Università degli Studi di Cagliari

DOTTORATO DI RICERCA

Scienze e Tecnologie Chimiche

XXXI Ciclo

Anilate-based Molecular Building Blocks for Metal-Organic Frameworks and Molecular Conductors

Settore scientifico disciplinare CHIM/03

Presentata da:	Suchithra Ashoka Sahadevan
Coordinatore Dottorato:	Prof. Stefano Enzo
Tutor:	Prof. Maria Laura Mercuri Dr. Narcis Avarvari

Esame finale anno accademico 2018/19

UNIVERSITE MATIERE BRETAGNE MOLECULES LOIRE ET MATERIAUX

université angers

THESE DE DOCTORAT DE

L'UNIVERSITE D'ANGERS
COMUE UNIVERSITE BRETAGNE LOIRE

ECOLE DOCTORALE N° 596
Matière Molécules et Matériaux
Spécialité: *Chimie des matériaux*

Par

ASHOKA SAHADEVAN SUCHITHRA

Anilate-based Molecular Building Blocks for Metal-Organic Frameworks and Molecular Conductors

Thèse présentée et soutenue à Cagliari, le 6 février 2019
Unité de recherche: Laboratoire MOLTECH-Anjou, Université d'Angers
Dipartimento di Scienze Chimiche e Geologiche, Università di Cagliari
Thèse N° : 161340

Rapporteurs avant soutenance:

Miguel Julve OLCINA, Professeur, Universitat de València (Spain)
Manuel ALMEIDA, Professeur, Universitat de lisbon (Portugal)

Composition du Jury:

Marius ANDRUH, Professeur, Université de Bucarest (Romania) Président
Olivier MAURY, Directeur de Recherche CNRS, Université de Lyon (France)
Adolfo SPEGHINI, Professeur, Université de Verona (France)
Maria laura MERCURI, Professeur, Université de Cagliari (Italy)
Narcis AVARVARI, Directeur de Recherche CNRS, Université de Angers (France)

This work has been performed in the framework of a Co-joint PhD thesis between the Dipartimento di Scienze Chimiche e Geologiche, University of Cagliari (Italy) and Moltech Anjou Laboratory, University of Angers (France).

Dedicated to my family...

Acknowledgments

Firstly, I would like to express my sincere gratitude to my supervisors, Prof. Maria Laura Mercuri and Dr. Narcis Avarvari, for their continuous support during my Ph.D.; for their patience, motivation and invaluable advices both in research as well as in career.

I wish to thank all the members of the research group (Cagliari University), Prof. Enzo Cadoni, my friends and the coworkers Mariangela Oggianu and Noemi Monni for the assistance and encouragement they provided at all levels of the research project. Special thanks to Noemi for all the endless discussions we had in professional and personal life and for being a great friend. I also thank my colleagues and friends Marco, Joanna and Rosita with whom I shared the office and for all the memorable moments we had. I also wish to thank all my Ph.D. colleagues with whom I could share all the stress and anxiety. Thanks Swapneel for all the fun-filled conversations which we had during the tea breaks. Thanks for being a great friend.

I would also like to acknowledge all the members from Moltech-Anjou Laboratory (Angers University), Alexandre Abhervé deserves special thanks for the support and the time we spent in fruitful discussions on several aspects of the work. Dr. Cécile Mézière, Dr. Flavia Pop, Dr. Magali Allain and Prof. Nicolas Mercier are also kindly acknowledged for all the assistance and discussions. I also thank all my groupmates and colleagues Cristina, Maurizio, Kevin, Oleg, Nataliya, Nabil and Marwa for all the fun we had during my stay at Angers. I am already missing our Coffee break discussions and barbeque time.

My sincere thanks to Prof. Masahiro Yamashita, who provided me an opportunity to spent a short-term research stay in his lab (Yamashita Lab, Tohoku University), and giving me all access to the laboratory and research facilities. I would also like to acknowledge Dr. Goulven Cosquer, who helped me with the magnetic measurements, Rasel, for the X-Ray measurements and throughout my stay there. I also thank all the other people from the lab especially Dr. Soumava Biswas, Dr. Leena Mandal, and Afrin.

I would also like to extend my sincere gratitude to all our collaborators.
Prof. Francesco Quochi and Prof. Giovanni Bongiovanni (Dipartimento di Fisica, Cagliari University) are greatly acknowledged for luminescent measurements and for all the discussions. Dr. Daniela Marongiu is also sincerely acknowledged for the AFM measurements. Prof. Carla Cannas (Dipartimento di Chimica, Cagliari University) is kindly acknowledged for the HR-TEM measurements and for the contribution to the discussions.

Prof. José Ramòn Galàn (Tarragona University) and Dr. Cristina Sàenz de Pipaon, are kindly acknowledged for magnetic measurements and their contributions to the discussion.

Dr. Pascale Auban-Senzier (Paris-Sud University) and Prof. Hengbo Cui (Condensed Molecular Materials Laboratory, Riken) are gratefully acknowledged for conductivity measurements and Prof. Enric Canadell (Barcelona University) is acknowledged for Band Structure calculations.

Dr. Bruno J. C. Vieira and Prof. João C. Waerenborgh (Universidade de Lisboa) are acknowledged for Mössbauer measurements

Prof. Pere Alemany (Universitat de Barcelona) is kindly acknowledged for theoretical calculations.

Dr. Valerie Bonin (Angers University) is acknowledged for elemental analyses, Dr. Ingrid Freuze (Angers University) are acknowledged for MS analyses and Dr. Sylvie Dabos-Seignon (University of Angers) are acknowledged for AFM characterization.

This work would not have been possible without the financial support from the ItalianMinistero dell'Istruzione e della Ricerca (MIUR), which has financed my PhD grant, and the Regione Autonoma della Sardegna, Cagliari and Angers Universities, INSTM, CNRS and Fondazione Banco di Sardegna.

I wish to thank all my Indian friends in Cagliari Ranjth, Swapneel, Barnali, Amitash, Rahul, Hema, and Ashish for making a home away from home.

Last but not the least, I would like to thank my family: my parents for encouraging and inspiring me to follow my dreams and to my sisters Smitha and Soorya with whom I grew together sharing and supporting all the moments and and special thanks to Kiran for supporting me along the way.

ABSTRACT

This work reports on the design, synthesis and characterization of novel anilate-based functional molecular materials showing luminescent, magnetic and/or conducting properties. The family of anilate ligands comprises several derivatives obtained by introducing various substituents (H, F, Cl, Br, I, CN, etc.) at the 3 and 6 positions of the common 2,5-dihydroxy-1,4-benzoquinone framework. Their electronic/structural features, coordination modes, ability to mediate magnetic exchange interactions between coordinated d and/or f-metal centers, and to work as efficient antenna ligands towards NIR lanthanide ions, make them suitable candidates for the preparation of the materials reported.

In **Chapter 1**, the synthesis of a multifunctional mixed-valence $Fe^{II}Fe^{III}$ anilate-based coordination polymer, obtained by using the chlorocyanilate ligand ($ClCNAn^{2-}$), formulated as $[TAG][Fe^{II}Fe^{III}(ClCNAn)_3]\cdot$(solvate) (TAG = tris(amino)-guanidinium) is reported. This compound is characterized by single crystal X-Ray, at 150K and 10K, magnetic, mössbauer and conductivity measurements. Moreover, correlation of conductivity difference between anilate and pioneer oxalate based $Fe^{II}Fe^{III}$ 2D coordination polymers are explained using theoretical calculations (small-polaron hopping model).

In **Chapter 2**, the series of 2D layered coordination polymers based on chlorocyanilate ligand as building blocks formulated as $[Ln_2(ClCNAn)_3(DMF)_6]\cdot(DCM)_x$ (Ln^{III} = Yb (1) (x = 0), Nd (2) and Er (3) (x = 2)) are reported. The synthesis, structural characterization, photophysical studies, time-resolved photoluminescence studies performed on both the bulk and nanosheets, effects induced by the exfoliation process on the photo-physical properties of the nanosheets are discussed.

In **Chapter 3**, the new family of NIR-emitting lanthanide coordination polymers based on chlorocyanilate ligand and carboxylate ligands (di-hydroxy-terephthalic acid (DOBDC) and tetrafluoroterephthalic acid (F_4-BDC)), which are the commonly used ligands to obtain 2D layered materials are reported. These systems are formulated as $[Ln_4(ClCNAn)_5(DOBDC)_1(DMSO)_{10}]\cdot(DMSO)_2$ (Ln^{III} - Yb (1), Er (2)) $[Ln_2(ClCNAn)_2(F_4\text{-}BDC)(DMSO)_6]$ (Ln^{III} – Yb (3), Er (4)). Structural characterizations along with time-resolved photoluminescence studies on these compounds are described.

In **Chapter 4**, series of 2D layered coordination polymers based on chlorocyanilate ligand and Dy^{III} are reported. These compounds are formulated as $[Dy_2(ClCNAn)_3(DMSO)_6]$ (1), $[Dy_2(ClCNAn)_6(DMSO)_6]$ (1'), $[Dy_2(ClCNAn)_3(DMF)_6](CH_2Cl_2)$ (3), $(Me_2NH_2)_2[Dy_2(ClCNAn)_4(H_2O)_2]\cdot(DMF)$ (4). The synthesis, structural characterization along with its magnetic characterization is described.

In **Chapter 5**, using the above-mentioned anilate ligands with the BEDT-TTF organic donor, purely organic semiconductors formulated as $[BEDT\text{-}TTF]_2[HClCNAn]$ (1) and $[BEDT\text{-}TTF][HCl_2An]$ (2) are obtained by electrocrystallization. Their structural characterization, transport properties and band structure calculation are reported.

In **Chapter 6**, structural diversity and physical properties of Π-d hybrid multifunctional paramagnetic molecular conductors obtained by combining BEDT-TTF and $[Fe(ClCNAn)_3]^{3-}$ as conducting and magnetic carrier respectively are reported. These compounds are formulated as $[BEDT\text{-}TTF]_4[Fe(ClCNAn)_3]\cdot 3H_2O$ (1) and $[BEDT\text{-}TTF]_5[Fe(ClCNAn)_3]_2\cdot 2CH_3CN$ (2). Their structural characterization, transport properties and magnetic properties are described.

The framework of the thesis is as follows:

Part I - **General Introduction** on Molecular Materials, State of the Art on Anilate-based MOFs and Coordination Polymers and Molecular Conductors together with aim of the work.

Part II - **Results and discussions**, which is divided into 6 Chapters whose content has been summarized above.

Part III - **Conclusions and the Perspectives**.

Part IV - **Annexes** where additional information (overview on anilate ligands, exfoliation, fundamentals of lanthanide luminescence, electrocrystallization technique, fundamentals of conductivity and molecular magnetism) are discussed.

LIST of ACRONYMS

A	
AC	alternate current
AFM	atomic force microscopy
An	anilate
B	
BEDO-TTF	bis-(ethylenedioxy)-tetrathiafulvalene
BEDT-TTF	bis-(ethylenedithio)-tetrathiafulvalene
BETS	bis(ethylenedithio)tetraselenafulvalene
BDC^{2-}	1,4-benzenedicarboxylate
C	
H_2Cl_2An	chloranilic acid
$ClCNAn^{2-}$	chlorocyanilate ligand
CP	coordination polymer
CT	charge transfer
D	
D	donor
DC	direct current
DLS	dynamic light scattering
DOBDC	2,5-dihydroxyterephthalic acid
$DOBDC^{2-}$	2,5-dihydroxyterephthalate
DR	diffuse reflectance
DM-BEDT-TTF	dimethyl-bis-(ethylenedithio)-tetrathiafulvalene
DFT	density functional theory
E	
EDT-TTF	ethylenedithio-tetrathiafulvalene
eMChA	electrical magneto-chiral anisotropy
EPR	electron paramagnetic resonance
Et	ethyl
F	
F_4BDC	tetrafluoroterephthalic acid
F_4BDC^{2-}	tetrafluoroterephthalate
FT-IR	fourier transform-InfraRed
FWHM	full width at half maximum
HOMO	highest occupied molecular orbital
H	
HR-TEM	high-resolution transmission electron microscopy
KHClCNAn	potassium chlorocyananilate
L	
LMCT	ligand to metal charge transfer
Ln	lanthanide
LUMO	lowest occupied molecular orbitals
M	
Me	methyl
MOF	Metal- Organic Framework

MOs	Molecular Orbitals
O	
ox	oxalate
P	
Ph	phenyl
phz	phenazine
PL	photoluminescence
Pr	propyl
PXRD	powder X-ray diffraction
R	
r.t.	room temperature
S	
SEM	scanning electron microscope
SMM	single molecule magnet
T	
TAG	tris(amino)-guanidinium
TCNQ	7,7,8,8-tetracyano-p-quinodimethane
TGA	thermogravimetric analysis
Th	thiophene
TM-BEDT-TTF	tetramethyl-bis-(ethylenedithio)-tetrathiafulvalene
TM-TSF	tetramethyl-tetraselenafulvalene
TTF	tetrathiafulvalene
U	
UV-Vis	ultraviolet-visible
X	
XRD	x-ray diffraction
Z	
ZFS	zero field splitting
1D	one-dimensional
2D	two-dimensional
3D	three-dimensional

Chart 1 - Ligands

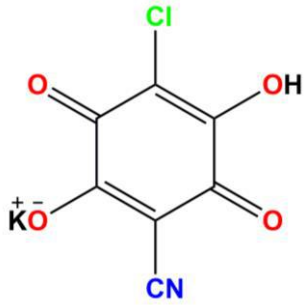

HKClCNAn

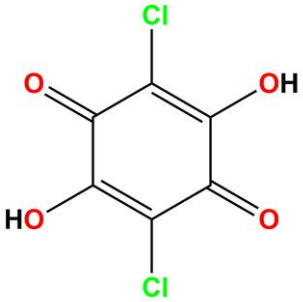

H_2Cl_2An

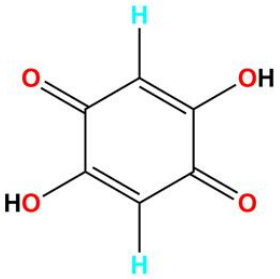

H_2An

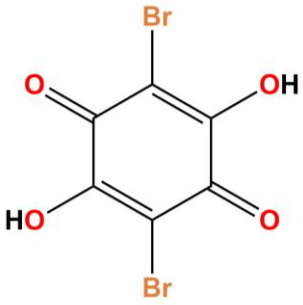

H_2Br_2An

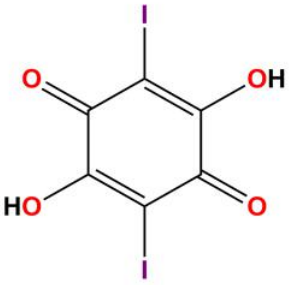

H_2I_2An

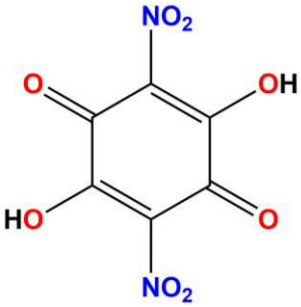

H_2NO_2An

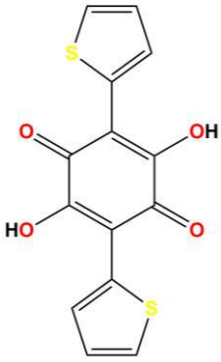

H_2Th_2An

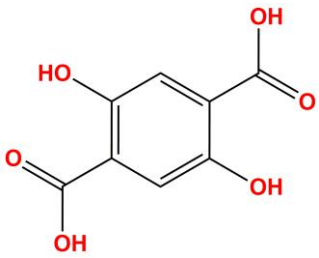

DOBDC

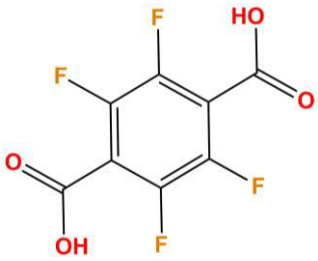

F_4BDC

Chart 2 - Donors

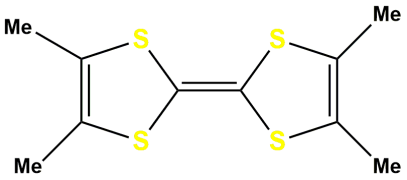

TM-TTF

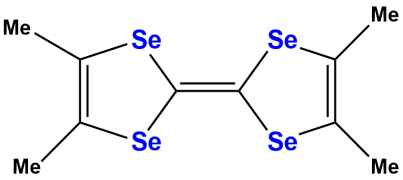

TM-TSF

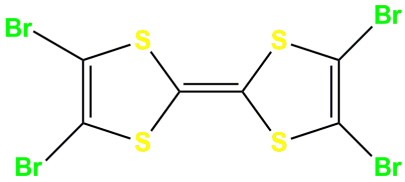

TTF-Br_4

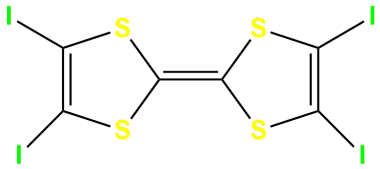

TTF-I_4

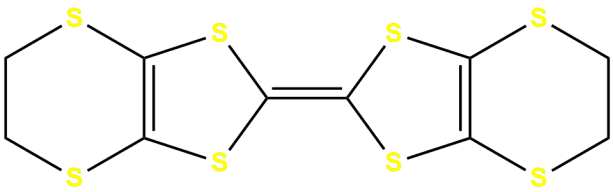

BEDT-TTF

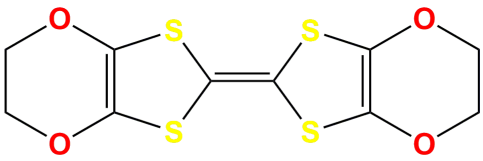

BEDO-TTF

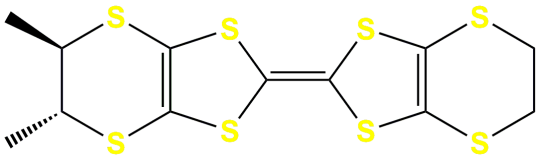

S,S DM-BEDT TTF

Table of Contents

Chapter 2. Anilate-based NIR-emitting lanthanide 2D Coordination Polymers

Chapter 3. Heteroleptic 2D Coordination Polymers based on Anilate and Carboxylate ligands

Chapter 4. Structural diversity in 2D Dy^{III}-Anilate-Based Magnetic MOFs/ Coordination Polymers

Chapter 5. Anilate-Based Organic Molecular Conductors

Chapter 6. Anilate-Based Magnetic Molecular Conductors

Part III - Conclusions and Perspectives

Part IV – Annexes

PART I
General Introduction

PART I

1.1 Molecular Materials

Molecular materials, namely materials built from molecular building blocks, are promising materials for the future generation of electronic devices and technologically important systems at the nanoscale level because of their chemical and physical properties. In the last decade, there have been tremendous developments in molecule-based materials, especially in the field of electrical conductivity, magnetism and optics. Since their synthesis and physical properties can be tuned by using the conventional synthetic methods of organic, coordination and supramolecular chemistry, this opens unprecedented possibilities for the design of objects with the desired chemical and electronic properties. Owing to their important perspectives in both fundamental sciences and applications in molecular electronics, considerable efforts are in course to design and investigate new molecule-based materials showing improved or novel physical properties.

The area of molecular materials with interesting technological properties started almost 85 years ago with the discovery of the first metal complex showing spin-crossover transition $[Fe(S_2CNEt_2)_2Cl]$.[1–3] Since then, the field of molecular materials has been enlarged including systems showing spin-crossover transitions,[5-8] ferri-/ferromagnets, single-molecule magnets,[14] metals and semi-/superconductors,[9-13] chromophores for non-linear optics,[15-16] and Vis-NIR emitters based on lanthanide complexes. Some of the important discoveries in this field related to conductivity, magnetism, and luminescence are reported as follows.

In 1842, Knop et al.[4] reported on the first molecular metal based on the tetracyanoplatinate anion. This system was later studied in detail and was formulated as $K_2[Pt(CN)_4]Br_{0.3}\cdot 3H_2O$, with conductivity values of 300 S cm^{-1} ($\sigma_{\parallel, RT}$) and 10^{-5} S cm^{-1} ($\sigma_{\perp, RT}$).[5] In 1973, the discovery of the first organic metal, the TTF-TCNQ system, represents an important milestone in the field of molecular conductors.[6,7] This compound is a charge-transfer salt formed by combining the TTF donor and the TCNQ acceptor, showing a r.t. electrical conductivity (σ_{RT}) of 500 S cm^{-1}. Molecular conductors based on metal-dithiolenes complexes also had a great impact in this field. Among them, $[(H_3O)_{0.33}Li_{0.8}][Pt(mnt)_2](H_2O)_{1.67}$ represents the first metal-like conductor[8] and $[TTF][Ni(dmit)_2]_2$ system represents the first superconductor,[9] with a Tc of 1.62 K under a pressure of 7 kbar).

In 1967, the pioneer work of Wickman et al.,[1–3] with the discovery of $[Fe(S_2CNEt_2)_2Cl]$, showing a magnetic ordering at T= ca. 2.5 K, was the start of the field of Molecular Magnetism. In this compound, the Fe^{III} ion is found in S = 3/2 spin state,

intermediate between the high spin (S = 5/2) and the low spin (S = 1/2) states. In 1968, Ito et al.,[10] reported $Fe^{III}_4[Fe^{II}(CN)_6]_3 \cdot xH_2O$, also known as "Prussian Blue", exhibiting ferromagnetic ordering with a Tc of 5.5 K. In this system, superexchange magnetic interactions are mediated by bridging ligands connected between paramagnetic d metal centers. Since then, other important achievements were reported: i) $[Cr^{III}(NH_3)_6][Cr^{III}(CN)_6]$ and $[Cr^{III}(NH_3)_6][Fe^{III}Cl_6]$ bimetallic systems, showing ferromagnetic (Tc = 0.66 K) and ferrimagnetic ordering (Tc = 2.85 K) respectively, by Reiff and Carlin;[11,12] ii) the heterobimetallic polymeric compounds of general formula $[N(Bu)_4][M^{II}Cr^{III}(ox)_3]$, a novel class of molecular ferromagnets, by Okawa et al.,[13] in 1992. In these systems, the oxalate ligand acts as a bridging ligand between two paramagnetic metals Cr^{III} and M^{II} (M^{II} = Mn, Fe, Co, Ni, Cu,) and it is able to mediate superexchange magnetic interactions, leading to long-range ferromagnetic ordering with Tc between 6 and 15 K, as a function of the coordinated metal ions. In 1993, Sessoli, Gatteschi et al.,[14] reported on the $Mn^{III}_8Mn^{IV}_4O_{12}(O_2CH_3)_{16}(H_2O)_4] \cdot 4H_2O \cdot 2CH_3COOH$ cluster, the first example of a new class of molecular magnets commonly called single-molecule magnets (SMMs).

In addition to mono-functional materials, a more recent and appealing goal in the field of material science is multifunctionality. Integrating independent properties which typically do not occur at the same time in a single crystal lattice or in conventional inorganic solids is the fundamental scientific challenge. The proper selection of molecular building blocks allows for the combination of two or more physical properties such as magnetism and conductivity to coexist in a single material.[15] The first example of multifunctional magnetic molecular conductors showing coexistence of two different physical properties, was the $[perilene]_2[M(mnt)_2]$ system.[16,17] Since then, different combinations of multifunctional materials have been synthesized and fully characterized. Some of the most recent and significant advances in this field are: (i) the first paramagnetic superconductor[18] [BEDT-TTF]$_4$ $[H_3OFe^{III}(ox)_3] \cdot C_6H_5CN$;[18](ii) the first antiferromagnetic superconductor λ-$(BETS)_2[FeBr_4]$;[19] (iii) the first ferromagnetic metal, $[BEDT\text{-}TTF]_3[Mn^{II}Cr^{III}(ox)_3]$;[20] (iv) the first chiral conductor showing coexistence of ferromagnetism, metal-like conductivity, and chirality, $[(S,S,S,S)\text{-}TM\text{-}BEDT\text{-}TTF]x[MnCr(ox)_3] \cdot CH_2Cl_2$;[21] (v) the first chiral conductor showing eMChA effect,[22] (S,S)- or (R,R)-$[DM\text{-}EDT\text{-}TTF]_2ClO_4$, and (vi) $[\{Mn^{II}_2Mn^{III}_2(hmp)_6(MeCN)_2\}\{Pt(mnt)_2\}_4][Pt(mnt)_2]_2$ (hmp^- = 2-hydroxymethyl-pyridinate; mnt^{2-} = maleonitriledithiolate), the first hybrid material exhibiting SMM behavior and

electronic conductivity in the same system, formed by tetranuclear [Mn_4] as SMM, and conductive [$Pt(mnt)_2]_2$.[23] (More details of these systems are discussed in Section 1.3)

A summary of the most appealing applications of these materials in different fields ranging from data storage to telecommunication is reported in Scheme 1.

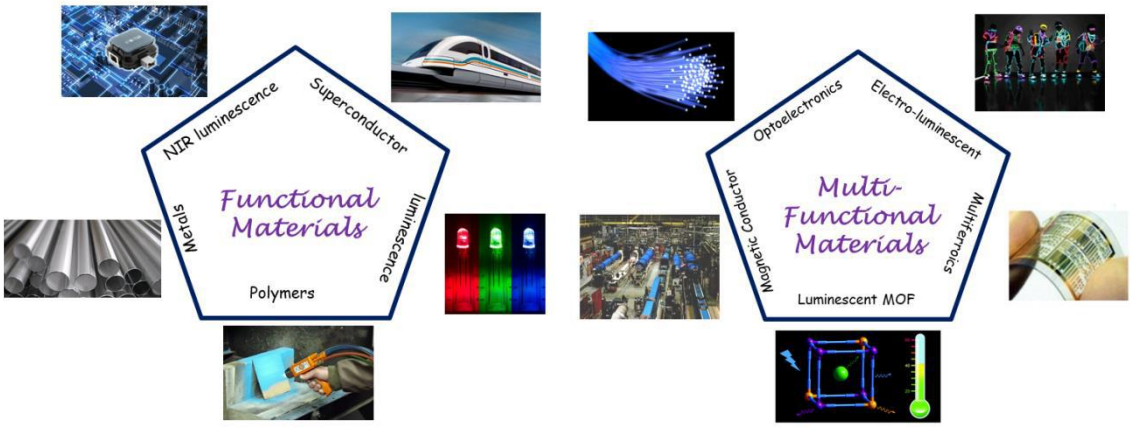

Scheme 1

Since the discovery of graphene, the search for other atomically thin layers grows up rapidly and a new and less explored field has emerged with 2D CPs, enclosing CPs and MOFs, which are layered inorganic materials that, in bulk, show stacked structures with weak van der Waals interactions between adjacent sheets, but with strong covalent bonding within each sheet (*vide infra*).[24,25] These 2D materials have the potential to be exfoliated micromechanically into nano-sized sheets, but owing to the fragility of the starting crystals, there are only few reports on stable crystalline ultrathin nano-sheets. More details on the exfoliation methods are reported in Annexes 2.

1.2 Metal-Organic Frameworks and Coordination Polymers

Recently, there has been intense scientific interest in MOFs and CPs owing to their designability, in terms of the combination of their organic bridging ligands and metal nodes. According to **IUPAC 2013,**[26] the definition and explanation for Coordination Polymers is *"A coordination compound with repeating coordination entities extending in 1, 2, or 3 dimensions".*

"Comment- Coordination polymers do not need to be crystalline; therefore, the more appropriate terms (for crystalline states) 1-periodic, 2-periodic, and 3-periodic cannot be used throughout. These compounds may even be regarded as salts in some cases, such as those mainly formed by carboxylates. The prefix 1D-, 2D-, or 3D- is acceptable for indicating the degree of extension of the coordination polymer."

And for MOFs as *"A metal–organic framework, abbreviated to MOF, is a coordination network with organic ligands containing potential voids".*[26]

"Comment- This wording accounts for the fact that many systems are dynamic and changes in structure and thus corresponding changes in potential porosity or solvent and/or guest filled voids may occur depending on temperature, pressure, or other external stimuli. For these reasons it is also not required that a MOF is crystalline. Arguments based on both theory and experiment can be used, suggesting that some of these CPs (i.e., those that can be described as salts) with direct anion-cation binding are more prone to form structures with open frameworks exhibiting permanent porosity than those forming positively charged networks. However, the grey zone between these extremes is large and increasing a definition based on such a charge distinction would be too restrictive."

One of the criteria a MOF needs to fulfill is that it contains potential voids, but no physical measurements of porosity or other properties are demanded.

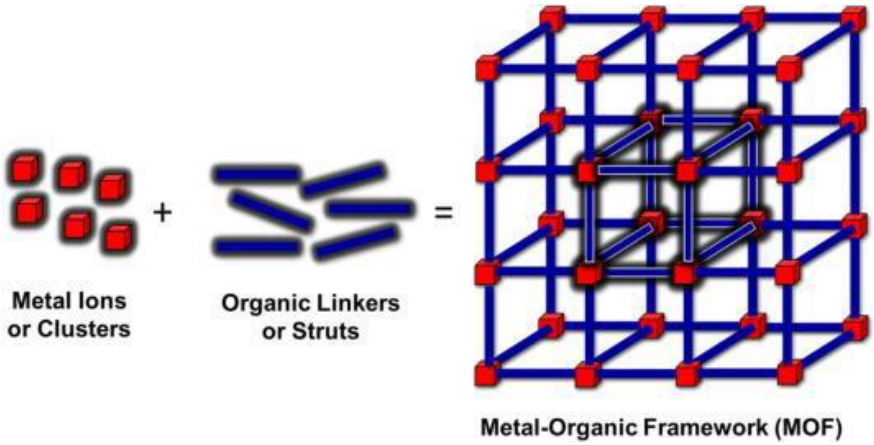

Scheme 2. Schematic representation of MOFs. Reprinted with the permission from Ref.[27]

MOFs are an emerging class of porous materials with potential applications in gas storage, separations, catalysis, biological and chemical sensing etc. Schematic representations of their most appealing applications are shown in Scheme 3.

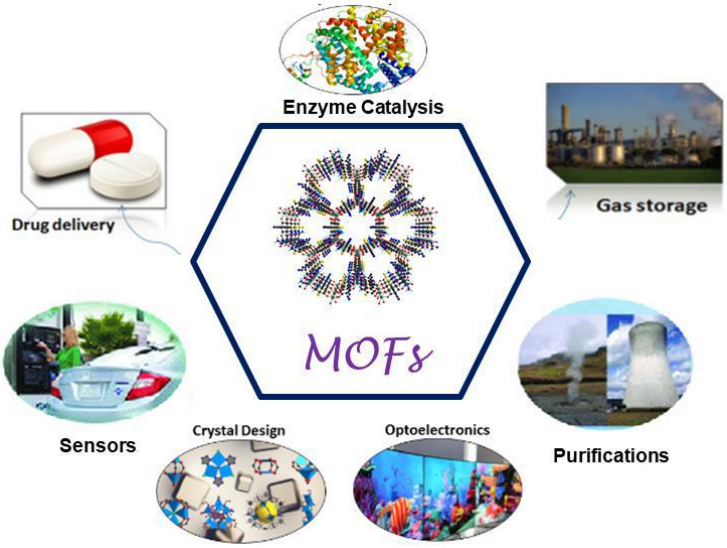

Scheme 3. Some of MOFs applications

MOFs with peculiar porosities are recently reported: (i) $Zn_4O(BTE)(BPDC)$, where BTE^{3-}=4,4′,4″-[benzene-1,3,5-triyl-tris(ethyne-2,1-diyl)]tribenzoate and $BPDC^{2-}$=biphe-nyl-4,4′-dicarboxylate (MOF-210), has Brunauer-Emmett-Teller (BET) and Langmuir surface areas of 6240 and 10,400 m^2/g, respectively, and a total carbon dioxide storage capacity of 2870 m^2/g;[28,29] (ii) $Zn_4O(BTB)_2$, where BTB^{3-}=1,3,5-benzenetribenzoate (MOF-177), has a surface area of 4526 m^2/g, it adsorbs between 4.2 and 9.3 molecules of H_2 per formula unit. (iii) $Zn_4O(BDC)_3$ (MOF-5) has a surface area of 2500-3000 m^2/g;[30,31] (iv) $M_2(dobdc)_3$, (M^{II} = Mg, Co, Ni) has BET surface area of 1525 m^2/g for Mg^{II}.[28,32,33] (Scheme 4)

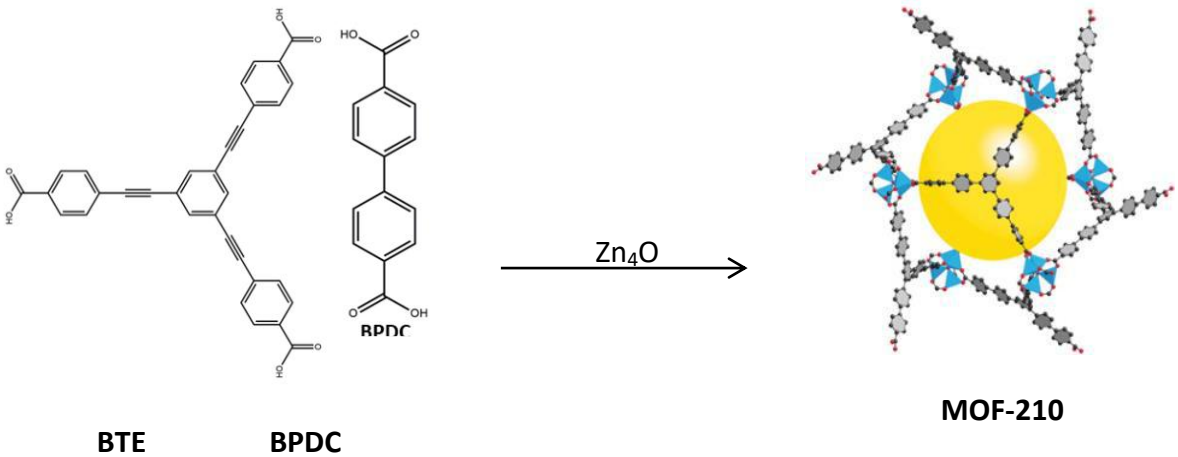

BTE **BPDC**

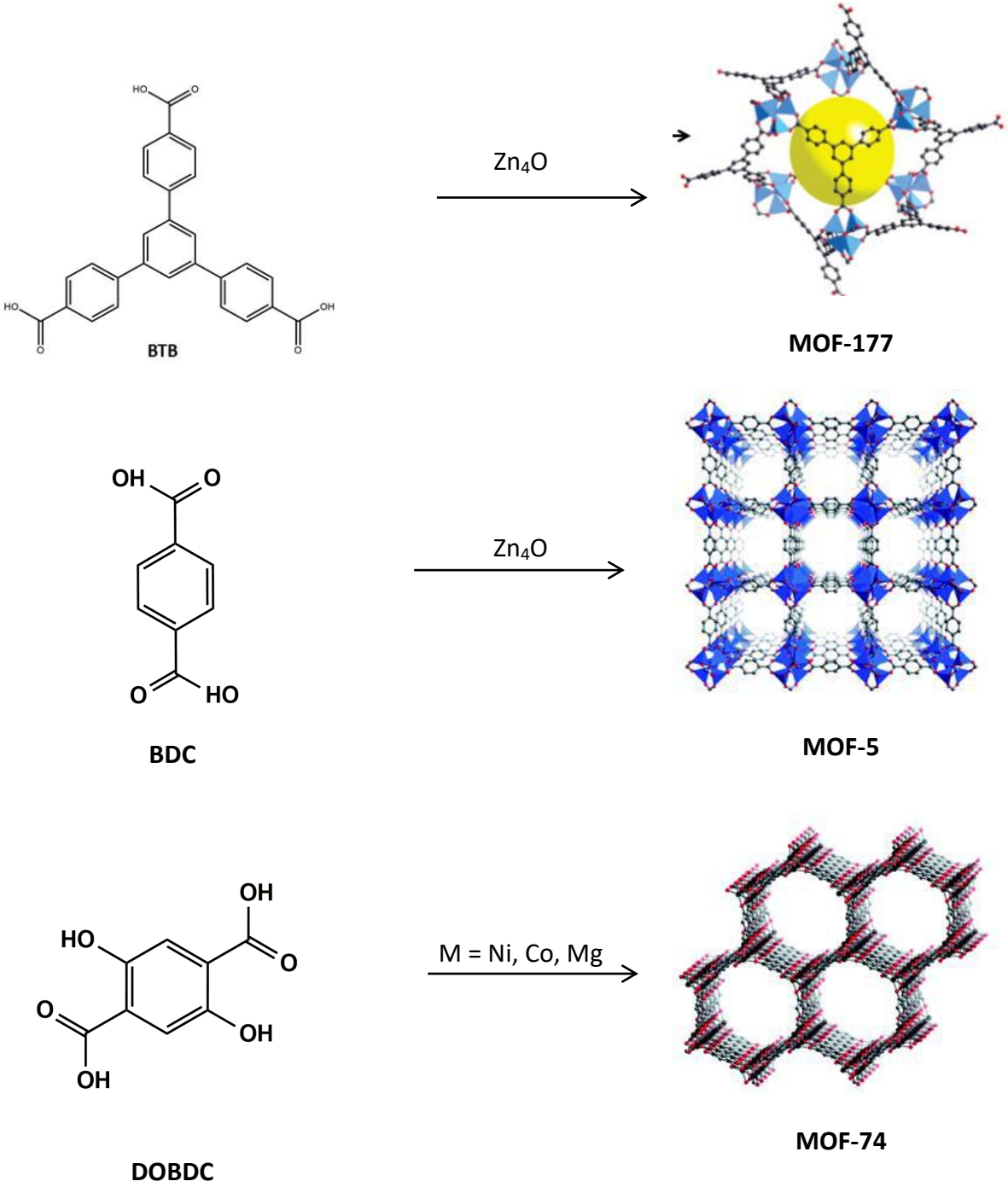

Scheme 4. Schematic representation of organic linkers (*vide supra*) and their corresponding MOFs.

The surface areas of MOFs can be generally controlled by the ligand design. In general, when the ligand length is extended, the surface area of the material is increased.[34] For instance, the $[Zn_4O(NTB)_2]\cdot 3DEF\cdot EtOH$ (DEF = N,N'-diethylformamide) porous MOF, obtained by solvothermal reaction in of $Zn(NO_3)_2$ with 4,4',4" -nitrilotrisbenzoate $(NTB_3)_3$ has a surface area of 1121 m^2g^{-1}, while the $[Zn_4O\text{-}(TCBPA)_2]\cdot 19DMA\cdot 4H_2O$ MOF, (SNU-77H) constructed with the extended ligand ($TCBPA^{3-}$ = tris(4-carboxybiphenyl)amine) that

contains one more phenyl ring on the branches of the ligand,[35] has a greater surface area (3670 m^2g^{-1}) than the NTB^{3-}-based MOF.[36] (Scheme 5)

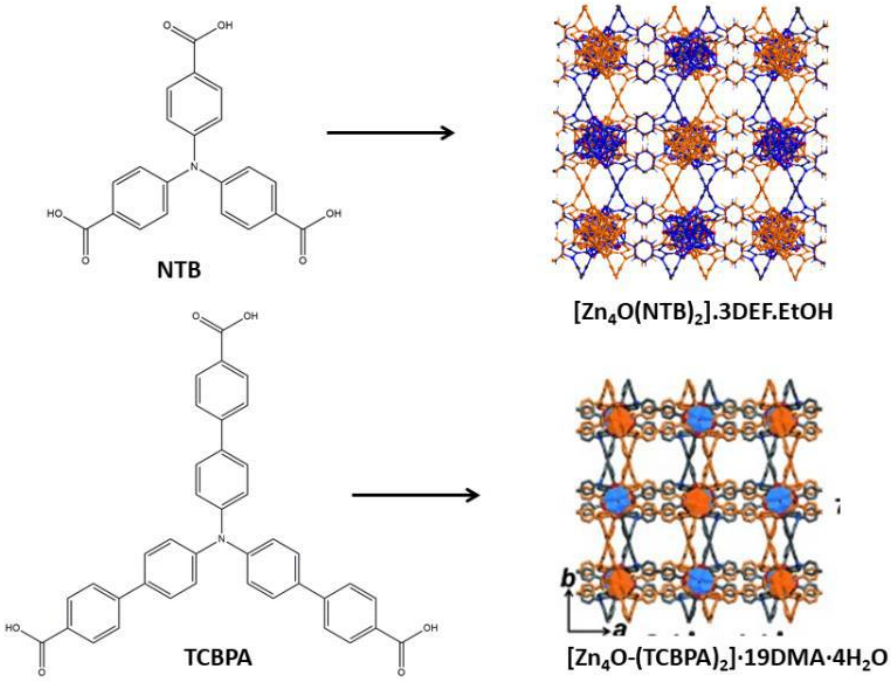

Scheme 5. Crystal packing of $[Zn_4O(NTB)_2]_3$·DEF·EtOH and $[Zn_4O\text{-}(TCBPA)_2]$· 19DMA·$4H_2O$ with their corresponding linkers, highlighting the difference in void size.

Despite numerous advantages, applications of several MOFs are ultimately limited by their stability. Structural transformation (Guest-induced crystal-to-amorphous and crystal-to-crystal transformation) with the removal or exchange of solvent molecules from the voids is a major concern regarding their stability. It can be largely controlled by the structure and the nature of the chemical bonds with the organic ligands.[37,38] With this perspective, the search for new ligands for the synthesis of MOFs is also of great importance in this field. The most commonly used ligands for the synthesis of MOFs and 2D CPs are shown in Figure 1.

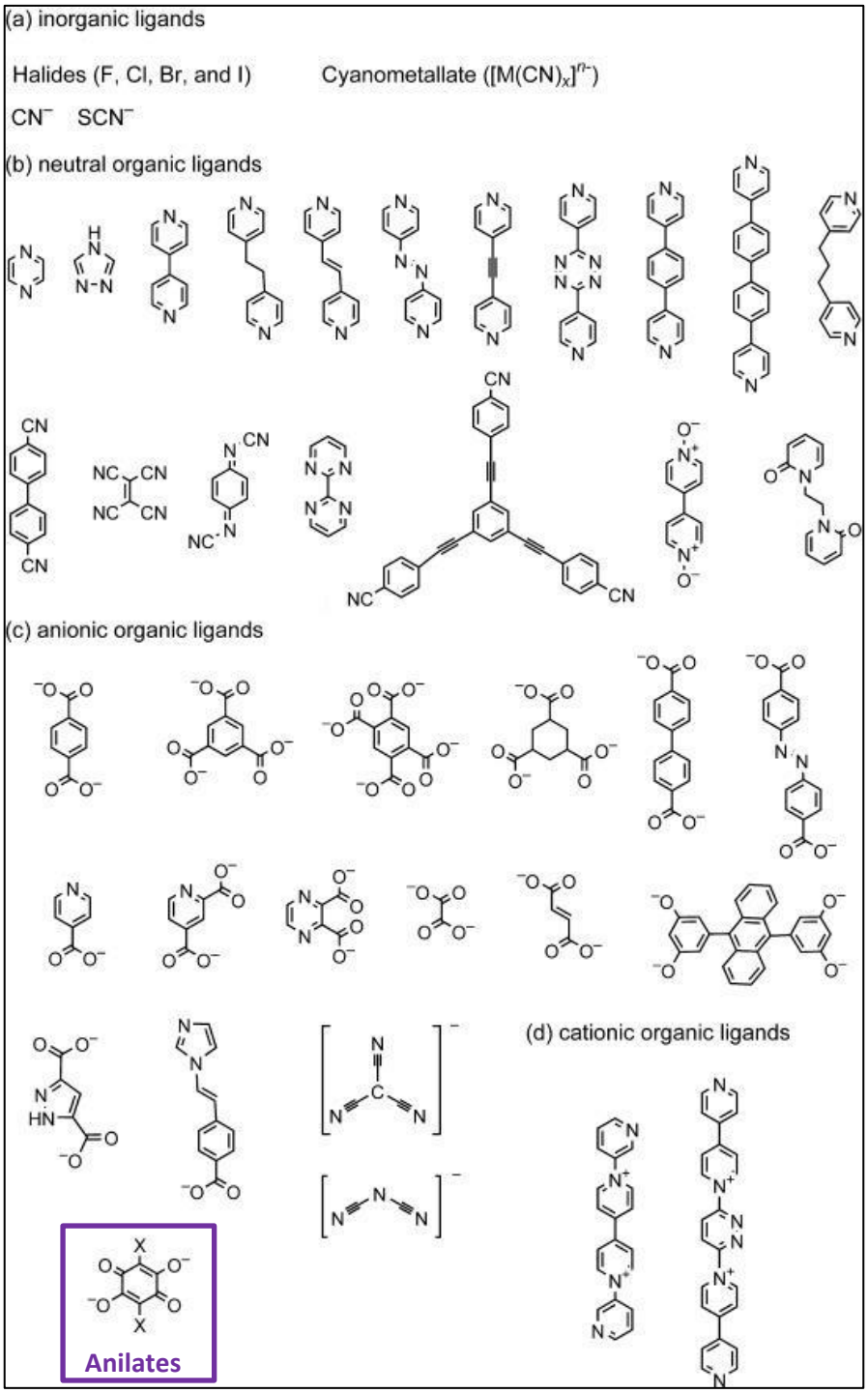

Figure 1. Commonly used ligands for the synthesis of MOFs and CPs.

1.2.1 MOFs and Coordination Polymers Based on Anilates

Anilate ligands have shown to be excellent candidates for the construction of novel supramolecular frameworks of different dimensionality.[39] It includes both finite and extended molecular assemblies, particularly the honeycomb packing pattern, where six metal ions are coordinated by anilate ligands forming a hexagonal motif.[40] Kawata et. al. [39,40] reported on

several straight and zig-zag infinite chain structures formed by M^{II} ions and the bis-chelating chloranilate anions; the first known example of hydrogen-bonded 2D layers, formulated as $\{[Cu(Cl_2An)(H_2O)_2](G)\}_n$, (G= dimethylpyrazine (dmpyz) and phz), was also reported, where phz molecules are intercalated to form columns stacked at a distance of 3.18 Å[39](Figure 2).

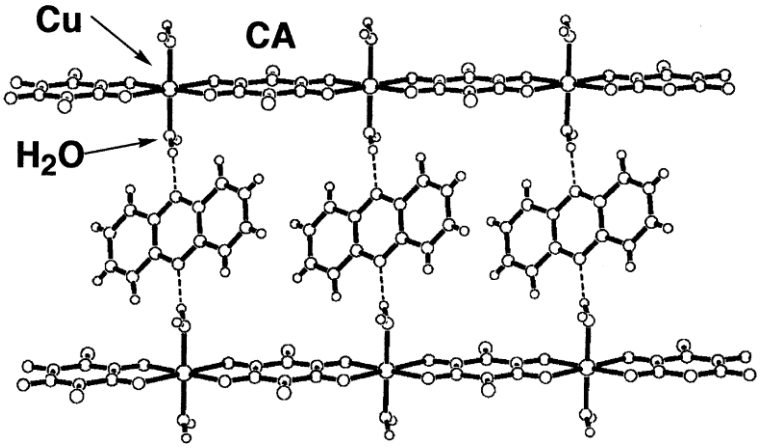

Figure 2. Crystal structure of $\{[Cu(Cl_2An)(H_2O)_2](phz)\}_n$. Dotted lines show hydrogen bond link between coordinated water and phz. Reprinted with the permission from Ref. [39].

Thereafter, a lot of anilato-based structures were obtained, mainly 1D-2D chains, and compounds forming honeycomb layers showing a (6,3)-topology*(see footnote).[41–45] For the first time, Abrahams et. al.,[43,44] reported on a series of 2D neutral CPs with lanthanides and anilato-bridged ligands. These are formed with two M^{III} ions and the reported examples include the $[M_2(H_2An)_3]\cdot 24H_2O$ (M^{III} = Y, La, Ce, Gd, Yb and Lu), $[M_2(Cl_2An)_3]\cdot 12H_2O$ (M^{III} = Sc, Y, La, Pr, Nd, Gd, Tb, Yb, Lu) and $[Y_2(Br_2An)_3]\cdot 12H_2O$ systems. (Figure 3)

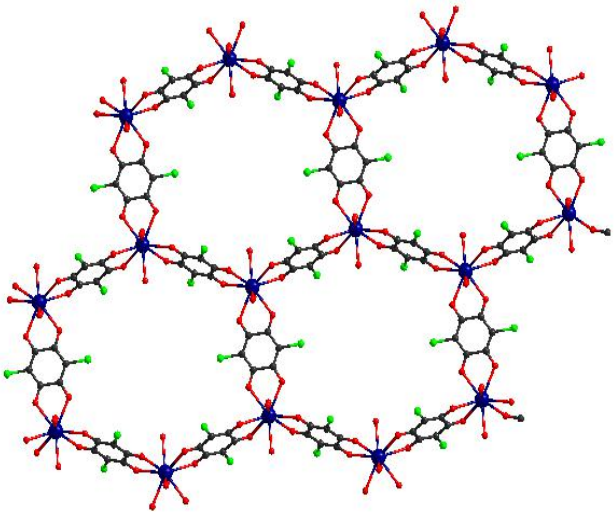

Figure 3. Crystal Structure of $[Ce_2(Cl_2An)_3]\cdot 12H_2O$. Solvent molecules are omitted for clarity

** (m,n) 2D toplogy means that n-connecting centres are linked to form m-membered rings in the 2D network*

Further interest for the anilate ligands is related to their ability to form 3D structures with the (10,3)-*a* topology. This 3D systems, $[(n\text{-}Bu)_4N]_2[M^{II}_2(H_2An)_3]$ (M^{II} = Mn, Fe, Ni, Co, Zn and Cd) and $[(n\text{-}Bu)_4N]_2[Mn_2(Cl_2An)_3]$,[46] shows a double interpenetrating (10,3)-*a* lattice with opposite stereochemical configuration that afford an overall achiral structure. The versatility of the anilate-based derivatives is finally demonstrated by the formation of a 3D adamantane-like network in the $[Ag_2(Cl_2An)]$,[47] $[H_3O][Y(Cl_2An)_3]\cdot 8CH_3OH$ and $[Th(Cl_2An)_2]\cdot 6H_2O$[44] compounds.

In 2011 Nikitina et. al.,[48] obtained the first example of bimetallic 2D-anilate based network, in which chloranilate ligand coordinates Fe^{III} and Mn^{II}. In 2013, Mercuri et. al.,[49] synthetized a new family of compounds characterized by 2D honeycomb network, where Cr^{III} and Mn^{II} ions, are linked by anilate derivatives, formulated as $[(H_3O)(phz)_3][MnCr(Cl_2An)_3(H_2O)]$ and $[NBu_4][MnCr(X_2An)_3]$ (X= Cl, Br, I, H). The former compound, reported in Figure 4, presents a void volume of ca. 291 $Å^3$ (ca. 20% of the unit cell volume) which opens the way to the synthesis of MOFs by using anilate ligands as linkers (More details about anilates are given in Annex 1).

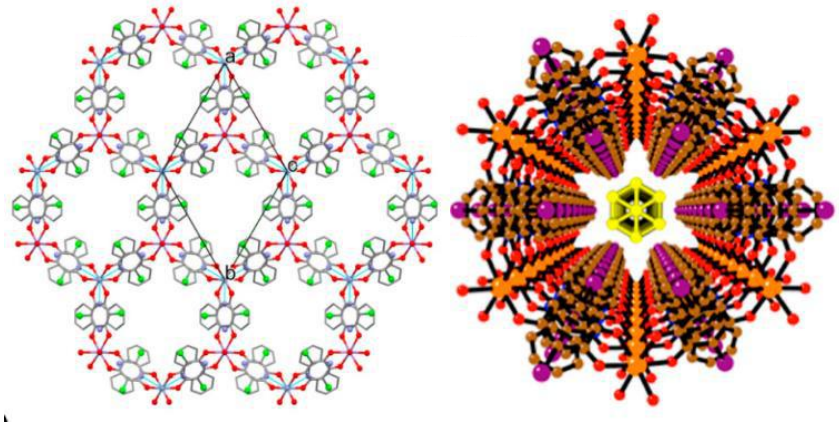

Figure 4. View of crystal structure of $[(H_3O)(phz)_3][MnCr(Cl_2An)_3(H_2O)]$ in the *ab* plane (left). Perspective view of one hexagonal channel running along the *c* direction with the solvent molecules in the center (in yellow) (right). Reprinted with permission from Ref.[49]

Ferrimagnetic interactions between Cr^{III} and Mn^{II} ions were mediated through the chloroanilate bridge, and this compound shows a T_c of 5.7 K. Noteworthy the T_c was influenced by changing the X substituent groups (X = Cl, Br, I, H) at the 3,6 positions of the anilato moiety, in particular as the electronegativity of X-substituents decreases; the T_c increases (Figure 5).

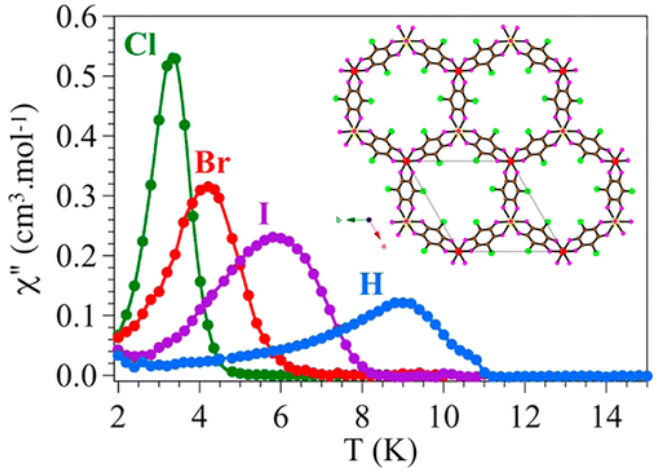

Figure 5. Magnetic properties of the series of $[NBu_4][MnCr(X_2An)_3]$, X = Cl , Br , I and H. Anionic layer in the inset. Reprinted with the permission from Ref. [49]

The first examples of 2D and 3D heterometallic lattices based on anilato ligands combining M^I and a M^{III} ions of chemical formula $(PBu_3Me)_2[NaCr(Br_2An)_3]$ and $(PPh_3Et)_2[KFe(Cl_2An)_3](DMF)_2$ have been obtained by Gomez et. al.[50] It shows that 2D lattices are formed by hexagonal $[M^IM^{III}(X_2An)_3]^{2-}$ anionic honeycomb layers, with $(PBu_3Me)^+$ or $(PPh_3Et)^+$ cations inserted between the layers. $(NBu_3Me)_2[NaCr(Br_2An)_3]$, is the first heterometallic 3D lattice based on anilato ligands (Figure 6).

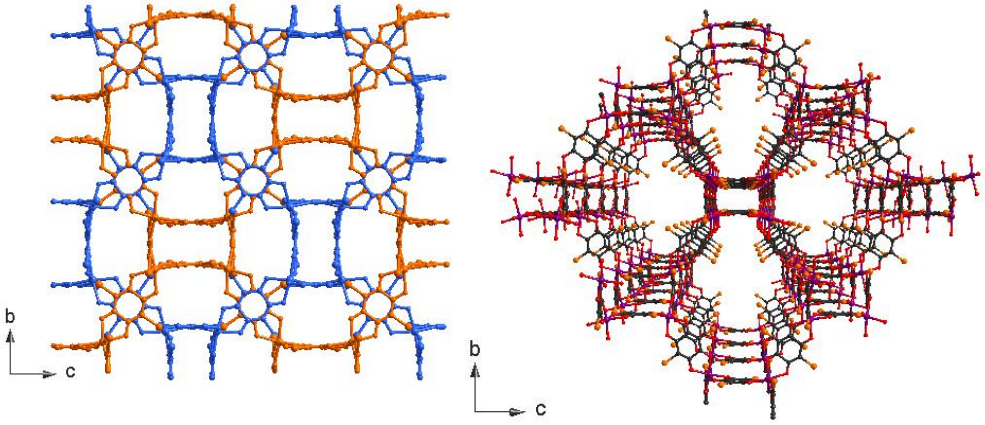

Figure 6. a) Structure of $NBu_3Me)_2[NaCr(Br_2An)_3]$ in *bc* plane. b) Central Projection of one layer. cations are omitted for clarity.

The first exfoliation study on 2D anilate-based layered CPs was performed by Abhervé, Coronado et al.[51] on $[Fe^{III}(sal_2\text{-trien})][Mn^{II}Cr^{III}(Cl_2An)_3](CH_2Cl_2)0.5(CH_3OH)(H_2O)\text{-}0.5(CH_3CN)_5$ compound, showing a typical alternated cation/anion layered structure with spin-crossover complexes as charge-compensating cationic species. The weak nature of the intermolecular interactions between the magnetic layers allows them to be exfoliated both *via* the Scotch-tape and liquid-assisted methods. The thicknesses of the flakes obtained by

solution methods (*ca.* 5 nm) were higher than those obtained by micromechanical methods, while the lateral size is significantly smaller (of the order of hundreds of nm) (Figure 7).

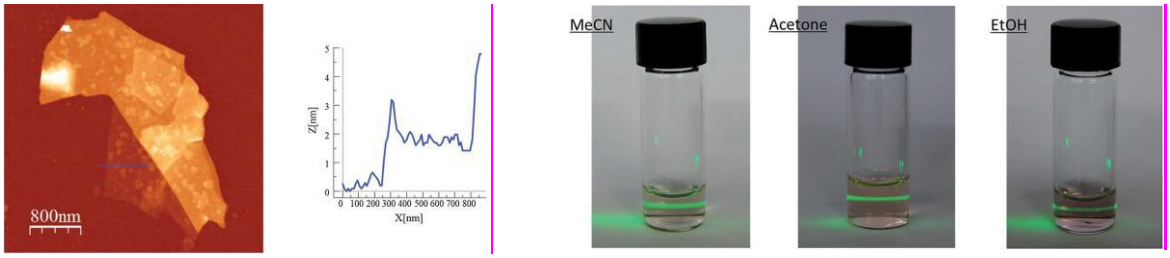

Figure 7. (a) Optical microscopy image (top), AFM image (bottom) and height profiles obtained by mechanical exfoliation on a 285 nm SiO_2/Si substrate. b) Tyndall effect of crystals obtained after liquid exfoliation. Reprinted from Ref. [51] with permission from the Royal Society of Chemistry.

Recently, J. Long et. al.,[52] reported a rare example of a 3D Multifunctional MOF, formulated as $(NBu_4)_2Fe^{III}_2(H_2An)_3$ composed by Fe^{III} bridged between the paramagnetic linkers, that additionally shows ligand-centered mixed-valence. H_2An is the parent member of the anilates which it is known that can afford the redox processes as reported in Scheme A1.2 (see Annex 1). This compound shows magnetic ordering[53] and a relevant value of r.t. conductivity (0.16(1) Scm^{-1}).

1.3 Molecular Conductors

Molecular conductors have attracted remarkably the interest of material scientists (*vide supra*) since the discovery, in 1973, of the TTF-TCNQ[54] charge-transfer salt, showing r.t. electrical conductivity of 500 Scm^{-1} and a metallic state down to *ca*. 55 K (Figure 8). These pioneeristic results addressed the scientific efforts to explore TTF-based derivatives, with the aim of increasing the intermolecular interactions between the donors, which are responsible for the metal-like conducting properties.

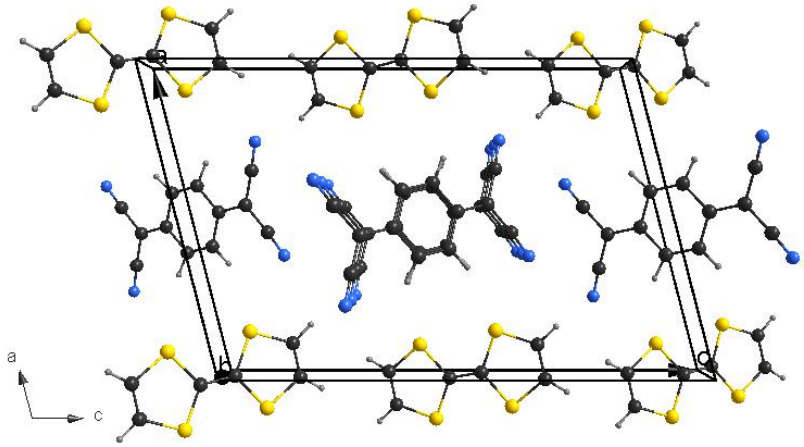

Figure 8. Crystal Structure of TTF-TCNQ in *ac* plane. Reproduced from Ref [55].

Subsequently, in 1980, Bechgaard et al.[56] reported on the first organic superconductor, the $[TM\text{-}TSF]_2[PF_6]$ system, showing a metal-superconductor transition at 1.2 K under the pressure of 10 kbar. The Bechgaard $(TM\text{-}TSF)_2X$ series (X= AsF_6, PF_6) was synthesized using the electrocrystallization technique which consists in the electrochemical oxidation of the organic donor on the surface of an electrode in a H-shaped cell (see Annex 4 for details) in the presence of a supporting electrolyte. The TM-TSF organic donor, in the presence of *n*-Bu_4NPF_6 or *n*-Bu_4NClO_4, afforded 1D single-chains organic metals and superconductors (Figure 9).

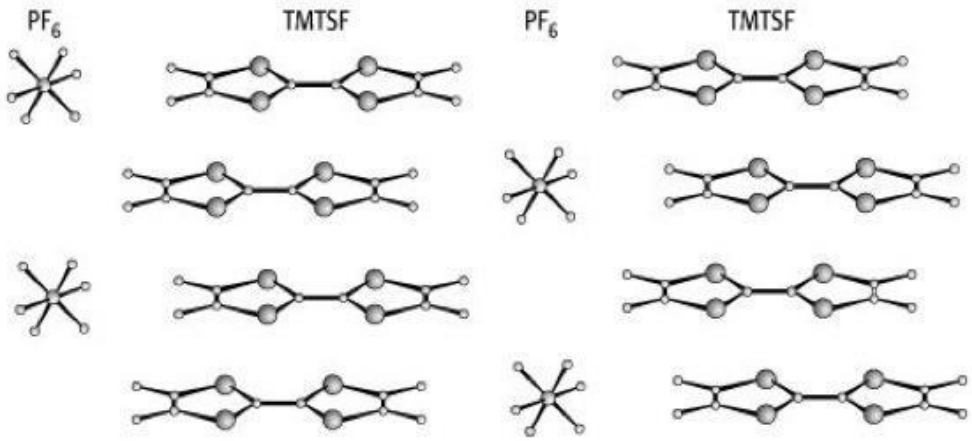

Figure 9. Crystal Structure of $[TM\text{-}TSF]_2[PF_6]$. Reprinted with the permission from Ref.[56]

Afterwards different TTF-based derivatives were synthesized and among them the BEDT-TTF organic donor, in particular, has been shown to be the most successful donor affording the largest number of molecular conductors and the majority of the known molecular superconductors. Among them, the κ-$[BEDT\text{-}TTF]_2[CuN(CN)_2Br]$ system shows a metal-superconductor transition temperature of ca. 11.6 K, which represents the highest Tc value for this class of compounds.[57]

The first paramagnetic superconductor, $[BEDT\text{-}TTF]_4[H_2OFe^{III}(ox)_3]\cdot C_6H_5CN$[18] (Figure 10) and the first ferromagnetic conductor, $[BEDT\text{-}TTF]_3[Mn^{II}Cr^{III}(ox)_3]$[20] (Figure 11) were successfully obtained by combining, *via* electrocrystallization, the mononuclear $[Fe(ox)_3]^{3-}$ and the $[Mn^{II}Cr^{III}(ox)_3]^-$ (2D honeycomb with oxalate bridges) charge-compensating anions with the BEDT-TTF organic donor, as magnetic and conducting carriers, respectively.

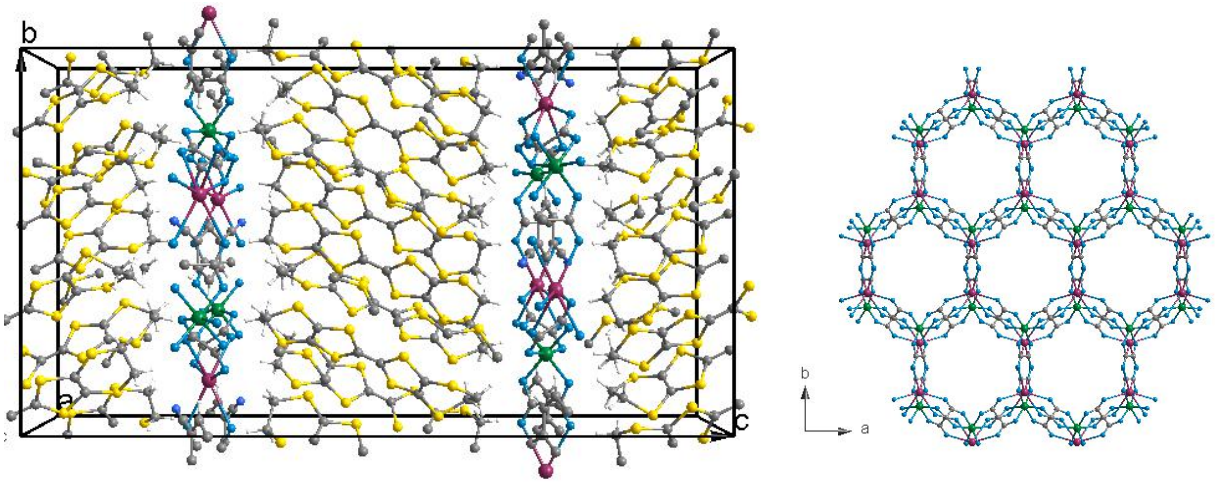

Figure 10. Left: Crystal Structure of $[BEDT\text{-}TTF]_4[H_2OFe^{III}(ox)_3]\cdot C_6H_5CN$ in *bc* plane. Right side shows anionic layer.

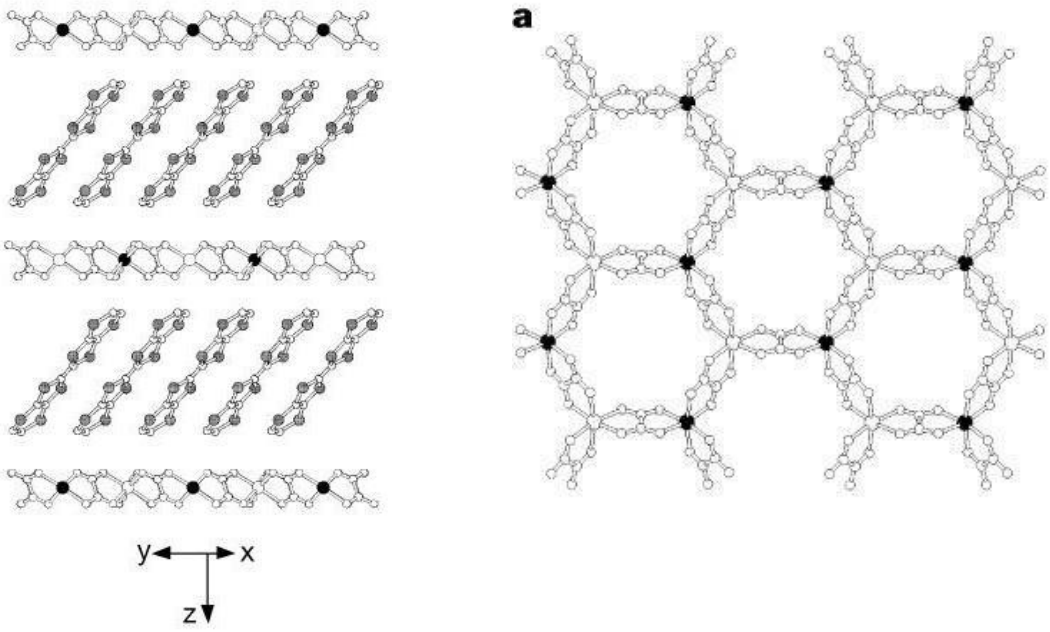

Figure 11. Left: Crystal Structure of $[BEDT\text{-}TTF]_3[Mn^{II}Cr^{III}(ox)_3]$; Right: honey-comb anionic layer. Reprinted with the permission from Ref.[20]

Furthermore, by combining the BETS molecule with the zero-dimensional $FeCl_4^-$ anion, a field-induced superconductivity with π-d interaction was observed which may be mediated through S···Cl interactions between the BETS molecule and the anion.[19]

The introduction of chirality in these materials represents one of the most recent advances in material science.[58] In 2010, Galán-Mascarós and Coronado et. al.,[21] reported the first chiral magnetic conductor, formulated as $[(S,S,S,S)\text{-}TM\text{-}BEDT\text{-}TTF]_x[MnCr(ox)_3]\cdot CH_2Cl_2$, showing coexistence of ferromagnetism, metal-like conductivity, and chirality. In this case,

the (S,S,S,S)-TM-BEDT-TTF chiral donor layers are responsible for both the electrical conductivity and optical activity and the layered bimetallic oxalate-based anionic network (heterobimetallic $[MnCr(ox)_3]^-$ layers) is responsible for the magnetic properties (Figure 12).

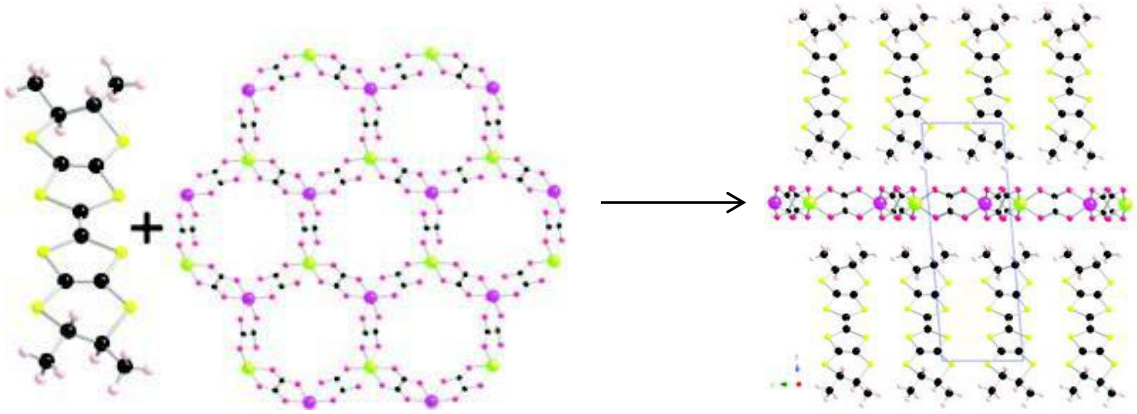

Figure 12. Packing of [(S,S,S,S)-TM-BEDT-TTF]x[$MnCr(ox)_3$] ·CH_2Cl_2 in *bc* plane.

In 2014, Avarvari, Rikken et al.,[22] demonstrated a synergy between chirality and conductivity, in the bulk crystalline chiral conductor, (S,S)- or (R,R)-[DM-EDT-TTF]$_2ClO_4$. In this system, two enantiomers show electrical magneto-chiral anisotropy (eMChA) effect with anisotropy factors opposite in sign, but equal in magnitude, field, and current dependencies (Figure 13). This system represents the most recent and significant advance in this field.

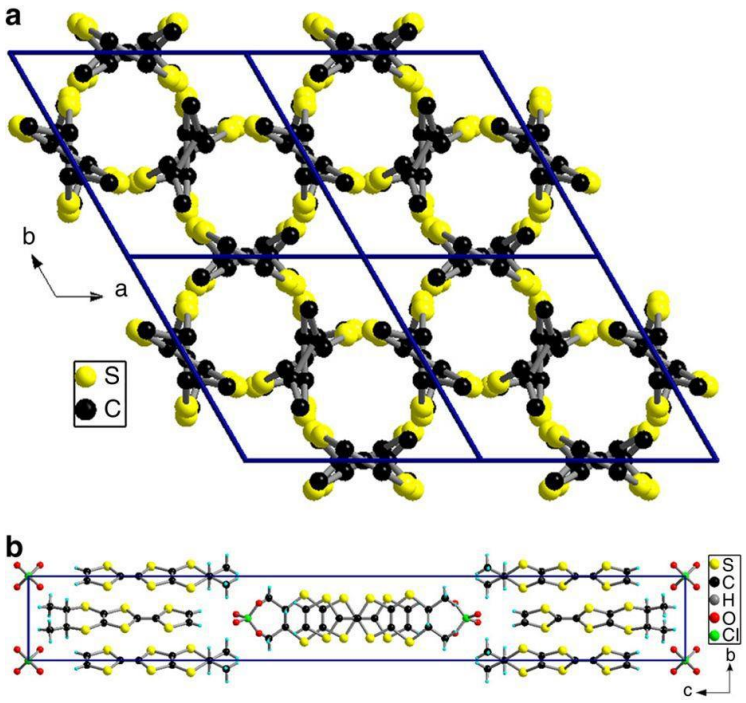

Figure 13. (a) Packing diagram of [(S,S)-DM-EDT-TTF]$_2ClO_4$ in the *ab* plane (H atoms and ClO_4 anions have been omitted for clarity). (b) Lateral view in the *bc* plane. Reprinted with the permission from Ref.[22]

1.3.1 Molecular Conductors Based on Anilates

The ability of the anilate moiety to work as molecular building block for molecular conductors has been recently explored. There are few examples of organic molecular conductors based on TTF and anilate derivatives. Among them following are the charge-transfer salts: (i) α′-(BEDT-TTF)$_2$HCNAn,[59] based on cyananilic acid (H_2CN_2An) and BEDT-TTF, showing a r.t. conductivity of 0.20–0.83 Scm^{-1} and activation energy of 0.15 eV; (ii) (TMTTF)$_2$HCNAn,[60] based on TM-TTF organic donor, showing a r.t. conductivity of 0.03 Scm^{-1} and activation energy of 0.05 eV.

The first family of magnetic molecular conductors based on BEDT-TTF and the tris(chloranilato)ferrate(III) anionic complex, were recently obtained by Mercuri and Avarvari et al.,[61] by using the electrocrystallisation technique. Three different hybrid systems, formulated as [BEDT-TTF]$_3$[Fe(Cl$_2$An)$_3$]·3CH$_2$Cl$_2$·H$_2$O, δ-[BEDT-TTF]$_5$[Fe(Cl$_2$An)$_3$]·4H$_2$O (r.t. conductivities of ca. 2 S·cm^{-1}) and α‴-[BEDT-TTF]$_{18}$[Fe(Cl$_2$An)$_3$]$_3$·3CH$_2$Cl$_2$·6H$_2$O systems (r.t. conductivities of ca. 8 S·cm^{-1}) were obtained by slightly changing the stoichiometric donor/anion ratio and the solvents (Figure 14). Subsequently Gomez et. al.,[62] reported on [(BEDT-TTF)$_6$[Fe(C$_6$O$_4$Cl$_2$)$_3$] ·(H$_2$O)$_{1.5}$·(CH$_2$Cl$_2$)$_{0.5}$, with a very unusual BEDT-TTF phase, called θ$_{21}$ with r.t. electrical conductivity of ca. 10 S cm^{-1}.

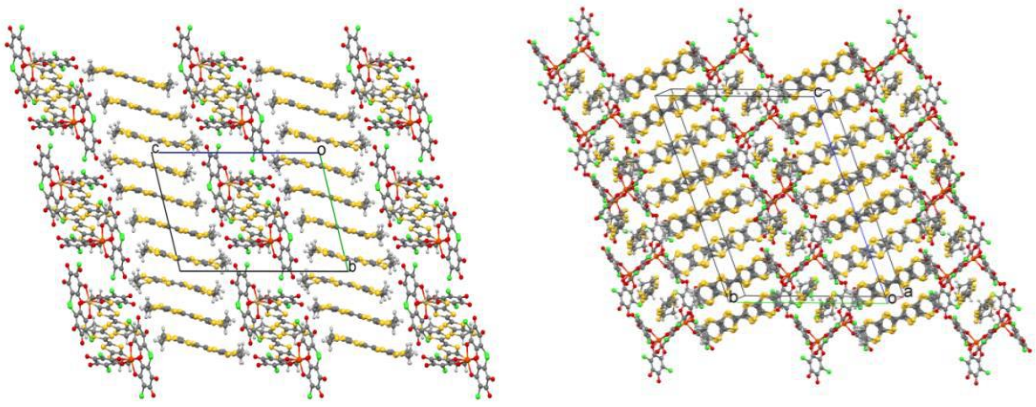

Figure 14. Crystal packing of δ-[BEDT-TTF]$_5$[Fe(Cl$_2$An)$_3$]·4H$_2$O and α‴-[BEDT-TTF]$_{18}$[Fe(Cl$_2$An)$_3$]$_3$·3CH$_2$Cl$_2$·6H$_2$O along the *bc* plane showing the organic-inorganic layer segregation. Reprinted with permission from Ref.[61]

The introduction of chirality in these materials was also reported by Avarvari, Mercuri et al.,[63] These systems, formulated as β-[(S,S,S,S)-TM-BEDT-TTF]$_3$PPh$_4$ [K^{I}Fe^{III}(Cl$_2$An)$_3$]·3H$_2$O, β-[(R,R,R,R)-TM-BEDT-TTF]$_3$PPh$_4$[K^{I}Fe^{III}(Cl$_2$An)$_3$]·3H$_2$O and β-[(rac)-TM-BEDT-TTF]$_3$PPh$_4$[K^{I}Fe^{III}(Cl$_2$An)$_3$]·3H$_2$O were successfully obtained by

combining the $[Fe^{III}(Cl_2An)_3]^{3-}$ anionic complex, K^+, forming 2D honeycomb anionic layers with chloranilate bridges and the chiral organic donor, as magnetic and conducting carriers respectively.

1.4 Aim of the Work

The aim of this thesis is to explore the versatility of anilate-ligands as molecular building blocks for constructing functional and multifunctional CPs, MOFs showing magnetic and/or conducting and/or luminescent properties and chiral/achiral Molecular Conductors.

Anilate derivatives have been selected as suitable ligands because of their electronic/structural features, coordination modes and redox properties and also for their ability to mediate magnetic exchange interactions between coordinated metal centers and to work as efficient antenna for lanthanides.

This family of ligands comprises several derivatives obtained by introducing various substituents (H, F, Cl, Br, I, NO_2, OH, CN, Me,..) at the 3 and 6 positions of the 2,5-dihyroxy-1,4-benzoquinone framework, and in this work we mainly focus on the only known asymmetric anilate ligand, $ClCNAn^{2-}$ because it is a green luminophore and its ability to mediate magnetic interactions and to be a component of multifunctional CPs and MOFs was scarcely investigated.

The present work has been particularly carried out as follows:

- Design, Synthesis, Structural and Physical properties (conducting/magnetic) of multifunctional homo- metallic CPs based on 3d-transition metal ions.
- Design, Synthesis, Structural and Luminescent properties of homoleptic CPs based on NIR emitting lanthanides (4f) and study of the $ClCNAn^{2-}$ ability to work as an efficient antenna towards NIR lanthanides. Design, Synthesis, Morphological and Luminescent studies of their corresponding Nanosheets and Comparison bulk/nanosheets.
- Design, Synthesis, Structural and Luminescent properties of heteroleptic (of $ClCNAn^{2-}$ /carboxylates) CPs based on NIR emitting lanthanides (4f); study of $ClCNAn^{2-}$ and carboxylate derivatives ability to work as an efficient antenna towards NIR lanthanides.
- Design, Synthesis, Structural and Conductivity properties of BEDT-TTF-based purely organic molecular conductors.
- Design, Synthesis, Structural and Conductivity properties of BEDT-TTF-based π–d paramagnetic molecular conductors.

References

(1) Wickmann, H. H.; Trozzolo, A. M. M.; Hull, G. W.; Merritt, F. R. *Phys. Rev.,* **1967**, *155*, 563.
(2) Wickmann, H. H. J. *Chem. Phys.,* **1972**, *56*, 976.
(3) Defotis, G. C.; Palacio, F.; O' Connor, C. J.; Bhaatia, S. N.; Carlin, R. L. *J. Am. Chem. Soc.,* **1977**, *99*, 8314–8315.
(4) Knop, W. *Justus Liebig's Ann. Chem.,* **1842**, *43*, 111.
(5) Krogmann, K. .; Hausen, H. D. Z. *Anorg. Allg. Chem.,* **1968**, *358*, 67.
(6) Coleman, L. B.; Cohen, M. J.; Sandman, D. J.; Yamagishi, F. G.; Garito, A. F.; Ferris, A. *J Solid State. Commun.,* **1973**, *12*, 1125–1202.
(7) Farris, A. J.; Cowan, D. O.; Walatka Jr., V.; Perlstein, J. H. *J. Am. Chem. Soc.,* **1973**, *95*, 948–949.
(8) Underhill, A. E.; Ahmad, M. M. *J. Chem. Soc. Chem. Commun.,* **1981**, 67–68.
(9) Brossard, L.; Ribault, M.; Bousseau, M.; Valade, L.; Cassoux, P. C. R. *Acad Sci Paris, Série II* **1986**, *302*, 205.
(10) Ito, A.; Suenaga, M.; Ono, K. *J. Chem. Phys.,* **1968**, *48*, 3597.
(11) Helms, J. H.; Hatfield, W. E.; Kwiecien, M. J.; Reiff, W. M. J. *Chem. Phys.,* **1986**, *84*, 3994.
(12) Burriel, R.; Casabo, J.; Pons, J.; Carnegie, D. E.; Carlin, R. L. *Physica,* **1986**, *13B*, 185.
(13) Tamaki, H.; Zhong, Z. J.; Matsumoto, N.; Kida, S.; Koikawa, M.; Achiwa, N.; Hashimoto, Y.; Okawa, H. *J. Am. Chem. Soc.,* **1992**, *114*, 6974–6979.
(14) Sessoli, R.; Gatteschi, D.; Caneschi, A.; Novak, M. A. *Nature.,* **1993**, *365*, 141–143.
(15) Coronado, E.; Miguel Clemente-Leo´; Romeroab, C. M.-G. F. M. *Chem. Soc. Rev.,* **2011**, *40*, 473–497.
(16) Alcacer, L.; Maki, A. H. *J. Phys. Chem.,* **1974**, *78*, 215–217.
(17) Alcacer, L.; Maki, A. H. *J. Phys. Chem.,* **1976**, *80*, 1912–1916.
(18) Kurmoo, M.; Graham, A. W.; Day, P.; Coles, S. J.; Hursthouse, M. B.; Caulfield, J. L.; Singleton, J.; Pratt, F. L.; Hayes, W.; Ducasse, L.; et al. *J. Am. Chem. Soc.,* **1995**, *117*, 12209–12217.
(19) Uji, S.; Shinagawa, H.; Terashima, T.; Yakabe, T.; Terai, Y.; Tokumoto, M.; Kobayashi, A.; Tanaka, H.; Kobayashi, H. *Nature,* **2001**, *410*, 908–910.
(20) Coronado, E.; Galán-Mascarós, J. R.; Gómez-García, C. J.; Laukhin, V. *Nature,* **2000**, *408*, 447–449.
(21) Galán-Mascarós, J. R.; Coronado, E.; Goddard, P. A.; Singleton, J.; Coldea, A. I.; Wallis, J. D.; Coles, S. J.; Alberolá, *J. Am. Chem. Soc.,* **2010**, *132*, 9271–9273.
(22) Pop, F.; Auban-Senzier, P.; Canadell, E.; Rikken, G.L.J.A.; Avarvari, N. *Nat. Commun.,* **2014**, *5*, 3757.
(23) Kazuya Kubo, Hiroki Hiraga, Hitoshi Miyasaka, A.; Yamashita, M. Multifunctionalities of Single Molecule Magnets and Electrical Conductivities. In *Multifunctional Molecular Materials*; Ouahab, L., Ed.; Stanford Publishing, 2013; 61–95.
(24) K. S. Novoselov; Geim, A. K.; Morozov, S. V.; Jiang, D.; Zhang, Y.; Dubonos, S. V.; Grigorieva, I. V.; Firsov, A. A. *Science,* **2004**, *306*, 666–669.
(25) López-Cabrelles, J.; Mañas-Valero, S.; Vitórica-Yrezábal, I. J.; Bereciartua, P. J.; Rodríguez-Velamazán, J. A.; Waerenborgh, J. C.; Vieira, B. J. C.; Davidovikj, D.; Steeneken, P. G.; van der Zant, H. S. J.; et al. *Nat. Chem.,* **2018**, *10*, 1001–1007.
(26) Batten, S. R.; Champness, N. R.; Chen, X.-M.; Garcia-Martinez,Javier Kitagawa, S.; Öhrström, L.; O'Keeffe, M.; Suh, M. P.; Reedijk, J. *Pure Appl. Chem.,* **2013**, *85*, 1715–1724.
(27) Liu, Y.; Howarth, A. J.; Vermeulen, N. A.; Moon, S.; Hupp, J. T.; Farha, O. K. *Coord. Chem. Rev.*, **2017**, *346*, 101–111.
(28) Wang, C.; Liu, D.; Lin, W. *J. Am. Chem. Soc.,* **2013**, *135*, 13222–13234.
(29) Furukawa, H.; Ko, N.; Go, Y. B.; Aratani, N.; Choi, S. B.; Choi, E.; Yazaydin, A. Ö.; Snurr, R. Q.; O'Keeffe, M.; Kim, J.; Yagi, O.M. *Science,* **2010**, *329*, 424–428.
(30) Rowsell, J. L. C.; Spencer, E. C.; Eckert, J.; Howard, J. A. K.; Yaghi, O. M. *Science,* **2005**, *309*, 1350–1354.

(31) Chae, H. K.; Siberio-Pérez, D. Y.; Kim, J.; Go, Y.; Eddaoudi, M.; Matzger, A. J.; O'Keeffe, M.; Yaghi, O. M. A *Nature,* **2004**, *427*, 523.
(32) Kapelewski, M. T.; Geier, S. J.; Hudson, M. R.; Stück, D.; Mason, J. A.; Nelson, J. N.; Xiao, D. J.; Hulvey, Z.; Gilmour, E.; Fitzgerald, S. A.; et al. *J. Am. Chem. Soc.,* **2014**, *136*, 12119–12129.
(33) Nandasiri, M. I.; Jambovane, S. R.; McGrail, B. P.; Schaef, H. T.; Nune, S. K. *Coord. Chem. Rev.,* **2016**, *311*, 38–52.
(34) Suh, M. P. *Bull. Jpn. Soc. Coord. Chem.,* **2015**, *65*,9-22.
(35) HJ Park, DW Lim, WS Yang, TR Oh, M. S. *Chem. Eur. J.***, 2011**,*17*, 7251–7260.
(36) Lee, E. Y.; Jang, S. Y.; Suh, M. P. *J. Am. Chem. Soc.,* **2005**, *127*, 6374–6381.
(37) Yuan, S.; Feng, L.; Wang, K.; Pang, J.; Bosch, M.; Lollar, C.; Sun, Y.; Qin, J.; Yang, X.; Zhang, P.; et al. *Adv. Matr.*, **2018**, *30*, 1704303.
(38) Kitagawa, S.; Kitaura, R.; Noro, S. *Angew. Chemie Int. Ed.,* **2004**, *43*, 2334–2375.
(39) Kawata, S.; Kitagawa, S.; Kumagai, H.; Kudo, C.; Kamesaki, H.; Ishiyama, T.; Suzuki, R.; Kondo, M.; Katada, M. *Inorg. Chem.,* **1996**, *35*, 4449–4461.
(40) Kitagawa, S.; Kawata, S. *Coord. Chem. Rev.,* **2002**, *224*, 11–34.
(41) Weiss, A.; Riegler, E.; Robl, C. *Zeitschrift fuer Naturforschung, Tl B Anorg Chemie, Org. Chemie.,* **1986**, *41*, 1501–1505.
(42) Luo, T. T.; Liu, Y. H.; Tsai, H. L.; Su, C. C.; Ueng, C. H.; Lu, K. L. *Eur. J. Inorg. Chem.,* **2004**, *2*, 4253–4258.
(43) Abrahams, B. F.; Coleiro, J.; Hoskins, B. F.; Robson, R. *Chem. Commun.,* **1996**, *2*, 603.
(44) Abrahams, B. F.; Coleiro, J.; Ha, K.; Hoskins, B. F.; Orchard, S. D.; Robson, R. *J Chem. Soc. Dalt. Trans.,* **2002**, *2*, 1586.
(45) Mercuri, M. L.; Congiu, F.; Concas, G.; Ashoka Sahadevan, S. *Magnetochemistry.,* **2017**, *3* , 17.
(46) Abrahams, B. F.; Hudson, T. A.; McCormick, L. J.; Robson, R. *Cryst. Growth. Des.,* **2011**, *11*, 2717–2720.
(47) Frenzer, W.W., R.; Bode, H. *Zeitschrift für Krist - Cryst. Mater.,* **1997**, *212*, 237.
(48) Nikitina, Z. K.; Ovanesyan, N. S.; Makhaev, V. D.; Shilov, G. V.; Aldoshin, S. M. *Dokl. Chem.*, **2011**, *437*, 129–132.
(49) Atzori, M.; Benmansour, S.; Mínguez Espallargas, G.; Clemente-León, M.; Abhervé, A.; Gómez-Claramunt, P.; Coronado, E.; Artizzu, F.; Sessini, E.; Deplano, P.; et al. *Inorg. Chem.,* **2013**, *52*, 10031–10040.
(50) Benmansour, S.; Vallés-García, C.; Gómez-Claramunt, P.; Mínguez Espallargas, G.; Gómez-García, C. J. *Inorg. Chem.,* **2015**, *54*, 5410–5418.
(51) Abhervé, A.; Mañas-Valero, S.; Clemente-León, M.; Coronado, E. *Chem. Sci.,* **2015**, *6*, 4665–4673.
(52) Darago, L. E.; Aubrey, M. L.; Yu, C. J.; Gonzalez, M. I.; Long, J. R. *J. Am. Chem. Soc.,* **2015**, *137*, 15703–15711.
(53) Miller, J. S. *Chem. Soc. Rev.,* **2011**, *40*, 3266–3296.
(54) Ferraris, J.; Cowan, D. O.; Walatka, V.; Perlstein, J. H. *J. Am. Chem. Soc.,* **1973**, *95*, 948–949.
(55) Schultz, A. J.; Stucky, G. D.; Blessing, R. H.; Coppens, P. *J. Am. Chem. Soc.,* **1976**, *98*, 3194–3201.
(56) D. Jérome, A. Mazaud, M. Ribault, K. B. *J. Physique Lett.,* **1980**, *41*, 95–98.
(57) Kini, A. M.; Geiser, U.; Wang, H. H. et al. *Inorg. Chem.,* **1990**, *29*, 2555–2557.
(58) Avarvari, N.; Wallis, J. D. *J. Mater. Chem.,* **2009**, *19*, 4061.
(59) Zaman, M. B.; Toyoda, J.; Morita, Y.; Nakamura, S.; Yamochi, H.; Saito, G.; Nishimura, K.; Yoneyama, N.; Enoki, T.; Nakasuji, K. *J. Mater. Chem.,* **2001**, *11*, 2211–2215.
(60) Zaman Md. Badruz , Morita Yasushi , Toyoda Jiro , Yamochi Hideki , Saito Gunzi , Yoneyama Naoki , Enoki Toshiaki, N. K. *Chem. Lett.,* **1997**, *26*, 729–730.
(61) Atzori, M.; Pop, F.; Auban-Senzier, P.; Gómez-García, C. J.; Canadell, E.; Artizzu, F.; Serpe, A.; Deplano, P.; Avarvari, N.; Mercuri, M. L. *Inorg. Chem.,* **2014**, *53*, 7028–7039.
(62) Benmansour, S.; Coronado, E.; Giménez-Saiz, C.; Gómez-García, C. J.; Rößer, C. *Eur. J. Inorg.*

Chem., **2014**, *2014*, 3949–3959.
(63) Atzori, M.; Pop, F.; Auban-Senzier, P.; Clérac, R.; Canadell, E.; Mercuri, M. L.; Avarvari, N. *Inorg. Chem.,* **2015**, *54*, 3643–3653.

PART II
Results and Discussion

CHAPTER 1

Anilate-Based Mixed Valence Multi-functional 2D Coordination Polymers

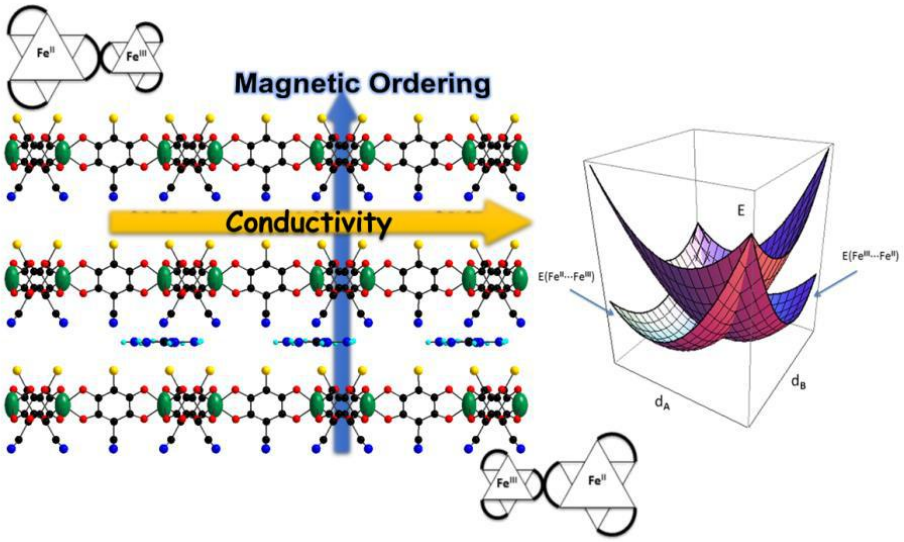

S. Ashoka Sahadevan, A. Abhervé, N. Monni, J. R. Galán-Mascarós, J. C. Waerenborgh, P. Auban-Senzier, C. Pasquier, S. Pillet, Marie-Bernadette Lepetit, P. Alemany, E. Canadell, M. L. Mercuri, and N. Avarvari. Conducting Anilate-Based Mixed-Valence Fe(II)Fe(III) Coordination Polymer: Small-polaron Hopping Model in Oxalate-Type Fe(II)Fe(III) 2D Networks., *J. Am. Chem. Soc*., **2018**, *140*, 12611-12621.

PART II

ABSTRACT

The mixed-valence $Fe^{II}Fe^{III}$ 2D CP formulated as $[TAG][Fe^{II}Fe^{III}(ClCNAn)^{3}]\cdot(solvate)$ (TAG = tris(amino)-guanidinium) crystallized in the polar trigonal space group *P*3. In the solid-state structure, determined both at 150 and at 10 K, anionic 2D honeycomb layers $[Fe^{II}Fe^{III}(ClCNAn)_3]^-$ establish in the *ab* plane, with an intralayer metal−metal distance of 7.860 Å, alternating with cationic layers of TAG. The similar Fe−O distances suggest electron delocalization and an average oxidation state of +2.5 for each Fe center. The cation imposes its C_3 symmetry to the structure and engages in intermolecular N−H···Cl hydrogen bonding with the ligand. Magnetic susceptibility characterization indicates magnetic ordering below 4 K and the presence of a hysteresis loop at 2 K with a coercive field of 60 Oe. Mössbauer measurements are in agreement with the existence of Fe (+2.5) ions at RT and statistic charge localization at 10 K. The compound shows semiconducting behavior with the in-plane conductivity of 2×10^{-3} Scm^{-1}, 3 orders of magnitude higher than the perpendicular one. A small-polaron hopping model has been applied to a series of oxalate-type $Fe^{II}Fe^{III}$ 2D CPs, providing a clear explanation on the much higher conductivity of the anilate-based systems than the oxalate ones.

PART II

1.1 INTRODUCTION

Molecular materials combining conducting (π-type, delocalized) and magnetic (d-type, localized) electrons have attracted major interest in molecular science since they can exhibit the coexistence of two distinct physical properties, furnished by the two independent networks, or novel and improved properties when they interact.[1–9] In this context, heterobimetallic oxalate bridged compounds have been thoroughly used as a magnetic lattice of multifunctional magnetic materials.[10] They are formed by anionic networks $[M^{II}M^{III}(ox)_3]^-$ with magnetic ions linked through bis-bidentate bridging oxalate ligands. The second property is provided by the charge compensating cation, thus combining the long-range magnetic ordering of the oxalate network with paramagnetism,[8,11] photochromism,[12,13] electrical conductivity,[14,15] proton conductivity,[16–19] ferroelectricity,[16] chirality,[20–22] or single-molecule magnet behavior.[23] In recent years, CPs based on the 3,5-disubstituted-2,6-dihydroxy-1,4-benzoquinone (H_2dhbq, see Chart 1), also called anilate ligand in its dianionic form (H_2An^{2-} or X_2An^{2-}), have been thoroughly developed.[24,25] They usually present 2D-layered or 3D-extended networks with larger cavities than those obtained in oxalate-based CPs due to the larger size of the bridging ligand.[24,26–30] More recently, Miyasaka et al. have been able to increase the magnetic ordering temperature in the previously reported ferrimagnet $(NBu_4)[Mn^{II}Cr^{III}(Cl_2An)_3]$ from 10 to 40 K.[31] Taking advantage of the porosity of the material, they inserted Li^+ ions into the pores of the 2D network in order to generate a radical $Cl_2An^{\bullet 3-}$ (S = 1/ 2) and produce a new exchange interaction between the radical ligand and the metal centers, thus giving further proof of the potential of the anilate ligand to enhance the magnetic coupling in the extended network. In this context, coexistence of electrical conductivity and magnetic ordering in Fe^{III} anilate based CPs has been reported simultaneously by two research groups in 2015.[32] In both cases, the conducting properties were attributed to the presence of radical anilate bridging ligand species. The role played by the Fe^{II}/Fe^{III} and L^{2-}/L^{3-} mixed valency was further discussed by Robson et al. with a more recent result based on an interpenetrated 3D network of formula $(NBu_4)[Fe_2(F_2An)_3]$.[32] Another advantage of the anilate ligand is that it can be substituted on the 3 and 6 positions of the aromatic ring by a large variety of substituents. Recently, the asymmetric ClCNAn[33] ligand has been combined to the redox-active molecule BEDT-TTF to prepare an organic semiconductor with formula $[HClCNAn]_2[BEDTTTF]$[34] and to lanthanide ions in a series of CPs of general formula $[Ln_2(ClCNAn)_3(DMF)_6]\cdot(CH_2Cl_2)x$ (Ln^{III} = Yb, x = 0; Ln^{III} = Nd or Er, x = 1) which present NIR emission properties as bulk and nanosheets.[35] In this work, we

investigated this nonsymmetric anilate ligand to prepare the mixed-valence CP of formula $[TAG][Fe^{II}Fe^{III}(ClCNAn)^3]\cdot$(solvate) (1), where TAG is the C_3-symmetric tris(amino)-guanidinium cation, never used so far in such CPs. Thorough structural characterization and study of the magnetic and conducting properties of this crystalline material are described. Since mixed-valence $Fe^{II}Fe^{III}$ oxalate-based CPs were previously reported to present a very poor conductivity, we also investigated the origin and mechanism of the transport properties in mixed-valence $Fe^{II}Fe^{III}$ networks based on oxalate-related bridging ligands, i.e., oxalate, squarate, H_2An^{2-}, and $ClCNAn^{2-}$.

1.2 EXPERIMENTAL SECTION

1.2.1 General Remarks.

Tris(amino)-guanidinium chloride (TAGCl) and KHClCNAn[33] were prepared according to the reported procedures. Reagents of analytical grade were purchased from Zentek (TCI) and used without further purification. The solvents, of HPLC grade, were purchased from Thermofisher Scientific Alfa-Aesar.

1.2.2 Synthesis

$[TAG][Fe^{II}Fe^{III}(ClCNAn)_3]\cdot$(solvate) (1) An aqueous solution (8 mL) of KHClCNAn (64 mg, 0.27 mmol) was placed in the bottom of a test tube, above was carefully layered a solution of TAGCl (42 mg, 0.3 mmol) in a mix of water (2 mL) and THF (2 mL), in the middle, and then a solution of $Fe(ClO_4)_2\cdot xH_2O$ (51 mg, 0.2 mmol) in acetone (3 mL) on top. After one week black hexagonal crystals appear at the interface suitable for XRD measurement. Elemental Anal. $C_{22}H_{67}N_9O_{41}Cl_3Fe_2$ calcd. C, 19.84; H, 5.07; N, 9.47 % found: C, 19.32; H, 5.23; N, 9.22 %. FT-IR (ν max/cm^{-1}): 2221 (νC≡N), 1631, 1492 (νC-O + νC-C), 869 (δC-Cl + νC-O).

1.2.3 Measurement details

X-ray Crystallography

Data collection was performed at 150 K on an Agilent Supernova diffractometer with Cu Kα (λ = 1.54184 Å). A single crystal of 1 was mounted on a glass fiber loop using a viscous hydrocarbon oil to coat the crystal and then transferred directly to the cold nitrogen stream for data collection. The structure was solved by direct methods with the SIR97 program and refined against all F2 values with the SHELXL-97 program using the WinGX graphical user interface. All non-hydrogen atoms were refined anisotropically except for the C and N atoms from the cationic entity $CN_6H_9^+$, and hydrogen atoms were placed in calculated positions and refined isotropically with a riding model. The program SQUEEZE from PLATON was used to calculate the potential solvent-accessible void volume and the nature of the disordered

solvent molecules. It has indicated a total void space of 885 $Å^3$ and 293 electrons/cell. This corresponds to 29 molecules of water that have been inserted in the formula of the compound. A summary of crystallographic data and refinement results are listed in Table 1.1.

Table 1.1. Crystallographic data for compound 1 at 150 K and 10 K.

	150 K	**10 K**
Empirical formula	$C_{22}H_{67}N_9O_{41}Cl_3Fe_2$	$C_{22}H_{67}N_9O_{41}Cl_3Fe_2$
Fw	1331.90	1331.90
Crystal color	black	black
Crystal size (mm^3)	0.20 * 0.20 * 0.05	0.22 × 0.19 × 0.06
Wavelength (Å)	1.54184	0.71073
Crystal system, Z	Trigonal, 1	Trigonal, 1
Space group	*P*3	*P*3
a (Å)	13.616(2)	13.5493(16)
b (Å)	13.616(2)	13.5493(16)
c (Å)	9.430(4)	9.484(3)
α (°)	90	90
β (°)	90	90
γ (°)	120	120
V ($Å^3$)	1514.1(8)	1507.8(6)
ρ_{calc} ($g.cm^{-3}$)	1.461	1.467
μ(CuKα) (mm^{-1})	5.994	0.653
θ range (°)	3.75–73.74	2.15-26.36
Data collected	3465	8947
Data unique	2610	3976
Data observed	1360	1612
R(int)	0.0459	0.0604
Nb of parameters / restraints	140/4	125/2
$R1(F)$,[a] $I > 2\sigma(I)$	0.0395	0.0715
$wR2(F^2)$,[b] all data	0.1258	0.2391
$S(F^2)$,[c] all data	0.891	1.095

[a] $R1(F) = \Sigma\|\|F_0\|-\|F_C\|\|/\Sigma|F_0|$; [b] $wR2(F^2) = [\Sigma w(F_0^2-F_C^2)^2/\Sigma wF_0^4]^{1/2}$; [c] $S(F^2) = [\Sigma w(F_0^2-F_C^2)^2/(n+r-p)]^{1/2}$.

Data collection was performed at 10 K on a SuperNova Microfocus diffractometer equipped with a two-dimensional ATLAS detector using Mo Kα radiation (λ = 0.71073 Å) and a Helijet He open-flow cryosystem. The unit-cell determination and data reduction were performed using the CrysAlisPRO program suite (Rigaku Oxford Diffraction, 2017) on the full data set. The data have been indexed using the trigonal setting with cell parameters a = b = 13.5493(16) Å and c = 9.484(3) Å. In addition, the diffraction pattern showed the presence of very weak (1/3 1/3 1/3) superstructure reflections, which were not taken into account in the structure determination. The corresponding crystal structure was refined on F2 by weighted full matrix least-squares methods using the SHELXL program (Sheldrick, 2008). All non-

hydrogen atoms were refined anisotropically except for the C and N atoms from the cationic entity $CN_6H_9^+$, and hydrogen atoms were placed in calculated positions and refined isotropically with a riding model. The program SQUEEZE from PLATON was used to calculate the potential solvent-accessible void volume and the nature of the disordered solvent molecules.

Raman spectroscopy

The Raman spectrum of 1 was carried out at room temperature on single crystals by using a micro Raman spectrometer (Horiba Labram 300) equipped with a He−Ne laser (λ = 632.81 nm) in the 80−2000 cm^{-1} range with a 20 LWD objective (with a Nd:YAG laser (λ = 1064 nm) in a backscattering geometry. No sample decomposition was observed during the experiments. The choice of the FT-Raman spectrometer was required because of the fluorescence of the ligand under He−Ne laser irradiation.

Magnetic measurements

Magnetic measurements were carried out on polycrystalline samples with a Quantum Design MPMS-XL-7T SQUID magnetometer (Quantum Design, Inc., San Diego, CA, USA). Magnetic measurements (dc) were carried out under an applied field of 1000 Oe. Zero-field-cooled/field-cooled/remanent magnetization (ZFC/FC/RM) were collected under an applied field of 25 Oe. Alternating current susceptibility measurements were carried out with an alternating magnetic field of 3.95 Oe in the 1− 1500 Hz frequency range.

Mössbauer spectroscopy

Mössbauer spectra were collected in transmission mode using a conventional constant-acceleration spectrometer and a 25 mCi 57Co source in a Rh matrix. The velocity scale was calibrated using α-Fe foil. Isomer shifts, IS, are given relative to this standard at room temperature. The low-temperature spectrum was collected in a bath cryostat with the sample in He exchange gas. The absorber was obtained by gently packing the powdered sample into a perspex holder. The spectra were fitted to Lorentzian lines using a nonlinear least-squares method.

Single-crystal transport measurements

Electrical transport measurements were performed on hexagonal-shaped single crystals. Gold wires (17 μm diameter) were glued with silver paste either on two edges or on both faces of the crystals (for conductivity measurements parallel and perpendicular to the 2D planes,

respectively). Two-probe dc measurements were performed applying a constant voltage in the range 0−5 V and measuring the current using a Keithley 6487 Picoammeter/Voltage Source. Low temperature was provided by a homemade cryostat equipped with a 4 K pulse tube.

Theoretical calculations

Density functional theory (DFT)- based calculations were carried out adopting the hybrid TPSSh functional,[35] which has been shown to give good high-spin−low-spin relative energies for spin-crossover complexes involving iron[35] and the standard double-ζ + polarization basis set 6-31G(d). Geometries were optimized forcing a D_3 symmetry and a high-spin configuration using the Gaussian 09 code.

1.3 RESULTS AND DISCUSSION

1.3.1 Synthesis

The synthesis of the mixed-valence compound 1 differs from that of the heterobimetallic oxalate and anilate based CPs. In such cases, the tetrabutylammonium salt of (tris-oxalato)metal(III) or (tris-anilato)- metal(III) complex was first prepared and isolated. The precursor thus obtained was then reacted with the second metal salt by diffusion techniques to grow the bimetallic extended network. Here we have slowly diffused a solution of $Fe^{II}ClO_4 \cdot xH_2O$ and a solution of TAGCl into a solution of KHClCNAn. Due to the partial oxidation of the Fe^{II} ions under aerobic conditions, black hexagonal crystals of the $Fe^{II}Fe^{III}$ compound 1 were obtained after 1 week.

1.3.2 Crystal Structure

Compound 1 crystallizes in the trigonal polar space group *P*3. The structure is formed by anionic 2D layers of formula $[Fe^{II}Fe^{III}(ClCNAn)_3]^-$ in the *ab* plane, alternating with cationic layers of TAG. The anionic layer presents the well-known honeycomb structure, which is similar to other extended oxalate[36,37] and anilate-based 2D networks.[28] It consists of a hexagonal layer with Fe^{II} and Fe^{III} ions linked through the anionic bis-bidentate $ClCNAn^{2-}$ ligands (Figure 1.1). As usual for this type of 2D networks, the two crystallographically independent metal centers present alternated chirality (*Δ*-configuration for Fe1 and *Λ*-configuration for Fe2 in the crystal used to solve the structure) (Figure 1.1c). The intralayer metal-metal distance is 7.860 Å. The average Fe-O distances are very similar between both metal centres (2.037(12) Å for Fe1 and 2.047(13) Å for Fe2), which may indicate an electron delocalization and an average oxidation state of +2.5 for each Fe center (*vide infra*). The cationic layer is formed by one crystallographically independent TAG cation and water

molecules. The TAG cation has an occupancy of 1/3, which is one-half of the Fe atoms, and is located only on one-half of the vertices of the hexagons. The structure of the cation is planar, with the C8− N2 and N2−N3 distances (1.394(15) and 1.558(17) Å respectively) in agreement with distances reported in the literature for other TAG-based compounds.[38] Anionic and cationic layers present intermolecular H-bonding interactions between the terminal amino groups of the TAG cation and the chloro substituents of the anilate ligands (Figure 1.1d).

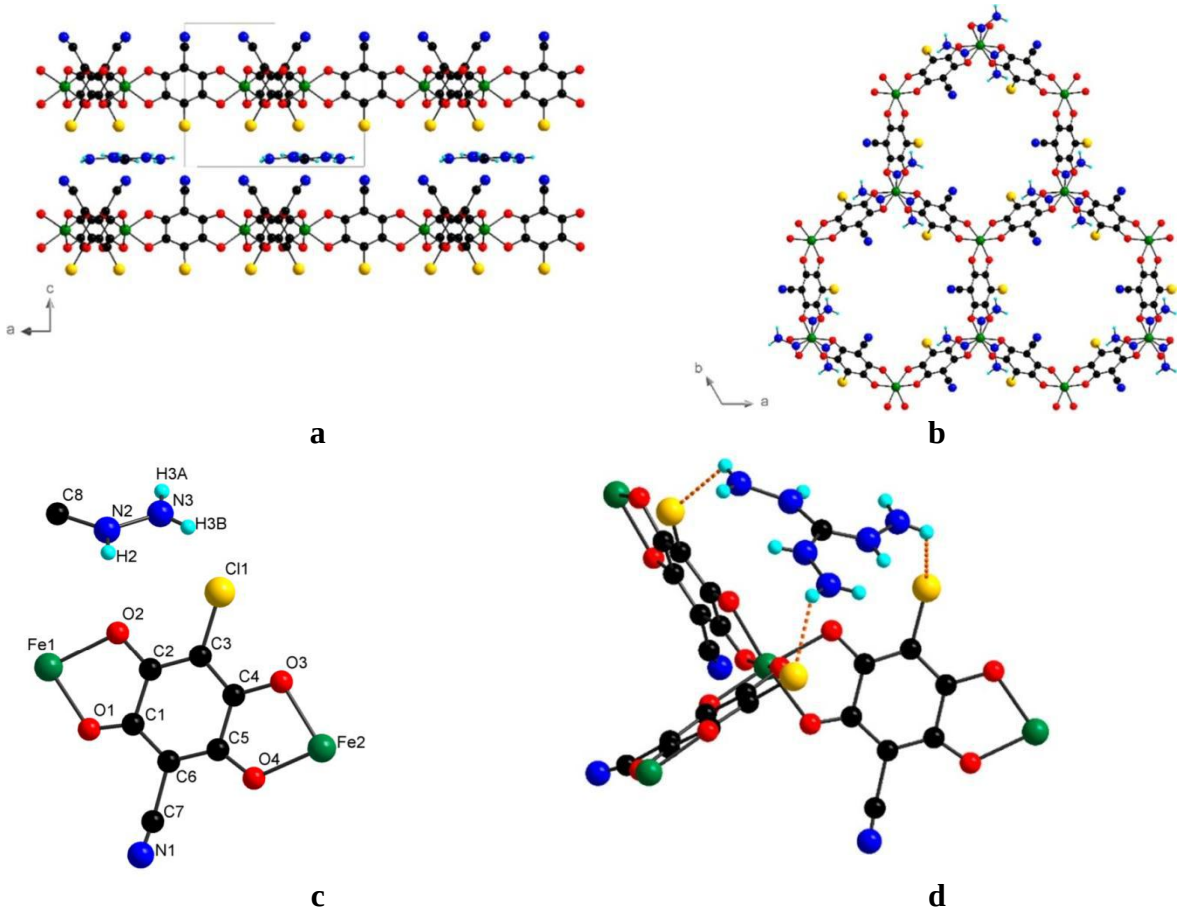

Figure 1.1. a) Structure of 1 in the *ac* plane and b) in the *ab* plane. c) Asymmetric unit d) H-bonding intermolecular interactions (dashed lines) between the cationic and anionic layers. Colour code: C, black; H, cyan; O, red; N, blue; Cl, yellow; Fe, green.

The distance between two anionic layers corresponds to the value of the c parameter (9.430(4) Å). The cationic and anionic 2D layers are eclipsed, leading to hexagonal channels along the c axis which are filled only by solvent molecules. When compared to the previously reported anilate-based layered CPs,[24,28,39] here the use of the smaller cation results in a drastic increase of the void space inside the hexagonal channels (885 $Å^3$). This represents 58% of the total volume, thus increasing the porosity of the 2D material (Figure 1.2).

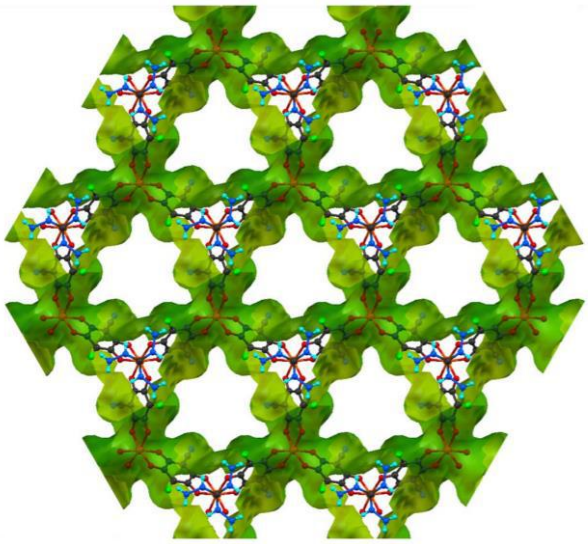

Figure 1.2. Structure of 1 showing the accessible void space inside the cavities along the *c* direction.

As a consequence, the compound shows a fast release of the solvent molecules after filtration, and the nature of these solvent molecules could not be attributed without ambiguity. In order to reach a good reliability factor and since 293 electrons per hexagonal cavity were determined by the SQUEEZE program, 29 molecules of water have been integrated in the empirical formula (see Table 1.1). However TGA analysis could not confirm the precise nature of the solvent molecules (Figure 1.3). Since a mixture of three solvents has been used during the synthesis (water, THF, and acetone), the formula of the compound should be defined as $[TAG][Fe^{II}Fe^{III}(ClCNAn)_3]\cdot(solvate)$.

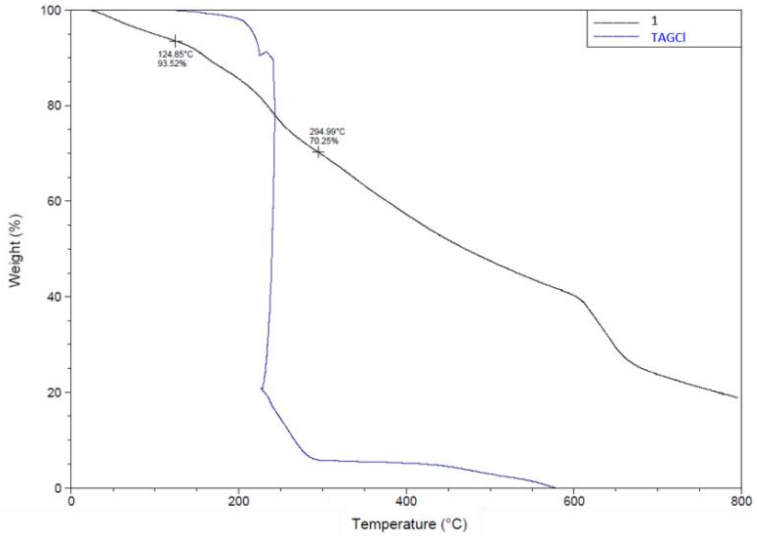

Figure 1.3. TGA analysis of 1 (black curve) and TAGCl (blue curve).

Table 1.2. Selected Fe-O bond distances (Å) in compound 1

Fe-O distances	150K (Å)	10K(Å)
Fe1—O1	2.000(6)	1.937(7)
Fe1—O2	2.086(6)	2.103(7)
Fe2—O3	2.073(7)	2.117(7)
Fe2—O4	2.018(6)	1.974(7)

By comparison with the 150 K crystal structure, the overall honeycomb 2D structural architecture in the trigonal *P*3 space group is retained at 10 K. Accordingly, the asymmetric unit still contains two symmetrically independent iron sites (Fe1 and Fe2). The unit cell parameters and unit cell volumes are slightly lower at 10 K, owing to usual thermal contraction effects. The intralayer metal−metal distance (7.8243(7) Å) and average Fe−O distances (2.020(14) Å for Fe1 and 2.043(14) Å for Fe2) are not significantly different from the 150 K values (Table 1.2). Accordingly, the 10 K crystal structure does not evidence a specific ordering of the Fe^{II} and Fe^{III} ions on the symmetrically independent Fe1 and Fe2 sites. We can therefore consider that in this description the Fe^{II} and Fe^{III} ions are spatially distributed and disordered over the two sites. As mentioned in the Experimental Section, very weak superstructure reflections were detected on the diffraction pattern, which indicates that the exact structural ordering may be more complex than this description in the *P*3 space group. However, the quality of the X-ray diffraction data, and especially the weakness of the superstructure reflections, does not allow going further. The current description leads to two Fe^{II} and two Fe^{III} different local environments in the crystal, which is consistent with the results from Mössbauer spectroscopy *(vide infra)*.

1.3.3 Raman Spectroscopy

Raman spectra are valuable probes to investigate the oxidation state of coordinated benzoquinone derivatives.[26] Therefore, in order to confirm the oxidation state of the bridging ligand a Raman study at room temperature was performed and a comparison between the Raman spectra of 1 and the free KHClCNAn ligand is reported in Figure 1.4. The strong and broad band centered at ca. 1574 cm^{-1} can be assigned to a ν(C=C) + ν(C=O) combination band, and the significant observed downshift from 1627 cm^{-1} for the free ligand can be attributed to a weakened double-bond character of these terminal groups because of the coordination with the metal ion; the weak band centered at ca. 1675 cm^{-1} present in the free ligand spectrum can be assigned to the ν(C=O) vibration mode for the uncoordinated C=O groups of the free ligand and in fact is not observed in 1. The two bands observed in the

1400−1250 cm^{-1} region are assigned to the ν(C−C) + ν(C−O) combination band and ν(C−C) vibration, respectively, and according to Harris et al.[40] confirm the assignment of ligand oxidation state as dianionic $ClCNAn^{2-}$, supporting structural findings. The observed band at 592 cm^{-1} can be assigned to a ν(Fe−O) + ν(C−C) combination stretching mode, as already found in previously reported dianionic anilate-based honeycomb-like networks.[32] No bands can be unambiguously assigned to Fe^{II}–O and Fe^{III}–O vibrational modes, thus supporting extensive electron delocalization between the Fe centers in 1 at room temperature, as clearly shown by Mössbauer spectra (*vide infra*).

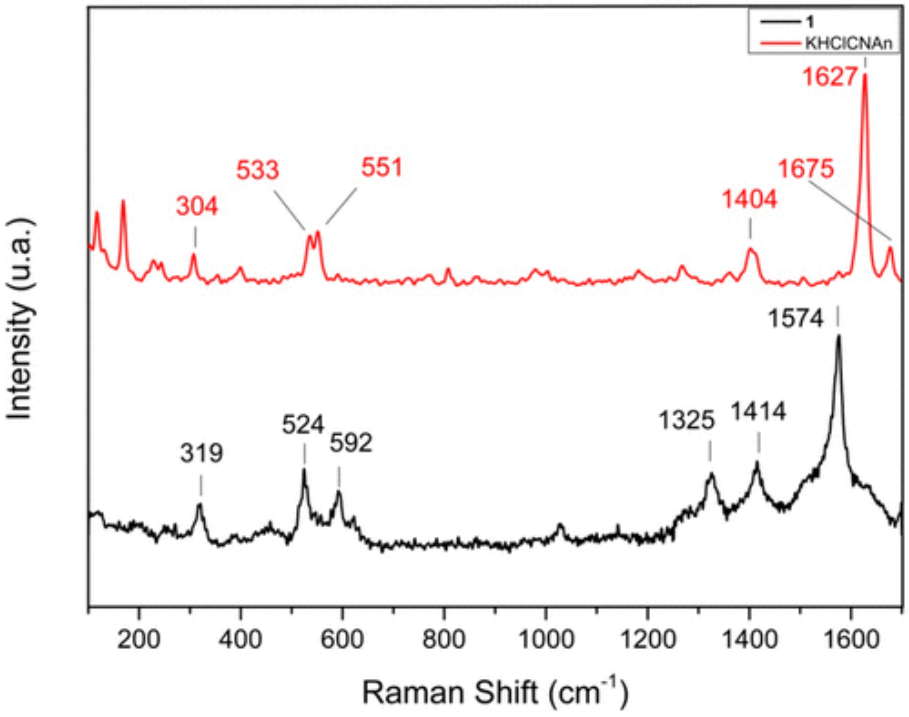

Figure 1.4. Comparison of Raman spectra of 1 and the KHClCNAn ligand, performed at room temperature with a He−Ne laser (λ = 632,81 nm) and a Nd:YAG (λ = 1064 nm), respectively.

1.3.4 Magnetic Properties

The magnetic properties were measured on a polycrystalline sample of 1. The product of the molar magnetic susceptibility times the temperature ($\chi_m T$) presents a value of 9.7 emu·K·mol^{-1} at 300 K, which corresponds to the expected spin-only value (7.38 emu·K·mol^{-1}) with a g = 2.2 (Figure 1.5). When the temperature is lowered, $\chi_m T$ slightly decreases, suggesting weak antiferromagnetic interactions between paramagnetic centers through the anilate bridges. Below 50 K, $\chi_m T$ increases until reaching a value of ~27 emu·K·mol^{-1} at 7 K, followed by a sharp decrease at lower temperatures. This suggests a magnetic ordering, which was confirmed by zero-field-cooled/field-cooled (ZFC/ FC) and remnant magnetization

measurements under a very low magnetic field (Figure 1.6). The ZFC and FC plots diverge below 3.5 K, indicating the appearance of an irreversibility or memory effect. The remnant magnetization becomes non negligible at the same temperature, confirming the existence of spontaneous magnetization below this temperature.

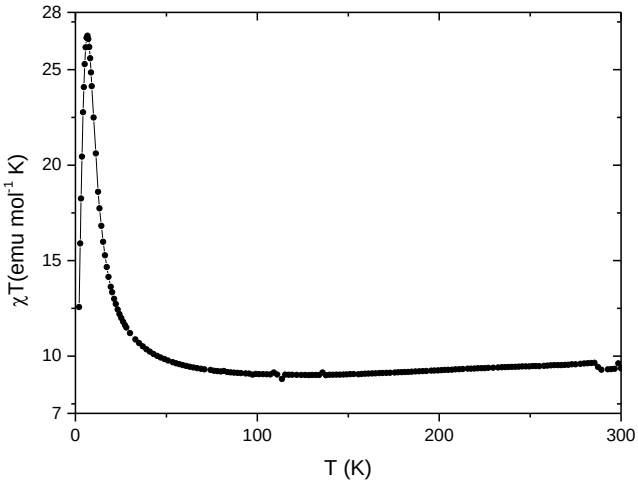

Figure 1.5. Temperature dependence of the product of the molar magnetic susceptibility times the temperature ($\chi_m T$) of 1 under an applied field of 1000 Oe.

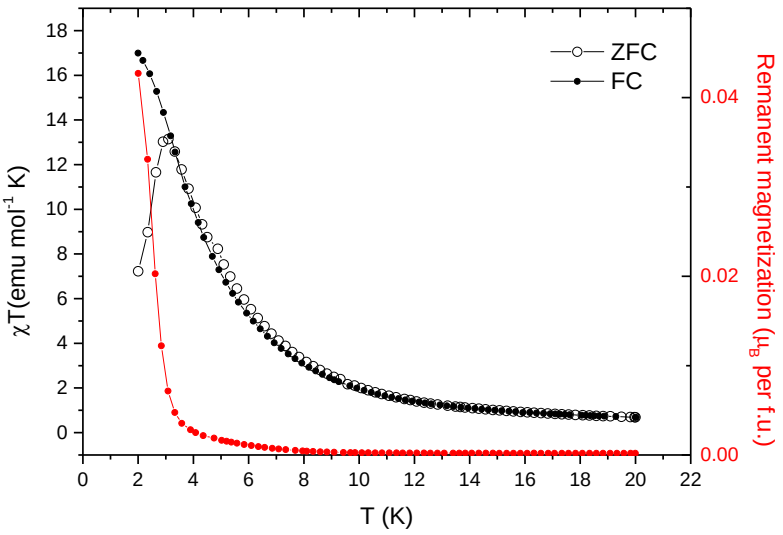

Figure 1.6. Temperature dependence of zero-field cooled (ZFC) and field cooled (FC) susceptibilities at 25 Oe and remanent magnetization (red curve) in the temperature range 2-20K.

The magnetic ordering was also confirmed by susceptibility measurements under alternating magnetic field (ac susceptibility, Figure 1.7a). This shows the appearance of an out-of phase signal and an ordering temperature Tc slightly dependent on the frequency, which can be observed for both super paramagnets and spin glasses.[41] The fitting of this frequency dependent behavior to a simple Arrhenius model (Figure 1.7b) yields parameters

with no physical meaning, including a $\tau_0 = 10^{-12}$, very different to what is found in super paramagnets (or single-molecule magnets, with values of τ_0 between 10^{-8} and 10^{-10} s).[42,43] This τ_0 value falls within the range reported for magnetic spin-glass systems (10^{-12}–10^{-14} s)[43,44] and is then consistent with a glassy magnet behavior as observed in many 2D magnetic materials.[45–47] Moreover, the Mydosh parameter φ, calculated from the ac data, has a value of 0.08, in good agreement with the expected values for a noncanonical spin glass.[32,48] Isothermal magnetization measurements at low temperatures show a fast increase of the magnetization at low fields that becomes more gradual at higher fields (Figure 1.8). The sharp increase at low fields (H<1000 Oe) also supports the appearance of spontaneous magnetization due to strong interactions between metal centers. The magnetization saturates at higher fields reaching ~5 μB, far from the expected 9 μB for parallel alignment of spin carriers. This confirms the ferrimagnetic nature of the spontaneous magnetization that stabilizes a ground state with an intermediate spin, characteristic of a glassy ferrimagnet as suggested by the initial decrease in the $\chi_m T$ at high temperatures. An additional proof of the magnetic ordering is the presence of a hysteresis loop at 2 K with a coercive field of 60 Oe.

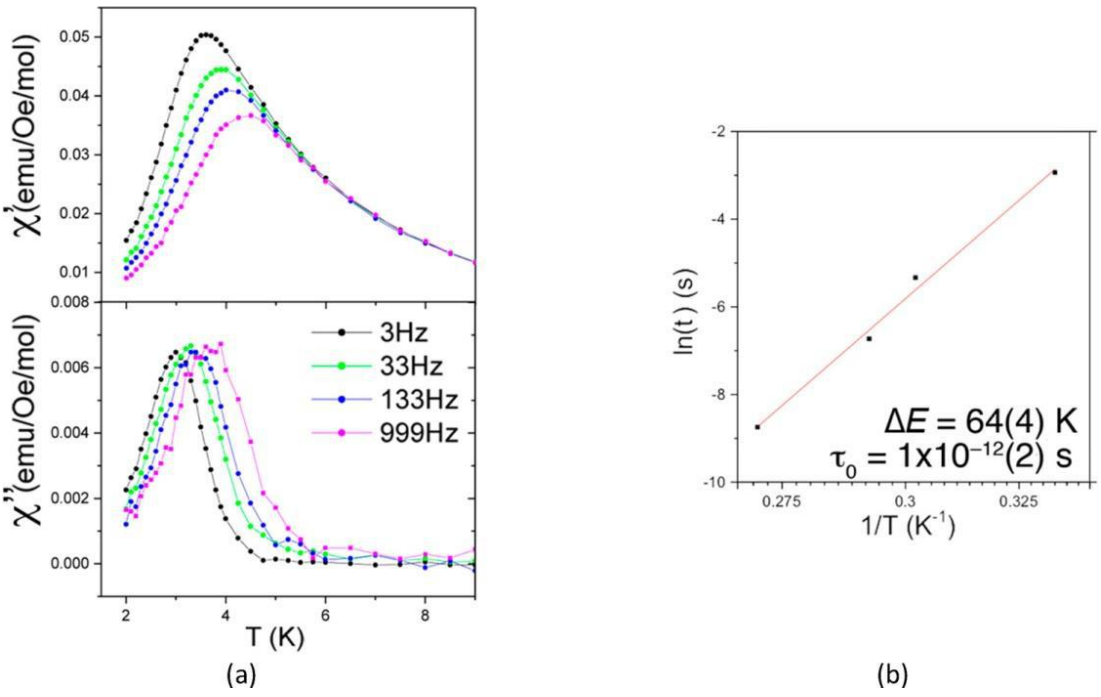

Figure 1.7. (a) Temperature dependence of the in-phase (χ′) and out-of-phase (χ″) ac susceptibility of 1, and (b) Arrhenius plot for the frequency dependence of the position of the peak in χ″ vs 1/*T*.

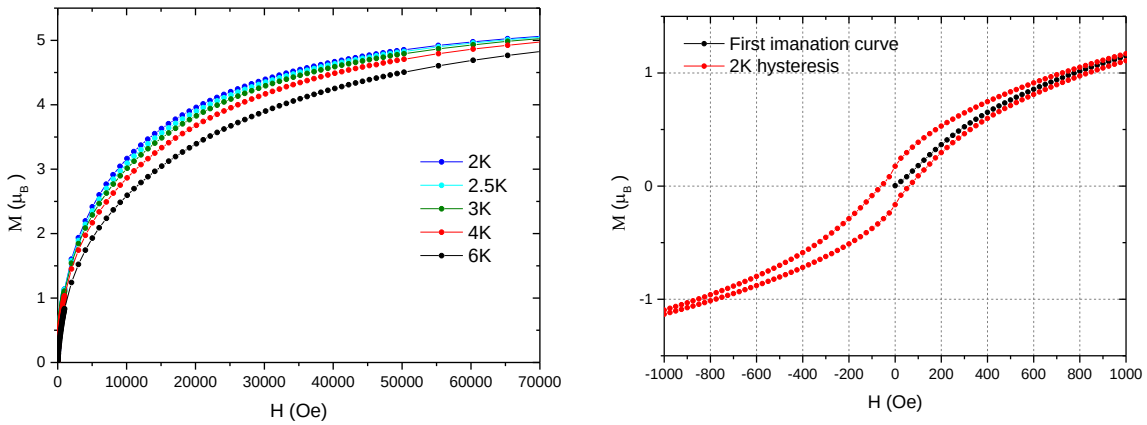

(a) (b)

Figure 1.8. (a) Isothermal magnetization of 1 at different temperatures and (b) magnetic hysteresis loop at 2K.

1.3.5 Mössbauer spectroscopy

Mössbauer spectroscopy has been used to confirm the oxidation state of the Fe metal centers (Figure 1.9). At 10 K three broad absorption peaks are observed. They may be interpreted by two quadrupole doublets. However, due to the large width of the absorption peaks a significantly better fit is obtained with four quadrupole doublets. The estimated isomer shift, IS, and quadrupole splitting, QS, are consistent with the presence of high-spin Fe^{III} and high-spin Fe^{II} in octahedral coordination by anionic oxygen atoms.[49] The estimated relative areas indicate that approximately one-half of the Fe cations are in the +3 state and the other half in the +2 state. The two doublets observed for each oxidation state are consistent with the occupation of Fe(1) and Fe(2) crystallographic sites by both Fe^{II} and Fe^{III}. The room-temperature spectrum shows only one asymmetric doublet with IS and QS consistent with an average oxidation state of +2.5.[50] The temperature dependence of the Mössbauer spectra of the anilate CP is similar to the behavior observed for other mixed-valence iron compounds, namely, molecular complexes.[51,52] The intermediate isomer shift at room temperature corresponds to a charge-delocalized state on the Mössbauer spectroscopy time scale of $\sim 10^{-7}$ s, i.e., a chargetransfer frequency $\geq 10^{8}$ s^{-1} . As the temperatures decreases, the frequency of charge delocalization gradually decreases, and at 10 K the Fe^{II} and Fe^{III} states are localized when compared to the Mössbauer effect time window (i.e., the lifetime of the Fe^{II} and Fe^{III} states becomes longer than 10^{-7} s).

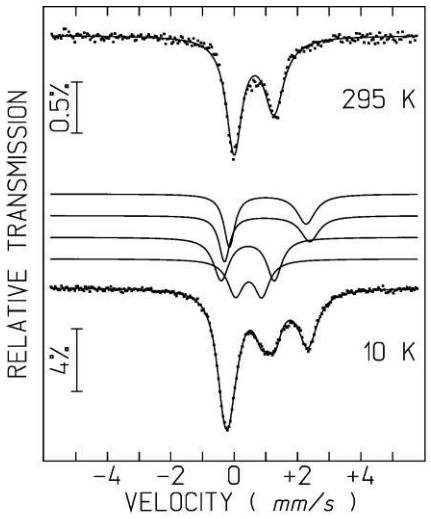

(a)

T	IS (mm/s)	QS (mm/s)	I (%)	Fe state
295 K	0.74	1.26	100%	$Fe^{2.5+}$
10 K	0.57	0.83	24%	Fe^{3+}
	0.54	1.68	29%	Fe^{3+}
	1.15	2.69	22%	Fe^{2+}
	1.17	2.42	25%	Fe^{2+}

(b)

Figure 1.9. (a) Mössbauer spectra of 1 taken at 295 and 10 K and (b) estimated parameters from the spectra. The lines over the experimental points are the calculated functions. On the spectrum taken at 10 K this function is the sum of four quadrupole doublets shown slightly shifted for clarity. IS, isomer shift relative to metallic α-Fe at 295 K; QS, quadrupole splitting; I, relative areas. Estimated errors are < 0.02 mm/s for IS, QS, < 2% for I.

1.3.6 Transport properties

Since a mixed-valence state and electron delocalization have been evidenced in 1, we could expect this CP to present transport properties; therefore, electrical conductivity measurements have been carried out on single crystals. The hexagonal shape of the crystals allows determining the direction of the {001} plane and then to measure the conductivity parallel ($\sigma^{\parallel}$) and perpendicular ($\sigma^{\perp}$) to the 2D layers, corresponding to the ab plane. The temperature dependence of the resistivity indicates that 1 is a semiconductor (Figure 1.10). The parallel roomtemperature conductivity value $\sigma^{\parallel}$ is about 2×10^{-3} S/cm, almost 3 orders of magnitude higher than the perpendicular room-temperature conductivity $\sigma^{\perp}$ (7×10^{-6} S/cm).

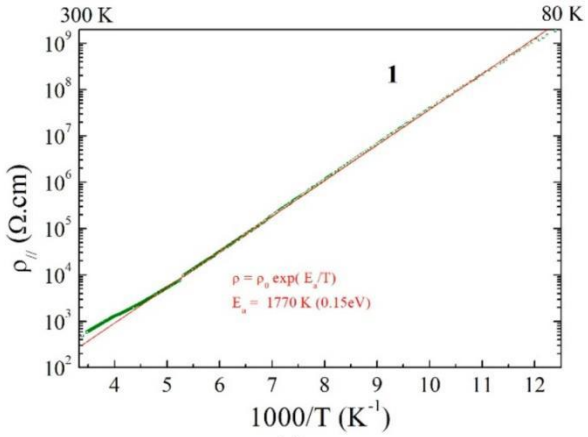

(a)

	ρ (kΩ.cm)	σ (S/cm)
//	0.5	2.10^{-3}
⊥	143	7.10^{-6}

(b)

Figure 1.10. (a) Electrical resistivity $\rho_{//}$ plotted as log $\rho_{//}$ versus the inverse temperature, measured with a 4V voltage applied in the ab plane. The red line is the fit to the data with the law $\rho = \rho_0 \exp(Ea/T)$ giving the activation energy Ea. (b) Room-temperature resistivity (ρ) and conductivity (σ) values measured along (//) and perpendicular (⊥) to the 2D layers.

1.3.7 Relationship between the electrical conductivity and the nature of the bridging ligand

The fairly good conductivity of compound 1 as well as of the few recently reported anilato-based $Fe^{II}Fe^{III}$ CPs[27,53] is in sharp contrast with the low conductivity found for the oxalate-based ones.[53] To gain insight into the origin of the good conductivity in our anilate-based CP and to point out the crucial role of the bridging ligand, we have undertaken a theoretical study on the electron transfer in 2D $Fe^{II}Fe^{III}$ networks based on bis(bidentate) oxalate-type ligands in which we consider the conductivity dominated by thermally activated small-polaron hopping. We are interested in a simple, pragmatic approach, highlighting the role of the bridging ligand, and in this comparative work, we decided to focus on four ligands: oxalate, squarate ($C_4O_4^{2-}$, dianion of 3,4- dihydroxycyclobut-3-ene-1,2-dione), $dhbq^{2-}$, and $ClCNAn^{2-}$, with different electron delocalization capabilities.

The basic reasoning behind the small-polaron hopping approach to the electron transfer process in either discrete or extended mixed-valence systems is qualitatively illustrated in Figure 1.11. Consider a system formed by two separated high-spin $Fe^{II}L_6$ ($t_{2g}^4e_g^2$) and high-spin $Fe^{III}L_6$($t_{2g}^3e_g^2$) complexes in close proximity. Although the electron transfer between them is between levels of the Fe t_{2g} orbital set, which are formally nonbonding, such transfer leads, in general, to an increase/decrease of the M–L distances in the $Fe^{II}/Fe^{III}L_6$ units due to the expansion/contraction of the electron cloud. As a consequence of the fact that electrons move much faster than nuclei, the much faster electron transfer occurs in such a way that the geometry cannot change during the process and the system cannot exchange thermal energy

with the surroundings. In other words, before the electron transfer can actually take place a Fe^{III} species with the Fe^{II} geometry (and viceversa) must be created. This rearrangement is however energetically unfavorable, so that the electron transfer will only occur when as a result of some vibrational process the two Fe centers reach equal coordination geometries (Figure 1.11a). Thus, to understand the differences in thermally activated conductivity one must focus on the evaluation of the energetic cost of such "equalization" of the two sites.

A simple yet usually very insightful analysis relies on the assumption that the structural distortion around each center may be described by a simple harmonic oscillator $E_i = 1/2\ k_i(d_i - d_0)^2$, where $k_i$is the force constant, d_i the Fe–L distance, and d_0 its equilibrium value. Within this approximation the energy of the whole system is $E_{tot} = k_{III}(d_A - d_{III})^2 + k_{II}(d_B - d_{II})^2$, where for the sake of simplicity the 1/2 factors have been included in the force constants. Here let us assume that complex A is in the Fe^{III} state and complex B in the Fe^{II} state, but there is a totally equivalent expression interchanging A and B. If we plot the two energy surfaces $E_{tot}(d_A,d_B)$ we see that they cross along the line $d_A = d_B$ (Figure 1.11b). The initial and final configurations (respectively, top and bottom configurations in Figure 1.11a) correspond to minima in the lower surface and the structures for which $d_A = d_B$ to the crossing seam. The situation is more conveniently analyzed by using a contour plot of the bottom surface (Figure 1.11c), obtained by joining the two bottom halves of the two intersecting surfaces. The two minima correspond to the configurations $Fe^{III}{}_A\cdots Fe^{II}{}_B$ (zone noted as F in Figure 1.11c) and $Fe^{II}{}_A\cdots Fe^{III}{}_B$ (noted as I). The point on the $d_A = d_B$ line for which the total energy is minimal (M) is found by taking the derivative of the energy function with $d_A = d_B = d_M$ and equating it to zero. It is found that $d_M = (k_{II}d_{II} + k_{III}d_{III})/(k_{II} + k_{III})$ and the corresponding energy $E_M = (k_{II}k_{III}/(k_{II} + k_{III}))(d_{II} - d_{III})^2$. In other words, the minimal energy required to make the coordination environments on both Fe centers equal, that is, the height of the barrier for thermally activated electron transfer, depends basically on the difference squared between the radii of the Fe^{III} and Fe^{II} coordination environments in their equilibrium geometries.

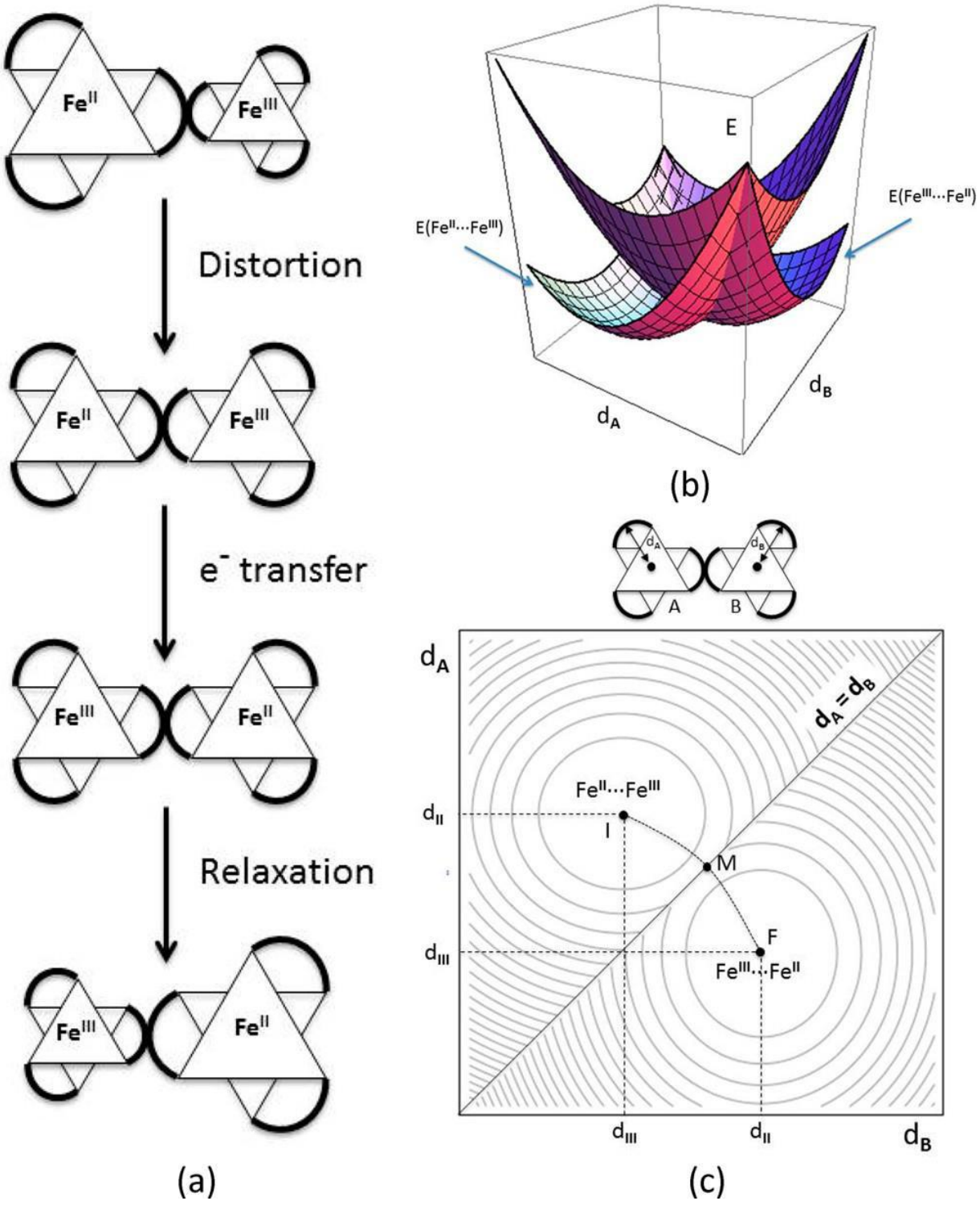

Figure 1.11. (a) Schematic representation of the three consecutive steps during the electron transfer with two neighboring pseudooctahedral Fe(chelate)$_3$ centers shown along the C_3 axis. (b) 3D plot of the energy surface E_{tot} as a function of d_A and d_B. (c) Contour plot of the bottom surface from the E_{tot} plot displayed in b.

The model can be more simply depicted by using a cut through the two surfaces in which we plot the energy along the dotted path joining the two minima through the M point, which is taken as the origin (Figure 1.12). This gives two parabolas corresponding to the energy of the whole system with either an $Fe^{II}Fe^{III}$ or an $Fe^{III}Fe^{II}$ configuration and crossing at the M point. Note that when the two complexes are not totally isolated from their surroundings, the energy necessary to distort the complexes has an additional contribution from the environment. This is particularly important in the case of 2D lattices where the distortion of one site contributes to the distortion of all its neighboring sites. This contribution is usually included considering a generic parameter λ, which is the vertical ionization energy from one minimum to the other curve or in other words the energy necessary to transfer the electron from A to B without considering a previous structural equalization of both centers. The barrier for thermal electron transfer in the absence of interaction (i.e., the energy difference between the minima and the crossing point of the two curves) is then simply λ/4. In the real case there is always some degree of electronic interaction between the two sites and a gap, $2V_{AB}$, is opened at point M, and the barrier for thermal electron transfer is consequently lowered to $\lambda/4 - V_{AB}$. Unfortunately, there is no simple way to evaluate V_{AB} without having recourse to long and costly computations, but since we are here interested only in looking for trends when the bridging ligand is changed, it seems safe to consider that λ/4 will be the leading term in the energy barrier, so that we can make our comparisons neglecting the effects of the nature of the ligands on V_{AB}.

It is now easy to relate the main parameters (mainly structural) of this simple model to the transport measurements. The diagram in Figure 1.12 is completely general and applicable to any electron transfer process. In an extended system, when the dimensions of the zone where the necessary atomic rearrangement controlling the electron transfer occurs are of the order of the coordination sphere of a single site as in the present case, one talks about a system with small polarons.[53] The polaron energy, W_P, is the energy gained when the system relaxes after addition of one electron. In this small-polaron scenario the conductivity is dominated by thermally activated electron hopping with the mobility given by the equation $\mu = \mu_0 e^{-W_H/k}$, where W_H is the electron hopping barrier, i.e., the energy cost to reach the geometry under which the electron transfer is possible. As far as it is assumed that the variation of energy is a quadratic function of the structural parameters, the energy cost per site to reach the "equalization" geometry is 1/4 W_P, and taking into account that there are two sites involved in the transfer, it follows that $W_H = 1/2\ W_P$. Since according to the Franck–Condon

principle the energy to optically excite one electron from one to the other site (i.e., λ in Figure 1.12) is twice the polaron energy it follows that $W_H = 1/2\ W_P = \lambda/4$. Therefore, $W_H = E_M = F(d_{II} - d_{III})^2$, with $F = k_{II}k_{III}/(k_{II} + k_{III})$ and $d_M = (k_{II}d_{II} + k_{III}d_{III})/(k_{II} + k_{III})$. In that way it is possible to correlate the transport (W_H) and structural (k_{II}, k_{III}, d_{II}, and d_{III}) features for a series of compounds.

How are these parameters tuned by the nature of the bridging ligand? The values of k_{II}, k_{III}, d_{II}, and d_{III} can be evaluated from density functional calculations (DFT). We carried out structural optimizations of $Fe^{II}L_3$ and $Fe^{III}L_3$ complexes with the four ligands oxalate, squarate, $dhbq^{2-}$, and $ClCNAn^{2-}$ using the TPSSh functional, which is known to give good high-spin–low-spin relative energies for spin-crossover complexes involving iron.[54] The geometries were optimized forcing a D_3 symmetry and a high-spin configuration. In that way we obtained the d_{M-L} parameter which is the distance between the Fe atom and the midpoint to the closest C–C bonds (between the C atoms bonded to the coordinating O atoms) which corresponds to d_{II} or d_{III} of the above discussion. Once the optimal d_{M-L} parameter for each Fe^{II} and each Fe^{III} complex was found, the values of k_{II} or k_{III} were obtained by reoptimizing the structure for fixed $d_{M-L} \pm \delta$ values and fitting the energy to a second-order polynomial. The results for the four ligands are reported in Figure 1.12b.

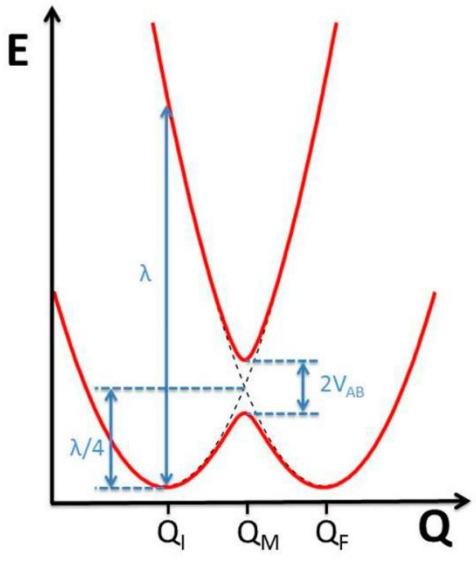

(a)

	Oxalate	Squarate	dhbq^{2-}	ClCNAn^{2-}
E_{III}	0	0	0	0
d_{III}	2.764	2.639	2.745	2.737
k_{III}	489	241	528	445
E_{II}	208	159	142	104
d_{II}	2.914	2.752	2.808	2.802
k_{II}	403	180	497	367
d_M	2.832	2.687	2.776	2.766
$(\Delta d)^2$	0.022	0.013	0.004	0.004
F	221	103	256	201
W_H	4.93	1.33	1.01	0.85

(b)

Figure 1.12. (a) Energy plot for a $Fe^{II}Fe^{III}$ to $Fe^{III}Fe^{II}$ electron transfer process. (b) Calculated parameters for the four studied bridging ligands. Distances are expressed in Angstroms, energies in kcal.mol^{-1}, and k and F in kcal.mol^{-1}·Å^{-2}.

According to the data in Figure 1.12b, W_H = 0.214, 0.057, 0.044, and 0.037 eV for oxalate, squarate, $dhbq^{2-}$, and $ClCNAn^{2-}$, respectively. Despite the simplicity of the approach,

these numbers are very reasonable when compared with W_H estimations based on experimental data for $Fe^{II}Fe^{III}$solids like magnetite (~0.15 eV) and partially substituted ferrites (~0.11 eV) which are in between those calculated for oxalate and the other three ligands. Thus, we believe that the simple approach captures the essence of the electron transfer process, although the activation energies are smaller than the experimental ones. This is not unexpected since the Fe sites are immersed in a quite rigid 2D network, which must lead to a noticeable increase in the parameter λ and hence in the barrier estimated here by λ/4. According to the values in Figure 12b electrons should be much less mobile in oxalate networks than in anilate ones, which is in good agreement with experimental observations.[27,55] What is the reason for this finding? The *F* values for the oxalate ligands are in between those for both the $dhbq^{2-}$ and the $ClCNAn^{2-}$ ones, yet W_H is five times larger. It is clear that the factor determining the large difference is $(\Delta d)^2$, i.e., the square of the difference in the *d* values for Fe in the two oxidation states. Because of the quadratic dependence, this term has an overwhelming influence on the final value of W_H. Comparing the $d_{II}$and d_{III} distances for the oxalate, $dhbq^{2-}$, and $ClCNAn^{2-}$ ligands in Figure 1.12b it is clear that whereas the d_{III} values are fairly similar, d_{II} for the oxalate ligand is markedly larger than those for the $dhbq^{2-}$ and $ClCNAn^{2-}$ ligands. Thus, the determining factor for the lower conductivity of the oxalate systems lies in the difficulty to cope with the extra electron of the high-spin Fe^{II} situation. The occurrence of extensive delocalization through the benzene ring of $dhbq^{2-}$ and $ClCNAn^{2-}$acts as a buffer for the electronic rearrangement needed by the presence of the extra electron. Note that when the ligands are more similar, the *F* factor depending on the force constants may become the key factor. According to Figure 1.12b this is, for instance, the case when comparing the $dhbq^{2-}$ and $ClCNAn^{2-}$ ligands. The squarate ligand is also associated with a small W_H value, not much different from those of the $dhbq^{2-}$ and $ClCNAn^{2-}$ ligands. However, the $(\Delta d)^2$ term is intermediate between those of the oxalate and $dhbq^{2-}$ and $ClCNAn^{2-}$ pair of ligands. Clearly, in that case the *F* term plays an important role. Both the geometrical constraints imposed by the four-member ring as well as the delocalization in the central part of the ligand influence the electron transfer tendency.

We thus conclude that the present approach provides a simple, yet insightful, model to rationalize the transport results for these $Fe^{II}Fe^{III}$ mixed-valence CPs and that the polymers based on the $dhbq^{2-}$ and $ClCNAn^{2-}$ ligands rank among the most effective ones in promoting the electron delocalization through a small-polaron hopping mechanism.

1.4 CONCLUSIONS

The mixed-valence $Fe^{II}Fe^{III}$ 2D CP [TAG][$Fe^{II}Fe^{III}$(ClCNAn)$_3$] based on the asymmetric chlorocyanoanilate ligand and containing, for the first time in such 2D networks, the TAG cation has been synthesized and crystallized in the polar noncentrosymmetric space group *P*3 thanks to the C_3 symmetry of the cation and its ability to engage in intermolecular hydrogen bonding with the chlorine atoms of the ligand. Magnetic susceptibility measurements in combination with Mössbauer spectroscopy are indicative of a spin-glass behavior with magnetic ordering below 4 K and the presence of intermediate Fe(+2.5) oxidation state at RT and charge localization $Fe^{II}Fe^{III}$ at 10 K, with a statistic occupational crystallographic site according to the 10 K Mössbauer spectra, also confirmed by the X-ray structure at 10 K. Single-crystal electron transport measurements in the 2D plane and perpendicular on it show semiconducting behavior of the material with a rather high RT value of 2×10^{-3} S/cm for the in-plane conductivity, much higher than the one reported in the oxalate-based 2D $Fe^{II}Fe^{III}$ CPs. In order to shed light on this difference and on the electron transport mechanism on these fast developing multifunctional families of 2D CPs, the small-polaron hopping approach to the electron transfer process has been applied to a series of mixed-valence $Fe^{II}Fe^{III}$ oxalate-related CPs containing as bridging ligands oxalate^{2-}, squarate^{2-}, dhbq^{2-}, and ClCNAn^{2-}. The results are clearly indicative of a much lower electron hopping barrier in the anilate complexes than in oxalates. These results open the way toward the use of the TAG cation in such multifunctional binuclear/bimetallic transition metal or lanthanide CPs, possibly endowed with multi ferroic properties thanks to the crystallization in polar space groups. Moreover, the mechanism of electron transport in the mixed-valence $Fe^{II}Fe^{III}$ CPs with bridging oxalate-type ligands has been disclosed, pointing out the higher "elasticity" of the anilate network compared to the oxalate one.

References

(1) Martin, L.; Turner, S. S.; Day, P.; Mabbs, F. E.; McInnes, E. J. L. *Chem. Commun.,* **1997**, *15*, 1367–1368.

(2) Uji, S.; Shinagawa, H.; Terashima, T.; Yakabe, T.; Terai, Y.; Tokumoto, M.; Kobayashi, A.; Tanaka, H.; Kobayashi, H. *Nature.,* **2001**, *410*, 908–910.

(3) Coronado, E.; Day, P. *Chem. Rev.,* **2004**, *11*, 5419–5448.

(4) Enoki, T.; Miyazaki, A. *Chem. Rev.,* **2004**, *104*, 5449–5477.

(5) Kobayashi, H.; Cui, H. B.; Kobayashi, A. *Chem. Rev.,* **2004**, *104*, 5265–5288.

(6) Rashid, S.; Turner, S. S.; Day, P.; Howard, J. A. K.; Guionneau, P.; McInnes, E. J. L.; Mabbs, F. E.; Clark, R. J. H.; Firth, S.; Biggs, T. *J Mater. Chem.,* **2001**, *11*, 2096–2102.

(7) Fujiwara, H.; Fujiwara, E.; Nakazawa, Y.; Narymbetov, B. Z.; Kato, K.; Kobayashi, H.; Kobayashi, A.; Tokumoto, M.; Cassoux, P. *J. Am. Chem. Soc.,* **2001**, *123*, 306–314.

(8) Kurmoo, M.; Graham, A. W.; Day, P.; Coles, S. J.; Hursthouse, M. B.; Caulfield, J. L.; Singleton, J.; Pratt, F. L.; Hayes, W.; Ducasse, L.; et al. *J. Am. Chem. Soc.,* **1995**, *117*, 12209–12217.

(9) Madalan, A. M.; Canadell, E.; Auban-Senzier, P.; Brânzea, D.; Avarvari, N.; Andruh, M. *New J. Chem.,* **2008**, *32*, 333–339.

(10) Coronado, E.; Miguel Clemente-Leo´; Romeroab, C. M.-G. F. M. *Chem. Soc. Rev.,* **2011**, *40*, 473–497.

(11) Coronado, E.; Galán-Mascarós, J. R.; Gómez-García, C. J.; Martínez-Agudo, J. M. *Adv. Mater.,* **1999**, *11*, 558–561.

(12) Bénard, S.; Yu, P.; Audière, J. P.; Rivière, E.; Clément, R.; Guilhem, J.; Tchertanov, L.; Nakatani, K. *J. Am. Chem. Soc.,* **2000**, *122*, 9444–9454.

(13) Aldoshin, S. M.; Sanina, N. A.; Minkin, V. I.; Voloshin, N. A.; Ikorskii, V. N.; Ovcharenko, V. I.; Smirnov, V. A.; Nagaeva, N. K. *J. Mol. Struct.,* **2007**, *826*, 69–74.

(14) Coronado, E.; Galán-Mascarós, J. R.; Gómez-García, C. J.; Laukhin, V. *Nature.,* **2000**, *408*, 447–449.

(15) Galán-Mascarós, J. R.; Coronado, E.; Goddard, P. A.; Singleton, J.; Coldea, A. I.; Wallis, J. D.; Coles, S. J.; Alberolá, A. A *J. Am. Chem. Soc.,* **2010**, *132*, 9271–9273.

(16) Pardo, E.; Train, C.; Gontard, G.; Boubekeur, K.; Fabelo, O.; Liu, H.; Dkhil, B.; Lloret, F.; Nakagawa, K.; Tokoro, H.; et al. *J. Am. Chem. Soc.,* **2011**, *133*, 15328–15331.

(17) Ōkawa, H.; Shigematsu, A.; Sadakiyo, M.; Miyagawa, T.; Yoneda, K.; Ohba, M.; Kitagawa, H. *J. Am. Chem. Soc.,* **2009**, *131*, 13516–13522.

(18) Ōkawa, H.; Sadakiyo, M.; Yamada, T.; Maesato, M.; Ohba, M.; Kitagawa, H. *J. Am. Chem. Soc.,* **2013**, *135*, 2256–2262.

(19) Sadakiyo, M.; Ōkawa, H.; Shigematsu, A.; Ohba, M.; Yamada, T.; Kitagawa, H. *J. Am. Chem. Soc.,* **2012**, *134*, 5472–5475.

(20) Andrés, R.; Gruselle, M.; Malézieux, B.; Verdaguer, M.; Vaissermann, J. *Inorg. Chem.,* **1999**, *38*, 4637–4646.

(21) Gruselle, M.; Li, Y.; Ovanesyan, N.; Makhaev, V.; Shilov, G.; Mushenok, F.; Train, C.; Aldoshin, S. *Chirality,* **2013***, 25*, 444–448.

(22) Clemente-León, M.; Coronado, E.; Dias, J. C.; Soriano-Portillo, A.; Willett, R. D. *Inorg. Chem.,* **2008**, *47*, 6458–6463.

(23) Clemente-León, M.; Coronado, E.; Gómez-García, C. J.; López-Jordà, M.; Camón, A.; Repollés, A.; Luis, F. *Chem. Eur. J.,***2013**, *20*, 1669–1676.

(24) Mercuri, M. L.; Congiu, F.; Concas, G.; Ashoka Sahadevan, S. *Magnetochemistry.,* **2017**, *3*, 17.

(25) Kitagawa, S.; Kawata, S.. *Coord. Chem. Rev.,* **2002**, *224*, 11–34.

(26) Abhervé, A.; Mañas-Valero, S.; Clemente-León, M.; Coronado, E. *Chem. Sci.,* **2015**, *6*, 4665–4673.

(27) Benmansour, S.; Abhervé, A.; Gómez-Claramunt, P.; Vallés-García, C.; Gómez-García, C. J. *ACS Appl. Mater. Interfaces.,* **2017**, *9*, 26210–26218.

(28) Atzori, M.; Benmansour, S.; Mínguez Espallargas, G.; Clemente-León, M.; Abhervé, A.; Gómez-Claramunt, P.; Coronado, E.; Artizzu, F.; Sessini, E.; Deplano, P.; et al. *Inorg. Chem.,* **2013**, *52*, 10031–10040.

(29) Abrahams, B. F.; Coleiro, J.; Ha, K.; Hoskins, B. F.; Orchard, S. D.; Robson, R. *J. Chem. Soc. Dal. Trans.,* **2002**, *2*, 1586.

(30) Abrahams, B. F.; Hudson, T. A.; McCormick, L. J.; Robson, R. *Cryst. Growth Des.,* **2011**, *11*, 2717–2720.

(31) Taniguchi, K.; Chen, J.; Sekine, Y.; Miyasaka, H. *Chem. Matr.,* **2017**, *29,* 10053−10059.

(32) Jeon, I.-R.; Negru, B.; Van Duyne, R. P.; Harris, T. D. *J. Am. Chem. Soc.,* **2015**, *137*, 15699–15702.

(33) Atzori, M.; Artizzu, F.; Marchiò, L.; Loche, D.; Caneschi, A.; Serpe, A.; Deplano, P.; Avarvari, N.; Mercuri, M. L. *Dalt. Trans.,* **2015**, *44*, 15786–15802.

(34) Ashoka Sahadevan, S.; Monni, N.; Abhervé, A.; Auban-Senzier, P.; Canadell, E.; Mercuri, M. L.; Avarvari, N. *Inorg. Chem.,* **2017**, *56*, 12564–12571.

(35) Ashoka Sahadevan, S.; Monni, N.; Abhervé, A.; Marongiu, D.; Sarritzu, V.; Sestu, N.; Saba, M.; Mura, A.; Bongiovanni, G.; Cannas, C.; et al. *Chem. Mater.,* **2018**, *30*, 6575–6586.

(36) Tamaki, H.; Matsumoto, N.; Koikawa, M.; Achiwa, N.; Okawa, H.; Zhong, Z. J.; Kida, S.; Hashimoto, Y. *J. Am. Chem. Soc.,* **1992**, *114*, 6974–6979.

(37) Clemente-León, M.; Coronado, E.; López-Jordà, M.; Espallargas, G. M.; Soriano-Portillo, A.; Waerenborgh, J. C. *Chem. - A Eur. J.,* **2010**, *16*, 2207–2219.

(38) Okaya, Y.; Pepinsky, R. *Acta Crystallogr.,* **1957**, *10*, 681–684.

(39) Abhervé, A.; Clemente-León, M.; Coronado, E.; Gómez-García, C. J.; Verneret, M. *Inorg. Chem.,* **2014**, *53*, 12014–12026.

(40) DeGayner, J. A.; Jeon, I.-R.; Sun, L.; Dincă, M.; Harris, T. D. *J. Am. Chem. Soc.,* **2017**, *139*, 4175–4184.

(41) Tholence, J. L. *Solid State Commun.,* **1980**, *35*, 113–117.

(42) Novak, M. A.; Folly, W. S. D.; Sinnecker, J. P.; Soriano, S. *J Magn. Magn. Mater.,* **2005**, *294*, 133–140.

(43) Novak, M. *J. Magn. Magn. Mater.,* **2004**, *272–276*, E707–E713.

(44) Gunnarsson, K.; Svedlindh, P.; Nordblad, P.; Lundgren, L.; Aruga, H.; Ito, A. *Phys. Rev. Lett.,* **1988**, *61*, 754–757.

(45) Sellers, S. P.; Korte, B. J.; Fitzgerald, J. P.; Reiff, W. M.; Yee, G. T. *J. Am. Chem. Soc.,* **1998**, *120*, 4662–4670.

(46) Ghosh, S.; Roy, S.; Liu, C.-M.; Mohanta, S. *Dalt. Trans.,* **2018**, *47*, 836–844.

(47) Krishnamohan Sharma, C. V; Chusuei, C. C.; Clérac, R.; Möller, T.; Dunbar, K. R.; Clearfield, A. *Inorg. Chem.,* **2003**, *42*, 8300–8308.

(48) Dalal, K. Y. C. and Z. W. and A. O. and J. van T. and H. D. Z. and C. R. W. and Y. S. and N. S. *J Phys. Condens. Matter.,* **2012**, *24*, 246001.

(49) Greenwood, N. N.; Gibb, T. C. *Mössbauer Spectroscopy*; Springer, Dordrecht, **1971**.

(50) Shilov, G. V.; Nikitina, Z. K.; Ovanesyan, N. S.; Aldoshin, S. M.; Makhaev, V. D. *Russ. Chem. Bull.,* **2011**, *60*, 1209–1219.

(51) Lupu, D.; Barb, D.; Filoti, G.; Morariu, M.; Tarină, D. *J. Inorg. Nucl. Chem.,* **1972**, *34*, 2803–2810.

(52) Maeda, Y. Mössbauer Spectroscopy. *J Nucl. Radiochem. Sci.,* **2006**, *7*, R13–R18.

(53) Darago, L. E.; Aubrey, M. L.; Yu, C. J.; Gonzalez, M. I.; Long, J. R. *J. Am. Chem. Soc.,* **2015**, *137*, 15703–15711.

(54) Jensen, K. P. *Inorg. Chem.,* **2008**, *47*, 10357–10365.

(55) Bhattacharjee, A.; Bhakat, D.; Roy, M.; Kusz, J. *Phys. B Condens. Matter.,* **2010**, *405*, 1546–1550.

CHAPTER 2

Anilate-based NIR-emitting lanthanide 2D Coordination Polymers

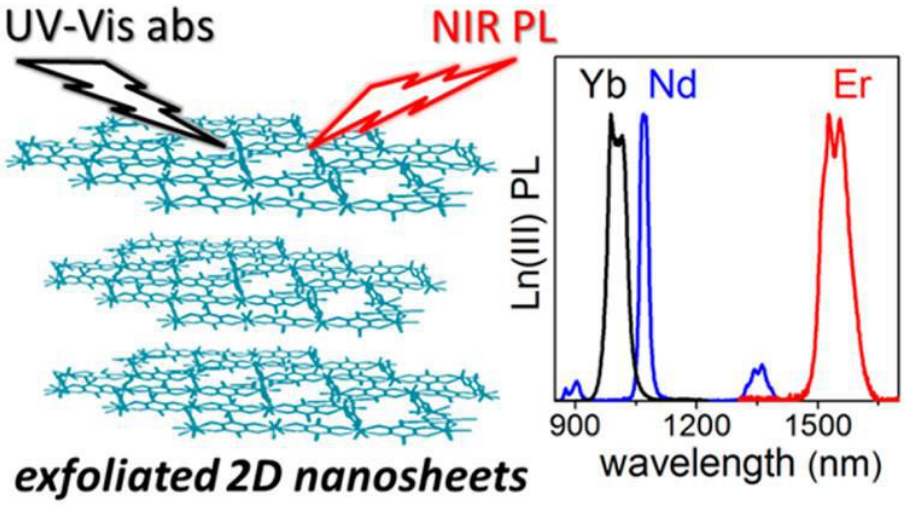

S. Ashoka Sahadevan, N. Monni, A. Abhervé, D. Marongiu, V. Sarritzu, N. Sestu, M. Saba, A. Mura, G. Bongiovanni, C. Cannas, F. Quochi, N. Avarvari and M. L. Mercuri, Nanosheets of 2D Neutral Coordination Polymers Based on NIR-Emitting Lanthanides and Chlorocyananilate Ligand., *Chem. Mater.*, **2018**, *30*, 6575-6586

PART II

ABSTRACT

The synthesis, structural characterization, photophysical studies and exfoliation of 2D layered CPs, formulated as $\{[Ln_2(ClCNAn)_3(DMF)_6]\cdot(DCM)_x\}_n$ (Ln^{III} = Yb(x=0), Nd, and Er (x=2)) based on the heterosubstituted $ClCNAn^{2-}$ ligand are herein reported. These compounds consist of neutral polymeric 2D networks of the $ClCNAn^{2-}$ ligand alternating with Ln^{III} ions. They form six-membered rings with rectangular cavities, where neighbor layers are eclipsed along the *a* axis (Yb), and a regular honeycomb-like structure, with hexagonal cavities filled by dichloromethane solvent molecules (Nd and Er), where neighbor layers are alternated along the *c* axis. Several interlayer interactions between lanthanide centers and DMF molecules, facing the cavities, are present in all compounds. Free-standing nanosheets, obtained by a top-down strategy involving sonication-assisted solution synthesis and characterized by AFM and HR-TEM, show lateral dimensions in the micrometer scale, thicknesses down to the monolayer, and the presence of lattice fringes. Time-resolved photoluminescence studies performed on both the bulk and nanosheets clearly demonstrate that the $ClCNAn^{2-}$ ligand acts as efficient antenna towards Ln^{III} ions and that the emission sensitization occurs as a multi-step relaxation process involving, in sequence, intersystem crossing and energy transfer from ligand triplet states to the Ln^{III} ions. Effects induced by the exfoliation process on the photophysical properties of the nanosheets are also discussed.

PART II

2.1 INTRODUCTION

Interest in anilate derivatives, has recently been revived because of their ability to construct 2D layered architectures with peculiar physical properties, from organic ferroelectrics,[1–3] purely organic molecular conductors,[4–7] layered magnets[8–12] (including spin-crossover systems) to magnetic conductors.[13–15] Conducting/magnetic Fe^{II}/Fe^{III} mixed-valence MOFs[10,16] and rare examples of conducting 2D iron-quinoid MOFs,[17,18] magnetically ordered up to Tc=105 K,[19] have been recently obtained by Harris et al.. Furthermore these magnetic hybrid CPs, being formed by a 2D anionic network and cations inserted within or between the layers, with interlayer weak van der Waals interactions, can behave as graphene related magnetic materials and the first attempts to successfully exfoliate spin-crossover systems[11,12] and MOFs into individual nanosheets have been reported very recently by Coronado et al.[11] and Gomez et al.,[10] respectively. It should be emphasized that 2D nanomaterials showing sheet-like structures are an emerging class of materials that exhibit unprecedented physical, chemical and optical properties due to their unique 2D structural features and promising applications[20] and the search for materials that can be exfoliated to the monolayer scale represents a hot topic in materials chemistry.

Anilates are scarcely investigated for the construction of lanthanide-based materials with respect to the plethora of ligands used in the classical lanthanide coordination[21] and supramolecular chemistry,[22] in CPs and hybrid materials[23] with strategic applications as OLEDs,[24] biomedical analysis, medical diagnosis and cell imaging.[25] Ligands, in fact, play a crucial role in determining the physical properties of lanthanide complexes since they either can work as antennas for efficient sensitization of the lanthanide-ion luminescence or their electronic properties can influence the magnetic properties of the related highly anisotropic lanthanides-based materials.[26] Since the report of Abrahams et al.[27,28] on a series of $Ln_2(H_2An)_3{\cdot}24H_2O$ (Ln= Ce, La, Yb, Y), a 3D monometallic lanthanoid assembly, $Na_5[Ho(THB)_2]_3{\cdot}7H_2O$), (THB=Tetrahydroxy-benzene),[29] showing peculiar magnetic properties (ferromagnetism with a Curie temperature of 11 K), a $[Ho_2(H_2An)_3(H_2O)_6]{\cdot}18H_2O$[30] 2D honeycombnetwork and a series of i) bimetallic CPs of formula $\{[Nd_2Ln_2(1–x)(H_2An)_3]{\cdot}24H_2O\}_n$ (Ln_2 = Gd, Ce)[31] and ii) 2D monometallic CPs, based on the hydranilate and chloranilate ligands, have been reported[32]. Recently, in our research group synthesized and fully characterized a new heterosubstituted anilate ligand, the ClCNAn, where a simple change of one chloro substituent on the chloranilate with a cyano group affects the electronic properties of the anilate moiety, inducing interesting

luminescence properties in the class of anilate-based ligands and their p- and d- transition metal complexes.[8,33–35] Very recently, new Ln^{III}-containing layered compounds, with general formula $\{[Ln_2(ClCNAn)_3(solv.)_6]\cdot nH_2O\}_n$ (n=0-2), have been reported by Gomez et al.[36] by combining the $ClCNAn^{2-}$ ligand with lanthanides ions (Ln^{III}=Ce, Pr, Yb and Dy) and three different solvents such as H_2O, DMSO and DMF. The role of the Ln^{III} size and the size and shape of the solvent on the crystal structure of the obtained compounds has been discussed in detail. The light-harvesting ability of the $ClCNAn^{2-}$ ligand towards the different lanthanides, especially the NIR emissive Yb^{III} ion, has not been instead studied, even though this ligand, is an interesting candidate for sensitizing efficiently the lanthanide emission since doesn't contain CH or OH groups, the most important IR quenchers. No fundamental studies on 2D layered materials containing the $ClCNAn^{2-}$ ligand and NIR-emissive lanthanides are reported so far, although Er^{III}, Yb^{III} and Nd^{III} complexes show ever-growing interest for their technological applications mainly in telecommunications[37] and biological imaging.[25,38] In this work we report a fundamental study on the synthesis, structural characterization and photophysical studies of 2D layered CPs, formulated as $\{[Ln_2(ClCNAn)_3(DMF)_6]\cdot(DCM)_x\}_n$ (Ln^{III}= Yb (x=0) and Nd, Er (x=2)), obtained by reacting Ln^{III} salts with the KHClCNAn, shown in Chart 1. The ability of the $ClCNAn^{2-}$ ligand to work as a valuable antenna in sensitizing the NIR-emitting Er^{III}, Yb^{III} and Nd^{III} lanthanides is investigated. The aim is to produce stable nanosized sheets by using the well-known top-down strategy involving the traditional sonication-assisted solution exfoliation, starting from fully characterized bulk 2D Neutral NIR-emissive CPs. The obtained 2D nanosheets are characterized by AFM,[39,40] HR-TEM, and continuous-wave transient (Cw/transient) optical spectroscopy. A comparison between the photophysical properties of the CPs as bulk and nanosheets, performed both in EtOH suspension and dropcast on a glass substrate, is also reported.

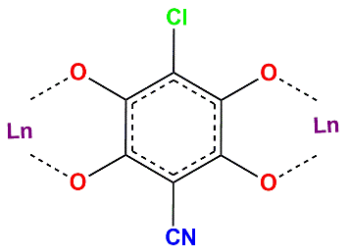

Chart 2.1. Coordination mode of the ligand in compounds 1-3.

2.2 EXPERIMENTAL SECTION

2.2.1 General Remarks

KHClCNAn was synthesized as reported in the literature.[35] Reagents of analytical grade were

purchased from Zentek (TCI) and used without further purification. The solvents, of HPLC grade, were purchased from Thermofisher Scientific Alfa-Aesar.

2.2.2 Synthesis

$[Yb_2(ClCNAn)_3(DMF)_6]_n$ (1) $Yb(NO_3)_3 \cdot 5H_2O$ (0.06 mmol, 26.94 mg) dissolved in 5 mL of DCM and 2 mL of DMF was placed in the bottom of the test tube. KHClCNAn (0.03 mmol, 7.2 mg) in 5 mL of DMF was carefully layered on the top with a blank solution of DMF (1 mL) in between. After three weeks red hexagonal crystals were formed. Crystals were suitable for XRD measurements.

$\{[Ln_2(ClCNAn)_3(DMF)_6] \cdot (DCM)_2\}_n$ (Ln = Nd (2), Er (3)) This compound was synthesized in a similar manner at an identical scale as mentioned for 1, except using $Nd(NO_3)_3 \cdot 5H_2O$ (0.06 mmol, 26.3 mg) for 2 and $Er(NO_3)_3 \cdot 5H_2O$ (0.06 mmol, 26.6 mg) for 3 instead of $Yb(NO_3)_3 \cdot 5H_2O$.

Nanosheets of compounds 1-3 (hereafter 1-NS-3-NS) were fabricated by a top down sonication-assisted liquid exfoliation method. Delamination was achieved by sonicating the dried powder of 1-3 (1 mg) samples in absolute anhydrous ethanol (EtOH, 2 mL) for 20 min at room temperature, according to literature.[41] After centrifugation, the suspensions were further diluted 10 times (100 µl suspension and 900 µl for EtOH) to allow DLS experiments (Malvern ZETASIZER NANO instrument) to fulfill all measurement requirements, even though DLS measurements on the pristine suspensions (1 mg/2 mL) yielded the same results. Undiluted 1-NS-3-NS suspensions in EtOH were deposited by drop-cast onto SiO_2/Si substrates (20 µl), glass substrates (200 µl) and carbon-coated copper grids (5 µl) for AFM, photophysical, and TEM measurements, respectively.

2.2.3 Measurement Details

X-ray Crystallography

Single crystals of the compounds were mounted on glass fiber loops using a viscous hydrocarbon oil to coat the crystal and then transferred directly to the cold nitrogen stream for data collection. Data collection was performed at 150 K on an Agilent Supernova with CuKα (λ = 1.54184 Å). The structures were solved by direct methods with the SIR97 program and refined against all F^2 values with the SHELXL-97 program using the WinGX graphical user interface. All non-hydrogen atoms were refined anisotropically except as noted, and hydrogen atoms were placed in calculated positions and refined isotropically with a riding model. A summary of crystallographic data and refinement results are listed in Table 2.1.

Table 2.1. Crystallographic data for compounds **1-3**.

	1	2	3
Empirical formula	$C_{39}H_{42}Cl_3N_9O_{18}Yb_2$	$C_{41}H_{46}Cl_7N_9O_{18}Nd_2$	$C_{41}H_{46}Cl_7N_9O_{18}Er_2$
Fw	1377.25	1489.50	1535.54
Crystal color	red	red	red
Crystal size (mm3)	0.10 * 0.05 * 0.02	0.10 * 0.05 * 0.03	0.10 * 0.07 * 0.05
Temperature (K)	150.00(10)	150.00(10)	150.00(10)
Wavelength (Å)	1.54184	1.54184	1.54184
Crystal system, Z	Monoclinic, 2	Monoclinic, 4	Monoclinic, 4
Space group	$P2_1/n$	$C2/c$	$C2/c$
a (Å)	9.7317(3)	13.8900(2)	13.7965(4)
b (Å)	13.5934(5)	23.0192(4)	22.5774(8)
c (Å)	19.6218(6)	18.1488(3)	17.9680(8)
α (°)	90	90	90
β (°)	96.451(3)	98.162(2)	98.075(4)
γ (°)	90	90	90
V (Å³)	2579.27(15)	5744.06(16)	5541.3(4)
ρcalc (g.cm-³)	1.773	1.722	1.829
μ(CuKα) (mm-1)	8.629	17.272	9.227
θ range (°)	3.96–73.51	3.74–76.34	3.78–74.01
Data collected	12606	14212	11988
Data unique	5034	5875	5493
Data observed	4160	5653	4820
Number of parameters/restraints	334/6	366/0	373/2
R(int)	0.0425	0.0255	0.0379
R1(F),a I > 2σ(I)	0.0427	0.0427	0.0500
wR2(F2),b all data	0.1224	0.1202	0.1376
S(F2),c all data	1.070	1.107	1.182

[a] $R1(F) = \Sigma\|F_0\|-\|F_C\|/\Sigma|F_0|$; [b] $wR2(F^2) = [\Sigma w(F_0^2-F_C^2)^2/\Sigma wF_0^4]^{1/2}$; [c] $S(F^2) = [\Sigma w(F_0^2-F_C^2)^2/(n+r-p)]^{1/2}$.

Morphological characterization

Nanosheets morphology was investigated by AFM (NT-MDT Smena instrument) operated in noncontact mode using sharp Si tips (NT-MDT ETALON HA_NC). Topography (height) images were analyzed using free software (WSxM 5.0).[42] TEM and HR-TEM images were obtained with a JEM 2010 UHR equipped with a Gatan Imaging Filter (GIF) with a 15 eV window and a 794 slow scan CCD camera.

Photophysical characterization

Continuous-wave (**Cw**) diffuse reflectance ($\boldsymbol{R_d}$) of grinded crystals, regular transmittance ($\boldsymbol{T_r}$) of nanosheet suspensions in EtOH, and total (specular/regular + diffuse) reflectance ($\boldsymbol{R}$)/transmittance ($\boldsymbol{T}$) of dropcast nanosheets were measured using a dual-beam spectrophotometer equipped with an integrating sphere accessory (Agilent Cary 5000 UV-

Vis-NIR). Optical absorptance (***A***) was estimated as 1-$\boldsymbol{R_d}$ for crystals, 1-$\boldsymbol{T_r}$ for nanosheet suspensions, and 1-***R***-***T*** for dropcast nanosheets. Ligand-centered photoluminescence was excited at 370 nm by 200-fs-long pulses delivered by an optical parametric amplifier (Light Conversion TOPAS-C) pumped by a regenerative Ti:Sapphire amplifier (Coherent Libra-HE) running at a repetition frequency of 1 kHz, and measured by a streak camera (Hamamatsu C10910) equipped with a grating spectrometer (Princeton Instruments Acton SpectraPro SP-2300). Lanthanide-centered photoluminescence was excited by a passively Q-switched powerchip laser (Teem Photonics PNV-M02510) delivering 310-ps-long pulses at 355 nm wavelength and 1 kHz repetition rate, wavelength dispersed by a grating spectrometer (Princeton Instruments Acton SpectraPro 2300i), and detected by a NIR array detector (Andor iDus InGaAs 1.7μm) for spectral measurements and a photomultiplier (Hamamatsu H10330A-75) connected to a 1 GHz digital oscilloscope (Tektronik TDS 5104) for time-resolved measurements. 10-mm (1-mm) quartz cuvettes were used for $\boldsymbol{T_r}$ (PL) measurements on nanosheet suspensions.

2.3 RESULTS AND DISCUSSION

2.3.1 Synthesis

ClCNAn^{2-}-based Ln^{III} compounds {[Ln_2(ClCNAn)$_3$(DMF)$_6$](CH_2Cl_2)$_x$}$_n$ (Ln = Yb (1), Nd (2), Er (3)) 1-3 have been synthesized by self-assembling the ClCNAn^{2-} ligand and the Ln^{III} ion as reported in Scheme 2.1. Crystals suitable for XRD were obtained by carefully layering a solution of the KHClCNAn, in DMF onto the top of a solution of the Ln^{III} salts in DCM/DMF mixture.

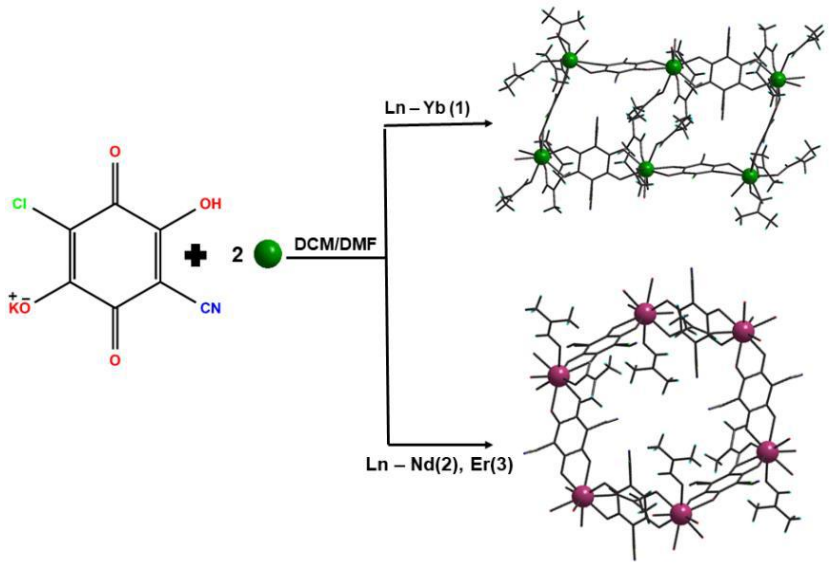

Scheme 2.1

2.3.2 Crystal Structures

Compounds 1-3 are neutral polymeric 2D networks of $ClCNAn^{2-}$ ligand alternating with Ln^{III} ions. Two types of networks can be observed depending on the Ln^{III} ion as shown in Scheme 2.1. The use of Yb^{III} has resulted in a solvent-free 2D network which crystallizes in the monoclinic space group $P2_1/n$, while the Nd^{III} and Er^{III} networks crystallize in the monoclinic space group $C2/c$ and contain one dichloromethane solvent molecule in the cavities of the layers. It is not uncommon in the lanthanides series to obtain different crystalline structures in spite of the similar experimental conditions used, a feature that is generally due to the slight differences between the ionic radii of the lanthanide. The asymmetric unit of 1 consists of one Yb^{III} ion, one and one- half molecules of $ClCNAn^{2-}$ ligand and three DMF molecules giving rise to the formula $[Yb_2(ClCNAn)_3(DMF)_6]_n$ (Figure 2.1a). In the anilate ligand, because of the inversion center, for the half-molecule of $ClCNAn^{2-}$, the chloro and cyano substituents are equally distributed over the same position.

The Yb^{III} ion is nine-coordinated in a slightly distorted monocapped square antiprismatic geometry, completed by six oxygen atoms from three $ClCNAn^{2-}$ ligands and three oxygen atoms from three DMF molecules (Figure 2.1b). Yb−O bond lengths and O−Yb−O angles fall in the range of 2.278−2.514 Å and 66−142°, respectively. The Yb^{III} centres are quite isolated as the shortest Yb···Yb distance is 8.633 Å. The structure shows 2D layers with (6,3) topology where each Yb^{III} ion is connected to three other Yb^{III} ions through bis-bidentate $ClCNAn^{2-}$ ligands forming six-membered rings with rectangular cavities along the *bc* plane (Figure 2.1c-d-e). Neighbor layers are eclipsed along the *a* axis. The coordinated DMF molecules face towards the cavities and towards neighboring layers. This results in a non-negligible overlap of the 2D layers (Figure 2.1d) and in numerous interlayer interactions between the DMF molecules of one layer and the Yb^{III} centers from the neighbor layer. All the interlayer contacts are detailed in Figure 2.2

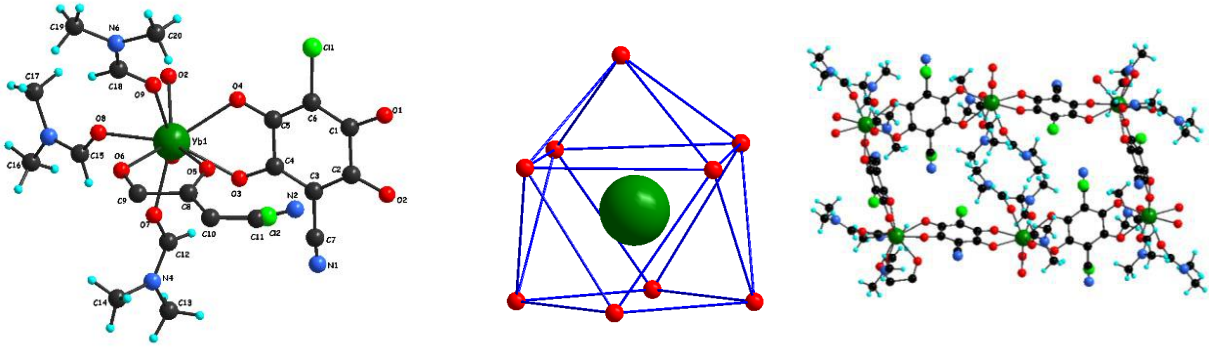

a b c

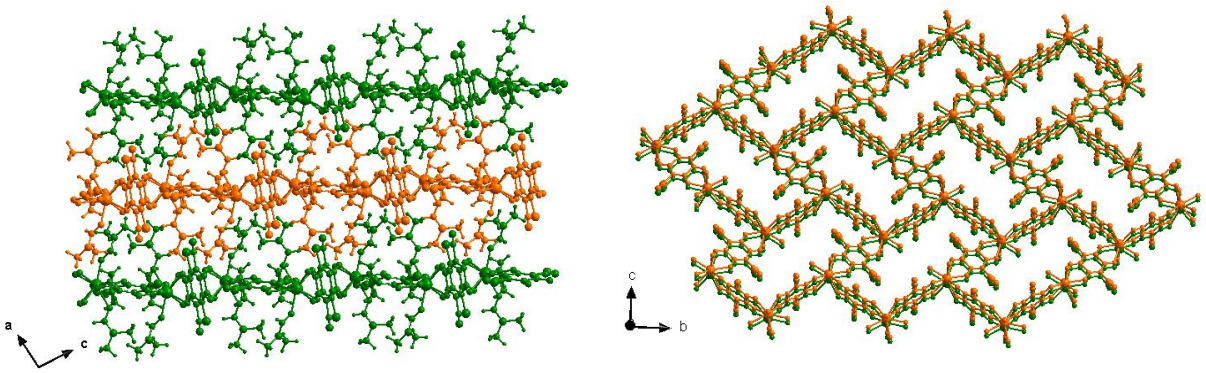

d e

Figure 2.1. Structure of compound 1. (a) Asymmetric unit with atom labelling scheme. (b) Distorted monocapped square antiprismatic coordination geometry of the Yb center. (c) View of one rectangular cavity. (d) View of three consecutive layers in the *ac* plane. (e) View of the eclipsed layers in the *bc* plane. DMF molecules are omitted for clarity. (f) Color code: Yb = green, O = red, Cl = light green, C = black, N = blue and H = cyan. In (d) and (e) different colors are used to represent the different layers.

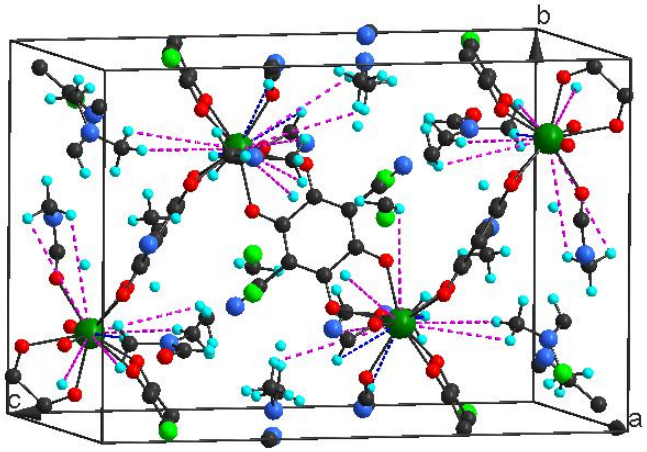

Figure 2.2. Unit cell of the compound 1 showing the H-contacts between Yb^{III} and the C-H oscillators, responsible of the quenching of lanthanide emission. Pink dotted lines are d(Ln^{III}···C-H) within 4-5 Å and blue dotted line corresponds to d(Ln^{III}···C-H) within 3-4 Å.

Compounds 2 and 3 are isostructural, therefore only the structure of 2 is discussed in detail hereafter. The asymmetric unit consists of one Nd^{III} ion, three half-molecules of $ClCNAn^{2-}$ ligand, three DMF molecules coordinated to the Nd^{III} center and one DCM solvent molecule giving rise to the formula $\{[Nd_2(ClCNAn)_3(DMF)_6]\cdot(DCM)_2\}_n$ (Figure 2.3a). The chloro and cyano substituents from the $ClCNAn^{2-}$ ligand are equally distributed over the same position as in 1.

The Nd^{III} ion is nine-coordinated and shows a tricapped trigonal prism geometry, completed

by six oxygen atoms from three ClCNAn^{2-} ligands and three oxygen atoms from three DMF molecules (Figure 2.3b). This different geometry of the Ln^{III} center compared to that of Yb^{III} in compound 1 results in a more regular honeycomb(6,3) topology structure, with hexagonal cavities (Figure 2.3c) filled by dichloromethane solvent molecules (two molecules per formula unit). Consecutive 2D layers are arranged in an alternated way along the *c* axis (Figure 2.3d-e). Nd−O bond lengths and O−Nd−O angles fall in the range of 2.419−2.561 Å and 64−142° respectively. The shortest distance between Nd^{III} centers is 8.93 Å. As in 1, there is an overlap of the 2D layers by the coordinated DMF molecules, and numerous interlayer interactions between Nd^{III} centers and methyl groups from the DMF molecules (see Figure 2.4).

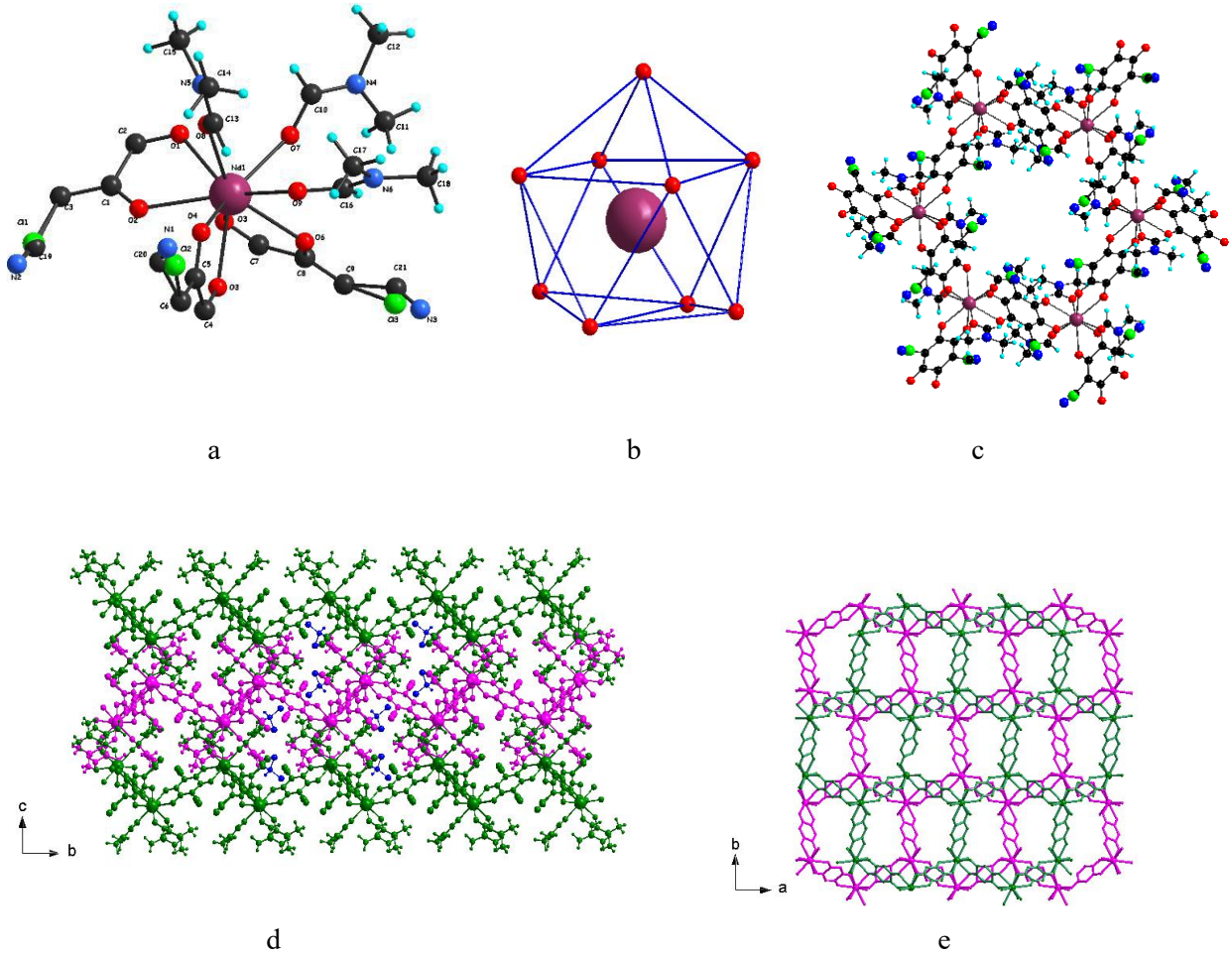

Figure 2.3. Structure of compound 2. (a) Asymmetric unit with atom labelling scheme. (b) Distorted tri-caped trigonal prismatic coordination geometry of the Nd center. (c) View of one hexagonal cavity. (d) View of three consecutive layers in the *ac* plane. Solvent molecules are omitted for clarity. (e) View of the alternated hexagonal layers in the *ab* plane. DMF and solvent molecules are omitted for clarity. Color code: Nd = purple, O = red, Cl = light green, C = black, N = blue and H = cyan. In (d) and (e) different colors are used to represent the different layers.

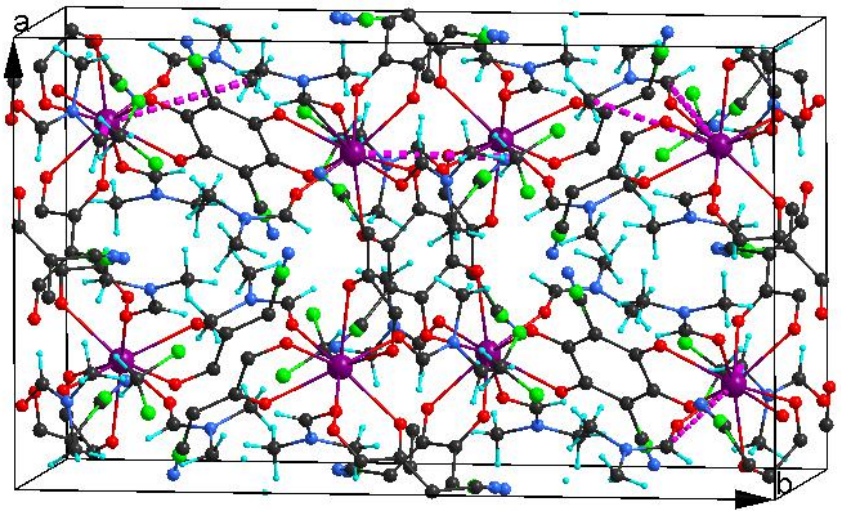

Figure 2.4. Unit cell of the compound 2 showing the H-contacts of $Nd^{III}\cdots$ C-H oscillators, responsible of the quenching of Ln^{III} emission. Pink dotted lines are distance of H and Ln^{III} (d($Nd^{III}\cdots$C-H)) within 3-5 Å.

The two different 2D networks we observed can be explained in terms of different sizes of the lanthanide ion as previously highlighted by Gomez et al..[36] In fact even small changes in the size of Ln^{III} ion play a key role in determining the shape and size of the cavities in compounds' structures. Indeed, despite the fact that the coordination number of the lanthanide ions are the same in the three structures, in compound 1 the Yb^{III} ion (the smallest one in this series) shows a different coordination geometry, which results in a stronger distortion of the cavities in the 2D layers (rectangular cavities) whereas in compounds 2 and 3 the Er^{III} and Nd^{III} adopt the same coordination geometry leading the usual regular honeycomb (6,3) topology structure, with hexagonal cavities.

Because in all compounds the coordinated DMF molecules are overlapped/interpenetrated with the neighbor layers, the overlapping distance has to be considered in order to determine the number of layers from the thickness of the exfoliated sheets. The height of a monolayer (h_0) and the inter-layer distance (d) can be easily calculated from the crystal structure (Figure 2.5). The number of layers ($\boldsymbol{n}$) of a 2D crystal slab of thickness h can thus be calculated as:

$$\boldsymbol{n = 1 + (h - h_0)/d}$$

A summary of these parameters is reported in Table 2.2 for compounds 1-3.

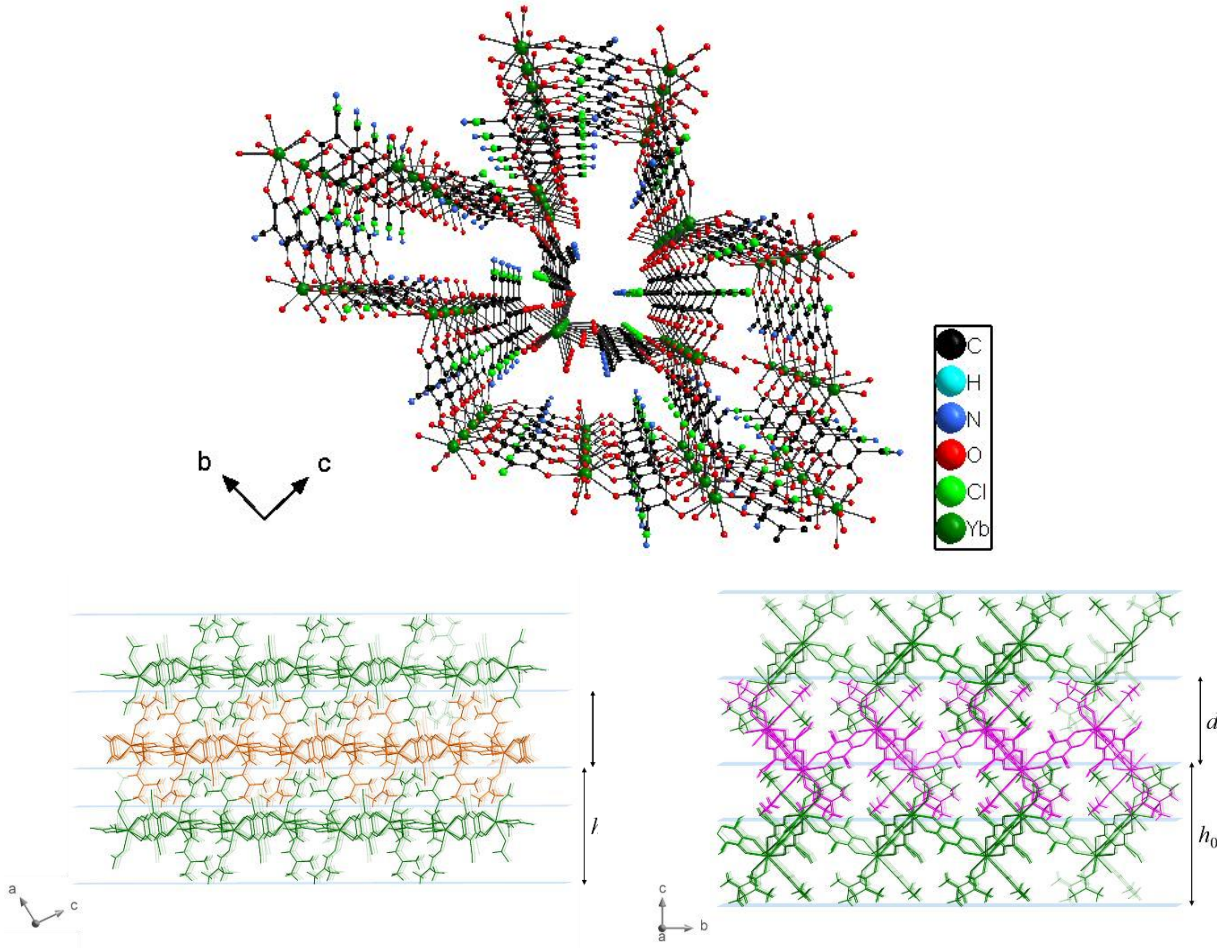

a b

Figure 2.5. Perspective view of 1 in the *bc* plane (top). View of 2D layers showing the thickness of the first monolayer (h_0) and inter-layer distance (d) in 1 (a) and 3 (b).

Table 2.2 Miller indexes of exfoliation plane (Σ), monolayer thickness (h_0) and inter-layer distance (d) of layered compounds 1-3.

Compound	**Σ**	h_0(Å)	d (Å)
1	101	12.39	8.30
2	001	14.83	8.98
3	001	14.48	9.00

2.3.3 Synthesis and Morphological Characterization

Exfoliation of crystals of compounds 1-3 was successfully achieved by a sonication-assisted solution method in different solvents such as acetone, methanol, ethanol and acetonitrile. DLS measurements performed at different times after sonication showed monomodal distributions of the hydrodynamic diameter of the nanosheets, with good stability over several days (Figures 2.6a-c). Stability of the nanosheet suspensions was visually confirmed by the long-

lived observation of Tyndall scattering of laser light (Figure 2.6d).

Morphological characterization of the exfoliated materials was carried out by AFM on 1-3-NS. Figures 2.7a-b display topography (height) scanning images over substrate areas covered with nanosheets of compounds 1 and 3, respectively. Randomly distributed nanosheets with lateral dimensions of up to a few micrometers are clearly evident, for which height profiles are depicted in Figures 2.7c-d. Lateral size of the nanosheets is clearly larger than their hydrodynamic diameter, which is, in fact, proportional through a shape factor to the diameter of the sphere of equal volume as the nanosheets.[43] The nanosheets exhibit a markedly quantized height distribution. According to the values of monolayer thickness and inter-layer distance reported in Table 2.2 and given the limited absolute accuracy (~0.5 nm) in determining the zero height level due to substrate roughness, results are consistent with a thickness distribution ranging from one to four layers. Repeated scans over the same nanosheet resulted in a progressive deterioration of its topography with the emergence of an increasing number of nanoholes as a possible consequence of the sample-tip interaction (Figure 2.8). Collected data clearly demonstrate that the sonication-assisted solution method was effective in providing exfoliation of 1-3 layered compounds down to the monolayer limit.

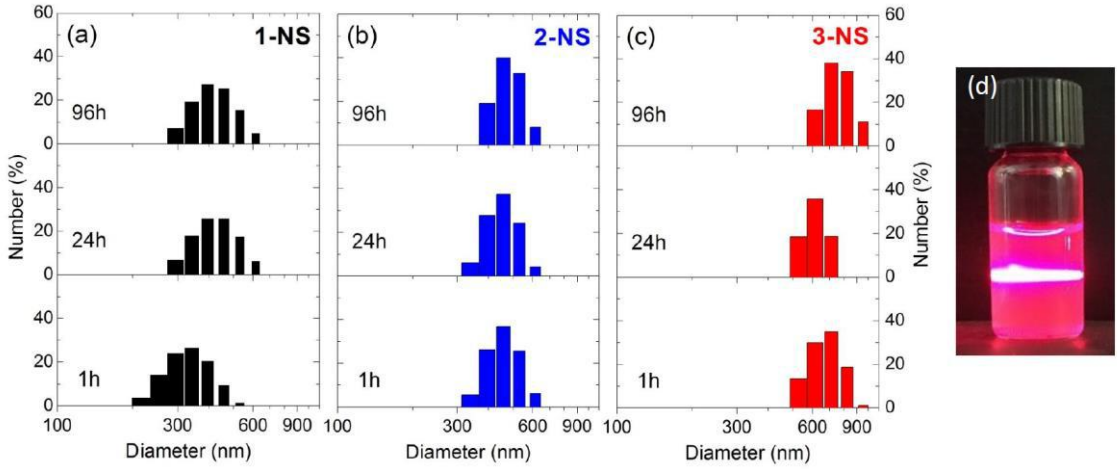

Figure 2.6. Hydrodynamic diameter distributions of 1-NS-3-NS suspensions in EtOH, measured at different times after preparation: (a) 1-NS; (b) 2-NS; (c) 3-NS. (d) Tyndall effect for 1-NS suspension in EtOH.

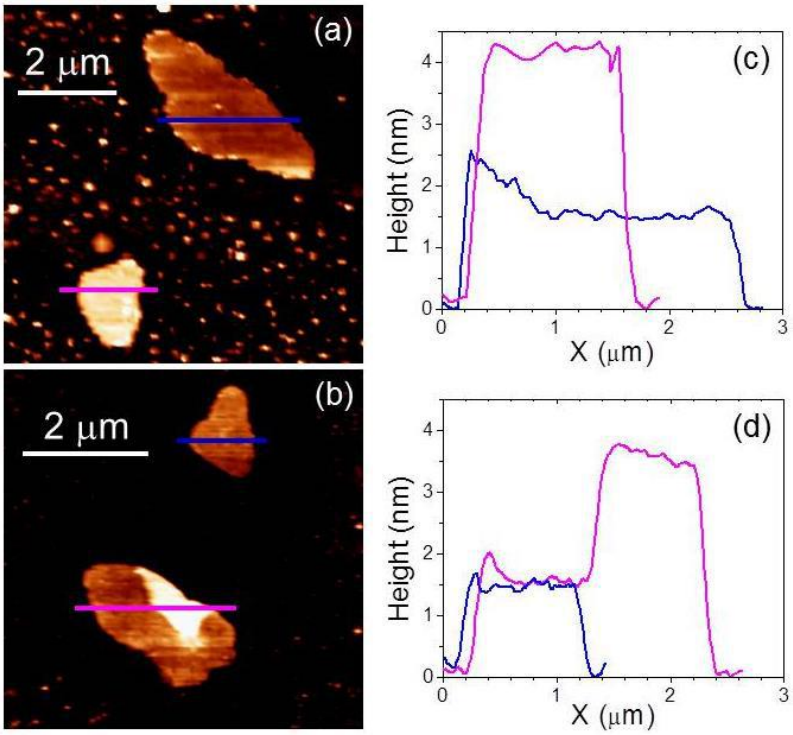

Figure 2.7. AFM characterization of nanosheets of compounds 1 and 3 obtained upon crystal exfoliation using the sonication-assisted method in EtOH solution, deposited on SiO_2/Si substrates. (a) Topography (height) image of nanosheets of compound 1 on a false-color scale. (b) Same as (a) but for compound 3. (c) Height profiles of nanosheets of compound 1 extracted along the lines drawn in panel (a). (d) Same as (c) but for compound 3.

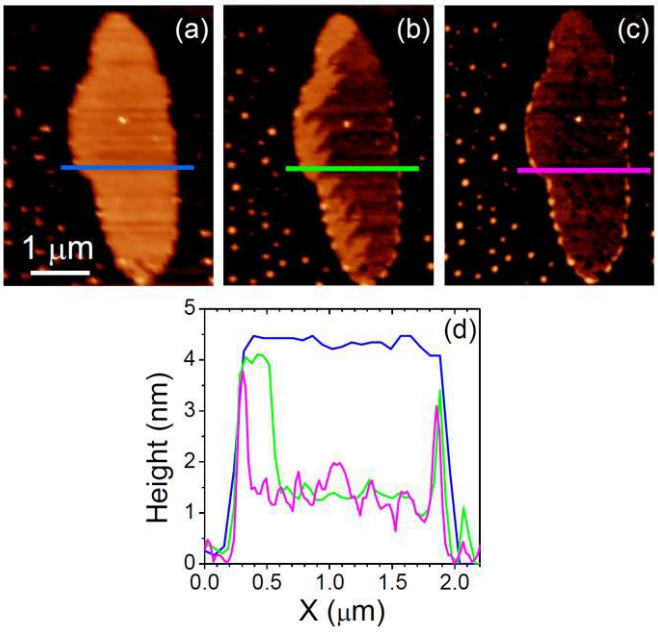

Figure 2.8. AFM topography kinetics for a selected nanosheet of compound 1 obtained by sonication-assisted liquid exfoliation in ethanol and deposited on a SiO_2/Si substrate. Topography

images were acquired in consecutive 10-min-long scans over the same sample area, one to two hours after deposition. (a) First scan; (b) second scan; (c) third scan. (d) Height profiles extracted along the lines drawn in panels (a), (b) and (c).

TEM images confirm the presence of overlapped sheets for both samples (Figure 2.9a-c). The contrast of the TEM images indicates that the layers are very thin. High resolution images for exfoliated compound 1 are reported in Figure 2.9d-f. For compound 1 we were able to observe well defined lattice fringes with interplanar average distances of 2.9 Å and 2.6 Å, which can be ascribed to the (-135) and (-3-15) planes of crystal 1 respectively (Figure 2.10). It is worth noting that due to possible sample degradation under electron beam irradiation, lattice fringes have so far been observed only in a few stable MOFs.[44,45]

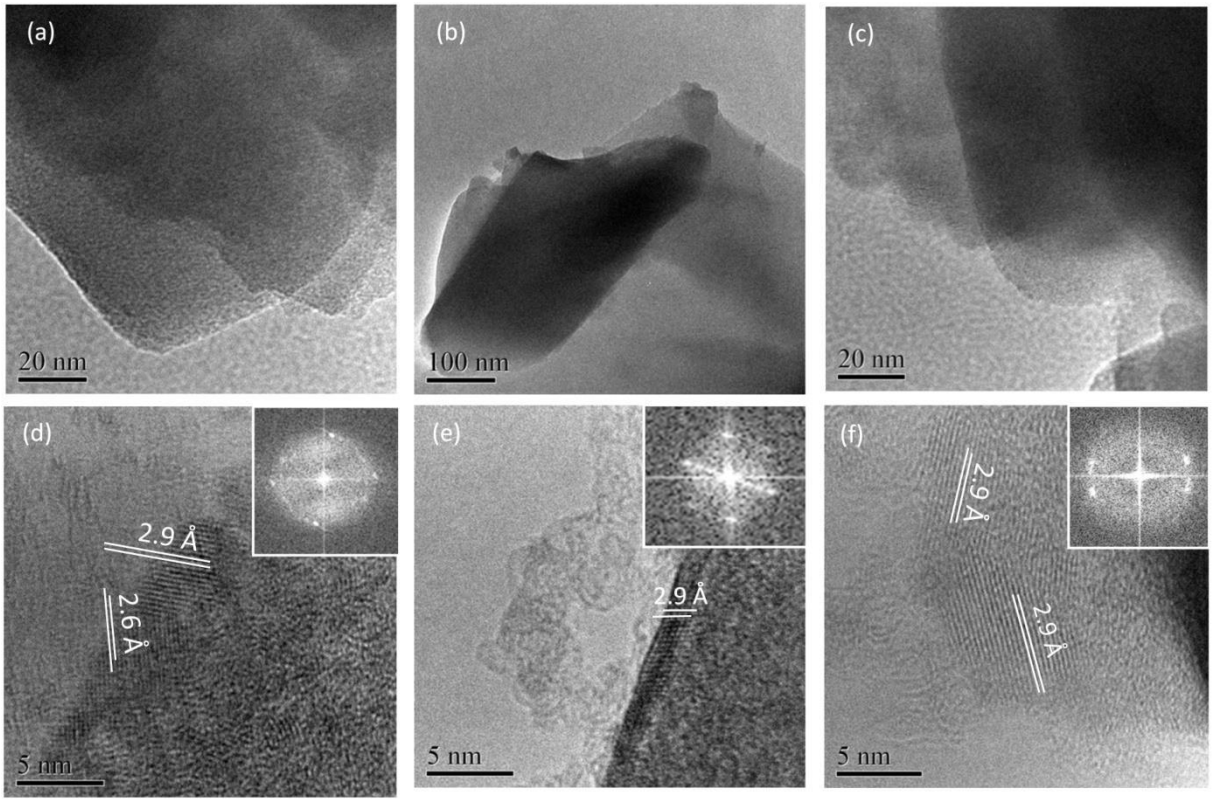

Figure 2.9. TEM images of samples 1 (a-b), 3 (c) and HR-TEM with FFT (inset) of sample 1 (d-f).

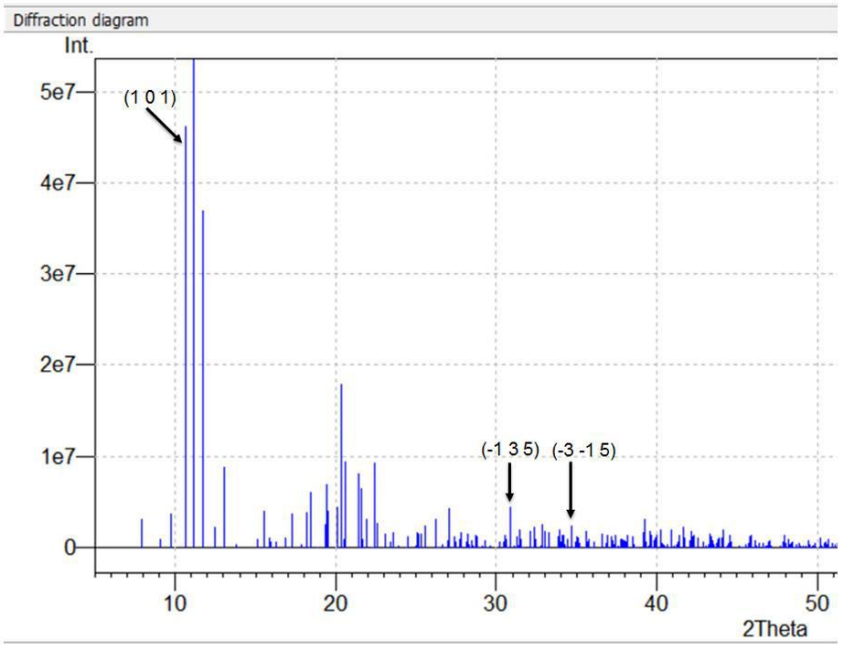

Figure 2.10. Theoretical XRD pattern calculated by CIF data of compound 1.

2.3.4 Photophysical Studies

Crystals of KHClCNAn and of Ln^{III} compounds 1-3 were investigated by absorption and photoluminescence spectroscopy. Cw absorptance spectra are depicted in Figure 2.11a. The absorption onset of the ligand is clearly visible at ~600 nm in KHClCNAn (4) and at ~650 nm in the Ln^{III} compounds. For longer wavelengths, Ln^{III} absorption transitions dominate the spectra.

PL spectroscopy was conducted with near-UV impulse excitation in the near UV above the ligand absorption onset; pulsed excitation enabled acquisition of excited-state lifetimes and emission spectra simultaneously. Given the maximum irradiation energy density of ~300 $\mu J/cm^2$ per pulse used in PL experiments, and assuming that at the pump wavelength, the ligand absorption cross-section yields a molar decadic absorption coefficient no larger than 10^3 $cm^{-1}mol^{-1}dm^3$ in solution,[35] an upper bound of ~2×10^{-3} excited states per ligand per pulse is estimated for the photoexcitation level reached in all compounds, meaning that both the excited-state dynamics and emission spectra were investigated in a regime of linear response.

Time-integrated PL spectra of all compounds are reported in Figure 2.11b. Ligand-centered emission (dots), which was identified based on the KHClCNAn emission band peaked at 650 nm, exhibits a ~50 nm red-shift with respect to the absorption onset in both KHClCNAn and lanthanide compounds. Ln^{III} emission lines peaked at ~980 nm in 1, at ~900, ~1070 and ~1350 nm in 2, and at ~1550 nm in 3 proving that the ligands act as optical antennas towards

the lanthanide ions. The Vis-NIR emission spectrum of 1 under UV photoexcitation shows strong similarities with the one reported very recently for a $ClCNAn^{2-}$-based Yb^{III} compounds.[46]

As shown in Figure 2.11c, the PL emission of KHClCNAn is short-lived, decaying monoexponentially with a characteristic time of 200(10) ps. Because to its short lifetime, the emission is ascribed to singlet radiative recombination, contrary to previous triplet assignment.[36] In the lanthanide compounds, the ligand-centered PL is strongly quenched; its emission lifetime decreases to ~40 ps in 3 and to ~30 ps in 1, while in 2 the ligand recombination dynamics is completely limited by resolution. PL lifetime shortening is attributed to enhanced intersystem (singlet-to-triplet) crossing due to the presence of the Ln^{III} ions, based on the well-known heavy-atom effect,[47] already reported in quinolinolate-based complexes of the same NIR-emissive lanthanides.[48] In lanthanide coordination compounds with organic ligands, enhancement of intersystem crossing can result in efficient sensitization of the Ln^{III} luminescence through energy transfer from the ligand triplet states to the Ln^{III} ions.[21,48] The quantum efficiency of intersystem crossing can be evaluated as $= \mathbf{1} - \boldsymbol{\tau} / \boldsymbol{\tau_0}$, where $\boldsymbol{\tau}$ and $\boldsymbol{\tau_0}$ are the ligand-centered PL lifetimes in the presence and in the absence of the heavy atom, respectively, and $\boldsymbol{\tau_0}$ is well approximated by the PL lifetime of KHClCNAn. A very high efficiency is thus inferred for intersystem crossing in all lanthanide compounds: $\boldsymbol{\eta}$ ~0.8 in 3, ~0.85 in 1 and >0.85 in 2.

Lanthanide-centered emission transients are reported in Figures-2.11d-e. As clearly visible in Figure 2.11d, Ln^{III}) emission sensitization takes place within a few tens of nanoseconds from the impulse excitation. The activation of the Ln^{III} emission exhibits an instantaneous component whose characteristic time is limited by the 1-ns temporal resolution of the NIR PL detection apparatus, superimposed to a delayed component occurring in the time scale of tens of nanoseconds. In compound 3, no instantaneous component is detected, and the time profile can be fitted with a single-component exponential rise function with characteristic time of 16 ns. This time constant is much longer than the 40 ps decay time of the ligand-centered emission, thereby corroborating our understanding of Ln^{III} emission sensitization as a multi-step relaxation process involving, in sequence, intersystem crossing and energy transfer from ligand triplet states to the Ln^{III} ions.

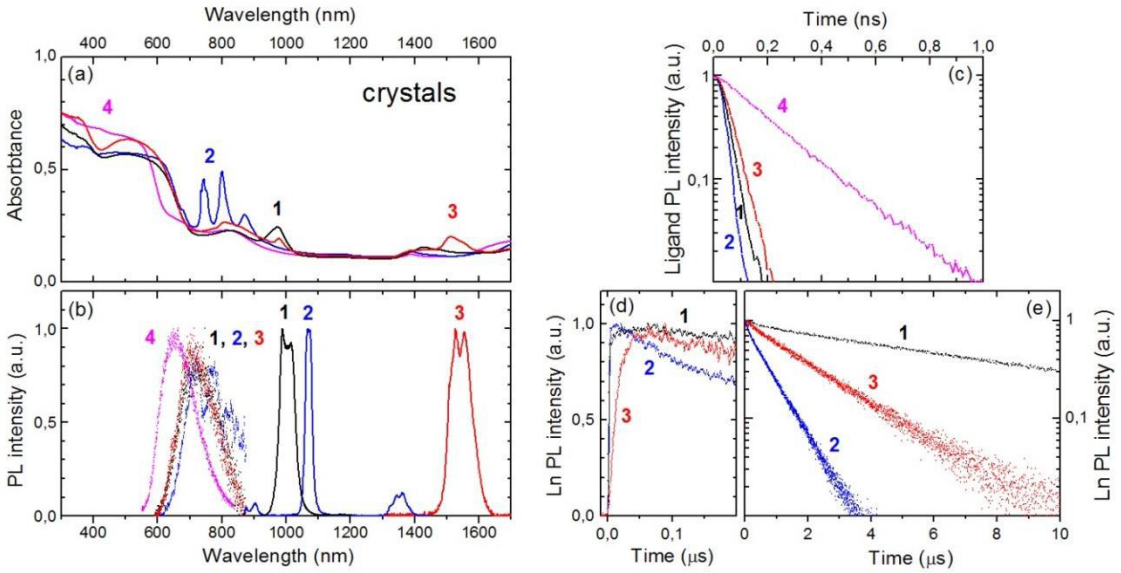

Figure 2.11. Optical absorption and photoluminescence (PL) characterization of crystals of 1-3 [1: Yb^{III} compound, black symbols; 2: Nd^{III} compound, blue symbols; 3: Er^{III} compound, red symbols] and of KHClCNAn (4, magenta symbols). All PL spectra and temporal traces were normalized to unity for better comparison among different compounds. (a) Cw absorptance spectra. (b) PL spectra: Ligand-centered PL (dots); Lanthanide-centered PL (continuous lines). (c) Ligand-centered PL decay transients. (d) Lanthanide-centered PL time traces shown on a 0.2-μs range to highlight PL signal activation. (e) Same as (d) but shown on a 10-μs range to visualize signal decay.

Ln^{III} emission decay occurs in the time scale of a few μs in all Ln^{III} compounds (Figure 2.11e). Nd^{III} and Er^{III} emissions decay monoexponentially with characteristic times of 0.79 and 2.1 μs, respectively, whereas the Yb^{III} emission transient is best fitted by a biexponential decay function with characteristic times of 1.2 and 9.7 μs, having fractional amplitudes of 0.13 and 0.87, respectively. The faster component, most likely arising from a distinct population of excited Yb^{III} ions undergoing more efficient nonradiative deactivation, could in fact be minimized upon careful selection of the photoexcited sample spot. The Ln^{III} excited-state lifetimes in compounds 1-3 are two to three orders of magnitudes shorter than the radiative lifetimes, which span from a fraction of a ms for Nd^{III} [49] and Yb^{III} [46,50] to a few ms for Er^{III}.[51–53] The observed lifetimes were traced back to vibrational deactivation of the Ln^{III} excited states[21,50,54–56] due to presence of the C-H groups of the coordinated (DMF) solvent molecules, lying at distances as short as 3-4 Å from the Ln^{III} ions (Figure 2.2 and 2.4).

Cw absorptance and transient PL measurements of nanosheet suspensions and dropcast nanosheets are reported in Figure 2.12 and Figure 2.13, respectively. In all nanosheet suspensions, absorptance spectra exhibit a strong wavelength dependent background arising

from loss of regular transmittance due to light diffusion (Figure 2.12a). The weak ligand-centered emission of the nanosheet suspensions is spectrally peaked at ~460 nm, occurring, in fact, in the same spectral region as the emission of the ligand anions in diluted EtOH solution, 5 (Figure 2.12b). The ligand-centered emission is still dominated by a fast component with a characteristic time as short as 56 ps (2-NS) and fractional amplitude >0.90 in all compounds (Figure 2.12c). The residual component with small (<0.10) fractional amplitude decays in the time scale of a few nanoseconds (not shown), as also observed in 5. As clearly visible from Figure 2.12b, lanthanide-centered emission spectra were only weakly perturbed by the exfoliation procedure. The activation of the lanthanide-centered emission is instantaneous within the resolution of the NIR PL detection apparatus (Figure 2.12d), while its decay is faster than in the crystals: Ln^{III} PL decay is monoexponential with characteristic time of 0.13 μs for Nd^{III} (2-NS) and biexponential for Yb^{III} (1-NS) and Er^{III} (3-NS) with amplitude-weighted average lifetimes of 0.88 and 0.13 μs, respectively (Figure 2.12e).

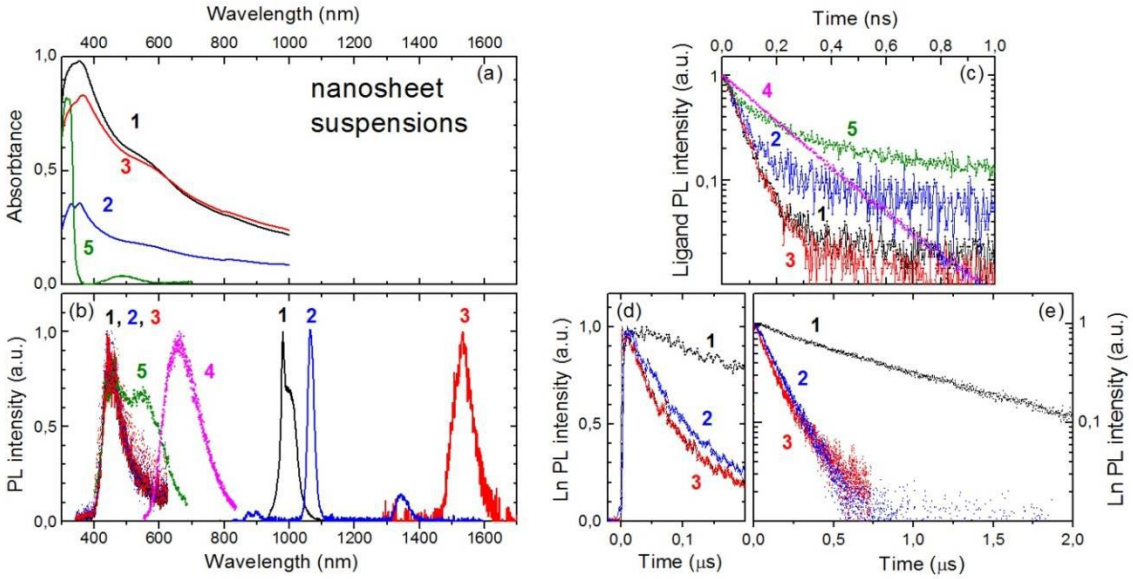

Figure 2.12. Optical absorption and PL characterization of suspensions of 1-NS-3-NS in EtOH. All PL spectra and temporal traces were normalized to unity for better comparison among different compounds. PL spectra and temporal traces of KHClCNAn crystals (4, magenta symbols) and $HClCNAn^{-}/ClCNAn^{2-}$ anions in EtOH solution at 5×10^{-4} mol·dm^{-3} concentration (5, green symbols) are shown for reference. (a) Cw absorptance spectra. (b) PL spectra: Ligand-centered PL (dots); Lanthanide-centered PL (continuous lines). (c) Ligand-centered PL decay transients. (d) Lanthanide-centered PL time traces shown on a 0.2-μs range. (e) Same as (d) but shown on a 2-μs range.

In dropcast nanosheets, absorption artifacts related to light diffusion were eliminated by inferring absorptance from total transmittance and reflectance measurements (Figure 2.13a).

The ligand-centered PL band peaked at ~460 nm is still present, and the red emission band centered at ~680-720 nm is clearly recovered (Figure 2.13b). The initial decay of the ligand-centered emission is nearly resolution-limited across the whole 400-800 nm spectral range both for 1-NS and 3-NS, whereas the red PL band of 2-NS decays monoexponentially with practically the same characteristic time as for KHClCNAn (Figure 2.13c). Further shortening of the Ln^{III} average lifetime down to 0.38 μs was observed for Yb^{III} in 1-NS; conversely, 1.8 and 2.2 fold increases in lifetime with respect to the nanosheet suspension were reported for Nd^{III} in 2-NS and Er^{III} in 3-NS, respectively (Figure 2.13e). A summary of Ln^{III} PL time constants is presented in Table 2.3.

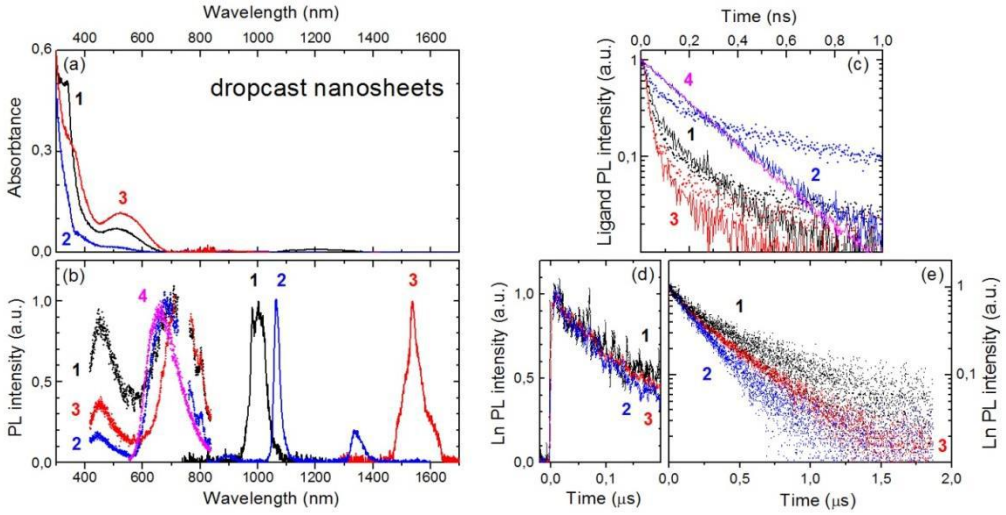

Figure 2.13. Optical absorption and PL characterization of 1-NS-3-NS dropcast onto glass substrates. All PL spectra and temporal traces were normalized to unity for better comparison among different compounds. PL spectrum and temporal trace of KHClCNAn crystals (4, magenta symbols) are shown for reference. (a) Cw absorptance spectra. (b) PL spectra: Ligand-centered PL (dots); Lanthanide-centered PL (continuous lines). (c) Ligand-centered PL decay transients integrated over 400-550 nm and 600-800 nm spectral windows (lines and dots, respectively). (d) Lanthanide-centered PL time traces shown on a 0.2-μs range. (e) Same as (d) but shown on a 2-μs range.

Table 2.3. Ln^{III} PL fractional amplitudes (A_i), time constants (τ_i), and amplitude-weighted average lifetimes (τ) in bulk and exfoliated crystals of 1-3.

Compound	A_1	τ_1 (μs)	A_2	τ_2 (μs)	τ (μs)
1	0.13	1.2	0.87	9.7	8.6
2	1	0.79	-	-	0.79
3	1	2.1	-	-	2.1
1-NS (suspension)	0.20	0.30	0.80	1.03	0.88
2-NS (suspension)	1	0.13	-	-	0.13

3-NS (suspension)	0.82	0.089	0.18	0.31	0.13
1-NS (dropcast)	0.33	0.11	0.67	0.52	0.38
2-NS (dropcast)	1	0.23	-	-	0.23
3-NS (dropcast)	0.41	0.12	0.59	0.41	0.29

The persistence of photophysical signatures of ligand-to-lanthanide coordination, that is, (i) the redshift of the fundamental absorption band, (ii) accelerated decay of ligand-centered emission, and (iii) UV sensitization of the NIR lanthanide emission upon materials sonication are demonstrations of successful exfoliation of these 2D layered CPs. The appearance of the blue emission band as well as the accelerated decay of the Ln^{III} PL in the nanosheets were ascribed to the creation of electronic defect states and nonradiative recombination centers by the exfoliation process. Effects of nanosheet-solvent interaction on the nanosheet emission properties were envisaged. In particular, partial recovery of the $Nd^{III}$and Er^{III} PL lifetimes observed upon nanosheet dropcasting onto the glass and solvent evaporation suggested that the C-H/O-H groups of the solvent molecules can contribute to vibrational quenching of the NIR nanosheet emission in the suspensions, and that the process is reversible. Last, deterioration of the NIR emission performance observed for Yb^{III} in dropcast 1-NS was attributed to nanosheet aggregation and/or nanosheet-substrate interaction effects.

2.4 CONCLUSIONS

A fundamental study of the synthesis, X-ray structure and photophysical properties of a new class of NIR-emissive Ln^{III} (Yb, Nd and Er) neutral 2D CPs, based on the asymmetric $ClCNAn^{2-}$, is reported. The three Ln^{III} ions are nine-coordinated by six oxygen atoms from anilates and three oxygen atoms from DMF molecules, within slightly distorted monocapped square antiprismatic geometry for Yb^{III} and tricapped trigonal prismatic geometry for $Nd^{III}$and Er^{III}. Formation of 2D coordination networks is observed for the three compounds. Exfoliation experiments upon sonication-assisted solution provided suspensions of ultrathin sheets of the materials in the micrometer lateral scale showing a thickness distribution down to the monolayer. It is noteworthy that HR-TEM images of nanosheets of the Yb^{III}-based compound show the presence of lattice fringes, never observed so far in anilate-based CPs and MOFs, showing good stability of the obtained nanosheets under electron-beam irradiation. Photophysical measurements demonstrated that the ligand works as an efficient antenna in sensitizing the Ln^{III} NIR emission both in bulk and nanosheets. Experimental findings hinted at possible exfoliation-induced electronic defects that have an impact on the nanosheet PL performances, while the C-H/O-H groups of the solvent molecules can contribute to

vibrational quenching of the NIR nanosheet emission in the suspensions.

Further studies on this novel class of materials will involve i) the preparation and characterization of nanosheets of these materials by the bottom-up strategy, by using the surfactant-assisted synthesis in order to improve their yield on planar substrates and to tune their thickness and ii) mixed lanthanides neutral CPs showing the same supramolecular architectures, as bulk and nanoparticles, since, noteworthy, these 2D layered CPs show emission bands in the 980-1350 nm spectral region, the so-called biological window and therefore can be envisaged for applications in biology and nanomedicine as luminescent dual-center nanothermometers.[57]

References

(1) Horiuchi, S.; Kumai, R.; Tokura, Y. *J. Am. Chem. Soc.,* **2013**, *135*, 4492–4500.

(2) Horiuchi, S.; Kumai, R.; Tokura, Y. *J. Am. Chem. Soc.,* **2005**, *127*, 5010–5011.

(3) Kagawa, F.; Horiuchi, S.; Minami, N.; Ishibashi, S.; Kobayashi, K.; Kumai, R.; Murakami, Y.; Tokura, Y. *Nano Lett.,* **2014**, *14*, 239–243.

(4) Zaman, M. B.; Toyoda, J.; Morita, Y.; Nakamura, S.; Yamochi, H.; Saito, G.; Nakasuji, K. *Synth. Met.,* **1999**, *102*, 1691–1692.

(5) Yamochi, H.; Nakamura, S.; Saito, G.; Zaman, M. B.; Toyoda, J.; Morita, Y.; Nakasuji, K.; Yamashita, Y. *Synth. Met.,* **1999**, *102*, 1729-1729.

(6) Zaman, M. B.; Toyoda, J.; Morita, Y.; Nakamura, S.; Yamochi, H.; Saito, G.; Nishimura, K.; Yoneyama, N.; Enoki, T.; Nakasuji, K. *J. Mater. Chem.,* **2001**, *11*, 2211–2215.

(7) Ashoka Sahadevan, S.; Monni, N.; Abhervé, A.; Auban-Senzier, P.; Canadell, E.; Mercuri, M. L.; Avarvari, N. *Inorg. Chem.,* **2017**, *56*, 12564–12571.

(8) Mercuri, M. L.; Congiu, F.; Concas, G.; Ashoka Sahadevan, S. *Magnetochemistry*., **2017**, *3*,17-17.

(9) Atzori, M.; Benmansour, S.; Mínguez Espallargas, G.; Clemente-León, M.; Abhervé, A.; Gómez-Claramunt, P.; Coronado, E.; Artizzu, F.; Sessini, E.; Deplano, P.; et al. *Inorg. Chem.,* **2013**, *52*, 10031–10040.

(10) Benmansour, S.; Abhervé, A.; Gómez-Claramunt, P.; Vallés-García, C.; Gómez-García, C. J. *ACS Appl. Mater. Interfaces,* **2017**, *9*, 26210–26218.

(11) Abhervé, A.; Mañas-Valero, S.; Clemente-León, M.; Coronado, E. *Chem. Sci.,* **2015**, *6*, 4665–4673.

(12) Abhervé, A.; Clemente-León, M.; Coronado, E.; Gómez-García, C. J.; Verneret, M. *Inorg. Chem.,* **2014**, *53*, 12014–12026.

(13) Benmansour, S.; Coronado, E.; Giménez-Saiz, C.; Gõmez-García, C. J.; Rößer, C. *Eur. J. Inorg. Chem.,* **2014**, *2014*, 3949–3959.

(14) Atzori, M.; Pop, F.; Auban-Senzier, P.; Gomez-Gacia, C. J.; Canadell, E.; Artizzu, F.; Serpe, A.; Deplano, P.; Avarvari, N.; Mercuri, M. L. *Inorg. Chem.,* **2014**, *53*, 7028–7039.

(15) Atzori, M.; Pop, F.; Auban-Senzier, P.; Clérac, R.; Canadell, E.; Mercuri, M. L.; Avarvari, N. *Inorg. Chem.,* **2015**, *54*, 3643–3653.

(16) Shilov, G. V; Nikitina, Z. K.; Ovanesyan, N. S.; Aldoshin, S. M.; Makhaev, V. D. *Russ. Chemi. Bull., Int. Ed.,* **2011**, *60*, 1209–1219.

(17) Darago, L. E.; Aubrey, M. L.; Yu, C. J.; Gonzalez, M. I.; Long, J. R. *J. Am. Chem. Soc.,* **2015**, *137*, 15703–15711.

(18) Jeon, I. R.; Negru, B.; Van Duyne, R. P.; Harris, T. D. *J. Am. Chem. Soc.,* **2015**, *137*, 15699–

15702.
(19) DeGayner, J. A.; Jeon, I. R.; Sun, L.; Dincă, M.; Harris, T. D. *J. Am. Chem. Soc.,* **2017**, *139*, 4175–4184.
(20) Tan, C.; Cao, X.; Wu, X. J.; He, Q.; Yang, J.; Zhang, X.; Chen, J.; Zhao, W.; Han, S.; Nam, G. H.; et al. *Chem. Rev.,* **2017**, *117*, 6225–6331.
(21) Bünzli, J. C. G. *Coord. Chem. Rev.,* **2015**, *293–294*, 19–47.
(22) Barry, D. E.; Caffrey, D. F.; Gunnlaugsson, T. *Chem. Soc. Rev.,* **2016**, *45*, 3244–3274.
(23) Bünzli, J. C. G. *Eur. J. Inorg. Chem.,* **2017**, *2017*, 5058–5063.
(24) Kuriki, K.; Koike, Y.; Okamoto, Y. *Chem. Rev.,* **2002**, *102*, 2347-2356.
(25) Bünzli, J. C. G. *Chem. Rev.,* **2010**, *110*, 2729–2755.
(26) Pointillart, F.; Le Guennic, B.; Cador, O.; Maury, O.; Ouahab, L. *Acc. Chem. Res.,* **2015**, *48* , 2834–2842.
(27) Abrahams, B. F.; Coleiro, J.; Ha, K.; Hoskins, B. F.; Orchard, S. D. *J. Chem. Soc. Dalt. Trans.*, **2002**, *2*, 1586-1594.
(28) Abrahams, B. F.; Coleiro, J.; Hoskins, B. F.; Robson, R. *Chem. Commun.,* **1996**, *0*, 603–604.
(29) Nakabayashi, K.; Ohkoshi, S. I. *Inorg. Chem.,* **2009**, *48*, 8647–8649.
(30) Nakabayashi, K.; Ohkoshi, S. *Acta Crystallogr. Sect. E Struct. Reports Online,* **2010**, *66*, m1300–m1300.
(31) Demars, T.; Boltoeva, M.; Vigier, N.; Maynadié, J.; Ravaux, J.; Genre, C.; Meyer, D. *Eur. J. Inorg. Chem.,* **2012**, 24, 3875–3884.
(32) Benmansour, S.; Pérez-Herráez, I.; López-Martínez, G.; Gómez García, C. J. *Polyhedron,* **2017**, *135*, 17–25.
(33) Kitagawa, S. *Coord. Chem. Rev.,* **2002**, *224*, 11–34.
(34) Atzori, M.; Marchio, L.; Cle, R.; Serpe, A.; Deplano, P.; Avarvari, N.; Mercuri, M. L. *Dalt. Trans.,* **2014**, *14*, 5938–5948.
(35) Atzori, M.; Artizzu, F.; Marchiò, L.; Loche, D.; Caneschi, A.; Serpe, A.; Deplano, P.; Avarvari, N.; Mercuri, M. L. *Dalt. Trans.,* **201**5, *44*, 15786–15802.
(36) Gómez-Claramunt, P.; Benmansour, S.; Hernández-Paredes, A.; Cerezo-Navarrete, C.; Rodríguez-Fernández, C.; Canet-Ferrer, J.; Cantarero, A.; Gómez-García, C. *Magnetochemistry,* **2018**, *4*, 6-6.
(37) Ye, H. Q.; Li, Z.; Peng, Y.; Wang, C. C.; Li, T. Y.; Zheng, Y. X.; Sapelkin, A.; Adamopoulos, G.; Hernández, I.; Wyatt, P. B.; et al. *Nat. Mater.,* **2014**, *13*, 382–386.
(38) Eliseeva, S. V.; Bünzli, J. C. G. *Chem. Soc. Rev.,* **2010**, *39*, 189–227.
(39) Li, J.-G.; Li, J.; Wang, X.; Zhu, Q.; Li, X.; Kim, B.-N.; Sun, X. *Dalt. Trans.,* **2017**, *46*, 12683–12691.
(40) Araki, T.; Kondo, A.; Maeda, K. *Chem. Commun.,* **2013**, *49*, 552–554.
(41) Xu, H.; Gao, J.; Qian, X.; Wang, J.; He, H.; Cui, Y.; Yang, Y.; Wang, Z.; Qian, G. *J. Mater. Chem. A,* **2016**, *4*, 10900–10905.
(42) Horcas, I.; Fernández, R.; Gómez-Rodríguez, J. M.; Colchero, J.; Gómez-Herrero, J.; Baro, A. M. *Rev. Sci. Instrum.,* **2007**, *78*, 1–9.
(43) Leith, D. *Aerosol Sci. Technol.,* **1987**, *6*, 153–161.
(44) Zhao, M.; Wang, Y.; Ma, Q.; Huang, Y.; Zhang, X.; Ping, J.; Zhang, Z.; Lu, Q.; Yu, Y.; Xu, H.; et al. *Adv. Mater.,* **2015**, *27*, 7372–7378.
(45) Lebedev, O. I.; Millange, F.; Serre, C.; Van Tendeloo, G.; Férey, G. *Chem. Mater.,* **2005**, *17*, 6525–6527.
(46) Hu, J.-Y.; Ning, Y.; Meng, Y.-S.; Zhang, J.; Wu, Z.-Y.; Gao, S.; Zhang, J.-L. *Chem. Sci.,* **2017**, *8*, 2702–2709.
(47) Lower, S. K.; El-Sayed, M. A. *Chem. Rev.,* **1966**, *66*, 199–241.
(48) Quochi, F.; Saba, M.; Artizzu, F.; Mercuri, M. L.; Deplano, P.; Mura, A.; Bongiovanni, G. *J. Phys. Chem. Lett.,* **2010**, *1*, 2733–2737.
(49) Yang, J.; Diemeer, M. B. J.; Sengo, G.; Pollnau, M.; Driessen, A. *IEEE J. Quantum Electron.,* **2010**, *46*, 1043–1050.

(50) Artizzu, F.; Quochi, F.; Saba, M.; Loche, D.; Mercuri, M. L.; Serpe, A.; Mura, A.; Bongiovanni, G.; Deplano, P. *Dalt. Trans.,* **2012**, *41*, 13147-13153.
(51) Quochi, F.; Artizzu, F.; Saba, M.; Cordella, F.; Mercuri, M. L.; Deplano, P.; Loi, M. A.; Mura, A.; Bongiovanni, G. *J. Phys. Chem. Lett.,* **2010**, *1*, 141–144.
(52) Sun, Q.; Yan, P.; Niu, W.; Chu, W.; Yao, X.; An, G.; Li, G. *RSC Adv.,* **2015**, *5*, 65856–65861.
(53) Ye, H. Q.; Peng, Y.; Li, Z.; Wang, C. C.; Zheng, Y. X.; Motevalli, M.; Wyatt, P. B.; Gillin, W. P.; Hernández, I. *J. Phys. Chem. C,* **2013**, *117*, 23970–23975.
(54) Quochi, F.; Orrù, R.; Cordella, F.; Mura, A.; Bongiovanni, G.; Artizzu, F.; Deplano, P.; Mercuri, M. L.; Pilia, L.; Serpe, A. *J. Appl. Phys.,* **2006**, *99*, 4–8.
(55) Tan, R. H. C.; Motevalli, M.; Abrahams, I.; Wyatt, P. B.; Gillin, W. P. *J. Phys. Chem. B,* **2006,** *110*, 24476–24479.
(56) Monguzzi, A.; Milani, A.; Mech, A.; Brambilla, L.; Tubino, R.; Castellano, C.; Demartin, F.; Meinardi, F.; Castiglioni, C. *Synth. Met.,* **2012**, *161*, 2693–2699.
(57) Rocha, J.; Brites, C. D. S.; Carlos, L. D. *Chem. - A Eur. J.,* **2016**, *22*, 14782–14795.

CHAPTER 3

Heteroleptic 2D Coordination Polymers based on Anilate and Carboxylate ligands

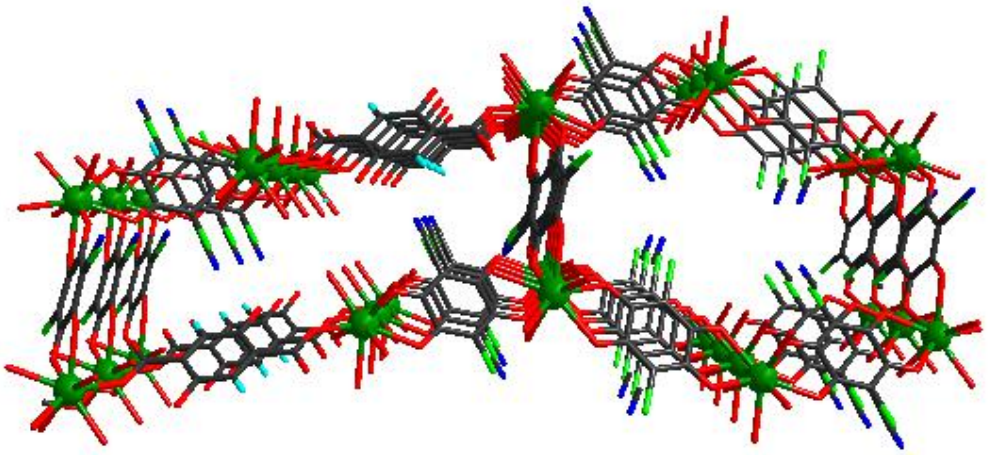

PART II

ABSTRACT

The synthesis, structural characterization and preliminary photophysical studies of 2D layered CPs, formulated as $[Ln_4(ClCNAn)_5(DOBDC)_1(DMSO)_{10}]_n.(DMSO)_2$ (Ln^{III} = Yb (1), Er (2)) and $[Ln_2(ClCNAn)_2(F_4BDC)(DMSO)_6]_n$ (Ln^{III} = Yb (3), Er (4)) based on mixed ligands ($ClCNAn^{2-}$ and carboxylate) are reported. These are 2D neutral polymeric porous networks formed by Ln^{III}, the mixed ligands, $ClCNAn^{2-}$, $DOBDC^{2-}$ and/or $F4BDC^{2-}$ and the DMSO solvent, obtained by using the conventional one-pot synthetic method. Compounds 1-2 form two types of cavities, hexagonal honeycomb cavities formed by Ln1 and $ClCNAn^{2-}$ and rectangular cavities formed by Ln2, $DODBC^{2-}$ and $ClCNAn^{2-}$ due to the presence of two crystallographically independent Ln^{III} ions with different coordination environment. Compounds 3-4 form parallelogram cavities formed by Ln^{III}, F_4BDC^{2-} and $ClCNAn^{2-}$. Preliminary Photophysical studies show that these ligands act as efficient antennas towards Ln^{III} ions.

PART II

3.1 INTRODUCTION

MOFs and CPs, have been an attractive field of current investigation due to their promising applications[1,2] in wide areas of gas adsorption[1] and storage,[3] luminescence,[4] chemical separation, catalysis,[5] and biomedicine.[6] Their crystalline frameworks holding intriguing structures depend mainly on the linkers/ligands used. Among the different organic linkers for the construction of MOFs, carboxylates, especially dicarboxylates, are the most popular ones, due to their versatile coordination modes depending on the metal ions. For example, BDC have been used for synthesis of some of the most frequently studied MOFs, like MOF-5,[7] MIL-53,[89] MIL-100,[10,11] *etc.* and for luminescent MOFs[12,13]and DOBDC has been used as a ligand for the synthesis of the M_2(m-dobdc) and M_2(dobdc) (M = Mn, Fe, Co, Ni) series of MOFs, showing BET surface area ranging from 1102 m^2/g (Mn_2(dobdc) to 1349 m^2/g (Mn_2(m-dobdc)[14] and [$Ln_2(DOBDC)_3(DMF)_4$]DMF[15] (Ln = La,Ce, Pr, Nd, Gd) with Ln^{III} ions[13]. Lanthanide MOFs/CPs,[4,13] hereafter Ln-MOFs, are of great interest for their practical applications as OLEDs,[16] biomedical analysis, sensors and cell imaging.[17] However, it is known that Ln^{III} centers cannot efficiently absorb light due to forbidden 4f–4f transitions. A strategy for the sensitization of Ln-MOFs is to incorporate chromophores as ligands, acting as antennas for absorption and then energy transfer to the Ln^{III} centers (antenna effect).[13,18] Numerous studies report on the use of π-conjugated organic molecules as efficient antenna ligands, in the synthesis of photo luminescent materials.[13,19,20] Recently, fluorinated linkers has attracted increasing attention, as these compounds are supposed to show enhanced adsorption properties[21–24] as well as improved luminescence[25] compared to CPs with typical organic ligands due to the fact that C–H vibrational quenching, which is typically an IR quencher, is not present in F_4BDC.[26] F_4BDC is also scarcely investigated as MOF linker and few series of Ln-CPs/MOFs are reported such as [$Ln(F_4BDC)_{1.5}(H_2O)_n$]·mH_2O}n (Ln = Ce – Yb, n=2, m=1; Ln = Pr and Nd, n= 1, m=2),[26] [$Ln(F_4BDC)(NO_3)(sol)_2$]·G (Ln^{III} = Eu, Gd, Tb, Ho, Tm, sol = DMF; Ln^{III} = Ho, Er and Tm, sol = DMSO) and [$Ln(F_4BDC)(CH_3COO)(FA)_3$]·3FA, ($Ln^{III}$ = Sm, Eu, FA = formamide).[27]

The ability of anilate derivatives to construct 2D layered architectures with lanthanides[28–32] and the light-harvesting capability of the ClCNAn^{2-} ligand towards these NIR emissive (Er^{III}, Yb^{III} and Nd^{III}) CPs,[33] [$Ln_2(ClCNAn)_3(DMF)_6$]·$(DCM)_x$}$_n$ (Ln^{III} = Yb (x = 0), Nd, and Er (x = 2)) are already been discussed in Chapter 2. Therefore in order to enlarge the family of anilate-based lanthanide MOFs/CPs the use of an ancillary ligand along with the anilate linker

would be advisable in order to achieve more robust supramolecular frameworks and/or improved luminescent properties.

Here we report a series of heteroleptic 2D layered CPs formulated as $[Ln_4(ClCNAn)_5(DOBDC)_1(DMSO)_{10}]_n.(DMSO)_2$ (Ln^{III} = Yb (1), Er (2)) and $[Ln_2(ClCNAn)_2(F_4BDC)(DMSO)_6]_n$ (Ln^{III} = Yb (3), Er (4)) obtained by the self-assembly of Ln^{III}, $ClCNAn^{2-}$, $DOBDC^{2-}$ or $F4BDC^{2-}$ by using conventional one-pot synthetic methods. The role of the mixed ligands on the Ln-MOFs/CPs supramolecular architectures will be investigated and a preliminary study of their photophysical properties will be reported.

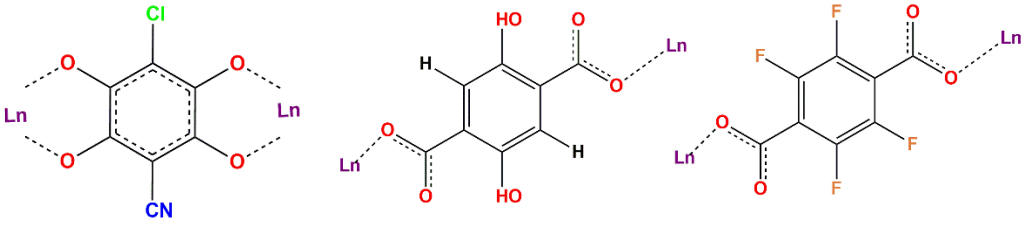

Mode I Mode II

Chart 3.1. Coordination modes of $ClCNAn^{2-}$, $DOBDC^{2-}$, F_4-BDC^{2-}

3.2 EXPERIMENTAL SECTION

3.2.1 Materials and Methods

KHClCNAn was synthesized as reported in the literature.[34] Reagents of analytical grade were purchased from Zentek (TCI) and used without further purification. The solvents, of HPLC grade, were purchased from Thermofisher Scientific Alfa-Aesar.

3.2.2 Synthesis

$[Yb_4(ClCNAn)_5(DOBDC)_2(DMSO)_{10}]_n.(DMSO)_2$ (1) An aqueous solution (5 mL) of $YbCl_3 \cdot 5H_2O$ (230 mg, 0.6 mmol) was added dropwise to an aqueous yellow solution (35 mL) of DOBDC (60 mg, 0.3 mmol) and NaOH (60 mg, 1.5 mmol) solution. KHClCNAn (72 mg, 0.3 mmol) was added to the mixture showing an immediate colour change from yellow to red. After *ca*. 4h of stirring at 90°C, the mixture was allowed to cool to room temperature, and the purple precipitate insoluble in water and in almost organic solvents was separated from the mother liquor by filtration, washed several times with fresh water and dried under vacuum. Compound 1 was recrystallized in DMSO to give after several weeks orange crystals suitable for X-ray analysis. Yield: 70%. From the reaction filtrate were obtained two more types of crystals corresponding to two complexes of formula $[Yb(HClCNAn)_2(H_2O)_4]Cl \cdot xH_2O$ (1a) and $[Yb_2(DOBDC)_2(H_2O)_{10}(\mu\text{-}ClCNAn)]Cl_2$ (1b).

$[Er_4(ClCNAn)_5(DOBDC)_1(DMSO)_{10}]_n.(DMSO)_2$ (2). This compound was synthesized in

a similar manner to 1, using $Er(NO_3)_3 \cdot 5H_2O$ (230 mg, 0.6 mmol) instead of $YbCl_3 \cdot 5H_2O$.

$[Yb_2(ClCNAn)_2(F_4BDC)(DMSO)_6]_n$ (3) This compound was synthesized in a similar manner to 1, using F_4BDC (60 mg, 0.3 mmol) and NaOH (60 mg, 1.5 mmol) instead of DOBDC.

$[Er_2(ClCNAn)_2(F_4BDC)(DMSO)_6]_n$ (4) This compound was synthesized in a similar manner to 3, using $Er(NO_3)_3 \cdot 5H_2O$ (230 mg, 0.6 mmol) instead of $YbCl_3 \cdot 5H_2O$.

3.2.3 Measurement Details

X-ray Crystallography.

Single crystals of the compounds were mounted on glass fiber loops using a viscous hydrocarbon oil to coat the crystal and then transferred directly to the cold nitrogen stream for data collection. Data collection was performed at 150 K on an Agilent Supernova with CuKα (λ = 1.54184 Å). The structures were solved by direct methods with the SIR97 program and refined against all F2 values with the SHELXL-97 program using the WinGX graphical user interface. All non-hydrogen atoms were refined anisotropically except as noted, and hydrogen atoms were placed in calculated positions and refined isotropically with a riding model. A summary of crystallographic data and refinement results are listed in Table 3.1.

Table 3.1. Crystallographic data for compounds 1-4

	1	**2**	**3**	**4**
Empirical formula	$C_{63}H_{74}Cl_5Yb_4N_5O_{38}S_{12}$	$C_{67}H_{76}Cl_5Er_4N_5O_{38}S_{12}$	$C_{34}H_{36}Cl_2Ybr_2F_4N_2O_{18}S_6$	$C_{67}H_{76}Cl_4Er_4F_8N_4O_{36}S_{12}$
Fw	2809.44	2790.34	1445.34	2860.94
Crystal color	orange	orange	red	red
Crystal size (mm3)	0.3*0.25*0.15	0.10 * 0.05 * 0.03	0.05 * 0.03 * 0.01	0.05 * 0.03 * 0.01
Temperature (K)	150	293	150	150
Wavelength (Å)	1.54184	1.54184	1.54184	1.54184
Crystal system, Z	Triclinic, 6	Triclinic, 2	Triclinic, 1	Triclinic, 1
Space group	P-1	P-1	P-1	P-1
a (Å)	9.3113(3)	9.3113(3)	9.2044(3)	9.1849(3)
b (Å)	10.7084(3)	10.7084(3)	9.8156(4)	9.7764(3)
c (Å)	24.9514(12)	24.9514(12)	14.7964(6)	14.8035(5)
α (°)	91.141(3)	91.141(3)	104.062(4)	103.718(3)
β (°)	100.381(4)	100.381(4)	93.533(3)	93.278(3)
γ (°)	90.467(3)	90.467(3)	107.249(4)	107.223(3)
V (Å³)	2446.50(16)	2446.50(16)	1225.47(8)	1221.78(8)
ρcalc (g.cm-³)	1.907	1.894	1.959	1.950
μ(CuKα) (mm-1)	11.172	10.469	12.258	10.361
θ range (°)	3.60-73.72	3.60–77.03	3.11-73.64	3.10-73.34
Data collected	19755	17423	8261	8509

Data unique	9522	9369	4703	4732
Data observed	7013	8558	4243	4541
R(int)	0.0568	0.0284	0.1409	0.0266
Nb of parameters / restraints	677/20	79/0	334/17	319/0
R1(F),a I > 2σ(I)	0.0619	0.0589	0.1042	0.0318
wR2(F2),b all data	0.1795	0.1528	0.2759	0.0880
S(F2),c all data	1.037	1.021	1.167	1.115

$^{a}R1(F) = \Sigma||F_0|-|F_C||/\Sigma|F_0|$; $^{b}wR2(F^2) = [\Sigma w(F_0^2-F_C^2)^2/\Sigma wF_0^4]^{1/2}$; $^{c}S(F^2) = [\Sigma w(F_0^2-F_C^2)^2/(n+r-p)]^{1/2}$.

Photophysical characterization.

Continuous-wave (Cw) diffuse reflectance (Rd) of ground crystals were measured using a dual-beam spectrophotometer equipped with an integrating sphere accessory (Agilent Cary 5000 UV−vis−NIR). The optical absorptance (fraction of absorbed irradiance, A) was estimated as 1 − Rd for crystals. Ligand-centered photo- luminescence was excited at 370 nm by 200 fs long pulses delivered by an optical parametric amplifier (Light Conversion TOPAS-C) pumped by a regenerative Ti:sapphire amplifier (Coherent Libra-HE) running at a repetition frequency of 1 kHz and measured by a streak camera (Hamamatsu C10910) equipped with a grating spectrometer (Princeton Instruments Acton SpectraPro SP-2300). Lanthanide- centered photoluminescence was excited by a passively Q-switched powerchip laser (Teem Photonics PNV-M02510) delivering 310 ps long pulses at a 355 nm wavelength and a 1 kHz repetition rate, wavelength dispersed by a grating spectrometer (Princeton Instruments Acton SpectraPro 2300i), and detected by a NIR array detector (Andor iDus InGaAs 1.7 μm) for spectral measurements and a photomultiplier (Hamamatsu H10330A-75) connected to a 1 GHz digital oscilloscope (Tektronik TDS 5104) for time-resolved measurements; 10 mm (1 mm) quartz cuvettes were used for Tr (PL).

3.3 RESULTS AND DISCUSSION

3.3.1 Synthesis

Compounds 1-2 were obtained by one-pot reaction of DOBDC, KHClCNAn, NaOH and Ln^{III} salts in water (Scheme 3.1), and the obtained solid was recrystallized in DMSO to get crystals suitable for X-Ray analysis. Compounds 3-4 were obtained by using F_4-BDC instead of DOBDC. The compounds $[Ln_4(ClCNAn)_5(DOBDC)_1(DMSO)_{10}]_n.(DMSO)_2$ (Ln- Yb (1), Er (2)) and $[Ln_2(ClCNAn)_2(F_4\text{-}BDC)(DMSO)_6]_n$ (Ln- Yb (3), Er (4)) are neutral polymeric 2D porous networks. Two more compounds were obtained from the mother liquor: a monomeric complex with Yb^{III} with $ClCNAn^{2-}$ of formula $[Yb(HClCNAn)_2(H_2O)_4]Cl\cdot xH_2O$

(1a) and a dimer with Yb^{III}, $ClCNAn^{2-}$ and DOBDC of formula $[Yb_2(DOBDC)_2(H_2O)_{10}(\mu\text{-}ClCNAn)]Cl_2$ (1b).

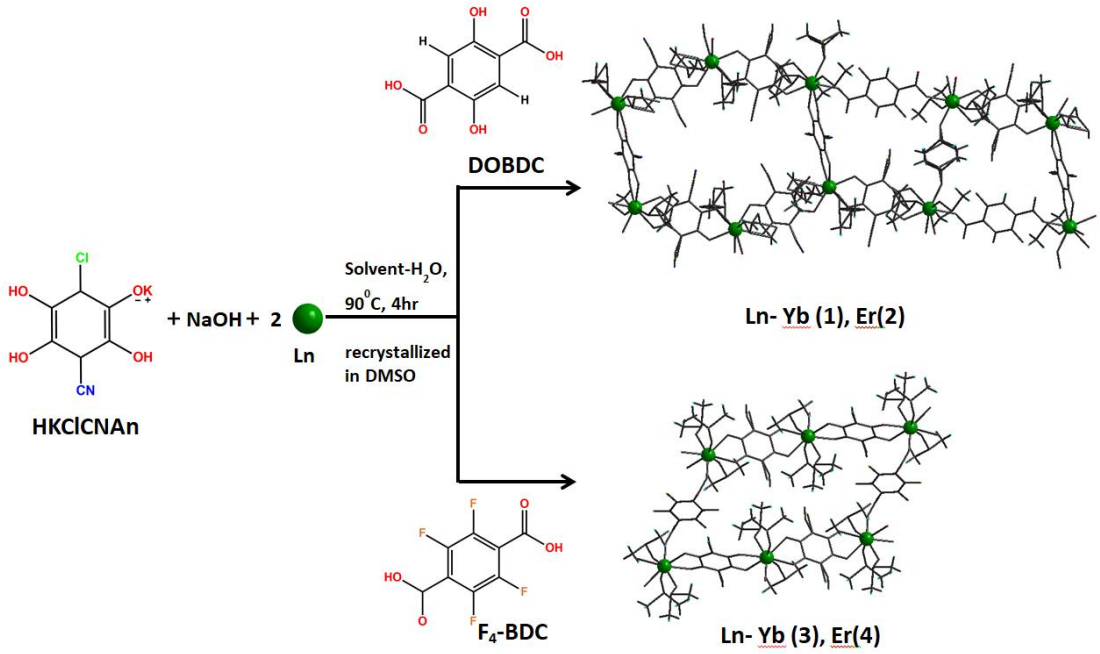

Scheme 3.1: General reaction scheme for the synthesis.

	$ClCNAn^{2-}$	
	$DOBDC^{2-}$	F_4BDC^{2-}
Yb(III)	**1**	**3**
Er(III)	**2**	**4**

3.3.2 Crystal Structures

Compounds 1-4 are 2D neutral porous CPs formed by Ln^{III} (Yb and Er) with mixed ligands, $ClCNAn^{2-}$, $DOBDC^{2-}$ and F_4BDC^{2-}. Since X-Ray crystal analysis of compounds 1-2 shows that they are isostructural, only the structure of compound 1 is discussed. Both compounds 1-2 crystallize in the triclinic *P*-1 space group. The asymmetric unit of 1 consists of two Yb^{III} ions, one $ClCNAn^{2-}$ ligand bridging two Yb^{III}, three half molecules of $ClCNAn^{2-}$, one half molecule of $DOBDC^{2-}$, five coordinated DMSO molecules and one non-coordinated DMSO solvent molecule giving rise to a 2D network of formula $[Yb_4(ClCNAn)_5(DOBDC)_1(DMSO)_{10}]_n\cdot(DMSO)_2$. The coordination modes of the two ligands $ClCNAn^{2-}$ and $DOBDC^{2-}$ are different. The $ClCNAn^{2-}$ ligands are coordinated to Ln^{III} in a bis-1,2 bidentate mode (Mode I), while the $DOBDC^{2-}$ are coordinated to Ln^{III} through a bis-monodentate mode (Mode II) as shown in Chart 3.1. Due to the inversion centre, in the anilate ligands the chloro and cyano substituents are disordered and equally distributed over two positions. S atoms

from the DMSO solvent molecules are disordered.

The coordination environment of the two independent Yb^{III} ions is different, depending on the coordinated ligand (Figure 3.1a). Yb1 ion is coordinated to eight oxygen atoms, four from two $ClCNAn^{2-}$ ligands, one from the $DOBDC^{2-}$ ligand and three from coordinated DMSO molecules, overall forming a Yb1O8 coordination environment with a distorted trigonal dodecahedron geometry. Yb2 ion is coordinated to eight oxygen atoms, six from three $ClCNAn^{2-}$ ligands and two from coordinated DMSO molecules, resulting in significantly distorted trigonal dodecahedron geometry (Figure 3.1b). Yb–O bond lengths and O–Yb–O angles are in the range 2.228 (7)-2.395(7) Å and 66–144°, respectively. The Yb^{III} centres are quite isolated as the shortest Yb1···Yb1, Yb2···Yb2 and Yb1···Yb2 distances are 11.507, 8.590 and 8.587 Å respectively.

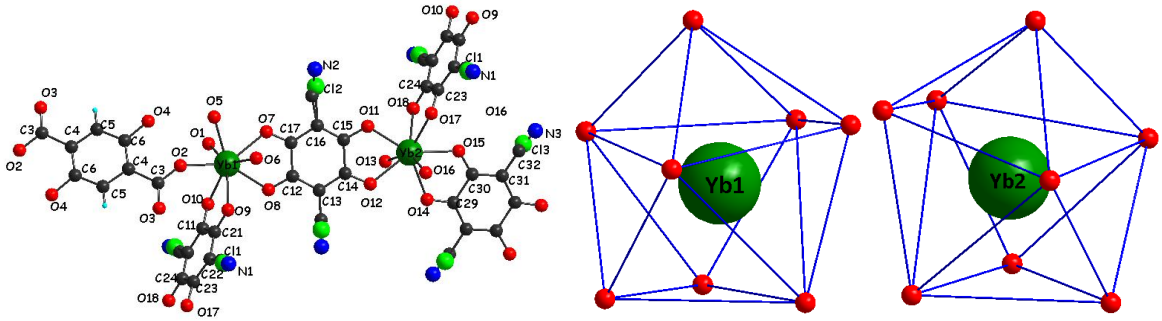

Figure 3.1. (a) The coordination environment of Yb^{III} centres in 1 with atom labelling scheme. Solvent molecules are omitted for clarity. (b) Distorted square antiprismatic coordination geometry of the two crystallographically independent Yb centres (Yb1 and Yb2).

In 1, $Yb(ClCNAn)_n$ zig-zag chains are formed by $ClCNAn^{2-}$ ligand bridging adjacent Yb1 and Yb2 along *b* axis (Figure 3.2 a). $ClCNAn^{2-}$ and $DOBDC^{2-}$ ligands are alternatively linked to these 1D chains to give a 2D $Ln(ClCNAn)_n$ layer along the *bc* plane, forming hexagonal cavities (noted as I, Figure 3.2 b) and rectangular cavities (noted as II, Figure 3.2 c) respectively. The layers are eclipsed along the *a* axis (Figure 3.2 d).

These 2D layers shows ladder-like arrangement (Figure 3.2c, down) with (6,3)-2D topology (see footnote in section 1.2.1), where each Yb1 ion is connected to three other Yb1 ions through bisbidentate $ClCNAn^{2-}$ ligands forming six-membered rings with hexagonal cavities (cavity I) filled with one DMSO solvent molecule. The different coordination mode of the $DOBDC^{2-}$ gives rise to larger rectangular cavities (cavity II) formed by six Yb ions, four $ClCNAn^{2-}$ and two $DOBDC^{2-}$ (Figure 3.2 f). In the *bc* plane, these cavities are alternatively arranged in the same layer. The coordinated DMSO molecules face towards the cavities and towards neighboring layers (Figure 3.3). This results in a non-negligible overlap of the 2D

layers and in numerous interlayer interactions between the DMSO molecules from one layer and the Yb^{III} centers from the neighboring layer.

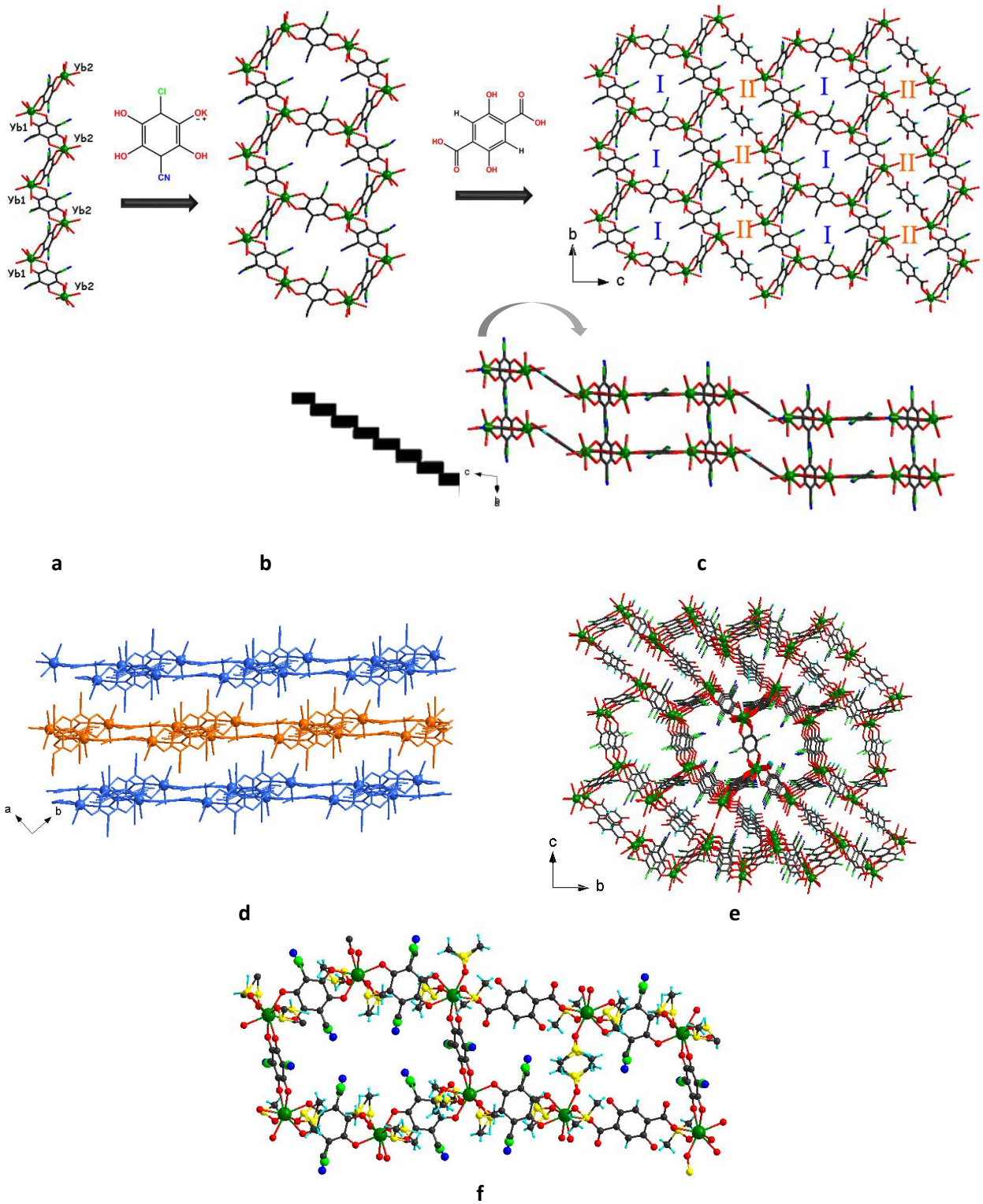

Figure 3.2. a) $Yb(ClCNAn)_n$ chain along *b* axis. (b) 2D $Ln(ClCNAn)_n$ sheet along *bc* plane (c) View of the 2D layers in the *bc* plane.(d) View of three consecutive layers in the *ab* plane with each layers coloured different. DMSO molecules are omitted for clarity. e) Perspective view along *a* axis f) View

of one hexagonal and rectangular cavities. Color code: Yb = green, O = red, Cl = light green, C = black, N = blue and H = cyan.

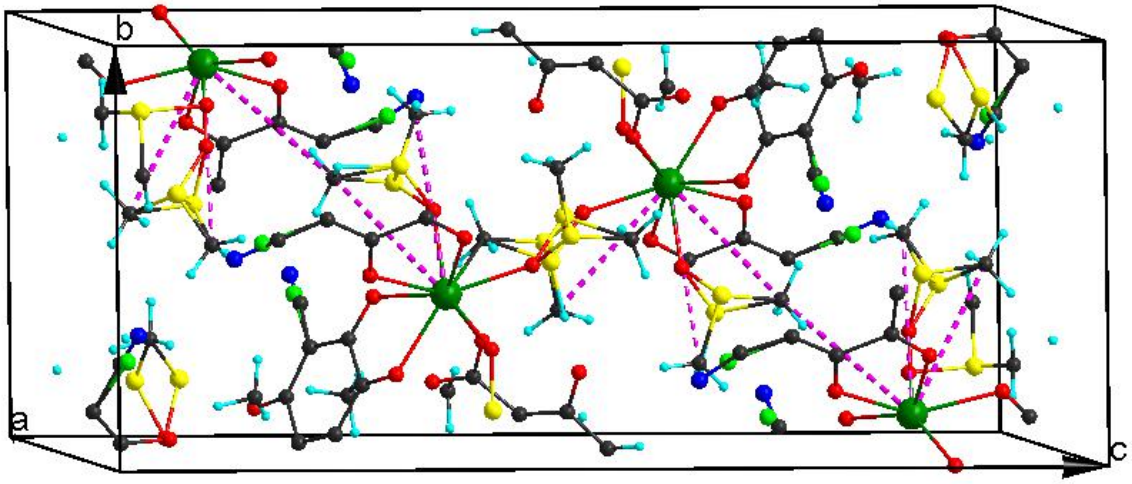

Figure 3.3. Unit cell showing the H contacts of Yb^{III}•••C-H oscillators, responsible of the quenching of Ln^{III} emission. Pink dotted lines are distance of H and Ln^{III} (d(Yb^{III}•••C-H)) within 4-5 Å.

Compound 1a crystallizes in the monoclinic *C*2/*m* space group. The asymmetric unit contains one half molecule of Yb^{III} ion, one $HClCNAn^-$ ligand, four half molecules of coordinated water molecules, one half molecule of Cl^- anion and two and half solvent water molecules giving rise to the $[Yb(HClCNAn)_2(H_2O)_4]Cl{\cdot}5H_2O$ formula. The $HClCNAn^-$ ligand is coordinated in the 1,2 bidentate coordination mode (Figure 3.4a). The Yb^{III} ion is coordinated to four oxygen atoms from two anilate ligands and four oxygen from four H_2O molecules and shows trigonal dodecahedron geometry (Figure 3.4b).

Compound 1b crystallizes in the triclinic *P*-1 space group. The asymmetric unit contains one Yb^{III} ion, one $DOBDC^-$ ligand, half molecule of $ClCNAn^{2-}$, five coordinated water molecules and one Cl^- anion giving rise to the formula $[Yb_2(DOBDC)_2(H_2O)_{10}(\mu\text{-}ClCNAn)]Cl_2$. The $ClCNAn^{2-}$ ligand is coordinated in the bis-1,2 bidentate coordination mode as in 1, while $DOBDC^-$ is coordinated in a monodentate coordination mode (Figure 3.4c). The chloro and cyano substituents from the $ClCNAn^{2-}$ are disordered and equally distributed over the two positions as in compound 1. The Yb^{III} ion is coordinated to eight oxygen atoms, two from $ClCNAn^{2-}$ ligand, one from $DOBDC^{2-}$ and four from H_2O molecules and shows a distorted square antiprismatic coordination geometry (Figure 3.4d).

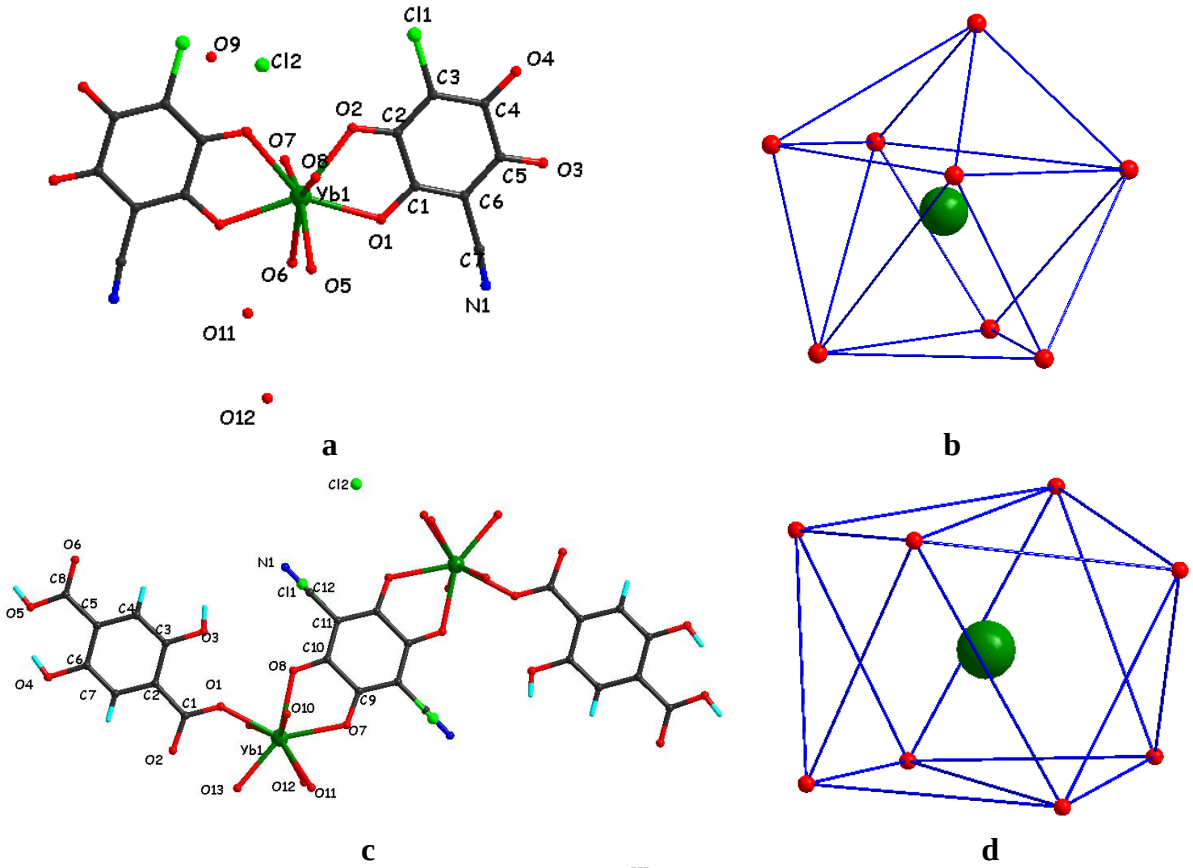

Figure 3.4. (a) The coordination environment of Yb^{III} centres in 1a with atom labelling scheme. (b) trigonal dodecahedron geometry of Yb^{III} centre in 1a. (c) The coordination environment of Yb^{III} centres in 1b with atom labelling scheme (d) Distorted square antiprismatic coordination geometry of Yb^{III} centre in 1b.

Compounds 3-4 crystallize in the triclinic *P*-1 space group. Since both compounds are isostructural, only the structure of 3 is described. The asymmetric unit of 3 contains one Yb^{III} ion, two half molecules of $ClCNAn^{2-}$, one half molecule of F_4BDC^{2-} and three coordinated DMSO solvent molecules giving rise to a 2D network of formula $[Yb_2(ClCNAn)_2(F_4BDC)_1(DMSO)_6]_n$ (Figure 3.5a). The coordination mode of the two ligands is the same as in compounds 1-2. The $ClCNAn^{2-}$ ligand is coordinated in the bis-1,2 bidentate coordination mode while F_4BDC^{2-} is coordinated through bis-monodentate coordination mode. The chloro and cyano substituents from the $ClCNAn^{2-}$ ligand are disordered and equally distributed over the two positions as in 1.

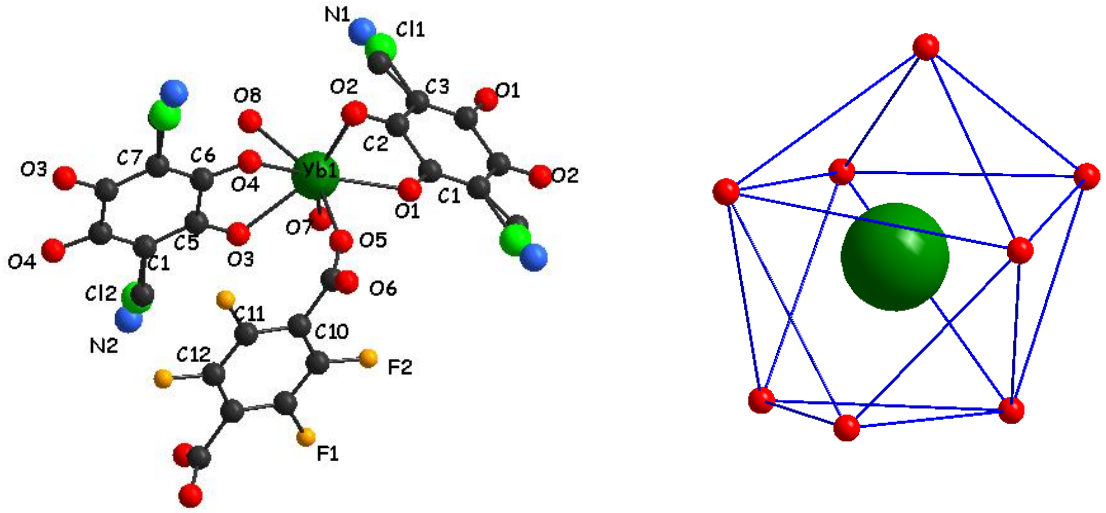

Figure 3.5. (a) The coordination environment of Yb^{III} centres in 3 with atom labelling scheme. Solvent molecules are omitted for clarity. (b) trigonal dodecahedron geometry of Yb^{III} centre in 3.

Yb^{III} ion is coordinated to eight oxygen atoms, six from three $ClCNAn^{2-}$, one from F_4BDC^{2-} and three from DMSO molecules, showing trigonal dodecahedron geometry (Figure 3.5b). Yb−O bond lengths and O−Yb−O angles are in the range 2.191(7) − 2.409(7) Å and 66−147°, respectively. The shortest distance between Yb^{III} centers is 8.596 Å.

Yb^{III} ions are linked to $ClCNAn^{2-}$ ligands to generate infinite chains in *bc* plane. These chains are linked to F_4BDC^{2-} ligands to finally form a 2D slanted grid-like layer with parallelogram cavities ((6, 3)-2D topology, (see footnote in section 1.2.1)) (Figure 3.6b top). In the *ac* plane, $ClCNAn^{2-}$ and F_4BDC^{2-} ligands are eclipsed forming wave-like layers (Figure 3.6b down). The 2D layers are eclipsed along the *a* axis (Figure 3.6d).

As in 1, there is a small overlap of the 2D layers by the coordinated DMSO molecules, with intralayer interactions between Yb^{III} centers and methyl groups from the DMSO molecules (Figure 3.7).

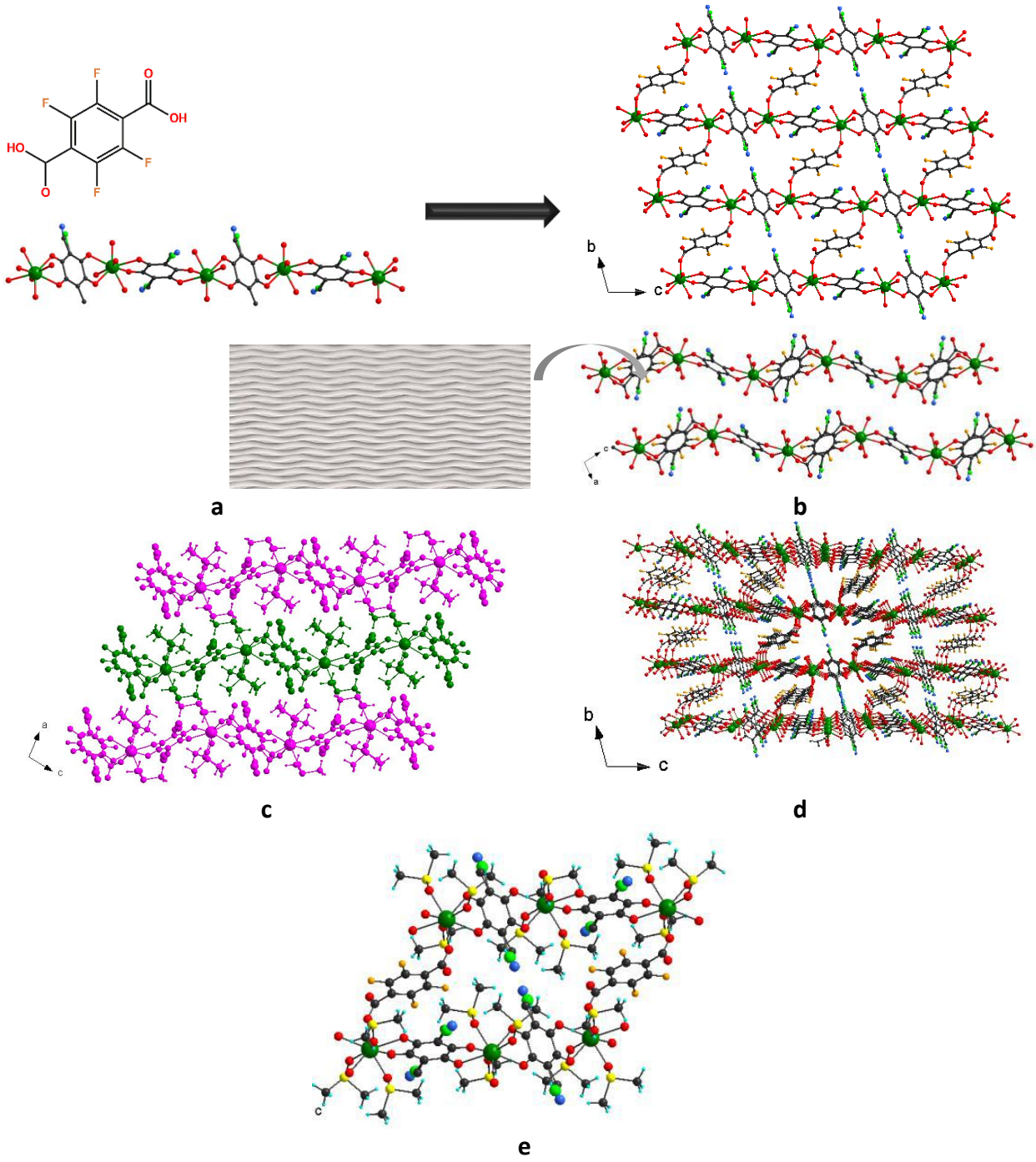

Figure 3.6. a) $[Yb(ClCNAn)]_n$ chain along *c* axis. b) View of the 2D layers in the *bc* plane. c) View of three consecutive layers in the *ac* plane with different colours. d) Perspective view along *a* axis e) View of one parallelogram cavity. Color code: Yb = green, O = red, Cl = light green, C = black, N = blue and H = cyan.

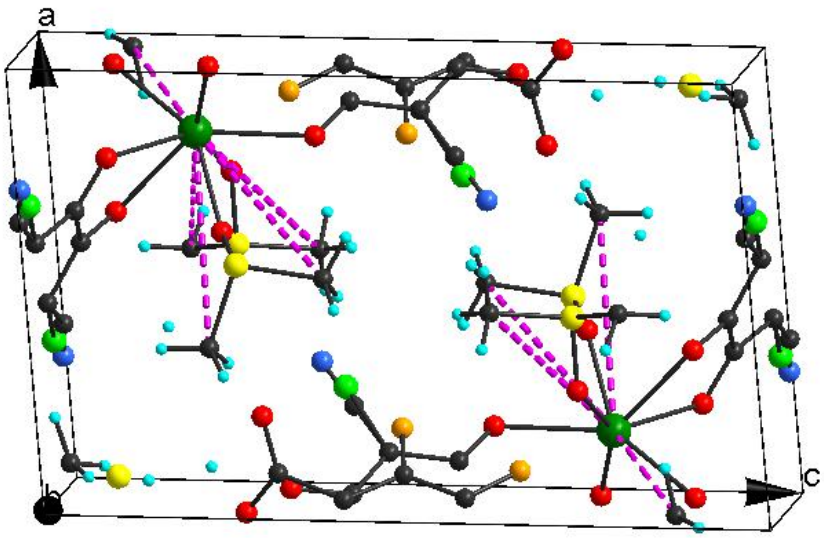

Figure 3.7. Unit cell showing the H contacts of Yb^{III}•••C-H oscillators, responsible of the quenching of Ln^{III} emission. Pink dotted lines are distance of H and Ln^{III} (d(Yb^{III}•••C-H)) within 4-5 Å.

Even though the ratio Ln^{III} salt/$ClCNAn^{2-}$/carboxylate ligand in the reaction is 2:1:1, the formula ratios are 2:2.5:0.5 for 1-2 and 2:2:1 for 3-4 respectively, indicating that the anilate ligand has a stronger affinity towards Ln^{III} than the carboxylate ligand.

Despite the fact that the coordination modes of $DOBDC^{2-}$ and F_4BDC^{2-} are the same, the shape of the 2D layers is different. In the case of $DOBDC^{2-}$, there are two crystallographically independent Ln^{III} ions with different coordination geometries and therefore two types of cavities inside the 2D layer: hexagonal honeycomb cavities formed by Ln1 and $ClCNAn^{2-}$ and rectangular cavities formed by Ln2, $DODBC^{2-}$ and $ClCNAn^{2-}$. With F_4BDC^{2-}, there is only one independent Ln^{III} ion and one type of cavity formed by Ln^{III}, F_4BDC^{2-} and $ClCNAn^{2-}$ resulting in parallelogram cavities.

3.3.3 Photophysical Studies

Crystals of compounds 1−4 were investigated by absorption and photoluminescence spectroscopy. Cw absorptance spectra are depicted in Figure 3.8a. The absorption onset of the ligand in the Ln^{III} compounds 1-4 is clearly visible at ~650 nm, showing a red shift from free ligand KHClCNAn ~600 nm.[33] It is difficult to differentiate the contribution from individual ligands as a broad peak is observed. For longer wavelengths, Ln^{III} absorption transitions dominate the spectra.

Ligand-centered emission in UV-visible spectra of compounds 1-4 is shown in Figure 3.8b (dots), identified on the basis of the ligand emission band that peaked at ~700 nm and exhibiting a ~50 nm red-shift with respect to the absorption onset in lanthanide compounds,

clearly indicate that the ligands act as optical antennas toward the Ln^{III} ions. The small spikes in the spectra ~720 nm and ~810 nm are ascribed to residual room light. Lanthanide-centered transient emissions are reported in Figure 6c. Ln^{III} emission decay occurs on the time scale of a few microseconds in all compounds (Figure 3.8c). These emissions decay monoexponentially with characteristic times of 11.1, 2.6, 0.57 and 3.83 μs for 1-4 respectively. The observed lifetimes of these compounds are not much different from homoleptic compounds (Yb^{III} 9.7 μs and Er^{III} 2.1 μs) described in Chapter 2, due to the presence of the C−H quenchers of the methyl groups of the coordinated (DMSO) solvent molecules, being as little as 4−5 Å away from the Ln^{III} ions. These are preliminary photoluminescence measurements; more measurements are required for a better understanding. As perspective, visible spectra will be repeated in quartz substrates in order to avoid background emission from the glass substrates and thin layers of drop-cast nanosheets of these compounds may allow us to distinguish the absorption bands of the individual ligands.

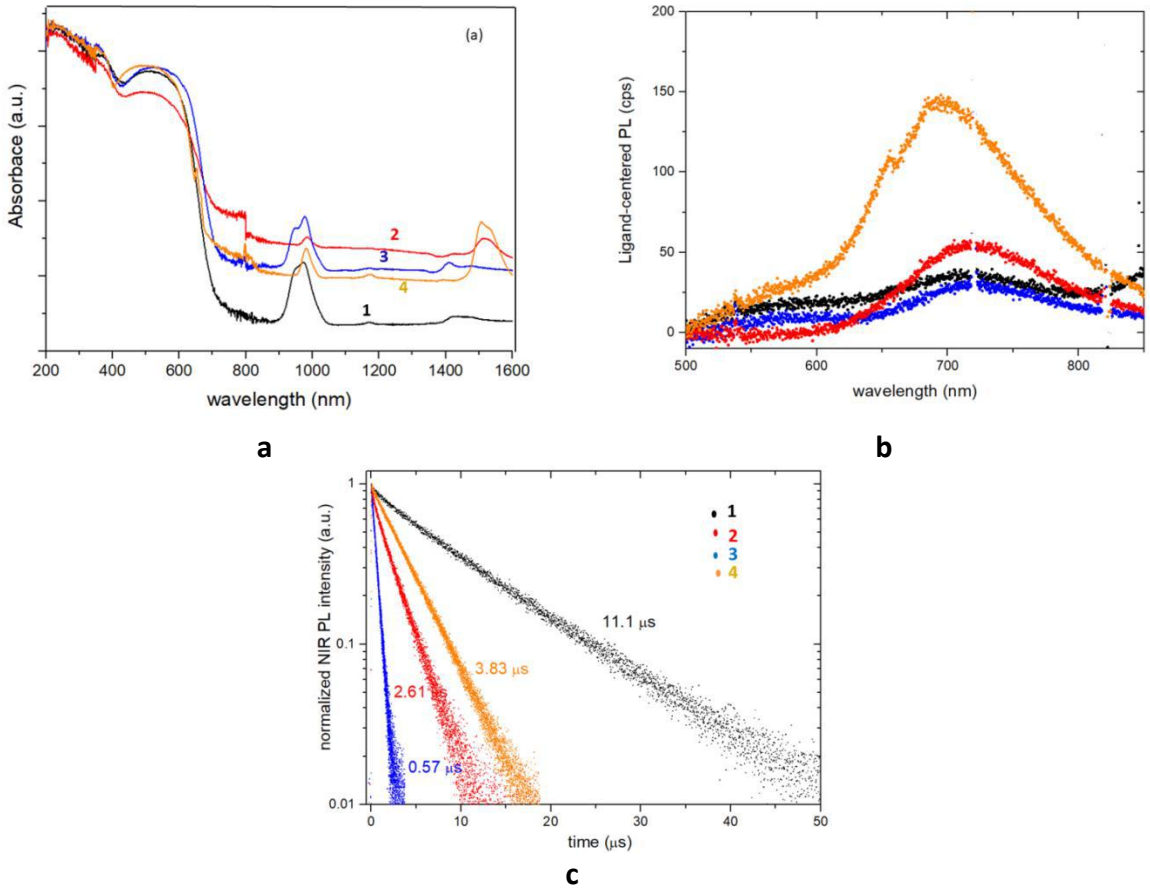

Figure 3.8. Optical absorption and PL characterization of crystals of 1−4 [1, Yb^{III}-ClCNAn/DOBDC compound, black symbols; 2, Er^{III}-ClCNAn/DOBDC compound, red symbols; 3, Yb^{III}-ClCNAn/F_4BDC compound, blue symbols; 4, Er^{III}-ClCNAn/ F_4BDC compound, orange symbols] (a)

Cw absorptance spectra (b) PL spectra: ligand-centered PL (dots) (c) Lanthanide-centered PL time traces shown over a 50 μs range to visualize signal decay.

3.4 CONCLUSIONS

A new series of heteroleptic NIR emisive lanthanide MOFs/CPs $[Ln_4(ClCNAn)_5(DOBDC)_1(DMSO)_{10}]_n.(DMSO)_2$ (Ln^{III} - Yb (1), Er (2)) and $[Ln_2(ClCNAn)_2(F_4BDC)(DMSO)_6]_n$ (Ln^{III} - Yb (3), Er (4)) with mixed ligands ($ClCNAn^{2-}$ and carboxylate ligands ($DOBDC^{2-}$, F_4BDC^{2-}) were prepared. The two Ln^{III} ions are eight-coordinated with two crystallographically independent Ln^{III} ions showing two different coordination environments: a distorted trigonal dodecahedron geometry for Ln1 (eight oxygen atoms, four from two $ClCNAn^{2-}$ ligands, one from the $DOBDC^{2-}$ ligand and three from coordinated DMSO molecules) and a more significantly distorted trigonal dodecahedron geometry for Ln2 (eight oxygen atoms, six from three $ClCNAn^{2-}$ ligands and two from coordinated DMSO molecules). Compounds 3-4 form a distorted trigonal dodecahedron geometry, being coordinated by six O from three $ClCNAn^{2-}$, one from F_4BDC^{2-} and three from DMSO molecules, showing only one coordination environment. This series represent the first family of heteroleptic lanthanide MOFs/CPs based on anilate and carboxylate ligands. Preliminary photophysical studies show that these ligands act as efficient antennas towards Ln^{III} ions, with Ln^{III} emissions decay monoexponentially with characteristic times of 11.1, 2.6, 0.57 and 3.83 μs for 1-4 respectively.

Further studies of this series involve: (i) photophysical studies in the visible region in order to investigate the capability of the individual ligands to work as valuable antennas; (ii) the preparation and full characterization of nanosheets of these materials by the bottom-up and top-down strategy for sensing applications; and (iii) mixed lanthanide, heteroleptic CPs/MOFs, as bulk and nanoparticles, because, as noteworthy, these 2D layered CPs show emission bands in the 980−1350 nm spectral region, the so-called biological window, and therefore can be envisaged for applications in biology and nanomedicine as luminescent dual-center nanothermometers.[35]

References

(1) Furukawa, H.; Cordova, K. E.; O'Keeffe, M.; Yaghi, O. M. *Science,* **2013**, *341*, 1230444.

(2) Wang, C.; Liu, D.; Lin, W. *J. Am. Chem. Soc.,* **2013**, *135*, 13222–13234.

(3) Barea, E.; Montoro, C.; Navarro, J. A. R. *Chem. Soc. Rev.,* **2014**, *43*, 5419–5430.

(4) Bünzli, J. C. G.; Piguet, C. *Chem. Rev.,* **2002**, *102*, 1897–1928.

(5) Nandasiri, M. I.; Jambovane, S. R.; McGrail, B. P.; Schaef, H. T.; Nune, S. K. *Coord. Chem. Rev.,* **2016**, *311*, 38–52.

(6) Horcajada, P.; Gref, R.; Baati, T.; Allan, P. K.; Maurin, G.; Couvreur, P.; Férey, G.; Morris, R. E.; Serre, C. *Chem. Rev.,* **2012**, *112*, 1232–1268.

(7) Li, H.; Eddaoudi, M.; O'Keeffe, M.; Yaghi, O. M. *Nature* **1999**, *402*, 276–279.

(8) Serre, C.; Millange, F.; Thouvenot, C.; Noguès, M.; Marsolier, G.; Louër, D.; Férey, G. *J. Am. Chem. Soc.,* **2002**, *124*, 13519–13526.

(9) Llewellyn, P. L.; Bourrelly, S.; Serre, C.; Filinchuk, Y.; Férey, G. *Angew. Chemie. Int. Ed.,* **2006**, *45*, 7751–7754.

(10) Latroche, M.; Surblé, S.; Serre, C.; Mellot-Draznieks, C.; Llewellyn, P. L.; Lee, J. H.; Chang, J. S.; Sung, H. J.; Férey, G. *Angew. Chemie. Int.Ed.,* **2006**, *45*, 8227–8231.

(11) Jeremias, F.; Khutia, A.; Henninger, S. K.; Janiak, C. *J. Mater. Chem.,* **2012**, *22*, 10148–10151.

(12) Zhang, H.; Zhou, L.; Wei, J.; Li, Z.; Lin, P.; Du, S. *J. Mater. Chem.,* **2012**, *22*, 21210–21217.

(13) Allendorf, M. D.; Bauer, C. A.; Bhakta, R. K.; Houk, R. J. T. *Chem .Soc. Rev.,* **2009**, *38*, 1330–1352.

(14) Kapelewski, M. T.; Geier, S. J.; Hudson, M. R.; Stück, D.; Mason, J. A.; Nelson, J. N.; Xiao, D. J.; Hulvey, Z.; Gilmour, E.; Fitzgerald, S. A.; et al. *J. Am. Chem. Soc.,* **2014**, *136*, 12119–12129.

(15) Nayak, S.; Nayek, H. P.; Pietzonka, C.; Novitchi, G.; Dehnen, S. *J. Mol. Struct.,* **2011**, *1004*, 82–87.

(16) Kuriki, K.; Koike, Y.; Okamoto, Y. *Chem. Rev.,* **2002**, *102*, 2347–2356.

(17) Bünzli, J.-C. G. *Chem. Rev.,* **2010**, *110*, 2729–2755.

(18) Monteiro, J. H. S. K.; De Bettencourt-Dias, A.; Sigoli, F. A. *Inorg. Chem.,* **2017**, *56*, 709–712.

(19) Bünzli, J.-C. G.; Eliseeva, S. V. *Chem. Sci.,* **2013**, *4*, 1939.

(20) Bünzli, J.-C. G. *Coord. Chem. Rev.,* **2015**, *293–294*, 19–47.

(21) Yang, C.; Wang, X.; Omary, M. A. *J. Am. Chem. Soc.,* **2007**, *129*, 15454–15455.

(22) Yang, C.; Wang, X.; Omary, M. A. *Angew. Chem. Int. Ed.,* **2009**, *48*, 2500–2505.

(23) Hulvey, Z.; Sava, D. A.; Eckert, J.; Cheetham, A. K. *Inorg. Chem.,* **2011**, *50*, 403–405.

(24) Zhang, D. S.; Chang, Z.; Li, Y. F.; Jiang, Z. Y.; Xuan, Z. H.; Zhang, Y. H.; Li, J. R.; Chen, Q.; Hu, T. L.; Bu, X. H. *Sci. Rep.,* **2013**, *3*, 1–7.

(25) Chen, B.; Yang, Y.; Zapata, F.; Qian, G.; Luo, Y.; Zhang, J.; Lobkovsky, E. B. *Inorg. Chem.,* **2006**, *45*, 8882–8886.

(26) Han, Y.; Yan, P.; Sun, J.; An, G.; Yao, X.; Li, Y.; Li, G. *Dalt. Trans.,* **2017**, *46*, 4642–4653.

(27) Sobieray, M.; Gode, J.; Seidel, C.; Poß, M.; Feldmann, C.; Ruschewitz, U. *Dalt. Trans.,* **2015**, *44*, 6249–6259.

(28) Benmansour, S.; Pérez-Herráez, I.; López-Martínez, G.; Gómez García, C. J. *Polyhedron.,* **2017**, *135*, 17–25.

(29) Gómez-Claramunt, P.; Benmansour, S.; Hernández-Paredes, A.; Cerezo-Navarrete, C.; Rodríguez-Fernández, C.; Canet-Ferrer, J.; Cantarero, A.; Gómez-García, C. J. *Magnetochemistry.,* **2018**, *4*, 6.

(30) Benmansour, S.; Hernández-Paredes, A.; Gómez-García, C. J. *J. Coord. Chem.,* **2018**, *71*, 845–863.
(31) Abrahams, B. F.; Coleiro, J.; Hoskins, B. F.; Robson, R. *Chem. Commun.,* **1996**, *2*, 603.
(32) Abrahams, B. F.; Coleiro, J.; Ha, K.; Hoskins, B. F.; Orchard, S. D.; Robson, R. *J Chem. Soc. Dalt.Trans.,* **2002**, *2*, 1586.
(33) Ashoka Sahadevan, S.; Monni, N.; Abhervé, A.; Marongiu, D.; Sarritzu, V.; Sestu, N.; Saba, M.; Mura, A.; Bongiovanni, G.; Cannas, C.; et al. *Chem. Mater.,* **2018**, *30*, 6575–6586.
(34) Atzori, M.; Artizzu, F.; Marchiò, L.; Loche, D.; Caneschi, A.; Serpe, A.; Deplano, P.; Avarvari, N.; Mercuri, M. L. *Dalt. Trans.,* **2015**, *44*, 15786–15802.
(35) Rocha, J.; Brites, C. D. S.; Carlos, L. D. *Chem. - A Eur. J.,* **2016**, *22*, 14782–14795.

CHAPTER 4

Structural diversity in 2D Dy^{III}-Anilate-Based Magnetic MOFs/Coordination Polymers

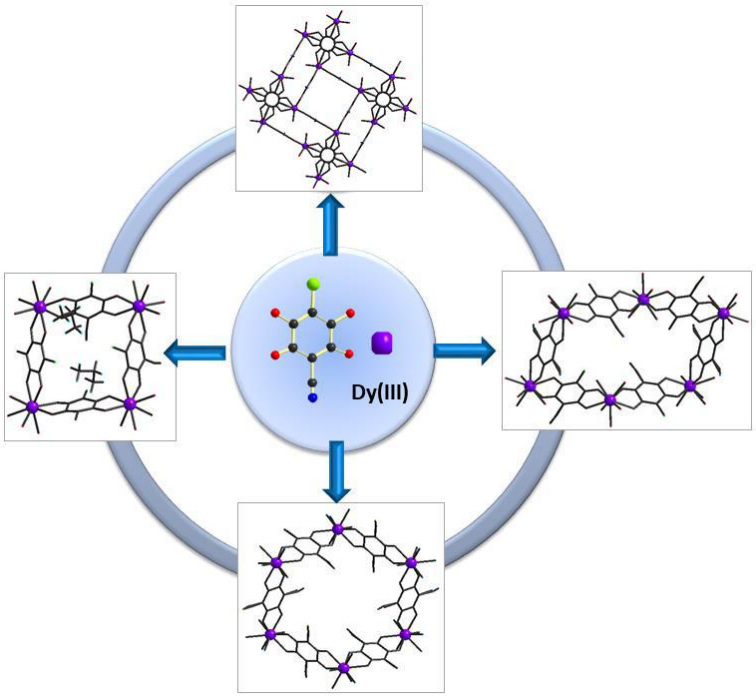

PART II

ABSTRACT

A new series of 2D layered CPs based on the heterosubstituted $ClCNAn^{2-}$ and Dy^{III} are herein reported. The resulting compounds are formulated as $[Dy_2(ClCNAn)_3(DMSO)_6]_n$ (1), $[Dy_2(ClCNAn)_3(DMSO)_6]_n$ (1'), $\{[Dy_2(ClCNAn)_3(DMF)_6]\cdot(DCM)_2\}_n$ (2), $\{[(Me_2NH_2)_2[Dy_2(ClCNAn)_4(H_2O)_2]\cdot(DMF)\}_n$ (3). Compounds 1-3 consist of neutral polymeric 2D networks of the $ClCNAn^{2-}$ ligand alternating with Dy^{III} ions, and 3 has 2D anionic layer $[Dy_2(ClCNAn)_4(H_2O)_2]^{2-}$ alternated with the cationic layer of $Me_2NH_2^+$ ions. These compounds have a very diverse topology, where compound 1 forms (8,3) and (4,3)-2D topology (see footnote in section 1.2.1) with eight-membered and four-membered ring with square cavities, 2 and 3 forms 2D (6,3)- topology with six-membered rings, (rectangular cavity for 2 and regular hexagonal cavity for 3) and 3 forms (4,4)-2D topology with distorted square cavities. The magnetic behavior of 1, 2 and 3 shows SMM behavior.

PART II

4.1 INTRODUCTION

Lanthanide-based CPs and MOFs attract considerable attention in material science because of their fascinating supramolecular architectures and richness in their optical[1] (Visible-NIR region, Eu^{III} and Tb^{III} and Nd^{III}, Er^{III} and Yb^{III} respectively) and magnetic properties (Ho^{III}, Tb^{III} and Dy^{III}) with applications in telecommunications, bioimaging and information storage.[2–4] The large anisotropic magnetic moment shown by the latter makes them appealing for the preparation of magnetic materials.[3,5–7] Recently, interest in anilate derivatives,[8–10] has been extensively renovated because of their ability to construct 2D layered architectures with peculiar physical properties, ranging from organic ferroelectrics,[11–13] layered magnets[10,14–18] (including spin-crossover systems) magnetic conductors[19,20] to multifunctional MOFs.[21,22] Anilates are also used for the construction of lanthanide-based materials, since the first report of Abrahams et al.[23,24] on a series of $Ln_2(H_2An)_3{\cdot}24H_2O$ (Ln = Ce, La, Yb, or Y) with hydranilate and chloranilate linkers. Afterwards, there were reported a series of (i) 2D monometallic CPs, based on the hydranilate and chloranilate ligands, (ii) 2D honeycomb network, and a series of bimetallic CPs with the formula $\{[Nd_2Ln_2(1-x)(H_2An)_3]\cdot 24H_2O\}_n$ (Ln_2 = Gd or Ce).[25] Recently, Gomez et.al.,[16,26] highlighted the key role of the solvents and size of lanthanides in the structures of the series of layered compounds, formulated as $[Ln_2(Br_2An)_3(solv.)n]$ G (Ln^{III}= Er, solv.= H_2O, DMF, DMSO; G = Guest) based on bromanilate ligands and $ClCNAn^{2-}$ ligands $[Ln_2(ClCNAn)_3(sol.)_6]{\cdot}G$ (Ln^{III} = Ce, Pr, solv= DMF; Yb, Pr, sol = DMSO; Dy, sol= H_2O) respectively. Very recently, our groups have reported[27] a series of 2D layered CPs based on NIR-emitting lanthanide ions formulated as $[Ln_2(ClCNAn)_3(DMF)_6]_n{\cdot}(DCM)x$ (Ln^{III}= Er, Nd and Yb). These compounds were also exfoliated to monolayers and their photophysical properties as bulk and nanosheets were discussed in chapter 2. Also, a novel series of heteroleptic 2D layered CPs based on anilate- and carboxylate-based ligands and NIR-emitting lanthanides (Yb^{III}, Er^{III}) were discussed in chapter 3. The aim of the present work is to investigate the magnetic properties of the systems based on $ClCNAn^{2-}$ and carboxylate derivatives DOBDC and F_4BDC, focusing on Dy^{III} lanthanide ion. The magnetic properties of lanthanide-anilate-based materials are in fact scarcely studied. There are few reports on (i) a 3D monometallic lanthanoid assembly, $Na_5[Ho(THB)_2]_3{\cdot}7H_2O$ (THB = tetrahydroxybenzene), showing ferromagnetism with a Curie temperature of 11 K;[28] (ii) a $[\{Ho_2(H_2An)_3(H_2O)_6\}{\cdot}18H_2O]_n$ complex based on hydranilate;[29] (iii) layered 2D compounds, $[Ln_2(ClCNAn)_3(sol.)_6]{\cdot}G$ (Ln^{III} = Ce, Pr, solv= DMF; Yb, Pr, sol = DMSO; Dy, sol= H_2O) showing weak antiferromagnetism;[16] (iv)

$[Ln_2(NO_2An)_3(H_2O)_{10}]\cdot 6H_2O$ (Ln^{III} = Sm, Gd, Tb, Dy, Ho and Er) forming dimers, showing weak antiferromagnetism;[30] (v) layered 2D compounds, $[Ln_2(Br_2An)_3(DMSO)_n]\cdot 2DMSO\cdot mH_2O$ with n = 6 and m = 0 for Ln = La, Ce, Pr, Nd, Sm, Eu and Gd ; n = 4 and m = 2 for Ln = Tb, Dy, Ho, Er, Tm and Yb showing weak antiferromagnetism.[26,30]

We report herein the synthesis and structural characterization of the series of compounds formulated as $[Dy_2(ClCNAn)_3(DMSO)_6]_n$ (1), $[Dy_2(ClCNAn)_3(DMSO)_6]_n$ (1'), $\{[Dy_2(ClCNAn)_3(DMF)_6]\cdot(DCM)_2\}_n$ (2) and $\{[(Me_2NH_2)_2[Dy_2(ClCNAn)_4(H_2O)_2]_n\cdot(DMF)\}_n$ (3). Surprisingly 1 and 1' are allotropes showing different crystal structures (Tetragonal and Monoclinic with Space Groups *I*4/*m* and *P*2/*n* respectively) and they represent the first example of allotropy observed in CPs. The magnetic properties shows the appearance of SMM behaviour.

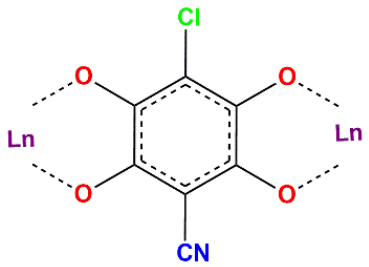

Chart 4.1. a) Coordination mode of the $ClCNAn^{2-}$ ligand in compounds 1-3.

4.2 EXPERIMENTAL SECTION

4.2.1 General Remarks

KHClCNAn was synthesized as reported in the literature.[9] Reagents of analytical grade were purchased from Zentek (TCI) and used without further purification. The solvents, of HPLC grade, were purchased from Thermofisher Scientific Alfa-Aesar.

4.2.2 Synthesis

$[Dy_2(ClCNAn)_3(DMSO)_6]_n$ (1)**:** An aqueous solution (5 mL) of $Dy(NO_3)_3\cdot 5H_2O$ (0.6 mmol, 290.14 mg) was added dropwise to an aqueous yellow solution (35 mL) of DOBDC (0.3 mmol, 60 mg) and NaOH (1.5 mmol, 60 mg) solution. KHClCNAn (0.3 mmol, 72 mg) was added to the mixture showing an immediate color change from yellow to red. After ca. 4h of stirring at 90°C, the mixture was allowed to cool at room temperature, and the purple solid insoluble in water and in almost organic solvents was separated from the mother liquor by filtration, washed several times with fresh water and dried under vacuum. Compound **1** was recrystallized in DMSO to give orange crystals suitable for X-ray analysis after several

weeks.

$[Dy_2(ClCNAn)_3(DMSO)_6]_n$ (1'): This compound was synthesized in a similar manner to **1**, by using F_4BDC (0.3 mmol, 71.4 mg) and NaOH (0.6 mmol, 24 mg) instead of DOBDC.

$\{[Dy_2(ClCNAn)_3(DMF)_6]\cdot(DCM)_2\}_n$ (2): This compound was synthesized in a similar manner as in literature[27] using $Dy(NO_3)_3\cdot 5H_2O$ (0.6 mmol, 290.14 mg) instead of $YbCl_3.5H_2O$.

$\{(Me_2NH_2)_2[Dy_2(ClCNAn)_4(H_2O)_2]\cdot(DMF)\}_n$ (3)**:** A 50ml Teflon-lined stainless-steel autoclave reactor was charged with $Dy(NO_3)_3\cdot 5H_2O$ (0.15 mmol, 72.5 mg) and KHClCNAn (0.45 mmol,108 mg) in solvent mixture of DMF (5ml) and H_2O (20ml) and placed in an oven (80°C) for 24h. The reactor was cooled to room temperature and the dark red crystals suitable for X-ray analysis were obtained.

4.2.3 Measurement details

X-ray Crystallography

Single crystals of the compound 1-3 were mounted on glass fiber loops using a viscous hydrocarbon oil to coat the crystal and then transferred directly to the cold nitrogen stream for data collection. X-ray diffraction data of 1-1' were collected with a Bruker APEX-II diffractometer (Mo-Kα, 0.71073) with a APEX II CCD detector. Data collection of 2-3 was performed at 150 K on an Agilent Supernova with CuKα (λ = 1.54184 Å). The structures were solved by direct methods with the SIR97 program and refined against all F^2 values with the SHELXL-97 program using the WinGX graphical user interface. All non-hydrogen atoms were refined anisotropically except as noted, and hydrogen atoms were placed in calculated positions and refined isotropically with a riding model.

Table 4.1. Crystallographic data for compounds 1, 1' and 3.

	1	**1'**	**3**
Empirical formula	$C_{66}H_{72}Cl_6Dy_4N_6O_{36}S_{12}$	$C_{16.50}H_{18}C_{11.50}DyN_{1.50}O_9S_3$	$C_{20}H_{10}Cl_3Dy_2N_3O_{14}$
Fw	2772.71	693.18	947.66
Crystal color	red	red	red
Crystal size (mm3)	0.10 * 0.05 * 0.02	0.10 * 0.05 * 0.03	0.10 * 0.07 * 0.05
Temperature (K)	293(2)	293(2)	150.00(10)
Wavelength (Å)	0.71073	0.71073	1.54184
Crystal system, Z	Tetragonal, 2	Monoclinic, 4	Monoclinic, 4
Space group	I4/m	P2/n	*C*2/*c*
a (Å)	20.1356(13)	9.7771(7)	11.5432(4)
b (Å)	20.1356	16.3575(13)	12.2497(5)
c (Å)	14.9195(10)	15.1790(11)	12.3357(6)
α (°)	90	90	62.654(4)

β (°)	90	94.493(2)	68.671(4)
γ (°)	90	90	68.807(4)
V (Å³)	6049.0(9)	2420.1(3)	1402.82(10)
ρcalc (g.cm-³)	1.522	1.902	1.829
μ(CuKα) (mm-1)	2.848	3.560	31.465
θ range (°)	1.699-17.725	1.833-27.153	4.15-73.47
Data collected	7808	17289	11400
Data unique	1063	5303	7015
Data observed	927	3187	6640
Number of parameters/restraints	184/6	318/0	621/3
R(int)	0.0322	0.1044	0.0497
R1(F),a I > 2σ(I)	0.0681	0.0645	0.0634
wR2(F2),b all data	0.2145	0.1285	0.1797
S(F2),c all data	1.131	1.052	1.096

[a] $R1(F) = \Sigma||F_0|-|F_C||/\Sigma|F_0|$; [b] $wR2(F^2) = [\Sigma w(F_0^2-F_C^2)^2/\Sigma wF_0^4]^{1/2}$; [c] $S(F^2) = [\Sigma w(F_0^2-F_C^2)^2/(n+r-p)]^{1/2}$.

Magnetic Studies

Magnetic measurements were performed on a crystalline powder by using a Quantum Design MPMS-XL magnetometer. The magnetic susceptibility data were recorded in the temperature range of 2−300 K in an external field of 1000 Oe. The diamagnetic corrections were calculated by using Pascal's constants.[31] The dynamic magnetic susceptibility data were obtained in the frequency range of 0.1−1000 Hz in an oscillating field of 3 Oe.

4.3 RESULTS AND DISCUSSION

4.3.1 Synthesis

The $ClCNAn^{2-}$-based Dy^{III} compounds $[Dy_2(ClCNAn)_3(DMSO)_6]_n$ (1), $[Dy_2(ClCNAn)_3(DMSO)_6]_n$ (1'), $\{[Dy_2(ClCNAn)_3(DMF)_6]_n\cdot(DCM)_2\}_n$ (2) and $\{[(Me_2NH_2)_2[Dy_2(ClCNAn)_4(H_2O)_2]_n\cdot(DMF)\}_n$ (3) have been synthesized by the self-assembly of the ClCNAn ligand and the Dy^{III} ion by using different synthetic strategies, as reported in Scheme 4.1. Compounds 1-3 are 2D layered porous polymeric networks formed by Dy^{III} and ClCNAn where 1-2 are neutral networks and 3 is formed by 2D $[Dy_2(ClCNAn)_4(H_2O)_2]^{2-}$ anionic layers and $Me_2NH_2^+$ cations.

The allotropes 1 and 1' were unexpectedly obtained by a one-pot reaction of DOBDC (F_4BDC), KHClCNAn, NaOH and Dy^{III} salts in water, as shown in Scheme 4.1, respectively. The obtained solid was recrystallized in DMSO to get crystals suitable for X-Ray studies. Although carboxylate ligands were used in the synthesis along with $ClCNAn^{2-}$, there is no coordination with the former unlike the heteroleptic $[Ln_4(ClCNAn)_5(DOBDC)_1(DMSO)_{10}]_n.(DMSO)_2$ $[Ln_2(ClCNAn)_2(F_4\text{-}BDC)(DMSO)_6]_n$ (Ln-

Yb, Er) CPs described in Chapter 3.

1 and 1' clearly show that $ClCNAn^{2-}$ has a greater affinity to coordinate Dy^{III} ions than DOBDC or F_4BDC, even though the role of the latter ligands in determining the observed allotropy needs to be investigated.

Compound 2 is obtained by carefully layering a solution of KHClCNAn in DMF onto the top of a solution of the Dy^{III} salt in DCM/DMF.

Compound 3 is obtained by solvothermal reaction of KHClCNAn and Dy^{III} salt in H_2O/DMF at high temperature. It is formed by 2D $[Dy_2(ClCNAn)_4(H_2O)_2]^{2-}$ anionic layers charge-compensated by $Me_2NH_2^+$ cations, which are generated in situ through decomposition of DMF in the autoclave.[21]

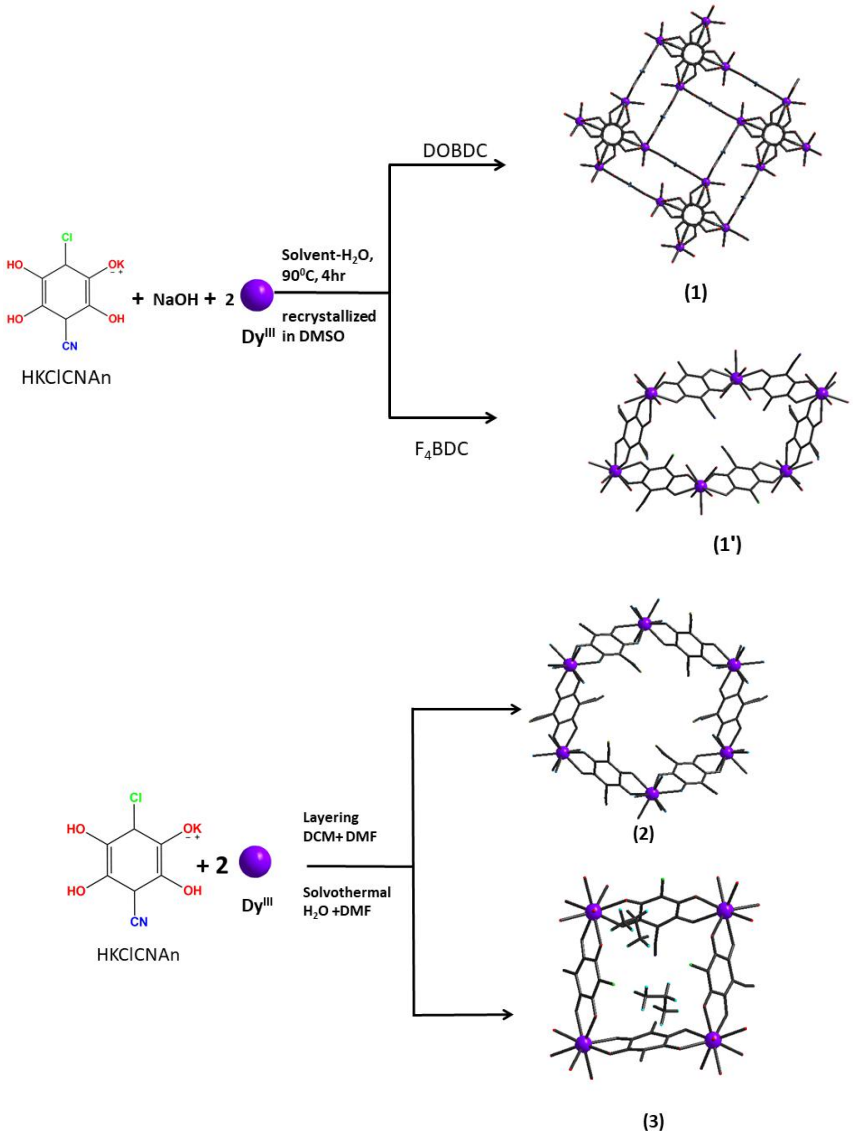

Scheme 4.1. Synthetic Strategy for compounds 1-3.

4.3.2 Crystal Structures

Compounds 1-3 are 2D polymeric coordination networks of $ClCNAn^{2-}$ with Dy^{III} ions. 1-2 are neutral networks while 3 are formed by 2D alternated anionic/cationic layers.

Compound 1 crystallizes in the tetragonal *I4/m* space group. The asymmetric unit contains one Dy^{III} ion of 0.5 occupancy, two half molecules of $ClCNAn^{2-}$ ligand with 1 and 0.5 occupancies and two DMSO molecules with occupancy factor of 1 and 0.5 giving rise to the formula $[Dy_2(ClCNAn)_3(DMSO)_6]_n$. In the anilate ligand, because of the inversion center, for the half independent molecule of $ClCNAn^{2-}$, the chloro and cyano substituents are equally distributed over the same position. S atoms from the DMSO solvent molecules are disordered.

The Dy^{III} ion is nine-coordinated in a slightly distorted monocapped square antiprismatic geometry, completed by six oxygen atoms from three $ClCNAn^{2-}$ ligands and three oxygen atoms from three DMSO molecules (Figure 4.1a). Dy−O bond lengths and O−Dy−O angles fall in the range of 2.283−2.46 Å and 64.3−139.9°, respectively.

Each Dy^{III} ion is connected to three other Dy^{III} ions through bis-bidentate ClCNAn ligands forming eight-membered and four-membered rings ((8,3) and (4,3)-2D topologies; (see footnote in section 1.2.1) with square cavities of different sizes along the *ba* plane (Figure 4.1 b, d). These square cavities are regular, with two close Dy-Dy diagonal distances (24.75 Å, 24.75 Å); (12.42 and 12.23 Å) and the orthogonal Dy-Dy-Dy angles inside the square (90◦ each) for the eight-membered and four-membered square cavity respectively. Neighbor layers are alternated following the sequence ...ABAB… generating square cavities along the *c* axis. (Figure 4.1 c-d).

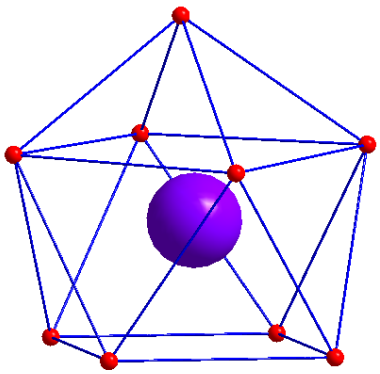

a

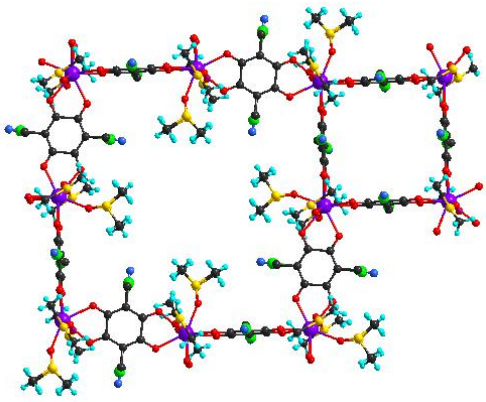

b

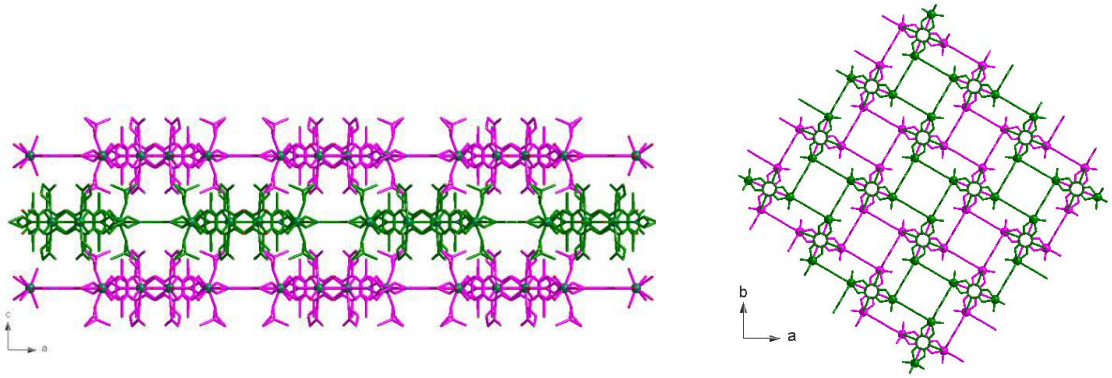

c d

Figure 4.1. Structure of compound 1. (a) Distorted monocapped square antiprismatic coordination geometry of the Dy^{III} center. (b) View of square cavity (eight membered and four membered). (c) View of three consecutive layers in the *ac* plane. (d) View of the alternated layers in the *ba* plane. Color code: Dy = violet, O = red, Cl = light green, C = black, N = blue and H = cyan. In (c) and (d) different colors are used to represent the different layers.

The allotrope 1' crystallizes in the Monoclinic *P*2/*n* space group. The asymmetric unit of 1' consists of one Dy^{III} ion, three half molecule of $ClCNAn^{2-}$ ligands and three DMSO molecules giving rise to the formula $[Dy_2(ClCNAn)_3(DMSO)_6]_n$. The chloro and cyano substituents from the asymmetric ClCNAn ligand are equally distributed over the same position as in 1. S atoms from the DMSO solvent molecules are disordered.

Dy^{III} ion is nine-coordinated in slightly distorted tricapped trigonal prism geometry, completed by six oxygen atoms from three $ClCNAn^{2-}$ ligands and three oxygen atoms from three DMSO molecules (Figure 4.2 b). Dy−O bond lengths and O−Dy−O angles fall in the range of 2.321−2.475 Å and 63.89−146.3°, respectively. The shortest Dy···Dy distance is 8.778 Å.

The structure shows corrugated layers with 2D (6,3)-topology, where each Dy^{III} ion is connected to three other Dy^{III} ions through bis-bidentate $ClCNAn^{2-}$ ligands forming six-membered rings with distorted hexagonal cavities along the *bc* plane (Figure 4.2 c-d-e). The two consecutive layers are parallel and are eclipsed forming distorted hexagonal cavities, that appear as rectangles along the *a* axis. The coordinated DMF molecules face towards the cavities and towards neighboring layers. Similar type of CPs was reported by Gomez. et. al.[16] with Pr^{III}.

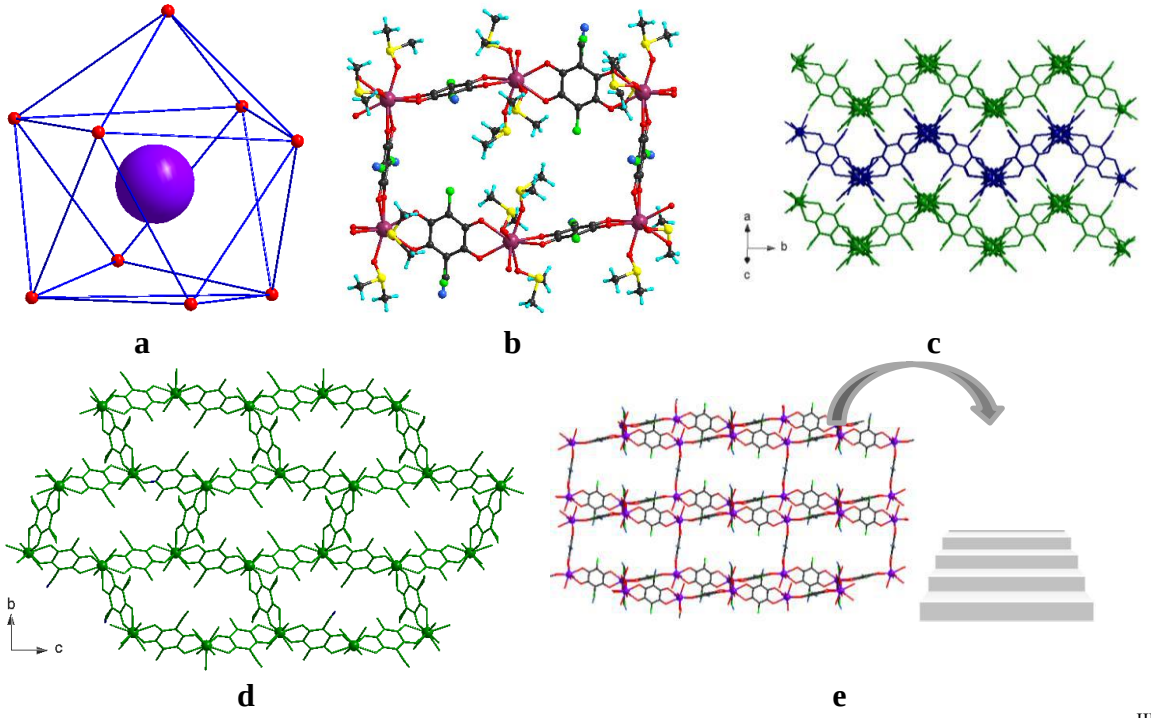

Figure 4.2. Structure of compound 1'. (a) Distorted tricapped trigonal prism geometry of the Dy^{III} center. (b) View of one rectangle cavity. (c) View of three consecutive layers in the *abc* plane. (d) View of the eclipsed layers in the *bc* plane. (e) View of one layer DMSO molecules are omitted for clarity. Color code: Dy = violet, O = red, Cl = light green, C = black, N = blue and H = cyan. In (c) and (d) different colors are used to represent the different layers.

Although, compounds 1 and 1' have the same formula, same solvent and coordination number (nine) around Dy^{III} ions, their coordination geometry is different (distorted monocapped square antiprismatic geometry (1) and distorted tricapped trigonal prism geometry for (1') and thus it is responsible for the observed different (8,3) and (4,3)-2D topologies forming square cavities for 1 and (6,3)-2D topology (see footnote in section 1.2.1), showing distorted hexagonal cavities, almost rectangles, for 1'.

Compound 2 crystallize in the monoclinic *C*2/*c* space group and is isostructural with the Nd^{III} and Er^{III} neutral CPs[27] described in Chapter 2 and thus they are not discussed here. 2 differs from 1-1' compounds for the coordination to Dy^{III} of DMF instead of DMSO with, and for the presence of two DCM molecules in the cavities. Although the number of solvent molecules in 1' and 2 is the same, the change of the solvent from DMF to DMSO produces a change in the coordination number (nine in compound 1' vs. eight in compound 2) leading to the change of the coordination geometry and the distortions of the hexagonal layers (2, forming honeycomb arrangement with regular hexagonal cavity, and 1', with more distorted hexagonal cavity, ultimately give rise to rectangular cavity), while keeping the same (6,3)

topology. This change can be attributed to the larger steric effect produced by DMSO compared to that produced by DMF as already been highlighted by Gomez et.al.[26]

Compound 3 crystallizes in the triclinic *P*1 space group. The asymmetric unit contains two independent Dy^{III} (Dy1 and Dy2) ion, four $ClCNAn^{2-}$ ligands, two water molecules and two $Me_2NH_2^+$ cations, giving rise to the general formula $\{(Me_2NH_2)_2[Dy_2(ClCNAn)_4(H_2O)_2]\cdot(DMF)\}_n$. The coordination environment around Dy1 and Dy2 is the same, being nine coordinated with tricapped trigonal prism geometry for Dy1 and with more distorted tricapped trigonal prism geometry for Dy2. The coordination sphere is completed by eight oxygen atoms from four $ClCNAn^{2-}$ ligands and one oxygen from crystallization water molecules in the capped position (Figure 4a). Dy−O bond lengths and O−Dy−O angles fall in the range of 2.354−2.498 Å and 64.3−142.6°, respectively. The shortest Dy···Dy distance is 8.683 Å.

The structure of compound 3 shows slightly corrugated layers in the anionic layer (Figure 4.3 c), with a (4,4)-2D square topology, where each Dy^{III} ion is connected to four other Dy^{III} ions through $ClCNAn^{2-}$ ligands, forming four-membered rings (Figure 4.3 b,d). These square cavities are distorted, as shown by the two close Dy-Dy diagonal distances (12.78 (Dy1-Dy1) and 11.53 Å (Dy2-Dy2)) and the Dy-Dy-Dy angles inside the square (82.83°, 94.45◦, 82.93°, 94.07°). The anionic layers are arranged in an eclipsed way, generating square channels along the *c* direction, with the $Me_2NH_2^+$ cations filling the large inter-layer space (Figure 4.3 c-d).

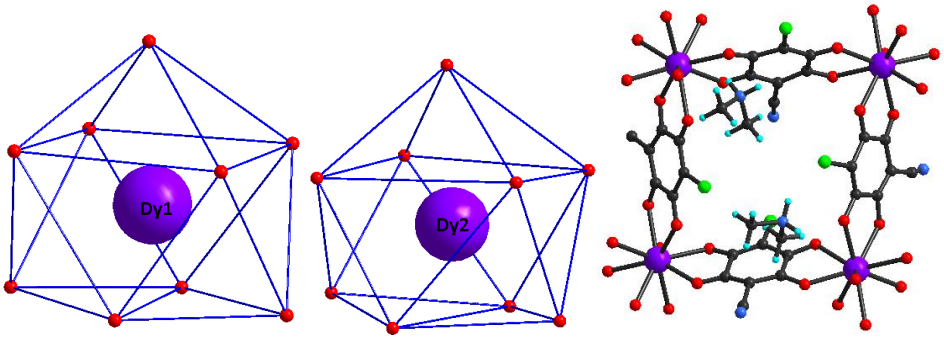

a b

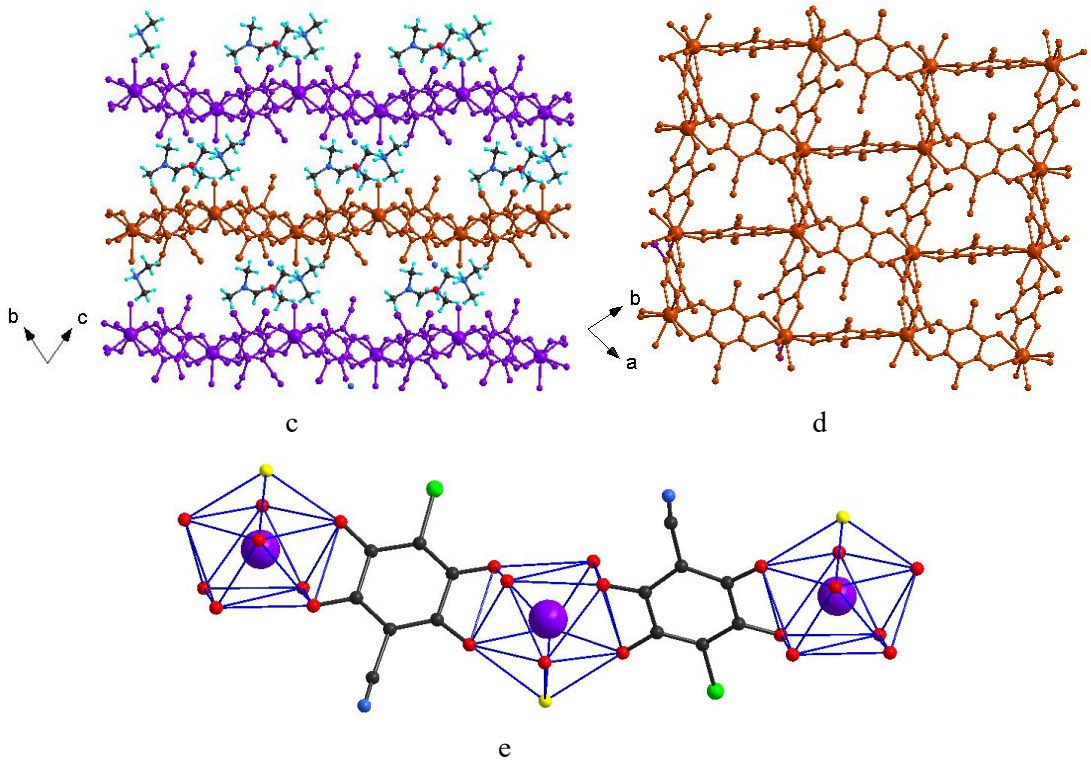

Figure 4.3. Structure of compound 3. (a) Distorted tri-capped trigonal prismatic coordination geometry of two Dy^{III} centers. (b) View of one square cavity. (c) View of three consecutive layers in the *bc* plane. (d) View of the eclipsed square layers in the *ab* plane. The cations are omitted for clarity. (e) ligand bridged between Dy^{III}, O atom from water molecule are highlighted in yellow. Color code: Dy= violet, O = red, Cl = light green, C = black, N = blue and H = cyan. In (c) and (d) different colors are used to represent the different layers.

The water molecule occupies one of the capped position of the tri-capped trigonal prism and the anilato ligands connect one position of the upper square with one of the bottom one (Figure 4.3e). This special disposition of the anilato ligands around the Dy^{III} ions generates the (4,4)-2D square lattice observed in compound 3. This similar kind of arrangement is also seen in the compound $[H_3O][Dy(ClCNAn)_2(H_2O)]\cdot 4H_2O$ reported by Gomez et. al.,[16] where Dy^{III} possess regular mono-capped square antiprismatic geometry giving rise to more regular square cavity. A summary of all compounds with their topology and cavity shape is reported in Table 4.2.

Table 4.2. Summary of compounds 1-3 described in the text.

Compounds	Coordination number	Topology , Cavity
$[Dy_2(ClCNAn)_3(DMSO)_6(DOBDC)_0]_n$ (1)	nine	(8,3) and (4,3)-2D, square
$[Dy_2(ClCNAn)_3(DMSO)_6(F_4BDC)_0]_n$ (1')	nine	(6,3)-2D, rectangle
$[Dy_2(ClCNAn)_3(DMF)_6](CH_2Cl_2)$ (2)	eight	(6,3)-2D, hexagon
$(Me_2NH_2)_2[Dy_2(ClCNAn)_4(H_2O)_2]\cdot(DMF)$ (3)	nine	(4,4)-2D, distorted square

4.3.3 Magnetic Studies

The three compounds 1, 2 and 3 show a similar magnetic behaviour. The room temperature $\chi_m T$ products for 1-3 (28.8, 27.1 and 25.9 $cm^3 \cdot K \cdot mol^{-1}$) are consistent with the expected value for magnetically diluted Dy cations, with small differences between them indicating slightly different single ion anisotropy. As temperature decreases, $\chi_m T$ decreases very fast, suggesting strong single ion anisotropy, although a contribution from magnetic superexchange between spin carriers promoted by the bridging ligands cannot be discarded at this point. Accordingly, the magnetization data at 2 K does not reach saturation even at 7 T, reaching ≈ 11 μ_B, away from the theoretical maximum saturation values.

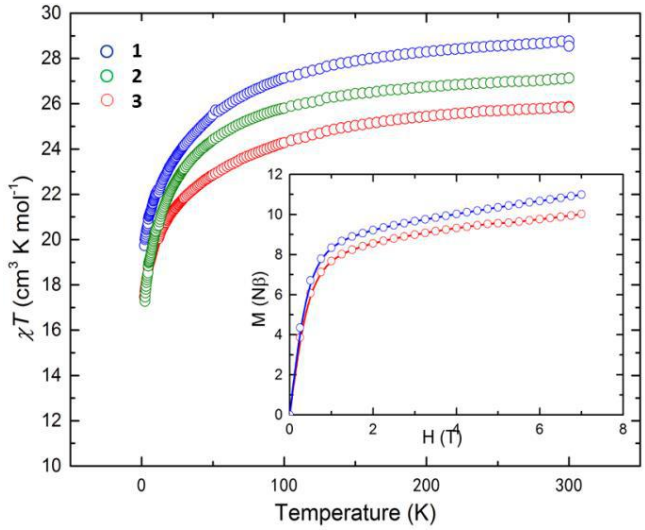

Figure 4.4. Magnetic susceptibility of the three complexes as a function of T.inset: Magnetisation curve for 1 and 3.

We studied ac magnetic measurements to determine the appearance of SMM behaviour (Figure 4.5). At first sight, no out-of-phase susceptibility signal was found for any of them. However, a detailed analysis of the data shows slightly differences for these materials, since in the case of 2 and 3, a weak but measurable χ''_m appears at very high frequencies. This suggests SMM behaviour is probably masked by fast quantum tunnelling of the magnetization (QTM). We carried out ac magnetic measurements in the presence of an external magnetic field, an easy experiment to suppress QTM.

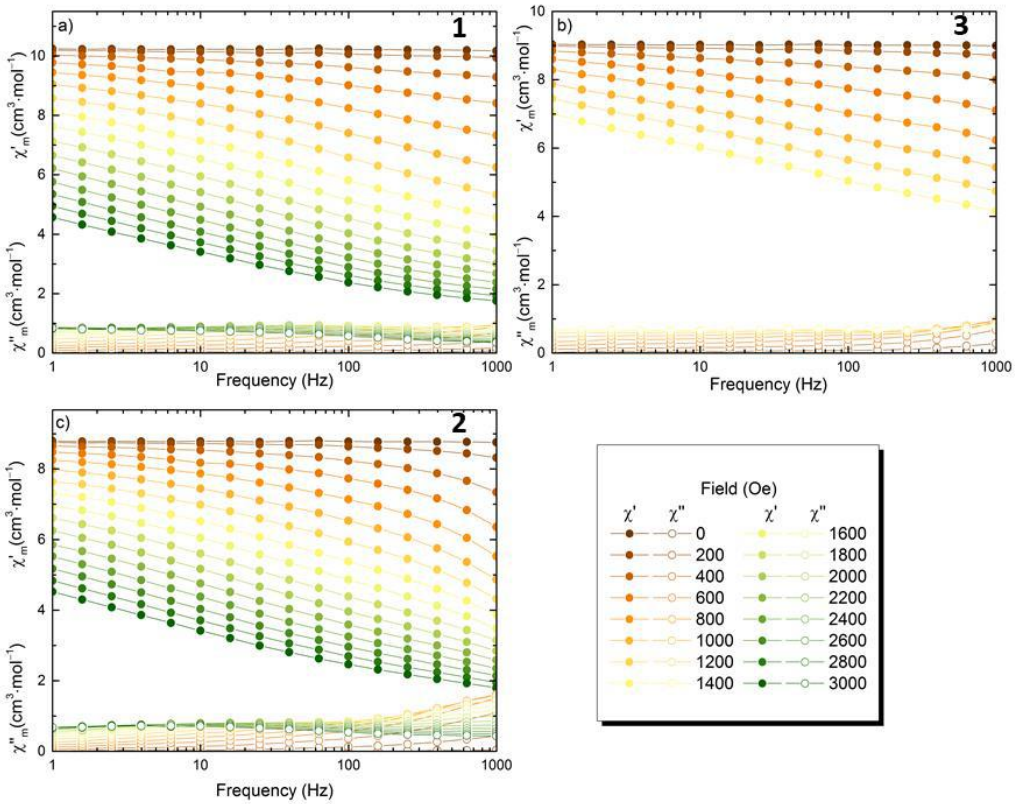

Figure 4.5. Frequency and field dependence of the in-phase (χ‘) and out-of-phase (χ“) signal of the susceptibility.

The magnetic studies of 1’ are under investigation.

4.4 CONCLUSIONS

A series of 2D layered CPs, based on the $ClCNAn^{2-}$ ligand and Dy^{III} ion, was synthesized by using different synthetic strategies such as conventional one-pot reactions, layering and solvothermal process.

Noteworthy two allotropes of neutral 2D CPs, never observed among the known CPs, have been obtained, formulated as $[Dy_2(ClCNAn)_3(DMSO)_6]_n$ (1) and $[Dy_2(ClCNAn)_3(DMSO)_6]_n$ (1'); $[Dy_2(ClCNAn)_3(DMF)_6]_n\cdot(DCM)_2$ (2) and $[(Me_2NH_2)_2[Dy_2(ClCNAn)_4(H_2O)_2]_n\cdot(DMF)$ (3) have been obtained as well. Compounds 1-2 consist of neutral 2D CPs of the ClCNAn ligand alternating with Dy^{III} ions, while 3 shows 2D alternated $[Dy_2(ClCNAn)_4(H_2O)_2]^{2-}$/ $Me_2NH_2^+$ anionic/cationic layers.

1-2 are porous CPs showing different cavity shapes, highlighting the ability of $ClCNAn^{2-}$ ligands to work as efficient linkers for the formation of MOFs. Compound 1 forms an unusual phase with (8,3) and (4,3)-2D topology forming square cavities of two different sizes, whereas 1' and 2 exhibit general (6,3)-2D topology with six membered rings (1', forming

rectangular cavities and 2 hexagonal cavities). Compound 3 forms (4,4)-2D topology with distorted square cavities.

Under an applied dc magnetic field, to remove tunneling, there observed an appearance of a frequency dependent out-of-phase susceptibility, which suggests SMM behavior. However, the blocking temperature is too low, and could not detect its maximum in χ" above 2 K.

Porosity measurements (Nitrogen Adsorption Measurements) of these compounds are in progress.

References

(1) Bünzli, J. C. G.; Piguet, C. *Chem. Rev.,* **2002**, *102*, 1897–1928.
(2) Ye, H. Q.; Li, Z.; Peng, Y.; Wang, C. C.; Li, T. Y.; Zheng, Y. X.; Sapelkin, A.; Adamopoulos, G.; Hernández, I.; Wyatt, P. B.; et al. *Nat. Mater.,* **2014**, *13*, 382–386.
(3) Bünzli, J.-C. G.; Eliseeva, S. V. *J. Rare. Earths.,* **2010**, *28*, 824–842.
(4) Pointillart, F.; le Guennic, B.; Cador, O.; Maury, O.; Ouahab, L. *Acc. Chem. Res.,* **2015**, *48*, 2834–2842.
(5) Eliseeva, S. V.; Bünzli, J.-C. G. *Chem. Soc. Rev.,* **2010**, *39*, 189–227.
(6) Bünzli, J.-C. G. *Coord. Chem. Rev.,* **2015**, *293–294*, 19–47.
(7) Bünzli, J.-C. G.; Eliseeva, S. V. *Chem. Sci.,* **2013**, *4*, 1939.
(8) Kitagawa, S. *Coord. Chem. Rev.,* **2002**, *224*, 11–34.
(9) Atzori, M.; Artizzu, F.; Marchiò, L.; Loche, D.; Caneschi, A.; Serpe, A.; Deplano, P.; Avarvari, N.; Mercuri, M. L. *Dalt. Trans.,* **2015**, *44*, 15786–15802.
(10) Mercuri, M. L.; Congiu, F.; Concas, G.; Ashoka Sahadevan, S. *Magnetochemistry.,* **2017**, *3*, 17.
(11) Horiuchi, S.; Kumai, R.; Tokura, Y. *J. Am. Chem. Soc.,* **2013**, *135*, 4492–4500.
(12) Horiuchi, S.; Kumai, R.; Tokura, Y. *J. Am. Chem. Soc.,* **2005**, *127*, 5010–5011.
(13) Kagawa, F.; Horiuchi, S.; Minami, N.; Ishibashi, S.; Kobayashi, K.; Kumai, R.; Murakami, Y.; Tokura, Y. *Nano. Lett.,* **2014**, *14*, 239–243.
(14) Atzori, M.; Benmansour, S.; Mínguez Espallargas, G.; Clemente-León, M.; Abhervé, A.; Gómez-Claramunt, P.; Coronado, E.; Artizzu, F.; Sessini, E.; Deplano, P.; Serpe, A; Mercuri, M.L.; Gómez García, C. J. *Inorg. Chem.,* **2013**, *52*, 10031–10040.
(15) Abhervé, A.; Mañas-Valero, S.; Clemente-León, M.; Coronado, E. *Chem. Sci.,* **2015**, *6*, 4665–4673.
(16) Gómez-Claramunt, P.; Benmansour, S.; Hernández-Paredes, A.; Cerezo-Navarrete, C.; Rodríguez-Fernández, C.; Canet-Ferrer, J.; Cantarero, A.; Gómez-García, C. J. *Magnetochemistry.,* **2018**, *4*, 6.
(17) Benmansour, S.; Abhervé, A.; Gómez-Claramunt, P.; Vallés-García, C.; Gómez-García, C. J. *ACS Appl. Mater. Interfaces.,* **2017**, *9*, 26210–26218.
(18) Sahadevan, S. A.; Abhervé, A.; Monni, N.; Sáenz de Pipaón, C.; Galán-Mascarós, J. R.; Waerenborgh, J. C.; Vieira, B. J. C.; Auban-Senzier, P.; Pillet, S.; Bendeif, E.-E.; Alemany, P.; Canadell, E.; Mercuri, M. L.; Avarvari, N. *J. Am. Chem. Soc.,* **2018**, *140*, 12611–12621.
(19) Atzori, M.; Pop, F.; Auban-Senzier, P.; Clérac, R.; Canadell, E.; Mercuri, M. L.; Avarvari, N. *Inorg.Chem.,* **2015**, *54*, 3643–3653.
(20) Atzori, M.; Pop, F.; Auban-Senzier, P.; Gómez-García, C. J.; Canadell, E.; Artizzu, F.; Serpe, A.; Deplano, P.; Avarvari, N.; Mercuri, M. L. *Inorg. Chem.,* **2014**, *53*, 7028–7039.
(21) Jeon, I.-R.; Negru, B.; Van Duyne, R. P.; Harris, T. D. *J. Am. Chem. Soc.,* **2015**, *137*, 15699–15702.

(22) DeGayner, J. A.; Jeon, I.-R.; Sun, L.; Dincă, M.; Harris, T. D. *J. Am. Chem. Soc.,* **2017**, *139*, 4175–4184.
(23) Abrahams, B. F.; Coleiro, J.; Ha, K.; Hoskins, B. F.; Orchard, S. D.; Robson, R. *J. Chem. Soc. Dalt .Trans.,* **2002**, *2*, 1586.
(24) Abrahams, B. F.; Coleiro, J.; Hoskins, B. F.; Robson, R. *Chem. Commun.,* **1996**, *2*, 603.
(25) Demars, T.; Boltoeva, M.; Vigier, N.; Maynadié, J.; Ravaux, J.; Genre, C.; Meyer, D. *Eur. J. Inorg. Chem.,* **2012**, *2012*, 3875–3884.
(26) Benmansour, S.; Pérez-Herráez, I.; López-Martínez, G.; Gómez García, C. J. *Polyhedron.,* **2017**, *135*, 17–25.
(27) Ashoka Sahadevan, S.; Monni, N.; Abhervé, A.; Marongiu, D.; Sarritzu, V.; Sestu, N.; Saba, M.; Mura, A.; Bongiovanni, G.; Cannas, C.; Quochi, F.; Avarvari, N; Mercuri, M.L. *Chem. Mater.,* **2018**, *30*, 6575–6586.
(28) Nakabayashi, K.; Ohkoshi, S. *Inorg. Chem.,* **2009**, *48*, 8647–8649.
(29) Nakabayashi, K.; Ohkoshi, S. *Acta Crystallogr. Sect E. Struct. Reports Online.,* **2010**, *66*, m1300.
(30) Benmansour, S.; Hernández-Paredes, A.; Gómez-García, C. J. *J. Coord. Chem.,* **2018**, *71*, 845–863.
(31) Bain, G. A.; Berry, J. F. *J. Chem. Educ.,* **2008**, *85*, 532.

CHAPTER 5

Anilate-Based Organic Molecular Conductors

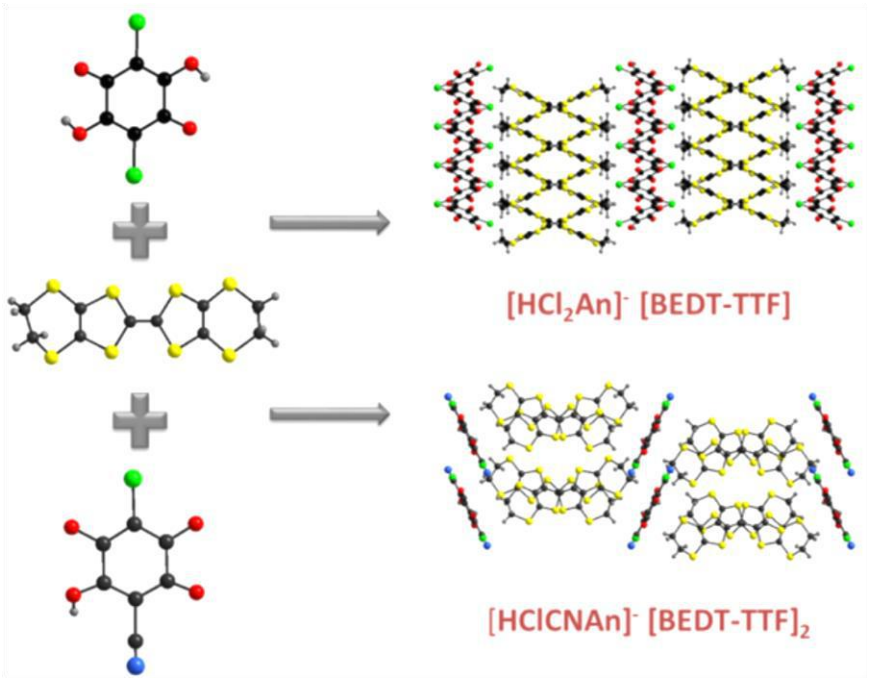

This work is partly published in the article S. Ashoka Sahadevan, N. Monni, A. Abhervé, P. Auban-Senzier, E. Canadell, M. L. Mercuri, N. Avarvari, Synthesis and Physical Properties of Purely Organic BEDT-TTF-based Conductors Containing Hetero-/Homosubstituted Cl/CN-Anilate Derivatives., *Inorg. Chem*. **2017**, 56, 12564–12571.

PART II

ABSTRACT

Radical cation salts composed of a BEDT-TTF donor with homo-/heterosubstituted Cl/CN anilic acids as purely organic molecular conducting materials formulated as [BEDT-TTF]$_2$[HClCNAn] (1) and [BEDT-TTF][HCl$_2$An] (2) have been prepared by electrocrystallization. Compounds 1 and 2 crystallized in the monoclinic space group *P*2/*c* for 1 and *I*2/*a* for 2, showing segregated donor-anion layers arranged in a α′-type donor packing pattern (1) and twisted parallel columns (2), respectively. Single-crystal conductivity measurements show that 1 and 2 are semiconductor with r.t. conductivity of 10^{-2} Scm^{-1}, 10^{-1} Scm^{-1} respectively.

5.1 INTRODUCTION

During the last 40 years molecular conductors have remarkably attracted the interest of material scientists since the pioneering work of Ferraris et al.,[1] where the TTF organic donor was combined with the TCNQ organic acceptor, yielding the charge transfer complex (TTF)(TCNQ). The new compound showed unique conducting properties comparable to those of a classical metal,[1] which have never been observed before in a purely organic material. Nevertheless, compounds containing radical species, e.g. $TTF^{\bullet+}Cl^{-}$ salt[2] or TCNQ-based systems with different metal cations,[3] were previously reported. With the aim of increasing the intermolecular interactions between the units that are responsible for the conducting properties, several TTF-based derivatives have been subsequently explored. In particular, the BEDT-TTF (Chart 2) has been shown to be the most successful donor, affording the largest number of 2D conducting materials,[4-6] ranging from Mott insulators and conductors to the majority of the known molecular superconductors. Most of these materials are formed of partially charged BEDT-TTF molecules and different types of closed-shell or magnetic inorganic anions,[4] while several examples of salts with organic ions such as polycyanocarbons,[7] fluoroalkyl sulfonates,[8] polynitrophenolates,[9] squarate and rhodizonate,[10] and haloanilates[11-13] have been described as well. Anilic acids (I; X = Cl, Br, I, NO_2, CN, etc.) are of special interest in the context of the band-filling control of organic conductors, since they give rise to anionic species with modulable charges such as monoanionic (II) and dianionic (III) forms, following a mono- or bis-deprotonation process of the two hydroxyl groups. The form III prevails in aqueous media due to the strong resonance stabilization of the negative charge (Scheme 5.1).

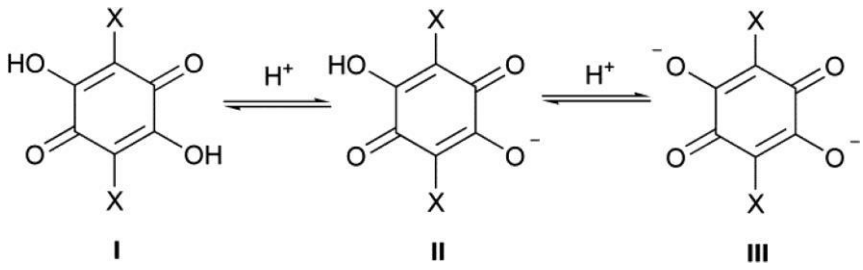

Scheme 5.1. Protonation Equilibria for a Generic Anilic Acid

Moreover, the interest in anilic acids has been recently renewed, since they have been used as molecular building blocks for obtaining different types of functional materials such as organic ferroelectrics or as components in their dianionic forms III of multifunctional molecular materials showing peculiar physical properties.[12,14-21] In fact anilates are very attractive

building blocks because of (i) their interesting redox properties, [22] (ii) their ability to mediate magnetic superexchange interactions when the ligand coordinates two metal ions in the 1,2-bis-bidentate coordination mode, [14] and (iii) the possibility of modulating the strength of this magnetic superexchange interaction by varying the substituents (X) on the 3,6-positions of the anilato ring. [23] Moreover, the presence of different substituents in the anilato moiety gives rise to intermolecular interactions such as H bonding, halogen bonding, π–π stacking, and dipolar interactions, which may influence the physical properties of the resulting material. In this context cyananilic acid, bearing two CN groups, H-bonding acceptor sites, has afforded 2:1 salts in which it is present in the monoanionic form II, a 1D antiferromagnetic CT salt with the TM-TTF organic donor and a Mott insulator with BEDT-TTF, respectively. [12,13,24,25] As a progression of these studies, we focus our scientific efforts on fully organic TTF salts based on hetero- and homosubstituted anilate derivatives in order to investigate the influence of the different substituents on the physical properties of the resulting radical cation salts.

We report herein the synthesis by electrocrystallization, thorough structural analysis, Raman studies, and physical properties of radical cation salts based on BEDT-TTF and the heterosubstituted X = Cl/CN anilate (1) and the homosubstituted X = Cl anilate (2). Band structure calculations of compound 1 will be also discussed in order to correlate the structure with the conducting properties.

5.2 EXPERIMENTAL SECTION

5.2.1 General Remarks

KHClCNAn was synthesized according to the literature procedure.[32] BEDT-TTF was prepared following the Larsen procedure.[33] H_2Cl_2An was purchased from Zentek (TCI) and used without further purification. Crystals were grown by the electrocrystallization technique. Solvents used for electrocrystallization experiments (HPLC grade) were dried under basic alumina and degassed with argon prior to use.

5.2.2 Synthesis

[BEDT-TTF]$_2$[HClCNAn] (1)**:** KHClCNAn (9.19mg) was dissolved in 8 mL of CH_2Cl_2 and placed in the cathode chamber of an H-shaped electrocrystallization cell. BEDT-TTF (5 mg) was dissolved in 8 mL of CH_2Cl_2 and placed in the anode chamber of the cell. A current density of 0.5 μA cm^{-2} was applied. Black prismatic single crystals of 1 were grown at 20 °C on the anode surface of a platinum-wire electrode over a period of 2 weeks.

[BEDT-TTF][HCl$_2$An] (2): H_2Cl_2An (8.08mg) was dissolved in 8 mL of CH_2Cl_2 and placed in the cathode chamber of an H-shaped electrocrystallization cell. BEDT-TTF (5 mg) was

dissolved in 8 mL of CH_2Cl_2 and placed in the anode chamber of the cell. A current density of 0.3 μA cm^{-2} was applied. Black prismatic single crystals of 2 were grown at 20 °C on the anode surface of a platinum-wire electrode over a period of 2 weeks.

5.2.3 Measurement details

X-ray Crystallography

Single crystals of the compounds were mounted on glass fiber loops using a viscous hydrocarbon oil to coat the crystal. Data collection was performed at 293 K on an Agilent Supernova instrument with Cu Kα radiation (λ = 1.54184 Å). The structures were solved by direct methods with the SIR97 program and refined against all F^2 values with the SHELXL-97 program using the WinGX graphical user interface. All non-hydrogen atoms were refined anisotropically except as noted, and hydrogen atoms were placed in calculated positions and refined isotropically with a riding model. A summary of crystallographic data and refinement results is given in Table 5.1.

Table 5.1. Crystallographic data for compounds 1 and 2.

	1	**2**
Empirical formula	$C_{27}H_{17}N_1O_4S_{16}Cl_1$	$C_{16}H_9O_4S_8Cl_2$
Fw	967.83	592.61
Crystal color	black	brown
Crystal size (mm^3)	0.15 * 0.15 * 0.03	0.10 * 0.05 * 0.03
Temperature (K)	293.00(10)	293.00(10)
Wavelength (Å)	1.54184	1.54184
Crystal system, Z	Monoclinic, 2	Monoclinic, 2
Space group	*P*2/*c*	*I*2/*a*
a (Å)	7.6647(3)	13.2766(4)
b (Å)	6.7891(3)	4.12130(10)
c (Å)	34.1205(12)	38.5124(15)
α (°)	90	90
β (°)	93.593(3)	92.935(3)
γ (°)	90	90
V (Å³)	1772.02(12)	2104.51(12)
ρ_{calc} ($g.cm^{-3}$)	1.814	1.870
μ(CuKα) (mm^{-1})	10.111	10.435
θ range (°)	2.60–73.85	4.60–73.43
Data collected	14654	6871
Data unique	3555	2086
Data observed	3381	1902
R(int)	0.0279	0.0389
Nb of parameters / restraints	234/0	140/0
$R1(F)$,[a] $I > 2\sigma(I)$	0.0775	0.0412
$wR2(F^2)$,[b] all data	0.1711	0.1327

$S(F^2)$,[c] all data	1.244	1.106

[a] $R1(F) = \Sigma\|F_0\|-\|F_C\|/\Sigma|F_0|$; [b] $wR2(F^2) = [\Sigma w(F_0^2-F_C^2)^2/\Sigma wF_0^4]^{1/2}$; [c] $S(F^2) = [\Sigma w(F_0^2-F_C^2)^2/(n+r-p)]^{1/2}$.

Raman Studies

Raman spectra were carried out at room temperature on single crystals by using a micro Raman spectrometer (Horiba Labram 300) equipped with a He–Ne laser (λ 632.81 nm) laser in the 80–2000 cm^{-1} range, with a 20 LWD objective (<0.25 $mW/\mu m^2$ on the crystal). A 180° reflective geometry was adopted. The samples were mounted on a glass microscope slide, and the scattering peaks were calibrated against a Si standard (n = 520.7 cm^{-1}). A typical spectrum was collected with a 300 s time constant at <1 cm^{-1} resolution and was averaged over three scans. No sample decomposition was observed during the experiments.

Single-Crystal Conductivity Measurements.

Electrical transport measurements were performed on platelet-shaped single crystals for 1. Gold contacts were evaporated on both faces of the crystals, and gold wires (17 μm diameter) were glued with silver paste on those contacts. Four-probe dc measurements were performed, applying a constant current of 1 μA and measuring the voltage using a Keithley 2401 source meter. Low temperature was provided by a homemade cryostat equipped with a 4 K pulse tube. For compound 2, electrical resistivity was measured on needle-shaped single crystals using a four or two contacts methods (depending on the size of the single crystals) on different single crystals of 2 in the temperature range of 300−150 K. dc measurements were performed, applying a constant current of 0.1 μA.

Band-Gap calculations

The tight-binding band structure calculations were of the extended Hückel type. [34] A modified Wolfsberg–Helmholtz formula[35] was used to calculate the nondiagonal $H_{\mu\nu}$ values. All valence electrons were taken into account in the calculations, and the basis set consisted of Slater-type orbitals of double-ζ quality for C 2s and 2p and S 3s and 3p and of single-ζ quality for H. The ionization potentials, contraction coefficients, and exponents were taken from previous work.[36]

5.3 RESULTS AND DISCUSSION

5.3.1 Synthesis

The KHClCNAn and H_2Cl_2An were combined in electrocrystallization experiments with the ET donor, using the same reagent stoichiometric ratios and solvent mixture at different current densities. Two crystalline salts formulated as $[BEDT\text{-}TTF]_2[HClCNAn]$ (1) and $[BEDT\text{-}TTF][HCl_2An]$ (2) were obtained.

5.3.2 Crystal Structures

The compound 1 crystallizes in the monoclinic space group *P*2/c. It consists of two BEDT-TTF donor molecules for one monoanionic $(HClCNAn)^-$ unit, with one independent donor and half of the anion in the asymmetric unit (Figure 5.1).

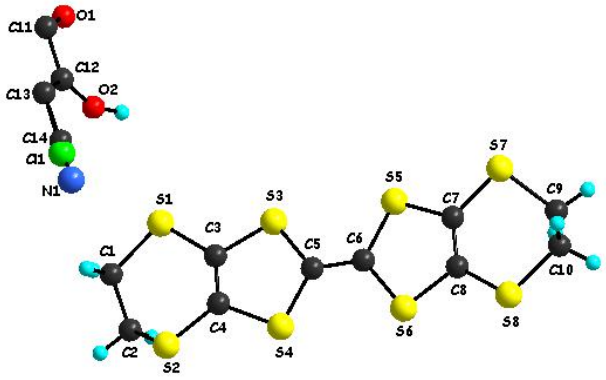

Figure 5.1. View of the independent molecule of donor and half of the anion in the structure of (**1**) together with the atom numbering scheme. H atoms are shown in cyan color.

The structure of the anion is planar with two different C–O distances, corresponding to two C═O bonds (1.215(8) Å) and two C–O bonds for one C–OH and one $C–O^-$ (intermediate value of 1.287(8) Å), which was expected as we started from the monoanionic salt KHClCNAn. As there is only one crystallographically independent molecule of BEDT-TTF for half an $(HClCNAn)^-$ anion, the average charge of each donor molecule is +0,5. This is consistent with the analysis of the bond lengths according to the procedure described by Day et al.,[26] which consists of the empirical equation $Q = 6.347 – 7.463\delta$, relating the charge *Q* to the parameter δ defined by $\delta = (b + c) – (a + d)$, where a–d represent averaged values of C═C and five-membered-ring C–S bonds, as illustrated in Table 5.2. Thus, the Q value for **1** amounts to +0.34 ± 0.1, clearly indicating a mixed valence state for the BEDT-TTF donors. With the knowledge that the estimated charge is very sensitive to the crystal quality, the difference from the expected value of +0.5 is not surprising.

The crystal packing shows segregation of BEDT-TTF molecules in the *ac* plane separated by layers of $(HClCNAn)^-$ and chains of organic donors along the *a* axis (Figure 5.2). The BEDT-TTF molecules inside a chain do not have the same orientation, the intrachain interactions being of the twisted mode (Figure 5.2 b,c).

Table 5.2. Bond distances analysis for the BEDT-TTF molecule in 1 and 2.

		1	2
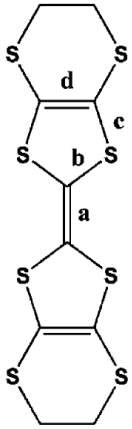	a	1.355(8)	1.367(6)
	b	1.738(6)	1.731(3)
		1.739(7)	1.742(3)
		1.730(7)	
		1.739(6)	
	c	1.751(6)	1.746(3)
		1.746(6)	1.742(3)
		1.751(7)	
		1.749(6)	
	d	1.330(10)	1.352(4)
		1.322(9)	
δ = (b+c) - (a+d)	δ	0.8047	0.7625
Q = 6.347 - 7.4638·δ	Q	0.34	0.66

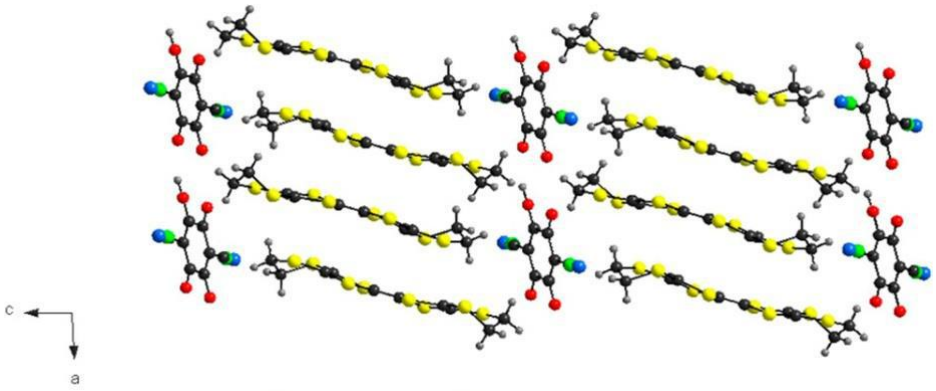

a

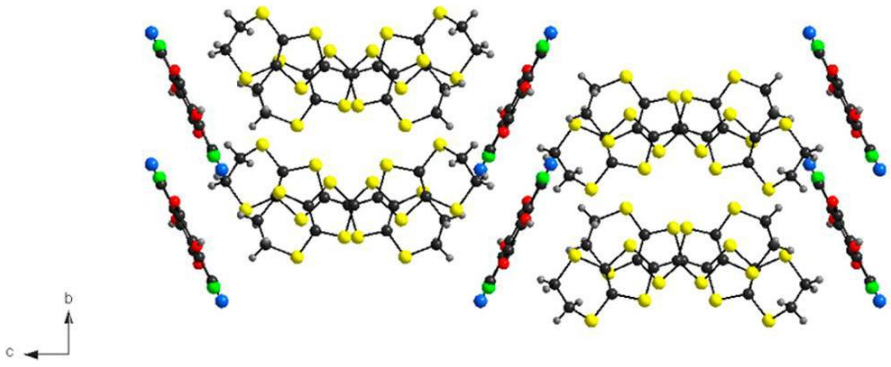

b

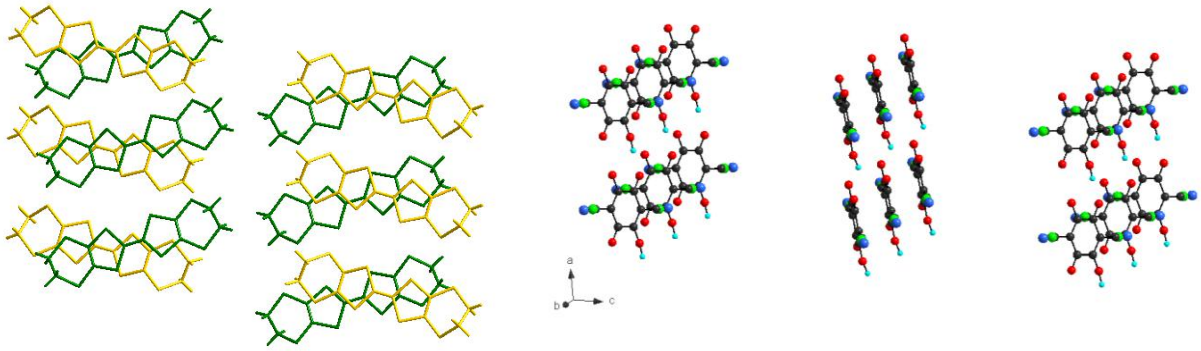

c d

Figure 5.2. View of the crystal structure of 1 along the *b* axis (a) and *a* axis (b). Color code: C, black; H, gray; N, blue; O, red; S, yellow; Cl, green. c) Crystal packing of donor layer of (**1**) in the crystallographic *bc* plane: Each donor molecule BEDT-TTF in the dimer is highlighted in different colors. d) Crystal packing of anilate layer in the crystallographic *ac* plane (bottom).

Due to the different types of interactions, the donor layer contains dimers of BEDT-TTF, for which we observe strong S···H hydrogen bonds between the terminal ethylenedithio groups and short S···S intermolecular contacts (Table 5.3). Similar to the case for the donor layer, in the anilate layer one can observe chains of $(HClCNAn)^-$ molecules along the *a* axis, with strong interactions via hydrogen bonds between C═O and C–OH/C–O^- groups (Table 5.4).

Table 5.3. Selected intermolecular short S···S contacts in 1

S···S	d(S···S) (Å)
S1···S8	4.2762
S2···S6	4.4961
S4···S6	3.6607
S3···S5	3.6081
S3···S6	3.8861
$S4^{ii}$···$S4^{iii}$	3.9335
S7···S8	3.5766

Symmetry transformations used to generate atoms:

(i)-x, -y, 1-z. (ii)1-x, 1-y,-z (iii) -1+x, 1-y, -0.5+z

Table 5.4. Hydrogen bonding parameters (distances in Å and angles in °) in 1

D–H···A	d(D···H)	d(H···A)	d(D ···A)	<(DHA)
C10-H10A···$O1^{i}$	0.9713	3.9394	4.1673	96.780
C10-H10B···O2	0.9691	2.5114	3.1392	122.399
C10-H10A···$O1^{ii}$	0.9713	3.4584	4.1340	128.53
C2-H2A···N1	0.9715	2.8338	3.7948	170.249
C1-H1A···Cl1	0.9692	4.0296	4.1508	90.883
C1-H1B···Cl1	0.9695	3.9559	4.1508	94.783
C10-H10B···Cl1	0.9691	3.5184	4.3385	143.811
C10-H10B···N1	0.9691	3.8950	4.7179	144.519

Symmetry transformations used to generate atoms: (i) x, 1+y, z (ii) x, -y, 0.5+z

Since the anion is located on an inversion center, the Cl and CN substituents are disordered with an sof value of 0.5. Finally, both chloro and cyano substituents present two types of interactions: one interchain interaction with a $(HClCNAn)^-$ from the upper and lower chains and one hydrogen bond with an ethylenedithio group from the neighboring BEDT-TTF molecules (Figure 5.3).

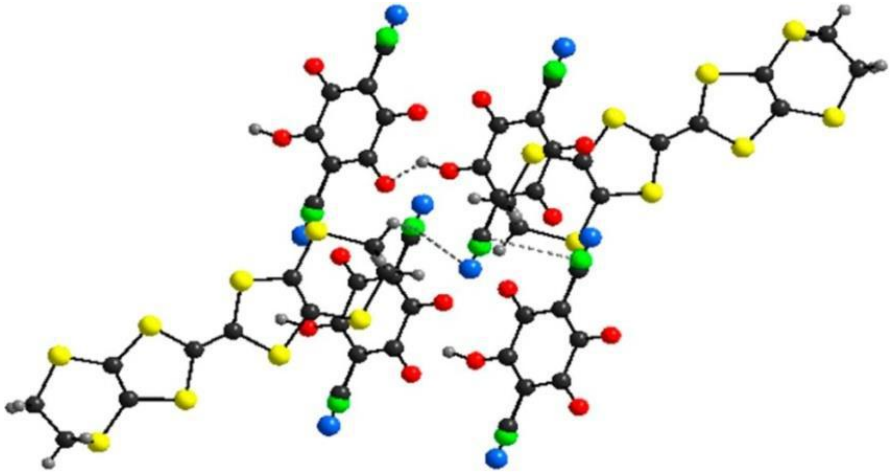

Figure 5.3. Intermolecular interactions (dashed lines) in the structure of 1. Color code: C, black; H, gray; N, blue; O, red; S, gold; Cl, light green.

Compound 2 crystallizes in the monoclinic space group *I2/a*, with one independent half of the donor and half of the anion both located on inversion centers in the asymmetric unit, thus affording a 1:1 stoichiometry (Figure 5.4).

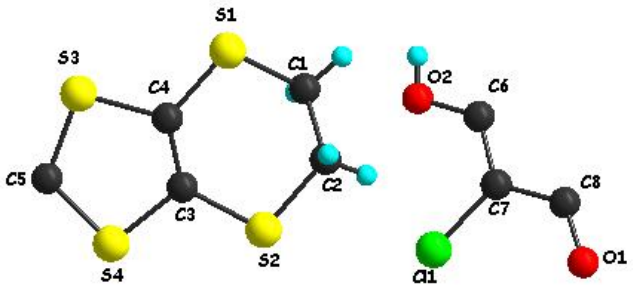

Figure 5.4. View of the independent half of molecules of donor and anion of the asymmetric unit in the structure of 2 together with the atom numbering scheme. H atoms are shown in cyan color.

Similar to the case for 1, the two independent C–O distances in the anilate molecule are consistent with the presence of two C═O (1.235(4) Å) and two C–O(H) bonds (1.294(4) Å). Since the electrocrystallization experiment was started with the H_2Cl_2An, one can conclude that partial deprotonation occurred during the process. As the stoichiometry of the salt is 1:1, one could argue that the anilate is under its monoanionic form II, and thus the donor would bear the charge +1. However, the inspection of the central C═C (1.367(6) Å) and internal C–S bonds (Table 5.2) of the donor would be more in favor of a mixed valence

state, all the more since the crystal structure is of excellent quality. Interestingly, the crystal packing shows donor/anion segregation in the *ac* plane, with formation of uniform chains of BEDT-TTF with no dimerization, separated by layers of anilate anions (Figure 5.5). In the donor layers, the chains develop along the b axis especially through CH···S intermolecular interactions. The intrachain S···S distances are rather long, with the shortest contact amounting to 3.93 Å for S2···S4. Lateral interchain S···S contacts established between donors from neighboring chains are much shorter, ranging from 3.44 to 3.74 Å (Table 5.5). The BEDT-TTF molecules lie parallel to one another along the b axis, but the orientation between donors from adjacent chains is twisted by 45°. This peculiar orientation implies that one BEDT-TTF donor establishes short S···S contacts with three donors from a neighboring chain. The same type of packing is observed for the anilate layer (Figure 5.5 d), although the $(HCl_2An)^-$ molecule is engaged in several interchain interactions with the neighboring anionic molecules, through hydrogen bonds between C═O and C–OH groups (Table 5.6). Finally, S···Cl donor–anion interactions are observed as well between the chloro substituents and the S atoms of ethylenedithio groups from the neighboring BEDT-TTF molecules (Figure 5.6).

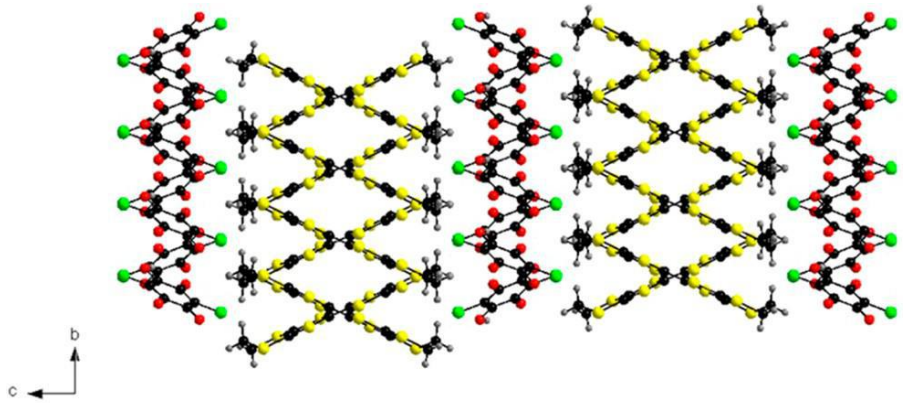

a

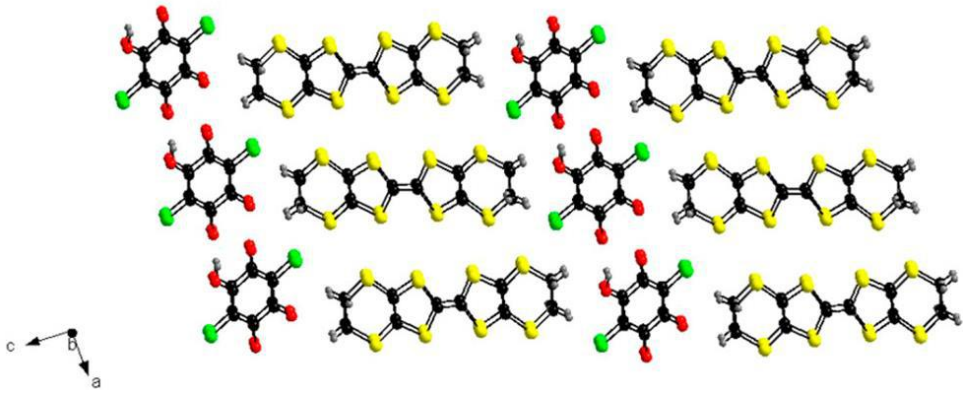

b

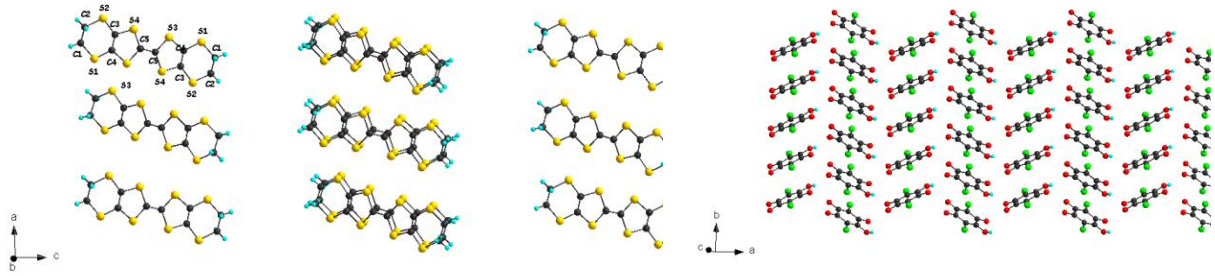

c d

Figure 5.5. View of the crystal structure of 2 along the *a* axis (top) and b axis (bottom). Color code: C, black; H, gray; O, red; S, gold; Cl, light green.

Table 5.5. Selected intermolecular short S···S contacts in 2

S···S	d(S···S) (Å)
S1···S2	3.4438
S2···S3	3.7461
S3···S4	4.8371

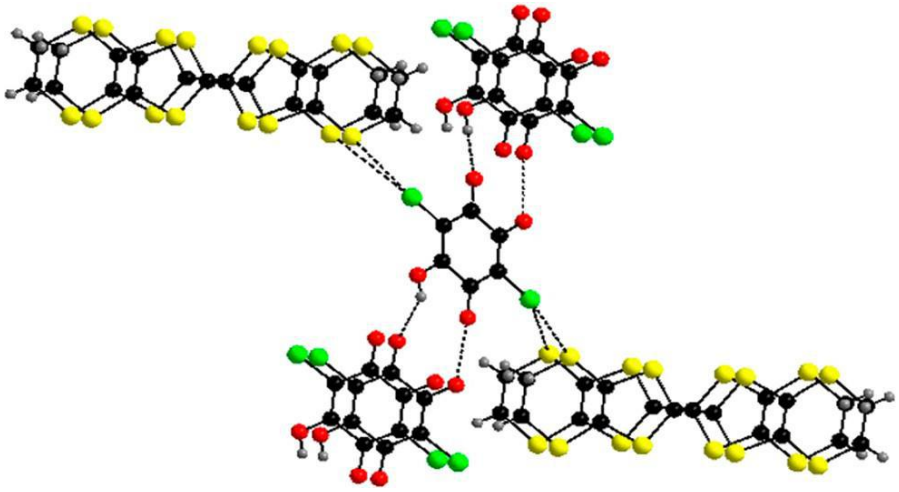

Figure 5.6. Intermolecular anion–anion and anion–donor interactions (dashed lines) in the structure of 2. Color code: C, black; H, gray; O, red; S, gold; Cl, light green.

Table 5.6. Hydrogen bonding parameters (distances in Å and angles in °) in 2

D–H···A	d(D···H)	d(H···A)	d(D ···A)	<(DHA)
O2-H···O1	0.8199	3.5284	3.9401	115.086
C1-H1A···O2	0.9702	3.1562	3.3461	92.745
C1-H1B···O2	0.9686	2.9271	3.3461	107.341
C2-H2B···O2	0.9706	3.3063	3.5162	94.378
C2-H2A···O2	0.9698	2.9459	3.5162	118.717
C1-H1B···Cl1	0.9686	2.9640	3.7759	142.152
C2-H2B···Cl1	0.9706	3.2843	3.4649	92.485
C1-H2A···Cl1	0.9698	3.1167	3.4649	61.254

Symmetry transformations used to generate atoms: i) -x, -y, 1-z.

5.3.3 Raman Studies

Raman measurements were performed on compounds 1 and 2 in order to gain information on the oxidation degree of BEDT-TTF molecules. An approximately linear dependence between

the charge degree of the donor and the Raman-active C═C stretching frequencies in insulating, conducting, and superconducting BEDT-TTF-based salts has previously been established. [27] The two totally symmetric Raman-active C═C stretching modes aν_3 and aν_4, with almost equal contributions of the stretching vibrations of the lateral C═C bonds and the central C═C bond of the BEDT-TTF donor, found in the 1400–1500 cm^{-1} range in most of the known BEDT-TTF-based salts, have been used as charge-sensitive vibrational probes. Raman spectra of 1 and 2 are reported in Figure 5.7. 1 shows a strong peak at 1470 cm^{-1} that can be assigned to the totally symmetric C═C stretching vibration aν_4 of the BEDT-TTF molecule, which is consistent with the observed 2:1 stoichiometry of this salt, where the donor possesses a +0.5 charge state. Two peaks at 1466 and 1495 cm^{-1} are observed instead in the Raman spectrum of 2 that may be assigned to the aν_4 and aν_3 totally symmetric C═C stretching vibrations of the BEDT-TTF molecule in a partial oxidation state. This is consistent with the Q value calculated by the bond distance analysis from the X-ray data (Table 5.2), suggesting a mixed valence (mixed protonation) character for compound 2.

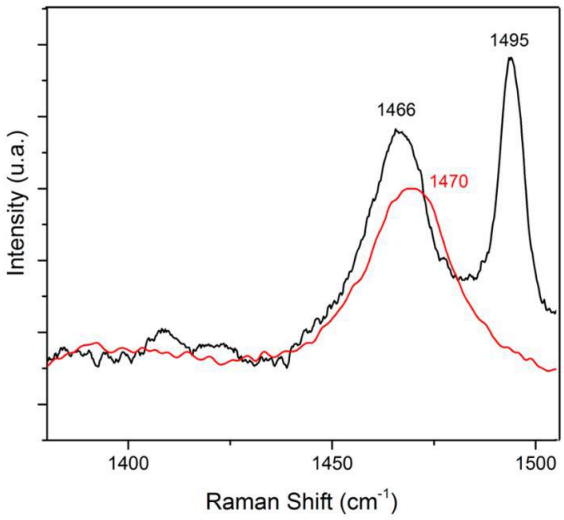

Figure 5.7. Raman spectra of 1 (red line) and 2 (black line) performed with a He–Ne laser (λ = 632.81 nm)

5.3.4 Transport Properties and Band Structure Calculations

The conductivity measurements in compound 1 shows a room-temperature conductivity value of 2×10^{-2} S cm^{-1} for 1 which is typical for a semiconductor. The temperature dependence of the resistivity indicates an activated regime (Figure 5.8, left). The Arrhenius plot of ln ρ vs $1/T$ shows a linear behavior that can be fitted to the law $\ln \rho = \ln \rho_0 + E_a/T$ with an activation energy E_a of 1900 K.

Compounds 2 show a room-temperature conductivity, 10^{-1} S cm^{-1} (four contacts), and 10^{-2} S cm^{-1} (two-contact), semiconducting behavior as shown by the increase of the resistivity as the temperature is decreased (Figure 5.8, right), with activation energies of ca. 4300 K.

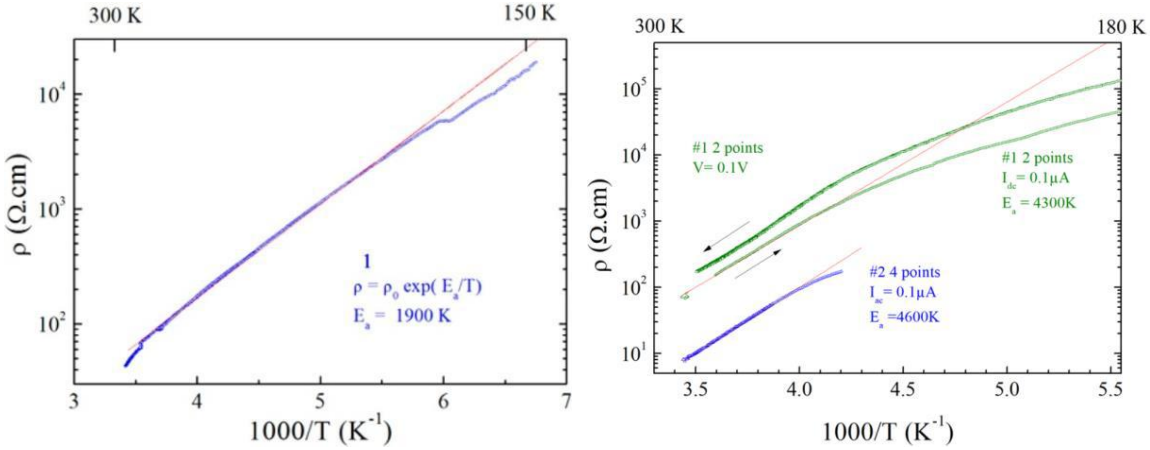

Figure 5.8. Electrical resistivity ρ for single crystals of compounds 1 (left), 2 (right) plotted as log ρ versus the inverse temperature. The red line is the fit to the data with the law $\rho = \rho_0 \exp(E_a/T)$ giving the activation energy Ea.

In order to get deeper insight into the activated conductivity of compound 1, tight-binding band structure calculations of the extended Hückel type were performed. The donor layers of compound 1 contain two symmetry-equivalent molecules making four different intermolecular interactions (labeled I–IV in Figure 5.9). The S···S contacts smaller than 4.0 Å associated with the different interactions are reported in Table 5.7. There are two intrachain (I and II) and two interchain (III and IV) interactions. The intrachain interactions are of the twisted mode, although the two interactions are not exactly of the same type. The shift of the center of the two C═C bonds is small for interaction I but considerably larger for interaction II. As a result, the C–H group of the terminal ethylenedithio groups pointing toward the other donor makes four S···H hydrogen bonds in interaction I (3.020 (×2), 3.046 (×2) Å) but two in interaction II (2.971 (×2) Å). This leads to a series of noticeably shorter S···S interactions and a tighter HOMO–HOMO overlap for interaction I (i.e., the S atoms of the five-membered rings, which are those bearing the stronger coefficients in the HOMO, are those associated with the shorter S···S contacts). In the understanding of the transport properties of this salt we need to have a hint as to the strength of the HOMO···HOMO interactions for I–IV, since there are the HOMO bands which are going to be partially emptied by oxidation. This may be done by looking at the absolute value of the so-called HOMO···HOMO interaction energy, $|\beta_{HOMO-HOMO}|$, associated with each interaction. The calculated values for the four interactions are reported in Table 5.7.

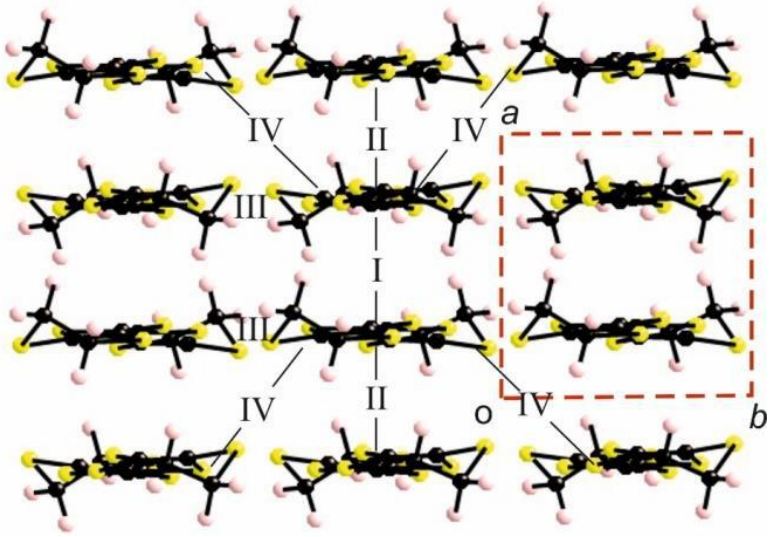

Figure 5.9. Donor layer of the salt 1 where the four different intermolecular interactions are labeled.

Table 5.7. S···S distances shorter than 3.9 Å and absolute values of the βHOMO-HOMO interaction energies (eV) for the different donor···donor interactions in the compound 1 at room temperature.

Interaction	S...S (<3.9 Å)	|βHOMO-HOMO| (eV)
I	3.550 (×2), 3.622 (×2), 3.822 (×2), 3.900	0.4482
II	3.759 (×2), 3.790 (×2), 3.790, 3.886 (×2)	0.2255
III	3.536, 3.553, 3.562, 3.566, 3.822	0.1217
IV	3.838	0.0437

In agreement with the previous structural analysis the strength of interaction I is twice as strong as interaction II. Thus, the chains are strongly dimerized as far as the HOMO···HOMO interactions are concerned. The coupling between these chains depends on the strength of interactions III and IV. Interaction III is associated with the shorter S···S contacts. However, these contacts are of the lateral type associated with moderate π type interactions so that the interaction is only modest. Finally, interaction IV is not very favorable in terms of both distance and orientation, its value thus being much smaller. However, every donor is associated with two of these interactions at both ends of the donor. Because of these interactions, the intrachain and interchain interactions are interrelated. Thus, the donor layers of compound 1 may be described as a series of fairly interacting strongly dimerized chains along *a*.

The previous analysis is substantiated by the calculated band structure shown in Figure 5.10. The band structure along the chain direction (Γ–X) shows two bands with opposite curvature with a large dimerization gap at X, as expected for a strongly dimerized chain. Consequently,

the upper band is built from the antibonding combination of the two HOMO orbitals (ψ^-) of the dimer associated with interaction I, whereas the lower band is built from the bonding combination (ψ^+). In addition, the full dispersion of the upper band is almost the same as that along the chain direction, whereas for the lower band the full dispersion is considerably larger than the dispersion along the chain. This means that the interchain interactions have a relatively small influence on the interactions of the antibonding ψ^- orbital of the dimers of different chains but noticeably affect those of the bonding ψ^+ orbital. In the upper band interactions III and IV tend to cancel along a large part of the Brillouin zone, whereas in the lower band they add up. This is very clear when one looks, for instance, at the Γ–Y direction (i.e., the interchain direction) in Figure 5.10. Ultimately this is due to the bonding vs antibonding character of the ψ^+ and ψ^- orbitals of the dimers.

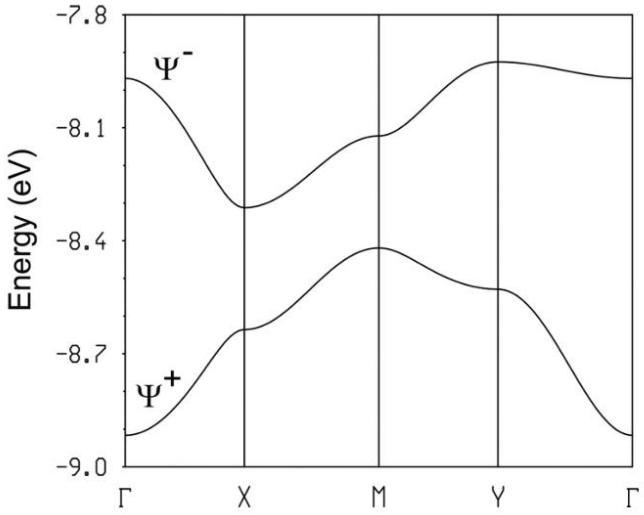

Figure 5.10. Calculated band structure for the donor layers of compound 1 where Γ = (0, 0), X = (a*/2, 0), Y = (0, b*/2), M = (a*/2, b*/2), and S = (−a*/2, b*/2).

The previous observations are relevant in understanding the origin of the activated conductivity of 1. Because of the 2:1 stoichiometry and the fact that the anion carries a single negative charge, the HOMO bands must contain one hole. Thus, the lower HOMO band in Figure 5.10 is full and the upper is half filled. Consequently, the activated conductivity is not a consequence of the occurrence of a gap in the band structure but of the localization of electrons in the upper band. This is likely because of the strong dimerization and the weak interaction between the dimeric units of the layer as far as the ψ orbital is concerned. In other words, the electrons tend to stay localized in the antibonding ψ^- orbital of the dimeric units (interaction I), according to the so-called Mott localization mechanism, and an activation energy is required to jump between units. The occurrence of disorder does not seem to play an

important role in triggering the localization. The particular nature of the donor lattice, with both a strong dimerization along the chains and competing interdimer interactions, lies at the origin of the activated conductivity of this salt.

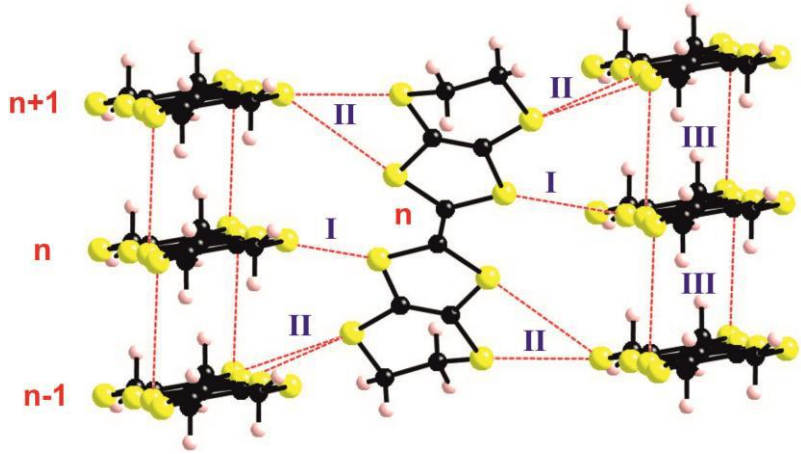

Figure 5.11. Donor···donor interactions in [BEDT-TTF][HCl_2An]**.** Only one molecule of the central uniform chain is shown. The labels n, n+1,…. Refer to the different molecules within a chain; the midpoint of the central C=C bond of molecules with the same index (n, n+1,…) are at the same height along the b direction.

The donor network in [BEDT-TTF][HCl_2An] is built from a series of uniform chains running along the b-direction and parallel to each other but twisted by 45°. As shown in Fig. 10 each donor of one chain (n) makes short S···S contact with three donors of the next chain (n+1, n and n-1), two of them being of the same type (II in Figure 5.11). As shown in Table 5.8, these lateral contacts are considerably shorter than those along the uniform chains. Since every donor makes a total of six contacts along the interchain direction but only two along the intrachain direction one could suspect that the dominant HOMO···HOMO interactions would be those along the interchain direction. This feature may be relevant in understanding the transport properties of this salt since analysis of the crystal structure suggest a partial oxidation state of the BEDT-TTF, something that must be related to an incomplete deprotonation of the chloranilic acid. Thus, one could maybe have some control over this parameter and influence the number of holes in the BEDT-TTF donors.

Table 5.8. S···S distances shorter than 4.0 Å and absolute values of the $\beta_{HOMO-HOMO}$ interaction energies (eV) for the different donor···donor interactions in 2**.**

Interaction	S...S (<4.0 Å)	|βHOMO-HOMO| (eV)
I	3.678	0.0423
II	3.444, 3,746	0.0151
III	3.939 (x2)	0.1348

A convenient way to have a hint on the strength of different HOMO···HOMO interaction is to calculate the absolute value of the so-called HOMO···HOMO interaction energy, $|\beta_{HOMO\text{-}HOMO}|$, associated with each interaction.[28] The calculated values for the three interactions are reported in Table 5.8. It is immediately clear that the lateral interactions, even if associated with S···S contacts which are considerably shorter than the intrachain ones, play only a secondary role. This is specially so for interaction II associated with a very short contact of 3.444 Å. Since the intrachain interaction (III) is substantial and taking into account the number and strength of interchain interactions, the band structure of 2 should exhibit a pseudo-1D behavior with stronger interactions along *b*.

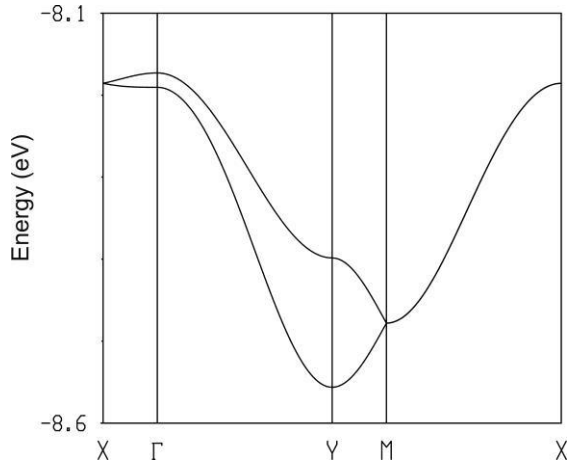

Figure 5.12. Calculated band structure for the donor layers of [BEDT-TTF][HCl_2An] where Γ = (0, 0), X = (a*/2, 0), Y = (0, b*/2) and M = (a*/2, b*/2).

The calculated band structure is shown in Figure 5.12. The total dispersion of the HOMO bands is quite sizable (~ 0.4 eV) and the dispersion along the chain direction is three times larger than that along the interchain direction. This is in agreement with the previous analysis. With a 1:1 stoichiometry and from the one-electron viewpoint half of these levels would be empty and the system should be metallic. However, as it is well known,[37] half-filled 1D systems are almost invariably non-metallic because large electron repulsion effects tend to localize one electron at every site. To predict if a partial doping of the system, by filling these bands with additional electrons because of the incomplete deprotonation of the H_2Cl_2An, would lead to a metallic behavior or not is a challenging question. Both the strength of the transfer integral along the chain, on-site electron-electron repulsions and the possible influence of the random potential of the anilate layer (because of the presence of H_2Cl_2An in both its deprotonated and neutral forms) should be taken into account. Certainly, the HOMO···HOMO interactions are quite sizable and not far, even if smaller, than those found

in some metallic conductors when studied with the same computational approach. In other words, the effective mass of the doping electrons will be relatively large. The fact that the system is not strictly 1D (Figure 5.12) may help in either stabilizing the metallic state or conferring activated but high conductivity to the system. In any case, pressure could most likely have a strong impact on the strength of the interactions along the chain and maybe stabilize the metallic state.

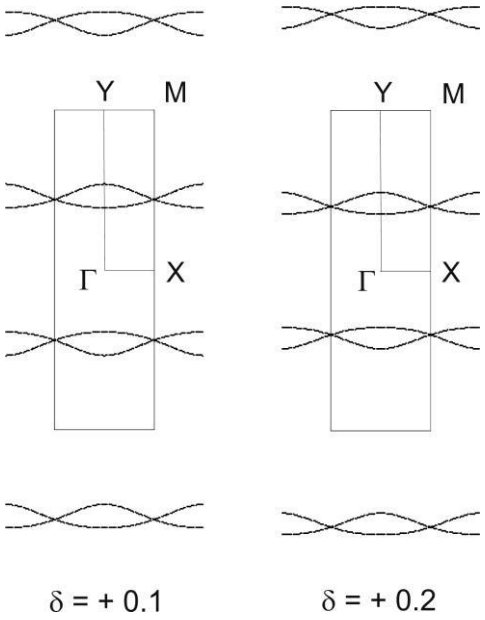

Figure. 5.13. Calculated Fermi surface for the donor layers of [BEDT-TTF][HCl_2An] when δ is +0.1 (left) and +0.2 (right).

If the metallization can be realized it is interesting to know if the metallic state could survive until low temperatures. shown in Figure 5.13 are the hypothetical Fermi surfaces calculated when the average charge of BEDT-TTF is (1-δ) for δ values of 0.1 and 0.2 (i.e. 100×δ is the percentage of neutral BEDT-TTF donors or, equivalently, of non deprotonated H_2Cl_2An molecules). They correspond to pseudo-1D systems as predicted. Note that the warping of the two lines is not really the same (see the zone around Γ) so that the nesting of the Fermi surface is only partial and the usual metal to insulator transition of 1D metallic systems, which in the present case would lead to incommensurate modulations with wave vector q = a*/2+(1+δ)b*/2, could be maybe avoided. In that case the system would keep the metallic state up to low temperatures.

5.4 CONCLUSIONS

Two radical cation salts based on BEDT-TTF and the organic anions chlorocyanoanilate and chloranilate have been prepared by electrocrystallization starting from the KHClCNAn

and the H_2Cl_2An, respectively. While for the first anion a 2:1 salt crystallized with a clear mixed valence state for the donor and −1 charge for the anion, the second salt showed a 1:1 stoichiometry. In both compounds donor–anion segregation occurs, with an arrangement of the donor molecules either in a α′-type donor packing pattern or in parallel columns twisted by 45° with respect to each other, respectively. The anions play a very important role, as they can tune the oxidation state of BEDT-TTF by the deprotonation degree and influence the solid-state architecture through establishment of a complex set on intermolecular interactions. The salt $(BEDT\text{-}TTF)_2(HClCNAn)$ shows activated conductivity supported by band structure calculations which suggest a Mott localization to explain the semiconducting behavior. The salt $(BEDT\text{-}TTF)(HCl_2An)$ is rather intriguing, as the bond distances within the donor are in agreement with a partial oxidation state of BEDT-TTF which would involve an incomplete deprotonation of the starting H_2Cl_2An, and no dimerization is observed within the chains. Moreover, a combination of other BEDT-TTF related donors, including chiral ones,[21,29-31] with diverse hetero-/homosubstituted anilates is envisaged in our groups.

References

(1) Ferraris, J.; Cowan, D. O.; Walatka, V.; Perlstein, J. H. *J. Am. Chem. Soc.,* **1973**, *95*, 948– 949

(2) Wudl, F.; Smith, G. M.; Hufnagel, E. J. *J. Chem. Soc., D* **1970**, *0*, 1453– 1454

(3) Siemons, W. J.; Bierstedt, P. E.; Kepler, R. G. *J. Chem. Phys.,* **1963**, *39*, 3523– 3528

(4) (a) Williams, J. M.; Ferraro, J. R.; Thorn, R. J.; Carlson, K. D.; Geiger, U.; Wang, H. H.; Kini, A. M.;Whangbo, M. H. (b) Coronado, E.; Day, P. *Chem. Rev.,* **2004**, *104*, 5419– 5448

(5) Gómez-García, C. J.; Coronado, E.; Curreli, S.; Giménez-Saiz, C.; Deplano, P.; Mercuri, M. L.; Pilia, L.;Serpe, A.; Faulmann, C.; Canadell, E. *Chem. Commun.,* **2006**, *0*, 4931–4933

(6) Coronado, E.; Curreli, S.; Giménez-Saiz, C.; Gómez-García, C. J.; Deplano, P.; Mercuri, M. L.; Serpe, A.;Pilia, L.; Faulmann, C.; Canadell, E. *Inorg. Chem.,* **2007**, *46*, 4446– 4457

(7) Yamochi, H.; Tada, C.; Sekizaki, S.; Saito, G.; Kusunoki, M.; Sakaguchi, K.-I. *Cryst. Sci. Technol., Sect. A,* **1996**, *284*,379– 390

(8) Dong, J.; Musfeldt, J. L.; Schlueter, J. A.; Williams, J. M.; Nixon, P. G. *Phys. Rev. B: Condens. Matter Mater. Phys.,* **1999**, *60*, 4342

(9) Nishimura, K.; Kondo, T.; Drozdova, O.O.; Yamochi, H.; Saito, G. *J.Mater.Chem.,* **2000**, *10*, 911– 919

(10) Seitz, G.; Imming, P. *Chem. Rev.,* **1992**, *92*, 1227– 1260

(11) Murata, T.; Morita, Y.; Yakiyama, Y.; Fukui, K.; Yamochi, H.; Saito, G.; Nakasuji, K. *J. Am. Chem. Soc.,* **2007**,129, 10837– 10846

(12) Zaman, M.B.; Toyoda, J.; Morita, Y.; Nakamura, S.; Yamochi, H.; Saito, G.; Nishimura, K.; Yoneya ma, N.; Enoki, T.; Nakasuji, K. *J. Mater. Chem.,* **2001**, *11*, 2211– 2215

(13) Zaman, M.B.; Toyoda, J.; Morita, Y.; Nakamura, S.; Yamochi, H.; Saito, G.; Nakasuji, K. *Synth. Met.,* **1999**, *102*, 1691– 1692

(14) Atzori, M.; Benmansour, S.; MínguezEspallargas, G.; ClementeLeón, M.; Abhervé, A.;Gómez-Claramunt, P.; Coronado, E.; Artizzu, F.; Sessini, E.; Deplano, P.; Serpe, A.; Mercuri, M. L.;Gómez García, C. J. *Inorg. Chem.,* **2013**, *52*, 10031– 10040.

(15) Atzori, M.; Pop, F.; Auban-Senzori, P.; GómezGarcía, C.J.; Canadell, E.; Artizzu, F.; Serpe, A.; Deplano, P.;Avarvari, N.; Mercuri, M. L. *Inorg. Chem.,* **2014**, 53, 7028– 7039

(16) Mercuri, M. L.; Congiu, F.; Concas, G.; Sahadevan, S. A. *Magnetochemistry.,* **2017**, 3, 17

(17) Horiuchi, S.; Kumai, R.; Tokura, Y. *J. Am. Chem. Soc.,* **2013**,*135*, 4492– 4500

(18) Kagawa, F.; Horiuchi, S.; Minami, N.; Ishibashi, S.; Kobayashi, K.; Kumai, R.; Murakami, Y.; Tokura, Y. *Nano Lett.,* **2014**, *14*, 239– 243

(19) Murata, T.; Yakiyama, Y.; Nakasuji, K.; Morita, Y. *Cryst. Eng. Comm.,* **2011**, 13, 3689– 3691

(20) Horiuchi, S.; Kumai, R.; Tokura, Y. *J. Am. Chem. Soc.,* **2005**,*127*, 5010– 5011

(21) Atzori, M.; Pop, F.; Auban-Senzier, P.; Clérac, R.; Canadell, E.; Mercuri, M. L.; Avarvari, N. *Inorg. Chem.,* **2015**, *54*,3643– 3653

(22) Ward, M. D.; McCleverty, J. a. *J. Chem. Soc. Dalt. Trans.,* **2002**, *0*, 275–288

(23) Tinti, F.; Verdaguer, I. M.; Kahn, O.; Savariault, J. *Inorg. Chem.,* **1987**, *26*, 2380– 2384

(24) Zaman, B.; Morita, Y.; Toyoda, J.; Yamochi, H.; Sekizaki, S.; Nakasuji, K. *Mol. Cryst. Liq. Cryst. Sci. Technol., Sect. A,* **1996**, *287*, 249– 254

(25) Yamochi, H.; Nakamura, S.; Saito, G.; Zaman, M.B.; Toyoda, J.; Morita, Y.; Nakasuji, K.; Yamashita, Y. *Synth. Met.,* **1999**, *102*,1729

(26) Guionneau, P.; Kepert, C.J.; Bravic, G.; Chasseau, D.; Truter, M.; Kurmoo, M.; Day, P. *Synth. Met.,* **1997**, *86*, 1973– 1974

(27) (a) Wang, H. H.; Ferraro, J. R.; Williams, J. M.; Geiser, U.; Schlueter, J. A. *J. Chem. Soc., Chem. Commun.,* **1994**, 1893– 1894 (b) Girlando, A. *J. Phys. Chem. C,* **2011**, *115*, 19371– 19378

(28) Whangbo, M.-H.; Williams, J. M.; Leung, P. C. W.; Beno, M. A.; Emge, T. J.; Wang, H. H. *Inorg. Chem.,* **1985**, *24*, 3500– 3502

(29) Pop, F.; Auban-Senzier, P.; Canadell, E.; Rikken, G. L. J. A.; Avarvari, N. *Nat. Commun.,* **2014**, *5*, 3757

(30) Pop, F.; Auban-Pop,Senzier, P.; Frąckowiak, A.; Ptaszyński, K.; Olejniczak, I.; Wallis, J.D.; Canadell, E.;Avarvari, N. *J. Am. Chem. Soc.,* **2013**,*135*, 17176– 17186.

(31) Pop, F.; Auban-Senzier, P.; Canadell, E.; Avarvari, N. *Chem. Commun.,* **2016**, *52*,12438– 12441

(32) Atzori, M.; Artizzu, F.; Marchiò, L.; Loche, D.; Caneschi, A.; Serpe, A.; Deplano, P.; Avarvari, N.; Mercuri, M. L. *Dalton. Trans*, **2015**, *44*, 15786– 15802.

(33) Larsen, J.; Lenoir, C. *Synthesis.,* **1989**, *1989*,134

(34) Whangbo, M.-H.; Hoffmann, R. *J. Am. Chem. Soc.,***1978**, *100*, 6093– 6098

(35) Ammeter, J. H.; Bürgi, H.-B.; Thibeault, J.; Hoffmann, R. *J. Am. Chem. Soc.,* **1978**, *100*, 3686–3692

(36) Pénicaud, A.; Boubekeur, K.; Batail, P.; Canadell, E.; Auban-Senzier, P.; Jérome, D. *J. Am. Chem. Soc.,* **1993**, *115*, 4101– 4112.

(37) Lieb, E. H.; Wu, F. Y. *Phy. Rev. Lett.,* **1968**, *20*, 1445–1448.

CHAPTER 6

Anilate-based Magnetic Molecular Conductors

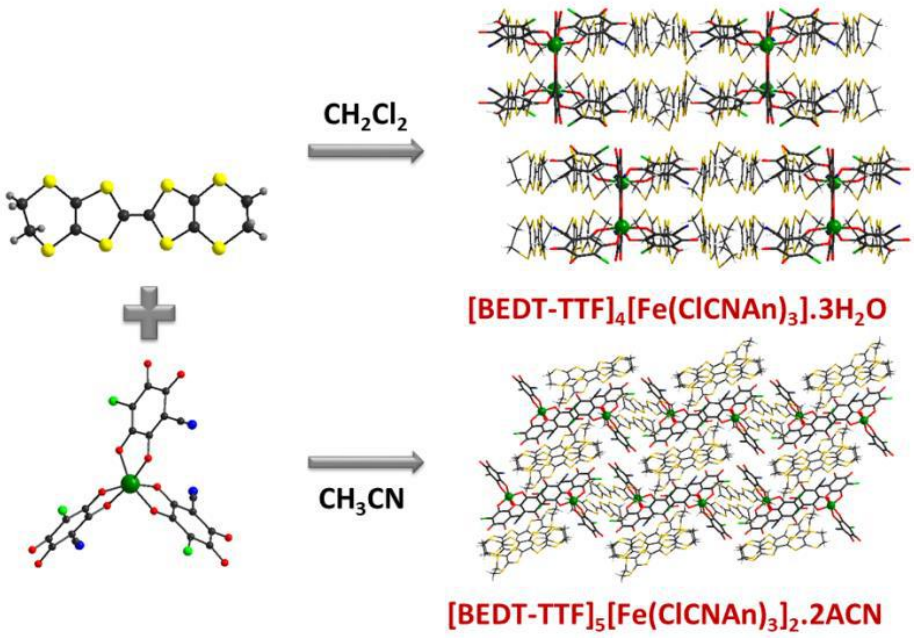

PART II

ABSTRACT

Electrocrystallization of the BEDT-TTF organic donor in the presence of the $[Fe(ClCNAn)_3]^{3-}$ tris(chlorocyanilato)ferrate(III) paramagnetic chiral anion in different stoichiometric ratios and solvent mixtures afforded two different hybrid systems formulated as $[BEDT\text{-}TTF]_4[Fe(ClCNAn)_3]\cdot 3H_2O$ (1) and $[BEDT\text{-}TTF]_5[Fe(ClCNAn)_3]_2\cdot 2CH_3CN$ (2). Compounds 1 and 2 present unusual structures without the typical alternating organic and inorganic layers, where layers of 1 are formed by Λ and Δ enantiomers of the anionic paramagnetic complex, together with mixed-valence BEDT-TTF tetramers and layers of 2 are formed by Λ and Δ enantiomers of the paramagnetic complex, together with dicationic BEDT-TTF dimers. Compounds 1 and 2 show semiconducting behaviors with r.t. conductivities of ca. 6 x 10^{-3} S cm^{-1} and 10^{-3} S cm^{-1} respectively, due to strong dimerization between the donors.

6.1 INTRODUCTION

π-d molecular materials, i.e., systems where delocalized π-electrons of the organic donor are combined with localized d-electrons of magnetic counter ions, have attracted considerable attention in current materials science for their potential applications in molecular electronics since they can exhibit coexistence of two distinct physical properties, furnished by the two networks, or novel and improved properties due to the interactions established between them.[1–6] As far as the magnetic and conducting properties are concerned, important milestones in the field of magnetic molecular conductors have been achieved using as molecular building blocks the BEDT-TTF organic donor[4,5,7] or its selenium derivatives, and charge-compensating anions ranging from simple mononuclear complexes $[MX_4]^{n-}$ ($M = Fe^{III}$, Cu^{II}; X = Cl, Br)[8–10] and $[M(ox)_3]^{3-}$ (ox = oxalate) to layered structures such as the bimetallic oxalate-based layers of the type $[M^{II}M^{III}(ox)_3]^-$ (M^{II} = Mn, Co, Ni, Fe, Cu; M^{III} = Fe, Cr). Anilato-based metal complexes[11–13] are interesting molecular building blocks to be used as paramagnetic counterions, as the presence of different substituents at the 3,6 positions of the anilato moiety gives rise to intermolecular interactions such as H bonding, halogen bonding, π–π stacking, and dipolar interactions, which may influence the physical properties of the resulting material making it versatile for the construction of the above-mentioned multifunctional conducting/magnetic molecule-based materials.[14–23] Recently, multifunctional magnetic molecular conductors based on the tris(chloranilato)ferrate(III) $[Fe(Cl_2An)_3]^{3-}$ anionic complex [11,12] as paramagnetic building block, with the BEDT-TTF organic donor as a potential building block of conducting layers, were reported by Mercuri, Avarvari et al.. By varying the stoichiometric ratio of the molecular components and the solvent mixture, three different hybrid systems formulated as $[BEDT\text{-}TTF]_3[Fe(Cl_2An)_3]\cdot 3CH_2Cl_2\cdot H_2O$, δ-$[BEDT\text{-}TTF]_5[Fe(Cl_2An)_3]\cdot 4H_2O$ and α‴-$[BEDT\text{-}TTF]_{18}[Fe(Cl_2An)_3]3\cdot 3CH_2Cl_2\cdot 6H_2O$ were obtained.[24] Very recently, a complete series of chiral magnetic molecular conductors based on chloranilate-bridged heterobimetallic network[25] and the chiral TM-BEDT-TTF,[26] as enantiopure (R,R,R,R and S,S,S,S) and racemic mixture, were also reported by Mercuri, Avarvari et al.. As a progression of these studies we reacted, by electrocrystallization, the BEDT-TTF organic donor with the heterosubstituted $TPPh_3[Fe(ClCNAn)_3]_3$ anilato complex, in two different solvents, in order to investigate the influence of the different substituents at the 3,6 positions of the anilato moiety as well as solvent effects on the crystal packing and physical properties of the resulting radical cation salts. Two different hybrid systems

formulated as $[BEDT\text{-}TTF]_4[Fe(ClCNAn)_3]\cdot 3H_2O$ (1) and $[BEDT\text{-}TTF]_5[Fe(ClCNAn)_3]_2\cdot 2CH_3CN$ (2) were obtained and we describe herein their synthesis, crystal structures and physical properties.

6.2 EXPERIMENTAL SECTION

6.2.1 General Remarks

$TPPh_3[Fe(ClCNAn)_3]$ was synthesized according to the literature procedure.[13] BEDT-TTF (Zentek, TCI) was used as received. Crystals were grown by the electrocrystallization technique. Solvents used for electrocrystallization experiments (HPLC grade), purchased from Termofisher Scientific Alfa-Aesar, were dried under basic alumina and degassed with argon prior to use.

6.2.2 Synthesis.

$[BEDT\text{-}TTF]_4[Fe(ClCNAn)_3]\cdot 3H_2O$ (1). $TPPh_3[Fe(ClCNAn)_3]$ was dissolved in 8 mL of CH_2Cl_2 and placed in the cathode chamber of an H-shape electrocrystallization cell. BEDT-TTF (5 mg) was dissolved in 8 mL of CH_2Cl_2 and placed in the anode chamber of the cell. A current density of 1 μA cm^{-2} was applied. Black blocks of single crystals of 1 were grown at 20 °C on the anode electrode over a period of three weeks.

$[BEDT\text{-}TTF]_5[Fe(ClCNAn)_3]_2\cdot 2CH_3CN$ (2). $TPPh_3[Fe(ClCNAn)_3$ was dissolved in 8 mL of CH_3CN and placed in the cathode chamber of an H-shape electrocrystallization cell. BEDT-TTF (5 mg) was dissolved in 8 mL of CH_3CN and placed in the anode chamber of the cell. A current density of 3 μA cm^{-2} was applied. Black prismatic single crystals of 2 were grown at 20 °C on the anode electrode over a period of one month.

6.2.3 Measurement details

X-ray Crystallography.

Data collection was performed at 150 K on an Agilent Supernova diffractometer with Cu Kα (λ = 1.54184 Å). Single crystals of 1 and 2 were mounted on a glass fiber loop using a viscous hydrocarbon oil to coat the crystal and then transferred directly to the cold nitrogen stream for data collection. The structure was solved by direct methods with the SIR97 program and refined against all F2 values with the SHELXL-97 program using the WinGX graphical user interface. All non-hydrogen atoms were refined anisotropically except as noted, and hydrogen atoms were placed in calculated positions and refined isotropically with a riding model. The program SQUEEZE from PLATON was used for 1 to calculate the potential solvent-accessible void volume and the nature of the disordered solvent molecules. It has indicated a

total void space of 378.8 $Å^3$ and 127 electrons/cell. This corresponds to 3 molecules of water that have been inserted in the formula of the compound. A summary of crystallographic data and refinement results are listed in Table 6.1.

Table 6.1. Crystallographic data for compounds 1 and 2.

	1	**2**
Empirical formula	$C_{61}H_{38}Cl_3FeN_3O_{15}S_{32}$	$C_{48}H_{23}Cl_3FeN_4O_{12}S_{20}$
Fw	2241.06	1651.10
Crystal color	black	black
Crystal size (mm3)	0.2 * 0.1 * 0.08	0.2 * 0.1 * 0.08
Temperature (K)	150.00(10)	150.00(10)
Wavelength (Å)	1.54184	1.54184
Crystal system, Z	Monoclinic, 4	Triclinic, 2
Space group	$P2_1/c$	P-1
a (Å)	18.2791(10)	13.8508(5)
b (Å)	21.9785(10)	14.5382(6)
c (Å)	22.4369(11)	18.3072(7)
α (°)	90	67.487(4)
β (°)	111.722(6)	79.770(3)
γ (°)	90	61.563(4)
V ($Å^3$)	8373.9(7)	2994.6(2)
ρcalc ($g.cm^{-3}$)	1.778	1.831
μ(CuKα) (mm-1)	10.334	10.338
θ range (°)	2.60–72.80	2.61-73.62
Data collected	36687	23006
Data unique	16234	11621
Data observed	12047	9812
Number of parameters/restraints	1021/15	793/4
R(int)	0.0626	0.0472
R1(F),a I > 2σ(I)	0.1459	0.0788
wR2(F2),b all data	0.3882	0.2174
S(F2),c all data	1.056	1.023

[a] $R1(F) = \Sigma\|F_0\|-\|F_C\|/\Sigma|F_0|$; [b] $wR2(F^2) = [\Sigma w(F_0^2-F_C^2)^2/\Sigma wF_0^4]^{1/2}$; [c] $S(F^2) = [\Sigma w(F_0^2-F_C^2)^2/(n+r-p)]^{1/2}$.

Single Crystal Conductivity Measurements.

Conductivity measurements were carried out on different single crystals of compound 1 with the two contacts methods in the temperature range of 300−150K. The Electrical transport measurements were performed on block-shaped single crystals. Compound 2 was measured on platelet-shaped single crystals.

6.3 RESULTS AND DISCUSSIONS

6.3.1 Synthesis

The tris(chlorocyanaanilato)ferrate(III) complex $[PPh_4]_3[Fe(ClCNAn)_3]$[13] and the BEDT-TTF donor were combined in electrocrystallization experiments, by using the same experimental conditions, except solvents and current density. Two different hybrid systems formulated as $[BEDT\text{-}TTF]_4[Fe(ClCNAn)_3]\cdot 3H_2O$ (1) and $[BEDT\text{-}TTF]_5[Fe(ClCNAn)_3]_2\cdot 2CH_3CN$ (2) were obtained as reported in Scheme 6.1. These systems mainly differ in the donor/anion ratio of 4:1 and 5:2 phase in 1 and 2 respectively which, along with the different crystallization solvent molecules present in the structures, influence the crystal packing motif exhibited by the BEDT-TTF molecules and the resulting physical properties (*vide infra*).

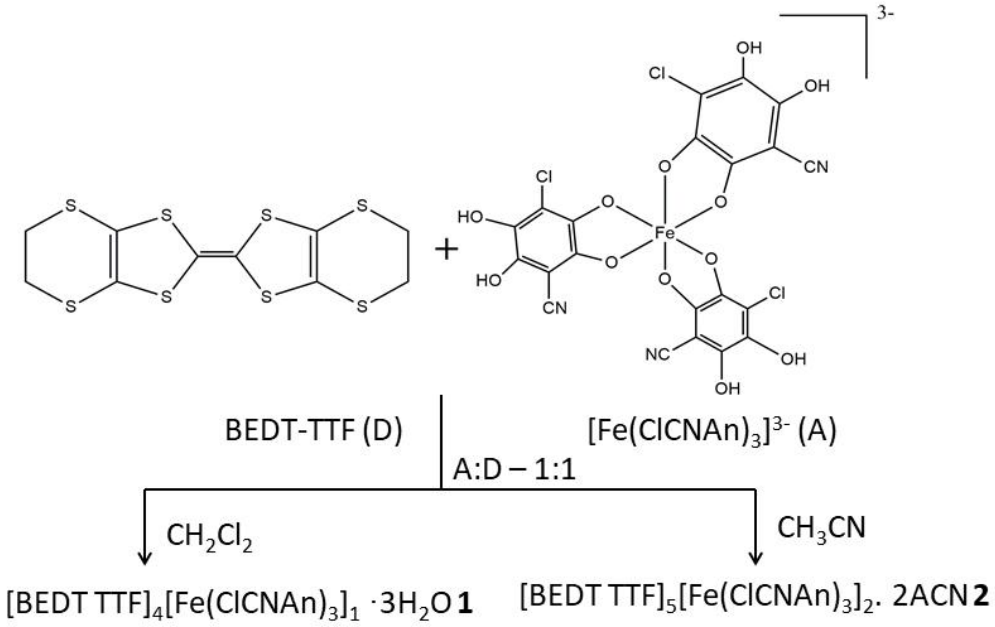

Scheme 6.1. BEDT-TTF Organic Donor (D), $[Fe(ClCNAn)_3]^{3-}$ Anionic Complex (A) and Experimental Conditions Used for the synthesis of Compounds 1−2.

6.3.2 Crystal Structures

The crystals structures of the two hybrid systems consist of homoleptic tris-chelated anionic complexes and BEDT-TTF radical cations. In each system, the metal complexes exhibit octahedral coordination geometry, with the Fe^{III} ion surrounded by six oxygen atoms of three $ClCNAn^{2-}$ chelating ligands. These complexes are chiral according to the metal coordination, but both Λ and Δ enantiomers are present in the crystal lattices with Fe···Fe distances of ca. 9.322Å and 11.77 Å for 1 and 11.7606 Å and 13.145 Å for 2. In Figure 6.1, the molecular structure of the anionic complex in 2 is reported.

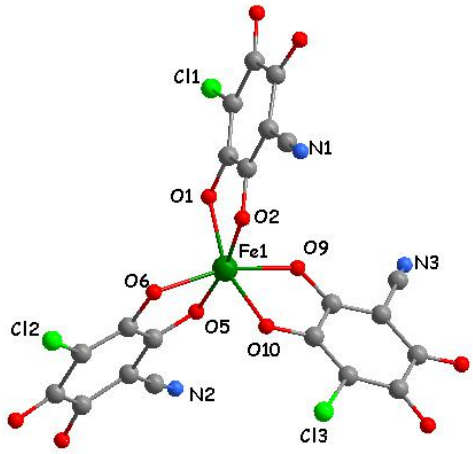

Figure 6.1. ORTEP drawing for the tris(chlorocyanilato)ferrate(III) anionic complex (Δ enantiomer) in 2.

The metal−oxygen bond distances in compounds 1 and 2 vary in the 1.987(5)−2.034(4) Å range (Table 6.2) and are similar to the distances observed in the corresponding BEDT-TTF radical cation salt with the homosubstituted chloranilate complex[24].

Table 6.2. Fe−O Bond Distances (Å) for the Anionic Complex in Compounds 1 and 2

Bonds	**Distances (Å)**	
	1	**2**
Fe-O(1)	2.003(9)	2.006(4)
Fe-O(2)	1.997(8)	2.022(4)
Fe-O(5)	2.001(9)	2.026(4)
Fe-O(6)	2.011(9)	1.987(5)
Fe-O(9)	2.018(9)	2.034(4)
Fe-O(10)	2.004(9)	2.015(4)
Average	2.006	2.015

The C−O bond distances are influenced by the coordination to the metal center. The oxygen atoms coordinated to the metal have C−O distances slightly longer than those of the peripheral oxygen atoms, which show a major double bond character.

Compound 1 crystallizes in the monoclinic space group $P2_1/c$. The asymmetric unit consists of four independent BEDT-TTF donor molecules (indicated as A, B, C and D) for one $[Fe(ClCNAn)_3]^{3-}$ complex (Figure 6.2).

The crystal packing of 1 is unusual and consists of hybrid organic-inorganic layers formed by repeating units of D-A-B-C BEDT-TTF molecules along *ba* plane intercalated by $[Fe(ClCNAn)_3]^{3-}$ complexes of opposite chirality as shown in Figure 6.3. Very short S···S contacts (3.29−3.61 Å) less than the sum of the van der Waals radii (3.65 Å) are present between the B and C molecules which form strong dimers (Figure 6.4).

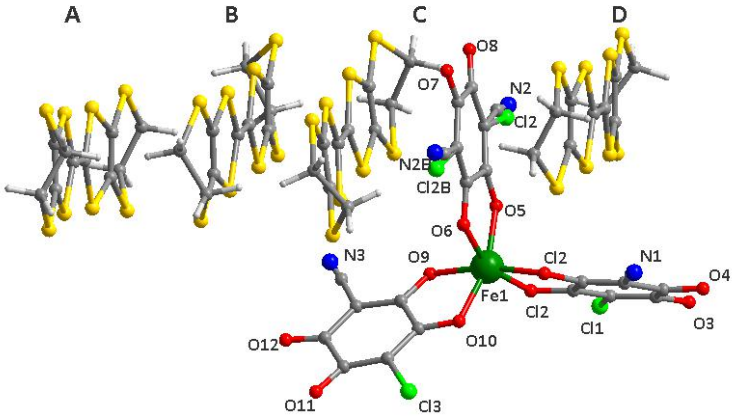

Figure 6.2. Asymmetric Unit of 1: BEDT-TTF molecules are labeled as A, B, C, D.

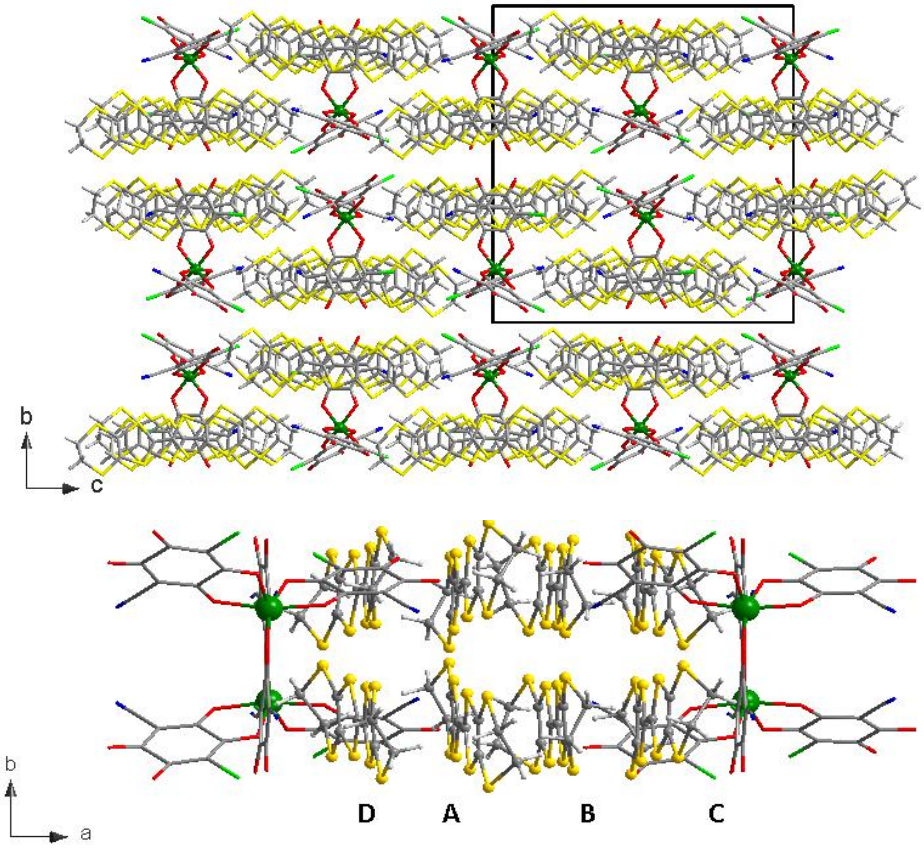

Figure 6.3. View of the crystal packing of 1 along the *bc* plane (top); *ba* plane with labeled A, B, C and D BEDT-TTF molecules (bottom).

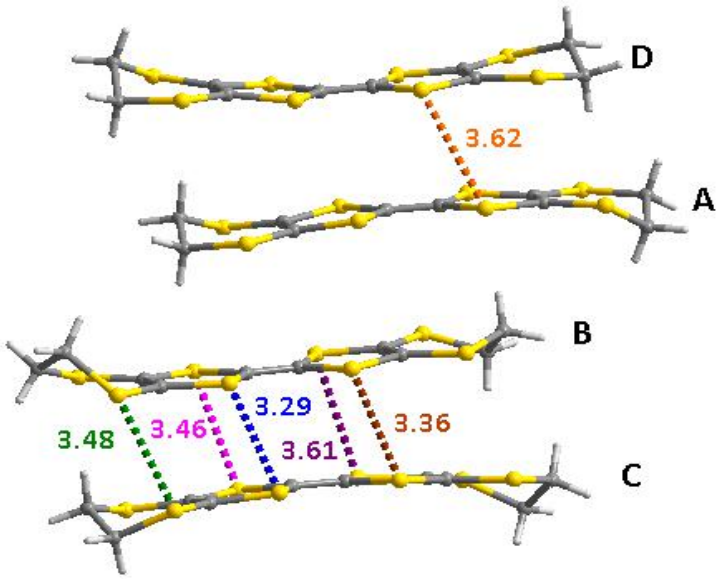

Figure 6.4. S···S contacts (Å) less than the sum of the van der Waals radii (3.65 Å) :S4A-S28D 3.62, S16B-S24C 3.48, S13B-S21C 3.46, S14B-S22C 3.29, S11B-S19C 3.61, S12B- S20C 3.36.

The role of the intermolecular interactions is crucial in templating this type of hybrid organic-inorganic molecular packing since the anionic complexes establish Cl···S and N···S interactions with the BEDT-TTF molecules (Figure 6.5).

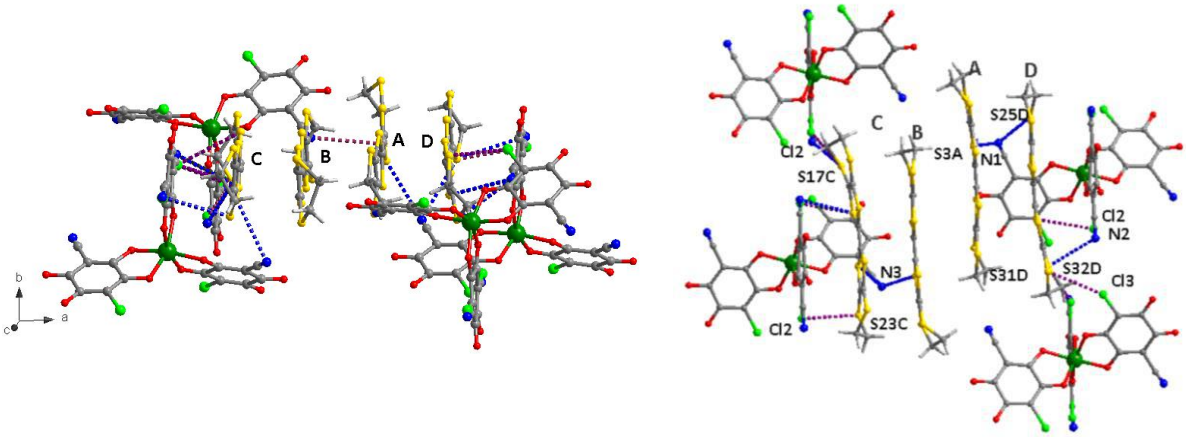

Figure 6.5. DABC BEDT-TTF molecules surrounded by metal complexes. Intermolecular Cl···S (violet) and N···S interactions (blue) lower than the sum of the van der Waals radii between the BEDT-TTF molecules and the ClCNAn ligands are highlighted are highlighted (Å). Cl2-S17C 3.53, Cl2-S19C 3.44, Cl2-S23C 3.61, Cl2-S29D 3.52, Cl2B-S31D 3.45, Cl3-S32D 3.60, N3-S21C 3.60, N2-S17C 3.40, N2-S21C 3.63, N1-S3A 3.63.

The analysis of the bond distances for each crystallographically independent BEDT-TTF molecule, according to the procedure described by Day et. al.,[27] consists of the empirical equation Q = 6.347 − 7.463δ, relating the charge Q to the parameter δ defined by δ =(b + c) − (a + d), where a−d represent averaged values of C=C and five-membered-ring C− S bonds, as

illustrated in Table 2. Thus, the calculated Q value for compound 1 is +3, as expected from the sum of the charge calculated for each of the four BEDT-TTF donor molecules present in this salt (Table 6.2).

Table 6.2: Bond Distance Analysis and Selected Bond Distances (Å) for the BEDT-TTF Donor Molecules in 1

		A	B	C	D
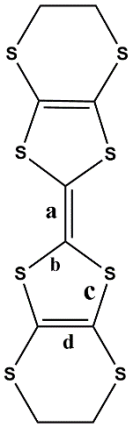	a	1.372(22)	1.373(20)	1.425(20)	1.351(16)
	b	1.721(14)	1.716(13)	1.711(12)	1.735(11)
		1.739(15)	1.715(13)	1.705(12)	1.735(11)
		1.721(15)	1.733(14)	1.704(13)	1.725(11)
		1.744(14)	1.722(14)	1.712(14)	1.737(11)
	c	1.762(14)	1.724(14)	1.751(12)	1.750(13)
		1.746(14)	1.736(12)	1.767(12)	1.750(11)
		1.758(13)	1.733(14)	1.757(13)	1.739(12)
		1.765(11)	1.750(14)	1.725(11)	1.718(12)
	d	1.329(18)	1.388(20)	1.336(18)	1.354(18)
		1.347(18)	1.322(20)	1.344(18)	1.347(18)
δ=(b+c)-(a+d)	δ	0.779	0.729	0.693	0.770
Q= 6.347-7.4638·δ	Q	0.53	0.90	1.17	0.59

The analysis of the central C=C and internal C−S bond lengths confirms that B and C molecules associated in dimers bears a charge of +1, whereas D and A molecules are present in a mixed-valence state.

The BEDT-TTF molecular packing in compound 1, along with the mixed-valence state of the A, D donor molecules, bearing 0.53 and 0.59 positive charge, respectively, allows for delocalization of the charge, in agreement with transport properties.

Compound 2 crystallizes in the triclinic centrosymmetric space group *P*–1. The asymmetric unit consists of two and half independent BEDT-TTF molecules (indicated as A−C), one $[Fe(ClCNAn)_3]^{3-}$ anionic complex and one acetonitrile solvent molecule (Figure 6.6). The crystal packing of 2 shows pseudo-segregation of organic and hybrid organic-inorganic layers (Figure 6.7).

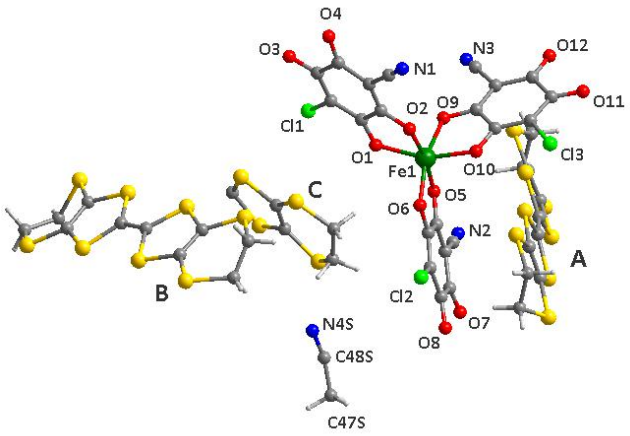

Figure 6.6. Asymmetric Unit of 2. BEDT-TTF molecules are labeled as A, B, C.

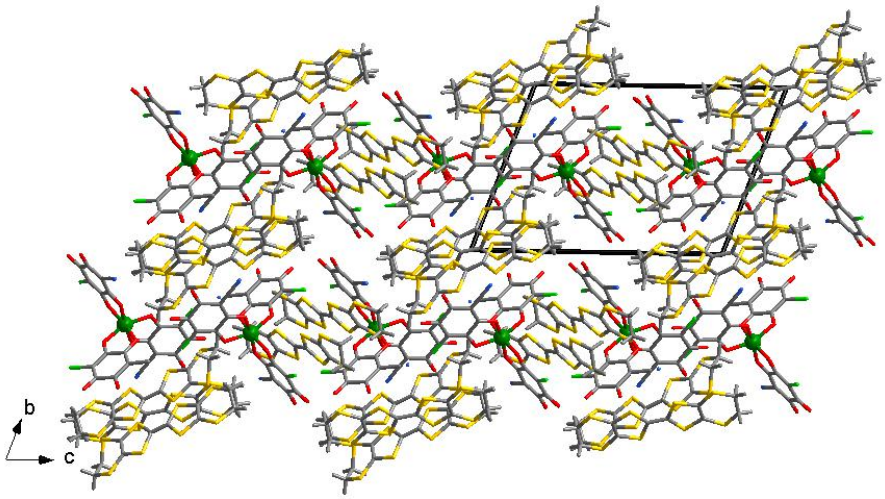

Figure 6.7: Crystal packing of 2 in *bc* plane. Solvent molecules are omitted for clarity.

The hybrid organic-inorganic layer consists of BEDT-TTF dimers (AA) surrounded by metal complexes of opposite chirality in the *bc* plane establishing Cl···S and N···S interactions (Figure 6.8). The organic donor layer is unusual and consists of B and C molecules arranged almost perpendicular to each other: B molecules interact in face-to-face manner forming strong dimers (BB) (Figure 6.9b) while the C molecules, which are almost perpendicular to B, interact laterally. Intra- and inter-layer interactions between donor molecules are highlighted in Figure 6.9b-d.

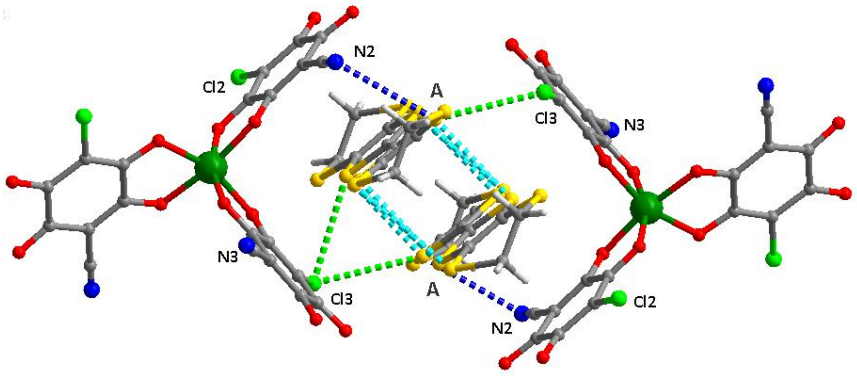

Figure 6.9. AA dimer surrounded by metal complexes of opposite chirality. S···S contacts and intermolecular interactions lower than the sum of the van der Waals radii between the BEDT-TTF molecules and the ClCNAn ligands are highlighted. Cl···S contacts in green, N···S contacts in dark blue; S···S contacts in blue (Å). S3A-S6A 3.33, S4A-S5A 3.44, Cl3-S3A 3.46, Cl3-S6A 3.46, N2-S6A 3.48.

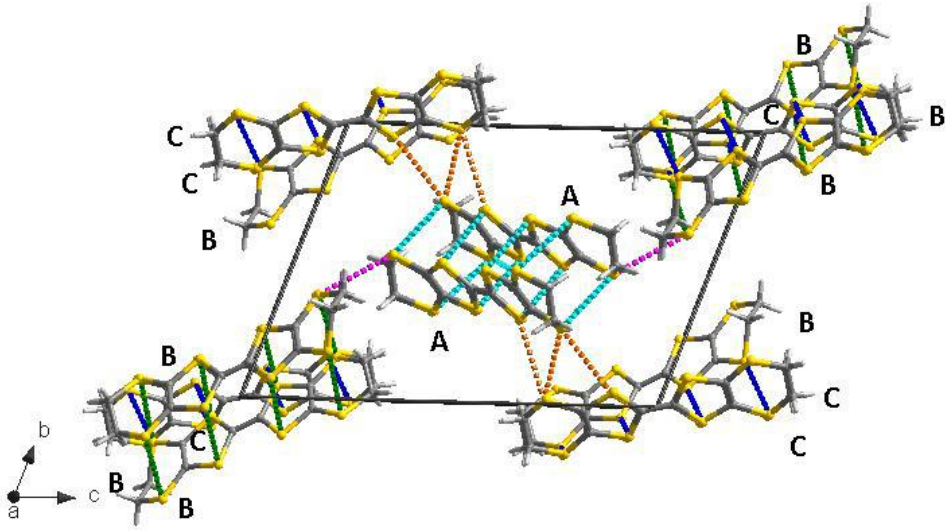

a

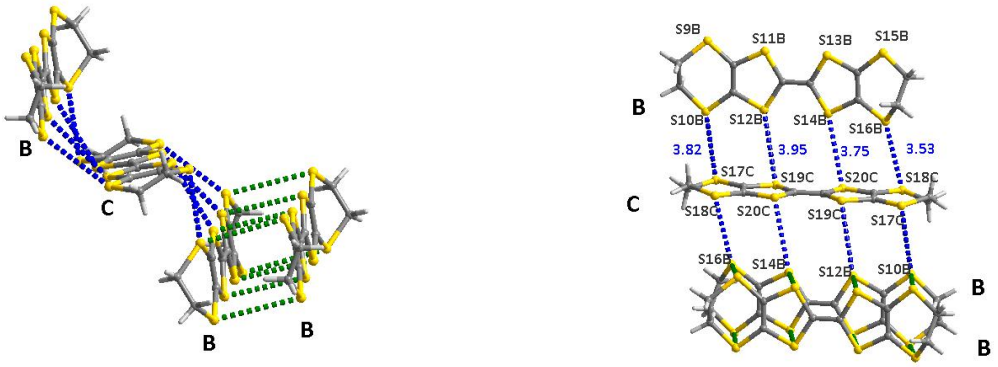

b

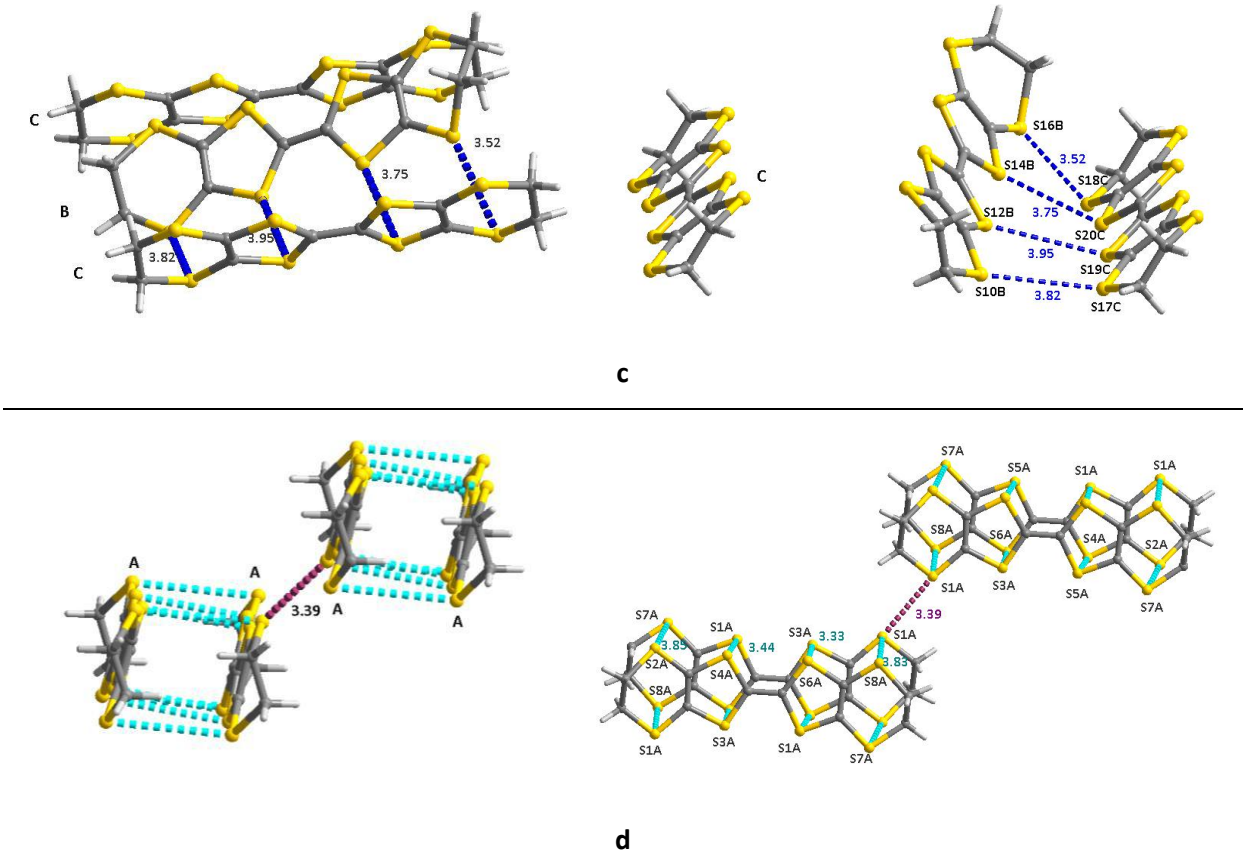

Figure 6.9. a) Unit cell showing the BEDT-TTF molecules. b-d) zoom pictures highlighting the interactions in the BEDT-TTF layer. Intra- and Inter-layer S···S contacts are highlighted. Face-to-face interactions are highlighted in A-A blue, B-B green. side-to-side interactions between B-C in dark blue, A-B in pink, A-A in violet, A-C in orange.

The analysis of the central C=C and internal C−S bond lengths confirms that the A molecule, forming dimers surrounded by the metal complexes, bears a charge of +0.97, whereas B molecules in dimer bears a charge of +1.05 and C molecule are over-oxidised (charge of +1.94), which is clear from longer C=C and shorter C−S bonds for C when compared to A and B (neutral form).

Table 6.3. Bond Distance Analysis and Selected Bond Distances (Å) for the BEDT-TTF Donor Molecules in 2.

		A	B	C
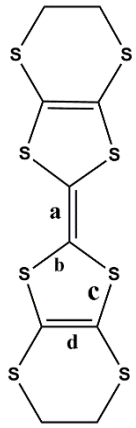	a	1.389(10)	1.391(9)	1.448(10)
	b	1.700(7)	1.718(7)	1.700(7)
		1.723(6)	1.714(8)	1.696(5)
		1.719(6)	1.722(8)	
		1.711(6)	1.718(7)	
	c	1.751(8)	1.734(9)	1.708(6)
		1.724(10)	1.726(6)	1.725(7)
		1.746(9)	1.745(6)	
		1.728(8)	1.740(8)	
	d	1.339(11)	1.360(12)	1.376(8)
		1.344(10)	1.348(11)	
δ=(b+c)-(a+d)	δ	0.72	0.70925	0.5905
Q= 6.347-7.4638·δ	Q	0.97	1.05	1.94

Noteworthy by using the same experimental conditions: the BEDT-TTF organic donor, CH_2Cl_2 and CH_3CN solvents, but by simply replacing $[PPh_4]_3[Fe(Cl_2An)_3]$ tris(chloranilate)ferrate(III) complex with $[PPh_4]_3[Fe(ClCNAn)_3]$ tris(chlorocyananilate) ferrate(III) complex, different radical cation salts with 4:1 and 5:2 D:A ratio instead of 3:1 and 5:1 D:A[18] have been obtained as highlighted in Table 6.4. The intermolecular interactions such as Cl···S and N···S contacts play a role in the crystal packing of compound 1 and 2.

Table 6.4. Comparison of radical-cation salts obtained by using $[PPh_4]_3[Fe(ClCNAn)_3]$ and $[PPh_4]_3[Fe(Cl_2An)_3]$ in CH_2Cl_2 (DCM) and CH_3CN (ACN) solvents.

Solvent	**BEDT-TTF (D)**			
	$[PPh_4]_3[Fe(ClCNAn)_3]$ (A)		**$[PPh_4]_3[Fe(Cl_2An)_3]$ (A)**	
		D:A		**D:A**
DCM	$[BEDT\text{-}TTF]_4[Fe(ClCNAn)_3]\cdot 3H_2O$ **(1)**	**4:1**	$BEDT\text{-}TTF]_3[Fe(Cl_2An)_3]\cdot 3CH_2Cl_2\cdot H_2O$	**3:1**
ACN	$[BEDT\text{-}TTF]_5[Fe(ClCNAn)_3]_2\cdot 2ACN$ **(2)**	**5:2**	δ-$[BEDT\text{-}TTF]_5[Fe(Cl_2An)_3]\cdot 4H_2O$	**5:1**

6.3.3 Transport Properties

The conductivity measurements in compound 1 show r.t. conductivity between ca. 2 x 10^{-3} $S.cm^{-1}$ and 10^{-4} $S.cm^{-1}$ (depending on the quality of crystals). This conductivity decreases as the sample is cooled in agreement with semiconducting behavior (Figure 6.10, left) with average activation energy E_a of *ca.* 1905K.

Compound 2 shows a r.t. conductivity between 10^{-3} S.cm^{-1} (at 12.9 GPa) and 2 x 10^{-4} 10 S.cm^{-1} (at 2.1 GPa). It shows a semiconducting behavior as shown by the increase of the resistivity as the temperature is decreased (Figure 6.10, right), with an activation energy of 92 meV at 12.9 GPa.

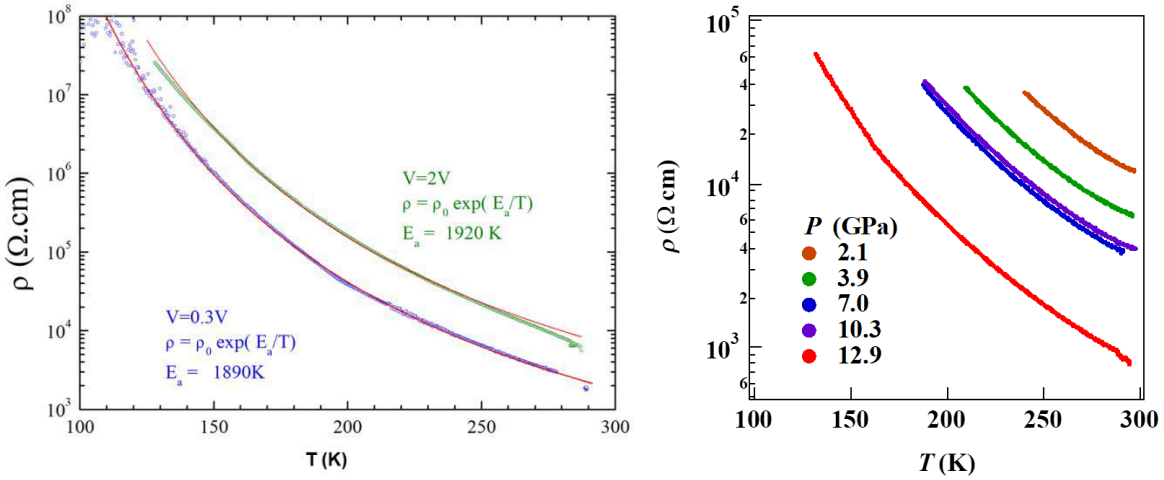

Figure 6.12. Temperature dependence of the electrical resistivity ρ for single crystals of compounds 1 (left) and 2 (right).

Raman studies to confirm the organic donor charge calculated from structural data, band structure calculations and magnetic measurements of 1 and 2 compounds are in progress.

6.4 CONCLUSIONS

Two radical cation salts based on BEDT-TTF and $[Fe(ClCNAn)_3]^{3-}$ tris(chlorocyanilato) ferrate(III) anionic complex have been prepared by electrocrystallization, by using CH_2Cl_2 for 1 and CH_3CN for 2. In CH_2Cl_2, a 4:1 donor:anion salt, 1, was obtained showing a combination of partial and neutral state for the donor; while 2 showed a 5:2 donor:anion ratio with a combination of neutral and over-oxidized charge state for the donor. 1 and 2 compounds present unusual donor–anion segregation and both are semiconductors. The role of Cl···S and N···S intermolecular interactions on the crystal packing of compound 1 and 2 is highlighted.

As perspective, novel BEDT-TTF-based radical cation salts where the tris(chlorocyananilato)ferrate(III) anion is replaced by its Br or I analogues at the 3,6 positions of the anilato moiety, will be prepared, in order to perform a systematic study on the influence of the electronic nature and strength of the intermolecular interactions, due to the different halogen substituents, in affecting the crystal packing and then, the corresponding physical properties.

References

(1) Kobayashi, H.; Cui, H. B.; Kobayashi, A. *Chem. Rev.* **2004**, *104*, 5265–5288.
(2) Enoki, T.; Miyazaki, A. *Chem. Rev.* **2004**, *104*, 5449–5477.
(3) Coronado, E.; Giménez-Saiz, C.; Gómez-García, C. J. *Coord Chem Rev*; 2005; 249, 1776–1796.
(4) Rashid, S.; Turner, S. S.; Day, P.; Howard, J. A. K.; Guionneau, P.; McInnes, E. J. L.; Mabbs, F. E.; Clark, R. J. H.; Firth, S.; Biggs, T. *J. Mater. Chem.* **2001**, *11*, 2095–2101.
(5) Martin, L.; Turner, S. S.; Day, P.; Mabbs, F. E.; McInnes, E. J. L. *Chem. Commun.* **1997**, 15, 1367–1368.
(6) Uji, S.; Shinagawa, H.; Terashima, T.; Yakabe, T.; Terai, Y.; Tokumoto, M.; Kobayashi, A.; Tanaka, H.; Kobayashi, H. *Nature* **2001**, *410*, 908–910.
(7) Kurmoo, M.; Graham, A. W.; Day, P.; Coles, S. J.; Hursthouse, M. B.; Caulfield, J. L.; Singleton, J.; Pratt, F. L.; Hayes, W.; Ducasse, L.; et al. *J. Am. Chem. Soc.* **1995**, *117*, 12209–12217.
(8) Fujiwara, H.; Fujiwara, E.; Nakazawa, Y.; Narymbetov, B. Z.; Kato, K.; Kobayashi, H.; Kobayashi, A.; Tokumoto, M.; Cassoux, P.; Narbonne, R. De; et al. *J. Am. Chem. Soc.* **2001**, *123*, 306–314.
(9) Day, P.; Kurmoo, M.; Mallah, T.; Marsden, I.R.; Friend, R.H.; Pratt, F.L.; Hayes, W.; Chasseau, D.; Gaultier, J. *J. Am. Chem. Soc.* **1992**, *114*, 10722–10729.
(10) Martin, L.; Day, P.; Clegg, W.; Harrington, R.W.; Horton, P.N.; Bingham, A.; Hursthouse, M.B.; McMillan, P.; Firth, S. *J. Mater. Chem.* **2007**, *17*, 3324–3329.
(11) Atzori, M.; Marchiò, L.; Clérac, R.; Serpe, A.; Deplano, P.; Avarvari, N.; Mercuri, M. L. *Cryst.Growth Des.* **2014**, *14*, 5938–5948.
(12) Atzori, M.; Artizzu, F.; Sessini, E.; Marchiò, L.; Loche, D.; Serpe, A.; Deplano, P.; Concas, G.; Pop, F.; Avarvari, N.; et al. *Dalton Trans* **2014**, *43*, 7006–7019.
(13) Atzori, M.; Artizzu, F.; Marchiò, L.; Loche, D.; Caneschi, A.; Serpe, A.; Deplano, P.; Avarvari, N.; Mercuri, M. L. *Dalt. Trans.* **2015**, *44*, 15786–15802.
(14) Galán-Mascarós, J. R.; Coronado, E.; Goddard, P. A.; Singleton, J.; Coldea, A. I.; Wallis, J. D.; Coles, S. J.; Alberolá, A. *J. Am. Chem. Soc* **2010**, *132*, 9271–9273.
(15) Atzori, M.; Benmansour, S.; Mínguez Espallargas, G.; Clemente-León, M.; Abhervé, A.; Gómez-Claramunt, P.; Coronado, E.; Artizzu, F.; Sessini, E.; Deplano, P.; et al. *Inorg Chem* **2013**, *52*, 10031–10040.
(16) Gómez-Claramunt, P.; Benmansour, S.; Hernández-Paredes, A.; Cerezo-Navarrete, C.; Rodríguez-Fernández, C.; Canet-Ferrer, J.; Cantarero, A.; Gómez-García, C. J. *Magnetochemistry* **2018**, *4*, 6.
(17) Abhervé, A.; Clemente-León, M.; Coronado, E.; Gómez-García, C. J.; Verneret, M. *Inorg Chem* **2014**, *53*, 12014–12026.
(18) Atzori, M.; Pop, F.; Auban-Senzier, P.; Gómez-García, C. J.; Canadell, E.; Artizzu, F.; Serpe, A.; Deplano, P.; Avarvari, N.; Mercuri, M. L. *Inorg Chem* **2014**, *53*, 7028–7039.
(19) Benmansour, S.; Pérez-Herráez, I.; López-Martínez, G.; Gómez García, C. J. *Polyhedron* **2017**, *135*, 17–25.
(20) Coronado, E.; Galàn-Mascaròs, J. R.; Gomez-Garcia, C.; Laukhin, V. *Nature* **2000**, *408*, 447–449.
(21) Benmansour, S.; Coronado, E.; Giménez-Saiz, C.; Gómez-García, C. J.; Rößer, C. *Eur. J. Inorg. Chem.* **2014**, *2014*, 3949–3959.
(22) Benmansour, S.; Abhervé, A.; Gómez-Claramunt, P.; Vallés-García, C.; Gómez-García, C. J. *ACS Appl Mater Interfaces* **2017**, *9*, 26210–26218.
(23) Benmansour, S.; Vallés-García, C.; Gómez-Claramunt, P.; Mínguez Espallargas, G.; Gómez-García, C. J. *Inorg. Chem.* **2015**, *54*, 5410–5418.
(24) Mercuri, M. L.; Congiu, F.; Concas, G.; Ashoka Sahadevan, S. *Magnetochemistry* **2017**, *3*, 17.
(25) Ashoka Sahadevan, S.; Monni, N.; Abhervé, A.; Auban-Senzier, P.; Canadell, E.; Mercuri, M. L.; Avarvari, N. *Inorg. Chem.* **2017**, *56*, 12564–12571.
(26) Atzori, M.; Pop, F.; Auban-Senzier, P.; Clérac, R.; Canadell, E.; Mercuri, M. L.; Avarvari, N.

Inorg. Chem. **2015**, *54*, 3643–3653.
(27) Guionneau, P.; Kepert, C. J.; Bravic, G.; Chasseau, D.; Truter, M. R.; Kurmoo, M.; Day, P. *Synth. Met.* **1997**, *86*, 1973–1974.

PART II

PART III
Conclusions & Perspectives

PART III

CONCLUSIONS

The obtained results highlight the versatility of anilate-based ligands as molecular building blocks for the synthesis of new functional and multifunctional materials combining magnetism, conductivity and luminescence. Among the anilate ligands, the only known heterosubstituted anilate with Cl/CN substituents at the 3,6 positions, $ClCNAn^{2-}$, have been selected for preparing a novel family of 2D layered CPs and MOFs with both 3d metal ions and 4f lanthanide ions, through a general and straightforward synthetic strategy. Scheme 1 summarizes the obtained results.

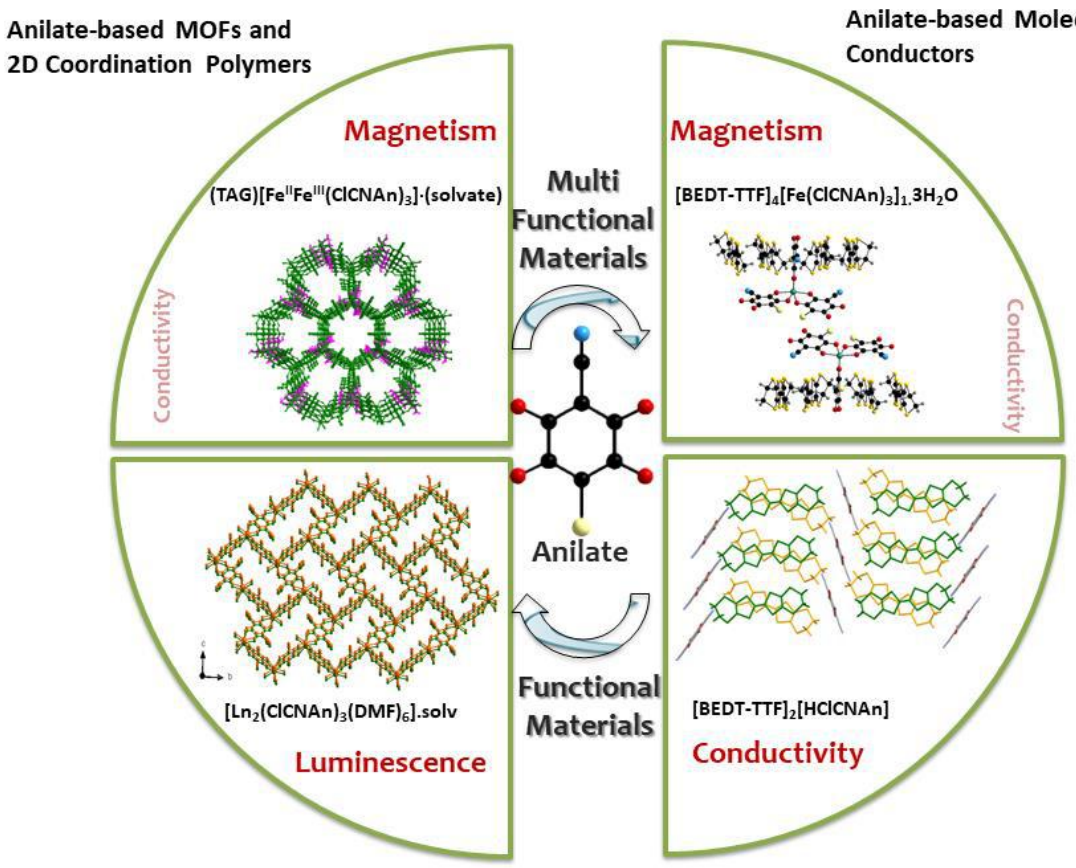

Scheme 1

The mixed-valence $Fe^{II}Fe^{III}$ 2D CP, formulated as $[TAG][Fe^{II}Fe^{III}(ClCNAn)_3]$, containing, for the first time in such 2D networks, the tris(amino)-guanidinium (TAG) cation has been synthesized. This system has been thoroughly characterized through X-ray diffraction analysis, magnetic, conductivity, Raman and Mössbauer studies.

2D CPs based on NIR-emitting lanthanides (Yb^{III}, Nd^{III}, Er^{III}) and the $ClCNAn^{2-}$ ligand, formulated as $[Ln_2(ClCNAn)_3(DMF)_6]\cdot(DCM)_x$ (Ln^{III} = Yb (x = 0)(1), Nd (2) and Er(3) (x = 2)), have been prepared and fully characterized. These layered compounds were

exfoliated to nanosheets, by a top-down strategy involving sonication-assisted solution synthesis and characterized by atomic-force microscopy and high-resolution transmission electron microscopy. Time-resolved photoluminescence studies performed on both the bulk and nanosheets clearly demonstrate that the $ClCNAn^{2-}$ ligand acts as efficient antenna towards Ln^{III} ions and that the emission sensitization occurs as a multi-step relaxation process involving, in sequence, intersystem crossing and energy transfer from ligand triplet states to the Ln^{III} ions. Effects induced by the exfoliation process on the photo physical properties of the nanosheets were also highlighted.

A novel family of heteroleptic 2D CPs based on NIR-emitting lanthanides $[Ln_4(ClCNAn)_5(DOBDC)_1(DMSO)_{10}].(DMSO)_2$ (Ln^{III}- Yb (1), Er (2)) $[Ln_2(ClCNAn)_2(F_4$-BDC$)(DMSO)_6]$ (Ln- Yb(3), Er(4)) and mixed ligands ($ClCNAn^{2-}$ and carboxylate ligands (DOBDC and F_4-BDC)), were prepared and characterized. Photo physical measurements show that these ligands act as efficient antenna for Ln^{III} ions.

A novel family of 2D CPs, formulated as $[Dy_2(ClCNAn)_3(DMSO)_6]$ (1), $[Dy_2(ClCNAn)_3(DMSO)_6]$ (1'), $[Dy_2(ClCNAn)_3(DMF)_6]\cdot(DCM)_2$ (2), $[(Me_2NH_2)_2[Dy_2(ClCNAn)_4(H_2O)_2]\cdot(DMF)$ (3) based on Dy^{III} and $ClCNAn^{2-}$ were prepared in order to investigate their magnetic properties. They were structurally characterized and magnetic measurements were done. The magnetic measurements show SMM behaviour.

Furthermore, the ability of the anilate ligands to work as components of BEDT-TTF-based molecular conductors has been demonstrated through the synthesis, via electrocrystallization technique. Two different crystalline radical cation salts the $[BEDT\text{-}TTF]_2[HClCNAn]$(1) and $[BEDT\text{-}TTF][HCl_2An]$(2) compounds, were structurally characterized and transport properties were studied. 1 and 2 are semiconductors with r.t. conductivities of 10^{-2} Scm^{-1} and 10^{-1} Scm^{-1}, respectively.

Π-d hybrid multifunctional paramagnetic molecular conductors were prepared by combining BEDT-TTF and tris(chlorocyanilato)ferrate(III) anion, formulated as $[BEDT\text{-}TTF]_4[Fe(ClCNAn)_3]\cdot 3H_2O$ (1) and $[BEDT\text{-}TTF]_5[Fe(ClCNAn)_3]_2\cdot 2CH_3CN$ (2). Two systems with different stotiometric ratios, D: A of 4:1 and 5:2, were obtained by changing the solvent mixture, i.e. CH_2Cl_2 and CH_3CN respectively. 1 and 2 show semiconducting behavior with r.t. conductivities of ca. 6 x 10^{-3} S cm^{-1} and 10^{-3} S cm^{-1} respectively.

PERSPECTIVES

On the basis of the obtained results, the following perspectives can be envisaged:

I. As far as the mixed valence Fe^{III}/Fe^{II} CP is concerned, it is noteworthy that (i) this compound crystallize in the Polar trigonal space group *P*3, therefore the ferroelectric properties on this compound are worth to be investigated. (ii) new homologue systems where the $ClCNAn^{2-}$ ligand is replaced by its Cl, Br or I analogues will be prepared. This could allow for a systematic study on the crystalline structure and properties of obtained materials due to the different electronic nature of substituents.

II. Novel heterobimetallic ClCNAn-based (M^{III}/M^{II}) complexes will be prepared with TAG^{+} as cation (M^{III} = Fe, Cr; M^{II} = Mn, Co), in order to investigate their magnetic and/or ferroelectric properties. In this context, a heterobimetallic system with Fe^{III} and Co^{II}, on $ClCNAn^{2-}$ as building block, was prepared and preliminary characterized by SEM and Elemental Analysis. It can be formulated as $TPPh_3[Fe^{III}Co^{II}(ClCNAn)_3]$ and its structural characterization and physical properties studies are in progress.

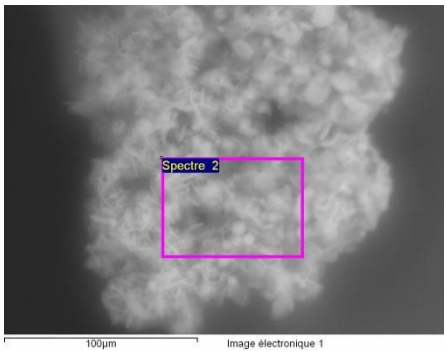

Elément	%Masse	%Atomique
P K	18.34	25.23
Cl K	30.41	36.55
Fe K	29.27	22.33
Co K	21.98	15.89
Totaux	100.00	

Figure1. SEM image of $TPPh_3[Fe^{III}Co^{II}(ClCNAn)_3]$

III. Novel homometallic ClCNAn-based complexes will be prepared in order to perform a sistematic study on the effects of metal ion substitution on electronic structure across a series of isostructural frameworks. In this context the novel series of 2D compounds has been obtained which can be formulated as $(TPPh_3)_2[M^{II}_2(ClCNAn)_3]_n\cdot$(solvate) ($M^{II}$ = Mn, Co).

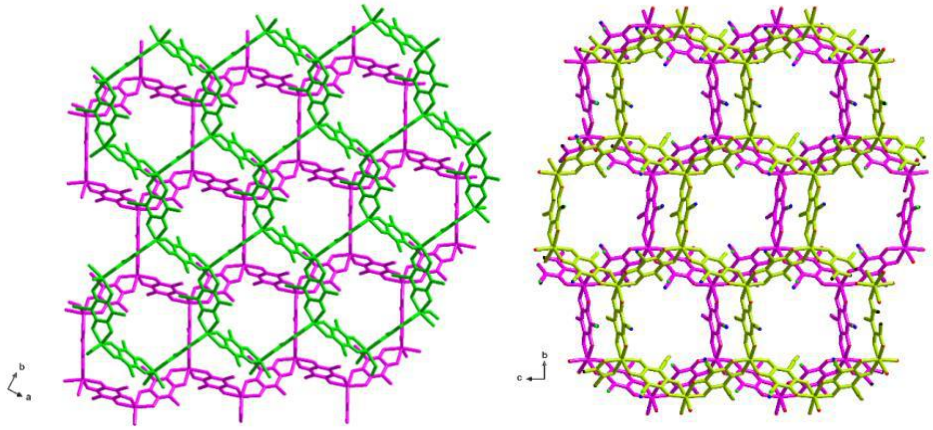

Figure 2. Anionic layer of $[M^{II}_2(ClCNAn)_3]^{2-}$ (M^{II} = Mn (left), Co (right))

IV. As far as the NIR-Lanthanide MOFs/CPs materials are concerned, novel ClCNAn-based 2D CPs/MOFs with NIR-emitting lanthanides and different antenna ligands will be prepared in order to study the capability of the individual ligands to work as valuable antennas towards lanthanides; the photophysical properties of the obtained bulk materials will be investigated by time-resolved photoluminescence spectroscopy. Nanosheets of the most promising materials, in terms of luminescence, will be prepared by the bottom-up and/or top-down strategy and synthetic protocols will be optimized for sensing applications. Furthermore, mixed lanthanide, 2D homo-/heteroleptic CPs/MOFs, will be prepared and characterized as bulk and nanoparticles, because, as noteworthy, these 2D layered CPs show emission bands in the 980−1350 nm spectral region, the so-called biological window, and therefore these systems can be envisaged for applications in biology and nanomedicine as luminescent dual-center nanothermometers.

V. As far as magnetic molecular conductors are concerned, new systems will be prepared by combining tris-chelated octahedral anilate-based anionic complexes with chiral/achiral TTF- derivatives, in order to perform a systematic study on different TTF-based organic donors for establishing a structure/property relationship in anilate-based charge-transfer radical salts. The influence of chirality on the physical properties of obtained materials is of ever-grown interest in material science, especially the electrical magneto-chiral anisotropy effect, which is scarcely investigated. In this context: (i) by combining tris(chlorocyanilato)ferrate anion ($TPPh_3[Fe(ClCNAn)_3]$) with tetramethyltetrathiofulvalene (TM-TTF) and tetramethyltetraselenafulvalene (TM-TSF), new compounds, formulated as $[TM\text{-}TTF]_4[Fe(ClCNAn)_3]$ and $[TM\text{-}TSF]_3[Fe(ClCNAn)_3]$, respectively, were obtained. Their crystal stucture is shown in Figure 3.

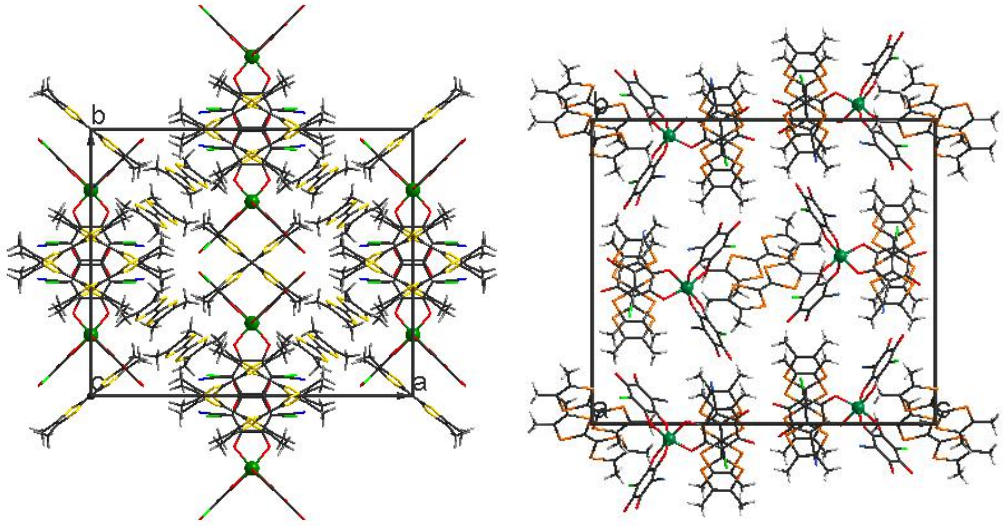

.

Figure 3. (left)Unit cell content of $[TM\text{-}TTF]_4[Fe(ClCNAn)_3]$ in *ba* plane. (right) Unit cell content of $[TM\text{-}TSF]_3[Fe(ClCNAn)_3]$ in *bc* plane

The physical properties of these systems are under investigation.

(ii) by combining the enantiopure (*S*,*S*)-DM-BEDT-TTF donor with the $[TPPh_3][Fe(ClCNAn)_3]$ anionic complex, a chiral molecular conductor, formulated as $[(S,S)\text{-DM-BEDT-TTF}]_6[Fe(ClCNAn)_3]_2$, was obtained. Its physical properties are under investigation.

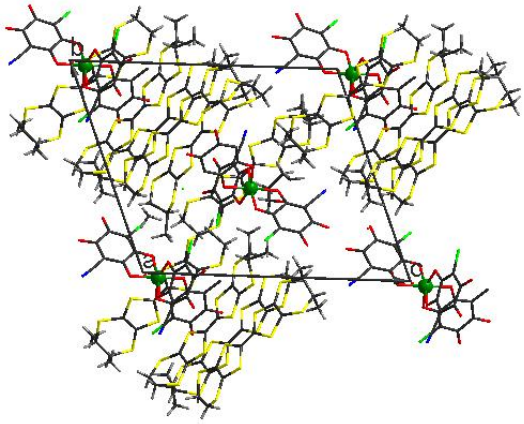

Figure 4. Unit cell content of $(S,S)\text{-}[DM\text{-}BEDT\text{-}TTF]_6[Fe(ClCNAn)_3]_2$ in *bc* plane.

(iii) New BEDT-TTF systems where the heterosubstituted chlorocyananilato ligand in the tris(chlorocyananilato)ferrate(III) anionic complex is replaced by its Br or I analogues will be prepared. A systematic study of the influence of the electronic nature of the X = Br and I on the crystal packing and the conducting properties of the obtained materials due to different intermolecular interactions will be performed.

(iv) the introduction of chirality in the anilato derivatives by functionalization of the 3,6 position of the anilato moiety with chiral groups represent a great challenge for constructing novel multifunctional materials showing a combination and/or interplay of chirality, magnetism and conductivity.

PART IV
Annexes

Annex 1
Overview on Anilate Ligands

The anilic acids are derived from 2,5-dihydroxy-1,4-benzoquinone (DHBQ), changing the hydrogen in 3 and 6 position with a different functional groups or halogens. Molecular formula of anilic acids can be written as $H_2X_2C_6O_4$ (H_2X_2An), where X indicates the substituent and C_6O_4 indicates the anilate moiety (An). (Table A1.1)

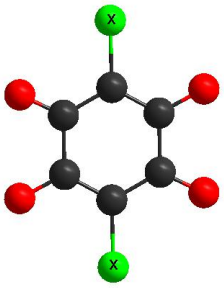

X_2An^{2-}

Table A1.1. Names, molecular formulas and acronyms of the anilic acids reported in the literature to date.

Substituent	Formula	Anilic acid name	Acronyms	Anilate dianion name	Acronyms	Ref
H	$H_4C_6O_4$	Hydranilic acid	H_2H_2An	Hydranilate	H_2An^{2-}	1
F	$H_2F_2C_6O_4$	Fluoranilic acid	H_2F_2An	Fluoranilate	F_2An^{2-}	2
Cl	$H_2Cl_2C_6O_4$	Chloranilic acid	H_2Cl_2An	Chloranilate	Cl_2An^{2-}	3
Br	$H_2Br_2C_6O_4$	Bromanilic acid	H_2Br_2An	Bromanilate	Br_2An^{2-}	4
I	$H_2I_2C_6O_4$	Iodanilic acid	H_2F_2An	Iodanilate	I_2An^{2-}	4
NO_2	$H_2N_2C_6O_8$	Nitranilic acid	$H_2(NO_2)_2An$	Nitranilate	$(NO_2)_2An^{2-}$	5
OH	$H_4C_6O_6$	Hydroxyanilic acid	$H_2(OH)_2An$	Hydroxyanilate	$(OH_2)_2An^{2-}$	6
CN	$H_2N_2C_8O_4$	Cyananilic acid	$H_2(CN)_2An$	Cyananilate	$(CN)_2An^{2-}$	7
Cl/CN	$H_2ClNC_7O_4$	Chlorocyananilic acid	$H_2ClCNAn$	Chlorocyan anilate	$ClCNAn^{2-}$	8
NH_2	$H_6N_2C_6O_4$	Aminanilic acid	$H_2(NH_2)_2An$	Aminanilate	$(NH_2)_2An^{2-}$	9
CH_3	$H_8C_8O_4$	Methylanilic acid	H_2Me_2An	Methylanilate	Me_2An^{2-}	10
CH_2CH_3	$H_{12}C_{10}O_4$	Ethylanilic acid	H_2Et_2An	Ethylanilate	Et_2An^{2-}	10
iso-C_3H_7	$H_{16}C_{12}O_4$	Isopropylanilic acid	H_2*iso*-Pr_2An	Isopropylanilate	*iso*-Pr_2An^{2-}	11
C_6H_5	$H_{12}C_{18}O_4$	Phenylanilic acid	H_2Ph_2An	Phenylanilate	Ph_2An^{2-}	12
C_4H_3S	$H_8C_{14}O_4S_2$	Thiophenyl anilic acid	H_2Th_2An	Thiophenyl anilate	Th_2An^{2-}	13
$C_6H_5O_2S$	$H_{12}C_{18}O_8S_2$	3,4-ethylene dioxythiophenyl anilic acid	H_2EDOT_2An	3,4-ethylene dioxythiophenyl anilate	$EDOTAn^{2-}$	13
C_4H_9	$H_{20}C_{14}O_4$	2,3,5,6-tetrahydroxy-1,4-benzo quinone	H_2THBQ	2,5-di-tert-butyl-3,6-dihydroxy-1,4-benzoquinonate	$THBQ^{2-}$	14

Anilic acids (I) undergo a mono and double deprotonation process of the two hydroxyl groups giving rise to the monoanionic (II) and dianionic (III) forms (Scheme A1.2: III prevails in aqueous media due to the strong resonance stabilization of the negative charge).

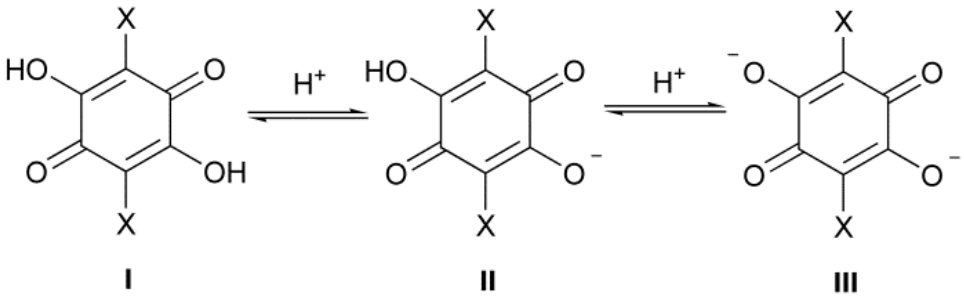

Scheme A1.2 Protonation equilibria for a generic anilic acid.

The molecular and crystal structures of the protonated anilic acids are characterized by. (i) a centrosymmetric quasi-quinonoid structure with C=O and C=C distances in the 1.215–1.235 Å and 1.332–1.355 Å ranges, respectively; (ii) a planar structure of the benzoquinone ring; and (iii) moderate-strong H-Bonding and π-stacking interactions in the crystal structure. It should be noted that the crystal structure of $H_2(NO_2)_2$ hexaydrate and $H_2(CN)_2An$ hexahydrate reveal the presence of hydronium nitranilates and hydronium cyananilates, respectively, as a result of their strong acidity (pKa values for $H_2(NO_2)_2An$: −3.0 and −0.5). The structure of the nitranilic acid hexahydrate is characterized by the presence of the Zundel cation, $(H_5O_2)^{2+}$, whose proton dynamic has been recently studied by using a multi-technique approach. Interestingly, the structure of $H_2(NH_2)_2An$ reveals the presence of an highly polarized zwitterionic structure with the protons located on the amino groups. The molecular and crystal structures of alkali metal salts of some anilic acids have also been reported. The X-ray analysis reveals that the carbon ring system for the anilate in their dianionic form takes the planar conformation but is not in a quinoidal form, having four C–C bonds of equal length (1.404–1.435 Å range) and two considerably longer C–C bonds (1.535–1.551 Å range) whose bond distances vary as a function of the substituents. Moreover, the four C–O bonds are of equal length (1.220–1.248 Å range). This description can be represented with four resonance structures that, in turn, can be combined in one form with delocalized π-electrons along the O–C–C(–X)–C–O bonds (Scheme A1.2).

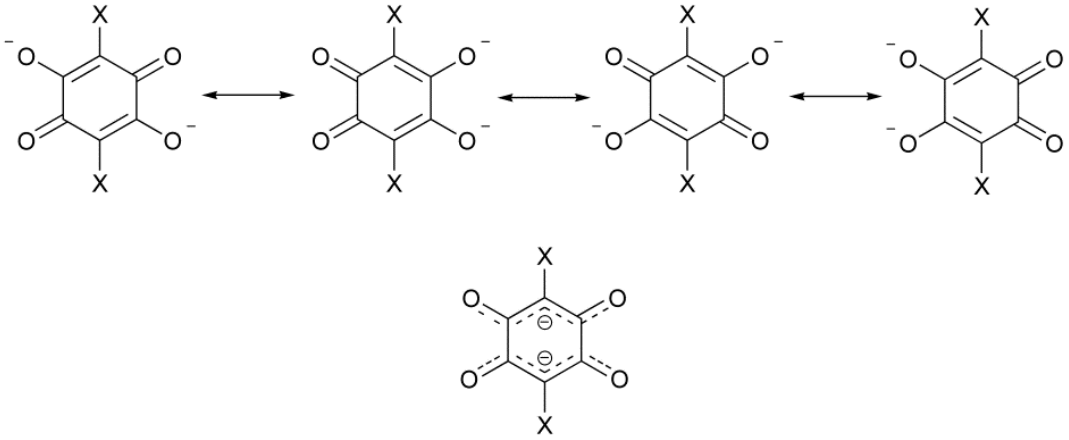

Scheme A1.2. Resonance structures for a generic anilate dianion. The π-electron delocalization over the O-C-C(-X)-C-O bonds is highlighted.

Despite the remarkable similarity in their molecular structure (*vide infra*), the various substituted anilic acids cannot be prepared by a common synthetic procedure. In the following, an overview of the synthetic methods reported in the literature to achieve the anilic acids reported are reported in Scheme A1.3, Scheme A1.4 and Scheme A1.5 respectively.

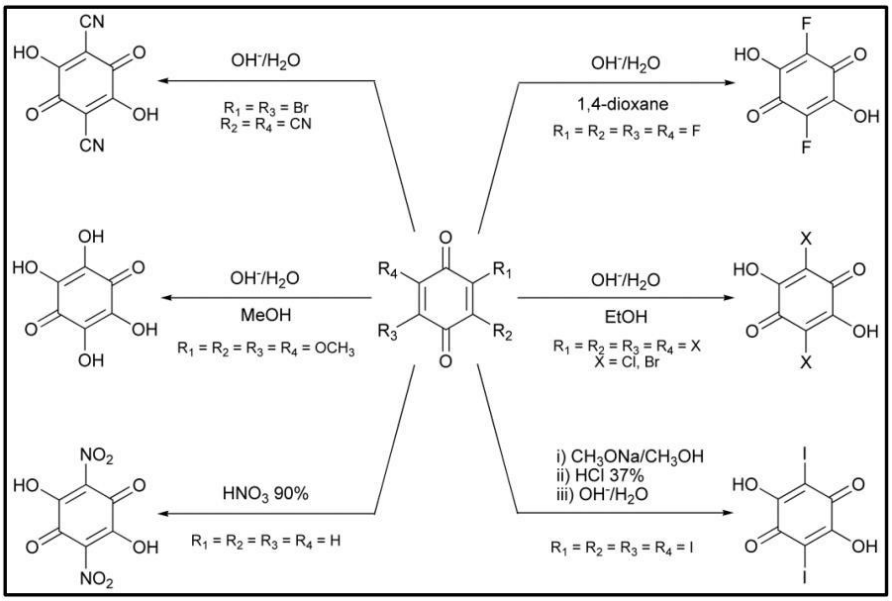

Scheme A1.3. Overview of the synthetic procedures for the preparation of the H_2X_2An (X = F, Cl, Br, I, NO_2, OH, CN) anilic acids. The corresponding anilate dianions, generated in solution, afford the protonated forms by simple acidification.

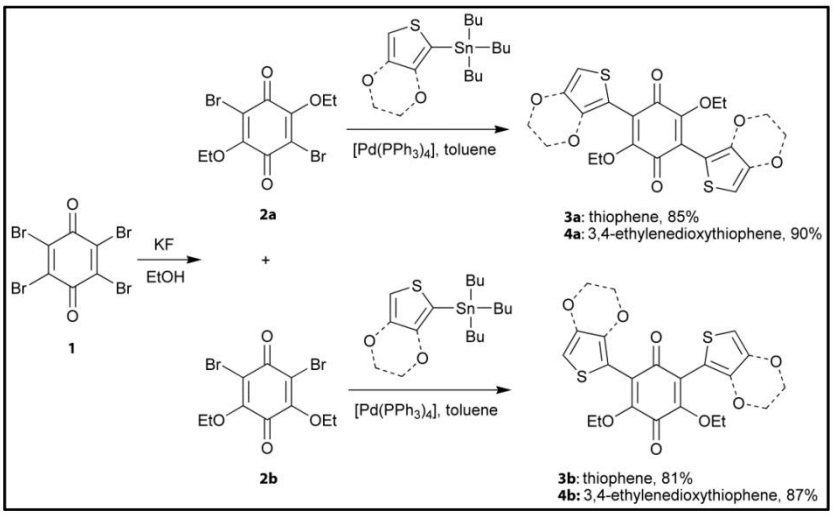

Scheme A1.4. Synthesis of thiophenyl (3a,b) and 3,4-ethylenedioxythiophenyl (4a,b) derivatives of 1,4-benzoquinone.

A simple change of one chloro substituent on the chloranilate ligand with a cyano group affects the electronic properties of the anilate moiety inducing unprecedented luminescence properties in the class of anilate-based ligands and their metal complexes. $ClCNAn^{2-}$ is a unique example of a heterosubstituted anilate ligand, was synthesized by treating 2,3-dicyano-5,6-dichloro-1,4-benzoquinone with a concentrated water solution of potassium hydroxide, and then acidifying with concentrated hydrochloric acid, as shown in SchemeA1.3. The dianionic form of this ligand ($ClCNAn^{2-}$) is a green luminophore, with maximum emission band around 550 nm.

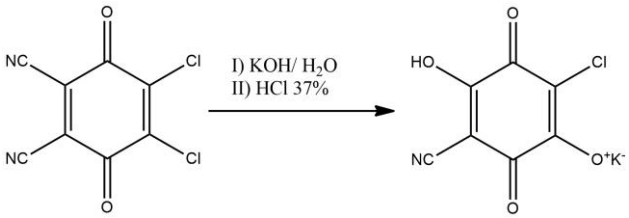

Scheme A1.5. Synthetic procedure for the preparation of KHClCNAn.

An overview of the coordination modes shown by the anilate dianions is reported in Scheme A1.6. It is noteworthy that among the described coordination modes, I and II are the most common, whereas III, IV and V have been only rarely observed.

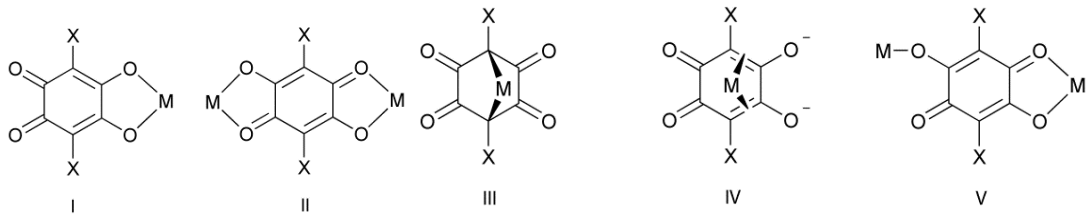

Scheme A1.6. Coordination modes exhibited by the anilate dianions: 1,2-bidentate (**I**), bis-1,2-bidentate (**II**), 1,4-bidentate (**III**), π-bonding (**V**), 1,2-bidentate/monodentate (**V**).

When X_2An^{2-} coordinates in the 1,2 bidentate mode (**I**) exhibits the o-quinone-like form with coordinating C-O bonds that are considerably longer than the uncoordinated C-O bonds, but when anilate acts as bridging ligand the coordination mode is bis-1,2-bidentate(**II**). 1,4-bidentate coordination mode (**III**) is when the ligand coordinates the metal by means of the carbon atoms in 1,4-position showing the bis-carbanion form. It can also coordinate by localized π-electrons in the π-bonding coordination mode (**IV**). Furthermore, it can act as a bridging ligand but contrary to mode II, one of the two sides coordinates with only one oxygen, in the 1,2-bidentate/monodentate coordination mode (**V**). This wide range of coordination modes make the anilate ligands very versatile, moreover the presence of different substituents on the benzoquinone ring yield different intermolecular interactions (H-Bonding, Halogen-Bonding, π–π stacking and dipolar interactions) inside the material. Changing the nature of substituent in 3,6-position is also possible to tune the properties of these materials.

Anilates are interesting building blocks because of: (i) their interesting redox properties; (ii) their ability to mediate magnetic superexchange interactions when the ligand coordinates two metals ions in the 1,2-bis-bidentate coordination mode; (iii) the possibility of modulating the strength of this magnetic superexchange interaction by varying the substituents (X) on the 3,6 position of the anilato-ring; moreover the presence of different substituents in the anilato moiety give rise to intermolecular interactions such as H-Bonding, Halogen-Bonding, π–π stacking and dipolar interactions which may influence the physical properties of the resulting material. Therefore these features provide an effective tool for engineering a great variety of new materials with unique physical properties. [15,16,17]

References

(1) Barltrop, J. A.; Burstall, M. L. *J Chem Soc* **1959**, 2183–2186.
(2) Wallenfels, K.; Friedrich, K. **1960**, 3070–3082.
(3) Stenhouse, J. On Chloranil and Bromanil. **1868**, 6, 6–14.
(4) Torrey, H. A.; Hunter, W. H. The Action of Iodides on Bromanil. Iodanil and Some of Its

Derivatives. **1912**, *555* (1905).
(5) Meyer, H. *Berichte der Dtsch Chem Gesellschaft (A B Ser* **1923**, *56*, 326–328.
(6) Fatiadi, A. J.; Sager, W. F. *Org Synth* **1962**, *42*, 90.
(7) Zaman, B.; Morita, Y.; Toyoda, J.; Yamochi, H.; Sekizaki, S.; Nakasuji, K. *Mol Cryst Liq Cryst* **1996**, *287*, 249–254.
(8) Rehwoldt, R. E.; Chasen, B. L. *Anal Chem* **1966**, *38*, 1018–1019.
(9) Akutagawa, T.; Nakamura, T. *Cryst Growth Des* **2006**, *6*, 70–74.
(10) Kogl, F.; Lang, A. *Chem Ber* **1926**, *59*, 910–913.
(11) Fichter, F.; Willmann, A. *Berichte der Dtsch Chem Gesellschaft* **1904**, *37*, 2384–2390.
(12) Fichter, F. *Justus Liebigs Ann Chem* **1908**, *361*, 363–402.
(13) Atzori, M.; Pop, F.; Cauchy, T.; Mercuri, M. L.; Avarvari, N. *Org Biomol Chem* **2014**, *12*, 8752–8763.
(14) Schultz, A. J.; Stucky, G. D.; Blessing, R. H.; Coppens, P. *J Am Chem Soc* **1976**, *98*, 3194–3201.
(15) Mercuri, M. L.; Congiu, F.; Concas, G.; Ashoka Sahadevan, S. *Magnetochemistry* **2017**, *3*, 17.
(16) Kitagawa, S. *Coord Chem Rev* **2002**, *224*, 11–34.
(17) M. Atzori, "Anilate-based Functional Molecular Materials with Conducting and Magnetic Properties", PhD Thesis, University of Cagliari and Angers, 2014.

Annex 2
Exfoliation

The study of 2D materials is a hot topic in material science and nanotechnology since graphene was first discovered by Novoselov[1] in 2004, by using adhesive tapes for mechanical exfoliation. Owing to the ultrathin thickness at atomic scale, these materials possess novel properties in many fields, such as carrier concentration, mobility and thermal conductivity.

In order to prepare 2D materials, there are two methods: top-down exfoliation[2,3] and bottom-up synthesis.[4–7] The bottom-up approach is so-called because it typically requires precursors that are reacted together in their molecular form to synthesize sheets of 2D materials. The top-down exfoliation involves the exfoliation of a bulk layered material down to monolayer or few layer 2D sheets. Most commonly used methods for top-down exfoliation are:

(i) Micromechanical exfoliation (also called scotch-tape method), which is simple and efficient way to produce the cleanest, highly crystalline and atomically thin microsheets of a layered material. However, it is difficult to get uniform samples through mechanical exfoliation, as it gives randomly dispersed layers on the substrates. And the process to find proper samples is time-consuming[8].

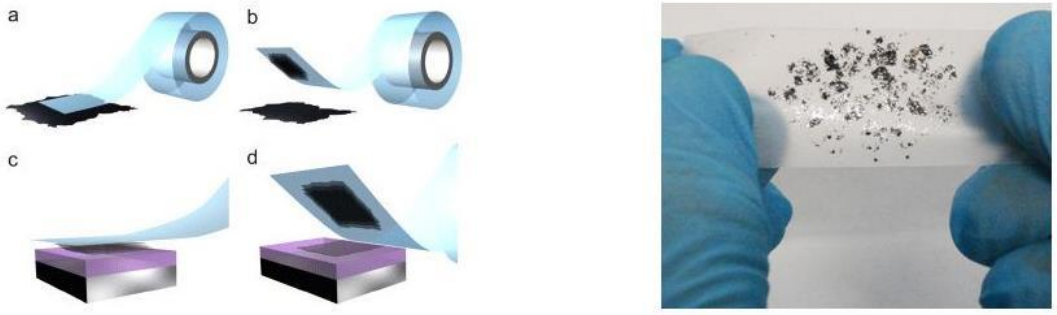

Figure A2.1. Schematic representation of Scotch-tape mechanical exfoliation

(ii) liquid exfoliation. It include ion intercalation, ion exchange and sonication-assisted exfoliation. Nanosheets can be made by soaking the bulk materials into appropriate solvents[8,9] and using proper ultrasound. The mechanism is as follows: first, ions are intercalated between the layers in a liquid environment, weakening the interlayer interactions. Then, sonication results in an exfoliated dispersion nanosheet formation. In “good” solvents, i.e. those with appropriate surface energy, the exfoliated nanosheets are stabilised against reaggregation. Otherwise, with “bad” solvents, reaggregation and sedimentation will occur. Ultrasonication does not allow good control over the size and thickness of flakes; however, the ability to

produce large quantities of 2D materials dispersed in liquid makes it quite useful. Compared with mechanical exfoliation, it has a high yield with rather low cost.

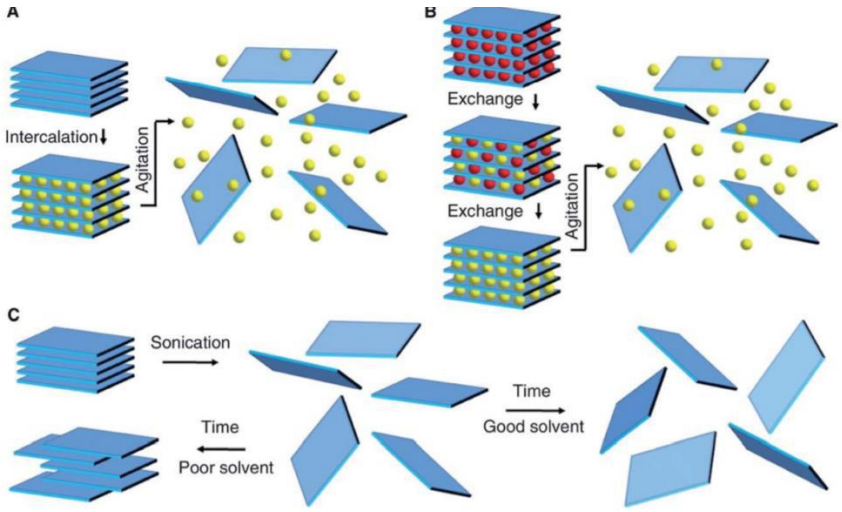

Figure A2.2. Schematic representation of liquid exfoliation mechanisms (A) Ion intercalation. (B) Ion exchange. (C) Sonication-assisted exfoliation. Reprinted with the permission from Ref.[10]

These 2D exfoliated materials can be characterized by using a wide array of techniques. The most commonly used tools for determining their morphology and dimensionality are optical microscopy, AFM, TEM, and Raman spectroscopy.

References

(1) K. S. Novoselov; Geim, A. K.; Morozov, S. V.; Jiang, D.; Zhang, Y.; Dubonos, S. V.; Grigorieva, I. V.; Firsov, A. A. *Science,* **2004**, *306*, 666–669.

(2) Zhao, M.; Wang, Y.; Ma, Q.; Huang, Y.; Zhang, X.; Ping, J.; Zhang, Z.; Lu, Q.; Yu, Y.; Xu, H.; et al. *Adv Mater* **2015**, *27*, 7372–7378.

(3) Tour, J. M. *Chem Mater* **2014**, *26*, 163–171.

(4) Pustovarenko, A.; Goesten, M. G.; Sachdeva, S.; Shan, M.; Amghouz, Z.; Belmabkhout, Y.; Dikhtiarenko, A.; Rodenas, T.; Keskin, D.; Voets, I. K.; Weckhuysen, B. M.; Eddaoudi, M.; de Smet, L. C. P. M; Sudhölter, E. J. R.; Kapteijn, F.; Seoane, B; Gascon J. *Adv Mater* **2018**, *30*, 1–8.

(5) Peng, L.; Mei, X.; He, J.; Xu, J.; Zhang, W.; Liang, R.; Wei, M.; Evans, D. G.; Duan, X. *Adv Mater* **2018**, *30*, 1–10.

(6) Ma, W.; Wang, L.; Xue, J.; Cui, H. *RSC Advances*. 2016, 85367–85373.

(7) Bosi, M. *RSC Adv* **2015**, *5*, 75500–75518.

(8) Huo, C.; Yan, Z.; Song, X.; Zeng, H. *Sci Bull* **2015**, *60*, 1994–2008.

(9) Nicolosi, V.; Chhowalla, M.; Kanatzidis, M. G.; Strano, M. S.; Coleman, J. N. *Science,* **2013**, *340*, 72–75.

(10) Nicolosi, V.; Chhowalla, M.; Kanatzidis, M. G.; Strano, M. S.; Coleman, J. N. *Science,* **2013**, *340*, 1226419.

(11) López-Cabrelles, J.; Mañas-Valero, S.; Vitórica-Yrezábal, I. J.; Bereciartua, P. J.; Rodríguez-Velamazán, J. A.; Waerenborgh, J. C.; Vieira, B. J. C.; Davidovikj, D.; Steeneken, P. G.; van der Zant, H. S. J.; Mínguez Espallargas, G.; Coronado, E. *Nat Chem* **2018**, *10*, 1001–1007.

Annex 3
Fundamentals of Lanthanide Luminescence

3.1 General Introduction of lanthanides

In the periodic table, lanthanide series comprises 15 elements ranging from lanthanum (Z= 57) to lutetium (Z= 71) having general configurations of $[Xe]4f^n5d^16s^2$. Lanthanide elements form +3 oxidation states as a stable oxidation state in the whole series, with some exceptions of Ce^{IV}, Eu^{II}, Sm^{II}, Yb^{II} and Tb^{IV} due to the presence of an empty, half-filled or completely-filled 4f shell. The electronic configuration of trivalent, Ln^{III} ions is $[Xe]4f^n$ (n = 0–14); some divalent Ln^{II} ions have similar f-electronic configuration $[Xe]4f^{n+1}$ (n = 3, 5, 6, 9, 12, 13; Ln = Nd, Sm, Eu, Dy, Tm, Yb), while the electronic configuration of the others is $[Xe]4f^n5d^1$ (n = 0, 1, 2, 7, 8, 10, 11, 14; Ln = La, Ce, Pr, Gd, Tb, Ho, Er, Lu). The 4f orbitals (Figure A3.1) are well shielded by the Xe core, transforming the valence 4f orbitals into "inner orbitals." As a consequence, there is a gradual decrease in the atomic and ionic radii in the lanthanide series from Ce (Z= 58), to Ln (Z =71) due to the poor shielding of nuclear charge by 4f electrons; the 6s electrons are drawn towards the nucleus, thus resulting in a smaller atomic radius. This phenomenon is termed as **lanthanide contraction.**

Ln^{III} ions are hard Lewis acids and, they preferentially bind to hard bases, ie ligands having negatively charged donor atoms, forming stronger bonds (O > N > S). Ln^{III} ions usually exhibit coordination numbers from 6 to 12 with eight and nine being most common.

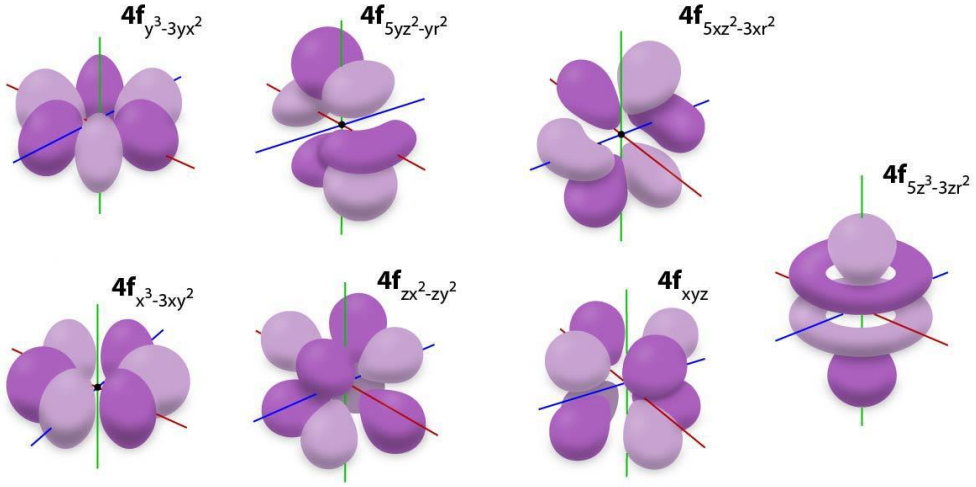

Figure A3.1. Representation of 4f orbitals

An important feature of the lanthanide ions is their photoluminescence. Several lanthanide ions show luminescence in the visible or near-infrared spectral regions upon irradiation with

ultraviolet radiation. For instance, Tm^{3+} emits blue light, Sm^{III}, orange light, Eu^{III}, red light, Tb^{III}, green light, and Nd^{III}, Er^{III}, and Yb^{III} are well-known for their near-infrared luminescence. This lanthanide luminescence has diverse potential applications ranging from displays, lasers, telecommunications, barcoding, molecular thermometers, immunoassays, to bioimaging and optical amplifiers.

3.2 Lanthanide spectroscopy

As already mentioned, the 4f electrons of the lanthanides are well shielded from the environment by the closed $5s^2$ and $5p^6$ outer shells and therefore the spectroscopic and magnetic properties of these ions (e.g., electronic spectra and crystal-field splitting) are largely independent of environment (solvent, coordinated ligands, etc.).

The degeneracy (N) of a $4f^n$ electronic configuration is given by

$$N = \frac{14!}{n!\,(14-n)!}, 1 \leq n \leq 13$$

n = number of 4f electrons.

This degeneracy is partly or totally lifted by several interactions acting on the Ln^{III} ion such as *electron repulsion* (electrostatic interaction between electrons in the 4f shell), *spin–orbit coupling* (interaction between spin magnetic moment of electron and magnetic field created by the movement of electron around the nucleus), *crystal-field effect* (interactions between the 4f electrons and the electrons of ligands) and eventually the *Zeeman effect* (due to the external magnetic field).

After the introduction of electron repulsion, spin multiplicity, 2S + 1 is further splitted into several J terms due to spin-orbit coupling and each free-ion level is characterized by $2S+1L_J$ terms (Russell–Saunders coupling scheme, also called LS coupling scheme)), where, S = total spin quantum number, L = total orbital angular momentum quantum number and J = total angular momentum.

When the lanthanide ion is surrounded by ligands, the 4f electron distribution is perturbed both by nephelauxetic effects (a drift of ligand electron density into the lanthanide ion causes an expansion of the 4f shell and reduces the 4f-4f interactions) and crystal field effects. In the latter case, the surrounding ligands destroy the spherical symmetry of the “free-ion” inducing a partial removal of the degeneracy of individual 4f terms, thus making f–f transitions slightly allowed, *ie*, the individual *J*-levels are split up further by the crystal field, *J* mixing is allowed. These levels are called crystal-field levels (or Stark levels). Due to the shielding by the

external 5s and 5p orbitals the magnitude of this splitting is moderate and the average energy gap between the levels by the crystal-field effect is of the order of a 10^2 cm^{-1}.

The position of both the absorption and emission bands of the lanthanide ions does not change significantly upon coordination with respect to the free ion spectra, thus each band can be easily recognised and provides the fingerprints for the corresponding lanthanide ion. However, in systems with an orthorhombic or lower symmetry, all degeneracy is lifted by the crystal field. When the lanthanide is placed in a magnetic field, there is an additional perturbation: the Zeeman perturbation. All remaining degeneracy is destroyed. The number of Stark sublevels depends on the site symmetry of the lanthanide ion, and these can be thermally populated at room temperature, yielding emission spectra that are more complex.

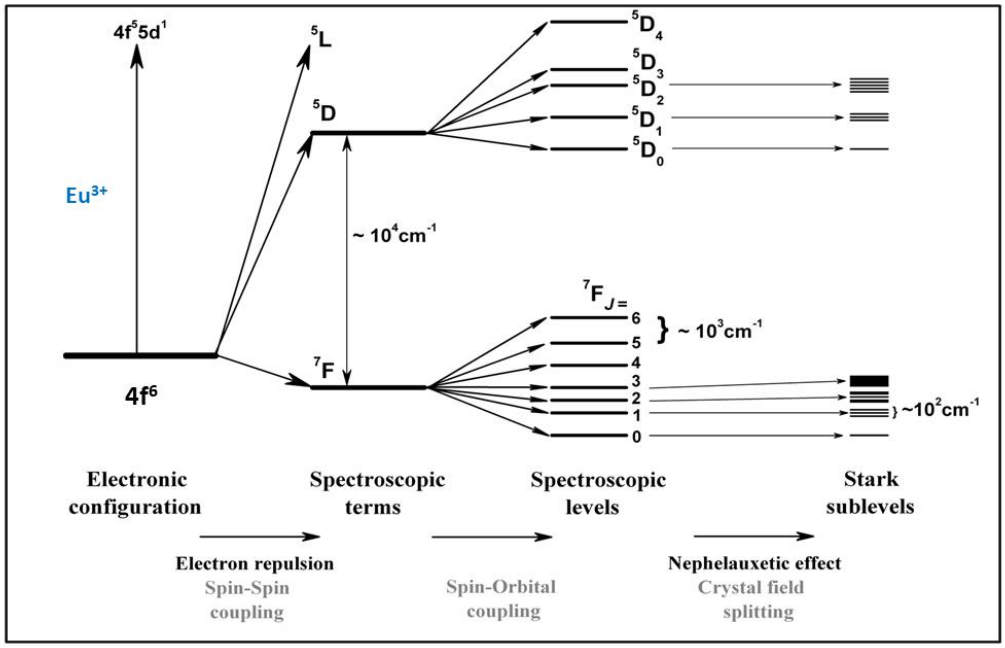

Figure A3.2: Energy levels splitting for the Eu^{3+} ions with $4f^6$ configuration.

According to Hund's rule the ground term for the free ion can be explained by:

- Rule 1: highest spin multiplicity.
- Rule 2: In case, if there is more than one term with the same spin multiplicity, the term with the highest total orbital angular momentum (or L value) is the ground state.
- Rule 3: For electronic shells that are less than half-filled, the ground state has the lowest possible J value. For electronic shells that are more than half-filled, the ground state has the highest possible J value.

ie., J ranges from $L–S \leq J \leq L+S$ and takes, for the fundamental level, the value $J = L–S$ for $n < 7$ (La-Eu) and $J = L+S$ for $n \geq 7$ (Gd-Lu).

Ln^{III} Ion	$4f^n$	Magnetic Quantum Number of f orbital							L	S	J	Ground State
		3	2	1	0	-1	-2	-3			**J = L-S**	
La^{3+}	0								0	0	0	$^1S_0$
Ce^{3+}	1	↑							3	1/2	5/2	$^2F_{5/2}$
Pr^{3+}	2	↑	↑						5	1	4	$^3H_4$
Nd^{3+}	3	↑	↑	↑					6	3/2	9/2	$^4I_{9/2}$
Pm^{3+}	4	↑	↑	↑	↑				6	2	4	$^5I_4$
Sm^{3+}	5	↑	↑	↑	↑	↑			5	5/2	5/2	$^6H_{5/2}$
Eu^{3+}	6	↑	↑	↑	↑	↑	↑		3	3	0	$^7F_0$
											J = L+S	
Gd^{3+}	7	↑	↑	↑	↑	↑	↑	↑	0	7/2	7/2	$^8S_{7/2}$
Tb^{3+}	8	↑↓	↑	↑	↑	↑	↑	↑	3	3	6	$^7F_6$
Dy^{3+}	9	↑↓	↑↓	↑	↑	↑	↑	↑	5	5/2	15/2	$^6H_{15/2}$
Ho^{3+}	10	↑↓	↑↓	↑↓	↑	↑	↑	↑	6	2	8	$^5I_8$
Er^{3+}	11	↑↓	↑↓	↑↓	↑↓	↑	↑	↑	6	3/2	15/2	$^4I_{15/2}$
Tm^{3+}	12	↑↓	↑↓	↑↓	↑↓	↑↓	↑	↑	5	1	6	$^3H_6$
Yb^{3+}	13	↑↓	↑↓	↑↓	↑↓	↑↓	↑↓	↑	3	1/2	7/2	$^3F_{7/2}$
Lu^{3+}	14	↑↓	↑↓	↑↓	↑↓	↑↓	↑↓	↑↓	0	0	0	$^1S_0$

Figure A3.3. Energy levels splitting for the Eu^{3+} ions with $4f^6$ configuration.

However, the relative positions of the energy levels of the excited states can be determined only by calculations. The first synopsis of the $4f^n$ energy levels of all trivalent lanthanides spanning the entire UV, visible and NIR spectral ranges was given by G.H. Dieke.

Dieke diagram (Figure A3.4) shows that the energy levels of the emissive lanthanide ions are often markedly subdivided into two main groups consisting of closely spaced levels. The f–f transitions which originate the luminescent emission of lanthanide ions usually occur from the lowest level of the higher multiplet (populated by non-radiative cascade decay from the excited upper levels) to the ground manifolds.

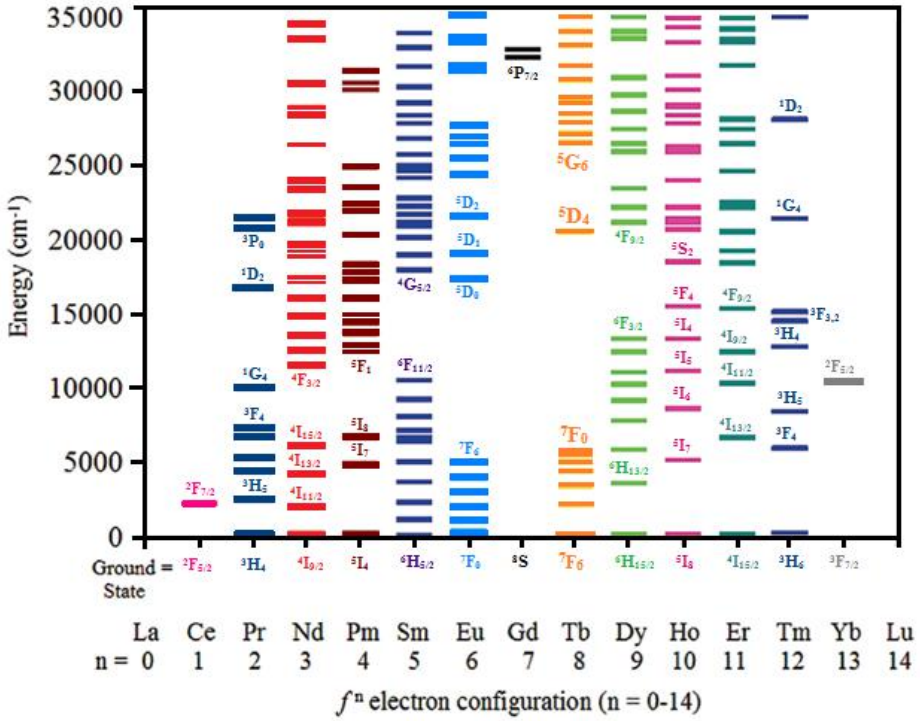

Figure A3.4. Dieke diagram of the energy levels of lanthanides.

3.3 Luminescence and Selection Rules

There are *three types of optical transitions* in lanthanide compounds:

1. Allowed f↔d transitions

Interconfigurational $4f^n \leftrightarrow 4f^{n-1}\ 5d^1$ transition are parity allowed. They show broader bands than f-f transitions and their energy is highly dependent on the ligand-field strength, since 5d orbitals have large radial expansion, allowing extensive tuning of the absorption and/or emission wavelengths. However, these transitions are highly energetic so that they are usually observed only for Ce^{III}, Pr^{III}, and Tb^{III}.

2. Allowed charge-transfer (CT) transitions

CT transitions, either LMCT or MLCT are also allowed. As they correspond to either reduction or oxidation of the metal ion, it usually occur at high energies. Typically, the lowest energies for LMCT transitions are associated with easily reducible ions such as Sm^{III} , Eu^{III}, Tm^{III}, or Yb^{III}.

3. Forbidden Intraconfigurational f↔f transitions

Absorption or emission of photons is promoted by operators linked to the nature of light:

- the odd-parity electric dipole operator (ED)
- the even-parity magnetic dipole operator (MD)
- the electric quadrupole operator (EQ)

Laporte's parity selection rule implies that ED 4f-4f transitions are forbidden. However, when the lanthanide ion undergoes the influence of a ligand-field, non-centrosymmetric interactions mix electronic states of opposite parity into 4f wavefunctions, which relax the selection rule and the transitions become partially allowed. These transitions are then called induced (or forced) electric dipole transition. Major contributions to their intensity are due to the mixing of $4f^n$ configuration with opposite parity $4f^{n-1}5d^1$ configuration, LMCT states, and/or vibrational levels.

Some induced ED transitions are highly sensitive to small changes in the chemical environment of the metal ion and are denoted hypersensitive or sometimes pseudo-quadrupolar transitions because they follow the selection rules of EQ transitions. While the intensity of regular ED transitions varies by factors 2-5 depending on the composition of the inner coordination sphere of the metal ion, hypersensitive transitions can be enhanced up to 200-fold.

Magnetic dipole transitions are parity allowed but their intensity is much smaller while the very weak EQ transitions have rarely been identified. In addition to the parity selection rule, other rules are operative, on ΔS, ΔL, ΔJ (see Table A3.1), as well as symmetry-related selection rules that can be derived from group-theoretical considerations.

Table A3.1. Selection Rules

Electric dipolar Transitions (ED)	Magnetic dipolar Transitions (MD)	Electric-quadrupole transitions (EQ)
opposite parity	same parity	same parity
$\Delta S = 0$	$\Delta S = 0$	$\Delta S = 0$
$\Delta L \leq 6$	$\Delta L = 0$	$\Delta L = 0, \pm 1, \pm 2$
$\Delta J \leq 6$, $\Delta J = 2,4,6$ if J or J'=0	$\Delta J = 0, \pm 1$	$\Delta J = 0, \pm 1, \pm 2$

Important parameters characterizing the emission of light from an Ln^{III} ion are the lifetime of the excited state, $\tau_{obs} = 1/k_{obs}$ and the quantum yield Q:

$$Q = \frac{\text{number of photons emitted}}{\text{number of photons absorbed}}$$

The quantum yield depends on the rate at which the excited level is depopulated, k_{obs}, and on the radiative rate k_{rad}:

$$Q_{Ln}^{Ln} = \frac{k_{rad}}{k_{obs}} = \frac{\tau_{obs}}{\tau_{rad}}$$

where subscript and superscript "Ln" mean that excitation has been performed directly into the 4f excited state and is called the intrinsic quantum yield. The rate constant k_{obs} is the sum

of the rate constants characterizing the various radiative and radiation-less deactivation processes. (*vide infra*, Section 3.5)

3.4 Sensitized lanthanide luminescence

As most of the 4f transitions are forbidden by selection rules, and, although several mechanisms, such as the coupling with vibrational states, may relax them to some extent, the absorption cross section (molar extinction coefficient: $\varepsilon < 10$ $mol^{-1}dm^3cm^{-1}$) and the emission intensity after a direct excitation of the lanthanide ion remain, however, very low.

A way to overcome this drawback is to encapsulate the lanthanide ion with a suitable organic ligand (chromophore) ("antenna effect") which can allow indirect excitation of the lanthanide ion by populating its higher levels by means of an energy transfer mechanism (sensitized emission). This two-step excitation process makes the considerable Stokes shift between the excitation and the emission wavelength allows the separation of the wavelengths due to scattered radiation or ligand photoluminescence.

The mechanism of energy transfer from organic ligands to the lanthanide ion involves mainly three steps:

(i) ligand absorption from the ground singlet state (S_0) to the excited singlet state (S_1) ($S_0 \rightarrow S_1$);

(ii) S_1 state decays non-radiatively to the triplet state (T_1) of ligand via InterSystem Crossing (ISC: $S_0 \rightarrow T_1/T_2$)

(iii) nonradiative energy transfer from the long-lived T_1 state of the ligand to nearest low-lying 4f levels of the Ln^{III} ion excited states. In some cases the direct energy-transfer from the S_1 singlet state to the excited Ln^{III} levels is also observed. But, this state is short-lived and the process is much less probable than ISC or radiative or non-radiative decays.

After the indirect excitation by energy transfer, the lanthanide ion may undergo a radiative transition to a lower 4f-state by a characteristic line-like photoluminescence, or may be deactivated by radiationless processes (section 3.5). The scheme of the processes is shown in Scheme A1.1.

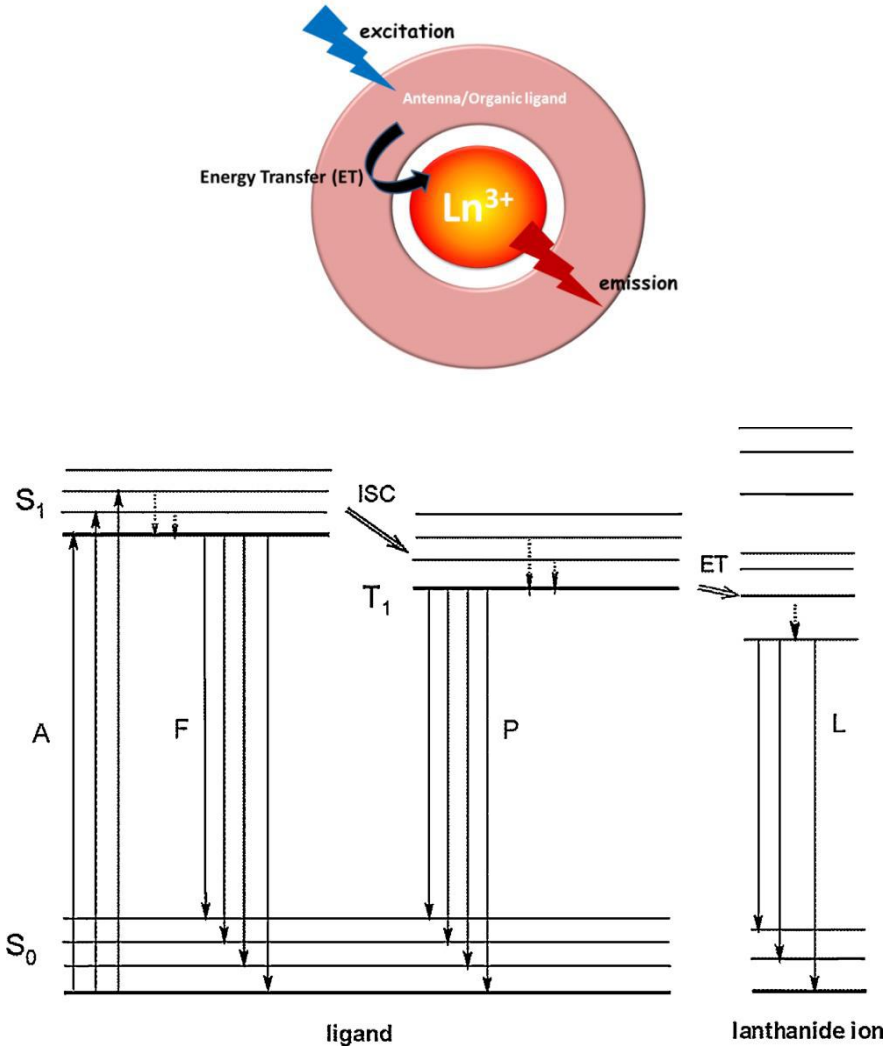

Scheme A1.1. Schematic representation of antenna effect and sensitized luminescence. A, absorption; F, fluorescence; P, phosphorescence; L, lanthanide-centered luminescence; ISC, intersystem crossing; ET, energy transfer; S, singlet; T, triplet. Full vertical lines: radiative transitions, dotted vertical lines: non-radiative transitions.

In a simplified model, the luminescence quantum yield Q_{Ln}^{L} of sensitized luminescence from a lanthanide complex can be written as:

$$Q_{Ln}^{L} = \eta_{ISC}\eta_{ET}Q_{Ln}^{Ln}$$

where, Q_{Ln}^{L} = quantum yield for direct excitation of the lanthanide ion, η_{ISC} = efficiency of the intersystem crossing process, η_{ET} = effectiveness of the ligand triplet state ($3\pi\pi^*$)–Ln transfer

The ligand-to-Ln^{III} energy transfer process can be schematically depicted in the Jablonski diagram:

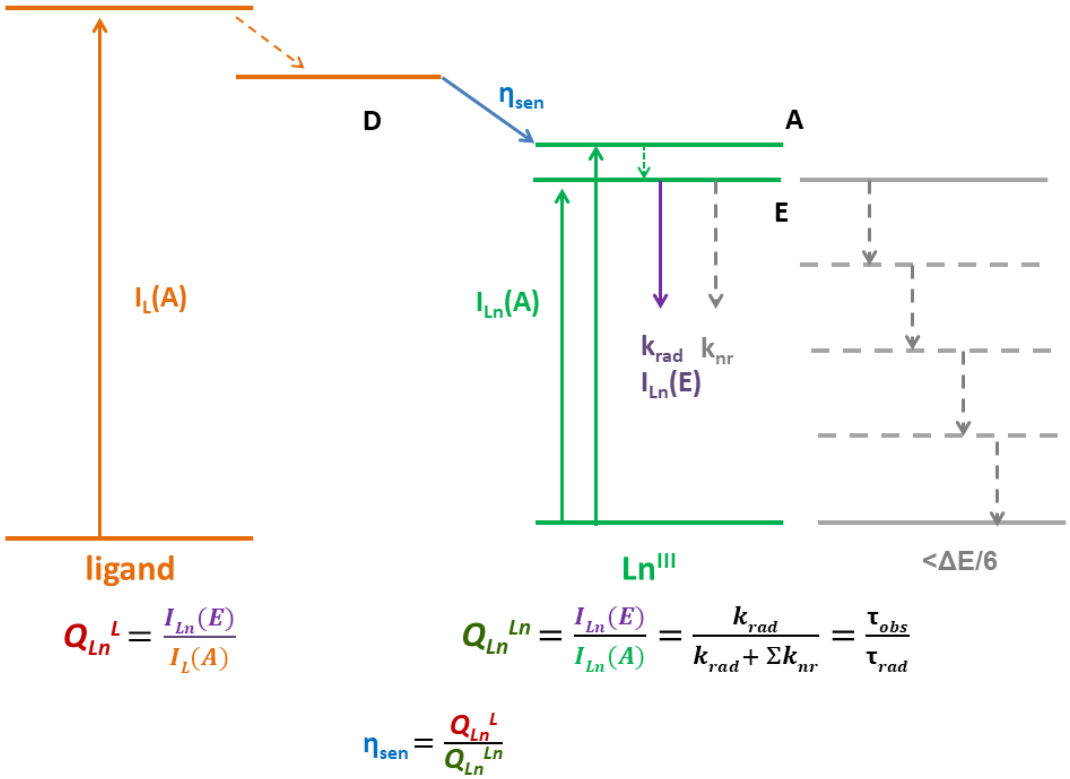

Scheme A3.2: Simplified energy diagram of sensitized luminescence. A = absorption, E = emission, D = donor state. Reprinted from Ref.[1]

The high spin-orbit coupling between the heavy, paramagnetic, lanthanide ion and the ligand, considerably favours the ISC mechanism (heavy atom effect) which populates the ligand triplet state (usually $3\pi\pi^*$) and produces an intramolecular energy transfer to the 4f states rather than a radiationless thermal decay that usually takes place in the absence of the lanthanide ion.

3.4.1 Ligand-to-metal charge-transfer

The ligand-to-metal energy transfer can be described on the basis of two theoretical models considering different dipolar-multipolar donor (ligand) - acceptor Ln^{III} interactions.

1. Dexter Energy Transfer (Exchange mechanism)

After the excitation of ligand, the electron in the triplet state is transferred to one of the excited Ln^{III} states. Simultaneously, an electron from the highest occupied 4f orbital is transferred to the ligand, filling up the gap created by the initial photo excitation. The rate of transfer depends on (i) the overlap integral J_{DA} between the emission spectrum of the donor (ligand) and the absorption spectrum of the acceptor (Ln^{III} ion) and (ii) the distance between the donor and the acceptor, r_{DA}, according to an exponentially decreasing function, $e^{-\beta r_{DA}}$

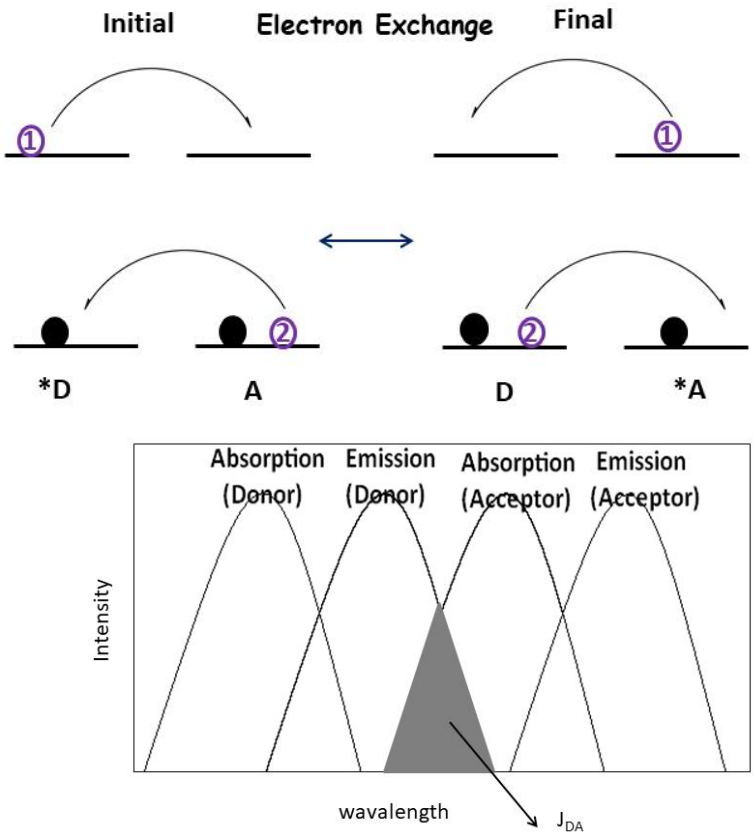

2. Förster Energy Transfer (Dipole-Dipole)

After the excitation of the ligand, to the donor triplet state (via, singlet state and ISC), the excited electron returns to its initial orbital, while, transition dipole moments of the ligand and Ln^{III} ion couple resulting in excitation of the electron Ln^{III} states. The rate of energy transfer via this mechanism depends on (i) the spectral overlap J_{DA} defined above, (ii) the luminescence quantum yield of the donor Q_D, (iii) the lifetime of the donor excited state, (iv) the relative orientation of the donor and acceptor transition dipoles κ, and (v) the distance between the donor and the acceptor according to a $1/r_{DA}^6$ dependence.

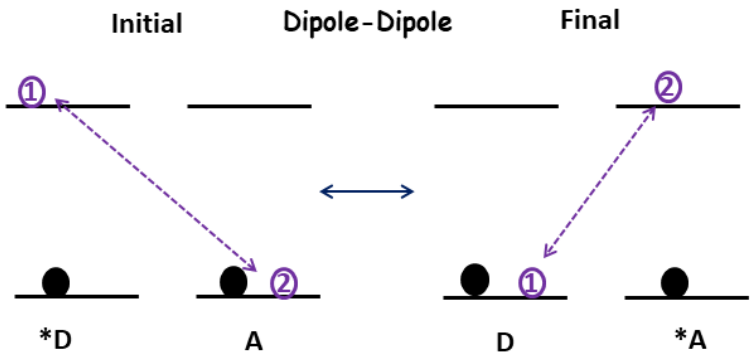

Selection Rules for these energy transfer process:-

• $\Delta J = 0, \pm 1$ ($J = J' = 0$ excluded) for a Dexter mechanism;

• ΔJ = ± 2, ± 4, ± 6 for a Förster mechanism; where ΔJ is referred to a transition from the lanthanide ground state.

In general, the sensitization of the lanthanide ion seems to occur from the ligand triplet state via a Dexter mechanism although, in some cases, energy transfer from singlet states cannot be ruled out. For efficient energy transfer to the lanthanide ion, the triplet states of the ligand must be closely matched to or slightly above the metal ion's emitting resonance levels. These mechanisms are summarized in Table A3.2.

Table A3.2 Dexter and Förster Energy-Transfer processes

Dexter	**Förster**
Electronic exchange implying an overlap between the ligand and the metal orbitals (through bond)	Columbic or dipole-dipole interaction between the dipole moments associated with the T1 state and the 4f orbitals, (through space)
Short range 6-20Å	Long range 30-100 Å
spectral overlap is independent of the oscillator strength of the transitions	spectral overlap depends on the oscillator strengths of D* → D and A → A* transitions
Singlet-Singlet and Triplet –Triplet transfer	Singlet - Singlet transfer only
Rate constant of exchange transfer , $K_{dexter} \sim e^{\frac{-2R}{L}}$	$K_{Forster} \sim {}^{1}/_{R}\,6$
ΔJ = 0, ± 1 (J = J' = 0 excluded)	ΔJ = ± 2, ± 4, ± 6
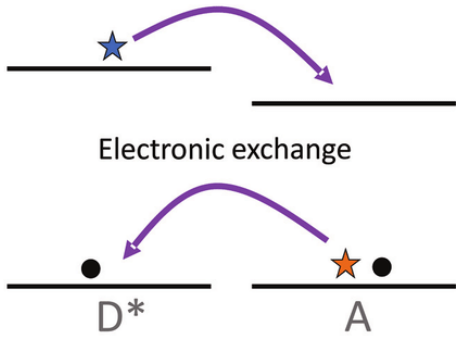	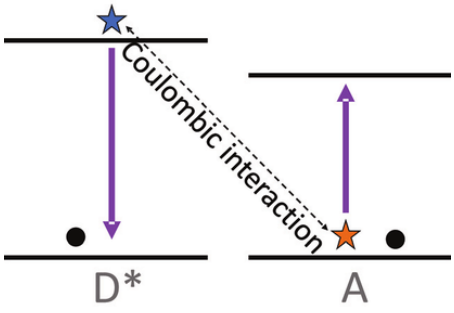

3.5 Luminescence Quenching

The excited states of lanthanide ions do not decay solely by radiative processes. If the excited state and the next lower state energy gap is relatively small, luminescence will be in strong competition with the non-radiative decay of the excited state. The electronic excitation energy can also be dissipated by vibrations of the matrix, by a process known as multiphonon relaxation. In other words, phonon relaxations correspond to the collisional decay of an

excited energy level, due to the crystalline lattice vibrations. It can occur through coupling of the lanthanide energy levels with the vibrational modes in the direct surrounding of the lanthanide ion.

As the quantum yield of a luminescent lanthanide ion depends on the energy gap between the lowest-lying excited state of the metal ion and the highest sublevel of its ground multiplet, the smaller this gap, easier is its de-excitation by non-radiative deactivation processes, for instance through vibrations of bound ligands, particularly high energy vibrations such as O–H or C–H.

These quenching effects lead to shorten luminescent lifetimes (τ_{obs}) some orders of magnitude than the natural radiative emission lifetime (τ_r) of the free lanthanide ion. The overall rate constant (κ_{obs}) for such deactivation processes, is inversely proportional to the measured lifetime, is given by:

$$\kappa_{obs} = {}^{1}/_{\tau obs}$$

Regarding radiationless deactivation, not only vibrations intervene but, also, back energy-transfer processes as well as quenching by charge-transfer states occurs, which are not always easy to identify.

The best way to minimize vibration-induced deactivation processes is to design a rigid metal-ion environment, devoid of high-energy oscillators and protecting the Ln^{III} ion from solvent interaction. Such an environment contributes to reduce collision- induced deactivation in solution. However, considerable weakening of the quenching ability of O-H vibrations is observed in some cases if the coordinated water molecules are involved in strong intra- or inter-molecular H-bonding.

The efficiency of the NIR Ln^{III} ion luminescence is severely limited by quenching phenomena, as relatively low energy-gap between excited and ground states of NIR Ln^{III} ions can easily be bridged by high-energy vibrations (O–H, N–H, C–H, C–O, etc.) and their overtones (Figure A3.5).

To overcome this situation, deuteration (C–D) and halogenation (C–F) of the organic ligands has been proven as remedy: absorptions are decreased (C–D) or absent (C–F) because the third overtone of C–D is located at 1.5 μs and the third overtone of C–F is located at 2.6 μs. Halogenation is preferred for the C-band window (infrared) because the third overtone of the C–D vibration absorbs in it. In addition, fluorination does not modify significantly the energy of the triplet levels, so the resonant transfer to the lanthanide ion is not affected. In the late

1990s, several papers were reported with the improved NIR photoluminescence of several deuterated and fluorinated Nd^{III} β-diketonate complexes in solution. [1,2,11,3–10]

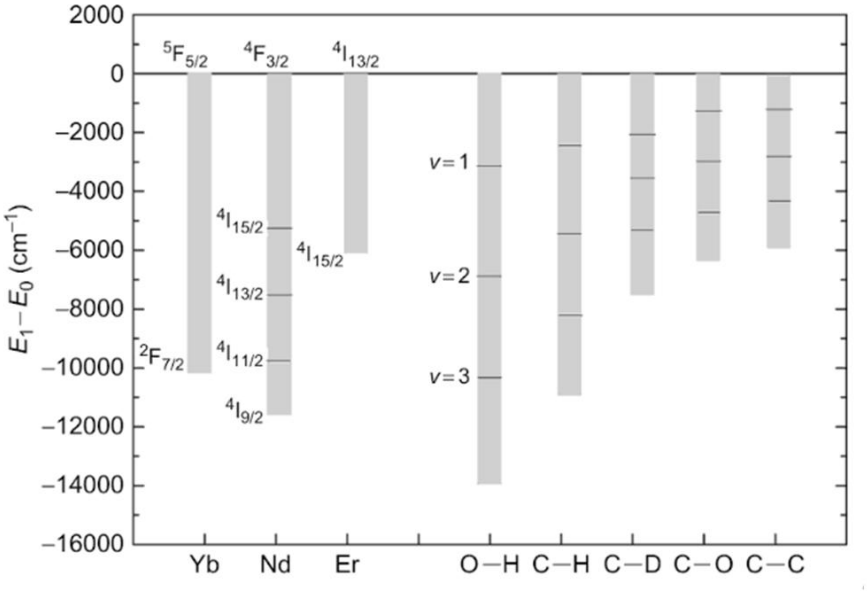

Figure A3.5. Representation of radiative transition energies of NIR emitting Ln^{III} ions (Nd, Er, Yb) and vibrational energy of O-H, C-H, C-D, C-O and C-C.

References

(1) Bünzli, J.-C. G. *Coord. Chem. Rev.,* **2015**, *293–294*, 19–47.
(2) Bünzli, J.-C. G.; Eliseeva, S. V. *Chem. Sci.,* **2013**, *4* (5), 1939.
(3) Bünzli, J.-C. G.; Eliseeva, S. V. *J. Rare Earths.,* **2010**, *28* (6), 824–842.
(4) Binnemans, K.. *Coord. Chem. Rev.,* **2015**, *295*, 1–45.
(5) Shinde, K. N.. Basic Mechanisms of Photoluminescence. In *Phosphate Phosphors for Solid-State Lighting*; 2012; 41–59.
(6) Malba, C. M. Synthesis and Characterization of Lanthanide Based Luminescent Materials, PhD Thesis, Università Ca' Foscari Venezia, 2013.
(7) Artizzu, F. Near-Infrared Luminescent Lanthanide Complexes of Quinolinol Ligands: Structure/Properties Relationship, PhD Thesis, Università degli Studi di Cagliari, 2007.
(8) Eliseeva, S. V.; Bünzli, J.-C. G. *Chem. Soc. Rev.,* **2010**, *39*, 189–227.
(9) Hebbink, G. Luminescent Materials Based on Lanthanide Ions, PhD Thesis, University of Twente, 2002.
(10) Ungur, L. Introduction to the Electronic Structure, Luminescence, and Magnetism of Lanthanides. In *Lanthanide-Based Multifunctional Materials*; Martín-Ramos, P., Ramos Silva, M., Eds.; Elsevier, 2018; pp 1–58.
(11) Bünzli, J.-C. G.; Piguet, C. *Chem. Soc. Rev.,* **2005**, *34*, 1048–1077.

Annex 4
Electrocrystallization Technique

Among the electrochemical techniques the electrocrystallization technique is widely used to obtain single crystals of high quality, which are essential for physical and chemical characterization, such as single-crystal X-Ray diffraction and four-probe conductivity measurements of molecular conductors and/or magnetic conductors.

Principle

The method requires an electroactive species, neutral or charged, whose electro-oxidation (or reduction) leads to a stable radical. If soluble, the generated radical species may diffuse into solution, but under optimum conditions of concentration, solvent, temperature, and current density, slow oxidation of the organic donor occurs and in the presence of the proper counterion it crystallizes on the electrode.

Once the experimental conditions are optimized, high quality single crystals suitable for the desired material can be obtained. Rate of crystal growth can be controlled by the use of a stable and constant direct current, which allows the number of electrons delivered to the electrode to be fine-tuned, thus controlling the local concentration of electroactive species. To ensure reproducible experimental conditions, the value of current density (the current intensity/electrode surface ratio) should be taken into account rather than the current intensity. The three other parameters, namely concentration, solvent, and temperature, essentially control the solubility of the crystalline phase. The choice of the solvent is limited by its ability to dissolve both the organic donor and the electrolyte, therefore sometimes, a mixture of two or more solvents are also used. Moreover, it plays an important role on the solubility of the starting materials and the final product, on the redox potentials of the species in solution, and on the electrode/solution and crystal/solution surface tension, affecting the crystals quality and, in some cases, the crystal phase. The appropriate combination of these factors, together with the use of high-purity starting materials, ultimately determines the success of the electrocrystallization experiment.

Let's consider the oxidation of a neutral donor molecule. The salt generated at the electrode may crystallize with a 1:1 stoichiometry as shown in the equation below:

$$D \xrightarrow{-e^-} D^{+\bullet} \xrightarrow{X^-} (D^{+\bullet},X^-)\downarrow$$

When the donor is a planar conjugated organic molecule with delocalized π electrons, the radical cation formed at the electrode associates with one or more neutral donor molecules, forming materials with different stoichiometries, for instance 1:2, 2:3, etc. This often leads to the formation of mixed-valence salts, which usually show good conducting properties.

$$n(D^{+\cdot}, X^{-}) + mD^{0} \rightarrow (nD^{+\cdot}, mD^{0}, nX^{-})\downarrow$$

Experimental Setup

Electrocrystallization is commonly performed in H-shape cell, where there are two chambers (anodic and cathodic) separated by a porous frit and each chamber contains a Pt electrode. In the anodic compartment, a degassed solution of the organic donor mixed with the counterion is placed, whereas in the cathodic compartment, only the counterion (which also works as electrolyte). The porous frit allows a slow diffusion of these two solutions. The electrodes are connected to a stable current source, which consequently affect the rate of crystal growth. The concentration of species in solution, solvent and temperature usually influence the solubility of the crystalline phase.

Figure A4.1. Picture of a generic H-shape electrocrystallization cell equipped with electrodes.

Due to the high number of parameters involved in the outcome of an electrosynthesis, several experiments are often required to optimize the experimental conditions for obtaining high quality single crystals. Moreover, the electrical properties of a material can be strongly dependent on the type and amount of its impurities. For this reason, in order to have reproducible results, great attention must be given to set up the experiment:

Cleaning of the H-cell

– chemical cleaning, by using aqua regia (HNO_3/HCl 1:3 v/v) or piranha solution (H_2SO_4 95-98%/H_2O_2 30% 3:1 v/v);

Cleaning of the electrode

– First, electrodes are cleaned thoroughly with fine sand paper

– electrochemical cleaning (or depolarization); placing the electrodes in a aqueous solution of diluted sulfuric acid (~1M) and connecting them to a DC generator. By periodically inverting the polarity of the electrodes, H_2 and O_2 are alternatively generated on their surface, allowing for the elimination by reduction or oxidation of all undesired impurities.

– Finally, washing several times with distillated water.

Solvents and Reagents

– Solvents of high-purity grade are dried on activated alumina or are distilled just prior to use.

– electrolyte, as well as the donors, are recrystallized, and the latter are ultimately purified by sublimation whenever possible.

An electrosynthesis usually lasts from few days to several weeks and it is performed in a thermostatic, free of vibrations and dark ambient.

Electrocrystallization is the most employed technique for the preparation of crystalline molecular conductors. However; it presents some disadvantages, such as the ultra-careful and accurate preparation of the experiments, duration of time, and the low yield (often few milligrams). Nevertheless, it allows to obtain the desired materials as high-quality single crystals, the morphological form suitable for their full structural and physical characterization.

Annex 5
Fundamentals of Conductivity

5.1 Molecular Conductors

Many of the molecular conductors known in the literature are charge-transfer (CT) salts or radical salts prepared *via* electrocrystallization (Annex 4). The milestone in this field was the discovery of the purely-organic metal-like conductor TTF-TCNQ *via* CT. Some of the important requirements to form conducting organic salts are (i) generation of charge carriers (ii) efficient packing promoting intermolecular interactions, thus, allowing a good flow of electrons. For instance, face-to-face stacks allows for a good overlap between adjacent orbitals. (iii) minimum columbic interactions to minimize electron repulsion.

Charge carriers are generated as stable charged species or neutral radicals. In CT salts, by the combination of two redox reagents; donor, (electron donating species with a relatively low ionization potential, I_D) and acceptor, (the electron acceptor species with a relatively high electron affinity, E_A), a fraction of the electron charge is transferred from the donor(s) to the acceptor(s) and forms the CT complex $D^{\bullet+}A^{\bullet-}$. Generally, donor and acceptors are planar molecules with an extended π-delocalization as shown in Figure A5.1.

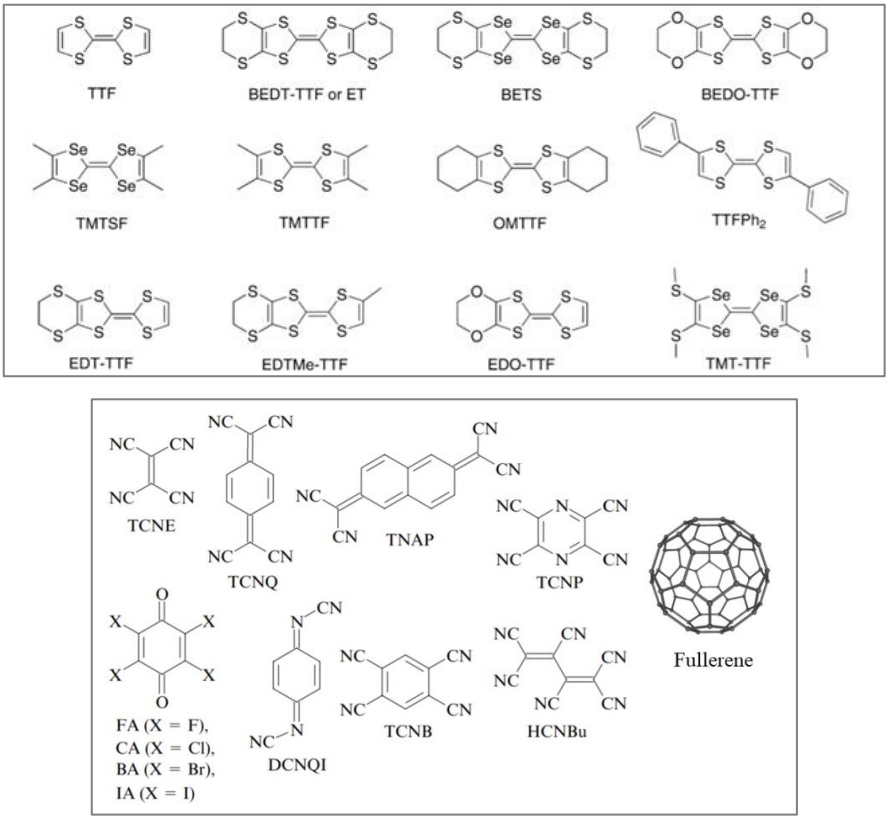

Figure A5.1 Some of the important donors and acceptors.

The CT in these systems can be generalized by the equation:

$$mD^0 + nA^0 \rightarrow D_m^{\rho+} + A_n^{\rho-}$$

where D, is the donor, A, the acceptor, and the exponent ρ quantifies the charge-transfer degree between the two molecules and can be complete (ρ = 1) or partial (0 < ρ < 1). The ρ value depends on the difference between the oxidation potential of the donor E_{ox}(D) and the reduction potential of the acceptor E_{red}(A), and also on the solid state structure of the D-A couple. Schematic representation of CT in the formation of TTF-TCNQ system is shown in Scheme A5.1.

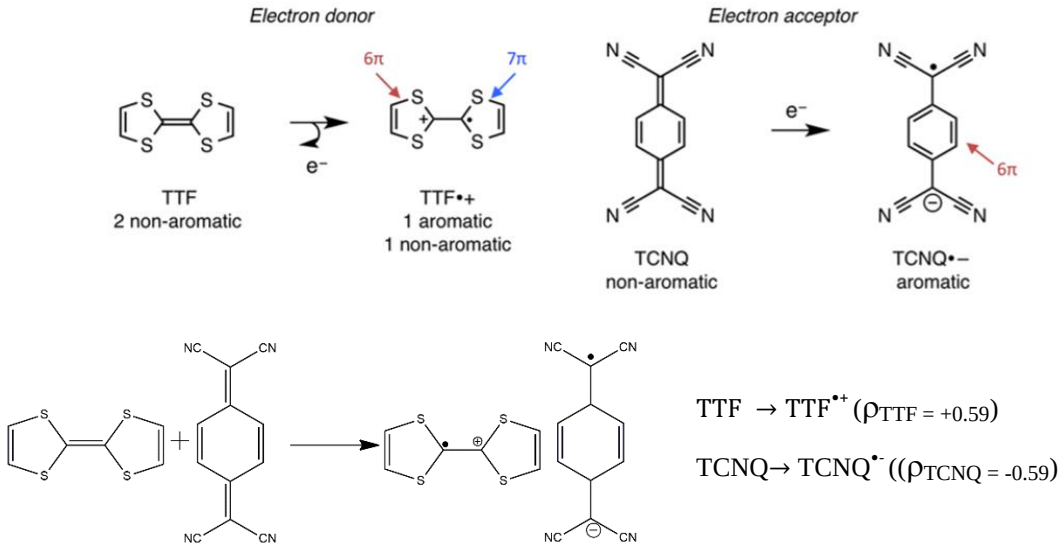

Scheme A5.1. TTF-TCNQ formation by radical formation in TTF and TCNQ molecule.

The functional properties of organic CT salts are strongly determined by ρ. For incomplete CT, ρ < 1, and segregated stacks systems show high conductivities (for instance TTF-TCNQ), whereas alkali metals with TCNQ, where CT is complete, (ρ =1), exhibit lower conductivity.

The CT energy is determined by the HOMO of the donor ($HOMO_D$) and the LUMO of the acceptor ($LUMO_A$), whose energies are equal to the negative of the ionization potential (I_D) and the electron affinity (E_A) of donor and acceptor respectively. For instance, in TTF-TCNQ system, the energy difference between the $HOMO_{TTF}$ and $LUMO_{TCNQ}$ is low (≈ 0.80 eV), which allows the electron transfer from the $HOMO_{TTF}$ to the $LUMO_{TCNQ}$, leading to a stable CT state. A common indicator of CT complex formation is the color change of donor-acceptor blend.

These materials are often characterized by 1D or 2D stacks. Generally, there are two types of stacks observed (Figure A5.2):

- Mixed stacks, where there is no segregation between donors and acceptors, alternated in a **-D-A-D-A-D-** sequence;

- Segregated stacks, where donors and acceptors form separated **-D-D-D-D-D-** and **-A-A-A-A-A-** stacks.

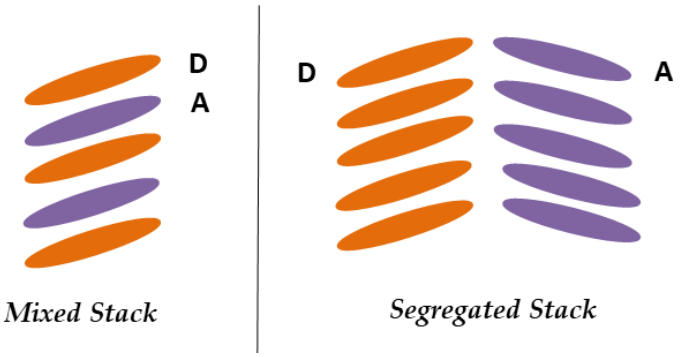

Figure A5.2. Schematic representation of mixed and segregated stacks. D represents donor and A represents acceptor

Segregated stacks of TTF donor and TCNQ acceptor in the TTF-TCNQ system is shown in Figure A5.3.

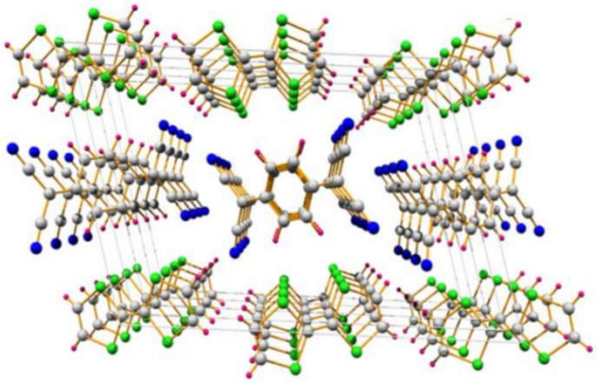

Figure A5.2. Segregated stacks of TTF and TCNQ molecules for the compound TTF-TCNQ

Another important feature determining the conductivity of molecular conductors is the intermolecular interactions (origin of the band structure) in the molecular packing. Along the stacks, conductivity has the maximum value, due to a favorable overlap between the MOs of the building units. The interactions between different stacks are instead usually weaker, resulting in lower conductivity in the direction perpendicular to them. Additionally, molecular materials are subjected to structural distortions, (Peierls distortion), that is, the dimerization between building blocks at low temperature. This results in a energy gap opening between the valence and conduction bands and, consequently, metal to insulator transition.

The concept of CT salts has been also extended to those systems where one of the components is a cationic or anionic species which acts as a counterion of the donor or the

acceptor bearing a fractional charge. This is the case for the systems prepared via the electrocrystallization technique (*vide supra*, Annex 4). In the case of radical cation salts, where only one species undergoes a partial oxidation or reduction process, the role of the counterion is of fundamental importance, as it can influence the arrangement of the donor molecules in the crystal lattice, and thus, the physical properties of the material depending on its molecular geometry, redox potential, and ability to give intermolecular interactions with donor molecules. The counter ion can also act as a carrier of an additional physical property, such as magnetic or optical properties, leading to a multifunctional molecular material.

Some of the important features that a good donor molecule should have are:

– high degree of π-delocalization, that allows for a charge stabilization and reduces the electrostatic repulsions between molecules, leading to a more efficient overlap between MOs;

– Maximum Polarization, mainly the presence of polarizable atoms in the molecule, which play a key role in promoting inter- and intra-stack contacts responsible for an increased dimensionality of the resulting material;

– good planarity, that allows for an effective superposition of the MOs, and thereby, good conducting properties.

There are different packing motifs exhibited by the donor molecules. Some of the most common molecular packing exhibited by the BEDT-TTF donors, shown in Figure A5.1 (*vide supra*) are reported in Figure A5.4.

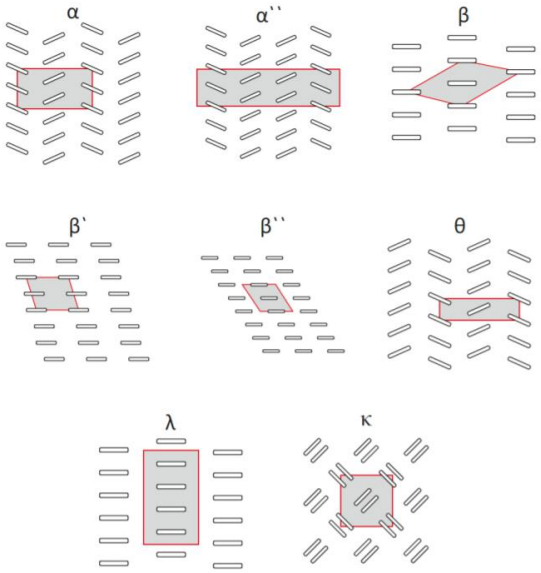

Figure A5.4. Schematic representation of the structural phases exhibited by the donor molecules and its derivatives with classification symbols.

5.2 Electrical conductivity

One of the most and interesting properties in solids is the electrical conductivity. σ is defined as:

$$\sigma = n\,Ze\,\mu$$

where, n is the number of charge carriers (electrons or holes) per unit volume, Ze is their charge (in the case of an electron, only e) and μ is their mobility i.e. the velocity of charge carriers in the presence of electric field. σ is the physical property that quantifies the ability of a given material to transport charge carriers when it is subjected to the action of an electric potential.

According to Ohm's law, which is the most fundamental law in electricity, there is a linear relationship between the electric potential, V and the electrical current of intensity I:

$$V = RI;\ \text{ where R is the resistance of the material}$$

The resistance value (R) is connected to the intrinsic nature of the material, *i.e.* its atomic and electronic structure, and to geometrical factors not correlated to its composition such as its length l and its section s, as stated by the Second Ohm's Law

$$R = \rho\frac{l}{s}$$

where, ρ is the resistivity or specific resistance and quantifies the resistance of a certain material independently from its geometrical features.

Conductivity or specific conductance, expressed in S cm^{-1}, is the reciprocal of the resistivity, as stated by the following expression

$$\sigma = \frac{1}{\rho} = \frac{1}{Rs} = \frac{i\,l}{\Delta V\,s}$$

Depending on the conductivity values σ, materials are classified as insulators ($\sigma < 10^{-6}$ S cm^{-1}), semiconductors ($10^{-6} < \sigma < 10$ S cm^{-1}), metals ($10 < \sigma < 10^{7}$ S cm^{-1}) or superconductors $\sigma > 10^{7}$ S cm^{-1}).

Metallic conductors either have a partially filled valence band, or an overlap between valence and conduction bands; as a consequence, in the applied electric field, electrons can move and generate the net flow of current; whereas insulators have a large gap (E_g) between the bands. Semiconductors have an energy gap which is sufficiently small, that the thermal energy can excite electrons from valence band to conduction band and these activated electrons are free to migrate (leaving holes in valence band) and can carry current (Figure A5.5). Therefore the

conductivity of a semiconductor increases with temperature, as greater number of electrons are mobilised.

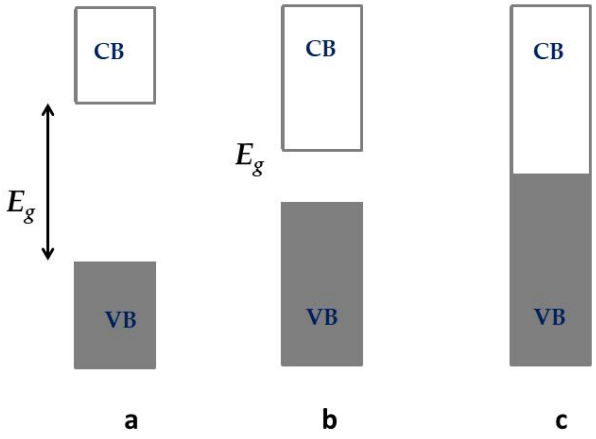

Figure A5.5. Energy bands for an insulator (a), semiconductor (b), metal (c); CB, conduction band; VB, valence band; and Eg, energy gap.

The number of activated electrons (n) in the conduction band can be expressed as a function of band gap E_g and temperature T given by:

$$\mathbf{n \propto exp(-E_g/2k_BT)}$$

Since the conductivity is proportional to the electrons in the conduction band, band gap of a semiconductor can be calculated from variable temperature conductivity measurements, using the Arrhenius-type equation:

$$\mathbf{\sigma_T = \sigma_0\, exp(-E_a/k_BT)}$$

where σ_T is the conductivity at temperature T, σ_0 is a material specific constant, E_a is the activation energy (defined as half the band gap), k_B is the Boltzmann constant and T is temperature. Thus, by plotting ln σ_T *vs* 1/T, the E_a can be calculated.

Reference

(1) Peierls, R. E. "Quantum Theory of Solids", Oxford University Press, 1995.
(2) Hoffmann, R. "Solid and Surfaces: A Chemist's View of Bonding in Extended Structures", Wiley-VCH, 1989. 58
(3) Coleman, L. B.; Cohen, M. J.; Sandman, D. J.; Yamagishi, F. G.; Garito, A. F.; Ferris, A. J. *Solid State Commun.*, **1973**, 12, 1125-1202.
(4) Farris, A. J.; Cowan, D. O.; Walatka, V.; Perlstein, J. H. *J. Am. Chem. Soc.*, **1973**, 95, 948-949.
(5) Jerome, D.; Mazaud, M.; Ribault, M.; Bechgaard, K. *J. Phys. Lett.*, **1980**, L95, 1416.
(6) Kobayashi, H.; Tomita, H.; Naito, T.; Kobayashi, A.; Sakai, F.; Watanabe, T.; Cassoux, P. *J. Am. Chem. Soc.*, **1996**, 118, 368-377.
(7) Mori, T. Bull. *Chem. Soc. Jpn.*, **1998**, 71, 2509-2526.
(8) Mori, T. Bull. *Chem. Soc. Jpn.* **1999**, 72, 2011-2027.
(9) M. Atzori, "Anilate-based Functional Molecular Materials with Conducting and Magnetic Properties", PhD Thesis, University of Cagliari and Angers, 2014.

Annex 6
Fundamentals of Molecular Magnetism

A magnetic field is produced by an electrical charge in motion, for example, electrical current flowing through a conductor. The imaginary lines that represents magnetic field showing the direction and intensity are called Lines of Force or more commonly "Magnetic Flux" (Φ). In the presence of magnetic field, ***H*,** all materials acquire a dipole moment and the response of the material is called Magnetic induction, ***B*** or flux density. In free space, the magnetic induction is a linear function of the magnetic field can be given by the relation:

$$\boldsymbol{B} = \mu_0 \mathbf{H}$$

where μ_0 is the universal constant, permeability of vacuum.

6.1 Physical Quantities

Some of the important physical quantities that represent the response of magnetic materials to the magnetic field are: magnetic moment, magnetization, susceptibility and permeability.

– Magnetic Moment

Magnetism arises from the electronic orbital and spin motion in an atom. The spin and orbital moments imparts magnetic moment on each electron, force them to behave as tiny magnets. The rotational force experienced by a magnet when placed in a magnetic field perpendicular to its magnetic axis is defined as the Magnetic Moment of a Magnet.

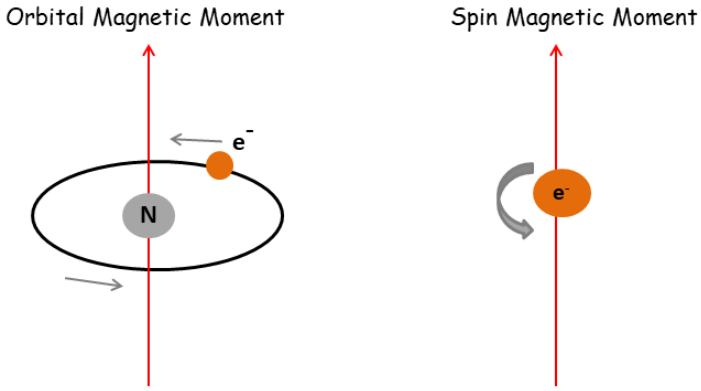

Figure A5.5. Schematic Representation of Orbital and Spin Magnetic Moment.

In a molecule, the overall magnetic moment is a combination of the following:

- magnetic moments due to its unpaired electron spins (paramagnetic contribution)
- orbital motion of its electrons (diamagnetic contribution)
- magnetic moment of its nuclear spins

– Magnetization

Magnetization, $\boldsymbol{M}$, is the density of permanent or induced magnetic dipole moments (i.e. the dipole per unit volume) in a magnetic material.

$$\mathbf{M} = \frac{magnetic\ moment\ (m)}{Volume\ (V)}$$

and the magnetic induction, $\boldsymbol{B}$, inside the material is given by the relation:

$$\boldsymbol{B} = \mu_0 \mathbf{M}$$

The relationship between $\boldsymbol{B}$, $\boldsymbol{H}$, and $\boldsymbol{M}$:

$$\boldsymbol{B} = \mu_0 (\boldsymbol{H} + \boldsymbol{M}) \qquad \text{eqn 1}$$

The unit of $\boldsymbol{H}$ is ampere per metre (A/m) and $\boldsymbol{B}$ in Tesla (T).

In general, the magnetization of a material depends on the magnetic field acting on it. For many materials, $\boldsymbol{M}$ is proportional to $\boldsymbol{H}$:

$$\boldsymbol{M} = \chi \boldsymbol{H} \qquad \text{eqn 2}$$

where, χ is the magnetic susceptibility. It is a dimensionless quantity since it is a property of the material. eqn 1 can be rewritten as:

$$\boldsymbol{B} = \mu_0 (1 + \chi) \boldsymbol{H} \qquad \text{eqn 3}$$
$$= \mu_0 \mu_r \boldsymbol{H}$$
$$= \mu H$$

where, μ_0 is the magnetic permeability of vaccum, μ is the magnetic permeability of any medium, equal to $\mu_0 (1 + \chi)$ and μ_r is the relative magnetic permeability, equal to $\frac{\mu}{\mu_0}$. Generally, χ and μ are used to characterize magnetic materials.

6.2 Types of Magnetism

Diamagnetism

In diamagnetic materials, atoms do not have permanent net magnetic moments, their diamagnetic susceptibility is due to the change in orbital motion of electrons caused by the influence of an external magnetic field. And the applied magnetic field induce a magnetic field in the opposite direction and hence diamagnetic materials are repelled by the magnetic field.

Although all materials exhibit diamagnetic susceptibility, not all are classified as diamagnets. Some materials have a net magnetic moment per atom due to an unpaired electron spin are classified as paramagnetism or even to ordered magnetic states as ferromagnetism. In either case the paramagnetic or ferromagnetic susceptibility is much greater than diamagnetic susceptibility and paramagnetism or ferromagnetism will be the dominant effects.

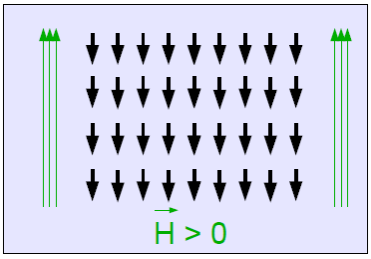

Magnetic moments (represented by small black arrows) of diamagnetic material in the presence of external magnetic field H.

Paramagnetism

Paramagnetism is observed in all materials having a permanent net magnetic moment per atom at high temperature. The atomic magnetic moments of a paramagnetic material are randomly orientated as a result of their thermal energy, but can be aligned in the direction of an external magnetic field.

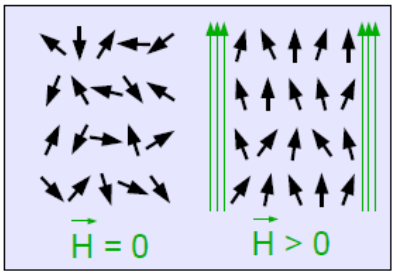

Both spin and orbital magnetic moments give contributions to the magnetization which lead to positive susceptibility values for paramagnets. The susceptibilities of paramagnets have typically values of the order 10^{-3}-10^{-5} and at low fields $\boldsymbol{M}$ is proportional to $\boldsymbol{H}$, although deviations from proportionality occur at very high fields where the magnetization begins to saturate. The paramagnetic behaviour of materials can be explained using different models.

- *The Curie law*

According to Curie's law, the susceptibilities of paramagnetic solids are inversely propotional with temperature, as shown in Figure A6.2. This dependence can be described using the equation

$$\chi = \frac{C}{T}$$

where C is the ***Curie constant***.

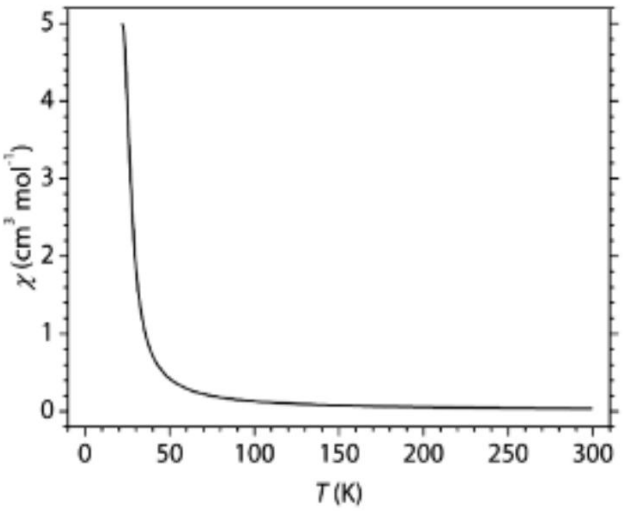

Figure A6.2 Temperature dependence of paramagnetic susceptibility for a Curie paramagnet.

The materials which obey this law are those in which the magnetic moments are localized at the atomic or ionic sites. These can be considered to be "diluted" magnetic materials, in which the magnetic atoms are surrounded by a number of nonmagnetic atoms, like transition metal complexes.

- The Curie-Weiss law

It is a modified or generalized version of the Curie law, which can be represented by the following equation

$$\chi = \frac{C}{(T - T_c)}$$

where C is again the Curie constant and T_c is another constant with dimensions of temperature.

T_c can be either positive, negative or zero. $T_c = 0$ corresponds, to the Curie law. Materials having $T_c > 0$ undergo a paramagnetic to ferromagnetic transition and are called ferromagnets, whereas materials having $T_c < 0$ undergo a paramagnetic to antiferromagnetic transition and are called antiferromagnets. The T_c constant is also indicated with the symbol θ and assumes the name of ***Weiss constant*** (Figure A6.3).

The real transition temperatures from a paramagnetic to ferromagnetic or antiferromagnetic state are both positive and are called ***Curie temperature*** and ***Néel temperature*** respectively. However, the susceptibility of ferromagnets and antiferromagnets only follows the Curie-Weiss law in the paramagnetic region. For lower temperatures, once the material becomes ordered, the susceptibility behaves in a more complicated way and no longer has a unique value for a given field strength.

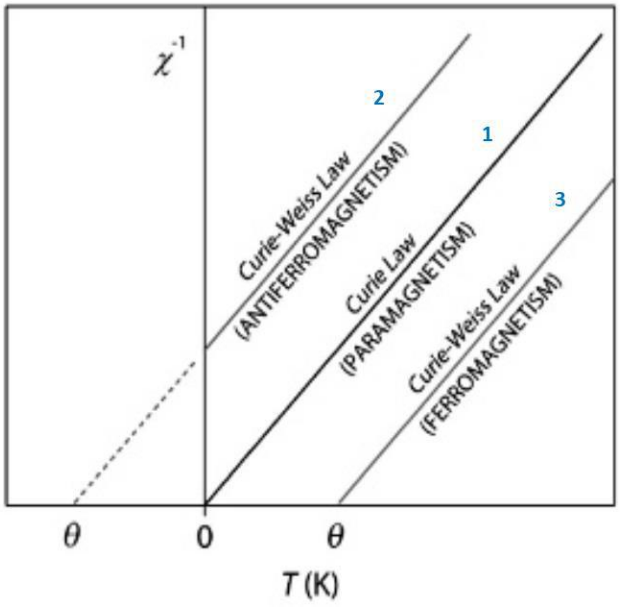

Figure A6.3 Thermal variation of the $1/\chi$ for a paramagnet. 1 represents paramagnet that follows Curie law ($\Theta = 0$); 2, a paramagnet that undergoes a paramagnetic transition to ferromagnetic transition and follows the Curie–Weiss law ($\Theta > 0$); 3, a paramagnet that undergoes a paramagnetic transition to antiferromagnetic and follows the Curie–Weiss law ($\Theta < 0$); the slope of each line is C^{-1}.

Ferromagnetism

In ferromagnetic materials like iron, each atom behaves as tiny magnet, and the magnetic moments are all aligned within microscopic portions of materials called magnetic domains. Below Curie temperature, these domains can align in the direction of an external magnetic field, leaving as permanent magnet.

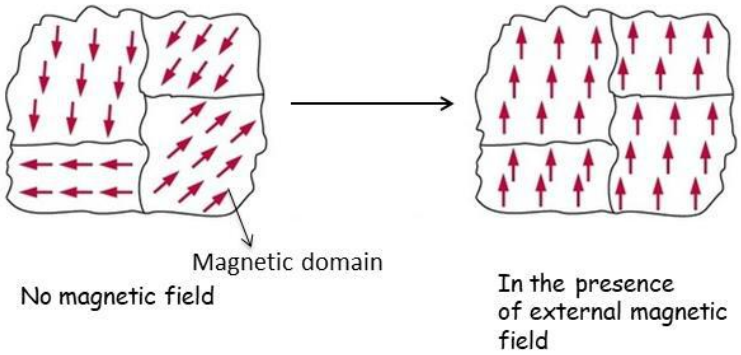

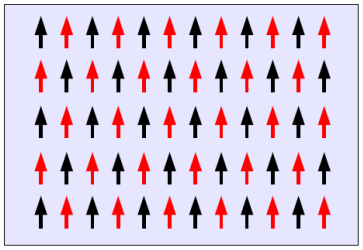

black and red arrows represent the net magnetic moment in a magnetic domain.

The variation of susceptibility and magnetization as a function of the temperature for a ferromagnet are reported in Figure A6.4.

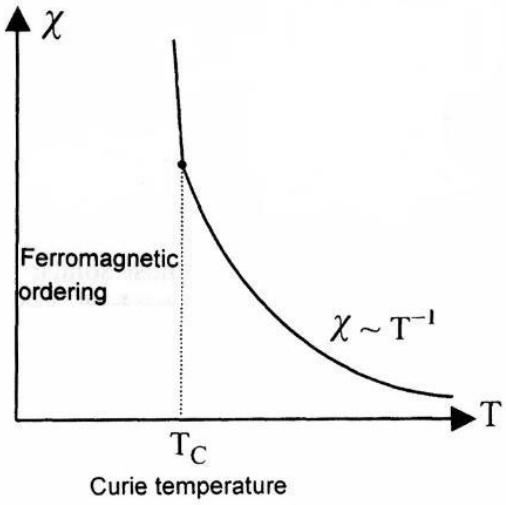

Figure A6.4. Variation of χ as a function of T for a typical ferromagnet.

The most important properties of ferromagnets is their high permeability, susceptibility and the permanent magnetization. So, in order to characterize the properties of a ferromagnetic material it is necessary to measure ***hysteresis curve***. A hysteresis loop shows the relationship between the induced magnetic induction (***B***) or flux density and the magnetic field (***H***) (Figure A6.5). It is well known that ferromagnets can be magnetized, *i.e.* once exposed to a magnetic field they retain their magnetization even when the field is removed. The retention of magnetization distinguishes ferromagnets from paramagnets which although they acquire a magnetization in an applied magnetic field, cannot retain the magnetization once the field is removed.

From magnetization measurements as a function of the applied field it can be seen that a ferromagnet in its initial state is not magnetized. Application of an external magnetic field ***H*** causes a magnetization increase in the direction of field. If ***H*** is increased indefinitely, magnetization reaches saturation at a value denoted as $\boldsymbol{M_S}$. This value represents a state where all the magnetic dipoles within the material are aligned in the direction of the magnetic field. When a ferromagnet is subjected to the action of an external magnetic field, once magnetized and the field is reduced to zero, the value of the magnetization does not assume the initial zero value but assume a certain nonzero value represented by the ***remanent magnetization*** $\boldsymbol{M_r}$. The remanent magnetization can be reduced to zero by applying a reverse magnetic field of strength $\boldsymbol{H_c}$ called ***coercive field***. This value is strongly correlated with the thermal history of the sample.

All ferromagnets when heated to sufficiently high temperatures become paramagnets. At T_C the permeability of the material drops suddenly and both coercivity and remanence become zero.

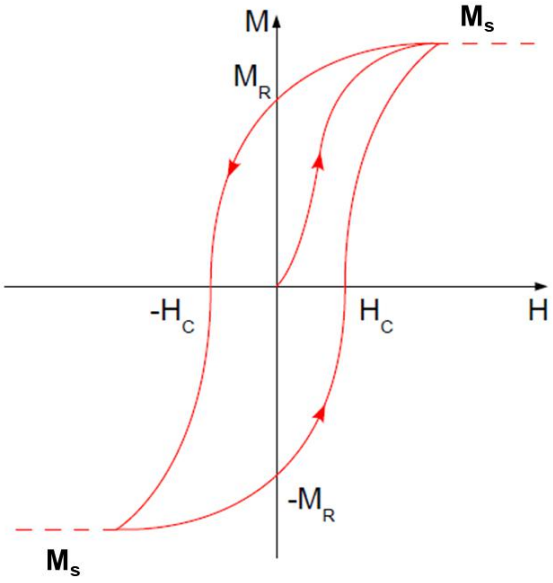

Figure A6.5. Hysterisis loop of typical ferromagnetic close to T = 0 K. H_C - coercivity field, M_R - remnant magnetization or retentivity.

Antiferromagnetism

Antiferromagnetic order, in which nearest-neighbour moments of same magnitude in a magnetic structure are, aligned anti-parallel and hence no net magnetization. This phenomenon is, analogous to ferromagnetism in that they both originate from (super)exchange magnetic coupling interactions extended over a magnetic structure and only differ in the direction of alignment of the magnetic moments in the ordered state, leading to strong differences in the resulting magnetic properties.

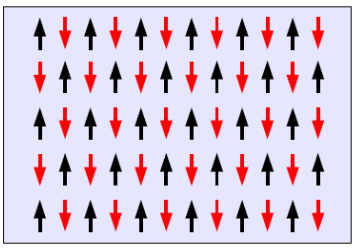

There are two ways to explain this behaviour. One consists in considering the magnetic material as divided in two magnetic sublattices A and B, with the magnetic moments of each sublattice interacting with a positive coupling coefficient, whereas the interactions between the two sublattices have a negative coefficient. This ensures that the magnetic moments of the

two sublattices point in different directions leading to an overall antiferromagnetic order. Another way is to describe the system with a negative interaction between nearest neighbors. The Curie-Weiss also applies to antiferromagnets for T values above the ordering temperature, the ***Néel temperature*** T_N, the Curie-Weiss law becomes

$$\chi = \frac{C}{T + T_C}$$

For antiferromagnets, the T_C appears as a negative temperature below the absolute zero, hence, the plot of $1/\chi$ against T intercepts the temperature axis in the negative region at $-T_C$. For $T_N > 0$, these materials undergo a transition from the ordered antiferromagnetic state to the disordered paramagnetic state. And for $T_N < 0$, the susceptibility does not follow the Curie-Weiss and behaves in a more complex way. The variation of the susceptibility as a function of the temperature is shown in Figure A6.6.

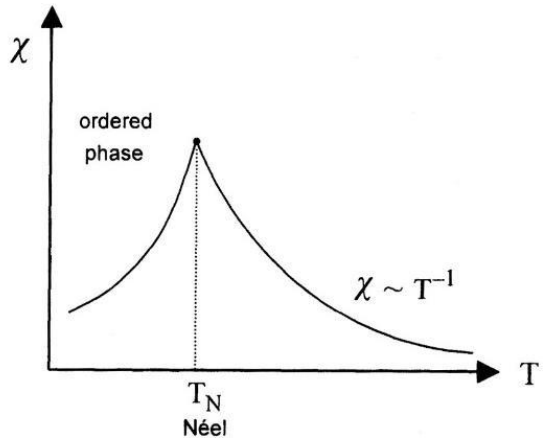

Figure A6.6. Variation of χ as a function of the T for an antiferromagnet; usually the maximum of the susceptibility, corresponding to T_N.

The Néel temperature of antiferromagnets is the analogous of the Curie temperature of ferromagnets. Both mark the transition temperature above which the material is disordered and becomes paramagnetic.

Below T_C		**Above T_C**
Ferromagnetic	↔	Paramagnetic
Ferrimagnetic	↔	Paramagnetic
Below T_N		**Above T_N**
Antiferromagnetic	↔	Paramagnetic

However, it should be pointed out that these two definitions of T_C and T_N are not somewhat equivalent. Some materials, in fact, can be antiferromagnetic and ferromagnetic ordered in different temperature regions and they can have both Curie and Néel temperatures.

Ferrimagnetism

Ferrimagnetism can be considered as a particular case of antiferromagnetism in which the magnetic moments of two A and B sublattices are aligned in an antiparallel way, but having a different magnitude give rise to an overall nonzero magnetization.

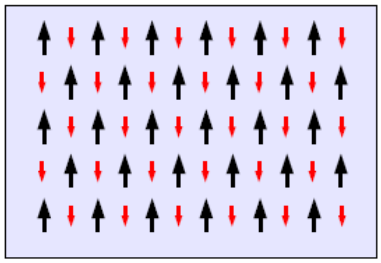

Ferrimagnets behave on a macroscopic scale as ferromagnets as they have a spontaneous magnetization below the critical temperature and are organized in domains, and they also exhibit hysteresis and a saturation magnetization. The general model used for the description of the ferrimagnetic order consists in considering the magnetic structure divided in two sublattices with magnetic moment of different magnitude. The magnetic moments are parallel coupled on the same sublattice, but are antiparallel coupled respect to the magnetic moments of the other sublattice.

Classification of materials by their magnetic properties are summarised in Table A6.1.

Table A6.1. Summary of magnetic materials by their properties

Class	Critical temperature	χ	Temperature dependence	Spin alignment
Diamagnetic	none	negative and small $\chi \approx -10^{-5}$	constant	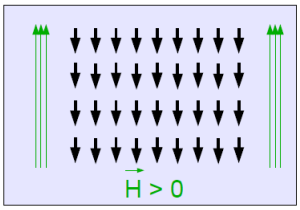
Paramagnetic	none	positive and small $\chi \approx 10^{-3}$-10^{-5}	$\chi = \frac{C}{T}$	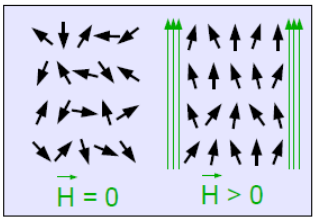
Ferromagnetic	Curie	positive	ferromagnetic	

	temperature	and large	below curie temperature and paramagnetic above	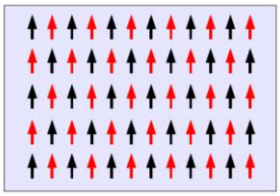
Antiferromagnetic	Neel temperature	positive and small	antiferromagnetic below neel temperature and paramagnetic above	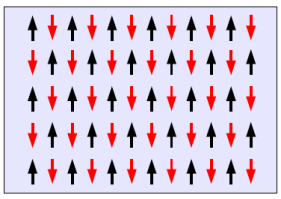
Ferrimagnetic	Curie temperature	positive and large	ferrimagnetic below curie temperature and paramagnetic above	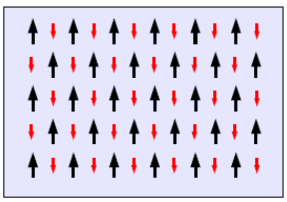

There are other materials, where conventional magnetic-range ordering (*vide supra*) is not possible, for instance, spin glasses. Spin glasses are disordered magnets characterised by the competition between ferromagnetism and antiferromagnetic interactions. Below a certain temperature (called the freezing temperature, T_f) the spins freeze into a highly irreversible metastable frozen state without the usual long-range spatial magnetic order.

The main features of a spin glass are:

- Paramagnetic behaviour above the freezing temperature T_f .
- Characteristic shape of zero-field cooling/field cooling magnetization, with small irreversibility.
- A peak in χ', accompanied by a relaxation process visible in χ''.
- A distorted hysteresis in magnetization versus field dependence in $T < T_f$, lack of saturation.

A detailed description of spin glasses magnetism can be found in ref.[3,4] An example of such materials is reported in Chapter 1.

References

(1) *Magnetism, Molecules to Materials II: Molecule-Based Materials*, Edited by Miller, J. S. and Drillon, M., **2002**, Wiley-VCH.
(2) Robertson, N. and Yee, G.T. *Molecular Materials, Chapter III: Magnetic Molecular Materials*, Edited by Bruce, D. W.; O'Hare, D.; Walton, R. I., **2010**, Wiley.
(3) J. A. Mydosh, *Spin Glasses/ An Experimental Introduction*, Taylor & Francis Ltd., 1993.
(4) K. Binder, A. P. *Young, Spin glasses: Experimental facts, theoretical concepts, and open questions*, Reviews of Modern Physics., **1986**, *58*, 801-976.

Publications

Published Articles

1. S. Ashoka Sahadevan, A. Abhervé, N. Monni, J. R. Galán-Mascarós, J. C. Waerenborgh, P. Auban-Senzier, C. Pasquier, S. Pillet, Marie-Bernadette Lepetit, P. Alemany, E. Canadell, M. L. Mercuri, and N. Avarvari, Conducting Anilate-Based Mixed-Valence Fe(II)Fe(III) Coordination Polymer: Small-polaron Hopping Model in Oxalate-Type Fe(II)Fe(III) 2D Networks. *J. Am. Chem. Soc.*, **2018**, *140*, 12611-12621. *(Chapter 1)*

2. S. Ashoka Sahadevan, N. Monni, A. Abhervé, D. Marongiu, V. Sarritzu, N. Sestu, M. Saba, A. Mura, G. Bongiovanni, C. Cannas, F. Quochi, N. Avarvari and M. L. Mercuri, Nanosheets of 2D Neutral CPs Based on NIR-Emitting Lanthanides and Chlorocyananilate Ligand., *Chem. Mater.*, **2018**, *30*, 6575-6586. *(Chapter 2)*

3. S. Ashoka Sahadevan, N. Monni, A. Abhervé, P. Auban-Senzier, E. Canadell, M. L. Mercuri, N. Avarvari, Synthesis and Physical Properties of Purely Organic BEDT-TTF-based Conductors Containing Hetero-/Homosubstituted Cl/CN-Anilate Derivatives., *Inorg. Chem*. **2017**, *56*, 12564–12571. (*Part of Chapter 5 is published in this article*)

4. M. L, Mercuri, F. Congiu, G. Concas, S. Ashoka Sahadevan, Recent Advances on Anilato-Based Molecular Materials with Magnetic and/or Conducting Properties., *Magnetochemistry*, **2017**, *3* ,17.

Articles Not Included in the Thesis

5. S. Ashoka Sahadevan, E. Cadoni, N. Monni, C. Sáenz de Pipaón, J.-R. Galan Mascaros, A. Abhervé, N. Avarvari, L. Marchiò, M. L. Mercuri, Halogen Interactions/Halogen-Bonding-Mediated Structural Diversity on a New Series of Halogenated Quinolyl Salicylaldimides-Based Fe(III) Compounds., *Cryst. Growth Des.* **2018**, *18*, 4187–4199.

6. N. Monni, V. Mameli, S. Ashoka Sahadevan, S. Gai, C. Cannas, M. Laura Mercuri, Raman Spectroscopy as a Probe for Monitoring the Zinc Presence in Zn-substituted Cobalt Ferrites, *J. Nanosci. Nanotechnol.* **2019**. (In Press)

Articles in Preparation

7. S. Ashoka Sahadevan, G. Cosquer, A. Abhervé, M. Yamashita, N. Avarvari, M. L. Mercuri, Structural diversity in two-dimensional Dy^{III}-Anilate-Based Coordination Polymers.

8. S. Ashoka Sahadevan, N. Monni, A. Abhervé, O. Mariangela, D. Marongiu, F. Quochi, N. Avarvari, M. L. Mercuri, Heteroleptic 2D Coordination Polymers based on Anilate and Carboxylate ligands.

9. S. Ashoka Sahadevan, A. Abhervé, N. Monni, P. Auban-Senzier, M. L. Mercuri, N. Avarvari, Structural diversity and Physical Properties of Paramagnetic Molecular Conductors Based on Bis(ethylenedithio)tetrathiafulvalene (BEDT-TTF) and the Tris(chlorocyanilato)ferrate(III) Complex.

JACS
JOURNAL OF THE AMERICAN CHEMICAL SOCIETY
Article
Cite This: J. Am. Chem. Soc. 2018, 140, 12611−12621
pubs.acs.org/JACS

Conducting Anilate-Based Mixed-Valence Fe(II)Fe(III) Coordination Polymer: Small-Polaron Hopping Model for Oxalate-Type Fe(II)Fe(III) 2D Networks

Suchithra Ashoka Sahadevan,[†,‡,§] Alexandre Abhervé,[†,§] Noemi Monni,[‡] Cristina Sáenz de Pipaón,[∥] José Ramón Galán-Mascarós,[∥,⊥] João C. Waerenborgh,[#] Bruno J. C. Vieira,[#] Pascale Auban-Senzier,[◊] Sébastien Pillet,[▽] El-Eulmi Bendeif,[▽] Pere Alemany,*[,□] Enric Canadell,*[,○] Maria Laura Mercuri,*[,‡] and Narcis Avarvari*[,†]

[†]Laboratoire MOLTECH-Anjou UMR 6200, UFR Sciences, CNRS, Université d'Angers, Bât. K, 2 Bd. Lavoisier, 49045 Angers, France

[‡]Dipartimento di Scienze Chimiche e Geologiche, Università degli Studi di Cagliari, I-09042 Monserrato (Cagliari), Italy

[∥]Institute of Chemical Research of Catalonia, The Barcelona Institute of Science and Technology (BIST), Avenida Països Catalans 16, 43007 Tarragona, Spain

[⊥]ICREA, Passeig Lluís Companys 23, 08010 Barcelona, Spain

[#]Centro de Ciências e Tecnologias Nucleares, Instituto Superior Técnico, Universidade de Lisboa, 2695-066 Bobadela LRS, Portugal

[◊]Laboratoire de Physique des Solides, UMR 8502, Bât. 510, CNRS-Université Paris-Sud, 91405 Orsay, France

[▽]Université de Lorraine, CNRS, CRM2, F-54000 Nancy, France

[□]Departament de Ciència de Materials i Química Física and Institut de Química Teòrica i Computacional (IQTCUB), Universitat de Barcelona, Martí i Franquès 1, 08028 Barcelona, Spain

[○]Institut de Ciència de Materials de Barcelona (CSIC), Campus de la UAB, E-08193 Bellaterra, Spain

Supporting Information

ABSTRACT: The mixed-valence $Fe^{II}Fe^{III}$ 2D coordination polymer formulated as $[TAG][Fe^{II}Fe^{III}(ClCNAn)_3]\cdot(solvate)$ **1** (TAG = tris(amino)-guanidinium, $ClCNAn^{2-}$ = chlorocyanoanilate dianionic ligand) crystallized in the polar trigonal space group *P*3. In the solid-state structure, determined both at 150 and at 10 K, anionic 2D honeycomb layers $[Fe^{II}Fe^{III}(ClCNAn)_3]^-$ establish in the *ab* plane, with an intralayer metal−metal distance of 7.860 Å, alternating with cationic layers of TAG. The similar Fe−O distances suggest electron delocalization and an average oxidation state of +2.5 for each Fe center. The cation imposes its C_3 symmetry to the structure and engages in intermolecular N−H···Cl hydrogen bonding with the ligand. Magnetic susceptibility characterization indicates magnetic ordering below 4 K and the presence of a hysteresis loop at 2 K with a coercive field of 60 Oe. Mössbauer measurements are in agreement with the existence of Fe(+2.5) ions at RT and statistic charge localization at 10 K. The compound shows semiconducting behavior with the in-plane conductivity of 2×10^{-3} S/cm, 3 orders of magnitude higher than the perpendicular one. A small-polaron hopping model has been applied to a series of oxalate-type $Fe^{II}Fe^{III}$ 2D coordination polymers, providing a clear explanation on the much higher conductivity of the anilate-based systems than the oxalate ones.

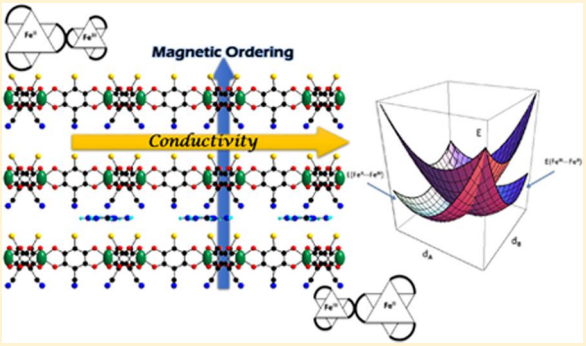

INTRODUCTION

Molecular materials combining conducting (π-type, delocalized) and magnetic (d-type, localized) electrons have attracted major interest in molecular science since they can exhibit the coexistence of two distinct physical properties, furnished by the two independent networks, or novel and improved properties when they interact.[1] In this context, heterobimetallic oxalate-bridged compounds have been thoroughly used as a magnetic lattice of multifunctional magnetic materials.[2] They are formed by anionic networks $[M^{II}M^{III}(ox)_3]^-$ (ox = oxalate) with magnetic ions linked through bis-bidentate bridging oxalate ligands. The second property is provided by the charge-compensating cation, thus combining the long-range magnetic

Received: August 4, 2018
Published: September 10, 2018

DOI: 10.1021/jacs.8b08032
J. Am. Chem. Soc. 2018, 140, 12611−12621

ordering of the oxalate network with paramagnetism,[3] photochromism,[4] electrical conductivity,[5] proton conductivity,[6] ferroelectricity,[7] chirality,[8] or single-molecule magnet behavior.[9] In recent years, coordination polymers based on the 3,5-disubstituted-2,6-dihydroxy-1,4-benzoquinone (H_2dhbq, see Scheme 1), also called anilate ligand in its dianionic form (dhbq^{2-} or X_2An^{2-}), have been thoroughly developed.[10] They usually present 2D-layered[11] or 3D-extended networks[12] with larger cavities than those obtained in oxalate-based coordination polymers due to the larger size of the bridging ligand. More recently, Miyasaka et al. have been able to increase the magnetic ordering temperature in the previously reported ferrimagnet $(NBu_4)[Mn^{II}Cr^{III}(Cl_2An)_3]$ (Cl_2An^{2-} = chloranilate) from 10 to 40 K.[13] Taking advantage of the porosity of the material, they inserted Li^+ ions into the pores of the 2D network in order to generate a radical $Cl_2An^{\bullet 3-}$ (S = 1/2) and produce a new exchange interaction between the radical ligand and the metal centers, thus giving further proof of the potential of the anilate ligand to enhance the magnetic coupling in the extended network. In this context, coexistence of electrical conductivity and magnetic ordering in Fe^{III} anilate-based coordination polymers has been reported simultaneously by two research groups in 2015.[14] In both cases, the conducting properties were attributed to the presence of radical anilate bridging ligand species. The role played by the Fe^{II}/Fe^{III} and L^{2-}/L^{3-} mixed valency was further discussed by Robson et al. with a more recent result based on an interpenetrated 3D network of formula $(NBu_4)[Fe_2(F_2An)_3]$ (F_2An^{2-} = fluoranilate).[12d] Another advantage of the anilate ligand is that it can be substituted on the 3 and 6 positions of the aromatic ring by a large variety of substituents.[15] Recently, the asymmetric chlorocyananilate ($ClCNAn^{2-}$, see Scheme 1)[16] ligand has been combined to the redox-active molecule bis(ethylenedithio)-tetrathiafulvalene (BEDT-TTF) to prepare an organic semiconductor with formula $[HClCNAn]_2[BEDT\text{-}TTF]$[17] and to lanthanide ions in a series of coordination polymers of general formula $[Ln_2(ClCNAn)_3(DMF)_6]\cdot(CH_2Cl_2)_x$ (Ln = Yb, x = 0; Ln = Nd or Er, x = 1) which present NIR emission properties as bulk and nanosheets.[18] In this work, we investigated this nonsymmetric anilate ligand to prepare the mixed-valence coordination polymer of formula $[TAG][Fe^{II}Fe^{III}(ClCNAn)_3]\cdot$(solvate) (**1**), where TAG is the C_3-symmetric tris(amino)-guanidinium cation, never used so far in such coordination polymers. Thorough structural characterization and study of the magnetic and conducting properties of this crystalline material are described. Since mixed-valence $Fe^{II}Fe^{III}$ oxalate-based coordination polymers were previously reported to present a very poor conductivity, we also investigated the origin and mechanism of the transport properties in mixed-valence $Fe^{II}Fe^{III}$ networks based on oxalate-related bridging ligands, i.e., oxalate, squarate, dhbq^{2-}, and $ClCNAn^{2-}$.

Scheme 1. 2,6-Dihydroxy-1,4-benzoquinone (H_2dhbq) and Potassium Chlorocyananilate (KHClCNAn)

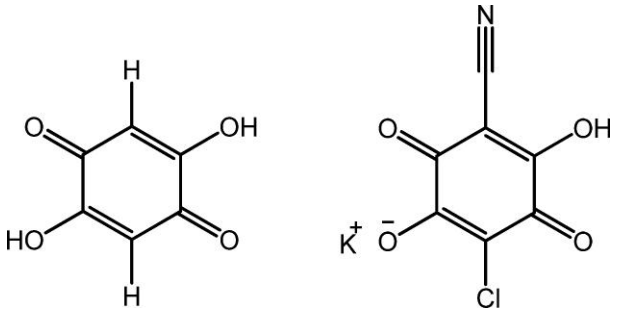

EXPERIMENTAL SECTION

Tris(amino)-guanidinium chloride (TAGCl)[19] and potassium chlorocyananilate (KHClCNAn)[16] were prepared according to the reported procedures. All other chemicals were commercially available and used as received without further purification.

Synthesis of $[TAG][Fe^{II}Fe^{III}(ClCNAn)_3]\cdot$(solvate) (1). An aqueous solution (8 mL) of KHClCNAn (64 mg, 0.27 mmol) was first placed in the bottom of a test tube, then it was carefully layered a solution of TAGCl (42 mg, 0.3 mmol) in a mixture of water (2 mL) and THF (2 mL) in the middle, and then a solution of $Fe(ClO_4)_2\cdot xH_2O$ (51 mg, 0.2 mmol) in acetone (3 mL) was added on the top. After 1 week black hexagonal crystals suitable for XRD measurement appeared at the interface. Anal. Calcd for $C_{22}H_{67}N_9O_{41}Cl_3Fe_2$: C, 19.84; H, 5.07; N, 9.47. Found: C, 19.32; H, 5.23; N, 9.22. FT-IR (ν max/cm^{-1}): 2221 ($\nu_{C\equiv N}$), 1631, 1492 (ν_{C-O} + ν_{C-C}), 869 (δ_{C-Cl} + ν_{C-O}).

Structural Characterization. Data collection was performed at 150 K on an Agilent Supernova diffractometer with Cu Kα (λ = 1.54184 Å). A single crystal of **1** was mounted on a glass fiber loop using a viscous hydrocarbon oil to coat the crystal and then transferred directly to the cold nitrogen stream for data collection. The structure was solved by direct methods with the SIR97 program and refined against all F^2 values with the SHELXL-97 program using the WinGX graphical user interface. All non-hydrogen atoms were refined anisotropically except for the C and N atoms from the cationic entity $CN_6H_9^+$, and hydrogen atoms were placed in calculated positions and refined isotropically with a riding model. The program SQUEEZE from PLATON was used to calculate the potential solvent-accessible void volume and the nature of the disordered solvent molecules. It has indicated a total void space of 885 Å^3 and 293 electrons/cell. This corresponds to 29 molecules of water that have been inserted in the formula of the compound. A summary of crystallographic data and refinement results are listed in Table 1.

Data collection was performed at 10 K on a SuperNova Microfocus diffractometer equipped with a two-dimensional ATLAS detector using Mo Kα radiation (λ = 0.71073 Å) and a Helijet He open-flow cryosystem. The unit-cell determination and data reduction were performed using the CrysAlisPRO program suite (Rigaku Oxford Diffraction, 2017) on the full data set. The data have been indexed using the trigonal setting with cell parameters a = b = 13.5493(16) Å and c = 9.484(3) Å. In addition, the diffraction pattern showed the presence of very weak (1/3 1/3 1/3) superstructure reflections, which were not taken into account in the structure determination. The corresponding crystal structure was refined on F^2 by weighted full matrix least-squares methods using the SHELXL program (Sheldrick, 2008). All non-hydrogen atoms were refined anisotropically except for the C and N atoms from the cationic entity $CN_6H_9^+$, and hydrogen atoms were placed in calculated positions and refined isotropically with a riding model. The program SQUEEZE from PLATON was used to calculate the potential solvent-accessible void volume and the nature of the disordered solvent molecules.

CCDC-1858728 (150 K) and 1858527 (10 K) contain the supplementary crystallographic data for this paper.

Raman Measurements. The Raman spectrum of **1** was carried out at room temperature on single crystals by using a micro Raman spectrometer (Horiba Labram 300) equipped with a He−Ne laser (λ = 632.81 nm) in the 80−2000 cm^{-1} range with a 20 LWD objective (<0.25 mW/μm^2 on the crystal). A 180° reflective geometry was adopted. The samples were mounted on a glass microscope slide, and the scattering peaks were calibrated against a Si standard (ν = 520.7 cm^{-1}). A typical spectrum was collected with a 300 s time constant at <1 cm^{-1} resolution and averaged over three scans. The KHClCNAn FT-Raman spectrum was recorded at room temperature on a capillary tube by using a Bruker RFS/100 FT-Raman spectrometer equipped

DOI: 10.1021/jacs.8b08032
J. Am. Chem. Soc. 2018, 140, 12611−12621

Table 1. Crystallographic Data for Compound 1 at 150 and 10 K

	150 K	10 K
empirical formula	$C_{22}H_{67}N_9O_{41}Cl_3Fe_2$	$C_{22}H_{67}N_9O_{41}Cl_3Fe_2$
fw	1331.90	1331.90
cryst color	black	black
cryst size (mm^3)	0.20 × 0.20 × 0.05	0.22 × 0.19 × 0.06
wavelength (Å)	1.54184	0.71073
cryst syst, Z	trigonal, 1	trigonal, 1
space group	$P\bar{3}$	$P\bar{3}$
a (Å)	13.616(2)	13.5493(16)
b (Å)	13.616(2)	13.5493(16)
c (Å)	9.430(4)	9.484(3)
α (deg)	90	90
β (deg)	90	90
γ (deg)	120	120
V (Å^3)	1514.1(8)	1507.8(6)
ρ_{calcd} ($g\cdot cm^{-3}$)	1.461	1.467
μ(Cu Kα) (mm^{-1})	5.994	0.653
θ range (deg)	3.75−73.74	2.15−26.36
data collected	3465	8947
data unique	2610	3976
data obsd	1360	1612
R(int)	0.0459	0.0604
no. of parameters/restraints	140/4	125/2
$R1(F)$,[a] $I > 2\sigma(I)$	0.0395	0.0715
$wR2(F^2)$,[b] all data	0.1258	0.2391
$S(F^2)$,[c] all data	0.891	1.095

[a] $R1(F) = \Sigma||F_0| - |F_C||/\Sigma|F_0|$. [b] $wR2(F^2) = [\Sigma w(F_0^2 - F_C^2)^2/\Sigma wF_0^4]^{1/2}$. [c] $S(F^2) = [\Sigma w(F_0^2 - F_C^2)^2/(n + r - p)]^{1/2}$.

with a Nd:YAG laser (λ = 1064 nm) in a backscattering geometry. No sample decomposition was observed during the experiments. The choice of the FT-Raman spectrometer was required because of the fluorescence of the ligand under He−Ne laser irradiation.

Magnetic Measurements. Magnetic measurements were carried out on polycrystalline samples with a Quantum Design MPMS-XL-7T SQUID magnetometer (Quantum Design, Inc., San Diego, CA, USA). Magnetic measurements (dc) were carried out under an applied field of 1000 Oe. Zero-field-cooled/field-cooled/remanent magnetization (ZFC/FC/RM) were collected under an applied field of 25 Oe. Alternating current susceptibility measurements were carried out with an alternating magnetic field of 3.95 Oe in the 1−1500 Hz frequency range.

Mössbauer Spectroscopy. Mössbauer spectra were collected in transmission mode using a conventional constant-acceleration spectrometer and a 25 mCi ^{57}Co source in a Rh matrix. The velocity scale was calibrated using α-Fe foil. Isomer shifts, IS, are given relative to this standard at room temperature. The low-temperature spectrum was collected in a bath cryostat with the sample in He exchange gas. The absorber was obtained by gently packing the powdered sample into a perspex holder. The spectra were fitted to Lorentzian lines using a nonlinear least-squares method.

Single-Crystal Transport Measurements. Electrical transport measurements were performed on hexagonal-shaped single crystals. Gold wires (17 μm diameter) were glued with silver paste either on two edges or on both faces of the crystals (for conductivity measurements parallel and perpendicular to the 2D planes, respectively). Two-probe dc measurements were performed applying a constant voltage in the range 0−5 V and measuring the current using a Keithley 6487 Picoammeter/Voltage Source. Low temperature was provided by a homemade cryostat equipped with a 4 K pulse tube.

Theoretical Calculations. Density functional theory (DFT)-based calculations were carried out adopting the hybrid TPSSh functional,[20] which has been shown to give good high-spin−low-spin relative energies for spin-crossover complexes involving iron[21] and the standard double-ζ + polarization basis set 6-31G(d).[22] Geometries were optimized forcing a D_3 symmetry and a high-spin configuration using the Gaussian 09 code.[23]

RESULTS AND DISCUSSION

Synthesis. The synthesis of the mixed-valence compound **1** differs from that of the heterobimetallic oxalate and anilate-based coordination polymers. In such cases, the tetrabutylammonium salt of (tris-oxalato)metal(III) or (tris-anilato)-metal(III) complex was first prepared and isolated. The precursor thus obtained was then reacted with the second metal salt by diffusion techniques to grow the bimetallic extended network. Here we have slowly diffused a solution of $Fe^{II}ClO_4\cdot xH_2O$ and a solution of tris(amino)-guanidinium chloride (TAGCl) into a solution of KHClCNAn. Due to the partial oxidation of the Fe^{II} ions under aerobic conditions, black hexagonal crystals of the $Fe^{II}Fe^{III}$ compound **1** were obtained after 1 week.

Crystal Structure. Compound **1** crystallizes in the trigonal polar space group $P\bar{3}$. The structure is formed by anionic 2D layers of formula $[Fe^{II}Fe^{III}(ClCNAn)_3]^-$ in the *ab* plane, alternating with cationic layers of TAG. The anionic layer presents the well-known honeycomb structure, which is similar to other extended oxalate[24] and anilate-based 2D networks.[11a−e] It consists of a hexagonal layer with Fe^{II} and Fe^{III} ions linked through the anionic bis-bidentate $ClCNAn^{2-}$ ligands (Figures 1 and S1 and S2). As usual for this type of 2D networks, the two crystallographically independent metal centers present alternated chirality (Δ configuration for Fe1 and Λ configuration for Fe2 in the crystal used to solve the structure). The intralayer metal−metal distance is 7.860 Å. The average Fe−O distances are very similar between both metal centers (2.037(12) Å for Fe1 and 2.047(13) Å for Fe2, see Table 2), which may indicate an electron delocalization and an average oxidation state of +2.5 for each Fe center (vide infra). The cationic layer is formed by one crystallographically independent TAG cation and water molecules. The TAG cation has an occupancy of 1/3, which is one-half of the Fe atoms, and is located only on one-half of the vertices of the hexagons. The structure of the cation is planar, with the C8−N2 and N2−N3 distances (1.394(15) and 1.558(17) Å respectively, see Table S1) in agreement with distances reported in the literature for other TAG-based compounds.[25] Anionic and cationic layers present intermolecular H-bonding interactions between the terminal amino groups of the TAG cation and the chloro substituents of the anilate ligands (Figure 1). The distance between two anionic layers corresponds to the value of the *c* parameter (9.430(4) Å). The cationic and anionic 2D layers are eclipsed, leading to hexagonal channels along the *c* axis which are filled only by solvent molecules. When compared to the previously reported anilate-based layered coordination polymers,[11a−h] here the use of the smaller cation results in a drastic increase of the void space inside the hexagonal channels (885 Å^3). This represents 58% of the total volume, thus increasing the porosity of the 2D material (Figure S3). As a consequence, the compound shows a fast release of the solvent molecules after filtration, and the nature of these solvent molecules could not be attributed without ambiguity. In order to reach a good reliability factor and since 293 electrons per hexagonal cavity were determined by the SQUEEZE program, 29 molecules of water have been integrated in the empirical formula (see Table 1). However,

DOI: 10.1021/jacs.8b08032
J. Am. Chem. Soc. 2018, 140, 12611−12621

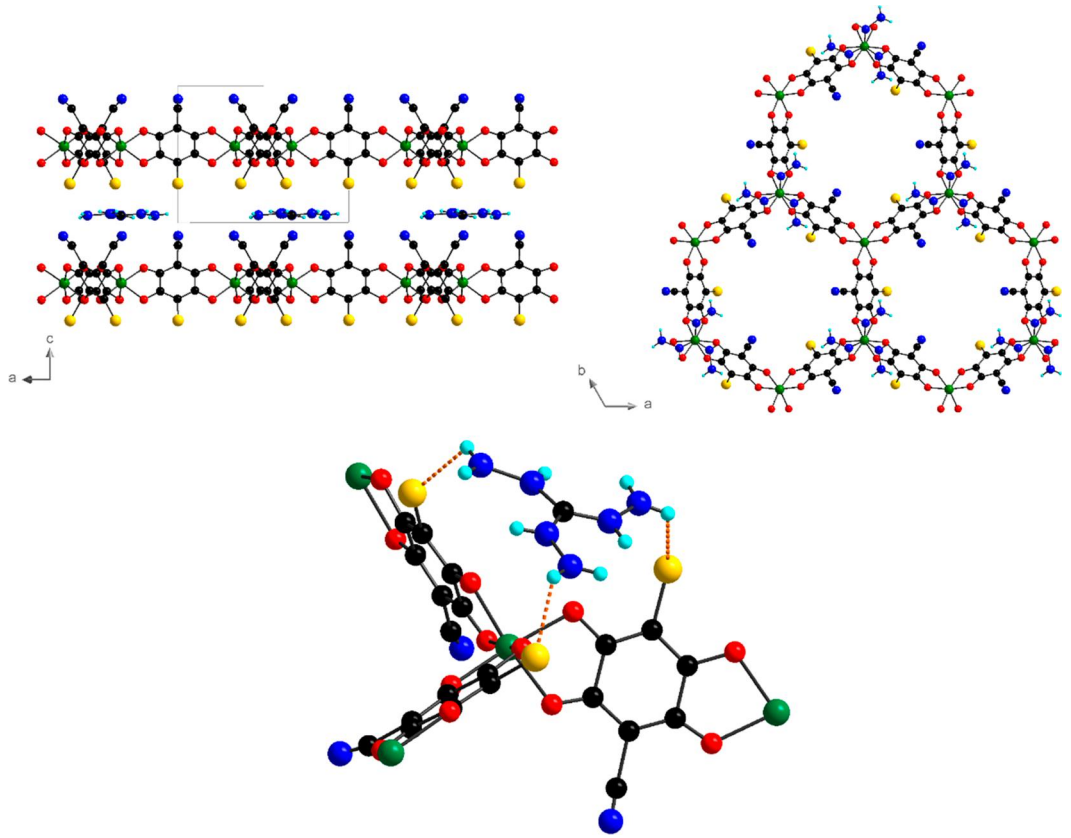

Figure 1. Structure of **1** in the *ac* plane (top left) and in the *ab* plane (top right). H-bonding intermolecular interactions (dashed lines) between the cationic and the anionic layers (bottom). Color code: C, black; H, cyan; O, red; N, blue; Cl, yellow; Fe, green.

Table 2. Selected Fe−O Bond Distances (Å) in Compound 1

Fe−O distances	150 K (Å)	10 K (Å)
Fe1−O1	2.000(6)	1.937(7)
Fe1−O2	2.086(6)	2.103(7)
Fe2−O3	2.073(7)	2.117(7)
Fe2−O4	2.018(6)	1.974(7)

TGA analysis could not confirm the precise nature of the solvent molecules (Figure S4). Since a mixture of three solvents has been used during the synthesis (water, THF, and acetone), the formula of the compound should be defined as $[TAG][Fe^{II}Fe^{III}(ClCNAn)_3]\cdot(solvate)$.

By comparison with the 150 K crystal structure, the overall honeycomb 2D structural architecture in the trigonal *P*3 space group is retained at 10 K. Accordingly, the asymmetric unit still contains two symmetrically independent iron sites (Fe1 and Fe2). The unit cell parameters and unit cell volumes are slightly lower at 10 K, owing to usual thermal contraction effects. The intralayer metal−metal distance (7.8243(7) Å) and average Fe−O distances (2.020(14) Å for Fe1 and 2.043(14) Å for Fe2) are not significantly different from the 150 K values. Accordingly, the 10 K crystal structure does not evidence a specific ordering of the Fe^{II} and Fe^{III} ions on the symmetrically independent Fe1 and Fe2 sites. We can therefore consider that in this description the Fe^{II} and Fe^{III} ions are spatially distributed and disordered over the two sites. As mentioned in the Experimental Section, very weak superstructure reflections were detected on the diffraction pattern, which indicates that the exact structural ordering may be more complex than this description in the *P*3 space group. However, the quality of the X-ray diffraction data, and especially the weakness of the superstructure reflections, does not allow going further. The current description leads to two Fe^{II} and two Fe^{III} different local environments in the crystal, which is consistent with the results from Mössbauer spectroscopy (vide infra).

Raman Spectroscopy. Raman spectra are valuable probes to investigate the oxidation state of coordinated benzoquinone derivatives.[26] Therefore, in order to confirm the oxidation state of the bridging ligand a Raman study at room temperature was performed and a comparison between the Raman spectra of **1** and the free KHClCNAn ligand is reported in Figure 2.

The strong and broad band centered at ca. 1574 cm^{-1} can be assigned to a ν(C═C) + ν(C═O) combination band, and the significant observed downshift from 1627 cm^{-1} for the free ligand can be attributed to a weakened double-bond character of these terminal groups because of the coordination with the metal ion; the weak band centered at ca. 1675 cm^{-1} present in the free ligand spectrum can be assigned to the ν(C═O) vibration mode for the uncoordinated C═O groups of the free ligand and in fact is not observed in **1**. The two bands observed in the 1400−1250 cm^{-1} region are assigned to the ν(C−C) + ν(C−O) combination band and ν(C−C) vibration, respectively, and according to Harris et al.[14c] confirm the assignment of ligand oxidation state as dianionic $ClCNAn^{2-}$, supporting structural findings. The observed band at 592 cm^{-1} can be assigned to a ν(Fe−O) + ν(C−C) combination stretching mode, as already found in previously reported dianionic anilate-based honeycomb-like networks.[14a] No bands can be unambiguously assigned to Fe^{II}−O and Fe^{III}−O vibrational

DOI: 10.1021/jacs.8b08032
J. Am. Chem. Soc. 2018, 140, 12611−12621

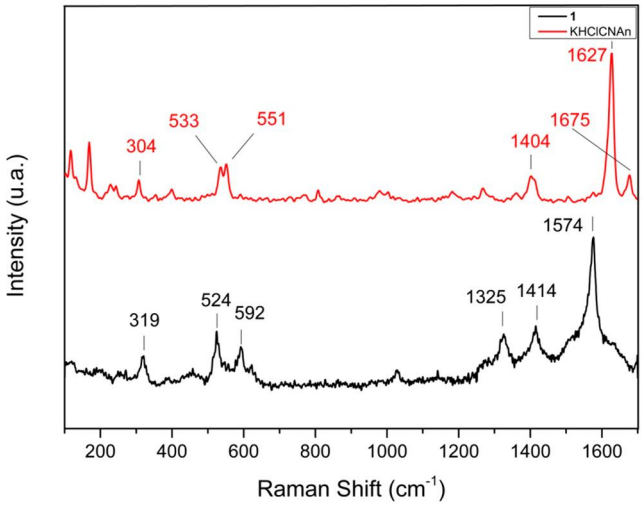

Figure 2. Comparison of Raman spectra of **1** and the KHClCNAn ligand, performed at room temperature with a He−Ne laser (λ = 632,81 nm) and a Nd:YAG (λ = 1064 nm), respectively.

modes, thus supporting extensive electron delocalization between the Fe centers in **1** at room temperature, as clearly shown by Mössbauer spectra (vide infra).

Magnetic Properties. The magnetic properties were measured on a polycrystalline sample of **1**. The product of the molar magnetic susceptibility times the temperature ($\chi_m T$) presents a value of 9.7 emu·K·mol^{-1} at 300 K, which corresponds to the expected spin-only value (7.38 emu·K·mol^{-1}) with a g = 2.2 (Figure 3). When the temperature is

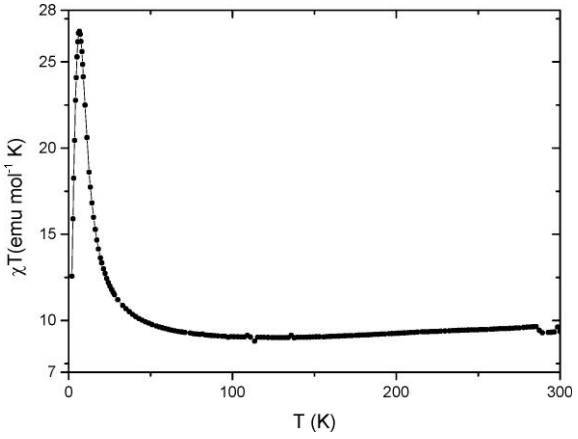

Figure 3. Temperature dependence of the product of the molar magnetic susceptibility times the temperature ($\chi_m T$) of **1** under an applied field of 1000 Oe.

lowered, $\chi_m T$ slightly decreases, suggesting weak antiferromagnetic interactions between paramagnetic centers through the anilate bridges. Below 50 K, $\chi_m T$ increases until reaching a value of ∼27 emu·K·mol^{-1} at 7 K, followed by a sharp decrease at lower temperatures. This suggests a magnetic ordering, which was confirmed by zero-field-cooled/field-cooled (ZFC/FC) and remnant magnetization measurements under a very low magnetic field (Figure S5). The ZFC and FC plots diverge below 3.5 K, indicating the appearance of an irreversibility or memory effect. The remnant magnetization becomes non-negligible at the same temperature, confirming the existence of spontaneous magnetization below this temperature.

The magnetic ordering was also confirmed by susceptibility measurements under alternating magnetic field (ac susceptibility, Figure 4a). This shows the appearance of an out-of-phase signal and an ordering temperature T_c slightly dependent on the frequency, which can be observed for both superparamagnets and spin glasses.[27] The fitting of this frequency-dependent behavior to a simple Arrhenius model (Figure 4b) yields parameters with no physical meaning, including a τ_0 = 10^{-12}, very different to what is found in superparamagnets (or single-molecule magnets, with values of τ_0 between 10^{-8} and 10^{-10} s).[28] This τ_0 value falls within the range reported for magnetic spin-glass systems (10^{-12}−10^{-14} s)[29] and is then consistent with a glassy magnet behavior as observed in many 2D magnetic materials.[30] Moreover, the Mydosh parameter φ, calculated from the ac data,[31] has a value of 0.08, in good agreement with the expected values for a noncanonical spin glass.[14a,32]

Isothermal magnetization measurements at low temperatures show a fast increase of the magnetization at low fields that becomes more gradual at higher fields (Figure 5). The sharp increase at low fields (H < 1000 Oe) also supports the appearance of spontaneous magnetization due to strong interactions between metal centers. The magnetization saturates at higher fields reaching ∼5 μ_B, far from the expected 9 μ_B for parallel alignment of spin carriers. This confirms the ferrimagnetic nature of the spontaneous magnetization that stabilizes a ground state with an intermediate spin, characteristic of a glassy ferrimagnet as suggested by the initial decrease in the $\chi_m T$ at high temperatures. An additional proof of the magnetic ordering is the presence of a hysteresis loop at 2 K with a coercive field of 60 Oe.

Mössbauer spectroscopy has been used to confirm the oxidation state of the Fe metal centers (Figure 6). At 10 K three broad absorption peaks are observed. They may be interpreted by two quadrupole doublets. However, due to the large width of the absorption peaks a significantly better fit is obtained with four quadrupole doublets. The estimated isomer shift, IS, and quadrupole splitting, QS, are consistent with the presence of high-spin Fe^{3+} and high-spin Fe^{2+} in octahedral coordination by anionic oxygen atoms.[33] The estimated relative areas indicate that approximately one-half of the Fe cations are in the +3 state and the other half in the +2 state. The two doublets observed for each oxidation state are consistent with the occupation of Fe(1) and Fe(2) crystallographic sites by both Fe^{2+} and Fe^{3+}. The room-temperature spectrum shows only one asymmetric doublet with IS and QS consistent with an average oxidation state of +2.5.[34] The temperature dependence of the Mössbauer spectra of the anilate coordination polymer is similar to the behavior observed for other mixed-valence iron compounds, namely, molecular complexes.[35] The intermediate isomer shift at room temperature corresponds to a charge-delocalized state on the Mössbauer spectroscopy time scale of ∼10^{-7} s, i.e., a charge-transfer frequency ≥ 10^8 s^{-1}. As the temperatures decreases, the frequency of charge delocalization gradually decreases, and at 10 K the Fe^{2+} and Fe^{3+} states are localized when compared to the Mössbauer effect time window (i.e., the lifetime of the Fe^{2+} and Fe^{3+} states becomes longer than 10^{-7} s).

Transport Properties. Since a mixed-valence state and electron delocalization have been evidenced in **1**, we could expect this coordination polymer to present transport properties; therefore, electrical conductivity measurements have been carried out on single crystals. The hexagonal shape of the

DOI: 10.1021/jacs.8b08032
J. Am. Chem. Soc. 2018, 140, 12611−12621

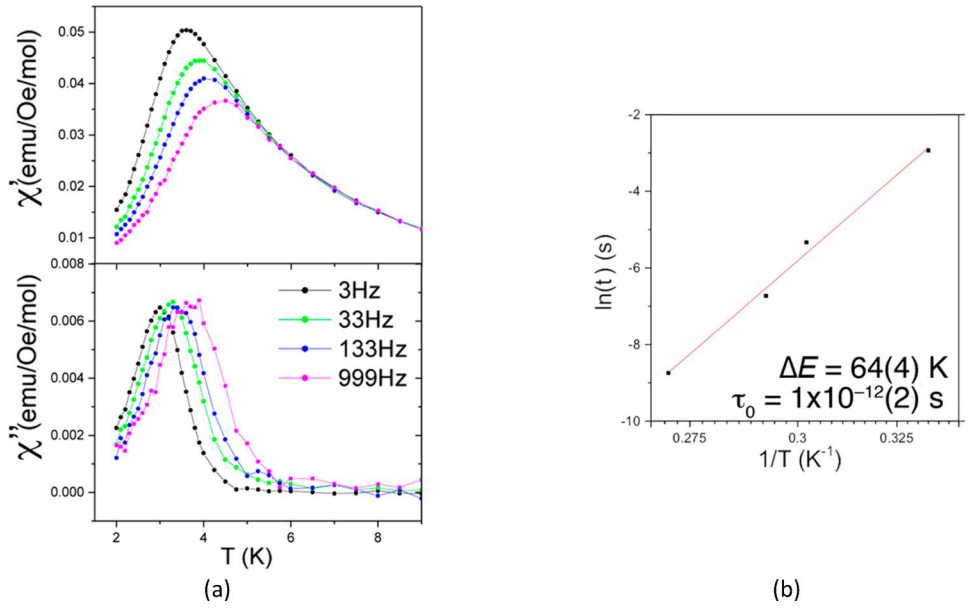

Figure 4. (a) Temperature dependence of the in-phase (χ') and out-of-phase (χ'') ac susceptibility of **1**, and (b) Arrhenius plot for the frequency dependence of the position of the peak in χ'' vs $1/T$.

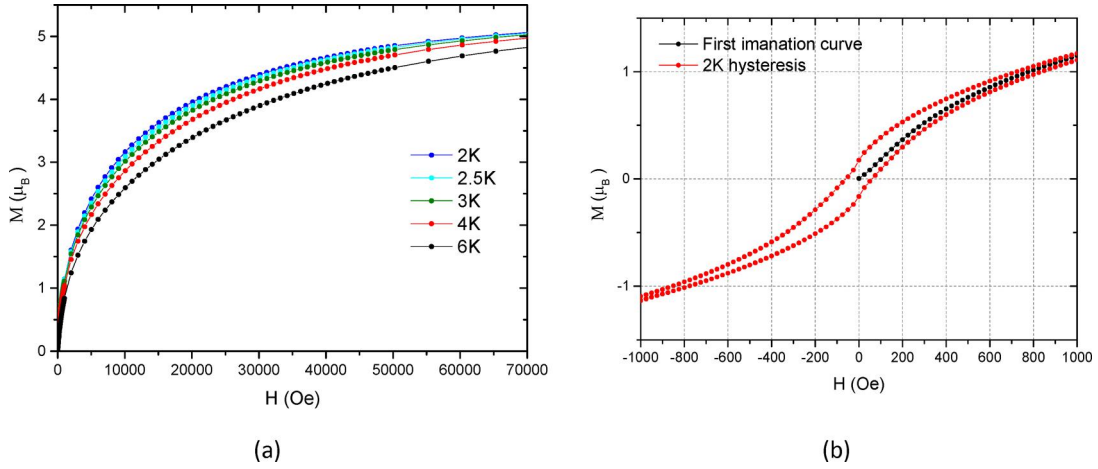

Figure 5. (a) Isothermal magnetization of **1** at different temperatures and (b) magnetic hysteresis loop at 2K.

crystals allows determining the direction of the {001} plane and then to measure the conductivity parallel ($\sigma_{\parallel}$) and perpendicular ($\sigma_{\perp}$) to the 2D layers, corresponding to the *ab* plane. The temperature dependence of the resistivity indicates that **1** is a semiconductor (Figure 7). The parallel room-temperature conductivity value $\sigma_{\parallel}$ is about 2×10^{-3} S/cm, almost 3 orders of magnitude higher than the perpendicular room-temperature conductivity $\sigma_{\perp}$ (7×10^{-6} S/cm).

Relationship between the Electrical Conductivity and the Nature of the Bridging Ligand. The fairly good conductivity of compound **1** as well as of the few recently reported anilato-based $Fe^{II}Fe^{III}$ coordination polymers[11g,14b] is in sharp contrast with the low conductivity found for the oxalate-based ones.[36] To gain insight into the origin of the good conductivity in our anilate-based coordination polymer and to point out the crucial role of the bridging ligand, we have undertaken a theoretical study on the electron transfer in 2D $Fe^{II}Fe^{III}$ networks based on bis(bidentate) oxalate-type ligands in which we consider the conductivity dominated by thermally activated small-polaron hopping. We are interested in a simple, pragmatic approach, highlighting the role of the bridging ligand, and in this comparative work, we decided to focus on four ligands: oxalate, squarate ($C_4O_4^{2-}$, dianion of 3,4-dihydroxycyclobut-3-ene-1,2-dione), $dhbq^{2-}$, and $ClCNAn^{2-}$, with different electron delocalization capabilities.

The basic reasoning behind the small-polaron hopping approach to the electron transfer process in either discrete or extended mixed-valence systems[37,38] is qualitatively illustrated in Figure 8. Consider a system formed by two separated high-spin $Fe^{II}L_6$ ($t_{2g}^4e_g^2$) and high-spin $Fe^{III}L_6$ ($t_{2g}^3e_g^2$) complexes in close proximity. Although the electron transfer between them is between levels of the Fe t_{2g} orbital set, which are formally nonbonding, such transfer leads, in general, to an increase/decrease of the M−L distances in the $Fe^{II}/Fe^{III}L_6$ units due to the expansion/contraction of the electron cloud. As a consequence of the fact that electrons move much faster than nuclei, the much faster electron transfer occurs in such a way that the geometry cannot change during the process and the system cannot exchange thermal energy with the surroundings. In other words, before the electron transfer

DOI: 10.1021/jacs.8b08032
J. Am. Chem. Soc. 2018, 140, 12611−12621

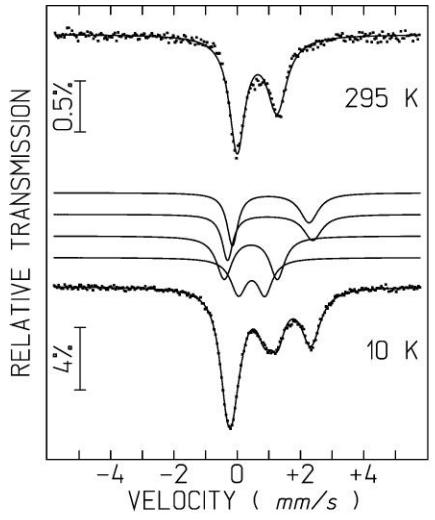

(a)

T	IS (mm/s)	QS (mm/s)	I (%)	Fe state
295 K	0.74	1.26	100%	$Fe^{2.5+}$
10 K	0.57	0.83	24%	Fe^{3+}
	0.54	1.68	29%	Fe^{3+}
	1.15	2.69	22%	Fe^{2+}
	1.17	2.42	25%	Fe^{2+}

(b)

Figure 6. (a) Mössbauer spectra of **1** taken at 295 and 10 K, and (b) estimated parameters from the spectra. Lines over the experimental points are the calculated functions. On the spectrum taken at 10 K this function is the sum of four quadrupole doublets shown slightly shifted for clarity. IS, isomer shift relative to metallic α-Fe at 295 K; QS, quadrupole splitting; I, relative areas. Estimated errors are <0.02 mm/s for IS and QS and <2% for I.

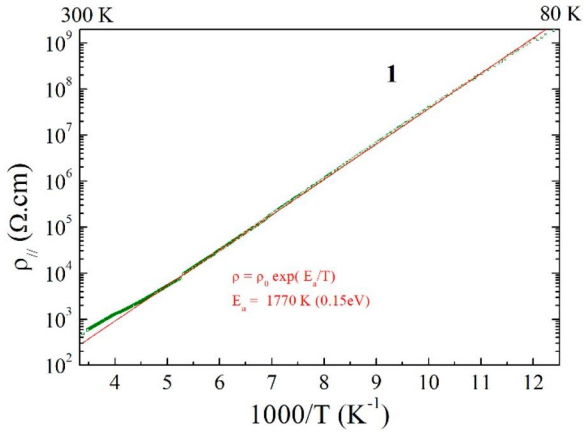

(a)

	ρ (kΩ.cm)	σ (S/cm)
//	0.5	2.10^{-3}
⊥	143	7.10^{-6}

(b)

Figure 7. (a) Electrical resistivity $\rho_{\parallel}$ plotted as log $\rho_{\parallel}$ versus the inverse temperature, measured with a 4 V voltage applied in the *ab* plane. Red line is the fit to the data with the law $\rho = \rho_0 \exp(E_a/T)$ giving the activation energy E_a. (b) Room-temperature resistivity (ρ) and conductivity (σ) values measured along (||) and perpendicular ($\perp$) to the 2D layers.

can actually take place a Fe^{III} species with the Fe^{II} geometry (and viceversa) must be created. This rearrangement is however energetically unfavorable, so that the electron transfer will only occur when as a result of some vibrational process the two Fe centers reach equal coordination geometries (see Figure 8a). Thus, to understand the differences in thermally activated conductivity one must focus on the evaluation of the energetic cost of such "equalization" of the two sites.

A simple yet usually very insightful analysis relies on the assumption that the structural distortion around each center may be described by a simple harmonic oscillator $E_i = 1/2\ k_i(d_i - d_0)^2$, where k_i is the force constant, d_i the Fe−L distance, and d_0 its equilibrium value. Within this approximation the energy of the whole system is $E_{tot} = k_{III}(d_A - d_{III})^2 + k_{II}(d_B - d_{II})^2$, where for the sake of simplicity the 1/2 factors have been included in the force constants. Here let us assume that complex A is in the Fe^{III} state and complex B in the Fe^{II} state, but there is a totally equivalent expression interchanging A and B. If we plot the two energy surfaces $E_{tot}(d_A,d_B)$ we see that they cross along the line $d_A = d_B$ (Figure 8b). The initial and final configurations (respectively, top and bottom configurations in Figure 8a) correspond to minima in the lower surface and the structures for which $d_A = d_B$ to the crossing seam. The situation is more conveniently analyzed by using a contour plot of the bottom surface (Figure 8c), obtained by joining the two bottom halves of the two intersecting surfaces. The two minima correspond to the configurations $Fe^{III}{}_A\cdots Fe^{II}{}_B$ (zone noted as F in Figure 8c) and $Fe^{II}{}_A\cdots Fe^{III}{}_B$ (noted as I). The point on the $d_A = d_B$ line for which the total energy is minimal (M) is found by taking the derivative of the energy function with $d_A = d_B = d_M$ and equating it to zero. It is found that $d_M = (k_{II}d_{II} + k_{III}d_{III})/(k_{II} + k_{III})$ and the corresponding energy $E_M = (k_{II}k_{III}/(k_{II} + k_{III}))(d_{II} - d_{III})^2$. In other words, the minimal energy required to make the coordination environ-

DOI: 10.1021/jacs.8b08032
J. Am. Chem. Soc. 2018, 140, 12611−12621

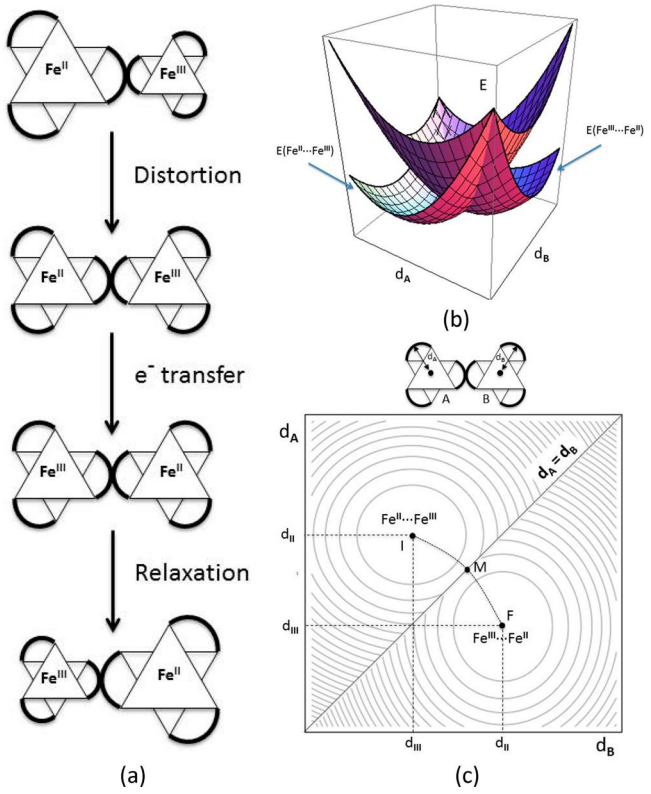

Figure 8. (a) Schematic representation of the three consecutive steps during the electron transfer with two neighboring pseudooctahedral Fe(chelate)$_3$ centers shown along the C_3 axis. (b) 3D plot of the energy surface E_{tot} as a function of d_A and d_B. (c) Contour plot of the bottom surface from the E_{tot} plot displayed in b.

ments on both Fe centers equal, that is, the height of the barrier for thermally activated electron transfer, depends basically on the difference squared between the radii of the Fe^{III} and Fe^{II} coordination environments in their equilibrium geometries.

The model can be more simply depicted by using a cut through the two surfaces in which we plot the energy along the dotted path joining the two minima through the M point, which is taken as the origin (Figure 9). This gives two parabolas corresponding to the energy of the whole system with either an $Fe^{II}Fe^{III}$ or an $Fe^{III}Fe^{II}$ configuration and crossing at the M point. Note that when the two complexes are not totally isolated from their surroundings, the energy necessary to distort the complexes has an additional contribution from the environment. This is particularly important in the case of 2D lattices where the distortion of one site contributes to the distortion of all its neighboring sites. This contribution is usually included considering a generic parameter λ, which is the vertical ionization energy from one minimum to the other curve or in other words the energy necessary to transfer the electron from A to B without considering a previous structural equalization of both centers. The barrier for thermal electron transfer in the absence of interaction (i.e., the energy difference between the minima and the crossing point of the two curves) is then simply $\lambda/4$. In the real case there is always some degree of electronic interaction between the two sites and a gap, $2V_{AB}$, is opened at point M, and the barrier for thermal electron transfer is consequently lowered to $\lambda/4 - V_{AB}$. Unfortunately, there is no simple way to evaluate V_{AB} without having recourse to long and costly computations, but since we are here interested only in looking for trends when the bridging ligand is changed, it seems safe to consider that $\lambda/4$ will be the leading term in the energy barrier, so that we can make our comparisons neglecting the effects of the nature of the ligands on V_{AB}.

It is now easy to relate the main parameters (mainly structural) of this simple model to the transport measurements. The diagram in Figure 9 is completely general and applicable to any electron transfer process. In an extended system, when the dimensions of the zone where the necessary atomic rearrangement controlling the electron transfer occurs are of the order of the coordination sphere of a single site as in the present case, one talks about a system with small polarons.[38] The polaron energy, W_P, is the energy gained when the system relaxes after addition of one electron. In this small-polaron scenario the conductivity is dominated by thermally activated electron hopping with the mobility given by the equation μ =

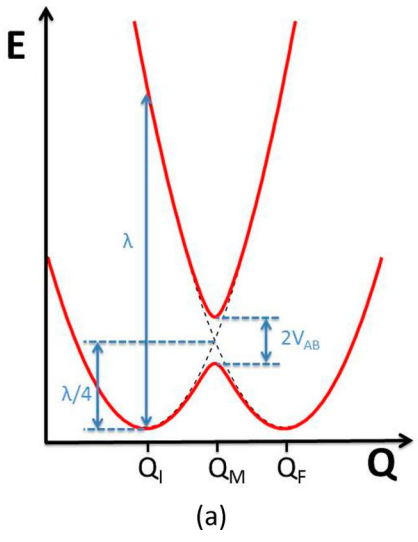

	Oxalate	Squarate	dhbq^{2-}	ClCNAn^{2-}
E_{III}	0	0	0	0
d_{III}	2.764	2.639	2.745	2.737
k_{III}	489	241	528	445
E_{II}	208	159	142	104
d_{II}	2.914	2.752	2.808	2.802
k_{II}	403	180	497	367
d_M	2.832	2.687	2.776	2.766
$(\Delta d)^2$	0.022	0.013	0.004	0.004
F	221	103	256	201
W_H	4.93	1.33	1.01	0.85

(b)

Figure 9. (a) Energy plot for a $Fe^{II}Fe^{III}$ to $Fe^{III}Fe^{II}$ electron transfer process. (b) Calculated parameters for the four studied bridging ligands. Distances are expressed in Angstroms, energies in kcal.mol^{-1}, and k and F in kcal.mol^{-1}·Å^{-2}.

DOI: 10.1021/jacs.8b08032
J. Am. Chem. Soc. 2018, 140, 12611−12621

$\mu_0 e^{-W_H/k}$, where W_H is the electron hopping barrier, i.e., the energy cost to reach the geometry under which the electron transfer is possible. As far as it is assumed that the variation of energy is a quadratic function of the structural parameters, the energy cost per site to reach the "equalization" geometry is 1/4 W_P, and taking into account that there are two sites involved in the transfer, it follows that $W_H = 1/2\ W_P$. Since according to the Franck−Condon principle the energy to optically excite one electron from one to the other site (i.e., λ in Figure 9) is twice the polaron energy it follows that $W_H = 1/2\ W_P = \lambda/4$. Therefore, $W_H = E_M = F(d_{II} - d_{III})^2$, with $F = k_{II}k_{III}/(k_{II} + k_{III})$ and $d_M = (k_{II}d_{II} + k_{III}d_{III})/(k_{II} + k_{III})$. In that way it is possible to correlate the transport (W_H) and structural (k_{II}, k_{III}, d_{II}, and d_{III}) features for a series of compounds.

How are these parameters tuned by the nature of the bridging ligand? The values of k_{II}, k_{III}, d_{II}, and d_{III} can be evaluated from density functional calculations (DFT). We carried out structural optimizations of $Fe^{II}L_3$ and $Fe^{III}L_3$ complexes with the four ligands oxalate, squarate, dhbq^{2-}, and ClCNAn^{2-} using the TPSSh functional, which is known to give good high-spin−low-spin relative energies for spin-crossover complexes involving iron.[21] The geometries were optimized forcing a D_3 symmetry and a high-spin configuration. In that way we obtained the d_{M-L} parameter which is the distance between the Fe atom and the midpoint to the closest C−C bonds (between the C atoms bonded to the coordinating O atoms) which corresponds to d_{II} or d_{III} of the above discussion. Once the optimal d_{M-L} parameter for each Fe^{II} and each Fe^{III} complex was found, the values of k_{II} or k_{III} were obtained by reoptimizing the structure for fixed $d_{M-L} \pm \delta$ values and fitting the energy to a second-order polynomial. The results for the four ligands are reported in Figure 9b.

According to the data in Figure 9b W_H = 0.214, 0.057, 0.044, and 0.037 eV for oxalate, squarate, dhbq^{2-}, and ClCNAn^{2-}, respectively. Despite the simplicity of the approach, these numbers are very reasonable when compared with W_H estimations based on experimental data for $Fe^{II}Fe^{III}$ solids like magnetite (∼0.15 eV)[38] and partially substituted ferrites (∼0.11 eV)[39] which are in between those calculated for oxalate and the other three ligands. Thus, we believe that the simple approach captures the essence of the electron transfer process, although the activation energies are smaller than the experimental ones. This is not unexpected since the Fe sites are immersed in a quite rigid 2D network, which must lead to a noticeable increase in the parameter λ and hence in the barrier estimated here by $\lambda/4$. According to the values in Figure 9b electrons should be much less mobile in oxalate networks than in anilate ones, which is in good agreement with experimental observations.[36,11f,14b] What is the reason for this finding? The F values for the oxalate ligands are in between those for both the dhbq^{2-} and the ClCNAn^{2-} ones, yet W_H is five times larger. It is clear that the factor determining the large difference is $(\Delta d)^2$, i.e., the square of the difference in the d values for Fe in the two oxidation states. Because of the quadratic dependence, this term has an overwhelming influence on the final value of W_H. Comparing the d_{II} and d_{III} distances for the oxalate, dhbq^{2-}, and ClCNAn^{2-} ligands in Figure 9b it is clear that whereas the d_{III} values are fairly similar, d_{II} for the oxalate ligand is markedly larger than those for the dhbq^{2-} and ClCNAn^{2-} ligands. Thus, the determining factor for the lower conductivity of the oxalate systems lies in the difficulty to cope with the extra electron of the high-spin Fe^{II} situation. The occurrence of extensive delocalization through the benzene ring of dhbq^{2-} and ClCNAn^{2-} acts as a buffer for the electronic rearrangement needed by the presence of the extra electron. Note that when the ligands are more similar, the F factor depending on the force constants may become the key factor. According to Figure 9b this is, for instance, the case when comparing the dhbq^{2-} and ClCNAn^{2-} ligands. The squarate ligand is also associated with a small W_H value, not much different from those of the dhbq^{2-} and ClCNAn^{2-} ligands. However, the $(\Delta d)^2$ term is intermediate between those of the oxalate and dhbq^{2-} and ClCNAn^{2-} pair of ligands. Clearly, in that case the F term plays an important role. Both the geometrical constraints imposed by the four-member ring as well as the delocalization in the central part of the ligand influence the electron transfer tendency.

We thus conclude that the present approach provides a simple, yet insightful, model to rationalize the transport results for these $Fe^{II}Fe^{III}$ mixed-valence coordination polymers and that the polymers based on the dhbq^{2-} and ClCNAn^{2-} ligands rank among the most effective ones in promoting the electron delocalization through a small-polaron hopping mechanism.

CONCLUSIONS

The mixed-valence $Fe^{II}Fe^{III}$ 2D coordination polymer [TAG]-[$Fe^{II}Fe^{III}$(ClCNAn)$_3$] based on the asymmetric chloro-cyanoanilate ligand and containing, for the first time in such 2D networks, the tris(amino)-guanidinium (TAG) cation has been synthesized and crystallized in the polar noncentrosymmetric space group $P3$ thanks to the C_3 symmetry of the cation and its ability to engage in intermolecular hydrogen bonding with the chlorine atoms of the ligand. Magnetic susceptibility measurements in combination with Mössbauer spectroscopy are indicative of a spin-glass behavior with magnetic ordering below 4 K and the presence of intermediate Fe(+2.5) oxidation state at RT and charge localization $Fe^{II}Fe^{III}$ at 10 K, with a statistic occupational crystallographic site according to the 10 K Mössbauer spectra, also confirmed by the X-ray structure at 10 K. Single-crystal electron transport measurements in the 2D plane and perpendicular on it show semiconducting behavior of the material with a rather high RT value of 2×10^{-3} S/cm for the in-plane conductivity, much higher than the one reported in the oxalate-based 2D $Fe^{II}Fe^{III}$ coordination polymers. In order to shed light on this difference and on the electron transport mechanism on these fast developing multifunctional families of 2D coordination polymers, the small-polaron hopping approach to the electron transfer process has been applied to a series of mixed-valence $Fe^{II}Fe^{III}$ oxalate-related coordination polymers containing as bridging ligands oxalate^{2-}, squarate^{2-}, dhbq^{2-}, and ClCNAn^{2-}. The results are clearly indicative of a much lower electron hopping barrier in the anilate complexes than in oxalates.

These results open the way toward the use of the TAG cation in such multifunctional binuclear/bimetallic transition metal or lanthanide coordination polymers, possibly endowed with multiferroic properties thanks to the crystallization in polar space groups. Moreover, the mechanism of electron transport in the mixed-valence $Fe^{II}Fe^{III}$ coordination polymers with bridging oxalate-type ligands has been disclosed, pointing out the higher "elasticity" of the anilate network compared to the oxalate one.

DOI: 10.1021/jacs.8b08032
J. Am. Chem. Soc. 2018, 140, 12611−12621

■ ASSOCIATED CONTENT

Supporting Information

The Supporting Information is available free of charge on the ACS Publications website at DOI: 10.1021/jacs.8b08032.

Full experimental section including description of the synthesis and characterization of all new materials and all of the techniques employed in the research reported here (PDF)
(CIF)
(CIF)

■ AUTHOR INFORMATION

Corresponding Authors

*p.alemany@ub.edu
*canadell@icmab.es
*mercuri@unica.it
*narcis.avarvari@univ-angers.fr

ORCID

José Ramón Galán-Mascarós: 0000-0001-7983-9762
Enric Canadell: 0000-0002-4663-5226
Maria Laura Mercuri: 0000-0002-4816-427X
Narcis Avarvari: 0000-0001-9970-4494

Author Contributions

§S.A.S. and A.A. contributed equally to this work.

Notes

The authors declare no competing financial interest.

■ ACKNOWLEDGMENTS

The work in France was supported by the CNRS, the University of Angers, the Erasmus program (mobility grant to N.M.), the RFI Regional project LUMOMAT (grant to A.A., project ASCO MMM), and the PIA project "Lorraine Université d'Excellence" (reference ANR-15-IDEX-04-LUE). This work was supported in Italy by the Fondazione di Sardegna-Convenzione triennale tra la Fondazione di Sardegna e gli Atenei Sardi, Regione Sardegna-L.R. 7/2007 annualità 2016-DGR 28/21 del 17.05.2015 "Innovative Molecular Functional Materials for Environmental and Biomedical Applications" and INSTM. Work in Spain was supported by the Spanish Ministerio de Economía y Competitividad (Grants FIS2012-37549-C05-05, FIS2015-64886-C5-4-P, CTQ2015-64579-C3-3-P, and CTQ2015-71287-R) and Generalitat de Catalunya (2014SGR301, 2017SGR797, and XRQTC and the CERCA program). E.C. acknowledges support of the Spanish MINECO through the Severo Ochoa Centers of Excellence Program under Grant SEV-2015-0496. J.C.W. and B.J.C.V. acknowledge Fundação para a Ciência e a Tecnologia (FCT, Portugal) through the project UID/Multi/04349/2013.

■ REFERENCES

(1) (a) Coronado, E.; Day, P. *Chem. Rev.* **2004**, *104*, 5419−5448. (b) Enoki, T.; Miyazaki, A. *Chem. Rev.* **2004**, *104*, 5449−5478. (c) Kobayashi, H.; Cui, H. B.; Kobayashi, A. *Chem. Rev.* **2004**, *104*, 5265−5288. (d) Kurmoo, M.; Graham, A. W.; Day, P.; Coles, S. J.; Hursthouse, M. B.; Caulfield, J. L.; Singleton, J.; Pratt, F. L.; Hayes, W.; Ducasse, L.; Guionneau, P. *J. Am. Chem. Soc.* **1995**, *117*, 12209−12217. (e) Martin, L.; Turner, S. S.; Day, P.; Mabbs, F. E.; McInnes, E. J. L. *Chem. Commun.* **1997**, *15*, 1367−1368. (f) Rashid, S.; Turner, S. S.; Day, P.; Howard, J. A. K.; Guionneau, P.; McInnes, E. J. L.; Mabbs, F. E.; Clark, R. J. H.; Firth, S.; Biggs, T. *J. Mater. Chem.* **2001**, *11*, 2095−2101. (g) Uji, S.; Shinagawa, H.; Terashima, T.; Yakabe, T.; Terai, Y.; Tokumoto, M.; Kobayashi, A.; Tanaka, H.; Kobayashi, H. *Nature* **2001**, *410*, 908−910. (h) Fujiwara, H.; Fujiwara, E.; Nakazawa, Y.; Narymbetov, B. Zh.; Kato, K.; Kobayashi, H.; Kobayashi, A.; Tokumoto, M.; Cassoux, P. *J. Am. Chem. Soc.* **2001**, *123*, 306−314. (i) Coronado, E.; Falvello, L. R.; Galán-Mascarós, J. R.; Giménez-Saiz, C.; Gómez-García, C. J.; Lauhkin, V. N.; Pérez-Benítez, A.; Rovira, C.; Veciana, J. *Adv. Mater.* **1997**, *9*, 984−987. (j) Madalan, A. M.; Canadell, E.; Auban-Senzier, P.; Brânzea, D.; Avarvari, N.; Andruh, M. *New J. Chem.* **2008**, *32*, 333−339. (k) Pop, F.; Allain, M.; Auban-Senzier, P.; Martínez-Lillo, J.; Lloret, F.; Julve, M.; Canadell, E.; Avarvari, N. *Eur. J. Inorg. Chem.* **2014**, *2014*, 3855−3862.

(2) Clemente-León, M.; Coronado, E.; Martí-Gastaldo, C.; Romero, F. M. *Chem. Soc. Rev.* **2011**, *40*, 473−497.

(3) (a) Clemente-León, M.; Coronado, E.; Galán-Mascarós, J. R.; Gómez-García, C. J. *Chem. Commun.* **1997**, 1727−1728. (b) Coronado, E.; Galán-Mascarós, J. R.; Gómez-García, C. J.; Martínez-Agudo, J. M. *Adv. Mater.* **1999**, *11*, 558−561. (c) Coronado, E.; Galán-Mascarós, J. R.; Gómez-García, C. J.; Ensling, J.; Gütlich, P. *Chem. - Eur. J.* **2000**, *6*, 552−563.

(4) (a) Bénard, S.; Yu, P.; Audière, J. P.; Rivière, E.; Clément, R.; Guilhem, J.; Tchertanov, L.; Nakatani, K. *J. Am. Chem. Soc.* **2000**, *122*, 9444−9454. (b) Aldoshin, S. M.; Sanina, N. A.; Minkin, V. I.; Voloshin, N. A.; Ikorskii, V. N.; Ovcharenko, V. I.; Smirnov, V. A.; Nagaeva, N. K. *J. Mol. Struct.* **2007**, *826*, 69−74.

(5) (a) Coronado, E.; Galán-Mascarós, J. R.; Gómez-García, C. J.; Laukhin, V. *Nature* **2000**, *408*, 447−449. (b) Alberola, A.; Coronado, E.; Galán-Mascarós, J. R.; Giménez-Saiz, C.; Gómez-García, C. J. *J. Am. Chem. Soc.* **2003**, *125*, 10774−10775. (c) Galán-Mascarós, J. R.; Coronado, E.; Goddard, P. A.; Singleton, J.; Coldea, A. I.; Wallis, J. D.; Coles, S. J.; Alberola, A. *J. Am. Chem. Soc.* **2010**, *132*, 9271−9273. (d) Coronado, E.; Galán-Mascarós, J. R.; Gómez-García, C. J.; Martínez-Ferrero, E.; Van Smaalen, S. *Inorg. Chem.* **2004**, *43*, 4808−4810. (e) Zhang, B.; Zhang, Y.; Zhu, D. *Chem. Commun.* **2012**, *48*, 197−199.

(6) (a) Okawa, H.; Shigematsu, A.; Sadakiyo, M.; Miyagawa, T.; Yoneda, K.; Ohba, M.; Kitagawa, H. *J. Am. Chem. Soc.* **2009**, *131*, 13516−13522. (b) Pardo, E.; Train, C.; Gontard, G.; Boubekeur, K.; Fabelo, O.; Liu, H.; Dkhil, B.; Lloret, F.; Nakagawa, K.; Tokoro, H.; Ohkoshi, S.-I.; Verdaguer, M. *J. Am. Chem. Soc.* **2011**, *133*, 15328−15331. (c) Sadakiyo, M.; Okawa, H.; Shigematsu, A.; Ohba, M.; Yamada, T.; Kitagawa, H. *J. Am. Chem. Soc.* **2012**, *134*, 5472−5475. (d) Okawa, H.; Sadakiyo, M.; Yamada, T.; Maesato, M.; Ohba, M.; Kitagawa, H. *J. Am. Chem. Soc.* **2013**, *135*, 2256−2262.

(7) (a) Endo, T.; Akutagawa, T.; Noro, S. I.; Nakamura, T. *Dalton Trans* **2011**, *40*, 1491−1496. (b) Pardo, E.; Train, C.; Liu, H.; Chamoreau, L.-M.; Dkhil, B.; Boubekeur, K.; Lloret, F.; Nakatani, K.; Tokoro, H.; Ohkoshi, S.-i.; Verdaguer, M. *Angew. Chem., Int. Ed.* **2012**, *51*, 8356−8360.

(8) (a) Andrés, R.; Gruselle, M.; Malézieux, B.; Verdaguer, M.; Vaissermann, J. *Inorg. Chem.* **1999**, *38*, 4637−4646. (b) Andrés, R.; Brissard, M.; Gruselle, M.; Train, C.; Vaissermann, J.; Malézieux, B.; Jamet, J. P.; Verdaguer, M. *Inorg. Chem.* **2001**, *40*, 4633−4640. (c) Clemente-León, M.; Coronado, E.; Dias, J. C.; Soriano-Portillo, A.; Willett, R. D. *Inorg. Chem.* **2008**, *47*, 6458−6463. (d) Train, C.; Gheorghe, R.; Krstic, V.; Chamoreau, L. M.; Ovanesyan, N. S.; Rikken, G. L. J. A.; Gruselle, M.; Verdaguer, M. *Nat. Mater.* **2008**, *7*, 729−734. (e) Train, C.; Nuida, T.; Gheorghe, R.; Gruselle, M.; Ohkoshi, S. *J. Am. Chem. Soc.* **2009**, *131*, 16838−16843. (f) Gruselle, M.; Li, Y.; Ovanesyan, N.; Makhaev, V.; Shilov, G.; Mushenok, F.; Train, C.; Aldoshin, S. *Chirality* **2013**, *25*, 444−448.

(9) Clemente-León, M.; Coronado, E.; Gómez-García, C. J.; López-Jordá, M.; Camón, A.; Repollés, A.; Luis, F. *Chem. - Eur. J.* **2014**, *20*, 1669−1676.

(10) (a) Kitagawa, S.; Kawata, S. *Coord. Chem. Rev.* **2002**, *224*, 11−34. (b) Mercuri, M. L.; Congiu, F.; Concas, G.; Sahadevan, S. A. *Magnetochemistry* **2017**, *3*, 17.

(11) (a) Atzori, M.; Benmansour, S.; Minguez Espallargas, G.; Clemente-León, M.; Abhervé, A.; Gómez-Claramunt, P.; Coronado, E.; Artizzu, F.; Sessini, E.; Deplano, P.; Serpe, A.; Mercuri, M. L.;

DOI: 10.1021/jacs.8b08032
J. Am. Chem. Soc. 2018, 140, 12611−12621

Gómez García, C. J. *Inorg. Chem.* **2013**, *52*, 10031−10040. (b) Atzori, M.; Pop, F.; Auban-Senzier, P.; Gómez García, C. J.; Canadell, E.; Artizzu, F.; Serpe, A.; Deplano, P.; Avarvari, N.; Mercuri, M. L. *Inorg. Chem.* **2014**, *53*, 7028−7039. (c) Abhervé, A.; Clemente-León, M.; Coronado, E.; Gómez-García, C. J.; Verneret, M. *Inorg. Chem.* **2014**, *53*, 12014−12026. (d) Abhervé, A.; Mañas-Valero, S.; Clemente-León, M.; Coronado, E. *Chem. Sci.* **2015**, *6*, 4665−4673. (e) Atzori, M.; Pop, F.; Auban-Senzier, P.; Clérac, R.; Canadell, E.; Mercuri, M. L.; Avarvari, N. *Inorg. Chem.* **2015**, *54*, 3643−3653. (f) Benmansour, S.; Gómez García, C. J. *Polymers* **2016**, *8*, 89. (g) Benmansour, S.; Abhervé, A.; Gómez-Claramunt, P.; Vallés-García, C.; Gómez-García, C. J. *ACS Appl. Mater. Interfaces* **2017**, *9*, 26210−26218. (h) Palacios-Corella, M.; Fernández-Espejo, A.; Bazaga-García, M.; Losilla, E. R.; Cabeza, A.; Clemente-León, M.; Coronado, E. *Inorg. Chem.* **2017**, *56*, 13865−13877. (i) Kingsbury, C. J.; Abrahams, B. F.; D'Alessandro, D. M.; Hudson, T. A.; Murase, R.; Robson, R.; White, K. F. *Cryst. Growth Des.* **2017**, *17*, 1465−1470. (j) DeGayner, J. A.; Jeon, I.-R.; Sun, L.; Dinca, M.; Harris, T. D. *J. Am. Chem. Soc.* **2017**, *139*, 4175−4184. (k) Benmansour, S.; Pérez-Herráez, I.; López-Martínez, G.; Gómez García, C. J. *Polyhedron* **2017**, *135*, 17−25. (l) Benmansour, S.; Hernández-Paredes, A.; Gómez-García, C. J. *J. Coord. Chem.* **2018**, *71*, 845.

(12) (a) Imaz, I.; Mouchaham, G.; Roques, N.; Brandès, S.; Sutter, J.-P. *Inorg. Chem.* **2013**, *52*, 11237−11243. (b) Benmansour, S.; Vallés-García, C.; Gómez-Claramunt, P.; Minguez Espallargas, G.; Gómez García, C. J. *Inorg. Chem.* **2015**, *54*, 5410−5418. (c) Sumida, K.; Hu, M.; Furukawa, S.; Kitagawa, S. *Inorg. Chem.* **2016**, *55*, 3700−3705. (d) Murase, R.; Abrahams, B. F.; D'Alessandro, D. M.; Davies, C. G.; Hudson, T. A.; Jameson, G. N. L.; Moubaraki, B.; Murray, K. S.; Robson, R.; Sutton, A. L. *Inorg. Chem.* **2017**, *56*, 9025−9035.

(13) Taniguchi, K.; Chen, J.; Sekine, Y.; Miyasaka, H. *Chem. Mater.* **2017**, *29*, 10053−10059.

(14) (a) Jeon, I.-R.; Negru, B.; Van Duyne, R. P.; Harris, T. D. *J. Am. Chem. Soc.* **2015**, *137*, 15699−15702. (b) Darago, L. E.; Aubrey, M. L.; Yu, C. J.; Gonzalez, M. I.; Long, J. R. *J. Am. Chem. Soc.* **2015**, *137*, 15703−15711. (c) DeGayner, J. A.; Jeon, I.-R.; Sun, L.; Dincă, M.; Harris, T. D. *J. Am. Chem. Soc.* **2017**, *139*, 4175−4184.

(15) (a) Rehwoldt, R. E.; Chasen, B. L.; Li, J. B. *Anal. Chem.* **1966**, *38*, 1018−1019. (b) Atzori, M.; Pop, F.; Cauchy, T.; Mercuri, M. L.; Avarvari, N. *Org. Biomol. Chem.* **2014**, *12*, 8752−8763.

(16) Atzori, M.; Artizzu, F.; Marchiò, L.; Loche, D.; Caneschi, A.; Serpe, A.; Deplano, P.; Avarvari, N.; Mercuri, M. L. *Dalton Trans* **2015**, *44*, 15786−15802.

(17) Ashoka Sahadevan, S.; Monni, N.; Abhervé, A.; Auban-Senzier, P.; Canadell, E.; Mercuri, M. L.; Avarvari, N. *Inorg. Chem.* **2017**, *56*, 12564−12571.

(18) Ashoka Sahadevan, S.; Monni, N.; Abhervé, A.; Marongiu, D.; Sarritzu, V.; Sestu, N.; Saba, M.; Mura, A.; Bongiovanni, G.; Cannas, C.; Quochi, F.; Avarvari, N.; Mercuri, M. L. *Chem. Mater.* **2018**, DOI: 10.1021/acs.chemmater.8b03399.

(19) Weiss, S.; Krommer, H. *Chem. Abstr.* **1986**, *104*, 206730.

(20) Tao, J. M.; Perdew, J. P.; Staroverov, V. N.; Scuseria, G. E. *Phys. Rev. Lett.* **2003**, *91*, 146401.

(21) Jensen, K. P. *Inorg. Chem.* **2008**, *47*, 10357−10365.

(22) Hariharan, P. C.; Pople, J. A. *Theor. Chim. Acta* **1973**, *28*, 213−222.

(23) Frisch, M. J.; Trucks, G. W.; Schlegel, H. B.; Scuseria, G. E.; Robb, M. A.; Cheeseman, J. R.; Scalmani, G.; Barone, V.; Mennucci, B.; Petersson, G. A.; Nakatsuji, H.; Caricato, M.; Li, X.; Hratchian, H. P.; Izmaylov, A. F.; Bloino, J.; Zheng, G.; Sonnenberg, J. L.; Hada, M.; Ehara, M.; Toyota, K.; Fukuda, R.; Hasegawa, J.; Ishida, M.; Nakajima, T.; Honda, Y.; Kitao, O.; Nakai, H.; Vreven, T.; Montgomery, J. A., Jr., Peralta, J. E.; Ogliaro, F.; Bearpark, M.; Heyd, J. J.; Brothers, E.; Kudin, K. N.; Staroverov, V. N.; Kobayashi, R.; Normand, J.; Raghavachari, K.; Rendell, A.; Burant, J. C.; Iyengar, S. S.; Tomasi, J.; Cossi, M.; Rega, N.; Millam, J. M.; Klene, M.; Knox, J. E.; Cross, J. B.; Bakken, V.; Adamo, C.; Jaramillo, J.; Gomperts, R.; Stratmann, R. E.; Yazyev, O.; Austin, A. J.; Cammi, R.; Pomelli, C.; Ochterski, J. W.; Martin, R. L.; Morokuma, K.; Zakrzewski, V. G.; Voth, G. A.; Salvador, P.; Dannenberg, J. J.; Dapprich, S.; Daniels, A. D.; Farkas, Ö.; Foresman, J. B.; Ortiz, J. V.; Cioslowski, J.; Fox, D. J. *Gaussian 09*, Revision B1; Gaussian, Inc.: Wallingford CT, 2009.

(24) (a) Tamaki, H.; Zhong, Z. J.; Matsumoto, N.; Kida, S.; Koikawa, M.; Achiwa, N.; Hashimoto, Y.; Okawa, H. *J. Am. Chem. Soc.* **1992**, *114*, 6974−6979. (b) Clemente-León, M.; Coronado, E.; López-Jordà, M.; Mínguez Espallargas, G.; Soriano-Portillo, A.; Waerenborgh, J. C. *Chem. - Eur. J.* **2010**, *16*, 2207−2219.

(25) Okaya, Y.; Pepinsky, R. *Acta Crystallogr.* **1957**, *10*, 681−684.

(26) Hartl, F.; Stufkens, D. J.; Vlček, A. *Inorg. Chem.* **1992**, *31*, 1687−1695.

(27) Tholence, J. L. *Solid State Commun.* **1980**, *35*, 113−117.

(28) (a) Novak, M. A. *J. Magn. Magn. Mater.* **2004**, *272*−*276*, e707−e713. (b) Novak, M. A.; Folly, W. S. D.; Sinnecker, J. P.; Soriano, S. *J. Magn. Magn. Mater.* **2005**, *294*, 133−140.

(29) (a) Gunnarsson, K.; Svedlindh, P.; Nordblad, P.; Lundgren, L.; Aruga, H.; Ito, A. *Phys. Rev. Lett.* **1988**, *61*, 754. (b) Laiho, R.; Lähderanta, E.; Salminen, J.; Lisunov, K. G.; Zakhvalinskii, V. S. *Phys. Rev. B: Condens. Matter Mater. Phys.* **2001**, *63*, 094405. (c) Mattsson, J.; Jonsson, T.; Nordblad, P.; Aruga Katori, H.; Ito, A. *Phys. Rev. Lett.* **1995**, *74*, 4305.

(30) (a) Sellers, S. P.; Korte, B. J.; Fitzgerald, J. P.; Reiff, W. M.; Yee, G. T. *J. Am. Chem. Soc.* **1998**, *120*, 4662−4670. (b) Kaul, B. B.; Durfee, W. S.; Yee, G. T. *J. Am. Chem. Soc.* **1999**, *121*, 6862−6866. (c) Buschmann, W. E.; Ensling, J.; Gütlich, P.; Miller, J. S. *Chem. - Eur. J.* **1999**, *5* (10), 3019−3028. (d) Clérac, R.; O'Kane, S.; Cowen, J.; Ouyang, X.; Heintz, R.; Zhao, H.; Bazile, M. J.; Dunbar, K. R. *Chem. Mater.* **2003**, *15*, 1840−1850. (e) Krishnamohan Sharma, C. V.; Chusuei, C. C.; Clérac, R.; Möller, T.; Dunbar, K. R.; Clearfield, A. *Inorg. Chem.* **2003**, *42*, 8300−8308. (f) Zhang, X.-M.; Li, P.; Gao, W.; Liu, J.-P.; Gao, E.-Q. *Dalton Trans* **2015**, *44*, 511−514. (g) Ghosh, S.; Roy, S.; Liu, C.-M.; Mohanta, S. *Dalton Trans* **2018**, *47*, 836−844.

(31) Mydosh, J. A. *Spin Glasses: an Experimental Introduction*; Taylor and Francis: London, 1993.

(32) Choi, K. Y.; Wang, Z.; Ozarowski, A.; van Tol, J.; Zhou, H. D.; Wiebe, C. R.; Skourski, Y.; Dalal, N. S. *J. Phys.: Condens. Matter* **2012**, *24*, 246001−6.

(33) Greenwood, N. N.; Gibb, T. C. *Mössbauer Spectroscopy*; Chapman and Hall, Ltd. Publishers: London, 1971.

(34) Shilov, G. V.; Nikitina, Z. K.; Ovanesyan, N. S.; Aldoshin, S. M.; Makhaev, V. D. *Russ. Chem. Bull.* **2011**, *60*, 1209−1219.

(35) For example: (a) Lupu, D.; Barb, D.; Filoti, G.; Morariu, M.; Tarina, D. *J. Inorg. Nucl. Chem.* **1972**, *34*, 2803−2810. (b) Maeda, Y. *J. Nucl. Radiochem. Sci.* **2006**, *7*, R13−R18.

(36) Bhattacharjee, A.; Bhakat, D.; Roy, M.; Kusz, J. *Phys. B* **2010**, *405*, 1546−1550.

(37) For a very pedagogic presentation of the basic methodology, see: Launay, J.-P.; Verdaguer, M. *Electrons in Molecules: From Basic Principles to Molecular Electronics*; Oxford University Press: Oxford, 2014; Chapter 3.

(38) Austin, I. G.; Mott, N. F. *Adv. Phys.* **1969**, *18*, 41−102.

(39) Tsuda, N.; Nasu, K.; Yanase, A.; Siratori, K. *Electronic conduction in Oxides*; Springer Series in Solid-State Sciences; Springer Verlag: Berlin Heidelberg, 1991; pp 163−168.

DOI: 10.1021/jacs.8b08032
J. Am. Chem. Soc. 2018, 140, 12611−12621

CHEMISTRY OF MATERIALS
Cite This: Chem. Mater. 2018, 30, 6575−6586
Article
pubs.acs.org/cm

Nanosheets of Two-Dimensional Neutral Coordination Polymers Based on Near-Infrared-Emitting Lanthanides and a Chlorocyananilate Ligand

Suchithra Ashoka Sahadevan,[†,§] Noemi Monni,[†] Alexandre Abhervé,[§] Daniela Marongiu,[∥] Valerio Sarritzu,[∥] Nicola Sestu,[∥] Michele Saba,[∥] Andrea Mura,[∥,‡] Giovanni Bongiovanni,[∥] Carla Cannas,[†,‡] Francesco Quochi,*[,∥,‡] Narcis Avarvari,*[,§] and Maria Laura Mercuri*[,†,‡]

[†]Dipartimento di Scienze Chimiche e Geologiche, Università degli Studi di Cagliari, I-09042 Monserrato, Cagliari, Italy
[‡]INSTM, Cagliari Unit, Via Giuseppe Giusti, 9, 50121 Firenze, Italy
[§]Laboratoire MOLTECH-Anjou UMR 6200, UFR Sciences, CNRS, Université d'Angers, Bât. K, 2 Bd. Lavoisier, 49045 Angers, France
[∥]Dipartimento di Fisica, Università degli Studi di Cagliari, I-09042 Monserrato, Cagliari, Italy

Supporting Information

ABSTRACT: The synthesis, structural characterization, photophysical studies, and exfoliation of two-dimensional (2D) layered coordination polymers, formulated as $\{[Ln_2(ClCNAn)_3(DMF)_6]\cdot(DCM)_x\}_n$ (Ln(III) = Yb(x = 0), Nd, and Er (x = 2)) based on the heterosubstituted chlorocyananilate ligand, are reported. These compounds consist of neutral polymeric 2D networks of the chlorocyananilate ligand alternating with Ln(III) ions. They form six-membered rings with rectangular cavities, where neighbor layers are eclipsed along the *a* axis (Yb), and a regular honeycomb-like structure, with hexagonal cavities filled by dichloromethane solvent molecules (Nd and Er), where neighbor layers alternate along the *c* axis. Several interlayer interactions between lanthanide centers and dimethylformamide molecules, facing the cavities, are present in all compounds. Free-standing nanosheets, obtained by a top-down strategy involving sonication-assisted solution synthesis and characterized by atomic force microscopy and high-resolution transmission electron microscopy, show lateral dimensions on the micrometer scale, thicknesses down to the monolayer, and the presence of lattice fringes. Time-resolved photoluminescence studies performed on both the bulk and nanosheets clearly demonstrate that the chlorocyananilate ligand acts as an efficient antenna toward Ln(III) ions and that emission sensitization occurs as a multistep relaxation process involving, in sequence, intersystem crossing and energy transfer from ligand triplet states to the Ln(III) ions. Effects induced by the exfoliation process on the photophysical properties of the nanosheets are also discussed.

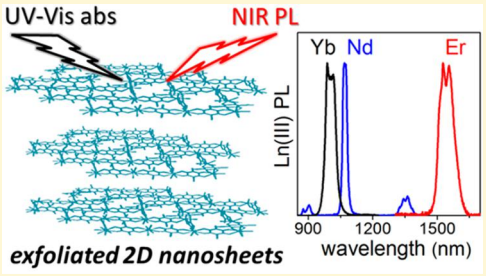

INTRODUCTION

Interest in anilate derivatives, namely 3,6-disubstituted 2,5-dihydroxybenzoquinones, has recently been revived because of their ability to construct two-dimensional (2D) layered architectures with peculiar physical properties, from organic ferroelectrics,[1−3] purely organic molecular conductors,[4−7] and layered magnets[8−12] (including spin-crossover systems) to magnetic conductors.[13−15] Conducting/magnetic Fe(II)/Fe(III) mixed-valence metal−organic frameworks (MOFs)[10,16] and rare examples of conducting 2D iron-quinoid MOFs,[17,18] magnetically ordered up to T_c = 105 K,[19] have recently been obtained by Harris et al. Furthermore, these magnetic hybrid coordination polymers (CPs), being formed by a 2D anionic network and cations inserted within or between the layers, with interlayer weak van der Waals interactions, can behave as graphene-related magnetic materials, and the first attempts to successfully exfoliate spin-crossover systems[11,12] and MOFs into individual nanosheets have been reported very recently by Coronado et al.[11] and Gomez et al.,[10] respectively. It should be emphasized that 2D nanomaterials showing sheetlike structures make up an emerging class of materials that exhibit unprecedented physical, chemical, and optical properties because of their unique 2D structural features and promising applications,[20] and the search for materials that can be exfoliated to the monolayer scale represents a hot topic in materials chemistry.

Anilates are scarcely investigated for the construction of lanthanide-based materials with respect to the plethora of ligands used in classical lanthanide coordination[21] and supramolecular chemistry,[22] in coordination polymers (CPs) and hybrid materials[23] with strategic applications as OLEDs,[24] biomedical analysis, medical diagnosis, and cell imaging.[25]

Received: August 9, 2018
Revised: August 21, 2018
Published: August 22, 2018

DOI: 10.1021/acs.chemmater.8b03399
Chem. Mater. 2018, 30, 6575−6586

Ligands, in fact, play a crucial role in determining the physical properties of lanthanide complexes because they can work as antennas for efficient sensitization of the lanthanide-ion luminescence or their electronic properties can influence the magnetic properties of the related highly anisotropic lanthanide-based materials.[26] Since the report of Abrahams et al.[27,28] on a series of $Ln_2(H_2An)_3{\cdot}24H_2O$ (Ln = Ce, La, Yb, or Y), a three-dimensional monometallic lanthanoid assembly, $Na_5[Ho(THB)_2]_3{\cdot}7H_2O$ (THB = tetrahydroxybenzene),[29] showing peculiar magnetic properties (ferromagnetism with a Curie temperature of 11 K), a $[\{Ho_2(H_2An)_3(H_2O)_6\}{\cdot}18H_2O]_n$[30] 2D honeycomb network, and a series of (i) bimetallic CPs with the formula $\{[Nd_2Ln_2(1-x)(H_2An)_3]{\cdot}24H_2O\}_n$ (Ln_2 = Gd or Ce)[31] and (ii) 2D monometallic CPs, based on the hydranilate and chloranilate ligands, have been reported.[32] Recently, some of us synthesized and fully characterized a new heterosubstituted anilate ligand, the chlorocyananilate ($ClCNAn^{2-}$), where a simple change of one chloro substituent on the chloranilate with a cyano group affects the electronic properties of the anilate moiety, inducing interesting luminescence properties in the class of anilate-based ligands and their p and d transition metal complexes.[8,33−35] Very recently, new Ln(III)-containing layered compounds, with the general formula $[Ln_2(ClCNAn)_3(Solv.)_6]{\cdot}nH_2O$ (n = 0−2), have been reported by Gomez et al.[36] by combining the chlorocyananilate ligand with Ln = Ce(III), Pr(III), Yb(III), and Dy(III) lanthanide ions and three different solvents such as H_2O, dimethyl sulfoxide (DMSO = Solv.), and dimethylformamide (DMF = Solv.). The role of the Ln(III) size and the size and shape of the solvent in the crystal structure of the obtained compounds has been discussed in detail. The light-harvesting ability of the chlorocyananilate ligand toward the different lanthanides, especially the near-infrared (NIR)-emissive Yb(III) ion, has not been studied, even though this ligand is an interesting candidate for sensitizing efficiently the lanthanide emission because does not contain CH or OH groups, the most important IR quenchers. No fundamental studies of 2D layered materials containing the chlorocyananilate ligand and NIR-emissive lanthanides have been reported so far, although Er(III), Yb(III), and Nd(III) complexes are attracting ever-growing interest because of their technological applications mainly in telecommunications[37] and biological imaging.[25,38] In this work, we report a fundamental study of the synthesis, structural characterization, and photophysical characteristics of 2D layered CPs, formulated as $[Ln_2(ClCNAn)_3(DMF)_6]_n{\cdot}(DCM)_x$ [Ln = Yb (x = 0) and Nd and Er (x = 2)], obtained by reacting Ln(III) salts with the monoprotonated chlorocyananilic acid (3-chloro-6-cyano-2,5-dihydroxybenzoquinone) (Chart 1). The ability of the chlorocyananilate ligand to work as a valuable antenna in sensitizing the NIR-emitting Er(III), Yb(III), and Nd(III) lanthanides is investigated. The aim is to produce stable nanosized sheets by using the well-known top-down strategy involving the traditional sonication-assisted solution exfoliation, starting from fully characterized bulk 2D neutral NIR-emissive CPs. The obtained 2D nanosheets are characterized by atomic force microscopy (AFM),[39,40] high-resolution transmission electron microscopy (HR-TEM), and continuous-wave transient optical spectroscopy. A comparison between the photophysical properties of the CPs as bulk and nanosheets, performed in an EtOH suspension and drop-cast on a glass substrate, is also reported.

Chart 1. Potassium Chlorocyananilate (left) and Coordination Mode of the Ligand in Compounds 1−3 (right)

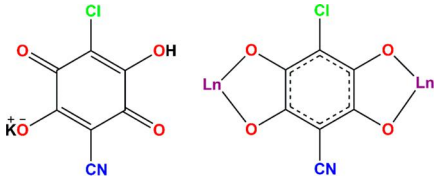

EXPERIMENTAL SECTION

Materials and Methods. Reagents of analytical grade were purchased from Sigma-Aldrich and used without further purification. The solvents were of high-performance liquid chromatography grade. Potassium chlorocyananilate (KHClCNAn) was synthesized as reported in the literature,[35] while $Er(NO_3)_3{\cdot}5H_2O$, $Yb(NO_3)_3{\cdot}5H_2O$, and $Nd(NO_3)_3{\cdot}6H_2O$ were purchased from Sigma-Aldrich and used without further purification.

Syntheses. *$[Yb_2(ClCNAn)_3(DMF)_6]_n$ (1).* $Yb(NO_3)_3{\cdot}5H_2O$ (0.06 mmol, 26.94 mg) dissolved in 5 mL of dichloromethane (DCM) and 2 mL of DMF was placed in the bottom of the test tube. KHClCNAn (0.03 mmol, 7.2 mg) in 5 mL of DMF was carefully layered on the top with a blank solution of DMF (1 mL) between the layers. After 3 weeks, red hexagonal crystals were formed. Crystals were suitable for X-ray diffraction (XRD) measurements.

$\{[Ln_2(ClCNAn)_3(DMF)_6]{\cdot}(DCM)_2\}_n$ [Ln = Nd (2) or Er (3)]. This compound was synthesized in a similar manner at an identical scale as mentioned for **1**, except using $Nd(NO_3)_3{\cdot}5H_2O$ (0.06 mmol, 26.3 mg) for **2** and $Er(NO_3)_3{\cdot}5H_2O$ (0.06 mmol, 26.6 mg) for **3** instead of $Yb(NO_3)_3{\cdot}5H_2O$.

Nanosheets of compounds **1**−**3** (hereafter **1-NS**−**3-NS**, respectively) were fabricated by a top-down sonication-assisted liquid exfoliation method. Delamination was achieved by sonicating the dried powder of samples of **1**−**3** (1 mg) in absolute anhydrous ethanol (EtOH, 2 mL) for 20 min at room temperature, according to the literature.[41] After centrifugation, the suspensions were further diluted 10 times (100 μL of suspension and 900 μL of EtOH) to allow dynamic light scattering (DLS) (Malvern ZETASIZER NANO instrument) to fulfill all measurement requirements, even though DLS measurements on the pristine suspensions (1 mg/2 mL) yielded the same results. Undiluted suspensions of **1-NS**−**3-NS** in EtOH were deposited by being drop-cast onto SiO_2/Si substrates (20 μL), glass substrates (200 μL), and carbon-coated copper grids (5 μL) for AFM, photophysical, and TEM measurements, respectively.

X-ray Crystallography. Single crystals of the compounds were mounted on glass fiber loops using a viscous hydrocarbon oil to coat the crystal and then transferred directly to the cold nitrogen stream for data collection. Data were collected at 150 K on an Agilent Supernova instrument with Cu Kα radiation (λ = 1.54184 Å). The structures were determined by direct methods with the SIR97 program and refined against all F^2 values with the SHELXL-97 program using the WinGX graphical user interface. All non-hydrogen atoms were refined anisotropically except as noted, and hydrogen atoms were placed in calculated positions and refined isotropically with a riding model.

Morphological Characterization. Nanosheet morphology was investigated by AFM (NT-MDT Smena instrument) performed in noncontact mode using sharp Si tips (NT-MDT ETALON HA_NC). Topography (height) images were analyzed using free software (WSxM version 5.0).[42] TEM and HR-TEM images were obtained with a JEM 2010 UHR instrument equipped with a Gatan Imaging Filter (GIF) with a 15 eV window and a 794 slow scan CCD camera.

Photophysical Characterization. Continuous-wave (Cw) diffuse reflectance (R_d) of ground crystals, regular transmittance (T_r) of nanosheet suspensions in EtOH, and total (specular/regular + diffuse) reflectance (R)/transmittance (T) of dropcast nanosheets

DOI: 10.1021/acs.chemmater.8b03399
Chem. Mater. 2018, 30, 6575−6586

Scheme 1

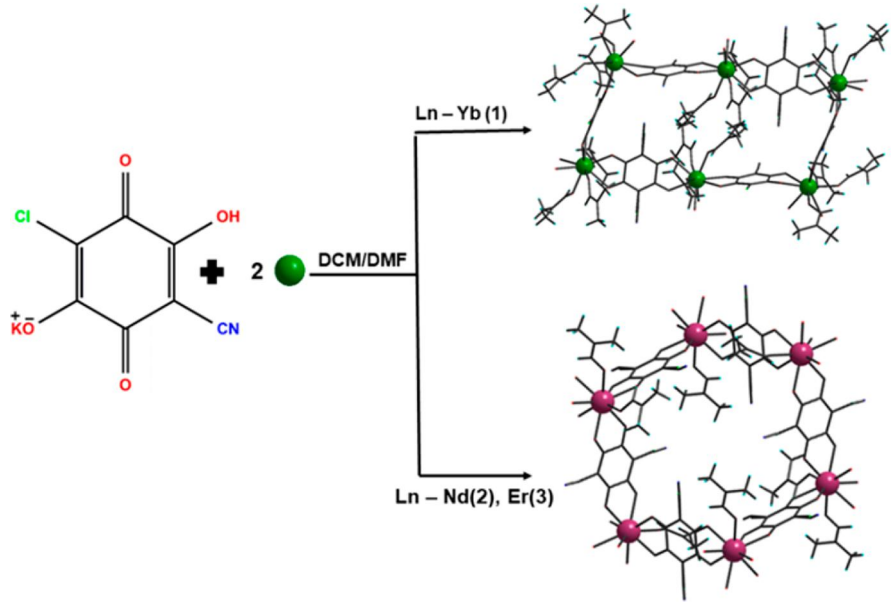

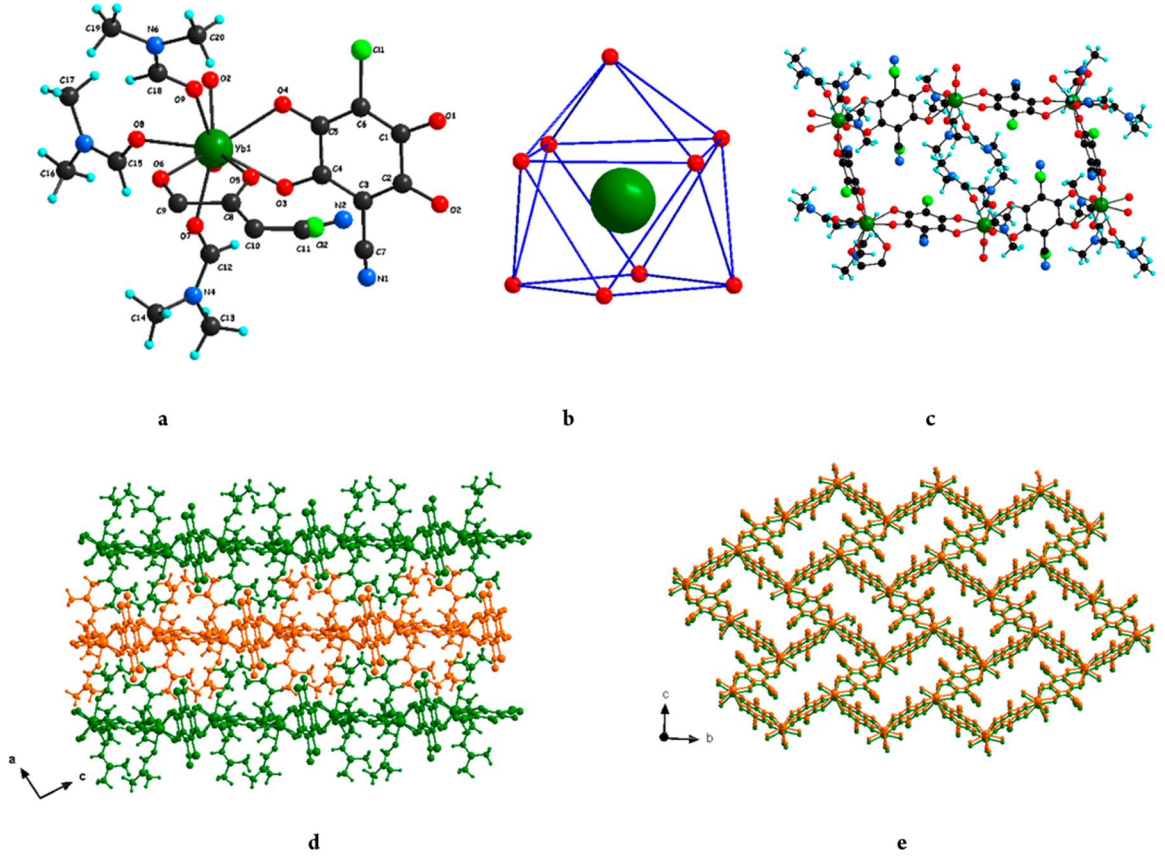

Figure 1. Structure of compound **1**. (a) Asymmetric unit with its atom labeling scheme. (b) Distorted monocapped square antiprismatic coordination geometry of the Yb center. (c) View of one rectangular cavity. (d) View of three consecutive layers in the *a*−*c* plane. (e) View of the eclipsed layers in the *b*−*c* plane. DMF molecules have been omitted for the sake of clarity. Color code: Yb, green; O, red; Cl, light green; C, black; N, blue; H, cyan. In panels d and e, different colors are used to represent different layers.

were measured using a dual-beam spectrophotometer equipped with an integrating sphere accessory (Agilent Cary 5000 UV−vis−NIR). The optical absorptance (fraction of absorbed irradiance, A) was estimated as $1 - R_d$ for crystals, $1 - T_r$ for nanosheet suspensions, and $1 - R - T$ for drop-cast nanosheets. Ligand-centered photoluminescence was excited at 370 nm by 200 fs long pulses delivered by an optical parametric amplifier (Light Conversion TOPAS-C) pumped by a regenerative Ti:sapphire amplifier (Coherent Libra-HE) running at a repetition frequency of 1 kHz and measured by a streak camera (Hamamatsu C10910) equipped with a grating spectrometer (Princeton Instruments Acton SpectraPro SP-2300). Lanthanide-centered photoluminescence was excited by a passively Q-switched

DOI: 10.1021/acs.chemmater.8b03399
Chem. Mater. 2018, 30, 6575−6586

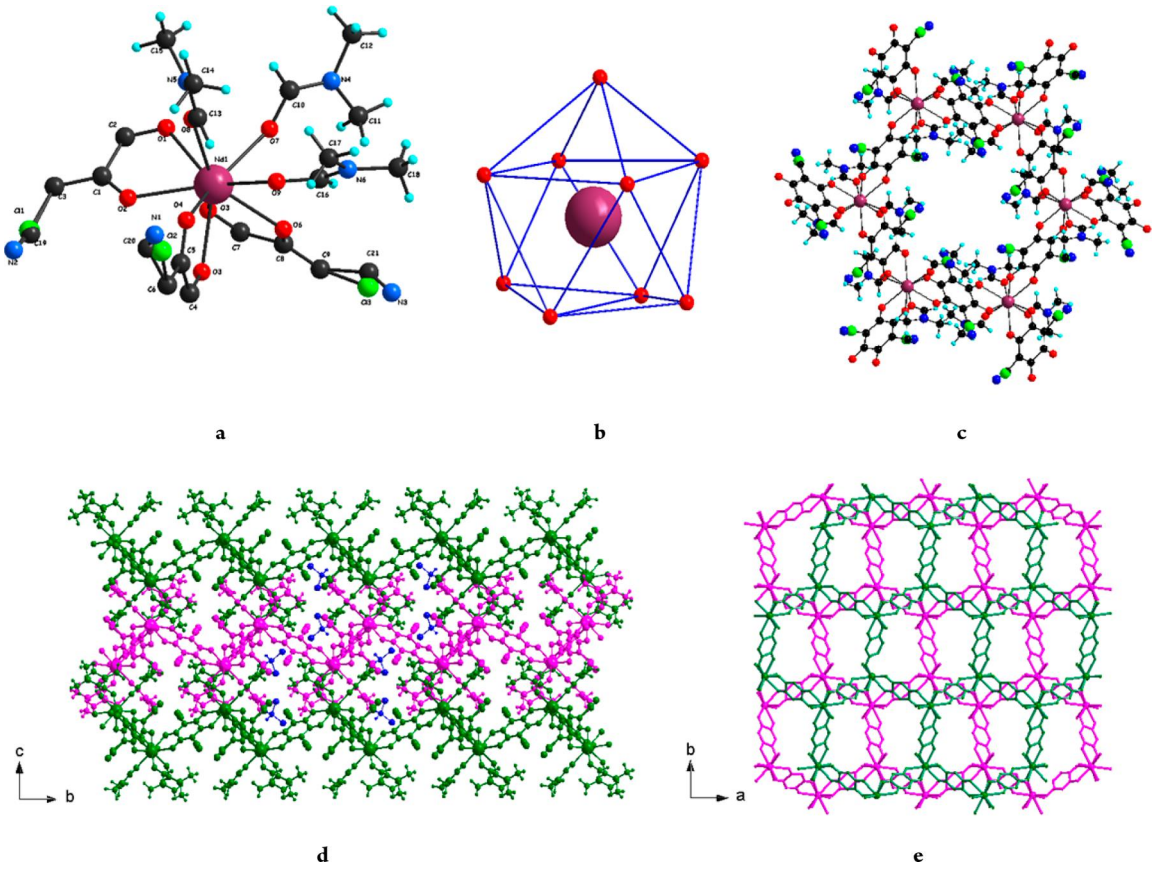

Figure 2. Structure of compound **2**. (a) Asymmetric unit with its atom labeling scheme. (b) Distorted tricapped trigonal prismatic coordination geometry of the Nd center. (c) View of one hexagonal cavity. (d) View of three consecutive layers in the $a-c$ plane. Solvent molecules have been omitted for the sake of clarity. (e) View of the alternate hexagonal layers in the $a-b$ plane. DMF and solvent molecules have been omitted for the sake of clarity. Color code: Nd, purple; O, red; Cl, light green; C, black; N, blue; H, cyan. In panels d and e, different colors are used to represent different layers.

powerchip laser (Teem Photonics PNV-M02510) delivering 310 ps long pulses at a 355 nm wavelength and a 1 kHz repetition rate, wavelength dispersed by a grating spectrometer (Princeton Instruments Acton SpectraPro 2300i), and detected by a NIR array detector (Andor iDus InGaAs 1.7 μm) for spectral measurements and a photomultiplier (Hamamatsu H10330A-75) connected to a 1 GHz digital oscilloscope (Tektronik TDS 5104) for time-resolved measurements; 10 mm (1 mm) quartz cuvettes were used for T_r (PL) measurements on nanosheet suspensions.

RESULTS AND DISCUSSION

Syntheses. Chlorocyananilate-based Ln(III) compounds $\{[Ln_2(ClCNAn)_3(DMF)_6](CH_2Cl_2)_x\}_n$ [Ln = Yb (**1**), Nd (**2**), or Er (**3**)] have been synthesized by self-assembling the chlorocyananilate ligand and the Ln(III) ion as reported in Scheme 1. Crystals suitable for XRD were obtained by carefully layering a solution of the potassium salt of the monoprotonated chlorocyananilate, KHClCNAn, in DMF onto the top of a solution of the Ln(III) salts in a DCM/DMF mixture.

Crystal Structures. Compounds **1**−**3** are neutral polymeric 2D networks of the chlorocyananilate ligand alternating with Ln(III) ions. Two types of networks can be observed depending on the Ln(III) ion as shown in Scheme 1. The use of Yb(III) has resulted in a solvent-free 2D network that crystallizes in monoclinic space group $P2_1/n$, while the Nd(III) and Er(III) networks crystallize in monoclinic space group $C2/c$ and contain one dichloromethane solvent molecule in the cavities of the layers. It is not uncommon in the lanthanides series to obtain different crystalline structures in spite of the similar experimental conditions used, a feature that is generally due to the slight differences between the ionic radii of the lanthanide. The asymmetric unit of **1** consists of one Yb^{3+} ion, one and one-half molecules of the $ClCNAn^{2-}$ ligand, and three DMF molecules giving rise to the formula $[Yb_2(ClCNAn)_3(DMF)_6]_n$ (Figure 1a). In the anilate ligand, because of the inversion center, for the half-molecule of asymmetric chlorocyananilate, the chloro and cyano substituents are equally distributed over the same position.

The Yb(III) ion is nine-coordinated in a slightly distorted monocapped square antiprismatic geometry, completed by six oxygen atoms from three $ClCNAn^{2-}$ ligands and three oxygen atoms from three DMF molecules (Figure 1b). Yb−O bond lengths and O−Yb−O angles fall in the range of 2.278−2.514 Å and 66−142°, respectively. The Yb(III) centers are quite isolated as the shortest Yb···Yb distance is 8.633 Å. The structure shows 2D layers with (6,3) topology in which each Yb(III) ion is connected to three other Yb(III) ions through bis-bidentate chlorocyananilate ligands forming six-membered rings with rectangular cavities along the $b-c$ plane (Figure 1c−e). Neighbor layers are eclipsed along the a axis. The coordinated DMF molecules face toward the cavities and toward neighboring layers. This results in a non-negligible overlap of the 2D layers (Figure 1d) and in numerous interlayer interactions between the DMF molecules of one

DOI: 10.1021/acs.chemmater.8b03399
Chem. Mater. 2018, 30, 6575−6586

Table 1. Crystallographic Data for Compounds 1−3

	1	2	3
empirical formula	$C_{39}H_{42}Cl_3N_9O_{18}Yb_2$	$C_{41}H_{46}Cl_7N_9O_{18}Nd_2$	$C_{41}H_{46}Cl_7N_9O_{18}Er_2$
Fw	1377.25	1489.50	1535.54
crystal color	red	red	red
crystal size (mm^3)	0.10 × 0.05 × 0.02	0.10 × 0.05 × 0.03	0.10 × 0.07 × 0.05
temperature (K)	150.00(10)	150.00(10)	150.00(10)
wavelength (Å)	1.54184	1.54184	1.54184
crystal system, Z	monoclinic, 2	monoclinic, 4	monoclinic, 4
space group	$P2_1/n$	$C2/c$	$C2/c$
a (Å)	9.7317(3)	13.8900(2)	13.7965(4)
b (Å)	13.5934(5)	23.0192(4)	22.5774(8)
c (Å)	19.6218(6)	18.1488(3)	17.9680(8)
α (deg)	90	90	90
β (deg)	96.451(3)	98.162(2)	98.075(4)
γ (deg)	90	90	90
V ($Å^3$)	2579.27(15)	5744.06(16)	5541.3(4)
ρ_{calc} (g cm^{-3})	1.773	1.722	1.829
μ(Cu Kα) (mm^{-1})	8.629	17.272	9.227
θ range (deg)	3.96−73.51	3.74−76.34	3.78−74.01
no. of data collected	12606	14212	11988
no. of unique data	5034	5875	5493
no. of data observed	4160	5653	4820
no. of parameters/restraints	334/6	366/0	373/2
R(int)	0.0425	0.0255	0.0379
R1(F),[a] $I > 2\sigma(I)$	0.0427	0.0427	0.0500
wR2(F2),[b] all data	0.1224	0.1202	0.1376
S(F2),[c] all data	1.070	1.107	1.182

[a] $R1(F) = \sum||F_0| - |F_C||/\sum|F_0|$. [b] $wR2(F2) = [\sum w(F_0^2 - F_C^2)^2/\sum wF_0^4]^{1/2}$. [c] $S(F2) = [\sum w(F_0^2 - F_C^2)^2/(n + r - p)]^{1/2}$.

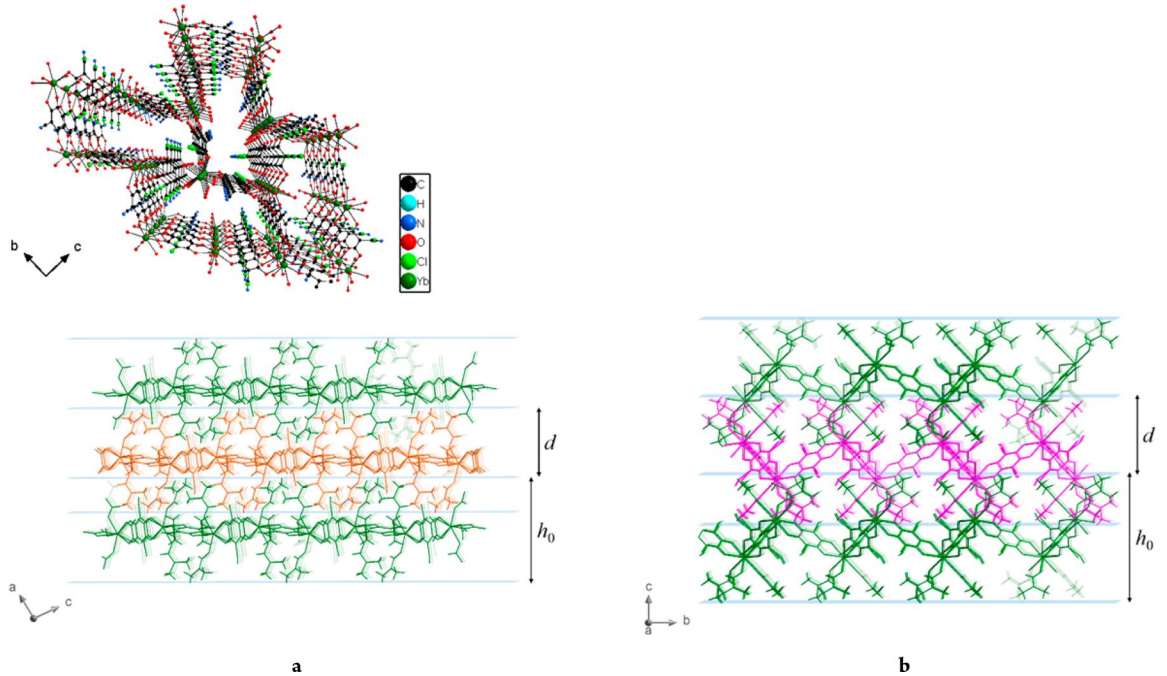

a **b**

Figure 3. Perspective view of **1** in the $b-c$ plane (top). View of 2D layers showing the thickness of the first monolayer (h_0) and interlayer distance (d) in (a) **1** and (b) **3**.

layer and the Yb(III) centers of the neighbor layer. All the interlayer contacts are detailed in Figure S1 and Table S1.

Compounds **2** and **3** are isostructural; therefore, only the structure of **2** is discussed in detail hereafter (see Figure S3 and Table S3 for compound **3**). The asymmetric unit consists of one Nd(III) ion, three half-molecules of the $ClCNAn^{2-}$ ligand, three DMF molecules coordinated to the Nd(III) center, and one DCM solvent molecule giving rise to the formula $\{[Nd_2(ClCNAn)_3(DMF)_6]\cdot(DCM)_2\}_n$ (Figure 2a). The chloro and cyano substituents from the asymmetric chlorocyananilate ligand are equally distributed over the same position as in **1**.

DOI: 10.1021/acs.chemmater.8b03399
Chem. Mater. 2018, 30, 6575−6586

The Nd(III) ion is nine-coordinated and shows a tricapped trigonal prism geometry, completed by six oxygen atoms from three $ClCNAn^{2-}$ ligands and three oxygen atoms from three DMF molecules (Figure 2b). This different geometry of the Ln(III) center compared to that of Yb(III) in compound **1** results in a more regular honeycomb(6,3) topology structure, with hexagonal cavities (Figure 2c) filled by dichloromethane solvent molecules (two molecules per formula unit). Consecutive 2D layers are arranged in an alternate way along the *c* axis (Figure 2d,e). Nd−O bond lengths and O−Nd−O angles fall in the range of 2.419−2.561 Å and 64−142°, respectively. The shortest distance between Nd(III) centers is 8.93 Å. As in **1**, there is an overlap of the 2D layers by the coordinated DMF molecules and numerous interlayer interactions between Nd(III) centers and methyl groups from the DMF molecules (see Figure S2 and Table S2). A summary of crystallographic data and refinement results are listed in Table 1.

The two different 2D networks we observed can be explained in terms of different sizes of the lanthanide ion as previously highlighted by Gomez et al.[36] In fact, even small changes in the size of Ln(III) ion play a key role in determining the shape and size of the cavities in the compounds' structures. Indeed, despite the fact that the coordination numbers of the lanthanide ions are the same in the three structures, in compound **1** the Yb(III) ion (the smallest one in this series) shows a different coordination geometry, which results in a stronger distortion of the cavities in the 2D layers (rectangular cavities), whereas in compounds **2** and **3**, the Er(III) and Nd(III) adopt the same coordination geometry leading the usual regular honeycomb(6,3) topology structure, with hexagonal cavities.

Because in all compounds the coordinated DMF molecules are overlapped/interpenetrated with the neighbor layers, the overlapping distance has to be considered to determine the number of layers from the thickness of the exfoliated sheets. The height of a monolayer (h_0) and the interlayer distance (d) can be easily calculated from the crystal structure (Figure 3). The number of layers (n) of a 2D crystal slab of thickness h can thus be calculated as

$$n = 1 + (h - h_0)/d$$

A summary of these parameters is reported in Table 2 for compounds **1**−**3**.

Table 2. Miller Indices of the Exfoliation Plane (Σ), Monolayer Thickness (h_0), and Interlayer Distance (d) of Layered Compounds 1−3

compound	Σ	h_0 (Å)	d (Å)
1	101	12.39	8.30
2	001	14.83	8.98
3	001	14.48	9.00

Synthesis and Morphological Characterization. Exfoliation of crystals of compounds **1**−**3** was successfully achieved by a sonication-assisted solution method in different solvents such as acetone, methanol, ethanol, and acetonitrile. DLS measurements performed at different times after sonication showed monomodal distributions of the hydrodynamic diameter of the nanosheets, with good stability over several days (Figure 4a−c). The stability of the nanosheet suspensions was visually confirmed by the long-lived observation of Tyndall scattering of laser light (Figure 4d).

Morphological characterization of the exfoliated materials was performed by AFM on **1-NS**−**3-NS**. Panels a and b of Figure 5 display topography (height) scanning images over substrate areas covered with nanosheets of compounds **1** and **3**, respectively. Randomly distributed nanosheets with lateral dimensions of up to a few micrometers are clearly evident, for which height profiles are depicted in panels c and d of Figure 5, respectively. The lateral size of the nanosheets is clearly larger than their hydrodynamic diameter, which is, in fact, proportional through a shape factor to the diameter of the sphere with the equal volume as the nanosheet.[43] The nanosheets exhibit a markedly quantized height distribution. According to the values of monolayer thickness and interlayer distance reported in Table 2 and given the limited absolute accuracy (∼0.5 nm) in determining the zero height level due to substrate roughness, results are consistent with a thickness distribution ranging from one to four layers. Repeated scans over the same nanosheet resulted in a progressive deterioration of its topography with the emergence of an increasing number of nanoholes as a possible consequence of the sample−tip interaction (Figure S4). Collected data clearly demonstrate that the sonication-assisted solution method was effective in providing exfoliation of **1**−**3** layered compounds down to the monolayer limit.

TEM images confirm the presence of overlapped sheets for both samples (Figure 6a−c). The contrast of the TEM images indicates that the layers are very thin. High-resolution images for exfoliated compound **1** are reported in Figure 6d−f. For compound **1**, we were able to observe well-defined lattice fringes with interplanar average distances of 2.9 and 2.6 Å, which can be ascribed to the (−135) and (−3−15) planes of crystal **1**, respectively (Figure S5). It is worth noting that because of possible sample degradation under electron-beam irradiation, lattice fringes have so far been observed in only a few stable MOFs.[44,45]

Photophysical Studies. Crystals of KHClCNAn and of Ln(III) compounds **1**−**3** were investigated by absorption and photoluminescence spectroscopy. Cw absorptance spectra are depicted in Figure 7a. The absorption onset of the ligand is clearly visible at ∼600 nm in KHClCNAn (**4**) and at ∼650 nm in the Ln(III) compounds. For longer wavelengths, Ln(III) absorption transitions dominate the spectra.

Photoluminescence (PL) spectroscopy was conducted with near-ultraviolet impulse excitation above the ligand absorption onset; pulsed excitation enabled acquisition of excited-state lifetimes and emission spectra simultaneously. Given the maximum irradiation energy density of ∼300 $\mu J/cm^2$ per pulse used in PL experiments, and assuming that at the pump wavelength, the ligand absorption cross section yields a molar decadic absorption coefficient no larger than 10^3 cm^{-1} mol^{-1} dm^3 in solution,[35] an upper bound of $\sim 2 \times 10^{-3}$ excited states per ligand per pulse is estimated for the photoexcitation level reached in all compounds, meaning that both the excited-state dynamics and emission spectra were investigated in a regime of the linear response.

Time-integrated PL spectra of all compounds are shown in Figure 7b. Ligand-centered emission (dots), which was identified based on the KHClCNAn emission band that peaked at 650 nm, exhibits an ∼50 nm red-shift with respect to the absorption onset in both KHClCNAn and lanthanide compounds. Ln(III) emission lines peaked at ∼980 nm in **1**,

DOI: 10.1021/acs.chemmater.8b03399
Chem. Mater. 2018, 30, 6575−6586

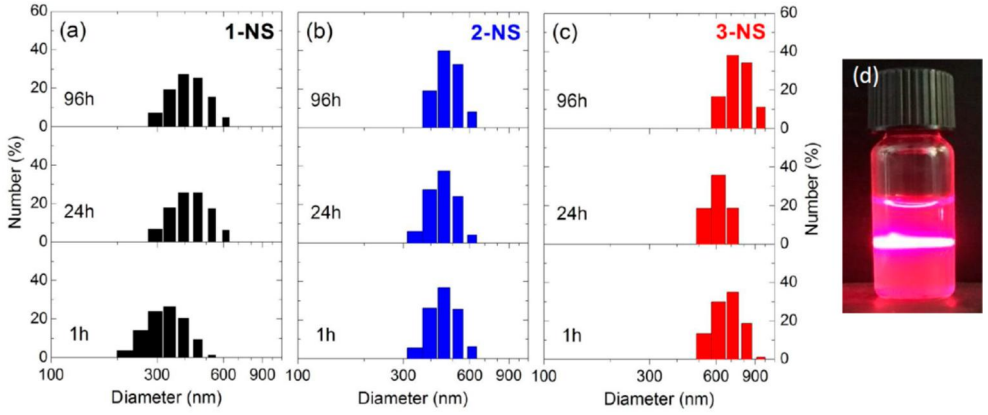

Figure 4. Hydrodynamic diameter distributions of suspensions of **1-NS**−**3-NS** in EtOH, measured at different times after preparation: (a) **1-NS**, (b) **2-NS**, and (c) **3-NS**. (d) Tyndall effect for the suspension of **1-NS** in EtOH.

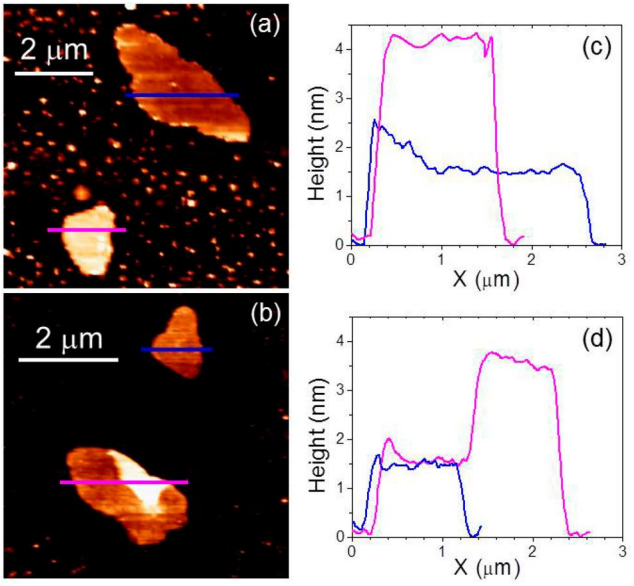

Figure 5. AFM characterization of nanosheets of compounds **1** and **3** obtained upon crystal exfoliation using the sonication-assisted method in an EtOH solution, deposited on SiO_2/Si substrates. (a) Topography (height) image of nanosheets of compound **1** on a false-color scale. (b) Same as panel a but for compound **3**. (c) Height profiles of nanosheets of compound **1** extracted along the lines drawn in panel a. (d) Same as panel c but for compound **3**.

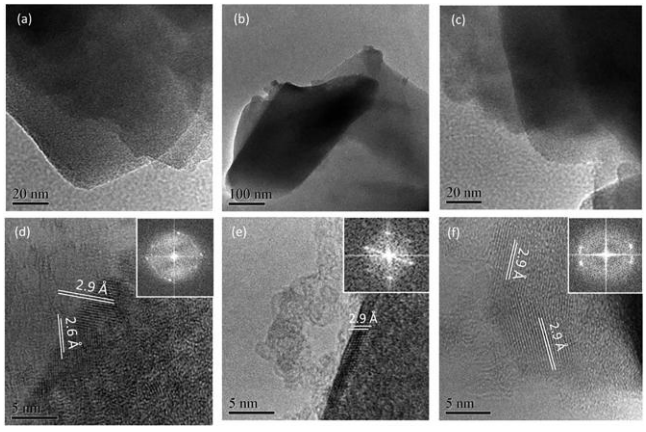

Figure 6. TEM images of samples (a and b) **1** and (c) **3** and (d−f) HR-TEM images with FFT (inset) of sample **1**.

~900, ~1070, and ~1350 nm in **2**, and ~1550 nm in **3**, proving that the ligands act as optical antennas toward the lanthanide ions. The visible−NIR emission spectrum of **1** under UV photoexcitation is strongly similar with the one reported very recently for a chlorocyananilate-based Yb(III) compound.[46]

As shown in Figure 7c, the PL emission of KHClCNAn is short-lived, decaying monoexponentially with a characteristic time of 200(10) ps. Because of its short lifetime, the emission is ascribed to singlet radiative recombination, contrary to previous triplet assignments.[36] In the lanthanide compounds, the ligand-centered PL is strongly quenched; its emission lifetime decreases to ~40 ps in **3** and ~30 ps in **1**, while in **2**, the ligand recombination dynamics is completely limited by resolution. PL lifetime shortening is attributed to enhanced intersystem (singlet-to-triplet) crossing due to the presence of the Ln(III) ions, based on the well-known heavy atom effect,[47] already reported by some of us in quinolinolate-based complexes of the same NIR-emissive lanthanides.[48] In lanthanide coordination compounds with organic ligands, enhancement of intersystem crossing can result in efficient sensitization of the Ln(III) luminescence through energy transfer from the ligand triplet states to the Ln(III) ions.[21,48] The quantum efficiency of intersystem crossing can be evaluated as $1 - \tau/\tau_0$, where τ and τ_0 are the ligand-centered PL lifetimes in the presence and absence of the heavy atom, respectively, and τ_0 is well-approximated by the PL lifetime of KHClCNAn. A very high efficiency (η) is thus inferred for intersystem crossing in all lanthanide compounds: ~0.8 in **3**, ~0.85 in **1**, and >0.85 in **2**.

Lanthanide-centered emission transients are reported in panels d and e of Figure 7. As one can clearly see in Figure 7d, Ln(III) emission sensitization takes place within a few tens of nanoseconds from the impulse excitation. The activation of the Ln(III) emission exhibits an instantaneous component whose characteristic time is limited by the 1 ns temporal resolution of the NIR PL detection apparatus, superimposed on a delayed component occurring on the time scale of tens of nanoseconds. In compound **3**, no instantaneous component is detected, and the time profile can be fitted with a single-component exponential rise function with a characteristic time of 16 ns. This time constant is much longer than the 40 ps decay time of the ligand-centered emission, thereby corroborating our understanding of Ln(III) emission sensitization as a multistep

DOI: 10.1021/acs.chemmater.8b03399
Chem. Mater. 2018, 30, 6575−6586

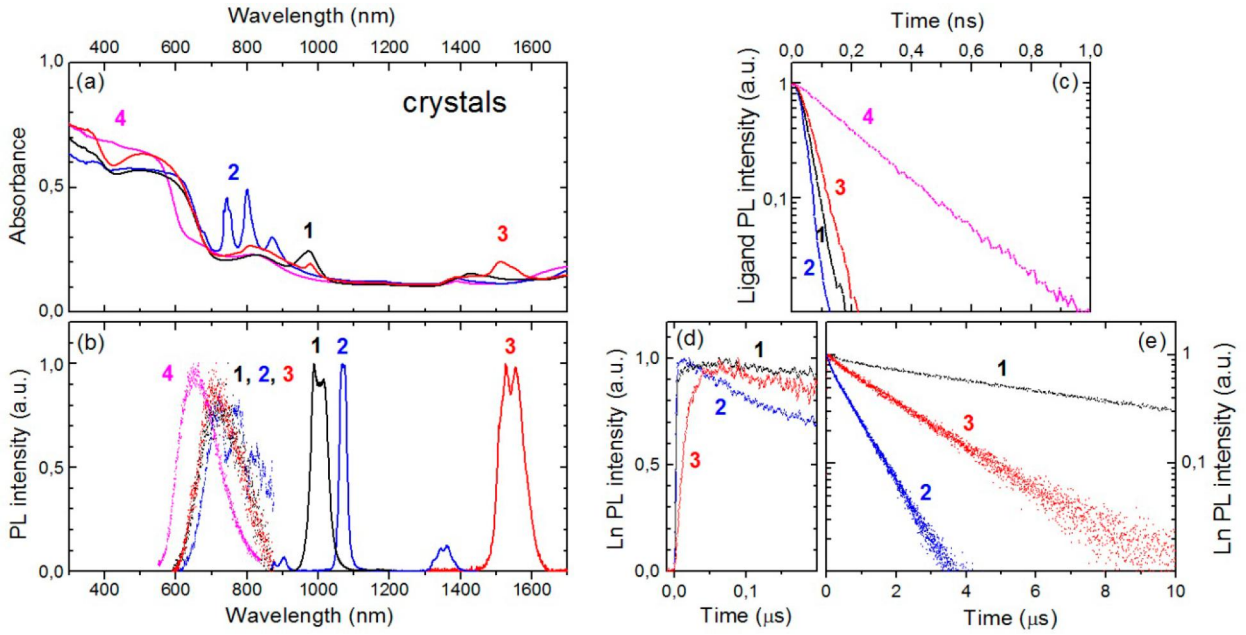

Figure 7. Optical absorption and photoluminescence (PL) characterization of crystals of **1**−**3** [**1**, Yb(III) compound, black symbols; **2**, Nd(III) compound, blue symbols; **3**, Er(III) compound, red symbols] and KHClCNAn (**4**, magenta symbols). All PL spectra and temporal traces were normalized to unity for better comparison among different compounds. (a) Cw absorptance spectra. (b) PL spectra: ligand-centered PL (dots) and lanthanide-centered PL (solid lines). (c) Ligand-centered PL decay transients. (d) Lanthanide-centered PL time traces shown over a 0.2 μs range to highlight PL signal activation. (e) Same as panel d but shown over a 10 μs range to visualize signal decay.

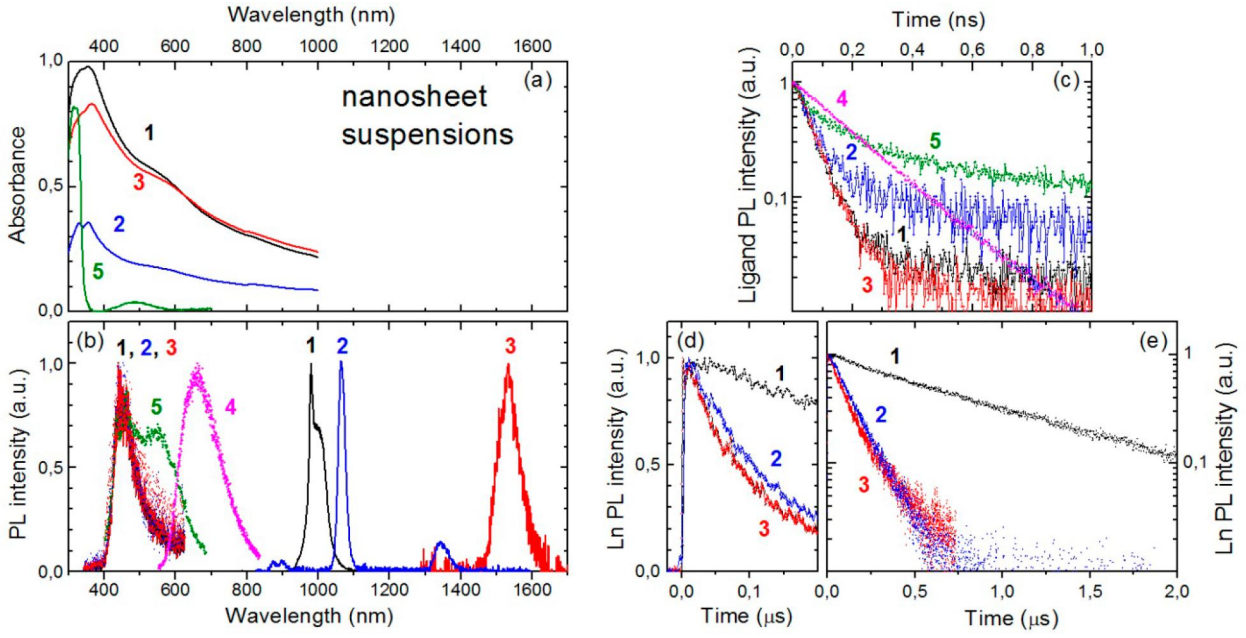

Figure 8. Optical absorption and photoluminescence (PL) characterization of suspensions of **1-NS**−**3-NS** in EtOH. All PL spectra and temporal traces were normalized to unity for better comparison among different compounds. PL spectra and temporal traces of KHClCNAn crystals (**4**, magenta symbols) and $HClCNAn^{-}/ClCNAn^{2-}$ anions in an EtOH solution at a 5×10^{-4} mol dm^{-3} concentration (**5**, green symbols) are shown for reference. (a) Cw absorptance spectra. (b) PL spectra: ligand-centered PL (dots) and lanthanide-centered PL (solid lines). (c) Ligand-centered PL decay transients. (d) Lanthanide-centered PL time traces shown over a 0.2 μs range. (e) Same as panel d but shown over a 2 μs range.

relaxation process involving, in sequence, intersystem crossing and energy transfer from ligand triplet states to the Ln(III) ions.

Ln(III) emission decay occurs on the time scale of a few microseconds in all Ln(III) compounds (Figure 7e). Nd(III) and Er(III) emissions decay monoexponentially with characteristic times of 0.79 and 2.1 μs, respectively, whereas the Yb(III) emission transient is best fitted by a biexponential decay function with characteristic times of 1.2 and 9.7 μs, having fractional amplitudes of 0.13 and 0.87, respectively. The faster component, most likely arising from a distinct population of excited Yb(III) ions undergoing more efficient nonradiative deactivation, could in fact be minimized upon careful selection of the photoexcited sample spot. The Ln(III)

DOI: 10.1021/acs.chemmater.8b03399
Chem. Mater. 2018, 30, 6575−6586

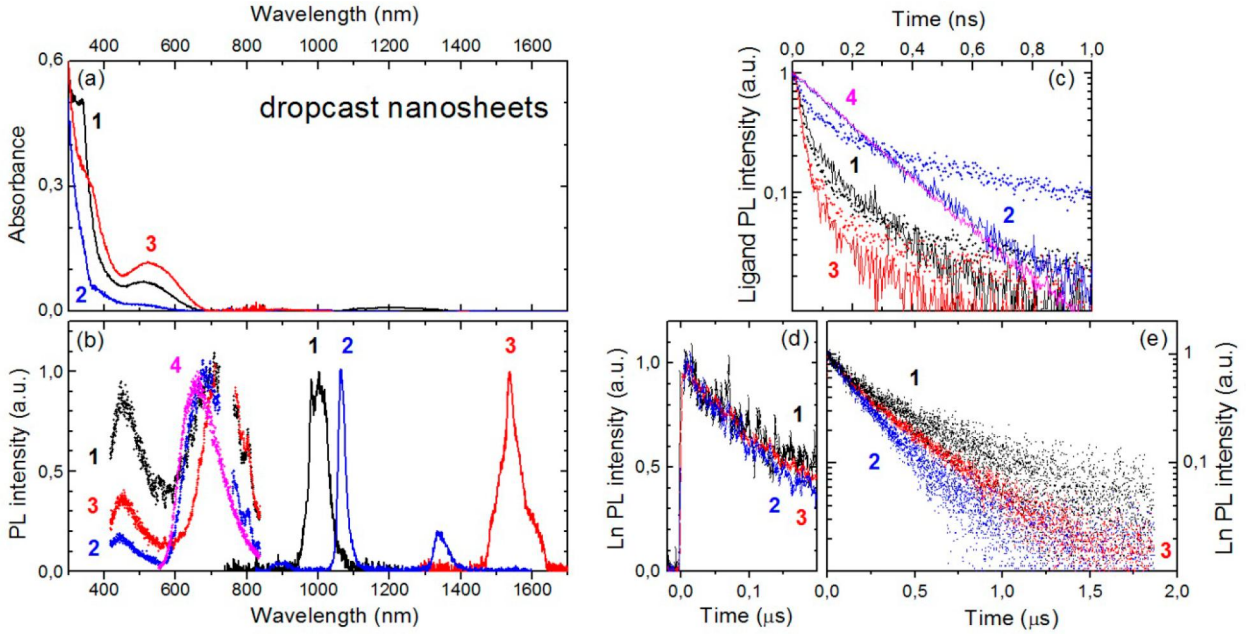

Figure 9. Optical absorption and photoluminescence (PL) characterization of **1-NS**−**3-NS** drop-cast onto glass substrates. All PL spectra and temporal traces were normalized to unity for better comparison among different compounds. The PL spectrum and temporal trace of KHClCNAn crystals (**4**, magenta symbols) are shown for reference. (a) Cw absorptance spectra. (b) PL spectra: ligand-centered PL (dots) and lanthanide-centered PL (solid lines). (c) Ligand-centered PL decay transients integrated over 400−550 and 600−800 nm spectral windows (lines and dots, respectively). (d) Lanthanide-centered PL time traces shown over a 0.2 μs range. (e) Same as panel d but shown over a 2 μs range.

excited-state lifetimes of compounds **1**−**3** are 2−3 orders of magnitude shorter than the radiative lifetimes, which range from a fraction of a millisecond for Nd(III)[49] and Yb(III)[46,50] to a few milliseconds for Er(III).[51−53] The observed lifetimes were traced back to vibrational deactivation of the Ln(III) excited states[21,50,54−56] due to the presence of the C−H groups of the coordinated (DMF) solvent molecules, being as little as 3−4 Å from the Ln(III) ions (Tables S1−S3).

Cw absorptance and transient PL measurements of nanosheet suspensions and drop-cast nanosheets are reported in Figures 8 and 9, respectively. In all nanosheet suspensions, absorptance spectra exhibit a strong wavelength-dependent background arising from the loss of regular transmittance due to light diffusion (Figure 8a). The weak ligand-centered emission of the nanosheet suspensions spectrally peaks at ∼460 nm, occurring, in fact, in the same spectral region as the emission of the ligand anions in a diluted EtOH solution, **5** (Figure 8b). The ligand-centered emission is still dominated by a fast component with a characteristic time as short as 56 ps (**2-NS**) and a fractional amplitude of >0.90 in all compounds (Figure 8c). The residual component with a small (<0.10) fractional amplitude decays on the time scale of a few nanoseconds (not shown), as also observed in **5**. As one can clearly see in Figure 8b, lanthanide-centered emission spectra were only weakly perturbed by the exfoliation procedure. The activation of the lanthanide-centered emission is instantaneous within the resolution of the NIR PL detection apparatus (Figure 8d), while its decay is faster than in the crystals. Ln(III) PL decay is monoexponential with a characteristic time of 0.13 μs for Nd(III) (**2-NS**) and biexponential for Yb(III) (**1-NS**) and Er(III) (**3-NS**) with amplitude-weighted average lifetimes of 0.88 and 0.13 μs, respectively (Figure 8e).

In drop-cast nanosheets, absorption artifacts related to light diffusion were eliminated by inferring absorptance from total transmittance and reflectance measurements (Figure 9a). The ligand-centered PL band that peaked at ∼460 nm is still present, and the red emission band centered at ∼680−720 nm is clearly recovered (Figure 9b). The initial decay of the ligand-centered emission is nearly resolution-limited across the whole 400−800 nm spectral range for both **1-NS** and **3-NS**, whereas the red PL band of **2-NS** decays monoexponentially with practically the same characteristic time as for KHClCNAn (Figure 9c). Further shortening of the Ln(III) average lifetime to 0.38 μs was observed for Yb(III) in **1-NS**; conversely, 1.8- and 2.2-fold increases in lifetime with respect to that of the nanosheet suspension were reported for Nd(III) in **2-NS** and Er(III) in **3-NS**, respectively (Figure 9e). A summary of Ln(III) PL time constants is presented in Table 3.

Table 3. Ln(III) PL Fractional Amplitudes (A_i), Time Constants (τ_i), and Amplitude-Weighted Average Lifetimes (τ) in Bulk and Exfoliated Crystals of 1−3

compound	A_1	τ_1 (μs)	A_2	τ_2 (μs)	τ (μs)
1	0.13	1.2	0.87	9.7	8.6
2	1	0.79	–	–	0.79
3	1	2.1	–	–	2.1
1-NS (suspension)	0.20	0.30	0.80	1.03	0.88
2-NS (suspension)	1	0.13	–	–	0.13
3-NS (suspension)	0.82	0.089	0.18	0.31	0.13
1-NS (drop-cast)	0.33	0.11	0.67	0.52	0.38
2-NS (drop-cast)	1	0.23	–	–	0.23
3-NS (drop-cast)	0.41	0.12	0.59	0.41	0.29

The persistence of photophysical signatures of ligand-to-lanthanide coordination, that is, (i) the red-shift of the fundamental absorption band, (ii) the accelerated decay of ligand-centered emission, and (iii) UV sensitization of the NIR lanthanide emission upon sonication of the materials, demonstrates the successful exfoliation of these 2D layered

DOI: 10.1021/acs.chemmater.8b03399
Chem. Mater. 2018, 30, 6575−6586

CPs. The appearance of the blue emission band and the accelerated decay of the Ln(III) PL in the nanosheets were ascribed to the creation of electronic defect states and nonradiative recombination centers by the exfoliation process. Effects of nanosheet−solvent interaction on the nanosheet emission properties were envisaged. In particular, partial recovery of the Nd(III) and Er(III) PL lifetimes observed upon nanosheet drop-casting onto the glass and solvent evaporation suggested that the C−H/O−H groups of the solvent molecules can contribute to vibrational quenching of the NIR nanosheet emission in the suspensions and that the process is reversible. Last, deterioration of the NIR emission performance observed for Yb(III) in dropcast **1-NS** was attributed to nanosheet aggregation and/or nanosheet−substrate interaction effects.

CONCLUSIONS

A fundamental study of the synthesis, X-ray structure, and photophysical properties of a new class of NIR-emissive Ln(III) (Ln = Yb, Nd, or Er) neutral 2D CPs, based on the asymmetric chlorocyananilate ligand ($ClCNAn^{2-}$), is reported. The three Ln(III) ions are nine-coordinated by six oxygen atoms from anilates and three oxygen atoms from DMF molecules, within a slightly distorted monocapped square antiprismatic geometry for Yb(III) and a tricapped trigonal prismatic geometry for Nd(III) and Er(III). Formation of 2D coordination networks is observed for the three compounds. Exfoliation experiments upon sonication-assisted solutions provided suspensions of ultrathin sheets of the materials on the micrometer lateral scale showing a thickness distribution down to the monolayer. It is noteworthy that HR-TEM images of nanosheets of the Yb(III)-based compound show the presence of lattice fringes, never observed so far in anilate-based CPs and MOFs, showing the good stability of the obtained nanosheets under electron-beam irradiation. Photophysical measurements demonstrated that the ligand works as an efficient antenna in sensitizing the Ln(III) NIR emission in both bulk and nanosheets. Experimental findings hinted at possible exfoliation-induced electronic defects that have an impact on the nanosheet PL performance, while the C−H/O−H groups of the solvent molecules can contribute to vibrational quenching of the NIR nanosheet emission in the suspensions.

Further studies of this novel class of materials will involve (i) the preparation and characterization of nanosheets of these materials by the bottom-up strategy, by using the surfactant-assisted synthesis to improve their yield on planar substrates and to tune their thickness, and (ii) mixed lanthanide neutral CPs showing the same supramolecular architectures, as bulk and nanoparticles, because, as worth noting, these 2D layered CPs show emission bands in the 980−1350 nm spectral region, the so-called biological window, and therefore can be envisaged for applications in biology and nanomedicine as luminescent dual-center nanothermometers.[57]

ASSOCIATED CONTENT

Supporting Information

The Supporting Information is available free of charge on the ACS Publications website at DOI: 10.1021/acs.chemmater.8b03399.

Figures S1−S5 and Tables S1−S3 (PDF)
X-ray crystallographic file for **1** (CIF)
X-ray crystallographic file for **2** (CIF)
X-ray crystallographic file for **3** (CIF)
checkCIF/PLATON report for **1** (PDF)
checkCIF/PLATON report for **2** (PDF)
checkCIF/PLATON report for **3** (PDF)

AUTHOR INFORMATION

Corresponding Authors

*E-mail: mercuri@unica.it. Fax: (+39)070 675 4456. Telephone: (+39)070 675 4474.
*E-mail: francesco.quochi@dsf.unica.it. Fax: (+39)070 675 3191. Telephone: (+39)070 675 4866.
*E-mail: narcis.avarvari@univ-angers.fr. Fax: (+33)02 41 73 5405. Telephone: (+33)02 41 73 50 84.

ORCID

Carla Cannas: 0000-0003-2908-7739
Narcis Avarvari: 0000-0001-9970-4494
Maria Laura Mercuri: 0000-0002-4816-427X

Notes

The authors declare no competing financial interest.
Crystallographic data for the structures were deposited in the Cambridge Crystallographic Data Centre, deposition numbers CCDC 1825214 (**1**), CCDC 1825213 (**2**), and CCDC 1825215 (**3**). These data can be obtained free of charge from The Cambridge Crystallographic Data Centre via www.ccdc.cam.ac.uk/data_request/cif.

ACKNOWLEDGMENTS

This work was supported in Italy by the Fondazione di Sardegna-Convenzione triennale tra la Fondazione di Sardegna e gli Atenei Sardi, Regione Sardegna-L.R. 7/2007 annualità 2016-DGR 28/21 del 17.05.2015 “Innovative Molecular Functional Materials for Environmental and Biomedical Applications”, and INSTM. The authors acknowledge the CeSAR (Centro Servizi d'Ateneo per la Ricerca) core facility of the University of Cagliari for the use of the Ultrafast Optical Spectroscopy Laboratory for photophysical measurements and the JEM 2010 UHR JEOL facility for TEM measurements. The work in France was supported by the CNRS, the University of Angers, the Erasmus program (mobility grant to N.M.), and the RFI Regional project LUMOMAT (grant to A.A., Project ASCO MMM). The authors thank Sylvie Dabos-Seignon (University of Angers) for preliminary AFM characterization, Andrea Ardu (University of Cagliari) for support with HR-TEM measurements, and Alessandro Mattoni (IOM-CNR Cagliari) for fruitful theoretical discussions. Mariangela Oggianu (University of Cagliari) is also greatly acknowledged for support with DLS measurements and nanosheets drop-cast on glass substrates.

REFERENCES

(1) Horiuchi, S.; Kumai, R.; Tokura, Y. High-Temperature and Pressure-Induced Ferroelectricity in Hydrogen-Bonded Supramolecular Crystals of Anilic Acids and 2,3-Di(2-Pyridinyl)pyrazine. *J. Am. Chem. Soc.* **2013**, *135*, 4492−4500.
(2) Horiuchi, S.; Kumai, R.; Tokura, Y. Room-Temperature Ferroelectricity and Gigantic Dielectric Susceptibility on a Supramolecular Architecture of Phenazine and Deuterated Chloranilic Acid. *J. Am. Chem. Soc.* **2005**, *127*, 5010−5011.
(3) Kagawa, F.; Horiuchi, S.; Minami, N.; Ishibashi, S.; Kobayashi, K.; Kumai, R.; Murakami, Y.; Tokura, Y. Polarization Switching Ability Dependent on Multidomain Topology in a Uniaxial Organic Ferroelectric. *Nano Lett.* **2014**, *14*, 239−243.

(4) Zaman, M. B.; Toyoda, J.; Morita, Y.; Nakamura, S.; Yamochi, H.; Saito, G.; Nakasuji, K. Hydrogen-Bonded CT-Complex of Cyananilic Acid with OMTTF: $(OMTTF)_3(HCNAn)_2$. *Synth. Met.* **1999**, *102*, 1691−1692.
(5) Yamochi, H.; Nakamura, S.; Saito, G.; Zaman, M. B.; Toyoda, J.; Morita, Y.; Nakasuji, K.; Yamashita, Y. Cyananilate Anion as Hydrogen Bonded Counter Ion in Conducting CT Complexes. *Synth. Met.* **1999**, *102*, 1729−1729.
(6) Zaman, M. B.; Toyoda, J.; Morita, Y.; Nakamura, S.; Yamochi, H.; Saito, G.; Nishimura, K.; Yoneyama, N.; Enoki, T.; Nakasuji, K. Preparation of a Mott Insulator Based on a BEDT-TTF Charge Transfer Complex of Hydrogen Cyananilate: α'-$(BEDT\text{-}TTF)_2HCNAn$. *J. Mater. Chem.* **2001**, *11*, 2211−2215.
(7) Ashoka Sahadevan, S.; Monni, N.; Abhervé, A.; Auban-Senzier, P.; Canadell, E.; Mercuri, M. L.; Avarvari, N. Synthesis and Physical Properties of Purely Organic BEDT-TTF-Based Conductors Containing Hetero-/Homosubstituted Cl/CN-Anilate Derivatives. *Inorg. Chem.* **2017**, *56*, 12564−12571.
(8) Mercuri, M. L.; Congiu, F.; Concas, G.; Sahadevan, S. A. Recent Advances on Anilato-Based Molecular Materials with Magnetic And/or Conducting Properties. *Magnetochemistry* **2017**, *3*, 17−72.
(9) Atzori, M.; Benmansour, S.; Mínguez Espallargas, G.; Clemente-León, M.; Abhervé, A.; Gómez-Claramunt, P.; Coronado, E.; Artizzu, F.; Sessini, E.; Deplano, P.; et al. A Family of Layered Chiral Porous Magnets Exhibiting Tunable Ordering Temperatures. *Inorg. Chem.* **2013**, *52*, 10031−10040.
(10) Benmansour, S.; Abhervé, A.; Gómez-Claramunt, P.; Vallés-García, C.; Gómez-García, C. J. Nanosheets of Two-Dimensional Magnetic and Conducting Fe(II)/Fe(III) Mixed-Valence Metal-Organic Frameworks. *ACS Appl. Mater. Interfaces* **2017**, *9*, 26210−26218.
(11) Abhervé, A.; Mañas-Valero, S.; Clemente-León, M.; Coronado, E. Graphene Related Magnetic Materials: Micromechanical Exfoliation of 2D Layered Magnets Based on Bimetallic Anilate Complexes with Inserted $[Fe^{III}(Acac_2\text{-}Trien)]^+$ and $[Fe^{III}(Sal_2\text{-}Trien)]^+$ Molecules. *Chem. Sci.* **2015**, *6*, 4665−4673.
(12) Abhervé, A.; Clemente-León, M.; Coronado, E.; Gómez-García, C. J.; Verneret, M. One-Dimensional and Two-Dimensional Anilate-Based Magnets with Inserted Spin-Crossover Complexes. *Inorg. Chem.* **2014**, *53*, 12014−12026.
(13) Benmansour, S.; Coronado, E.; Giménez-Saiz, C.; Gõmez-García, C. J.; Rõßer, C. Metallic Charge-Transfer Salts of Bis(ethylenedithio)tetrathiafulvalene with Paramagnetic tetrachloro(oxalato)rhenate(IV) and tris(chloranilato)ferrate(III) Anions. *Eur. J. Inorg. Chem.* **2014**, *2014*, 3949−3959.
(14) Atzori, M.; Pop, F.; Auban-Senzier, P.; Gómez-García, C. J.; Canadell, E.; Artizzu, F.; Serpe, A.; Deplano, P.; Avarvari, N.; Mercuri, M. L. Structural Diversity and Physical Properties of Paramagnetic Molecular Conductors Based on Bis(ethylenedithio)tetrathiafulvalene (BEDT-TTF) and the Tris(chloranilato)ferrate(III) Complex. *Inorg. Chem.* **2014**, *53*, 7028−7039.
(15) Atzori, M.; Pop, F.; Auban-Senzier, P.; Clérac, R.; Canadell, E.; Mercuri, M. L.; Avarvari, N. Complete Series of Chiral Paramagnetic Molecular Conductors Based on Tetramethyl-Bis(ethylenedithio)-Tetrathiafulvalene (TM-BEDT-TTF) and Chloranilate-Bridged Heterobimetallic Honeycomb Layers. *Inorg. Chem.* **2015**, *54*, 3643−3653.
(16) Shilov, G. V.; Nikitina, Z. K.; Ovanesyan, N. S.; Aldoshin, S. M.; Makhaev, V. D. Phenazineoxonium Chloranilatomanganate and Chloranilatoferrate: Synthesis, Structure, Magnetic Properties, and Mössbauer Spectra. *Russ. Chem. Bull.* **2011**, *60*, 1209−1219.
(17) Darago, L. E.; Aubrey, M. L.; Yu, C. J.; Gonzalez, M. I.; Long, J. R. Electronic Conductivity, Ferrimagnetic Ordering, and Reductive Insertion Mediated by Organic Mixed-Valence in a Ferric Semiquinoid Metal-Organic Framework. *J. Am. Chem. Soc.* **2015**, *137*, 15703−15711.
(18) Jeon, I. R.; Negru, B.; Van Duyne, R. P.; Harris, T. D. A 2D Semiquinone Radical-Containing Microporous Magnet with Solvent-Induced Switching from Tc = 26 to 80 K. *J. Am. Chem. Soc.* **2015**, *137*, 15699−15702.
(19) DeGayner, J. A.; Jeon, I. R.; Sun, L.; Dincă, M.; Harris, T. D. 2D Conductive Iron-Quinoid Magnets Ordering up to Tc = 105 K via Heterogenous Redox Chemistry. *J. Am. Chem. Soc.* **2017**, *139*, 4175−4184.
(20) Tan, C.; Cao, X.; Wu, X. J.; He, Q.; Yang, J.; Zhang, X.; Chen, J.; Zhao, W.; Han, S.; Nam, G. H.; et al. Recent Advances in Ultrathin Two-Dimensional Nanomaterials. *Chem. Rev.* **2017**, *117*, 6225−6331.
(21) Bünzli, J. C. G. On the Design of Highly Luminescent Lanthanide Complexes. *Coord. Chem. Rev.* **2015**, *293*−*294*, 19−47.
(22) Barry, D. E.; Caffrey, D. F.; Gunnlaugsson, T. Lanthanide-Directed Synthesis of Luminescent Self-Assembly Supramolecular Structures and Mechanically Bonded Systems from Acyclic Coordinating Organic Ligands. *Chem. Soc. Rev.* **2016**, *45*, 3244−3274.
(23) Bünzli, J. C. G. Rising Stars in Science and Technology: Luminescent Lanthanide Materials. *Eur. J. Inorg. Chem.* **2017**, *2017*, 5058−5063.
(24) Kuriki, K.; Koike, Y.; Okamoto, Y. Plastic Optical Fiber Lasers and Amplifiers Containing Lanthanide Complexes. *Chem. Rev.* **2002**, *102*, 2347−2356.
(25) Bünzli, J. C. G. Lanthanide Luminescence for Biomedical Analyses and Imaging. *Chem. Rev.* **2010**, *110*, 2729−2755.
(26) Pointillart, F.; Le Guennic, B.; Cador, O.; Maury, O.; Ouahab, L. Lanthanide Ion and Tetrathiafulvalene-Based Ligand as a "magic" Couple toward Luminescence, Single Molecule Magnets, and Magnetostructural Correlations. *Acc. Chem. Res.* **2015**, *48*, 2834−2842.
(27) Abrahams, B. F.; Coleiro, J.; Ha, K.; Hoskins, B. F.; Orchard, S. D.; Robson, R. Dihydroxybenzoquinone and Chloranilic Acid Derivatives of Rare Earth Metals. *J. Chem. Soc. Dalt. Trans.* **2002**, *2*, 1586−1594.
(28) Abrahams, B. F.; Coleiro, J.; Hoskins, B. F.; Robson, R. Gas hydrate-like pentagonal dodecahedral $M_2(H_2O)_{18}$ cages (M = lanthanide or Y) in 2,5-dihydroxybenzoquinone-derived coordination polymers. *Chem. Commun.* **1996**, *0*, 603−604.
(29) Nakabayashi, K.; Ohkoshi, S. I. Monometallic Lanthanoid Assembly Showing Ferromagnetism with a Curie Temperature of 11 K. *Inorg. Chem.* **2009**, *48*, 8647−8649.
(30) Nakabayashi, K.; Ohkoshi, S. Poly[[hexaaquatris[μ_2-2,5-Dihydroxy-1,4-benzoquinonato(2−)]diholmium(III)] Octadecahydrate]. *Acta Crystallogr., Sect. E: Struct. Rep. Online* **2010**, *66*, m1300−m1300.
(31) Demars, T.; Boltoeva, M.; Vigier, N.; Maynadié, J.; Ravaux, J.; Genre, C.; Meyer, D. From Coordination Polymers to Doped Rare-Earth Oxides. *Eur. J. Inorg. Chem.* **2012**, *2012*, 3875−3884.
(32) Benmansour, S.; Pérez-Herráez, I.; López-Martínez, G.; Gómez García, C. J. Solvent-Modulated Structures in Anilato-Based 2D Coordination Polymers. *Polyhedron* **2017**, *135*, 17−25.
(33) Kitagawa, S. Coordination Compounds of 1,4-Dihydroxybenzoquinone and Its Homologues. Structures and Properties. *Coord. Chem. Rev.* **2002**, *224*, 11−34.
(34) Atzori, M.; Marchio, L.; Clérac, R.; Serpe, A.; Deplano, P.; Avarvari, N.; Mercuri, M. L. Hydrogen-Bonded Supramolecular Architectures Based on Tris(Hydranilato)Metallate(III) (M = Fe, Cr) Metallotectons. *Cryst. Growth Des.* **2014**, *14*, 5938−5948.
(35) Atzori, M.; Artizzu, F.; Marchiò, L.; Loche, D.; Caneschi, A.; Serpe, A.; Deplano, P.; Avarvari, N.; Mercuri, M. L. Switching-on Luminescence in Anilate-Based Molecular Materials. *Dalt. Trans.* **2015**, *44*, 15786−15802.
(36) Gómez-Claramunt, P.; Benmansour, S.; Hernández-Paredes, A.; Cerezo-Navarrete, C.; Rodríguez-Fernández, C.; Canet-Ferrer, J.; Cantarero, A.; Gómez-García, C. Tuning the Structure and Properties of Lanthanoid Coordination Polymers with an Asymmetric Anilato Ligand. *Magnetochemistry* **2018**, *4*, 6−27.
(37) Ye, H. Q.; Li, Z.; Peng, Y.; Wang, C. C.; Li, T. Y.; Zheng, Y. X.; Sapelkin, A.; Adamopoulos, G.; Hernández, I.; Wyatt, P. B.; et al. Organo-Erbium Systems for Optical Amplification at Telecommunications Wavelengths. *Nat. Mater.* **2014**, *13*, 382−386.

DOI: 10.1021/acs.chemmater.8b03399
Chem. Mater. 2018, 30, 6575−6586

(38) Eliseeva, S. V.; Bünzli, J. C. G. Lanthanide Luminescence for Functional Materials and Bio-Sciences. *Chem. Soc. Rev.* **2010**, *39*, 189−227.
(39) Li, J.-G.; Li, J.; Wang, X.; Zhu, Q.; Li, X.; Kim, B.-N.; Sun, X. Two-Step Crystallization of a Phase-Pure $Ln_2(OH)_5NO_3 \cdot nH_2O$ Layered Compound for the Smallest Ln Ions of Tm, Yb and Lu, Anion Exchange, and Exfoliation. *Dalt. Trans.* **2017**, *46*, 12683−12691.
(40) Araki, T.; Kondo, A.; Maeda, K. The First Lanthanide Organophosphonate Nanosheet by Exfoliation of Layered Compounds. *Chem. Commun.* **2013**, *49*, 552−554.
(41) Xu, H.; Gao, J.; Qian, X.; Wang, J.; He, H.; Cui, Y.; Yang, Y.; Wang, Z.; Qian, G. Metal-Organic Framework Nanosheets for Fast-Response and Highly Sensitive Luminescent Sensing of Fe^{3+}. *J. Mater. Chem. A* **2016**, *4*, 10900−10905.
(42) Horcas, I.; Fernández, R.; Gómez-Rodríguez, J. M.; Colchero, J.; Gómez-Herrero, J.; Baro, A. M. WSXM: A Software for Scanning Probe Microscopy and a Tool for Nanotechnology. *Rev. Sci. Instrum.* **2007**, *78*, 013705.
(43) Leith, D. Drag on Nonspherical Objects. *Aerosol Sci. Technol.* **1987**, *6*, 153−161.
(44) Zhao, M.; Wang, Y.; Ma, Q.; Huang, Y.; Zhang, X.; Ping, J.; Zhang, Z.; Lu, Q.; Yu, Y.; Xu, H.; et al. Ultrathin 2D Metal-Organic Framework Nanosheets. *Adv. Mater.* **2015**, *27*, 7372−7378.
(45) Lebedev, O. I.; Millange, F.; Serre, C.; Van Tendeloo, G.; Férey, G. First Direct Imaging of Giant Pores of the Metal-Organic Framework MIL-101. *Chem. Mater.* **2005**, *17*, 6525−6527.
(46) Hu, J.-Y.; Ning, Y.; Meng, Y.-S.; Zhang, J.; Wu, Z.-Y.; Gao, S.; Zhang, J.-L. Highly near-IR Emissive Ytterbium(III) Complexes with Unprecedented Quantum Yields. *Chem. Sci.* **2017**, *8*, 2702−2709.
(47) Lower, S. K.; El-Sayed, M. A. The Triplet State and Molecular Electronic Processes in Organic Molecules. *Chem. Rev.* **1966**, *66*, 199−241.
(48) Quochi, F.; Saba, M.; Artizzu, F.; Mercuri, M. L.; Deplano, P.; Mura, A.; Bongiovanni, G. Ultrafast Dynamics of Intersystem Crossing and Resonance Energy Transfer in Er(III)-Quinolinolate Complexes. *J. Phys. Chem. Lett.* **2010**, *1*, 2733−2737.
(49) Yang, J.; Diemeer, M. B. J.; Sengo, G.; Pollnau, M.; Driessen, A. Nd-Doped Polymer Waveguide Amplifiers. *IEEE J. Quantum Electron.* **2010**, *46*, 1043−1050.
(50) Artizzu, F.; Quochi, F.; Saba, M.; Loche, D.; Mercuri, M. L.; Serpe, A.; Mura, A.; Bongiovanni, G.; Deplano, P. Silica Sol−gel Glasses Incorporating Dual-Luminescent Yb Quinolinolato Complex: Processing, Emission and Photosensitising Properties of the "antenna" Ligand. *Dalt. Trans.* **2012**, *41*, 13147−13153.
(51) Quochi, F.; Artizzu, F.; Saba, M.; Cordella, F.; Mercuri, M. L.; Deplano, P.; Loi, M. A.; Mura, A.; Bongiovanni, G. Population Saturation in Trivalent Erbium Sensitized by Organic Molecular Antennae. *J. Phys. Chem. Lett.* **2010**, *1*, 141−144.
(52) Sun, Q.; Yan, P.; Niu, W.; Chu, W.; Yao, X.; An, G.; Li, G. NIR Luminescence of a Series of Benzoyltrifluoroacetone Erbium Complexes. *RSC Adv.* **2015**, *5*, 65856−65861.
(53) Ye, H. Q.; Peng, Y.; Li, Z.; Wang, C. C.; Zheng, Y. X.; Motevalli, M.; Wyatt, P. B.; Gillin, W. P.; Hernández, I. Effect of Fluorination on the Radiative Properties of Er^{3+} Organic Complexes: An Opto-Structural Correlation Study. *J. Phys. Chem. C* **2013**, *117*, 23970−23975.
(54) Quochi, F.; Orrù, R.; Cordella, F.; Mura, A.; Bongiovanni, G.; Artizzu, F.; Deplano, P.; Mercuri, M. L.; Pilia, L.; Serpe, A. Near Infrared Light Emission Quenching in Organolanthanide Complexes. *J. Appl. Phys.* **2006**, *99*, 053520.
(55) Tan, R. H. C.; Motevalli, M.; Abrahams, I.; Wyatt, P. B.; Gillin, W. P. Quenching of IR Luminescence of Erbium, Neodymium, and Ytterbium β-Diketonate Complexes by Ligand C-H and C-D Bonds. *J. Phys. Chem. B* **2006**, *110*, 24476−24479.
(56) Monguzzi, A.; Milani, A.; Mech, A.; Brambilla, L.; Tubino, R.; Castellano, C.; Demartin, F.; Meinardi, F.; Castiglioni, C. Predictive Modeling of the Vibrational Quenching in Emitting Lanthanides Complexes. *Synth. Met.* **2012**, *161*, 2693−2699.
(57) Rocha, J.; Brites, C. D. S.; Carlos, L. D. Lanthanide Organic Framework Luminescent Thermometers. *Chem. - Eur. J.* **2016**, *22*, 14782−14795.

DOI: 10.1021/acs.chemmater.8b03399
Chem. Mater. 2018, 30, 6575−6586

Inorganic Chemistry

Article

pubs.acs.org/IC

Synthesis and Physical Properties of Purely Organic BEDT-TTF-Based Conductors Containing Hetero-/Homosubstituted Cl/CN-Anilate Derivatives

Suchithra Ashoka Sahadevan,[†,‡] Noemi Monni,[†] Alexandre Abhervé,[‡] Pascale Auban-Senzier,[§] Enric Canadell,[∥] Maria Laura Mercuri,*[,†] and Narcis Avarvari*[,‡]

[†]Dipartimento di Scienze Chimiche e Geologiche, Università degli Studi di Cagliari, S.S. 554-Bivio per Sestu, I09042 Monserrato (Cagliari), Italy

[‡]Laboratoire MOLTECH-Anjou UMR 6200, UFR Sciences, CNRS, Université d'Angers, Bât. K, 2 Bd. Lavoisier, 49045 Angers, France

[§]Laboratoire de Physique des Solides, UMR 8502, CNRS-Université Paris-Sud, Bât. 510, 91405 Orsay, France

[∥]Institut de Ciència de Materials de Barcelona (CSIC), Campus de la UAB, E-08193 Bellaterra, Spain

S *Supporting Information*

ABSTRACT: Radical cation salts composed of a bis(ethylenedithio)-tetrathiafulvalene (ET) donor with homo-/heterosubstituted Cl/CN anilic acids as purely organic molecular conducting materials formulated as [BEDT-TTF]$_2$[HClCNAn] (**1**) and [BEDT-TTF][HCl$_2$An] (**2**) have been prepared by electrocrystallization. Compounds **1** and **2** crystallized in the monoclinic space group *P*2/*c* for **1** and *I*2/*a* for **2**, showing segregated donor-anion layers arranged in a α'-type donor packing pattern (**1**) and twisted parallel columns (**2**), respectively. Single-crystal conductivity measurements show that **1** is a semiconductor with room-temperature conductivity of 10^{-2} S cm^{-1} and an activation energy E_a of 1900 K.

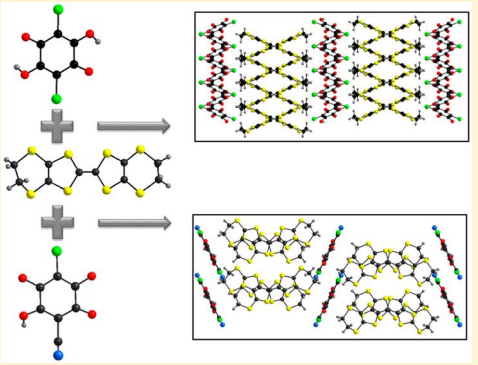

1. INTRODUCTION

During the last 40 years molecular conductors have remarkably attracted the interest of material scientists since the pioneering work of Ferraris et al.,[1] where the tetrathiafulvalene (TTF) organic donor was combined with the tetracyanoquinodimethane (TCNQ) organic acceptor, yielding the charge transfer complex (TTF)(TCNQ). The new compound showed unique conducting properties comparable to those of a classical metal,[1] which have never been observed before in a purely organic material. Nevertheless, compounds containing radical species, e.g. TTF$^{\bullet+}$Cl$^-$ salt[2] or TCNQ-based systems with different metal cations,[3] were previously reported. With the aim of increasing the intermolecular interactions between the units that are responsible for the conducting properties, several TTF-based derivatives have been subsequently explored. In particular, the bis(ethylenedithio)tetrathiafulvalene molecule (BEDT-TTF or ET, Chart 1) has been shown to be the most successful donor, affording the largest number of two-dimensional (2D) conducting materials,[4−6] ranging from Mott insulators and conductors to the majority of the known molecular superconductors. Most of these materials are formed of partially charged ET molecules and different types of closed-shell or magnetic inorganic anions,[4] while several examples of salts with organic ions such as polycyanocarbons,[7] fluoroalkyl sulfonates,[8] polynitrophenolates,[9] squarate and rhodizonate,[10] and haloanilates[11−13] have been described as well. Anilic acids (I; X = Cl, Br, I, NO$_2$, CN, etc.) are of special interest in the context of the band-filling control of organic conductors, since they give rise to anionic species with modulable charges such as monoanionic (II) and dianionic (III) forms, following a mono-

Chart 1. Compounds Discussed in the Text

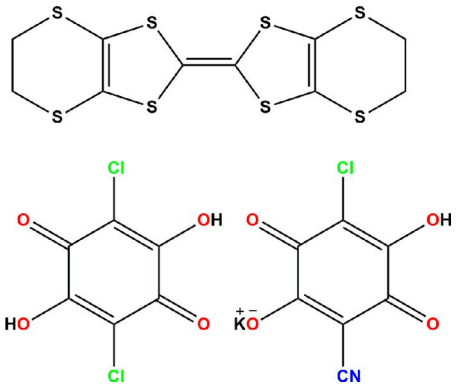

Received: August 9, 2017
Published: September 27, 2017

DOI: 10.1021/acs.inorgchem.7b01994
Inorg. Chem. 2017, 56, 12564−12571

or bis-deprotonation process of the two hydroxyl groups. The form III prevails in aqueous media due to the strong resonance stabilization of the negative charge (Scheme 1).

Scheme 1. Protonation Equilibria for a Generic Anilic Acid

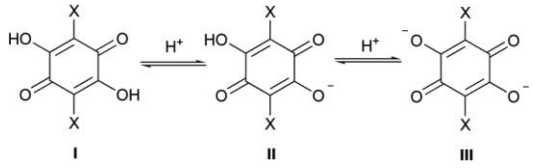

Moreover, the interest in anilic acids has been recently renewed, since they have been used as molecular building blocks for obtaining different types of functional materials such as organic ferroelectrics or as components in their dianionic forms III of multifunctional molecular materials showing peculiar physical properties.[12,14−21] In fact anilates are very attractive building blocks because of (i) their interesting redox properties,[22] (ii) their ability to mediate magnetic superexchange interactions when the ligand coordinates two metal ions in the 1,2-bis-bidentate coordination mode,[14] and (iii) the possibility of modulating the strength of this magnetic superexchange interaction by varying the substituents (X) on the 3,6-positions of the anilato ring.[23] Moreover, the presence of different substituents in the anilato moiety gives rise to intermolecular interactions such as H bonding, halogen bonding, $\pi-\pi$ stacking, and dipolar interactions, which may influence the physical properties of the resulting material. In this context cyananilic acid, bearing two CN groups, H-bonding acceptor sites, has afforded 2:1 salts in which it is present in the monoanionic form II, a 1D antiferromagnetic CT salt with the tetramethyl-TTF (TM-TTF) organic donor and a Mott insulator with ET, respectively.[12,13,24,25] As a progression of these studies, we focus our scientific efforts on fully organic TTF salts based on hetero- and homosubstituted anilate derivatives in order to investigate the influence of the different substituents on the physical properties of the resulting radical cation salts.

We report herein the synthesis by electrocrystallization, thorough structural analysis, Raman studies, and physical properties of radical cation salts based on BEDT-TTF and the heterosubstituted X = Cl/CN anilate (**1**) and the homosubstituted X = Cl anilate (**2**). Band structure calculations of compound **1** will be also discussed in order to correlate the structure with the conducting properties.

2. RESULTS AND DISCUSSION

Synthesis. The chlorocyananilic and chloroanilic acids were combined in electrocrystallization experiments with the ET donor, using the same reagent stoichiometric ratios and solvent mixture at different current densities. Two crystalline salts formulated as $[BEDT\text{-}TTF]_2[HClCNAn]$ (**1**) and $[BEDT\text{-}TTF][HCl_2An]$ (**2**) were obtained.

Crystal Structures. The compound **1** crystallizes in the monoclinic space group *P*2/c. It consists of two BEDT-TTF donor molecules for one monoanionic $(HClCNAn)^-$ unit, with one independent donor and half of the anion in the asymmetric unit (Figure S1 in the Supporting Information). The structure of the anion is planar with two different C−O distances, corresponding to two C═O bonds (1.215(8) Å) and two C−O bonds for one C−OH and one $C-O^-$ (intermediate value of 1.287(8) Å), which was expected as we started from the monoanionic salt KHClCNAn (Table S1 in the Supporting Information). As there is only one crystallographically independent molecule of BEDT-TTF for half an $(HClCNAn)^-$ anion, the average charge of each donor molecule is +0,5. This is consistent with the analysis of the bond lengths according to the procedure described by Day et al.,[26] which consists of the empirical equation $Q = 6.347 - 7.463\delta$, relating the charge Q to the parameter δ defined by $\delta = (b + c) - (a + d)$, where a–d represent averaged values of C═C and five-membered-ring C−S bonds, as illustrated in Table 1. Thus, the Q value for **1**

Table 1. Bond Distance Analysis for the BEDT-TTF Molecule in 1 and 2

		1	2
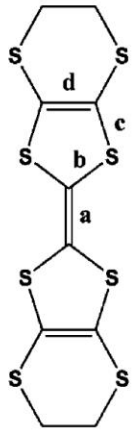	a	1.355(8)	1.367(6)
	b	1.738(6)	1.731(3)
		1.739(7)	1.742(3)
		1.730(7)	
		1.739(6)	
	c	1.751(6)	1.746(3)
		1.746(6)	1.742(3)
		1.751(7)	
		1.749(6)	
	d	1.330(10)	1.352(4)
		1.322(9)	
δ = (b+c) - (a+d)	δ	0.8047	0.7625
Q = 6.347 - 7.4638·δ	Q	0.34	0.66

amounts to +0.34 ± 0.1, clearly indicating a mixed valence state for the BEDT-TTF donors. With the knowledge that the estimated charge is very sensitive to the crystal quality, the difference from the expected value of +0.5 is not surprising. The crystal packing shows segregation of BEDT-TTF molecules in the *ac* plane separated by layers of $(HClCNAn)^-$ and chains of organic donors along the *a* axis (Figure 1). The BEDT-TTF molecules inside a chain do not have the same orientation, the intrachain interactions being of the twisted mode (Figure 1 and Figure S2 in the Supporting Information). Due to the different types of interactions, the donor layer contains dimers of BEDT-TTF, for which we observe strong S···H hydrogen bonds between the terminal ethylenedithio groups and short S···S intermolecular contacts (Table S2 in the Supporting Information). Similar to the case for the donor layer, in the anilate layer one can observe chains of $(HClCNAn)^-$ molecules along the *a* axis, with strong interactions via hydrogen bonds between C═O and C−OH/$C-O^-$ groups (Figure S3 and Table S3 in the Supporting Information).

Since the anion is located on an inversion center, the Cl and CN substituents are disordered with an sof value of 0.5. Finally, both chloro and cyano substituents present two types of interactions: one interchain interaction with a $(HClCNAn)^-$

DOI: 10.1021/acs.inorgchem.7b01994
Inorg. Chem. 2017, 56, 12564−12571

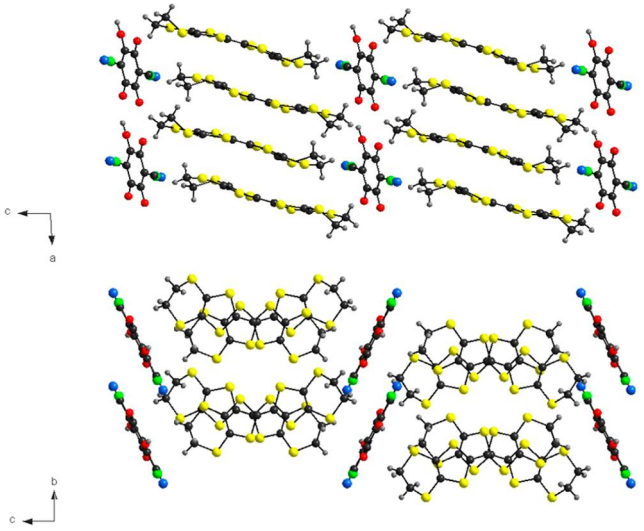

Figure 1. View of the crystal structure of **1** along the *b* axis (top) and *a* axis (bottom). Color code: C, black; H, gray; N, blue; O, red; S, yellow; Cl, green.

from the upper and lower chains and one hydrogen bond with an ethylenedithio group from the neighboring BEDT-TTF molecules (Figure 2).

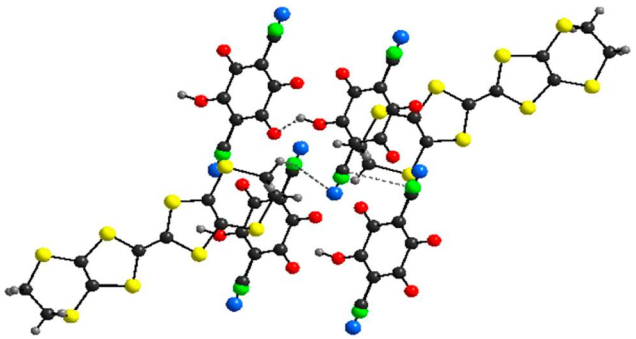

Figure 2. Intermolecular interactions (dashed lines) in the structure of **1**. Color code: C, black; H, gray; N, blue; O, red; S, gold; Cl, light green.

Compound **2** crystallizes in the monoclinic space group *I*2/*a*, with one independent half of the donor and half of the anion both located on inversion centers in the asymmetric unit, thus affording a 1:1 stoichiometry (Figure S4 in the Supporting Information). Similar to the case for **1**, the two independent C−O distances in the anilate molecule are consistent with the presence of two C═O (1.235(4) Å) and two C−O(H) bonds (1.294(4) Å). Since the electrocrystallization experiment was started with the chloranilic acid H_2Cl_2An, one can conclude that partial deprotonation occurred during the process. As the stoichiometry of the salt is 1:1, one could argue that the anilate is under its monoanionic form II, and thus the donor would bear the charge +1. However, the inspection of the central C═C (1.367(6) Å) and internal C−S bonds (Table S4 in the Supporting Information; see also Table 1) of the donor would be more in favor of a mixed valence state, all the more since the crystal structure is of excellent quality. Interestingly, the crystal packing shows donor/anion segregation in the *ac* plane, with formation of uniform chains of BEDT-TTF with no dimerization, separated by layers of anilate anions (Figure 3

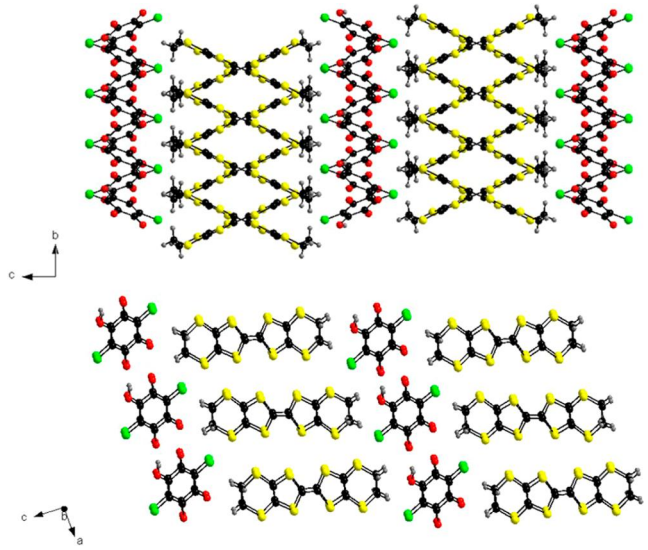

Figure 3. View of the crystal structure of **2** along the *a* axis (top) and *b* axis (bottom). Color code: C, black; H, gray; O, red; S, gold; Cl, light green.

and Figure S5 in the Supporting Information). In the donor layers, the chains develop along the *b* axis especially through CH···S intermolecular interactions. The intrachain S···S distances are rather long, with the shortest contact amounting to 3.93 Å for S2···S4. Lateral interchain S···S contacts established between donors from neighboring chains are much shorter, ranging from 3.44 to 3.74 Å (Table S5 in the Supporting Information). The BEDT-TTF molecules lie parallel to one another along the *b* axis, but the orientation between donors from adjacent chains is twisted by 45°. This peculiar orientation implies that one BEDT-TTF donor establishes short S···S contacts with three donors from a neighboring chain. The same type of packing is observed for the anilate layer (Figure S6 in the Supporting Information), although the $(HCl_2An)^-$ molecule is engaged in several interchain interactions with the neighboring anionic molecules, through hydrogen bonds between C═O and C−OH groups (Table S6 in the Supporting Information). Finally, S···Cl donor−anion interactions are observed as well between the chloro substituents and the S atoms of ethylenedithio groups from the neighboring BEDT-TTF molecules (Figure 4).

Raman Studies. Raman measurements were performed on compounds **1** and **2** in order to gain information on the

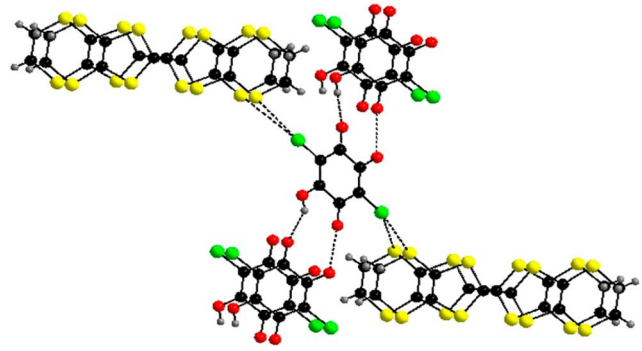

Figure 4. Intermolecular anion−anion and anion−donor interactions (dashed lines) in the structure of **2**. Color code: C, black; H, gray; O, red; S, gold; Cl, light green.

DOI: 10.1021/acs.inorgchem.7b01994
Inorg. Chem. 2017, 56, 12564−12571

oxidation degree of BEDT-TTF molecules. An approximately linear dependence between the charge degree of the donor and the Raman-active C═C stretching frequencies in insulating, conducting, and superconducting BEDT-TTF-based salts has previously been established.[27] The two totally symmetric Raman-active C═C stretching modes aν_3 and aν_4, with almost equal contributions of the stretching vibrations of the lateral C═C bonds and the central C═C bond of the BEDT-TTF donor, found in the 1400−1500 cm^{-1} range in most of the known BEDT-TTF-based salts, have been used as charge-sensitive vibrational probes. Raman spectra of **1** and **2** are reported in Figure 5. **1** shows a strong peak at 1470 cm^{-1} that

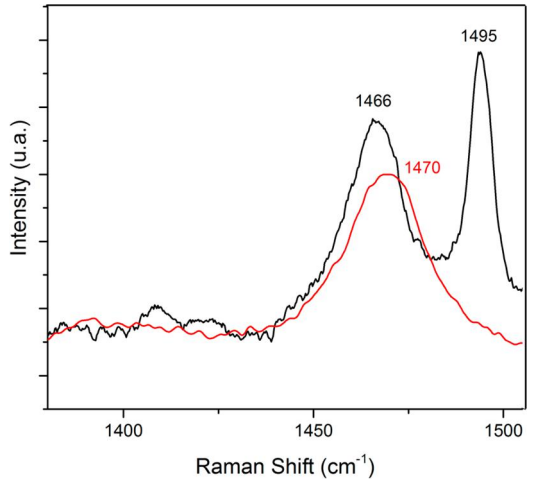

Figure 5. Raman spectra of **1** (red line) and **2** (black line) performed with a He−Ne laser (λ = 632.81 nm).

can be assigned to the totally symmetric C═C stretching vibration aν_4 of the BEDT-TTF molecule, which is consistent with the observed 2:1 stoichiometry of this salt, where the donor possesses a +0.5 charge state. Two peaks at 1466 and 1495 cm^{-1} are observed instead in the Raman spectrum of **2** that may be assigned to the aν_4 and aν_3 totally symmetric C═C stretching vibrations of the BEDT-TTF molecule in a partial oxidation state. This is consistent with the Q value calculated by the bond distance analysis from the X-ray data (Table 1), suggesting a mixed valence (mixed protonation) character for compound **2**.

Transport Properties and Band Structure Calculations. As the crystals of compound **2** were too small, conductivity measurements were performed only on single crystals of compound **1**. The room-temperature conductivity value of 2 × 10^{-2} S cm^{-1} for **1** is typical for a semiconductor. The temperature dependence of the resistivity indicates an activated regime (Figure 6).

The Arrhenius plot of ln ρ vs $1/T$ shows a linear behavior that can be fitted to the law ln ρ = ln ρ_0 + E_a/T with an activation energy E_a of 1900 K.

In order to get deeper insight into the activated conductivity of compound **1**, tight-binding band structure calculations of the extended Hückel type were performed. The donor layers of compound **1** contain two symmetry-equivalent molecules making four different intermolecular interactions (labeled I−IV in Figure 7). The S···S contacts smaller than 4.0 Å associated with the different interactions are reported in Table 2. There are two intrachain (I and II) and two interchain (III and IV) interactions. The intrachain interactions are of the twisted

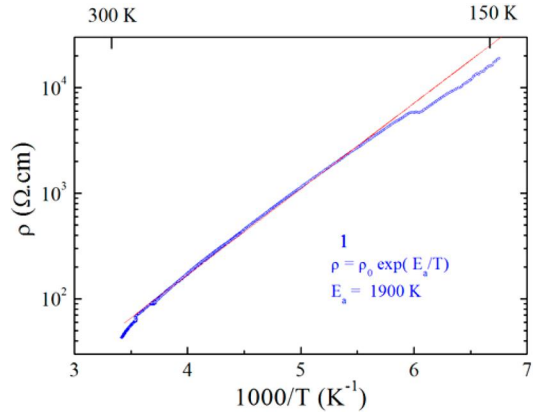

Figure 6. Electrical resistivity ρ for single crystals of compounds **1** plotted as log ρ versus the inverse temperature. The red line is the fit to the data with the law $\rho = \rho_0 \exp(E_a/T)$ giving the activation energy E_a.

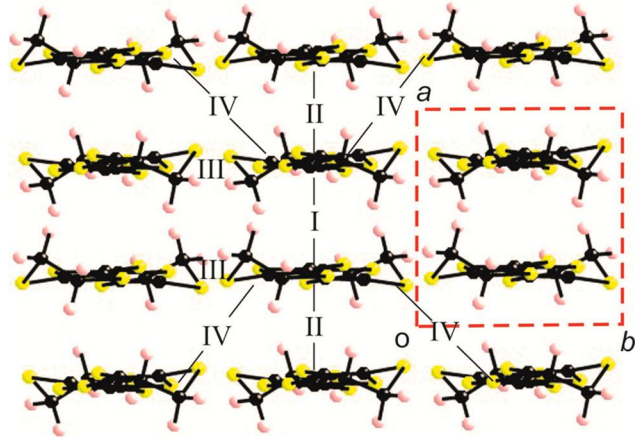

Figure 7. Donor layer of the salt **1** where the four different intermolecular interactions are labeled.

Table 2. S···S Distances Shorter Than 4.0 Å and Absolute Values of the $\beta_{HOMO-HOMO}$ Interaction Energies (eV) for the Different Donor···Donor Interactions in Compound 1 at Room Temperature

interaction	S···S (<4.0 Å)	$\lvert\beta_{HOMO-HOMO}\rvert$ (eV)
I	3.608 (×2), 3.661 (×2), 3.886 (×2), 3.933	0.4177
II	3.822 (×2), 3.847 (×2), 3.852, 3.902	0.2170
III	3.561, 3.566, 3.577, 3.586, 3.848	0.1224
IV	3.953	0.0436

mode, although the two interactions are not exactly of the same type. The shift of the center of the two C═C bonds is small for interaction I but considerably larger for interaction II. As a result, the C−H group of the terminal ethylenedithio groups pointing toward the other donor makes four S···H hydrogen bonds in interaction I (3.020 (×2), 3.046 (×2) Å) but two in interaction II (2.971 (×2) Å). This leads to a series of noticeably shorter S···S interactions and a tighter HOMO−HOMO overlap for interaction I (i.e., the S atoms of the five-membered rings, which are those bearing the stronger coefficients in the HOMO, are those associated with the shorter S···S contacts). In the understanding of the transport properties of this salt we need to have a hint as to the strength

DOI: 10.1021/acs.inorgchem.7b01994
Inorg. Chem. 2017, 56, 12564−12571

of the HOMO···HOMO interactions for I–IV, since there are the HOMO bands which are going to be partially emptied by oxidation. This may be done by looking at the absolute value of the so-called HOMO···HOMO interaction energy, $|\beta_{HOMO-HOMO}|$, associated with each interaction.[28] The calculated values for the four interactions are reported in Table 2.

In agreement with the previous structural analysis the strength of interaction I is twice as strong as interaction II. Thus, the chains are strongly dimerized as far as the HOMO···HOMO interactions are concerned. The coupling between these chains depends on the strength of interactions III and IV. Interaction III is associated with the shorter S···S contacts. However, these contacts are of the lateral type associated with moderate π type interactions so that the interaction is only modest. Finally, interaction IV is not very favorable in terms of both distance and orientation, its value thus being much smaller. However, every donor is associated with two of these interactions at both ends of the donor. Because of these interactions, the intrachain and interchain interactions are interrelated. Thus, the donor layers of compound **1** may be described as a series of fairly interacting strongly dimerized chains along *a*.

The previous analysis is substantiated by the calculated band structure shown in Figure 8. The band structure along the chain

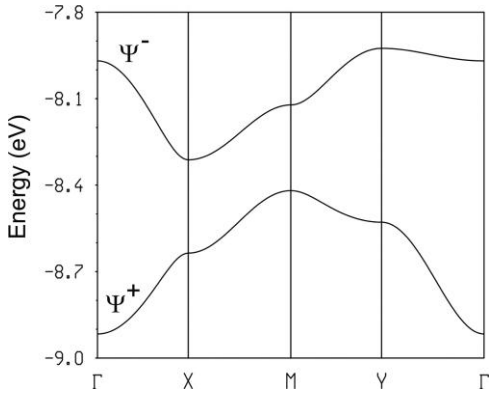

Figure 8. Calculated band structure for the donor layers of compound **1** where Γ = (0, 0), X = (a^*/2, 0), Y = (0, b^*/2), M = (a^*/2, b^*/2), and S = (−a^*/2, b^*/2).

direction (Γ–X) shows two bands with opposite curvature with a large dimerization gap at X, as expected for a strongly dimerized chain. Consequently, the upper band is built from the antibonding combination of the two HOMO orbitals (ψ^-) of the dimer associated with interaction I, whereas the lower band is built from the bonding combination (ψ^+). In addition, the full dispersion of the upper band is almost the same as that along the chain direction, whereas for the lower band the full dispersion is considerably larger than the dispersion along the chain. This means that the interchain interactions have a relatively small influence on the interactions of the antibonding ψ^- orbital of the dimers of different chains but noticeably affect those of the bonding ψ^+ orbital. In the upper band interactions III and IV tend to cancel along a large part of the Brillouin zone, whereas in the lower band they add up. This is very clear when one looks, for instance, at the Γ–Y direction (i.e., the interchain direction) in Figure 8. Ultimately this is due to the bonding vs antibonding character of the ψ^+ and ψ^- orbitals of the dimers.

The previous observations are relevant in understanding the origin of the activated conductivity of **1**. Because of the 2:1 stoichiometry and the fact that the anion carries a single negative charge, the HOMO bands must contain one hole. Thus, the lower HOMO band in Figure 8 is full and the upper is half filled. Consequently, the activated conductivity is not a consequence of the occurrence of a gap in the band structure but of the localization of electrons in the upper band. This is likely because of the strong dimerization and the weak interaction between the dimeric units of the layer as far as the ψ orbital is concerned. In other words, the electrons tend to stay localized in the antibonding ψ^- orbital of the dimeric units (interaction I), according to the so-called Mott localization mechanism, and an activation energy is required to jump between units. The occurrence of disorder does not seem to play an important role in triggering the localization. The particular nature of the donor lattice, with both a strong dimerization along the chains and competing interdimer interactions, lies at the origin of the activated conductivity of this salt.

3. CONCLUSIONS

Two radical cation salts based on BEDT-TTF and the organic anions chlorocyanoanilate and chloranilate have been prepared by electrocrystallization starting from the monopotassic chlorocyanoanilate salt and the chloroanilic acid, respectively. While for the first anion a 2:1 salt crystallized with a clear mixed valence state for the donor and −1 charge for the anion, the second salt showed a 1:1 stoichiometry. In both compounds donor–anion segregation occurs, with an arrangement of the donor molecules either in a α'-type donor packing pattern or in parallel columns twisted by 45° with respect to each other, respectively. The anions play a very important role, as they can tune the oxidation state of BEDT-TTF by the deprotonation degree and influence the solid-state architecture through establishment of a complex set on intermolecular interactions. The salt $(BEDT\text{-}TTF)_2(HClCNAn)$ shows activated conductivity supported by band structure calculations which suggest a Mott localization to explain the semiconducting behavior. The salt $(BEDT\text{-}TTF)(HCl_2An)$ is rather intriguing, as the bond distances within the donor are in agreement with a partial oxidation state of BEDT-TTF which would involve an incomplete deprotonation of the starting chloranilic acid, and no dimerization is observed within the chains. The balance between charge transfer on the donor and deprotonation degree of the acid in this compound is worthy of further investigation together with its conducting properties. Moreover, a combination of other BEDT-TTF related donors, including chiral ones,[21,29–31] with diverse hetero-/homosubstituted anilates is envisaged in our groups.

EXPERIMENTAL SECTION

General Considerations. KHClCNAn was synthesized according to the literature procedure.[32] BEDT-TTF was prepared following the Larsen procedure.[33] H_2Cl_2An was purchased (Sigma-Aldrich). Crystals were grown by the electrocrystallization technique. Solvents used for electrocrystallization experiments (HPLC grade) were dried under basic alumina and degassed with argon prior to use.

Synthesis. *[BEDT-TTF]$_2$[HClCNAn] (1).* KHClCNAn was dissolved in 8 mL of CH_2Cl_2 and placed in the cathode chamber of an H-shaped electrocrystallization cell. BEDT-TTF (5 mg) was dissolved in 8 mL of CH_2Cl_2 and placed in the anode chamber of the cell. A current density of 0.5 μA cm^{-2} was applied. Black prismatic single crystals of **1** were

DOI: 10.1021/acs.inorgchem.7b01994
Inorg. Chem. 2017, 56, 12564–12571

grown at 20 °C on the anode surface of a platinum-wire electrode over a period of 2 weeks.

*[BEDT-TTF][HCl_2An] (**2**).* H_2Cl_2An was dissolved in 8 mL of CH_2Cl_2 and placed in the cathode chamber of an H-shaped electrocrystallization cell. BEDT-TTF (5 mg) was dissolved in 8 mL of CH_2Cl_2 and placed in the anode chamber of the cell. A current density of 0.3 μA cm^{-2} was applied. Black prismatic single crystals of **2** were grown at 20 °C on the anode surface of a platinum-wire electrode over a period of 2 weeks.

X-ray Crystallography. Single crystals of the compounds were mounted on glass fiber loops using a viscous hydrocarbon oil to coat the crystal. Data collection was performed at 293 K on an Agilent Supernova instrument with Cu Kα radiation (λ = 1.54184 Å). The structures were solved by direct methods with the SIR97 program and refined against all F^2 values with the SHELXL-97 program using the WinGX graphical user interface. All non-hydrogen atoms were refined anisotropically except as noted, and hydrogen atoms were placed in calculated positions and refined isotropically with a riding model. A summary of crystallographic data and refinement results is given in Table 3.

Table 3. Crystallographic Data for Compounds 1 and 2

	1	2
empirical formula	$C_{27}H_{17}NO_4S_{16}Cl$	$C_{16}H_9O_4S_8Cl_2$
fw	967.83	592.61
cryst color	black	brown
cryst size (mm^3)	0.15 × 0.15 × 0.03	0.10 × 0.05 × 0.03
temp (K)	293.00(10)	293.00(10)
wavelength (Å)	1.54184	1.54184
cryst system, Z	monoclinic, 2	monoclinic, 2
space group	$P2/c$	$I2/a$
a (Å)	7.6647(3)	13.2766(4)
b (Å)	6.7891(3)	4.12130(10)
c (Å)	34.1205(12)	38.5124(15)
α (deg)	90	90
β (deg)	93.593(3)	92.935(3)
γ (deg)	90	90
V (Å^3)	1772.02(12)	2104.51(12)
ρ_{calc} (g cm^{-3})	1.814	1.870
μ(Cu Kα) (mm^{-1})	10.111	10.435
θ range (deg)	2.60–73.85	4.60–73.43
no. of data collected	14654	6871
no. of unique data	3555	2086
no. of obsd data	3381	1902
R(int)	0.0279	0.0389
no. of params/restraints	234/0	140/0
R1(F),[a] $I > 2\sigma(I)$	0.0775	0.0412
wR2(F^2),[b] all data	0.1711	0.1327
$S(F^2)$,[c] all data	1.244	1.106

[a] $R1(F) = \sum||F_o| - |F_c||/\sum|F_o|$. [b] $wR2(F^2) = [\sum w(F_o^2 - F_c^2)^2/\sum wF_o^4]^{1/2}$. [c] $S(F^2) = [\sum w(F_o^2 - F_c^2)^2/(n + r - p)]^{1/2}$.

Raman Measurements. Raman spectra were carried out at room temperature on single crystals by using a micro Raman spectrometer (Horiba Labram 300) equipped with a He–Ne laser (λ 632.81 nm) laser in the 80–2000 cm^{-1} range, with a 20 LWD objective (<0.25 mW/μm^2 on the crystal). A 180° reflective geometry was adopted. The samples were mounted on a glass microscope slide, and the scattering peaks were calibrated against a Si standard (n = 520.7 cm^{-1}). A typical spectrum was collected with a 300 s time constant at <1 cm^{-1} resolution and was averaged over three scans. No sample decomposition was observed during the experiments.

Single-Crystal Conductivity Measurements. Electrical transport measurements were performed on platelet-shaped single crystals. Gold contacts were evaporated on both faces of the crystals, and gold wires (17 μm diameter) were glued with silver paste on those contacts. Four-probe dc measurements were performed, applying a constant current of 1 μA and measuring the voltage using a Keithley 2401 source meter. Low temperature was provided by a homemade cryostat equipped with a 4 K pulse tube.

Band Structure Calculations. The tight-binding band structure calculations were of the extended Hückel type.[34] A modified Wolfsberg–Helmholtz formula[35] was used to calculate the non-diagonal $H_{\mu\nu}$ values. All valence electrons were taken into account in the calculations, and the basis set consisted of Slater-type orbitals of double-ζ quality for C 2s and 2p and S 3s and 3p and of single-ζ quality for H. The ionization potentials, contraction coefficients, and exponents were taken from previous work.[36]

■ ASSOCIATED CONTENT

Supporting Information

The Supporting Information is available free of charge on the ACS Publications website at DOI: 10.1021/acs.inorgchem.7b01994.

Additional figures and tables as mentioned in the text (PDF)

Accession Codes

CCDC 1566295–1566296 contain the supplementary crystallographic data for this paper. These data can be obtained free of charge via www.ccdc.cam.ac.uk/data_request/cif, or by emailing data_request@ccdc.cam.ac.uk, or by contacting The Cambridge Crystallographic Data Centre, 12 Union Road, Cambridge CB2 1EZ, UK; fax: +44 1223 336033.

■ AUTHOR INFORMATION

Corresponding Authors

*M.L.M.: e-mail, mercuri@unica.it; fax, (+39)0706754486; tel, (+39)0706754486.

*N.A.: e-mail, narcis.avarvari@univ-angers.fr; fax, (+33)02 41 73 5405; tel, (+33)02 41 73 50 84.

ORCID

Enric Canadell: 0000-0002-4663-5226

Narcis Avarvari: 0000-0001-9970-4494

Notes

The authors declare no competing financial interest.

■ ACKNOWLEDGMENTS

This work was supported in France by the CNRS, the University of Angers, the Erasmus program (mobility grant to N.M.), and the RFI Regional project LUMOMAT (grant to A.A.). The work in Italy was supported by the Fondazione di Sardegna-Convenzione triennale tra la Fondazione di Sardegna e gli Atenei Sardi, Regione Sardegna-L.R. 7/2007 annualità 2016-DGR 28/21 del 17.05.2015 "Innovative Molecular Functional Materials for Environmental and Biomedical Applicatons" and INSTM. Special thanks are due to Dr. Walter Marchione and Stefano Gai, HORIBA Italia S.r.l., for Raman measurements. E.C. acknowledges support by the MINECO (Spain) through Grant FIS2015-64886-C5-4-P and the Severo Ochoa Centers of Excellence Program (Grant SEV-2015-0496) as well as by Generalitat de Catalunya (2014SGR301).

■ REFERENCES

(1) Ferraris, J.; Cowan, D. O.; Walatka, V.; Perlstein, J. H. Electron Transfer in a New Highly Conducting Donor-Acceptor Complex. *J. Am. Chem. Soc.* **1973**, *95*, 948–949.

DOI: 10.1021/acs.inorgchem.7b01994
Inorg. Chem. 2017, 56, 12564–12571

(2) Wudl, F.; Smith, G. M.; Hufnagel, E. J. Bis-1,3-Dithiolium Chloride: An Unsually Stable Organic Radical Cation. *J. Chem. Soc. D* **1970**, 1453−1454.
(3) Siemons, W. J.; Bierstedt, P. E.; Kepler, R. G. Electronic Properties of a New Class of Highly Conductive Organic Solids. *J. Chem. Phys.* **1963**, *39*, 3523−3528.
(4) (a) Williams, J. M.; Ferraro, J. R.; Thorn, R. J.; Carlson, K. D.; Geiger, U.; Wang, H. H.; Kini, A. M.; Whangbo, M. H. In *Organic Superconductors: Synthesis, Structure, Properties and Theory*; Grimes, R. N., Ed.; Prentice Hall: Englewood Cliffs, NJ, 1992. (b) Coronado, E.; Day, P. Magnetic Molecular Conductors. *Chem. Rev.* **2004**, *104*, 5419−5448.
(5) Gómez-García, C. J.; Coronado, E.; Curreli, S.; Giménez-Saiz, C.; Deplano, P.; Mercuri, M. L.; Pilia, L.; Serpe, A.; Faulmann, C.; Canadell, E. A Chirality-Induced Alpha Phase and a Novel Molecular Magnetic Metal in the BEDT-TTF/tris(croconate)ferrate(III) Hybrid Molecular System. *Chem. Commun.* **2006**, 4931−4933.
(6) Coronado, E.; Curreli, S.; Giménez-Saiz, C.; Gómez-García, C. J.; Deplano, P.; Mercuri, M. L.; Serpe, A.; Pilia, L.; Faulmann, C.; Canadell, E. New BEDT-TTF/$[Fe(C_5O_5)_3]_3$- Hybrid System: Synthesis, Crystal Structure, and Physical Properties of a Chirality-Induced α Phase and a Novel Magnetic Molecular Metal. *Inorg. Chem.* **2007**, *46*, 4446−4457.
(7) Yamochi, H.; Tada, C.; Sekizaki, S.; Saito, G.; Kusunoki, M.; Sakaguchi, K.-I. Conductive Radical Cation Salts with Organic Anions of {RO-C[C(CN)$_2$]$_2$ }. *Mol. Cryst. Liq. Cryst. Sci. Technol., Sect. A* **1996**, *284*, 379−390.
(8) Dong, J.; Musfeldt, J. L.; Schlueter, J. A.; Williams, J. M.; Nixon, P. G. Optical Properties of β''-$(ET)_2SF_5CH_2CF_2SO_3$: A Layered Molecular Superconductor with Large Discrete Counterions. *Phys. Rev. B: Condens. Matter Mater. Phys.* **1999**, *60*, 4342.
(9) Nishimura, K.; Kondo, T.; Drozdova, O. O.; Yamochi, H.; Saito, G. Preparation of Metallic BEDT-TTF Charge Transfer Complex of 3,3′,5,5′-Tetranitro-4,4′-Biphenyldiol Dianion ($TNBP^{2-}$) Having Flexible Molecular Shape. *J. Mater. Chem.* **2000**, *10*, 911−919.
(10) Seitz, G.; Imming, P. Oxocarbons and Pseudooxocarbons. *Chem. Rev.* **1992**, *92*, 1227−1260.
(11) Murata, T.; Morita, Y.; Yakiyama, Y.; Fukui, K.; Yamochi, H.; Saito, G.; Nakasuji, K. Hydrogen-Bond Interaction in Organic Conductors: Redox Activation, Molecular Recognition, Structural Regulation, and Proton Transfer in Donor - Acceptor Charge-Transfer Complexes of TTF-Imidazole. *J. Am. Chem. Soc.* **2007**, *129*, 10837−10846.
(12) Zaman, M. B.; Toyoda, J.; Morita, Y.; Nakamura, S.; Yamochi, H.; Saito, G.; Nishimura, K.; Yoneyama, N.; Enoki, T.; Nakasuji, K. Preparation of a Mott Insulator Based on a BEDT-TTF Charge Transfer Complex of Hydrogen Cyananilate: A′-(BEDT-TTF)-2HCNAL. *J. Mater. Chem.* **2001**, *11*, 2211−2215.
(13) Zaman, M. B.; Toyoda, J.; Morita, Y.; Nakamura, S.; Yamochi, H.; Saito, G.; Nakasuji, K. Hydrogen-Bonded CT-Complex of Cyananilic Acid with OMTTF: $(OMTTF)_3(HCNAL)_2$. *Synth. Met.* **1999**, *102*, 1691−1692.
(14) Atzori, M.; Benmansour, S.; Mínguez Espallargas, G.; Clemente-León, M.; Abhervé, A.; Gómez-Claramunt, P.; Coronado, E.; Artizzu, F.; Sessini, E.; Deplano, P.; Serpe, A.; Mercuri, M. L.; Gómez García, C. J. A Family of Layered Chiral Porous Magnets Exhibiting Tunable Ordering Temperatures. *Inorg. Chem.* **2013**, *52*, 10031−10040.
(15) Atzori, M.; Pop, F.; Auban-Senzier, P.; Gómez-García, C. J.; Canadell, E.; Artizzu, F.; Serpe, A.; Deplano, P.; Avarvari, N.; Mercuri, M. L. Structural Diversity and Physical Properties of Paramagnetic Molecular Conductors Based on Bis(ethylenedithio)tetrathiafulvalene (BEDT-TTF) and the Tris(chloranilato)ferrate(III) Complex. *Inorg. Chem.* **2014**, *53*, 7028−7039.
(16) Mercuri, M. L.; Congiu, F.; Concas, G.; Sahadevan, S. A. Recent Advances on Anilato-Based Molecular Materials with Magnetic And/or Conducting Properties. *Magnetochemistry* **2017**, *3*, 17.
(17) Horiuchi, S.; Kumai, R.; Tokura, Y. High-Temperature and Pressure-Induced Ferroelectricity in Hydrogen-Bonded Supramolecular Crystals of Anilic Acids and 2,3-Di(2-Pyridinyl)pyrazine. *J. Am. Chem. Soc.* **2013**, *135*, 4492−4500.
(18) Kagawa, F.; Horiuchi, S.; Minami, N.; Ishibashi, S.; Kobayashi, K.; Kumai, R.; Murakami, Y.; Tokura, Y. Polarization Switching Ability Dependent on Multidomain Topology in a Uniaxial Organic Ferroelectric. *Nano Lett.* **2014**, *14*, 239−243.
(19) Murata, T.; Yakiyama, Y.; Nakasuji, K.; Morita, Y. Proton-Transfer Salts between an EDT-TTF Derivative Having Imidazole-Ring and Anilic Acids: Multi-Dimensional Networks by Acid−base Hydrogen-Bonds, π-Stacks and Chalcogen Atom Interactions. *CrystEngComm* **2011**, *13*, 3689−3691.
(20) Horiuchi, S.; Kumai, R.; Tokura, Y. Room-Temperature Ferroelectricity and Gigantic Dielectric Susceptibility on a Supramolecular Architecture of Phenazine and Deuterated Chloranilic Acid. *J. Am. Chem. Soc.* **2005**, *127*, 5010−5011.
(21) Atzori, M.; Pop, F.; Auban-Senzier, P.; Clérac, R.; Canadell, E.; Mercuri, M. L.; Avarvari, N. Complete Series of Chiral Paramagnetic Molecular Conductors Based on Tetramethyl-Bis(ethylenedithio)-Tetrathiafulvalene (TM-BEDT-TTF) and Chloranilate-Bridged Heterobimetallic Honeycomb Layers. *Inorg. Chem.* **2015**, *54*, 3643−3653.
(22) Ward, M. D.; McCleverty, J. a. Non-Innocent Behaviour in Mononuclear and Polynuclear Complexes: Consequences for Redox and Electronic Spectroscopic Properties. *J. Chem. Soc. Dalt. Trans.* **2002**, 275−288.
(23) Tinti, F.; Verdaguer, I. M.; Kahn, O.; Savariault, J. Interaction between Copper(II) Ions Separated by 7.6 A. Crystal Structure and Magnetic Properties of (Iodanilato)bis[(N,N,N′,N′-tetramethylethylenediamine)copper(II)]Diperchlorate. *Inorg. Chem.* **1987**, *26*, 2380−2384.
(24) Zaman, B.; Morita, Y.; Toyoda, J.; Yamochi, H.; Sekizaki, S.; Nakasuji, K. Convenient Preparation and Properties of 2, 5-Dichloro- and Benzoquinone (CDDQ and CBDQ): DDQ Analogs with Centrosymmetry. *Mol. Cryst. Liq. Cryst. Sci. Technol., Sect. A* **1996**, *287*, 249−254.
(25) Yamochi, H.; Nakamura, S.; Saito, G.; Zaman, M. B.; Toyoda, J.; Morita, Y.; Nakasuji, K.; Yamashita, Y. Cyananilate Anion as Hydrogen Bonded Counter Ion in Conducting CT Complexes. *Synth. Met.* **1999**, *102*, 1729.
(26) Guionneau, P.; Kepert, C. J.; Bravic, G.; Chasseau, D.; Truter, M.; Kurmoo, M.; Day, P. Determining the Charge Distribution in BEDT-TTF Salts. *Synth. Met.* **1997**, *86*, 1973−1974.
(27) (a) Wang, H. H.; Ferraro, J. R.; Williams, J. M.; Geiser, U.; Schlueter, J. A. Rapid Raman Spectroscopic Determination of the Stoichiometry of Microscopic Quantities of BEDT-ITF-Based Organic Conductors and Superconductors. *J. Chem. Soc., Chem. Commun.* **1994**, 1893−1894. (b) Girlando, A. Charge Sensitive Vibrations and Electron-Molecular Vibration Coupling in Bis(ethylenedithio)-tetrathiafulvalene (BEDT-TTF). *J. Phys. Chem. C* **2011**, *115*, 19371−19378.
(28) Whangbo, M.-H.; Williams, J. M.; Leung, P. C. W.; Beno, M. A.; Emge, T. J.; Wang, H. H. Role of the Intermolecular Interaction in the Two-Dimensional Ambient-Pressure Organic Superconductors B-$(ET)_2I_3$ and B-$(ET)_2IBr_2$. *Inorg. Chem.* **1985**, *24*, 3500−3502.
(29) Pop, F.; Auban-Senzier, P.; Canadell, E.; Rikken, G. L. J. A.; Avarvari, N. Electrical magneto-chiral anisotropy in a bulk chiral molecular conductor. *Nat. Commun.* **2014**, *5*, 3757.
(30) Pop, F.; Auban-Senzier, P.; Frąckowiak, A.; Ptaszyński, K.; Olejniczak, I.; Wallis, J. D.; Canadell, E.; Avarvari, N. Chirality Driven Metallic *versus* Semiconducting Behavior in a Complete Series of Radical Cation Salts Based on Dimethyl-Ethylenedithio-Tetrathiafulvalene (DM-EDT-TTF). *J. Am. Chem. Soc.* **2013**, *135*, 17176−17186.
(31) Pop, F.; Auban-Senzier, P.; Canadell, E.; Avarvari, N. Anion size control of the packing in the metallic versus semiconducting chiral radical cation salts (DM-EDT-TTF)$_2XF_6$ (X = P, As, Sb). *Chem. Commun.* **2016**, *52*, 12438−12441.
(32) Atzori, M.; Artizzu, F.; Marchiò, L.; Loche, D.; Caneschi, A.; Serpe, A.; Deplano, P.; Avarvari, N.; Mercuri, M. L. Switching-on luminescence in anilate-based molecular materials by substituent exchange. *Dalton Trans.* **2015**, *44*, 15786−15802.

DOI: 10.1021/acs.inorgchem.7b01994
Inorg. Chem. 2017, 56, 12564−12571

(33) Larsen, J.; Lenoir, C. Synthesis of Bis(ethylenedithio)-tetrathiafulvalene (BEDT-TTF). *Synthesis* **1989**, *1989*, 134.
(34) Whangbo, M.-H.; Hoffmann, R. The Band Structure of the Tetracyanoplatinate Chain. *J. Am. Chem. Soc.* **1978**, *100*, 6093−6098.
(35) Ammeter, J. H.; Bürgi, H.-B.; Thibeault, J.; Hoffmann, R. Counterintuitive Orbital Mixing in Semiempirical and ab Initio Molecular Orbital Calculations. *J. Am. Chem. Soc.* **1978**, *100*, 3686−3692.
(36) Pénicaud, A.; Boubekeur, K.; Batail, P.; Canadell, E.; Auban-Senzier, P.; Jérome, D. Hydrogen-bond tuning of macroscopic transport properties from the neutral molecular component site along the sries of metallic organic-inorganic solvates (BEDT-TTF)$_4$Re$_6$Se$_5$Cl$_9$.[guest], [guest = DMF, THF, dioxane]. *J. Am. Chem. Soc.* **1993**, *115*, 4101−4112.

DOI: 10.1021/acs.inorgchem.7b01994
Inorg. Chem. 2017, 56, 12564−12571

magnetochemistry

MDPI

Review

Recent Advances on Anilato-Based Molecular Materials with Magnetic and/or Conducting Properties

Maria Laura Mercuri [1,*], Francesco Congiu [2], Giorgio Concas [2] and Suchithra Ashoka Sahadevan [1]

[1] Dipartimento di Scienze Chimiche e Geologiche, Università degli Studi di Cagliari, S.S. 554—Bivio per'Sestu—I09042 Monserrato (CA), Italy; suchithra.sahadevan@unica.it

[2] Dipartimento di Fisica, Universitàdegli Studi di Cagliari, S.P. Monserrato'Sestu km 0,700—I09042 Monserrato (CA), Italy; franco.congiu@dsf.unica.it (F.C.); giorgio.concas@dsf.unica.it (G.C.)

* Correspondence: mercuri@unica.it; Tel./Fax: +39-70-675-4486

Academic Editor: Manuel Almeida

Received: 2 February 2017; Accepted: 7 April 2017; Published: 19 April 2017

Abstract: The aim of the present work is to highlight the unique role of anilato-ligands, derivatives of the 2,5-dioxy-1,4-benzoquinone framework containing various substituents at the 3 and 6 positions (X = H, Cl, Br, I, CN, etc.), in engineering a great variety of new materials showing peculiar magnetic and/or conducting properties. Homoleptic anilato-based molecular building blocks and related materials will be discussed. Selected examples of such materials, spanning from graphene-related layered magnetic materials to intercalated supramolecular arrays, ferromagnetic 3D monometallic lanthanoid assemblies, multifunctional materials with coexistence of magnetic/conducting properties and/or chirality and multifunctional metal-organic frameworks (MOFs) will be discussed herein. The influence of (i) the electronic nature of the X substituents and (ii) intermolecular interactions i.e., H-Bonding, Halogen-Bonding, π-π stacking and dipolar interactions, on the physical properties of the resulting material will be also highlighted. A combined structural/physical properties analysis will be reported to provide an effective tool for designing novel anilate-based supramolecular architectures showing improved and/or novel physical properties. The role of the molecular approach in this context is pointed out as well, since it enables the chemical design of the molecular building blocks being suitable for self-assembly to form supramolecular structures with the desired interactions and physical properties.

Keywords: benzoquinone derivatives; molecular magnetism; multifunctional molecular materials; spin-crossover materials; metal-organic frameworks

1. General Introduction

The aim of the present work is to highlight the key role of anilates in engineering new materials with new or improved magnetic and/or conducting properties and new technological applications. Only homoleptic anilato-based molecular building blocks and related materials will be discussed. Selected examples of para-/ferri-/ferro-magnetic, spin-crossover and conducting/magnetic multifunctional materials and MOFs based on transition metal complexes of anilato-derivatives, on varying the substituents at the 3,6 positions of the anilato moiety, will be discussed herein, whose structural features or physical properties are peculiar and/or unusual with respect to analogous compounds reported in the literature up to now. Their most appealing technological applications will be also reported.

Derivatives of the 2,5-dioxy-1,4-benzoquinone framework, containing various substituents at the 3 and 6 positions, constitute a well-known motif observed in many natural products showing important biological activities such as anticoagulant [1], antidiabetic [2], antioxidative [3], anticancer [4], etc. Structural modifications of the natural products afforded related compounds of relevant interest in medicinal chemistry [5,6]. Furthermore, the 2,5-dihyroxy-1,4-benzoquinone (DHBQ) represents the parent member of a family of organic compounds traditionally called anilic acids that, in their deprotonated dianionic form, act as valuable ditopic ligands towards transition metal ions [7].

Anilic acids are obtained when the hydrogens at the 3 and 6 positions of the DHBQ are replaced by halogen atoms or functional groups (see below). They can be formulated as $H_2X_2C_6O_4$ (H_2X_2An) where X indicates the substituent and C_6O_4 the anilate moiety (An). A summary of the anilic acids reported in the literature to the best of our knowledge is reported in Table 1.

Table 1. Names, molecular formulas and acronyms of the anilic acids reported in the literature to date.

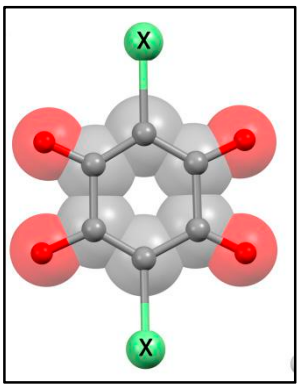

X_2An^{2-}

Substituent, X	Formula	Anilic Acid Name	Acronyms	Anilate Dianion Name	Acronyms	Ref.
H	$H_4C_6O_4$	Hydranilic acid	H_2H_2An	Hydranilate	H_2An^{2-}	[8–10]
F	$H_2F_2C_6O_4$	Fluoranilic acid	H_2F_2An	Fluoranilate	F_2An^{2-}	[11]
Cl	$H_2Cl_2C_6O_4$	Chloranilic acid	H_2Cl_2An	Chloranilate	Cl_2An^{2-}	[12,13]
Br	$H_2Br_2C_6O_4$	Bromanilic acid	H_2Br_2An	Bromanilate	Br_2An^{2-}	[14]
I	$H_2I_2C_6O_4$	Iodanilic acid	H_2F_2An	Iodanilate	I_2An^{2-}	[14]
NO_2	$H_2N_2C_6O_8$	Nitranilic acid	$H_2(NO_2)_2An$	Nitranilate	$(NO_2)_2An^{2-}$	[15]
OH	$H_4C_6O_6$	Hydroxyanilic acid	$H_2(OH)_2An$	Hydroxyanilate	$(OH_2)_2An^{2-}$	[16–20]
CN	$H_2N_2C_8O_4$	Cyananilic acid	$H_2(CN)_2An$	Cyananilate	$(CN)_2An^{2-}$	[21,22]
Cl/CN	$H_2ClNC_7O_4$	Chlorocyananilic acid	$H_2ClCNAn$	Chlorocyananilate	$ClCNAn^{2-}$	[23]
NH_2	$H_6N_2C_6O_4$	Aminanilic acid	$H_2(NH_2)_2An$	Aminanilate	$(NH_2)_2An^{2-}$	[24]
CH_3	$H_8C_8O_4$	Methylanilic acid	H_2Me_2An	Methylanilate	Me_2An^{2-}	[25]
CH_2CH_3	$H_{12}C_{10}O_4$	Ethylanilic acid	H_2Et_2An	Ethylanilate	Et_2An^{2-}	[25]
iso-C_3H_7	$H_{16}C_{12}O_4$	Isopropylanilic acid	H_2*iso*-Pr_2An	Isopropylanilate	*iso*-Pr_2An^{2-}	[26]
C_6H_5	$H_{12}C_{18}O_4$	Phenylanilic acid	H_2Ph_2An	Phenylanilate	Ph_2An^{2-}	[10,27]
C_4H_3S	$H_8C_{14}O_4S_2$	Thiophenylanilic acid	H_2Th_2An	Thiophenylanilate	Th_2An^{2-}	[28]
$C_6H_5O_2S$	$H_{12}C_{18}O_8S_2$	3,4-ethylene dioxythiophenyl anilic acid	H_2EDOT_2An	3,4-ethylene dioxythiophenyl anilate	$EDOTAn^{2-}$	[28]
C_4H_9	$H_{20}C_{14}O_4$	2,3,5,6-tetrahydroxy-1,4-benzo quinone	H_2THBQ	2,5-di-tert-butyl-3,6-dihydroxy-1,4-benzoquinonate	$THBQ^{2-}$	[29]

The synthetic methods to obtain the anilic acids described in Table 1 are reported in Schemes 1–3 respectively.

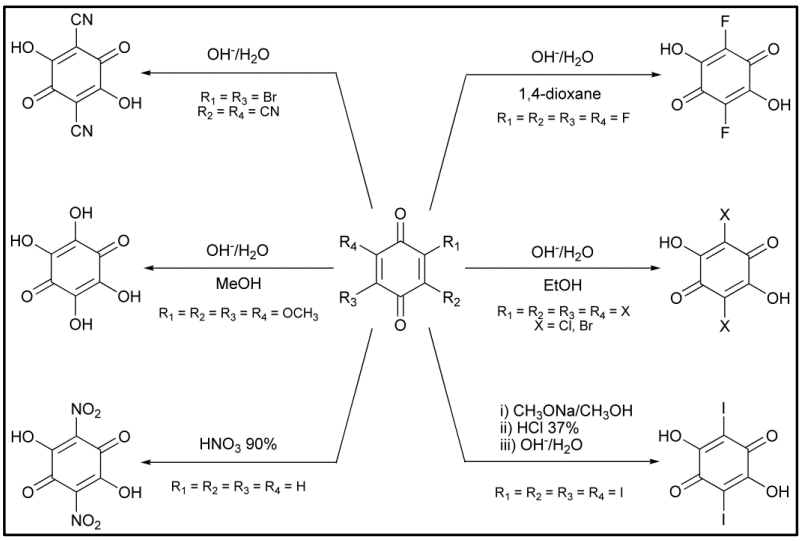

Scheme 1. Overview of the synthetic procedures for the preparation of the H_2X_2An (X = F, Cl, Br, I, NO_2, OH, CN) anilic acids. The corresponding anilate dianions, generated in solution, afford the protonated forms by simple acidification.

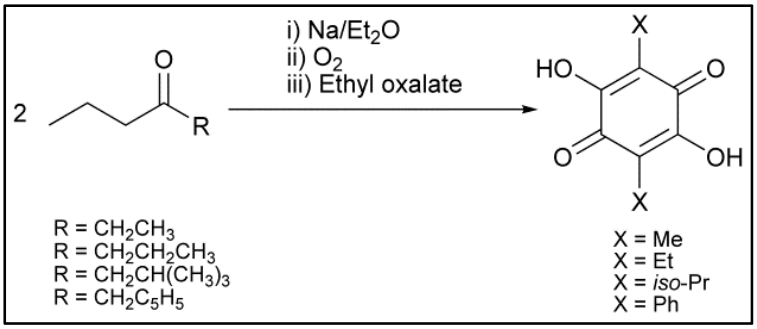

Scheme 2. Overview of the synthetic procedures for the preparation of the H_2X_2An (X = Me, Et, *iso*-Pr, Ph) anilic acids.

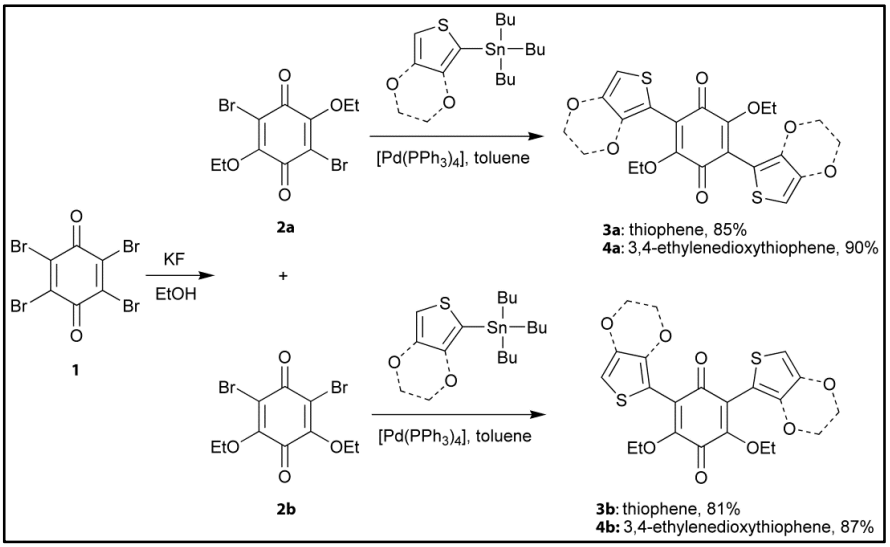

Scheme 3. Synthesis of thiophenyl (**3a**,**b**) and 3,4-ethylenedioxythiophenyl (**4a**,**b**) derivatives of 1,4-benzoquinone.

Anilic acids (**I**) undergo a mono and double deprotonation process of the two hydroxyl groups giving rise to the monoanionic (**II**) and dianionic (**III**) forms (Scheme 4: **III** prevails in aqueous media due to the strong resonance stabilization of the negative charge).

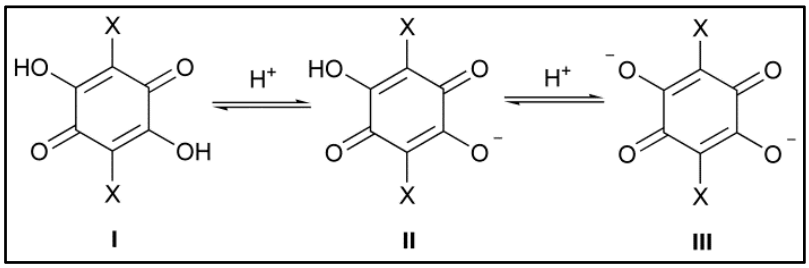

Scheme 4. Protonation equilibria for a generic anilic acid.

The molecular and crystal structures of the protonated anilic acids [24,30–38] are characterized by similar features: (i) a centrosymmetric quasi-quinonoid structure with C=O and C=C distances in the 1.215–1.235 Å and 1.332–1.355 Å ranges, respectively; (ii) a planar structure of the benzoquinone ring; and (iii) moderate-strong H-Bonding and π-stacking interactions in the crystal structure [30,32,36–38]. It should be noted that the crystal structure of $H_2(NO_2)_2An$ hexahydrate and $H_2(CN)_2An$ hexahydrate reveal the presence of hydronium nitranilates and hydronium cyananilates, respectively [35,36], as a result of their strong acidity (pK_a values for $H_2(NO_2)_2An$: −3.0 and −0.5) [11]. The structure of the nitranilic acid hexahydrate is characterized by the presence of the Zundel cation, $(H_5O_2)^{2+}$, whose proton dynamic has been recently studied by using a multi-technique approach [39]. Interestingly, the structure of $H_2(NH_2)_2An$ reveals the presence of an highly polarized zwitterionic structure with the protons located on the amino groups [24]. The molecular and crystal structures of alkali metal salts of some anilic acids have also been reported [40–47]. The X-ray analysis reveals that the carbon ring system for the anilates in their dianionic form takes the planar conformation but is not in a quinoidal form, having four C–C bonds of equal length (1.404–1.435 Å range) and two considerably longer C–C bonds (1.535–1.551 Å range) whose bond distances vary as a function of the substituents. Moreover, the four C–O bonds are of equal length (1.220–1.248 Å range). This description can be represented with four resonance structures that, in turn, can be combined in one form with delocalized π-electrons along the O–C–C(–X)–C–O bonds (Scheme 5) [34,35,38,41].

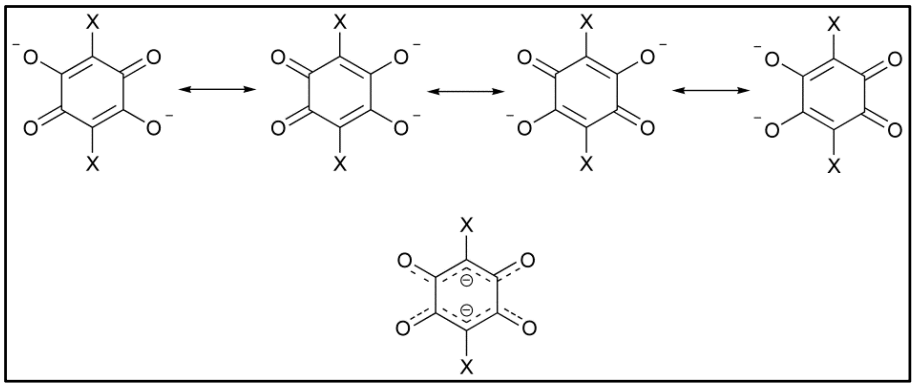

Scheme 5. Resonance structures for a generic anilate dianion. The π-electron delocalization over the O–C–C(–X) –C–O bonds is highlighted.

The crystal structures of the anilate anions are dominated by π-stacking interactions between quinoid rings. Since the dianions are characterized by (i) π-electron delocalization on the O–C–C(–X) –C–O bonds and (ii) strong repulsion due to double negative charges, their crystal structures are

dominated by parallel offset π-π stacking arrangement, similarly to what found in aromatic systems. Monoanionic alkali salts are, instead, able to stack in a perfect face-to-face parallel arrangement with no offset, where single bonds are sandwiched between double bonds and vice versa, with short distances of the ring centroids (3.25–3.30 Å), as thoroughly described by Molčanov et al. [43,45,46]. This arrangement minimizes of π-electrons repulsions while maximizing σ-π and dipolar attractions [45].

An overview of the coordination modes shown by the anilate dianions is reported in Scheme 6:

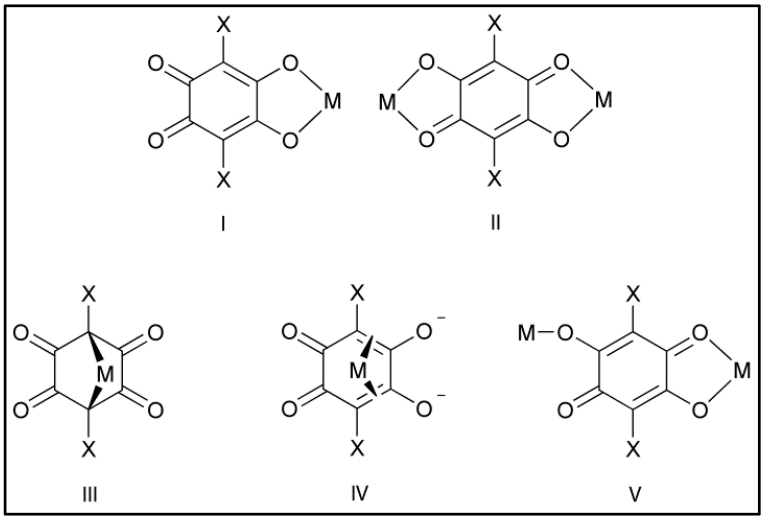

Scheme 6. Coordination modes exhibited by the anilate dianions: 1,2-bidentate (**I**), bis-1,2-bidentate (**II**), 1,4-bidentate (**III**), π-bonding (**IV**), 1,2-bidentate/monodentate (**V**).

It is noteworthy that among the described coordination modes, **I** and **II** are the most common, whereas **III**, **IV** and **V** have been only rarely observed.

Kitagawa and Kawata reported on the coordination chemistry of the anilic acids in their dianionic form (anilate ligands) with particular attention to the $DHBQ^{2-}$ (H_2An^{2-}) and its chloro derivative, chloranilate (Cl_2An^{2-}) [7]. Since the first observation of a strong magnetic interaction between paramagnetic metal ions and the H_2An^{x-} (x = 3, 1) radical species, reported by Gatteschi et al. [48] several types of metal complexes ranging from finite discrete homoleptic and heteroleptic mononuclear systems to extended homoleptic and heteroleptic polymeric systems showing a large variety of peculiar crystal structures and physical properties, have been obtained so far [7,49–60]. Valence Tautomerism is an essential phenomenon in anilato-based systems [29,61–64] and it has been observed for the first time by Sato et al. [64] in the heteroleptic dinuclear complex, $[(CoTPA)_2(H_2An)](PF_6)_3$, (TPA = tris(2-pyridylmethyl)amine) that exhibits a valence tautomeric transition with a distinct hysteresis effect (13 K) around room temperature and photoinduced valence tautomerism under low temperature.

Slow magnetic relaxation phenomena are also one of hot topic in magnetochemistry and very recently Ishikawa, Yamashita et al. [65] reported on the first example of slow magnetic relaxation observed in a chloranilato-based system, the new field induced single-ion magnet, $[Co(bpy)_2(Cl_2An)]\cdot EtOH$, (bpy = bipiridyl) a heteroleptic six-coordinate mononuclear high-spin cobalt(II) complex, formed by 1D π-π stacked chain-like structures through the bpy ligands. This compound undergoes spin-phonon relaxation of Kramers ions through two-phonon Raman and direct spin-phonon bottleneck processes and the observed slow relaxation of the magnetization is purely molecular in its origin.

The interest in the anilate chemistry has been recently renovated since uncoordinated anilic acids have been recently used as molecular building blocks for obtaining different types of functional materials such as organic ferroelectrics or as a component of charge transfer salts showing peculiar physical properties [66–69]. Anilates in fact are very challenging building blocks because of: (i) their

interesting redox properties [70]; (ii) their ability to mediate magnetic superexchange interactions when the ligand coordinates two metals ions in the 1,2-bis-bidentate coordination mode; (iii) the possibility of modulating the strength of this magnetic superexchange interaction by varying the substituents (X) on the 3,6 position of the anilato-ring [71]; moreover the presence of different substituents in the anilato moiety give rise to intermolecular interactions such as H-Bonding, Halogen-Bonding, π-π stacking and dipolar interactions which may influence the physical properties of the resulting material. Therefore, these features provide an effective tool for engineering a great variety of new materials with unique physical properties.

The aim of the present work is to highlight the key role of anilates in engineering new materials with new or improved magnetic and/or conducting properties and new technological applications. Only homoleptic anilato-based molecular building blocks and related materials will be discussed. Selected examples of para-/ferri-magnetic, spin-crossover and conducting/magnetic multifunctional materials based on transition metal complexes of anilato-derivatives, on varying the substituents at the 3,6 positions of the anilato moiety, will be discussed herein, whose structural features or physical properties are peculiar and/or unusual with respect to analogous compounds reported in the literature up to now. Their most appealing technological applications will be also reported.

2. Anilato-Based Molecular Magnets

2.1. Introduction

In the design of molecule-based magnets the choice of the interacting metal ions and the bridging ligand plays a key role in tuning the nature and magnitude of the magnetic interaction between the metal ions, especially when the bridge contains electronegative groups that may act as "adjusting screws. A breakthrough in this area is represented by the preparation in 1992 by Okawa et al. [72] of the family of layered bimetallic magnets based on the oxalate ($C_2O_4^{2-}$) ligand, formulated as [(*n*-Bu)$_4$N]M^{II}Cr(C_2O_4)$_3$] (M^{II} = Mn, Fe, Co, Ni and Cu) showing the well-known 2D hexagonal honeycomb structure [73,74]. These systems show ferromagnetic order (M^{III} = Cr) with ordering temperatures ranging from 6 to 14 K, or ferrimagnetic order (M^{III} = Fe) with T_c ranging from 19 to 48 K [75–79]. In these compounds the A^+ cations play a crucial role in tailoring the assembly of the molecular building-blocks and therefore controlling the dimensionality of the resulting bimetallic framework. In addition, the substitution of these electronically innocent cations with electroactive ones can increase the complexity of these systems, adding novel properties to the final material. In the last 20 years many efforts have been addressed to add in these materials a further physical property by playing with the functionality of the A^+ cations located between the bimetallic layers. This strategy produced a large series of multifunctional molecular materials where the magnetic ordering of the bimetallic layers coexists or even interacts with other properties arising from the cationic layers, such as paramagnetism [2,76–80], non-linear optical properties [2,81,82], metal-like conductivity [83,84], photochromism [2,81,85,86], photoisomerism [87], spin crossover [88–93], chirality [94–97], or proton conductivity [2,98,99]. Moreover, it is well-established that the ordering temperatures of these layered magnets are not sensitive to the separation determined by the cations incorporated between the layers, which slightly affects the magnetic properties of the resulting hybrid material, by emphasizing its 2D magnetic character [2,75–80,95,100,101]. The most effective way to tune the magnetic properties of such systems is to act directly on the exchange pathways within the bimetallic layers. This can be achieved either by varying M^{II} and M^{III} or by modifying the bridging ligand. So far, only the first possibility has been explored, except for a few attempts at replacing the bridging oxalate ligand by with the dithioxalate one, leading to a small variations of the ordering temperatures [102–105].

In this context, anilates, larger bis-bidentate bridging ligands than oxalates, are very challenging as their coordination modes are similar to the oxalato ones and it is well-known that they are able to provide an effective pathway for magnetic exchange interactions [7].

One of the most interesting anilato-based structures obtained so far are the H_2An^{2-}- and Cl_2An^{2-}-based honeycomb layers [47,106–110]. In these 2D compounds the structure is similar to that of the oxalate honeycomb layers, but all reported systems to date are homometallic (i.e., they contain two M^{II} or two M^{III} ions of the same nature type). The layers formed with two M^{II} ions contain a 2- charge per formula, $[M^{II}_2(X_2An)_3]^{2-}$ (X = Cl, H), and, accordingly, two monocations are needed to balance the charge. The only known examples of this $[M^{II}_2L_3]^{2-}$ series are the $[M_2(H_2An)_3]^{2-}$ (M = Mn and Cd) [106] and $[M_2(Cl_2An)_3]^{2-}$ (M = Cu, Co, Cd and Zn) systems [108]. The layers formed with two M^{III} ions are neutral and the reported examples include the $[M_2(H_2An)_3]\cdot 24H_2O$ (M^{III} = Y, La, Ce, Gd, Yb and Lu) [109,110], $[M_2(Cl_2An)_3]\cdot 12H_2O$ (M^{III} = Sc, Y, La, Pr, Nd, Gd, Tb, Yb, Lu) [2,47,110] and $[Y_2(Br_2An)_3]\cdot 12H_2O$ systems [47]. Further interest for the anilate ligands is related to their ability to form 3D structures with the (10,3)-*a* topology, similar to the one observed with the oxalate [111]; these structures are afforded when all the ML_3 units show the same chirality, in contrast with the 2D honeycomb layer, which requires alternating Λ-ML_3 and Δ-ML_3 units. This 3D structure with a (10,3)-*a* topology has been recently reported for the $[(n\text{-}Bu)_4N]_2[M^{II}_2(H_2An)_3]$ (M^{II} = Mn, Fe, Ni, Co, Zn and Cd) and $[(n\text{-}Bu)_4N]_2[Mn_2(Cl_2An)_3]$ systems [112], showing a double interpenetrating (10,3)-*a* lattice with opposite stereochemical configuration that afford an overall achiral structure. The versatility of the anilate-based derivatives is finally demonstrated by the formation of a 3D adamantane-like network in the compounds $[Ag_2(Cl_2An)]$ [113], $[H_3O][Y(Cl_2An)_3]\cdot 8CH_3OH$ and $[Th(Cl_2An)_2]\cdot 6H_2O$ [110]. Because these ligands are able to mediate antiferromagnetic exchange interactions, it should be expected that 2D heterometallic lattices of the $[M^{II}M^{III}(X_2An)_3]^{-}$ type, would afford ferrimagnetic coupling and ordering. Furthermore, if the magnetic coupling depends on the X substituents on the ligand, as expected, a change of X is expected to modify the magnetic coupling and the T_c. This is probably the most interesting and appealing advantage of the anilate ligands since they can act as the oxalate ligands, but additionally they show the possibility of being functionalized with different X groups. This should lead to a modulation of the electronic density in the benzoquinone ring, which, in turn, should result in an easy tuning of the magnetic exchange coupling and, therefore, of the magnetic properties (ordering temperatures and coercive fields) in the resulting 2D or 3D magnets. It should be highlighted that among the ligands used to produce the majority of known molecule-based magnets such as oxalato, azido, or cyano ligands, only the anilates show the this ability, to our knowledge.

A further peculiar advantage of these 2D materials is that the bigger size of anilate ligands compared with oxalate ones may enable the insertion within the anion layer of the charge-compensating counter-cation, leading to neutral layers that may be exfoliated using either mechanical or solvent-mediated exfoliation methods [114]. To date, examples of exfoliation of magnetic layered coordination polymers are rare and some of the few examples of magnetic 2D coordination polymers exfoliated so far are the Co^{2+} or Mn^{2+} 2,2-dimethylsuccinate frameworks showing antiferromagnetic ordering in the bulk [115].

2.2. Molecular Paramagnets

Two new isostructural mononuclear complexes of formula $[(Ph)_4P]_3[M(H_2An)_3]\cdot 6H_2O$ (M = Fe(III) (**1**) or Cr(III) (**2**) have been obtained by reacting the hydranilate anion with the Fe(III) and Cr(III) paramagnetic metal ions [116]. The crystal structure of **1** consists of homoleptic tris-chelated octahedral complex anions $[Fe(H_2An)_3]^{3-}$ surrounded by crystallization water molecules and $(Ph)_4P^{+}$ cations. The metal complexes are involved in an extensive network of moderately strong hydrogen bonds (HBs) between the peripheral oxygen atoms of the ligand and crystallization water molecules; HBs are responsible, as clearly shown by the analysis of the Hirshfeld surface, for the formation of supramolecular layers that run parallel to the *a* crystallographic axis, showing an unprecedented H-bonded 2D architecture in the family of the anilato-based H-bonded networks [116]. DFT theoretical calculations pointed out the key role of the H substituent on the hydranilato ligand in modulating the electron density of the whole complex and favoring the electron delocalization toward the peripheral

oxygen atoms of the ligands, compared with the other components of the family of halogenated tris-chelated anilato-based complexes (Figure 1); these peripheral oxygen atoms act, in turn, as suitable HB-acceptors in the observed supramolecular architecture. The magnetic properties of **1** show a typical paramagnetic behavior of quasi-isolated spin centers, while those of **2** are quite intriguing and might find their origin in some kind of charge transfer between the Cr metal ions and the hydranilate ligands, even though the observed magnetic behavior do not rule out the possibility to have extremely small magnetic coupling also mediated by HB interactions (Figure 2).

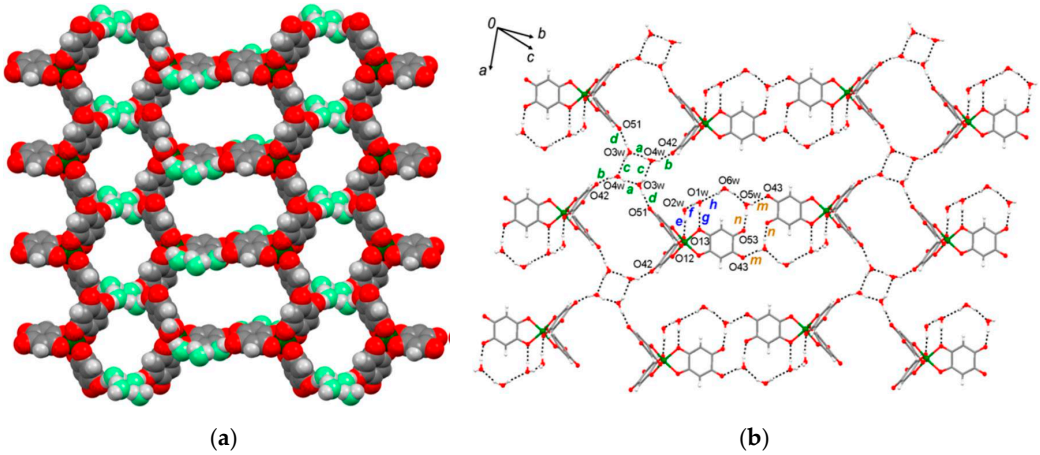

Figure 1. View of the crystal packing of **1**: (**a**) with metal complexes and water molecules in spacefill model highlighting the supramolecular topology; (**b**) highlighting the hydrogen bond (HB) interactions occurring between the water molecules and the metal complexes. The 11 HBs are indicated with colored letters. HB donors and acceptor are also indicated. Symmetry codes are omitted. Reprinted with permission from Reference [116]. Copyright 2014 American Chemical Society.

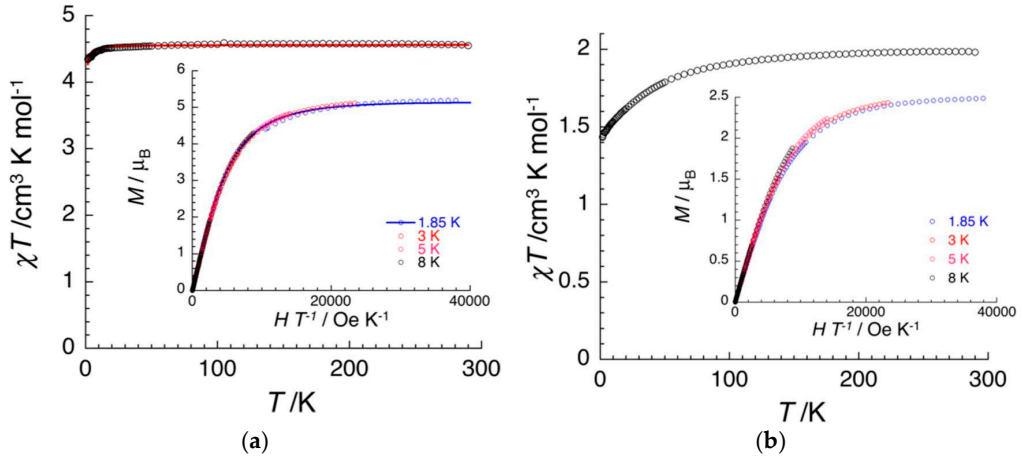

Figure 2. (**a**) Temperature dependence of χT product at 1000 Oe (where χ is the molar magnetic susceptibility equal to M/H per mole of Fe(III) complex) between 1.85 and 300 K for a polycrystalline sample of **1**. The solid line is the best fit obtained using a Curie-Weiss law. Inset shows field dependence of the magnetization for 1 between 1.85 and 8 K at magnetic fields between 0 and 7 T. The solid line is the best fit obtained using S = 5/2 Brillouin function; (**b**) Temperature dependence of χT product at 1000 Oe (where χ is the molar magnetic susceptibility equal to M/H per mole of Fe(III) complex) between 1.85 and 300 K for a polycrystalline sample of **2**. Inset shows field dependence of the magnetization for 2 between 1.85 and 8 K at magnetic fields between 0 and 7 T. Reprinted with permission from Reference [116]. Copyright 2014 American Chemical Society.

These compounds behave as versatile metallotectons, which are metal complexes able to be involved in well identified intermolecular interactions such as HBs and can therefore serve as building blocks for the rational construction of crystals, especially with HB-donating cations or size-tunable cationic metallotectons to afford porous coordination polymers or porous magnetic networks with guest-tunable magnetism (See Section 2.3).

By using the chloranilate ligand, Cl_2An^{2-}, the $[(TPA)(OH)Fe^{III}OFe^{III}(OH)(TPA)][Fe(Cl_2An)_3]_{0.5}(BF_4)_{0.5}\cdot 1.5MeOH\cdot H_2O$ (**3**) [TPA = tris(2-pyridylmethyl)amine] compound has been obtained by Miller et al. [117] in an atom economical synthesis. This is the first example of the formation of homoleptic trischelated $[Fe(Cl_2An)_3]^{3-}$ mononuclear anions. The core structure of **3** consists of two (dihydroxo)oxodiiron(III) dimer dications, the tris(chloranilato)ferrate(III) anion as well as a $[BF_4]^-$ (see Figure 3).

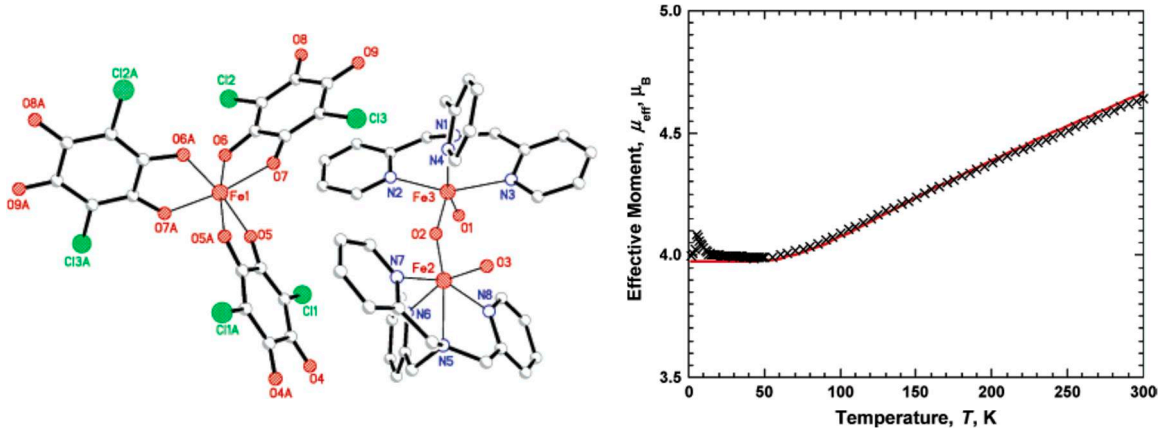

Figure 3. (**left**) ORTEP view of **3**. The atoms are represented by 50% probable thermal ellipsoids. Hydrogen atoms, solvent, and $[BF_4]^-$ are omitted for clarity; (**right**) $\mu_{eff}(T)$ for **3** taken at 300 Oe. The solid line is the best fit curve to the model. Reprinted with permission from [117]. Copyright 2006. American Chemical Society.

Variable-temperature magnetic measurements on a solid sample of **3** have been performed in the 2–300 K. At room temperature, the effective moment, $\mu_{eff}(T)$ is 2.93 μ_B/Fe, and $\mu_{eff}(T)$ decreases with decreasing temperature until it reaches a plateau at ca. 55 K, indicating a strong antiferromagnetic interaction within the $Fe^{III}OFe^{III}$ unit. Below 55 K, $\chi(T)$ is constant at 4.00 μ_B, which is attributed solely to $[Fe(Cl_2An)_3]^{3-}$. The $\chi(T)$ data were fit to a model for a coupled $S = 5/2$ dimer and an $S = 5/2$ Curie-Weiss term for the uncoupled $[Fe(Cl_2An)_3]^{3-}$. The best fit had J/kB of -165 K (115 cm^{-1}), $g = 2.07$, $\theta = -1$ K, and the spin impurity $\varrho = 0.05$. This experimentally determined J value for 3 is in the range observed for other oxo-bridged Fe(III) complexes with TPA as capping ligand, that is, $J = -107 \pm 10$ cm^{-1} [118].

By replacing X = H at the 3,6 positions of the benzoquinone moiety with X = Cl, Br, I, the new tris(haloanilato)metallate(III) complexes with general formula $[A]_3[M(X_2An)_3]$ (A = $(n\text{-}Bu)_4N^+$, $(Ph)_4P^+$; M = Cr(III), Fe(III); X_2An = chloranilate (Cl_2An^{2-}, see Chart 1), bromanilate (Br_2An^{2-}) and iodanilate (I_2An^{2-})), have been obtained [119]. To the best of our knowledge, except for the tris(chloranilato)ferrate(III) complex obtained by Miller et al. [117] no reports on the synthesis and characterization of trischelated homoleptic mononuclear complexes with the previously mentioned ligands are available in the literature so far.

Cation	Cl_2An^{2-}		Br_2An^{2-}		I_2An^{2-}	
	Cr(III)	Fe(III)	Cr(III)	Fe(III)	Cr(III)	Fe(III)
$(n\text{-}Bu)_4N^+$	4a	5a	6a	7a	8a	9a
$(Ph)_4P^+$	4b	5b	6b	7b	8b	9b
$(Et)_3NH^+$	4c	5c	-	-	-	-

Chart 1. $[A]_3[M(X_2An)_3]$ tris(haloanilato)metallate(III) complexes (A = $(n\text{-}Bu)_4N^+$, $(Ph)_4P^+$; M = Cr(III), Fe(III); Cl_2An^{2-} = chloranilate, Br_2An^{2-} = bromanilate and I_2An^{2-} = iodanilate).

The crystal structures of these Fe(III) and Cr(III) haloanilate complexes consist of anions formed by homoleptic complex anions formulated as $[M(X_2An)_3]^{3-}$ and $(Et)_3NH^+$, $(n\text{-}Bu)_4N$, or $(Ph_4)P^+$ cations. All complexes exhibit octahedral coordination geometry with metal ions surrounded by six oxygen atoms from three chelate ligands. These complexes are chiral according to the metal coordination of three bidentate ligands, and both Λ and Δ enantiomers are present in their crystal lattice. Interestingly the packing of $[(n\text{-}Bu)_4N]_3[Cr(I_2An)_3]$ (**8a**) shows that the complexes form supramolecular dimers that are held together by two symmetry related I···O interactions (3.092(8) Å), considerably shorter than the sum of iodine and oxygen van der Waals radii (3.50 Å). The I···O interaction can be regarded as a halogen bond (XB), where the iodine behaves as the XB donor and the oxygen atom as the XB acceptor (Figure 4a). This is in agreement with the properties of the electrostatic potential for $[Cr(I_2An)_3]^{3-}$ that predicts a negative charge accumulation on the peripheral oxygen atoms and a positive charge accumulation on the iodine. Also in $[(Ph)_4P]_3[Fe(I_2An)_3]$ (**9b**) each $[Fe(I_2An)_3]^{3-}$ molecule exchanges three I···I XBs with the surrounding complex anions. These iodine–iodine interactions form molecular chains parallel to the *b* axis that are arranged in a molecular layer by means of an additional I···I interaction with symmetry related I(33) atoms (3.886(2) Å), which may behave at the same time as an XB donor and acceptor. Additional XB interactions can be observed in the crystal packing of **9b** (Figure 4b).

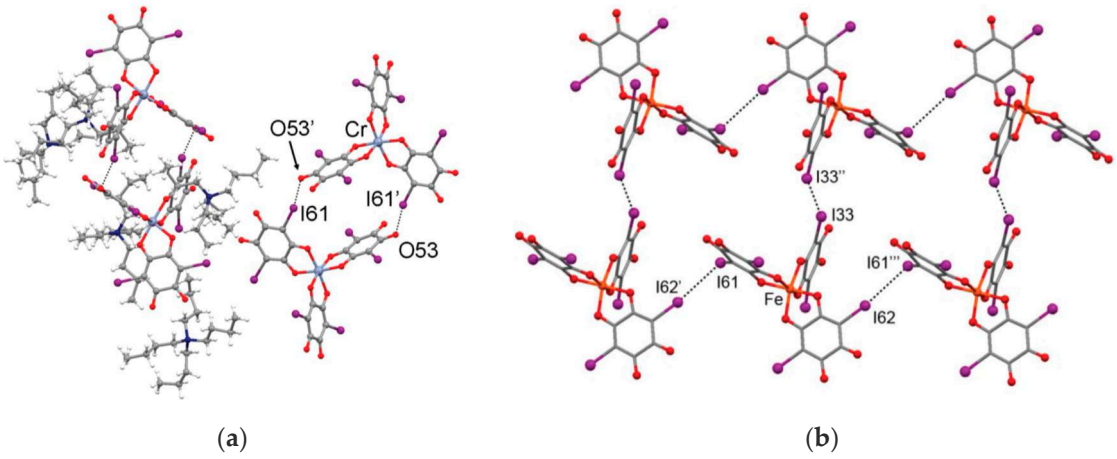

Figure 4. (**a**) Portion of the molecular packing of 8a where four complex anions are displayed (Symmetry code ′ = 1 − x; 1 − y; 1 − z); (**b**) halogen bonds between the complex anions (Symmetry codes ′ = x; y + 1; z, ″ = 3/2 − x; 3/2 − y; 1 − z, ‴ = x; y − 1; z). Adapted with permission from Reference [119]. Copyright 2014 American Chemical Society.

The magnetic behaviour of all complexes, except 8**a**, may be explained by considering a set of paramagnetic non-interacting Fe(III) or Cr(III) ions, taking into account the zero-field splitting effect similar to the Fe(III) hydranilate complex reported in Figure 2a. The presence of strong XB interactions in 8**a** are able, instead, to promote antiferromagnetic interactions among paramagnetic centers at

low temperature, as shown by the fit with the Curie-Weiss law, in agreement with the formation of halogen-bonded supramolecular dimers (Figure 5).

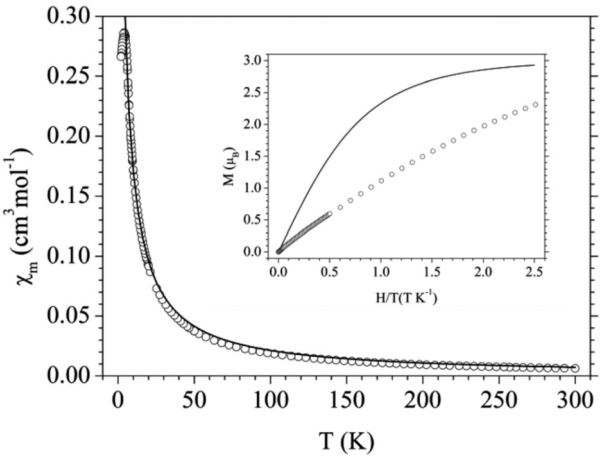

Figure 5. Thermal variation of χ_m for 8**a**. Solid line is the best fit to the Curie-Weiss law. Inset shows the isothermal magnetization at 2 K. Solid line represents the Brillouin function for an isolated S = 3/2 ion with g = 2. Anions. Reprinted with permission from Reference [119]. Copyright 2014 American Chemical Society.

A simple change of one chloro substituent on the chloranilate ligand with a cyano group affects the electronic properties of the anilate moiety inducing unprecedented luminescence properties in the class of anilate-based ligands and their metal complexes. The synthesis and full characterization, including photoluminescence studies, of the chlorocyananilate ligand ($ClCNAn^{2-}$), a unique example of a heterosubstituted anilate ligand has been recently reported [120], along with the tris-chelated metal complexes with Cr(III), (**10**) Fe(III), (**11**) and Al(III) (**12**) metal ions, formulated as $[A]_3[M^{III}(ClCNAn)_3]$ (A = $(n\text{-}Bu)_4N^+$ or $Ph4P^+$) shown in Chart 2.

Cation	$ClCNAn^{2-}$		
	Cr(III)	Fe(III)	Al(III)
$(n\text{-}Bu)_4N^+$	**10a**	**11a**	**12a**
$(Ph)_4P^+$	**10b**	**11b**	**12b**

Chart 2. $[A]_3[M(X_2An)_3]$ tris(haloanilato)metallate(III) complexes (A = $(n\text{-}Bu)_4N^+$, $(Ph)_4P^+$; M = Cr(III), Fe(III), Al(III); $ClCNAn^{2-}$ = chlorocyananilate).

The crystal structures of the M(III) chlorocyananilate complexes consist of homoleptic tris-chelated complex anions of formula $[M(ClCNAn)_3]^{3-}$ (M = Cr(III), Fe(III), Al(III)), exhibiting octahedral geometry and $[(n\text{-}Bu)_4N]^+$ or $[Ph_4P]^+$ cations. The 1**0a**–**12a** complexes are isostructural and their crystal packing is characterized by the presence of C–N$\cdots$Cl interactions between complex anions having an opposite stereochemical configuration (Λ, Δ), responsible for the formation of infinite 1D supramolecular chains parallel to the *a* crystallographic axis (Figure 6). The Cl$\cdots$N interaction can be regarded as a halogen-bond where the chlorine behaves as the halogen-bonding donor and the nitrogen atom as the halogen-bonding acceptor, in agreement with the electrostatic potential that predicts a negative charge accumulation on the nitrogen atom of the cyano group and a positive charge accumulation on the chlorine atom.

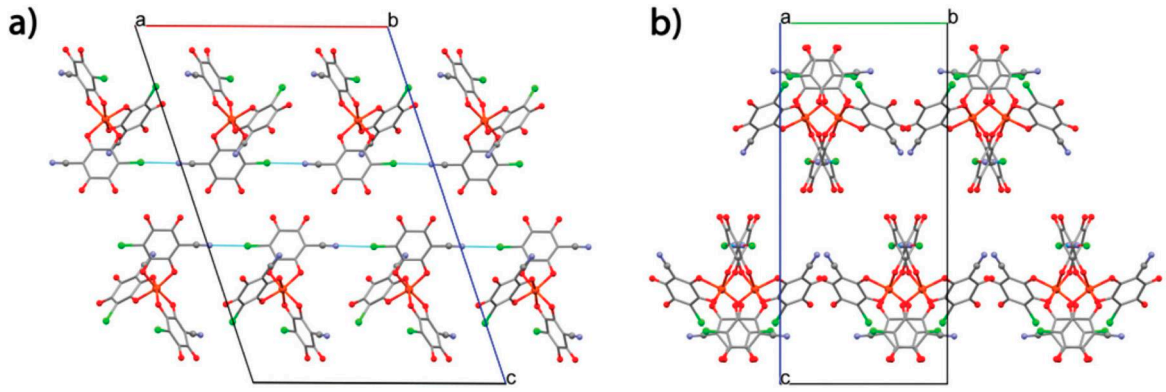

Figure 6. (**a**) Portion of the molecular packing of **11a** showing the Cl···N interactions occurring between the complex anions; (**b**) View of the supramolecular chains along the a axis. $[(n\text{-}Bu)_4N]^+$ cations are omitted for clarity. Reprinted with permission from Reference [120]. Copyright 2015 from The Royal Society of Chemistry.

10b–**12b** complexes are isostructural to the already reported analogous systems having chloranilate as ligand (vide supra). **10**, **12** (**a**, **b**) exhibit the typical paramagnetic behavior of this family of mononuclear complexes (vide supra). Interestingly TD-DFT calculations have shown that the asymmetric structure of the chlorocyananilate ligand affects the shape and energy distribution of the molecular orbitals involved in the electronic excitations. In particular, the HOMO → LUMO transition in the Vis region (computed at 463 nm) becomes partly allowed compare to the symmetric homosubstituted chloranilate and leads to an excited state associated with emission in the green region, at ca. λ_{max} = 550 nm, when exciting is in the lowest absorption band. Coordination to Al(III) (**12a**, **b**), does not significantly affect the luminescence properties of the free ligand, inducing a slight red-shift in the emission wavelength while maintaining the same emission efficiency with comparable quantum yields; thus the Al(III) complex **12a** still retains the ligand-centered emission and behaves as an appealing red luminophore under convenient visible light irradiation. **10a** and **11a** instead are essentially non-emissive, likely due to the ligand-to-metal CT character of the electronic transition in the Vis region leading to non-radiative excited states [120].

By combining $[A]_3[M^{III}(X_2An)_3]$ (A = Bu_3MeP^+, $(Ph)_3EtP^+$; M(III) = Cr, Fe; X = Cl, Br) with alkaline metal ions (M^I = Na, K) the first examples of 2D and 3D heterometallic lattices (**13**–**16**) based on anilato ligands combining M(I) and a M(III) ions have been obtained by Gomez et al. [121]. $(PBu_3Me)_2[NaCr(Br_2An)_3]$ (**13**) and $(PPh_3Et)_2[KFe(Cl_2An)_3](dmf)_2$ (**14**) show very similar 2D lattices formed by hexagonal $[M^IM^{III}(X_2An)_3]^{2-}$ anionic honeycomb layers with $(PBu_3Me)^+$ (**1**) or $(PPh_3Et)^+$ and dmf (**14**) charge-compensating cations inserted between the layers. While **13** and **14** show similar structures to the oxalato-based ones, a novel 3D structure, not found in the oxalato family is observed in $(NEt_3Me)[Na(dmf)]$-$[NaFe(Cl_2An)_3]$ (**14**) formed by hexagonal layers analogous to **1** and **14** interconnected through Na^+ cations. $(NBu_3Me)_2[NaCr(Br_2An)_3]$ (**16**), is the first heterometallic 3D lattice based on anilato ligands. This compound shows a very interesting topology containing two interpenetrated (10,3) chiral lattices with opposite chiralities, resulting in achiral crystals. This topology is unprecedented in the oxalato-based 3D lattices due to the smaller size of oxalateo compared to the anilato. Attempts to prepare **16** in larger quantities result in **16′**, the 2D polymorph of **16**, and as far as we know, this 2D/3D polymorphism has never been observed in the oxalato families showing the larger versatility of the anilato-ligands compared to the oxalato one. In Figure 7 the structures of **13**–**16** compounds are reported.

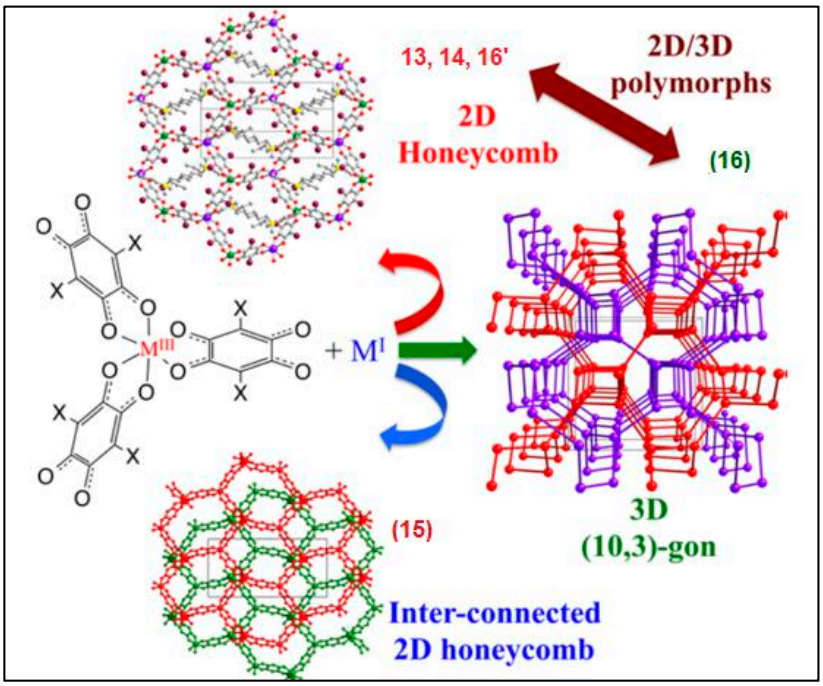

Figure 7. View of the hexagonal honeycomb layer in **13** with the $(PBu_3Me)^+$ cations in the hexagons. Color code: Cr = green, Na = violet, O = red, C = gray, Br = brown, and P = yellow. H atoms have been omitted for clarity. (Down) View of two adjacent layers in **15** showing the positions of the Fe(III) centers and the Na_2 dimers. H and Cl atoms have been omitted for clarity. (Right) Perspective view of the positions of the metal atoms in both interpenetrated sublattices (red and violet) in **16**. Adapted with permission from Reference [121]. Copyright 2015 American Chemical Society.

The magnetic measurements have been performed only on **13**, **15**, obtained and **16′** since only a few single crystals of **14** and **16** have been obtained. **13**, **15**, and **16′** show, as expected, paramagnetic behaviors that can be satisfactorily reproduced with simple monomer models including a zero field splitting (ZFS) of the corresponding S = 3/2 for Cr(III) in **13** and **16′** or S = 5/2 for Fe(III) in **15** (Figure 8a,b).

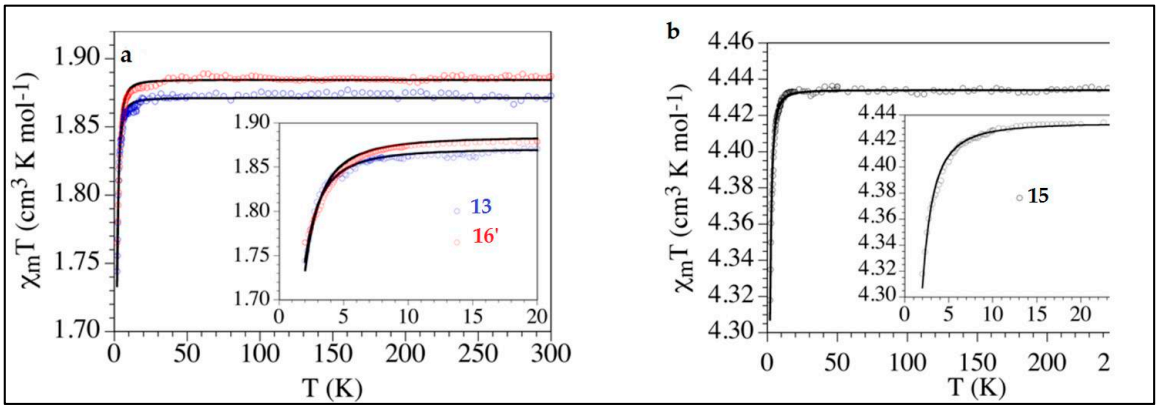

Figure 8. Thermal variation of χ_mT for (**a**) the Cr(III) compounds **13** and **16′** and (**b**) the Fe(III) compound **15**. Solid lines are the best fit to the isolated monomer models with zero field splitting (see text). Inset: low temperature regions. Reprinted with permission from Reference [121]. Copyright 2015 American Chemical Society.

In conclusion, this family of anionic complexes are versatile precursors (i) for constructing 2D molecule-based Ferrimagnets with tunable ordering temperature as a function of the halogen electronegativity (Section 2.2); (ii) as magnetic components for building up multifunctional molecular materials based on BEDT-TTF organic donors-based conductivity carriers (Section 3.2), in analogy with the relevant class of $[M(ox)_3]^{3-}$ tris-chelated complexes which have produced the first family of molecular paramagnetic superconductors [122–124]. Moreover, the ability of chlorocyananilate to work as the antenna ligand towards lanthanides, showing intense, sharp and long-lived emissions, represents a challenge due to the pletora of optical uses spanning from display devices and luminescent sensors to magnetic/luminescent multifunctional molecular materials.

2.3. Molecular Ferrimagnets

The novel family of molecule-based magnets formulated as $[Mn^{II}M^{III}(X_2An)_3]$ (A = $[H_3O(phz)_3]^+$, $(n\text{-}Bu)_4N^+$, phz = phenazine; M^{III} = Cr, Fe; X = Cl, Br, I, H), namely $[(H_3O)(phz)_3][Mn^{II}M^{III}(X_2An)_3]\cdot H_2O$, with M^{III}/X = Cr/Cl (**17**), Cr/Br (**18**) and Fe/Br (**19**) and $[(n\text{-}Bu_4)N][Mn^{II}Cr^{III}(X_2An)_3]$, with X = Cl (**20**), Br (**21**), I (**22**) and H (**23**) (Chart 3) have been synthesized and fully characterized [125]. These compounds were obtained by following the so-called "complex-as-ligand approach". In this synthetic strategy, a molecular building block, the homoleptic $[M^{III}(X_2An)_3]^{3-}$ tris(anilato)metallate octahedral complex (M^{III} = Cr, Fe; X = Cl, Br, I, H), is used as ligand towards the divalent paramagnetic metal ion Mn(II). 2D anionic complexes were formed leading to crystals suitable for an X-ray characterization in the presence of the $(n\text{-}Bu)_4N^+$ bulky organic cation or the $[H_3O(phz)_3]^+$ chiral adduct (Scheme 7).

Cationic Layer	Anionic Layer
$[H_3O(phz)_3]^+$	$Mn^{II}Cr^{III}$ (X-Cl) **17**
$[H_3O(phz)_3]^+$	$Mn^{II}Cr^{III}$ (X-Br) **18**
$[H_3O(phz)_3]^+$	$Mn^{II}Fe^{III}$ (X-Br) **19**
$[(n\text{-}Bu_4)N]^+$	$Mn^{II}Cr^{III}$ (X-Cl) **20**
$[(n\text{-}Bu_4)N]^+$	$Mn^{II}Cr^{III}$ (X-Br) **21**
$[(n\text{-}Bu_4)N]^+$	$Mn^{II}Cr^{III}$ (X-I) **22**
$[(n\text{-}Bu_4)N]^+$	$Mn^{II}Cr^{III}$ (X-H) **23**

Chart 3. $[Mn^{II}M^{III}(X_2An)_3]$ heterobimetallic complexes (A = $[H_3O(phz)_3]^+$, $(n\text{-}Bu)_4N^+$, phz = phenazine; M^{III} = Cr, Fe; M^{II} = Mn; X = Cl, Br, I, H).

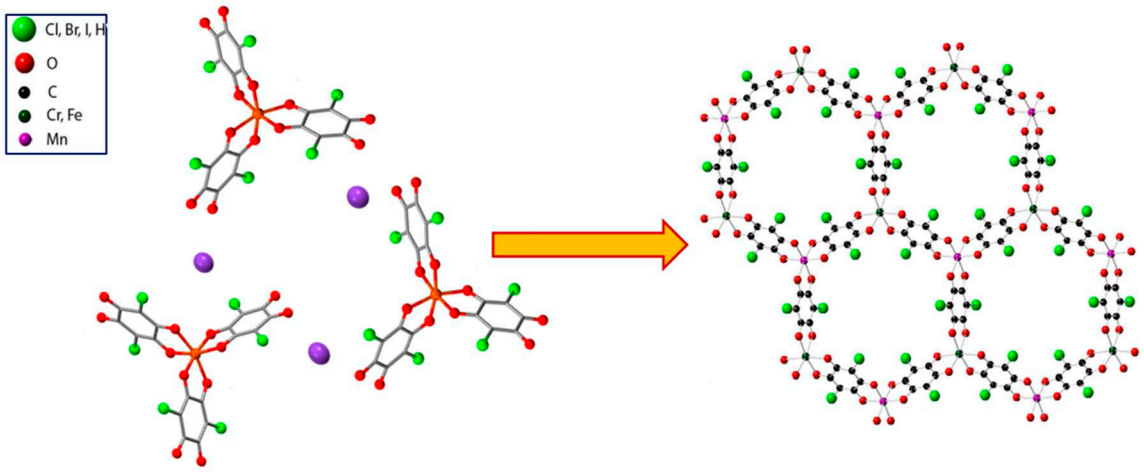

Scheme 7. Picture of the "complex-as-ligand approach" used for obtaining **17**–**23** compounds.

In these compounds, the monovalent cations act not only as charge-compensating counterions but also as templating agents controlling the dimensionality of the final system. In particular the chiral cation $[(H_3O)(phz)_3]^+$, obtained in situ by the interaction between phenazine molecules and hydronium cations, appears to template and favor the crystallization process. In fact, most of the attempts to obtain single crystals from a mixture of the $(n\text{-}Bu_4)N^+$ salts of the $[M^{III}(X_2An)_3]^{3-}$ precursors and Mn(II) chloride, yielded poorly crystalline products and only the crystal structure for the $[(n\text{-}Bu)_4N][MnCr(Cl_2An)_3]$ (**20**) system was obtained by slow diffusion of the two components.

Compounds $[(H_3O)(phz)_3][MnCr(Cl_2An)_3(H_2O)]$ (**17**), $[(H_3O)(phz)_3][MnCr(Br_2An)_3]\cdot H_2O$ (**18**) and $[(H_3O)(phz)_3][MnFe(Br_2An)_3]\cdot H_2O$ (**19**) are isostructural and show a layered structure with alternating cationic and anionic layers (Figure 9). The only differences, besides the change of Cl_2An^{2-} (**17**) with Br_2An^{2-} (**18**), or Cr(III) (**18**) with Fe(III) (**19**), are (i) the presence of an inversion center in **18** and **19** (not present in **17**) resulting in a statistical distribution of the M(III) and Mn(II) ions in the anionic layers; (ii) the presence of a water molecule coordinated to the Mn(II) ions in **16** (Mn-O1w 2.38(1) Å), in contrast with compounds **18** and **19** where this water molecule is not directly coordinated.

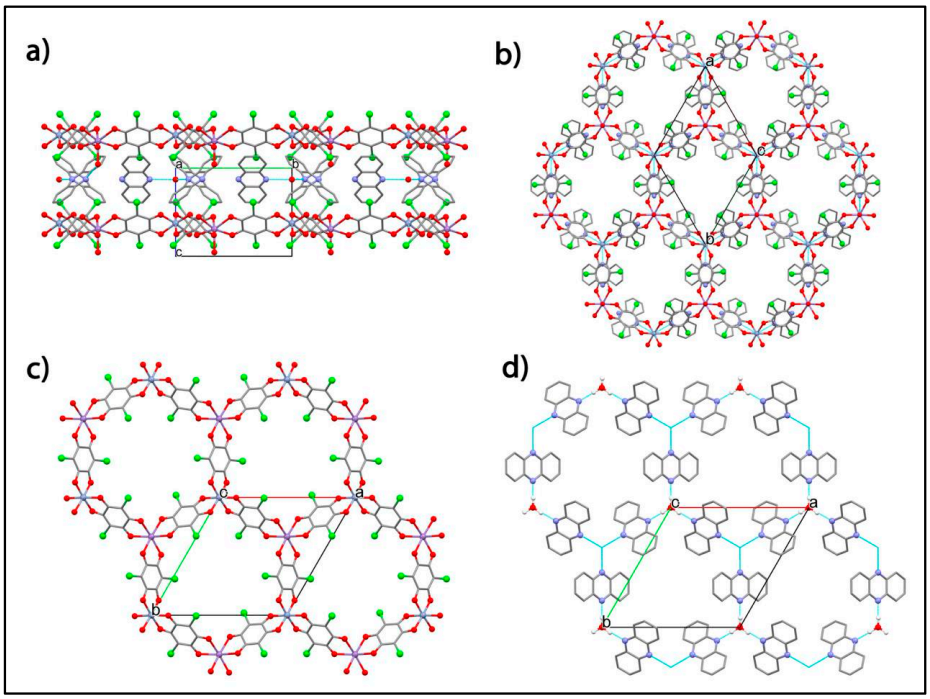

Figure 9. View of the crystal structure of **17**: (**a**) Side view of the alternating cationic and anionic layers; (**b**) Top view of the two layers; (**c**) Top view of the anionic layer; (**d**) Top view of the cationic layer showing the positions of the metal centers in the anionic layer (blue dashed hexagon). Reprinted with permission from Reference [125]. Copyright 2013 American Chemical Society.

The cationic layer is formed by chiral cations formulated as Δ-$[(H_3O)(phz)_3]^+$ (Figure 9d) resulting from the association of three phenazine molecules around a central H_3O^+ cation through three equivalent strong O–H···N hydrogen bonds. These Δ-$[(H_3O)(phz)_3]^+$ cations are always located below and above the Δ-$[Cr(Cl_2An)_3]^{3-}$ units, because they show the same chirality, allowing a parallel orientation of the phenazine and chloranilato rings (Figure 10b). This fact suggests a chiral recognition during the self-assembling process between oppositely charged $[Cr(Cl_2An)_3]^{3-}$ and $[(H_3O)(phz)_3]^+$ precursors with the same configuration (Δ or Λ).

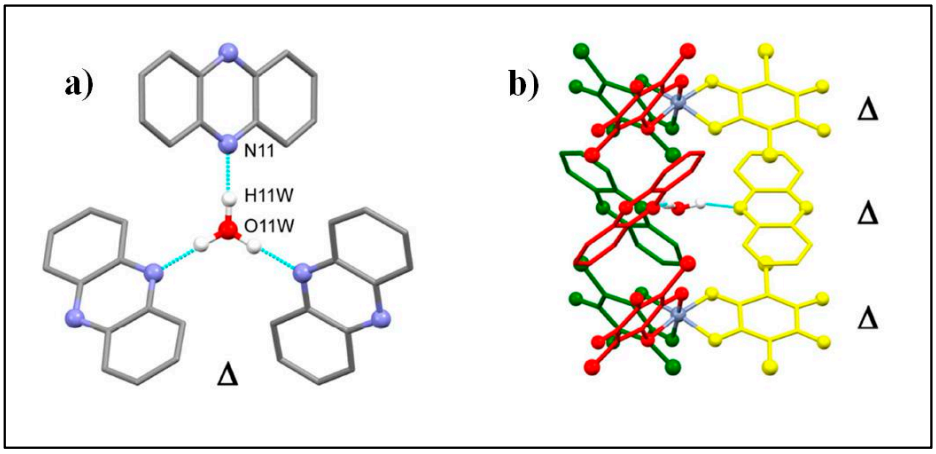

Figure 10. (**a**) Δ-$[(H_3O)(phz)_3]^+$ cation showing the O–H···N bonds as dotted lines; (**b**) side view of two anionic and one cationic layers showing Δ-$[(H_3O)(phz)_3]^+$ and the Δ-$[Cr(Cl_2An)_3]^{3-}$ entities located above and below. Parallel phenazine and anilato rings are shown with the same color. Color code: C, brown; O, pink; N, blue; H, cyan; Cl, green; Mn, yellow/orange; Cr, red. Reprinted with permission from Reference [125]. Copyright 2013 American Chemical Society.

An interesting feature of **17–19** is that they show hexagonal channels, which contain solvent molecules, resulting from the eclipsed packing of the cationic and anionic layers (Figure 11).

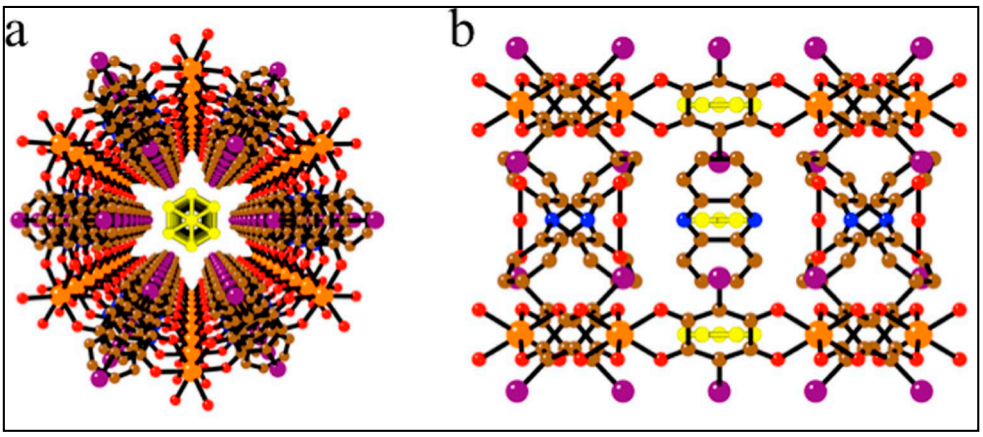

Figure 11. Structure of **18**: (**a**) perspective view of one hexagonal channel running along the c direction with the solvent molecules in the center (in yellow); (**b**) side view of the same hexagonal channel showing the location of the solvent molecules in the center of the anionic and cationic layers showing the O–H···N bonds as dotted lines. Reprinted with permission from Reference [125]. Copyright 2013 American Chemical Society.

20, the only compound with the $[NBu_4]^+$ cation whose structure has been solved, shows a similar layered structure as **17–19** but the main difference is the absence of hexagonal channels since the honeycomb layers are alternated and not eclipsed (Figure 12).

This eclipsed disposition of the layers generates an interesting feature of these compounds, i.e., the presence of hexagonal channels that can be filled with different guest molecules. **17–19** infact present a void volume of ca. 291 $Å^3$ (ca. 20% of the unit cell volume), where solvent molecules can be absorbed, opening the way to the synthesis of layered metal-organic frameworks (MOFs).

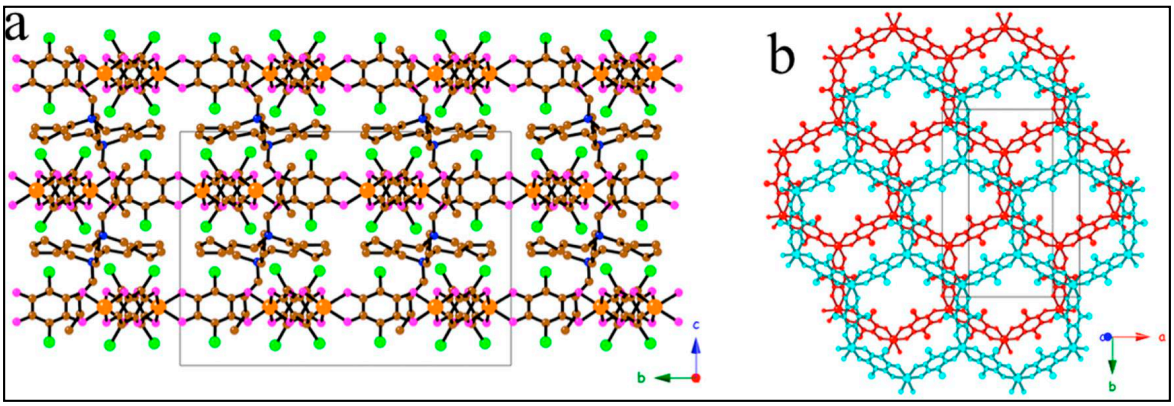

Figure 12. (**a**) Structure of **20**: (**a**) view of the alternating anionic and cationic layers; (**b**) projection, perpendicular to the layers, of two consecutive anionic layers showing their alternate packing. Reprinted with permission from Reference [125]. Copyright 2013 American Chemical Society.

All components of this series show ferrimagnetic long-range order as shown by susceptibility measurements, but the most interesting feature of this family is the tunability of the critical temperature depending on the nature of the X substituents: infact, as an example, an increase in Tc from ca. 5.5 to 6.3, 8.2, and 11.0 K (for X = Cl, Br, I, and H, respectively) is observed in the MnCr derivatives (Figure 13). Thus the different nature of the substituents on the bridging ligand play a key role in determining the critical temperature as shown by the linear correlation of the Tc as a function of the electronegativity of the substituents; Tc increases following the order X = Cl, Br, I, H and can be easily modulated by changing the X substituent. Both $[NBu_4]^+$ and Phenazinium salts, show similar magnetic behaviour showing an hysteretic behaviour with a coercive field of 5 mT.

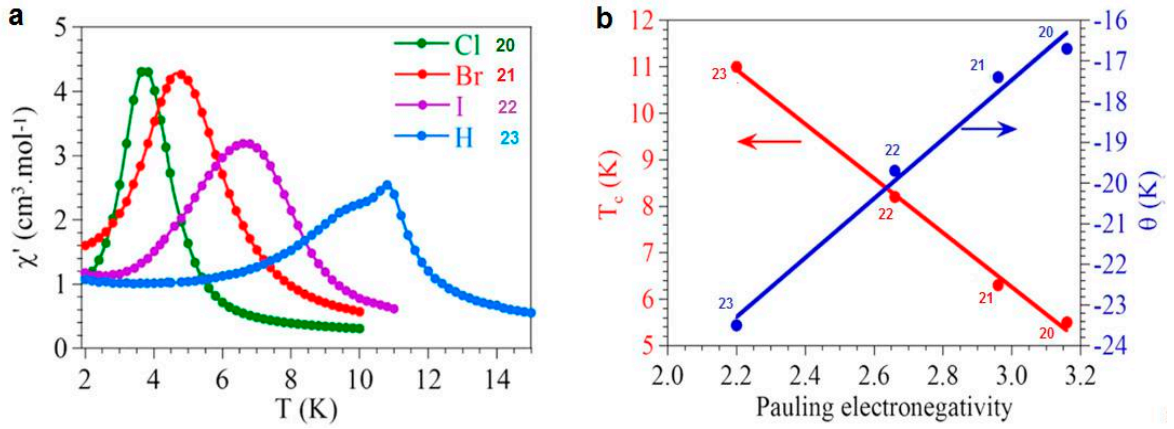

Figure 13. Magnetic properties of the $[NBu_4][MnCr(X_2An)_3]$ family, X = Cl (**20**), Br (**21**), I (**22**) and H (**23**): (**a**) Thermal variation of the in phase ($\chi m'$) AC susceptibility at 1 Hz.; (**b**) Linear dependence of the ordering temperature (Tc, left scale, red) and the Weiss temperature (θ, right scale, blue) with the electronegativity of the X group. Solid lines are the corresponding linear fits. Adapted with permission from Reference [125]. Copyright 2013 American Chemical Society.

17 is, therefore, the first structurally (and magnetically) characterized porous chiral layered magnet based on anilato-bridged bimetallic layers. This chirality is also expected to be of interest for studying the magnetochiral effect as well as the multiferroic properties, as has already been done in the oxalato family [94,107,121,126].

Moreover, the bigger size of the anilato compared to the oxalato ligand leads to hexagonal cavities that are twice larger than those of the oxalato-based layers. Therefore a larger library of cations can be used to prepare multifunctional molecular materials combining the magnetic ordering of the anionic layers with any additional property of the cationic one (the chirality of the phenazinium cation is only the first example). In the following section selected examples of cationic complexes spanning from chiral and/or achiral tetrathiafulvalene-based conducting networks to spin-crossover compounds to will be discussed.

3. Anilato-Based Multifunctional Molecular Materials

3.1. Introduction

π-*d* molecular materials, i.e., systems where delocalized π-electrons of the organic donor are combined with localized *d*-electrons of magnetic counterions, have attracted major interest in molecular science since they can exhibit coexistence of two distinct physical properties, furnished by the two networks, or novel and improved properties due to the interactions established between them[127–130]. The development of these π-*d* systems as multifunctional materials represents one of the main targets in current materials science for their potential applications in molecular electronics [78,127–130]. Important milestones in the field of magnetic molecular conductors have been achieved using as molecular building blocks the bis(ethylenedithio)tetrathiafulvalene (BEDT-TTF) organic donor[123,131–133] or its selenium derivatives, and charge-compensating anions ranging from simple mononuclear complexes $[MX_4]^{n-}$ (M = Fe^{III}, Cu^{II}; X = Cl, Br)[134–136] and $[M(ox)_3]^{3-}$ (ox = oxalate = $C_2O_4^{2-}$) with tetrahedral and octahedral geometries, to layered structures such as the bimetallic oxalate-based layers of the type $[M^{II}M^{III}(ox)_3]^-$ (M^{II} = Mn, Co, Ni, Fe, Cu; M^{III} = Fe, Cr) [123,124,131–133,137–140]. In these systems the shape of the anion and the arrangement of intermolecular contacts, especially H-bonding, between the anionic and cationic layers influence the packing motif of the BEDT-TTF radical cations, and therefore the physical properties of the obtained charge-transfer salt [141]. Typically, the structure of these materials is formed by segregated stacks of the organic donors and the inorganic counterions which add the second functionality to the conducting material. The first paramagnetic superconductor [BEDT-TTF]$_4$ $[H_3OFe^{III}(ox)_3]\cdot C_6H_5CN$ [123] and the first ferromagnetic conductor, $[BEDT\text{-}TTF]_3[Mn^{II}Cr^{III}(ox)_3]$ [49] were successfully obtained by combining, via electrocrystallization, the mononuclear $[Fe(ox)_3]^{3-}$ and the $[Mn^{II}Cr^{III}(ox)_3]^-$ (2D honeycomb with oxalate bridges) anions with the BEDT-TTF organic donor, as magnetic and conducting carriers, respectively. Furthermore, by combining the bis(ethylenedithio)tetraselenafulvalene (BETS) molecule with the zero-dimensional $FeCl_4^-$ anion, a field-induced superconductivity with π-*d* interaction was observed which may be mediated through S···Cl interactions between the BETS molecule and the anion [134]. Clues for designing the molecular packing in the organic network, carrier of conductivity, were provided by the use of the paramagnetic chiral anion $[Fe(croc)_3]^{3-}$ (croc = croconate = $C_5O_5^{2-}$) as magnetic component of two systems: α-$[BEDT\text{-}TTF]_5$ $[Fe(croc)_3]\cdot 5H_2O$ [142], which behaves as a semiconductor with a high room-temperature conductivity (ca. 6 S cm^{-1}) and β-$[BEDT\text{-}TTF]_5[Fe(croc)_3]\cdot C_6H_5CN$ [143], which shows a high room-temperature conductivity (ca. 10 S cm^{-1}) and a metallic behavior down to ca. 140 K. The BEDT-TTF molecules in the α-phase are arranged in a herring-bone packing motif which is induced by the chirality of the anions. Therefore, the packing of the organic network and the corresponding conducting properties can be influenced by playing with the size, shape, symmetry and charge of the inorganic counterions. The introduction of chirality in these materials represents one of the most recent advances [144] in material science and one of the milestones is represented by the first observation of the electrical magneto-chiral anisotropy (eMChA) effect in a bulk crystalline chiral conductor [145], as a synergy between chirality and conductivity [146–148]. However, the combination of chirality with electroactivity in chiral TTF-based materials afforded several other recent important results, particularly the modulation of the structural disorder in the solid state , [130–138] and hence a difference in conductivity between the enantiopure and racemic

forms [149–151] and the induction of different packing patterns and crystalline space groups in mixed valence salts of dimethylethylenedithio-TTF (DM-EDT-TTF), showing semiconducting (enantiopure forms) or metallic (racemic form) behaviour [152]. Although the first example of an enantiopure TTF derivative, namely the tetramethyl-bis(ethylenedithio)-tetrathiafulvalene (TM-BEDT-TTF), was described almost 30 years ago as the (*S*,*S*,*S*,*S*) enantiomer [153,154], the number of TM-BEDT-TTF based conducting radical cation salts is still rather limited. They range from semiconducting salts [155], as complete series of both enantiomers and racemic forms, to the [TM-BEDT-TTF]$_x$[MnCr(ox)$_3$] ferromagnetic metal [156], described only as the (*S*,*S*,*S*,*S*) enantiomer. The use of magnetic counterions, particularly interesting since they provide an additional property to the system, was largely explored in the case of the above-mentioned metal-oxalates $[M(ox)_3]^{3-}$ (M = Fe^{3+}, Cr^{3+}, Ga^{3+}, ox = oxalate) [124,140], present as Δ and Λ enantiomers in radical cation salts based on the BEDT-TTF donor. Other paramagnetic chiral anions, such as [Fe(croc)$_3$] [142,143] or $[Cr(2,2'\text{-bipy})(ox)_2]^-$ (bipy = bipyridine) [157], have been scarcely used up to now. However, in all these magnetic conductors the tris-chelated anions were present as racemic mixtures, except for the Δ enantiomer of $[Cr(ox)_3]^{3-}$ [158]. As far as the π-*d* systems are concerned, the number of conducting systems based on enantiopure TTF precursors is even scarcer [156,159]. One example concerns the above-mentioned ferromagnetic metal [TM-BEDT-TTF]$_x$[MnCr(ox)$_3$] [156], while a more recent one is represented by the semiconducting paramagnetic salts [DM-BEDT-TTF]$_4$[$ReCl_6$] [159]. In this context, anilate-based metal complexes [116,119] are very interesting molecular building blocks to be used as paramagnetic counterions, also because they offer the opportunity of exchange coupling at great distance through the anilate bridge (See Section 2.3), being therefore extremely versatile in the construction of the above mentioned achiral and chiral conducting/magnetic molecule-based materials.

Furthermore multifunctional materials with two functional networks responding to an external stimulus are also very challenging in view of their potential applications as chemical switches, memory or molecular sensors [160]. For the preparation of such responsive magnetic materials two-network compounds a magnetic lattice and spin-crossover complexes as the switchable molecular component are promising candidates. These molecular complexes, which represent one of the best examples of molecular bistability, change their spin state from low-spin (LS) to high-spin (HS) configurations and thus their molecular size, under an external stimulus such as temperature, light irradiation, or pressure [161,162]. Two-dimensional (2D) and three-dimensional (3D) bimetallic oxalate-based magnets with Fe(II) and Fe(III) spin-crossover cationic complexes have been obtained, where changes in size of the inserted cations influence the magnetic properties of the resulting materials [89,90,92,93]. By combining $[Fe^{III}(sal_2\text{-trien})]^+$ (sal_2-trien = N,N′-disalicylidene triethylenetetramine) cations with the 2D $Mn^{II}Cr^{III}$ oxalate-based network, a photoinduced spin-crossover transition of the inserted complex (LIESST effect), has been observed unexpectedely; this property infact is very unusual for Fe(III) complexes. The bigger size of anilates has the main advantage to enable the introduction of a larger library of cations, while the magnetic network, the family of layered ferrimagnets described in Section 2.3, showing higher Tc's, can be porous and/or chiral depending on the X substituent on the anilato moiety.

Interestingly, Miller et al. [29] reported on the formation and characterization of a series of heteroleptic isostructural dicobalt, diiron, and dinickel complexes with the TPyA = tris(2-pyridylmethyl)amine ligand and bridged by the 2,5-di-*tert*-butyl-3,6-dihydroxy-1,4-benzoquinonate (DBQ^{2-} or $DBQ^{\cdot 3-}$) anilato derivative, where the more electron donating *tert*-butyl group, has been targeted to explore its influence on the magnetic properties, e.g., spin coupling and spin crossover. In particular, Co-based dinuclear complex with $DBQ^{\cdot 3-}$ has shown valence tautomeric spin crossover behavior above room temperature, while Fe-based complexes exhibit spin crossover behavior. Spin crossover behavior or ferromagnetic coupling have been also observed in the heteroleptic dinuclear Fe(II) complexes $\{[(TPyA)Fe^{II}(DBQ^{2-})Fe^{II}(TPyA)](BF_4)_2$ and $\{[(TPyA)Fe^{II}(Cl_2An)\ Fe^{II}(TPyA)](BF_4)_2\}$, respectively [163], where the former does not exhibit thermal hysteresis, although shows ≈ room temperature SCO behavior. Thus, greater interdinuclear cation interactions are needed to induce

thermal hysteresis, maybe through the introduction of interdinuclear H-bonding. Therefore 2,3,5,6-tetrahydroxy-1,4-benzoquinone (H_2THBQ) has been used as bridging ligand and the [(TPyA)Fe^{II}($THBQ^{2-}$)FeII(TPyA)]$(BF_4)_2$ obtained complex shows coexistence of spin crossover with thermal hysteresis in addition to an intradimer ferromagnetic interaction [29].

3.2. Achiral Magnetic Molecular Conductors

The first family of conducting radical cation salts based on the magnetic tris(chloranilato)ferrate(III) complex have been recently obtained by reacting the BEDT-TTF donor (D) with the tris(chloranilato)ferrate(III) complex (A), via electrocrystallization technique, by slightly changing the stoichiometric donor: anion ratio and the solvents. Three different hybrid systems formulated as [BEDT-TTF]$_3$[Fe(Cl_2An)$_3$]·3CH_2Cl_2·H_2O (**24**), δ-[BEDT-TTF]$_5$[Fe(Cl_2An)$_3$]·4H_2O (**25**) and α′′′-[BEDT-TTF]$_{18}$[Fe(Cl_2An)$_3$]$_3$·3CH_2Cl_2·6H_2O (**26**), were obtained [164] as reported in Scheme 8.

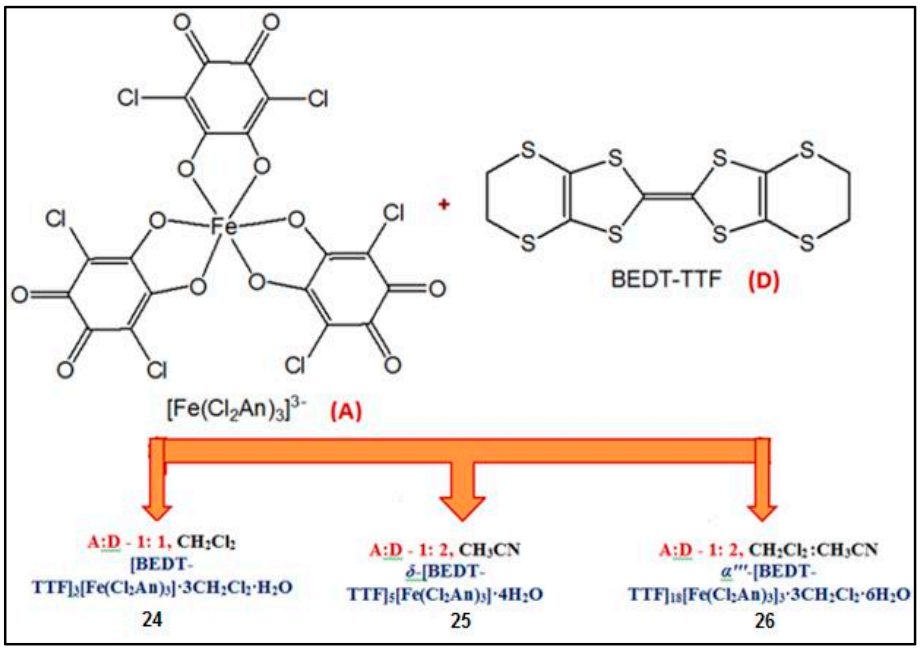

Scheme 8. Molecular structures for the complex anion [Fe(Cl_2An)$_3$]$^{3-}$ and the bis(ethylenedithio)tetrathiafulvalene (BEDT-TTF) organic donor, and experimental conditions used for obtaining **24**–**26** compounds.

The common structural feature for the three phases is the presence of dimerized oxidized BEDT-TTF units in the inorganic layer, very likely due to intermolecular S···Cl contacts and also electrostatic interactions. While in **24**, of 3:1 stoichiometry, the three BEDT-TTF molecules are fully oxidized in radical cations, in **25** and **26**, of 5:1 and 6:1 stoichiometry, respectively, only the donors located in the inorganic layers are fully oxidized, while those forming the organic slabs are in mixed valence state. **24** presents an unusual structure without the typical alternating organic and inorganic layers, whereas **25** and **26** show a segregated organic-inorganic crystal structure where layers formed by Λ and Δ enantiomers of the paramagnetic complex, together with dicationic BEDT-TTF dimers, alternate with layers where the donor molecules are arranged in the δ (**25**) and α′′′ (**26**) packing motifs.

The crystal packing of **25** and **26** plane showing the organic-inorganic layer segregation are reported in Figures 14 and 15 respectively.

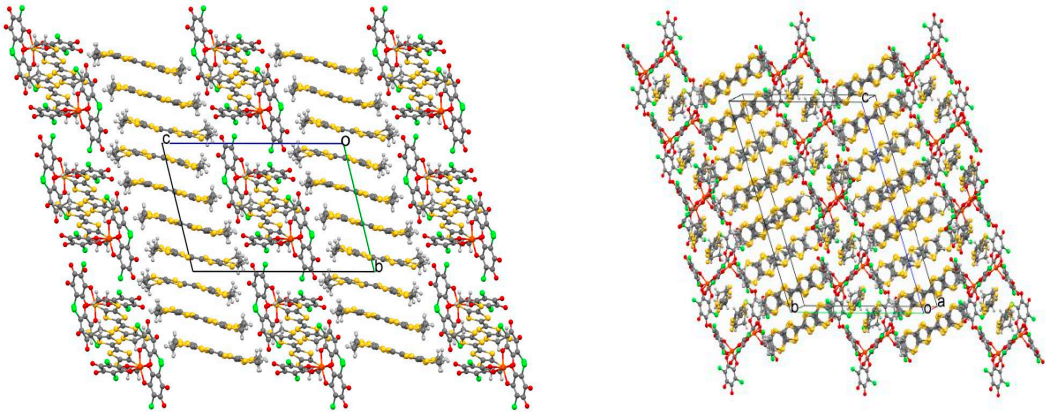

Figure 14. Crystal packing of **25** (**left**) and **26** (**right**) along the *bc* plane showing the organic-inorganic layer segregation. Crystallization water and CH_2Cl_2 molecules were omitted for clarity. Reprinted with permission from Reference [164]. Copyright 2014 American Chemical Society.

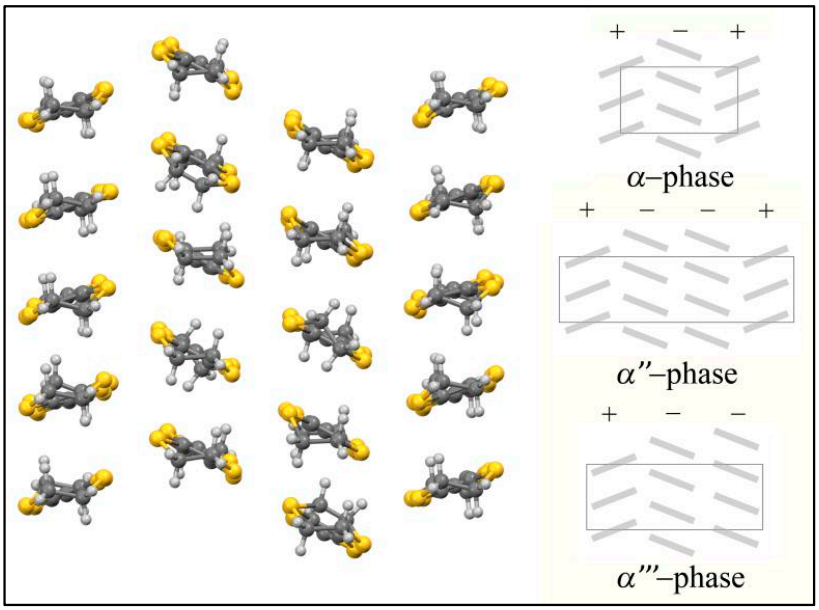

Figure 15. View of α′′′-packing of **26** along the *ac* plane (**left**); schematic representation of the BEDT-TTF molecules arranged in the α, α′′ and α′′′ packing motifs (**right**). Adapted with permission from Reference [164]. Copyright 2014 American Chemical Society.

The hybrid inorganic layers of **24**, **25** and **26** shows alternated anionic complexes of opposite chirality that surround dimers of mono-oxidized BEDT-TTF radical cations. This packing motif, shown in Figure 16 for **24**, points out the templating influence of the Cl···S interactions intermolecular interactions between the chloranilate ligand and the dimerized BEDT-TTF molecules.

The peculiar α′′′ structural packing motif observed in **26** is quite unusual [138,165]. In fact, the BEDT-TTF molecules stack in columns with an arrangement reminiscent of the α structural packing [165], but with a 2:1:2:1 alternation of the relative disposition of the molecules, instead of the classical 1:1:1:1 sequence (Figure 14). The α′′′-phase can be regarded as 1:2 hybrid of θ- and β′′- phases.

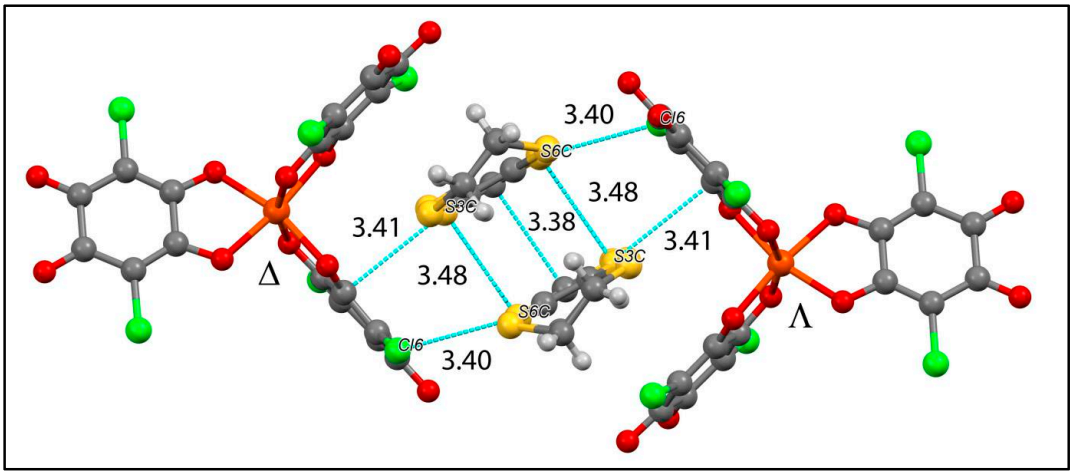

Figure 16. **C-C** dimer surrounded by two metal complexes of opposite chirality in **24**. Symmetry related S···S contacts and intermolecular interactions lower than the sum of the van der Waals radii between the BEDT-TTF molecules and the chloranilate ligands are highlighted. (Å): S3C···S6C 3.48, S4C···S5C 3.57, Cl6···S6C 3.40, C13C···S6C 3.41. Reprinted with permission from Reference [164]. Copyright 2014 American Chemical Society.

Single crystal conductivity measurements show semiconducting behavior for the three materials. **24** behaves as a semiconductor with a much lower conductivity due to the not-layered structure and strong dimerization between the fully oxidized donors, whereas **25** and **26** show semiconducting behaviors with high room-temperature conductivities of ca. 2 S cm^{-1} and 8 S cm^{-1}, respectively and low activation energies of 60–65 meV. Magnetic susceptibility measurements for **24** clearly indicate the presence of isolated high spin S = 5/2 Fe(III) ions, with a contribution at high temperatures from BEDT-TTF radical cations. These latter are evidenced also by EPR variable temperature measurements on single crystals of **26** (See Figure 17).

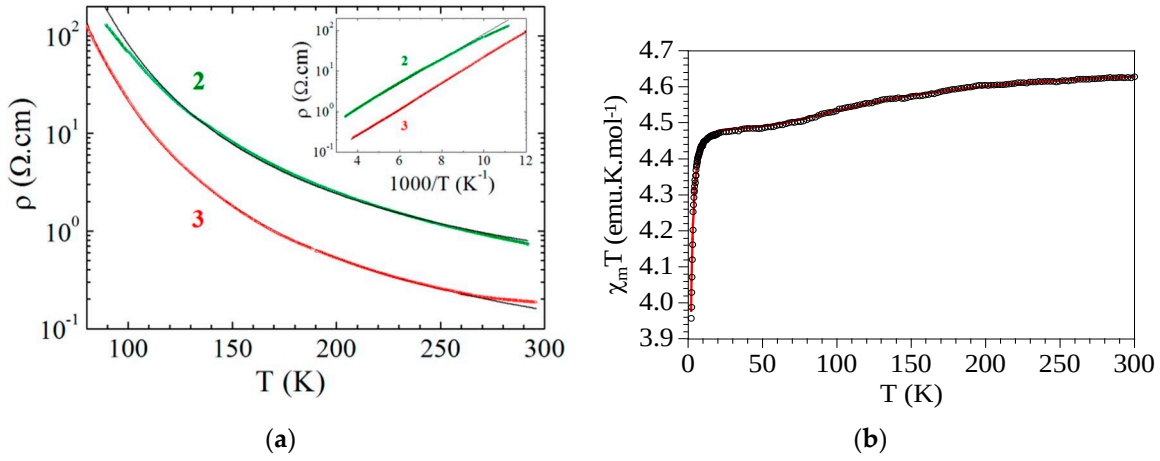

Figure 17. (**a**) Temperature dependence of the electrical resistivity ϱ for **25** and **26** single crystals. The inset shows the Arrhenius plot. The black lines are the fit to the data with the law $\varrho = \varrho_0 \exp(Ea/T)$ giving the activation energy Ea; (**b**) Thermal variation of the magnetic properties ($\chi_m T$) for **24**. Solid line is the best fit to the model (see text). Reprinted with permission from Reference [164]. Copyright 2014 American Chemical Society.

The correlation between crystal structure and conductivity behavior has been studied by means of tight-binding band structure calculations which support the observed conducting properties; and structure calculations for **25** and **26** are in agreement with an activated conductivity with low band gaps. A detailed analysis of the density of states and HOMO···HOMO interactions in **25** explains the origin of the gap as a consequence of a dimerization in one of the donor chains, whereas the challenging calculation of **26**, due to the presence of eighteen crystallographically independent BEDT-TTF molecules, represents a milestone in the band structure calculations of such relatively rare and complex crystal structures [164]. Recently Gomez et al. [166] has obtained a very unusual BEDT-TTF phase, called θ_{21}, by reacting the BEDT-TTF donor with the novel $(PPh_3Et)_3[Fe(C_6O_4Cl_2)_3]$ tris(chloranilato)ferrate(III) complex, via electrocrystallization technique, in the CH_2Cl_2/MeOH solvent mixture. The obtained compound $[(BEDT\text{-}TTF)_6[Fe(C_6O_4Cl_2)_3]\cdot(H_2O)_{1.5}\cdot(CH_2Cl_2)_{0.5}$ **(27)** shows the same layered structure and physical properties as **26**. In Figure 18, a view of the θ_{21} BEDT-TTF packing motif is reported.

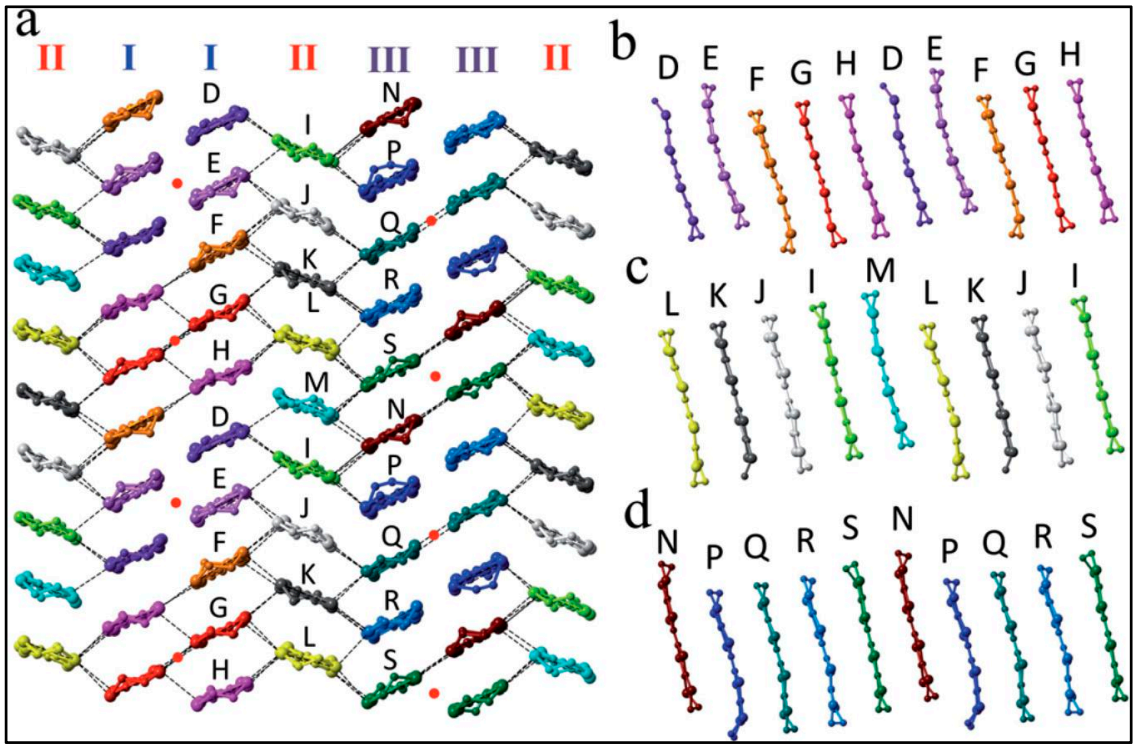

Figure 18. View of the θ_{21} BEDT-TTF packing motif in **27**. Copyright (2014) Wiley Used with permission from [166].

3.3. Chiral Magnetic Molecular Conductors

The first family of chiral magnetic molecular conductors [167] formulated as β-[(*S*,*S*,*S*,*S*)-TM-BEDT-TTF]$_3PPh_4[K^IFe^{III}(Cl_2An)_3]\cdot 3H_2O$ (**28**), β-[(*R*,*R*,*R*,*R*)-TM-BEDT-TTF]$_3PPh_4$ $[K^IFe^{III}(Cl_2An)_3]\cdot 3H_2O$ (**29**) and β-[(*rac*)-TM-BEDT-TTF]$_3$ $PPh_4[K^IFe^{III}(Cl_2An)_3]\cdot 3H_2O$ (**30**) have been afforded by electrocrystallization of the tetramethyl-bis(ethylenedithio)-tetrathiafulvalene (TM-BEDT-TTF) chiral donor in its forms: enantiopure (*S*,*S*,*S*,*S*)- and (*R*,*R*,*R*,*R*)- (TM-BEDT-TTF) donors, as well as the racemic mixture, in the presence of potassium cations and the tris(chloranilato)ferrate(III) $[Fe(Cl_2An)_3]^{3-}$ paramagnetic anion (Scheme 9).

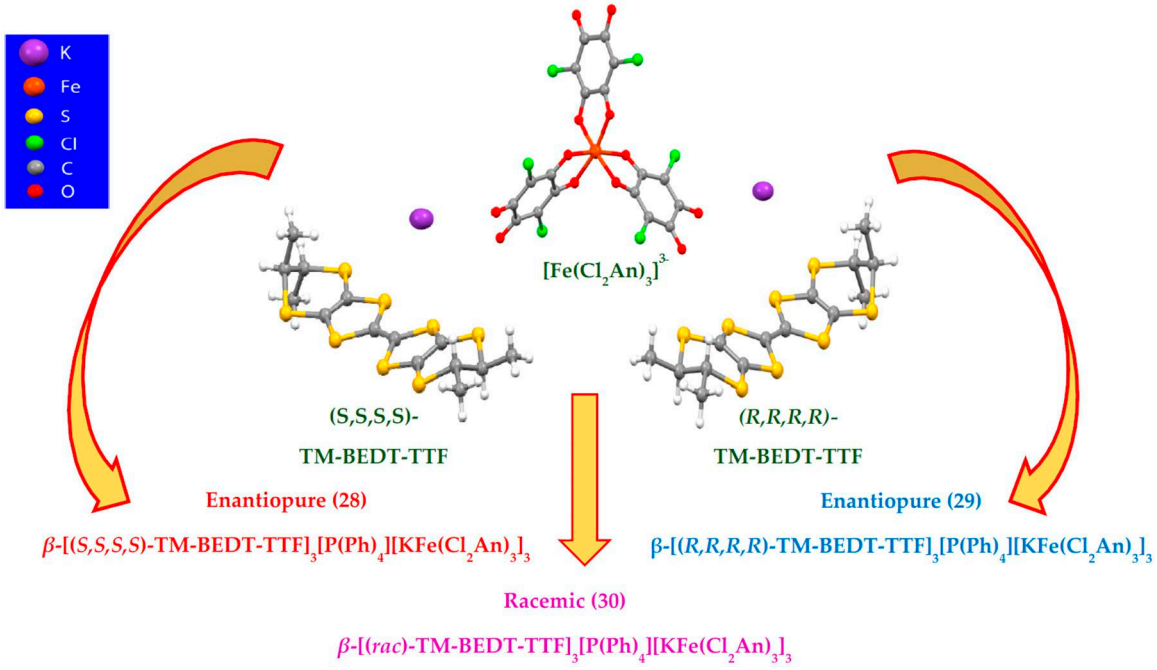

Scheme 9. Molecular structures for the $[Fe(Cl_2An)_3]^{3-}$ complex anion and the enantiopure (*S*,*S*,*S*,*S*)- and (*R*,*R*,*R*,*R*)- TM-BEDT-TTF donors, as well as the racemic mixture, in the presence of potassium cations. Adapted with permission from Reference [167]. Copyright 2015 American Chemical Society.

Compounds **28**–**30** are isostructural and crystallize in the triclinic space group (*P*1 for **28** and **29**, *P*-1 for **30**) showing the usual segregated organic—inorganic crystal structure, where anionic chloranilate-bridged heterobimetallic honeycomb layers obtained by self-assembling of the Λ and Δ enantiomers of the paramagnetic complex with potassium cations, alternate with organic layers where the chiral donors are arranged in the β packing motif (Figure 19).

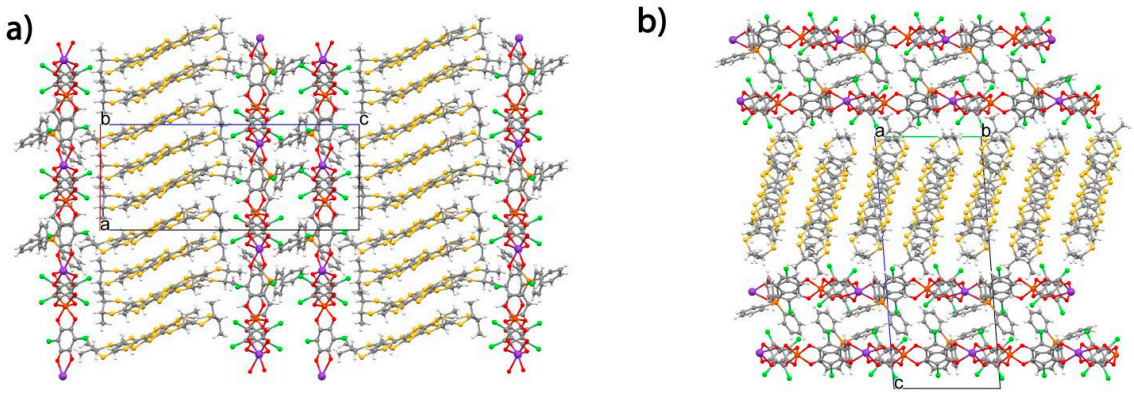

Figure 19. Crystal packing of **29** (**a**) in the *ac* plane; (**b**) in the *bc* plane, showing the organic-inorganic layer segregation. Crystallization water molecules were omitted for clarity. Reprinted with permission from Reference [167]. Copyright 2015 American Chemical Society.

The use of the "complex as ligand approach" during the electrocrystallization experiments has been successful for obtaining these systems where the self-assembling of the tris(chloranilato)ferrate(III) anion with potassium cations afforded anionic layers, that further template the structure in segregated organic and inorganic layers. The common structural features of the three systems are: (i) the presence of inorganic layers associated in double-layers, as a result of two major intermolecular interactions,

Cl···Cl and π-π stacking, between the chloranilate ligands and the $[(Ph)_4P]^+$ charge-compensating cations (Figure 19b) and (ii) the simultaneous presence of two different conformations of the TM-BEDT-TTF donor in the crystal packing, very likely due to the diverse interactions of the terminal methyl groups with the oxygen atoms of the chloranilate ligands. Therefore the molecular packing of **28**–**30** is strongly influenced by the topology of the inorganic layers. **28**–**30** behave as molecular semiconductors with room temperature conductivity values of ca. 3×10^{-4} S cm^1 and an activation energy E_a of ca. 1300–1400 K corresponding to ca. 110–120 meV, as expected from the presence of one neutral TM-BEDT-TTF donor in the crystal packing and the presence of a slight dimerization between the partially oxidized molecules. No significant difference between the enantiopure and the racemic systems is observed. Magnetic susceptibility measurements for **30** indicate the presence of quasi-isolated high spin $S = 5/2$ Fe(III) ions, since the M···M distances between paramagnetic metal centers (ca. 13.6 Å through space and ca. 16.2 Å through the bridging ligands) are too large to allow significant magnetic interactions, with a negligible contribution from the TM-BEDT-TTF radical cations (Figure 20 a,b).

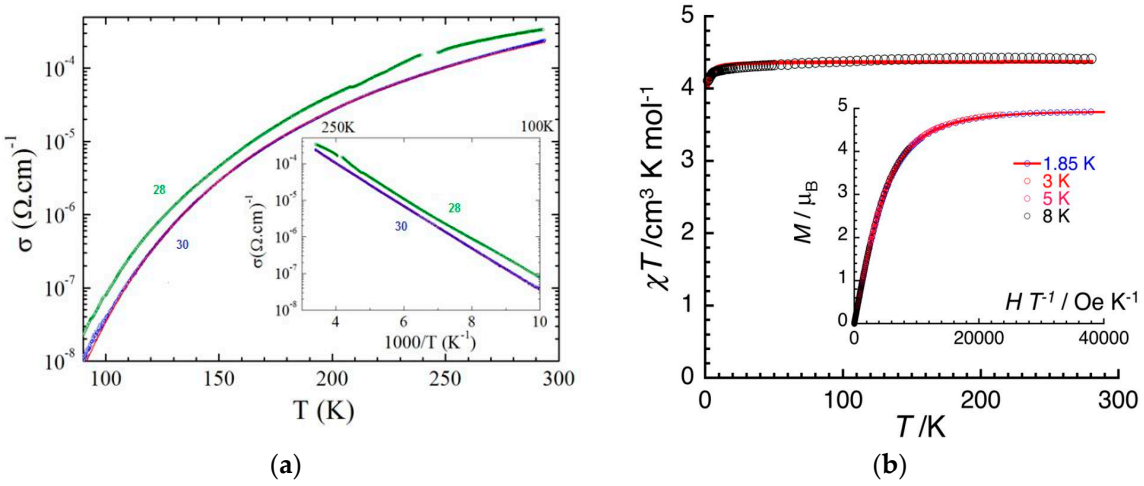

Figure 20. (**a**) Thermal variation of the electrical conductivity for **28** and **30.** The inset shows the Arrhenius plot. The red line is the Arrhenius fit to the data for **30**; (**b**) Thermal variation of magnetic properties (χT product) at 1000 Oe (where χ is the molar magnetic susceptibility equal to the ratio between the magnetization and the applied magnetic field, M/H, per mole of Fe(III) complex) between 1.85 and 280 K for a polycrystalline sample of **30**. The solid line is the Curie-Weiss best fit. Inset: M vs. H/T plot for **30** between 1.85 and 8 K at magnetic fields between 0 and 7 T. The solid line is the best fit obtained using $S = 5/2$ Brillouin function. Adapted with permission from Reference [167]. Copyright 2015 American Chemical Society.

The structural analyses and the band structure calculations are in agreement with the intrinsic semiconducting behaviour shown by the three materials (Figure 21).

This first family of isostructural chiral conducting radical cation salts based on magnetic chloranilate-bridged heterobimetallic honeycomb layers demonstrates (i) the versatility of these anions for the preparation of *π-d* multifunctional molecular materials where properties such as charge transport, magnetism and chirality coexist in the same crystal lattice; (ii) they are fundamental importance for a rational design of chiral conductors showing the eMChA effect as a synergy between chirality and conductivity.

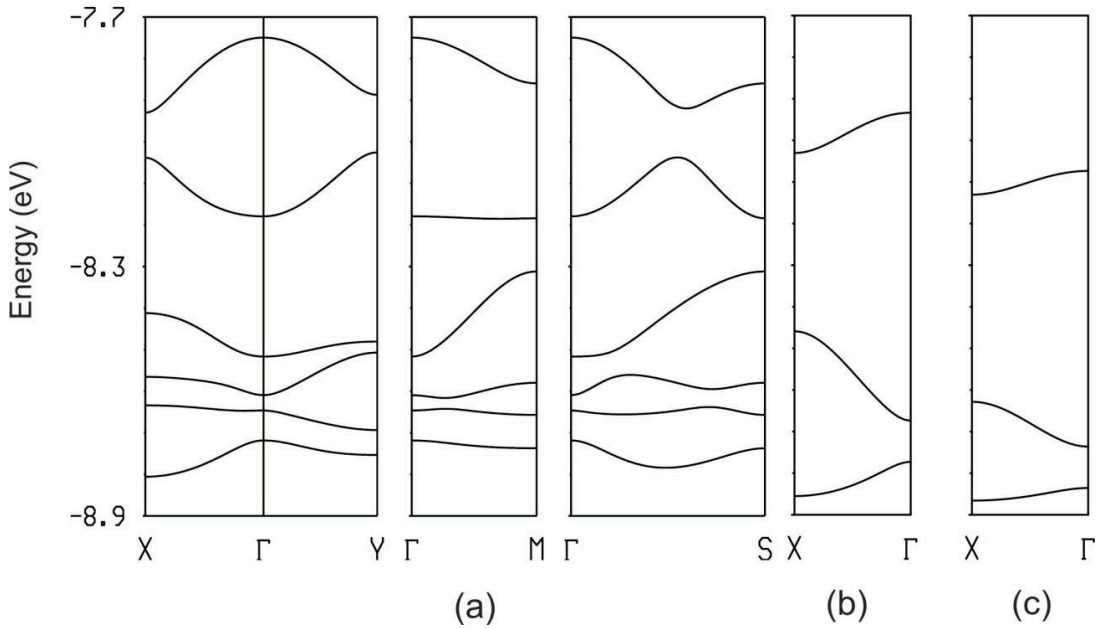

Figure 21. Electronic structure for **28**. Calculated band structure of: (**a**) the $[(TM\text{-}BEDT\text{-}TTF)_6]^{2+}$ donor layers; (**b**) the isolated **–B–E–C–** chains and (**c**) the isolated **–A–D–F–** chains, where Γ = (0, 0), X = ($a^*/2$, 0), Y = (0, $b^*/2$), M = ($a^*/2$, $b^*/2$) and S = ($-a^*/2$, $b^*/2$). Reprinted with permission from Reference [167]. Copyright 2015 American Chemical Society.

3.4. Spin-Crossover Complexes

The family of bimetallic Mn ^{II} Cr ^{III} anilate (X_2An; X = Cl, Br)-based ferrimagnets with inserted the following spin-crossover cationic complexes: $[Fe^{III}(sal_2\text{-trien})]^+$, (X = Cl) (**31**) and its derivatives, $[Fe^{III}(4\text{-OH-}sal_2\text{-trien})]^+$, (X = Cl) (**32**), $[Fe^{III}(sal_2\text{-epe})]^+$, (X = Br) (**33**), $[Fe^{III}(5\text{-Cl-}sal_2\text{-trien})]^+$, (X = Br) (**34**), and $[Fe^{II}(tren(imid)_3)]^{2+}$, (X = Cl) (**35**), (Chart 4a,b) have been prepared and fully characterized [168]. In Chart 4a, the ligands of the Fe(III) and Fe(II) spin crossover complexes are shown. The structures of **32**–**34** consist of bimetallic anionic layers with a 2D bimetallic network of formula $[Mn^{II}Cr^{III}(X_2An)_3]$ (X = Cl, Br) with inserted Fe(III) cationic complexes and solvent molecules. The bimetallic anilate layer show the well-known honeycomb structure, which is similar to that found for other extended oxalate or anilate-based networks (Figure 22). A consequence of the replacement of oxalate by the larger anilate ligands is the presence of pores in the structures, which are filled with solvent molecules.

In contrast to the 2D compounds obtained with $[Fe^{III}(sal_2\text{-trien})]^+$ and derivatives, the structure of **35** is formed by anionic 1D $[Mn^{II}Cl_2Cr^{III}(Cl2An)_3]^{3-}$ chains surrounded by $[Fe^{II}(tren(imid)_3)]^{2+}$, Cl^- and solvent molecules. These chains are formed by $[Cr^{III}(Cl_2An)_3]^{3-}$ complexes coordinated to two Mn(II) ions through two bis-bidentate chloranilate bridges, whereas the third choranilate is a terminal one. The octahedral coordination of Mn(II) ions is completed with two chloride ions in cis. This type of structure has been found for other oxalate-based [169] and homometallic anilate-based compounds [7,170,171], but it is the first time that it is obtained for heterometallic anilate-based networks (Figure 23).

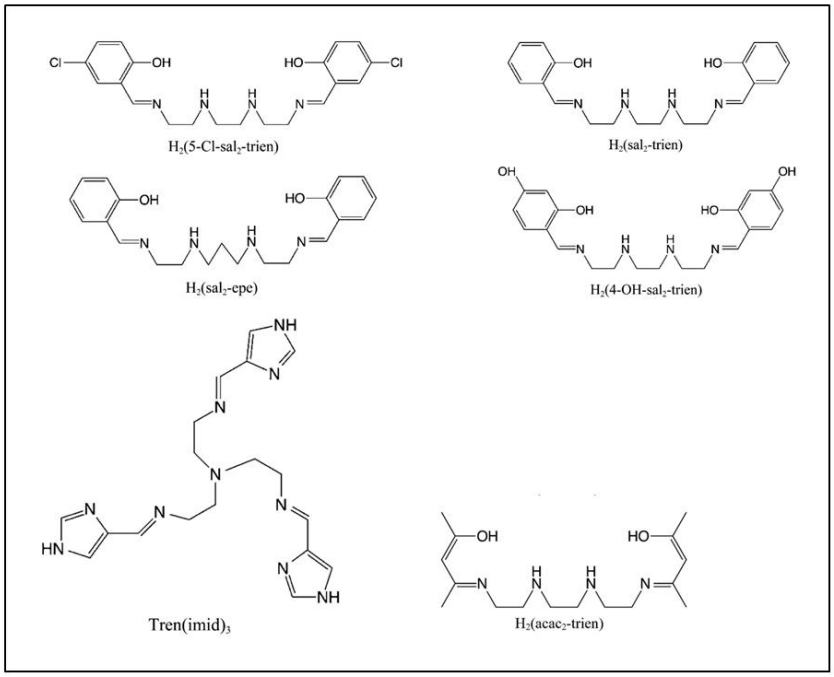

(**a**)

Spin CrossOver Cationic Complexes	
$[Fe^{III}(sal_2\text{-trien})]^+$	MnCr(X-Cl) **31**
$[Fe^{III}(4\text{-OH-sal}_2\text{-trien})]^+$	MnCr(X-Cl) **32**
$[Fe^{III}(sal_2\text{-epe})]^+$	MnCr(X-Br) **33**
$[Fe^{III}(5\text{-Cl-sal}_2\text{-trien})]^+$	MnCr(X-Br) **34**
$[Fe^{II}(tren(imid)_3)]^{2+}$	MnCr(X-Cl) **35**
$[Fe^{III}(acac_2\text{-trien})]^+$	MnCr(X-Cl) **36** MnCr(X-Br) **37**
$[Ga^{III}(acac_2\text{-trien})]^+$	MnCr(X-Br) **38**

(**b**)

Chart 4. Ligands of Fe(III) and Fe(II) complexes (**a**,**b**).

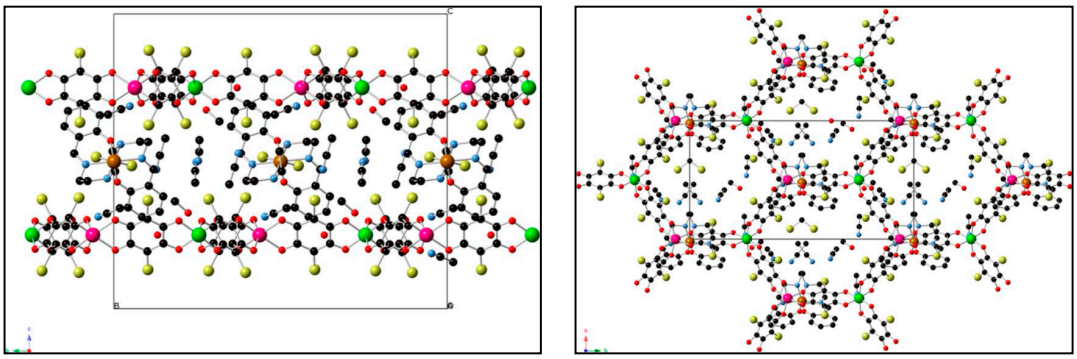

(**a**) (**b**)

Figure 22. Projection of **31** in: (**a**) the *bc* plane; (**b**) the *ab* plane, showing one anionic layer and one cationic layer. (Fe (brown), Cr (green), Mn (pink), C (black), N (blue), O (red) Cl (yellow)). Hydrogen atoms have been omitted for clarity. Adapted with permission from Reference [168]. Copyright 2014 American Chemical Society.

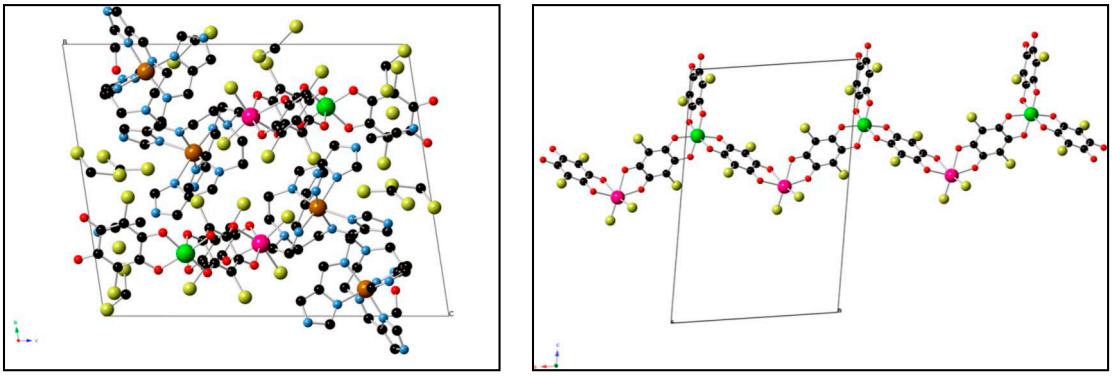

(**a**) (**b**)

Figure 23. Projection of **35** in the bc plane (**a**); $[Mn^{II}Cl_2Cr^{III}(Cl_2An)_3]^{3-}$ chains in the structure of **35** (**b**). (Fe (brown), Cr (green), Mn (pink), C (black), N (blue), O (red) Cl (yellow)). Hydrogen atoms have been omitted for clarity. Adapted with permission from Reference [168]. Copyright 2014 American Chemical Society.

Magnetic studies show that **31**–**34** undergo a long-range ferrimagnetic ordering at ca. 10 K (ca. 10 K for **31**, 10.4 K for **32**, 10.2 K for **33**, and 9.8 K for **34**) with most of the Fe(III) of the inserted cations in the HS state (**31**–**33**), or LS state (**34**). These values are much higher than those found for the $[NBu_4]^+$ and $[(H_3O)(phz)_3]^+$ salts containing similar $[Mn^{II}Cr^{III}(X_2An)_3]^-$ (X = Cl, Br) layers (5.5 and 6.3 K, respectively) (see Section 2.3), in contrast to oxalate-based 2D compounds, where Tc remains constant for a given 2D $[M^{II}M^{III}(ox)_3]^-$ lattice, independently of the inserted cation. Therefore, the magnetic coupling and, accordingly, the ordering temperatures of these heterometallic 2D anilate-based networks are much more sensitive to the changes of the inserted cations than the corresponding oxalate ones. This effect is maybe due to the presence of π-π and NH···O and NH···Cl/Br intermolecular interactions between the anilate ligands and Fe(III) complexes which may increase the Mn(II)–Cr(III) coupling constant through the anilate ligand an thus the Tc. Interestingly, this modulation of Tc with the inserted cation (or even with solvent molecules), besides the already observed modulation with the X substituents on the benzoquinone moiety, represents an additional advantage of the anilate-based networks compared with the oxalate ones.

Differently from **28**–**34**, **35** do not show π-π stacking interactions with the anilate ligands and therefore half of the inserted Fe(II) cations undergo a complete and gradual spin crossover from 280 to 90 K which coexists with a ferrimagnetic coupling within the chains that gives rise to a magnetic ordering below 2.6 K. The Temperature dependence of the product of the molar magnetic susceptibility times the temperature of **31**–**35** is reported in Figure 24.

When using the $[M^{III}(acac_2\text{-trien})]^+$ (M^{III}—Fe or Ga complex, which has a smaller size than the $[Fe^{III}(sal_2\text{-trien})]^+$ spin-crossover complex, three novel magnetic compounds $[Fe^{III}(acac_2\text{-trien})][Mn^{II}Cr^{III}(Cl_2An)_3]_3(CH_3CN)_2$ (**36**), $[Fe^{III}(acac_2\text{-trien})][Mn^{II}Cr^{III}(Br_2An)_3]_3(CH_3CN)_2$ (**37**), $[Ga^{III}(acac_2\text{-trien})][Mn^{II}Cr^{III}(Br_2An)_3]_3(CH_3CN)_2$ (**38**), have been prepared and characterized by Coronado et al. [172]. The 2D anilate-based networks show the common honeycomb anionic packing pattern but a novel type of structure where the cations are placed into the hexagonal channels of the 2D network has been afforded due to the smaller size of the $[Fe^{III}(acac_2\text{-trien})]^+$ or $[Ga^{III}(acac_2\text{-trien})]^+$ complex with respect to the templating cations used in previous compounds of this type, where they are placed in between the anionic layers. An important decrease of the interlayer separation between the anilate-based layers (Figure 25a,b) is observed.

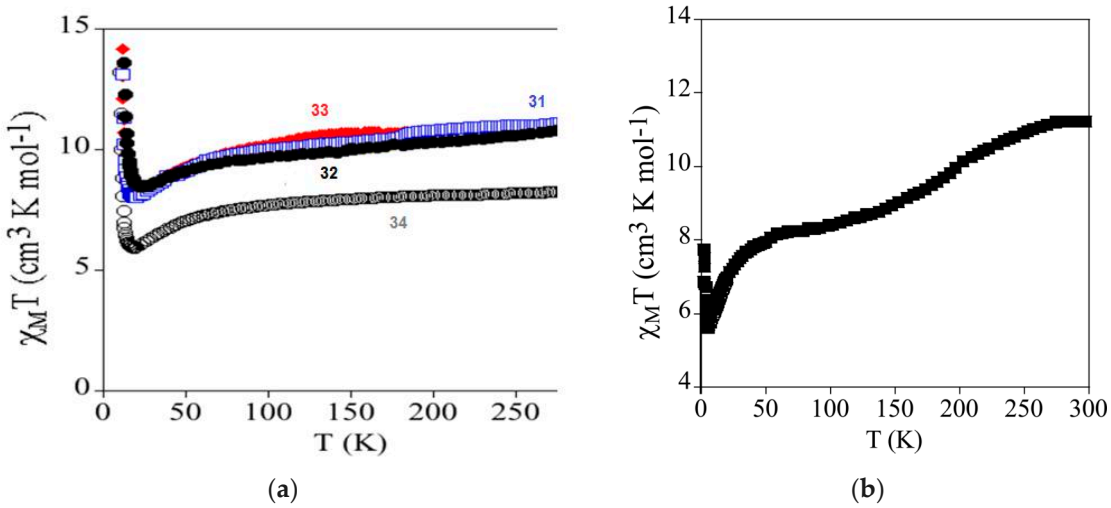

(**a**) (**b**)

Figure 24. Thermal variation of magnetic properties (χ_mT product vs. T) at an applied field of 0.1 mT of: (**a**) **31** (empty blue, squares), **32** (full circles), **33** (full red diamonds), and **34** (empty circles); (**b**) **35.** Adapted with permission from Reference [168]. Copyright 2014 American Chemical Society.

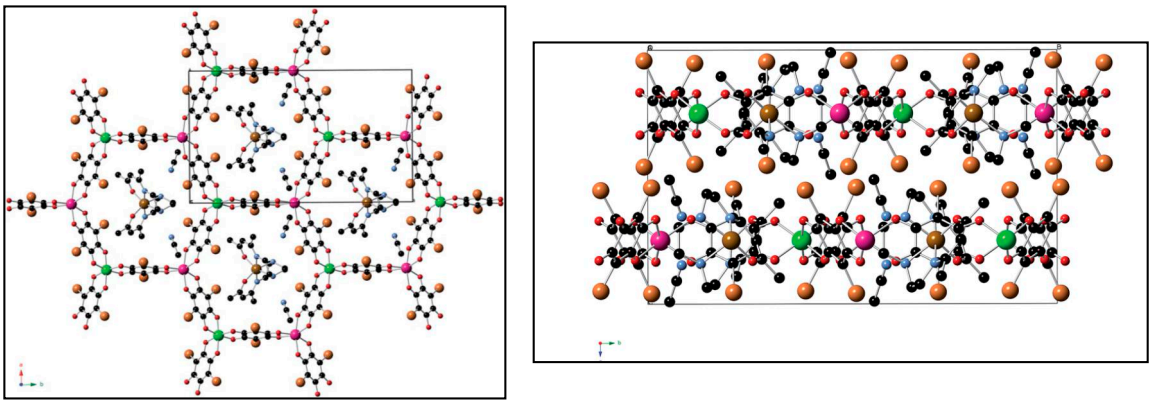

(**a**) (**b**)

Figure 25. Projection of **36** in the *ab* plane (**a**) and in the *bc* plane (**b**). ((Fe (brown), Cr (green), Mn (pink) C (black), N (blue), O (red), Br (orange)). Hydrogen atoms have been omitted for clarity. Reprinted from Reference [172] with permission from The Royal Society of Chemistry.

The anilate-based layers with inserted $[Fe^{III}(acac_2\text{-trien})]^+$ complexes may be viewed as neutral layers that interact with each other via van der Waals interactions. Thus, in **37**, the shortest contacts between neighbouring layers involve Br atoms from Br_2An ligands and CH_2 and CH_3 groups from $[Fe^{III}(acac_2\text{-trien})]^+$ complexes of neighbouring layers. This type of structure, formed by neutral layers, has never been observed previously in oxalate or anilate-based 2D networks. The close contact of the cationic complexes with the magnetic network results in an increase of the T_c (ca. 11 K) with respect to that of previous anilate-based compounds (ca. 10 K), even though to not favour the spin crossover of the inserted complexes which remain the HS state. The weak natures of the intermolecular interactions between the magnetic neutral layers play a crucial role for the exfoliation of the layers. In fact this new magnetic network is very peculiar since it can be easily exfoliated by using the so-called Scotch tape method which is a micromechanical method, capable to produce in a very efficient way, highly crystalline thin microsheets of a layered material [173–175]. To the best of our knowledge this method has never been applied to such layered materials. Flakes of **37**, with different sizes and thicknesses randomly distributed over the substrate have been obtained. AFM topography images revealed that the

they show maximum lateral dimensions of ca. 5 mm, with well-defined edges and angles (Figure 26). The heights of the largest flakes of **37** are around 10–20 nm, while smaller microsheets with heights of less than 2 nm were also found.

The presence of terraces with different heights indicatse that this magnetic network is layered. Interestingly the Scotch tape method has been successful used also to exfoliate the 2D anilate-based compound $[Fe^{III}(sal_2\text{-trien})][Mn^{II}Cr^{III}(Cl_2An)_3](CH_2Cl_2)_{0.5}(CH_3OH)(H_2O)_{0.5}(CH_3CN)_5$, (**31**), described above [168], which exhibits the typical alternated cation/anion layered structure. In this case rectangular flakes of larger lateral size than those isolated in **37** (up to 20 microns) have been obtained with well-defined terraces and a minimum thickness of ca. 2 nm, which may correspond to that of a single cation/anion hybrid layer (ca. 1.2 nm).

31 and **37** have been also successfully exfoliated by solution methods. Tyndall light scattering of the colloidal suspensions of both compounds has been observed, as shown in Figure 27 for **37**, and dynamic light scattering (DLS) measurements confirm the efficiency of the liquid exfoliation.

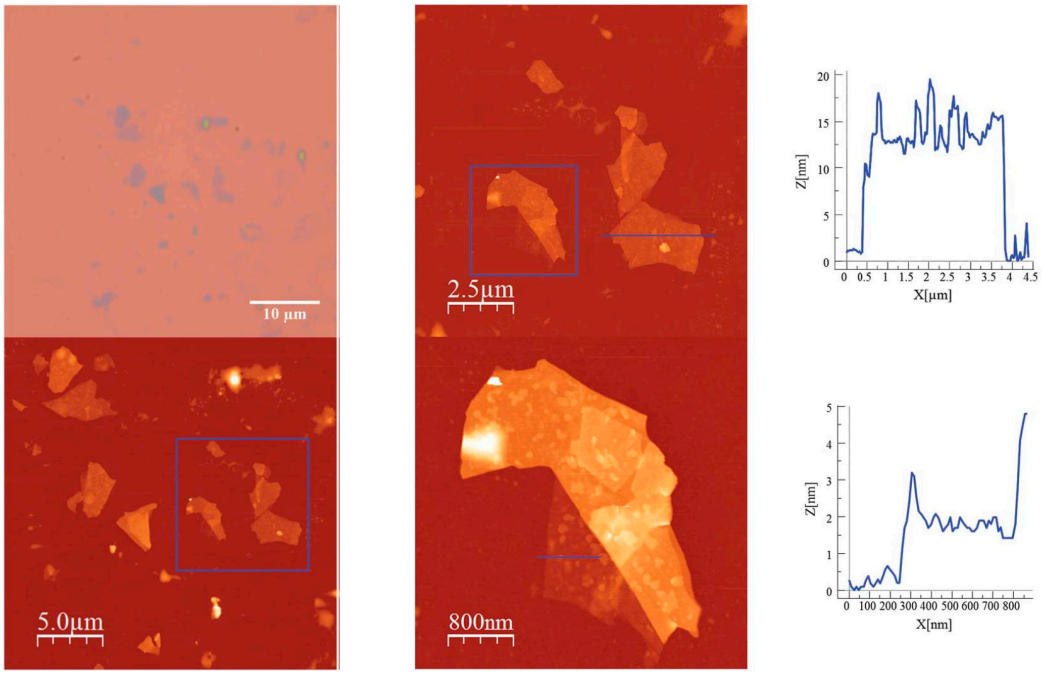

Figure 26. Images of flakes of **37**, obtained by mechanical exfoliation on a 285 nm SiO_2/Si substrate, by Optical microscopy (**left**), AFM (atomic force microscopy) (**middle**) and height profiles (**right**). Reprinted from Reference [172] with permission from The Royal Society of Chemistry.

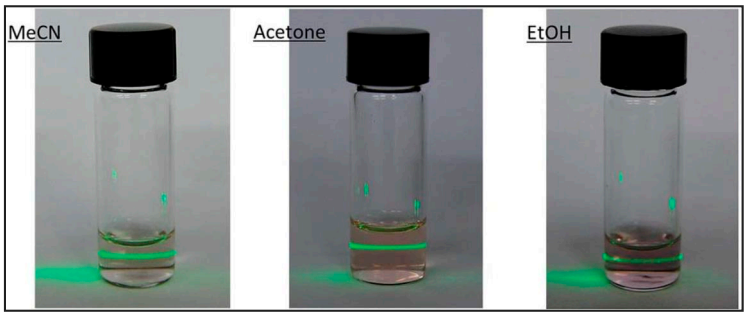

Figure 27. Tyndall effect of crystals of **37** after suspension in acetone, ethanol or acetonitrile (1.0 mg in 1 mL) overnight and then ultrasonicating for 1 min. Reprinted from Reference [172] with permission from The Royal Society of Chemistry.

These results show that it is possible to exfoliate 2D coordination polymers formed by a 2D honeycomb anionic network and cations inserted within or between the layers. The thicknesses of the flakes obtained by micromechanical methods are clearly lower than those obtained by solution methods (ca. 5 nm), where the lateral size of the flakes is of the order of hundreds of nm (significantly smaller). The solution-based exfoliation procedure is less effective in the neutral coordination polymers which can be completely delaminated (with a thickness ca. 1–1.5 nm) [115,170,176–183]. The stronger interlayer interactions in these hybrid compounds compared with the weaker van der Waals interactions observed in neutral 2D coordination polymers could be responsible of the lower degree of exfoliation.

The hybrid nature of these layered materials, providing the opportunity to produce smart layers where the switching properties of the cationic complexes can tune the cooperative magnetism of the anionic network, represents the real challenge of these results.

3.5. Guests Intercalation of Hydrogen-Bond-Supported Layers

A successful strategy to control the molecular packing in molecule-based materials takes advantage of more flexible hydrogen bonds in combination with metal-ligand bonds (Scheme 10 to control the rigidity of a supramolecular framework.

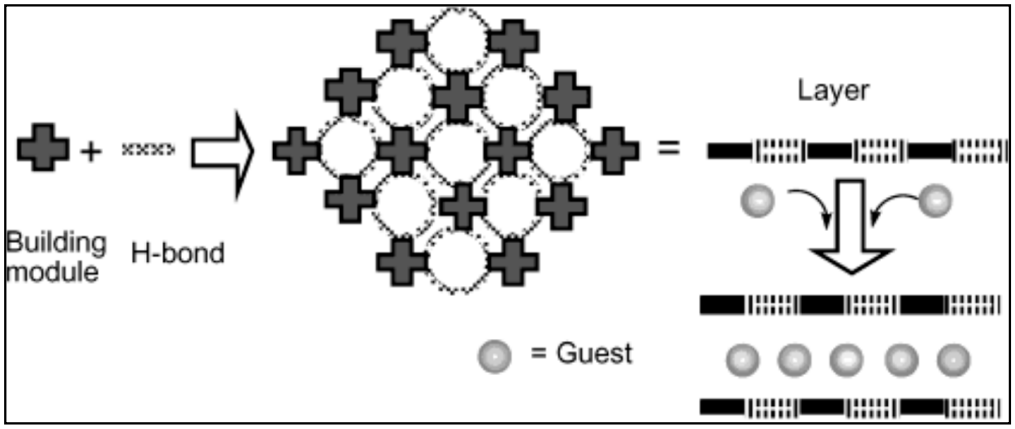

Scheme 10. Reprinted with permission from Reference [184]. Copyright 2003 American Chemical Society.

Novel intercalation compounds formed by 2D hydrogen-bond mediated Fe(III)-chloranilate layers and cationic guests, carrier of additional physical properties, $\{(H_{0.5}phz)_2[Fe(Cl_2An)_2(H_2O)2]â2H_2O\}_n$ (**39**), $\{[Fe(Cp)_2][Fe(Cl_2An)_2(H_2O)_2]\}n$ (**40**), $\{[Fe(Cp^*)_2][Fe(Cl_2An)_2(H_2O)_2]\}_n$ (**41**), and $\{(TTF)_2[Fe(Cl_2An)_2(H_2O)_2]\}_n$ (**42**) (phz = phenazine, $[Fe(Cp)_2]$ = ferrocene, $[Fe(Cp^*)_2]$ = decamethyl ferrocene, TTF = tetrathiafulvalene) are reported by Kawata et al. [184]. The cationic guests are inserted between the $\{[Fe(Cl_2An)_2(H_2O)_2]\}^{m-}$ layers and are held together by electrostatic (**39**–**42**) and π-π stacking (**41**, **42**) interactions. The $\{[Fe(Cl_2An)_2(H_2O)_2]\}^{m-}$ layers are very flexible and depending on the guest sizes and electronic states they can tune their charge distribution and interlayer distances. Especially **42** is a rare example of hydrogen-bonded layer of monomeric complexes, which can intercalate different charged guests, thus showing a unique electronic flexibility.

In **41** decamethylferrocene cations are stacked in tilted columns inserted in the channels created by the chlorine atoms of chloranilate dianions. In **42** TTF cations are stacked face to face with two types of S···S distances (type A; 3.579(3) Å, and type B; 3.618(3) Å) leading to 1D columns. The TTF cations in the stacked column have a head-to-tail arrangement with respect to the iron-chloranilate layer. Interestingly, slight differences are observed in the **39**–**42** structures built from the common anionic layer, caused by the intercalation of different types of guests that influence the crystal packing. The main difference in fact is in the interlayer distances (Fe(1)-Fe(1′′)) 14.57 Å (**39**), 9.79 Å (**40**), 13.13 Å

(**41**), and 13.45 Å (**42**) as shown in Scheme 11. Interestingly chlorine atoms form channels between the layers and by changing their tilt angles and stacking distances depending on their sizes and shapes, modify layers structure (Scheme 12.)

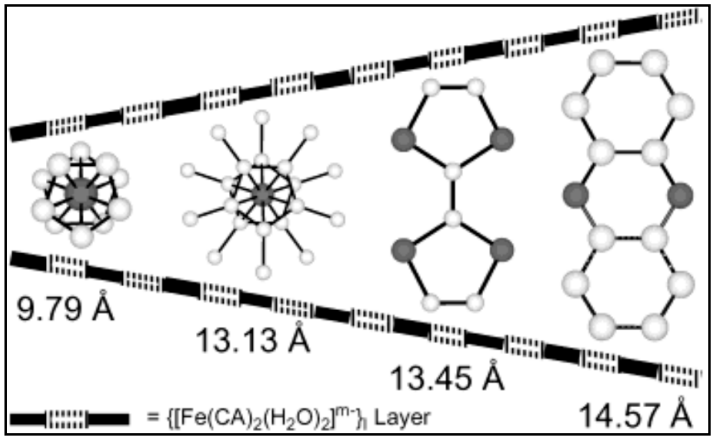

Scheme 11. Reprinted with permission from Reference [184]. Copyright 2003 American Chemical Society.

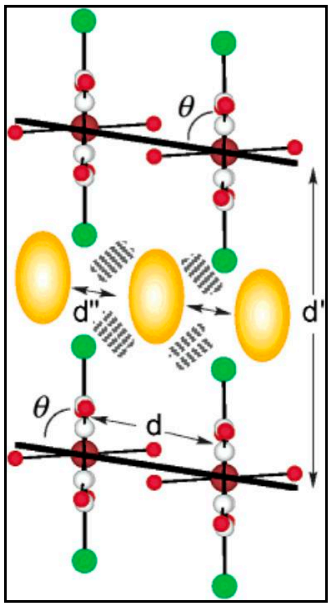

Scheme 12. Reprinted with permission from Reference [184]. Copyright 2003 American Chemical Society.

Mossbauer spectra suggests that: (i) in **41** high-spin (S = 5/2) iron(III) ions are present in $\{[Fe(Cl_2An)_2(H_2O)_2]\}^{m-}$ anions while low-spin (S = 1/2) iron(III) ions in $[Fe(Cp^*)_2]^+$ cations; (ii) in **42**, the anionic layer of iron-chloranilate has a valence-trapped mixed-valence state since high-spin iron(II) and iron(III) ions are present. **39**, **40**, and **41** are EPR silent, in the 77–300 K range, whereas the EPR spectrum of **42** shows two types of signals with g = 2.008 indicating the TTF is present as radical species (Figure 28).

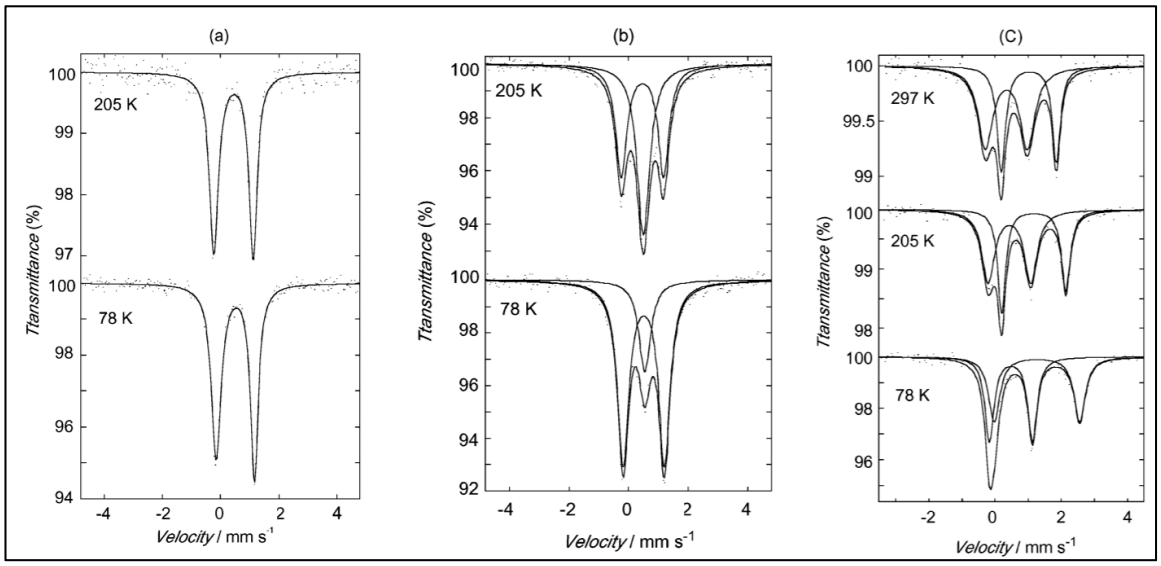

Figure 28. ^{57}Fe Mössbauer spectra of: (**a**) **39**; (**b**) **41**, showing the overlap of one singlet and one quadrupole doublet typical of low-spin iron(III) and high-spin iron(III) respectively; and (**c**) **42**. Reprinted with permission from Reference [184]. Copyright 2014 American Chemical Society.

The thermal variation of the magnetic properties ($\chi_M T$ product vs. T) for **39**–**42** compounds, measured in the 2–300 K temperature range, under an applied field of 0.5 T, are shown in Figure 29. The $\chi_M T$ product in **39**, **40**, and **41** shows a slight decrease with decreasing temperature and at lower temperature they show a major decrease, suggesting the existence of weak antiferromagnetic interactions.

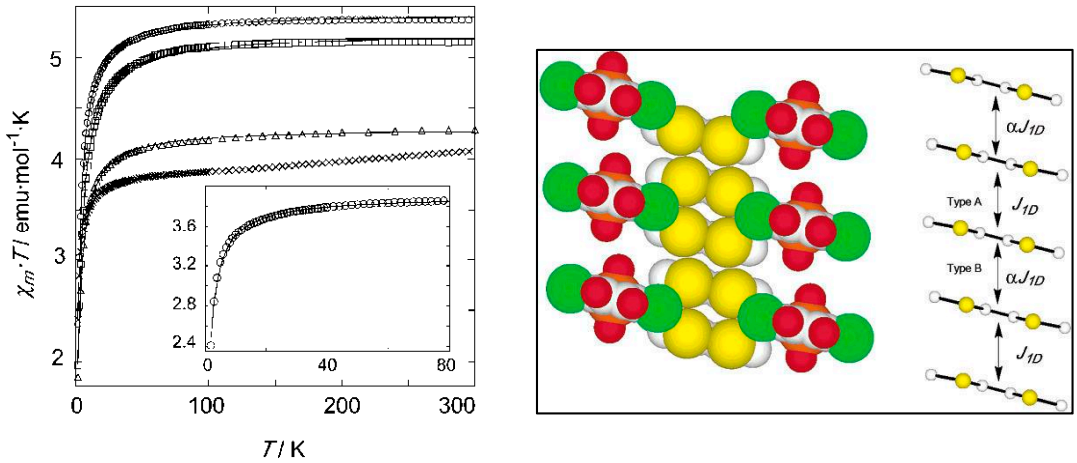

Figure 29. (**left**) Thermal variation of the magnetic properties ($\chi_M T$ vs. T) for **39** (open triangles), **40** (open squares), **41** (open circles), and **42** (cross marks). Inset, magnetic susceptibility of **42** below 80 K. Solid lines are theoretical fits of the data with the parameters listed in Reference [184]; (**right**) S···S stacking interactions of A and B types. Reprinted with permission from Reference [184]. Copyright 2003 American Chemical Society.

The observed χ_M values of **40**, **41**, and **42** are the sum of the guest and host contributions; no exchange has been observed between the two spin sublattices while are observed magnetic-field dependent susceptibility (**40**, **41**) and strong antiferromagnetic coupling around 300 K (**42**). These peculiar magnetic behaviors are due to the intrachain coupling in guests which are arranged in 1D columns. In the case of **42** the antiferromagnetic interactions through the column dominates the layers structure above 80 K and this is due to the 1D columns with rare S···S contacts of TTF cations. As shown in

Figure 29 (right), the values of J_{1D} and αJ_{1D} reflect two types of S···S stacking interactions and indicate that the magnetic exchange is stronger between the stacked TTF cations located at smaller distances.

4. Anilato-Based Multifunctional Organic Frameworks (MOFs)

A rare example of Metal Organic Framework MOF composed by Fe^{III} bridged by paramagnetic linkers that additionally shows ligand mixed-valency has been reported by J. Long et al. [185]. These materials are based on 2,5-dihyroxy-1,4-benzoquinone (DHBQ) or hydranilate with R=H, the parent member of the anilates which can afford the redox processes shown in Scheme 13:

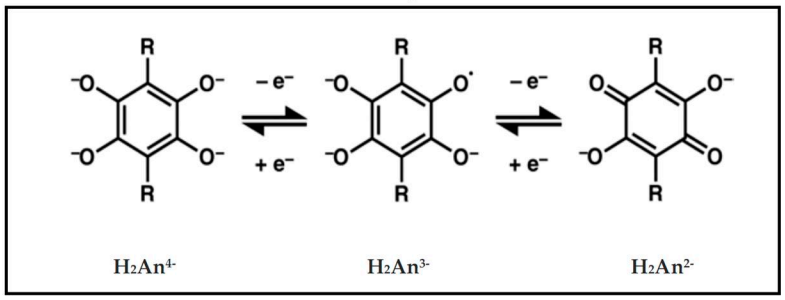

Scheme 13. Redox states of linkers deriving from 2,5-dihydroxybenzoquinone that have previously been observed in metal—organic molecules. Notably, $\mathbf{H_2An^{3-}}$ is a paramagnetic radical bridging ligand.

$(NBu_4)_2Fe^{III}{}_2(H_2An)_3$ (**43**) shows a very rare topology for H_2An^{2-}-based coordination compounds [81,112,121,125], with two interpenetrated (10,3)-a lattices of opposing chiralities where neighboring metal centers within each lattice are all of the same chirality (Figure 30b,c), generating a three-dimensional structure (Figure 30a–d). This topology differs from the classic 2D honeycomb structure type frequently observed for hydranilates and derivatives, where neighboring metal centers are of opposing chiralities [108,125].

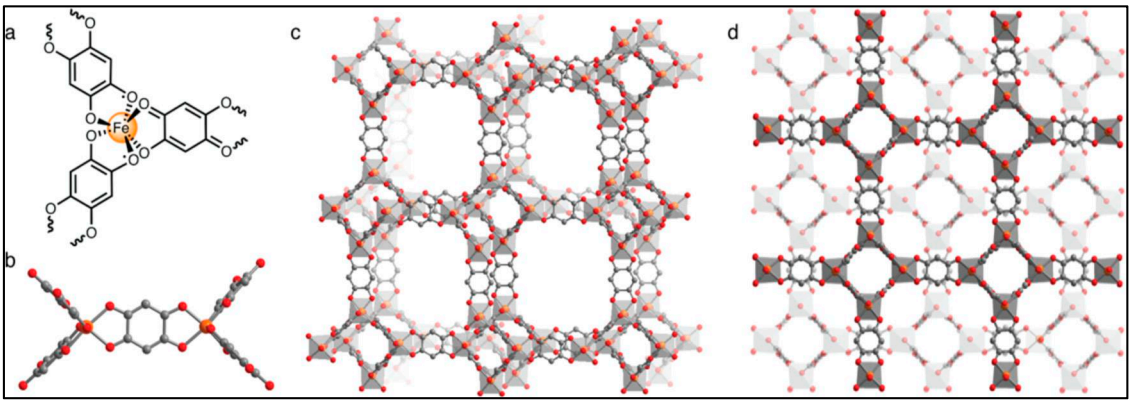

Figure 30. (**a**) Molecular structure of a single Fe^{III} center in $(NBu_4)_2Fe^{III}{}_2(H_2An)_3$, showing that two radical (H_2An^{3-}) bridging ligands and one diamagnetic (H_2An^{2-}) bridging ligand are coordinated to each metal site; (**b**) A portion of its crystal structure, showing the local environment of two H_2An^{n-}-bridged Fe^{III} centers; (**c**) A larger portion of the crystal structure, showing one of the two interpenetrated (10,3)-a nets that together generate the porous three-dimensional structure; (**d**) The two interpenetrated (10,3)-a lattices of opposing chiralities. Charge-balancing NBu_4^+ cations are not depicted for clarity. Reprinted with permission from Reference [185]. Copyright 2015 American Chemical Society.

The tetrabutylammonium countercations are crucial for templating the 3D structure, compared with other 1D or 2D hydranilate-based materials [7,108,125,186–188] since were located inside the pores and appear to fill the pores almost completely with no large voids present. Similar cation-dependent morphology changes have been observed for transition metal—oxalate coordination compounds with analogous chemical formula $[A^+]_2M^{II}_2(ox)_3$ [72,81,189–191]. The electronic absorption spectrum broad absorbance extending across the range 4500–14,000 cm^{-1}, with ν_{max} = 7000 cm^{-1}. This intense absorption features are attributed to ligand-based IVCT. Notably, a solid-state UV-vis-NIR spectrum of a molecular Fe^{III} semiquinone—catecholate compound shows a similar, though narrower, IVCT band at ν_{max} = 5200 cm^{-1} [192]. Since all the iron centers are trivalent as confirmed by Mössbauer spectroscopy, the origin of the IVCT must be the organic $dhbq^{2-/3-}$ moieties. Interestingly a very sharp absorption edge is observed at low energy (4500 cm^{-1}), one of the best-known signatures of Robin—Day Class II/III mixed-valency[193–196]. This represents the first observation of a Class II/III mixed-valency in a MOF which is also indicative of thermally activated charge transport within the lattice. **43** infact behaves as an Arrhenius semiconductor with a room-temperature conductivity of 0.16(1) S/cm and activation energy of 110 meV and it has been found to be Ohmic within ±1 V of open circuit. To the best of our knowledge, this is the highest conductivity value yet observed for a 3D connected MOF. The chemical reduction of **43** by using a stoichiometric amount of sodium naphthalenide in THF, for a stoichiometric control of the ligand redox states, affords **44**, formulated as $(Na)_{0.9}(NBu_4)_{1.8}Fe^{III}_2(H_2An)_3$, which shows a highly crystalline powder X-ray diffraction (PXRD) pattern that overlays with that simulated for **45** and is much closer to a fully H_2An^{3-}—bridged framework. **44** shows a lower conductivity of 0.0062(1) S/cm at 298 K and a considerably larger activation energy of 180 meV which is consistent with a further divergence of the H_2An^{3-}/H_2An^{2-} ligand ratio from the optimal mixed-valence ratio of 1:1 (Figure 31).

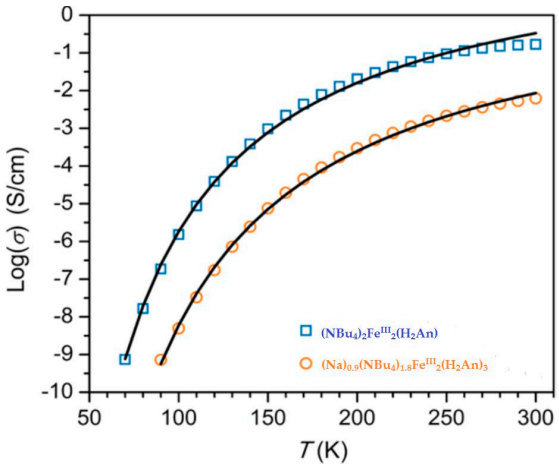

Figure 31. Variable-temperature conductivity data for **43** and **44**, shown by blue squares and orange circles, respectively. Arrhenius fits to the data are shown by black lines. Adapted with permission from Reference [185]. Copyright 2015 American Chemical Society.

Due to the presence of H_2An^{3-} radicals a peculiar magnetic behavior is expected on the basis of previously studied metal—organic materials with transition metals bridged by organic radicals which have shown strong magnetic coupling, leading to high temperature magnetic ordering [197]. Variable-temperature dc magnetic measurements under an applied magnetic field of 0.1 T revealed strong metal-radical magnetic interactions, leading to magnetic ordering less than 8 K (Figure 32) due to the strong magnetic coupling that has previously been observed in Fe^{III} H_2An^{3-} complexes [198].

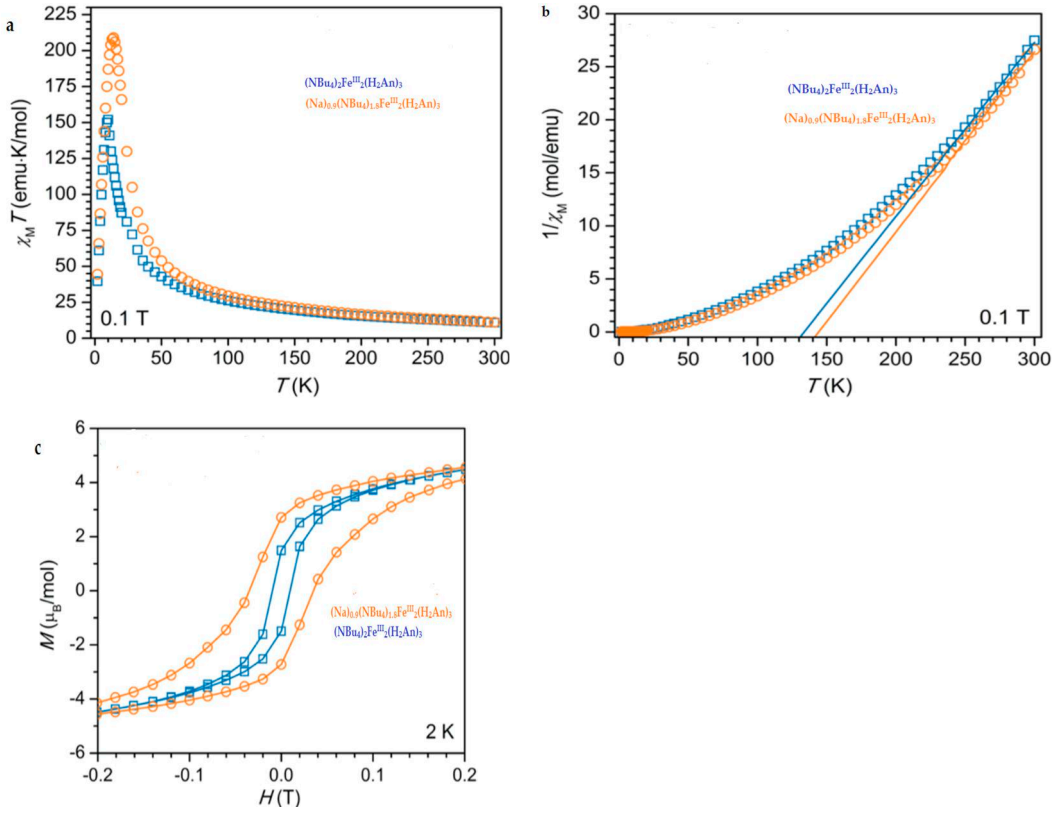

Figure 32. (**a**) DC magnetic susceptibility data for **43** (blue squares) and **44** (orange circles); (**b**) Inverse of magnetic susceptibility versus temperature for **43** and **44**. Curie-Weissfits to the data in the temperature range 250–300 K are shown by solid blue (**43**) and orange lines (**44**); (**c**) Magnetization (M) versus applied dc magnetic field (H) data for **43** and **44** in blue and orange, respectively. Hysteresis loops were recorded at a sweep rate of 2 mT/s. Solid lines are guides for the eye**.** Adapted with permission from Reference [185]. Copyright 2015 American Chemical Society.

Below 250 K the observed strong deviations from the Curie-Weiss behavior, observed in systems with strong π-d interactions [199], have been attributed to the competition between ferromagnetic and antiferromagnetic interactions, both maybe present in **43**, leading to magnetic glassiness [200]. A Curie-Weiss fit of the inverse magnetic susceptibility data from 250 to 300 K results in a Curie temperature of θ = 134 K and a Curie constant of C = 6.1 emu·K/mol. The positive Curie temperature reveals that ferromagnetic interactions are dominant at high temperature and its magnitude suggests that quite high temperature magnetic coupling occurs. In contrast, the magnetic behavior at low temperature indicates that ferrimagnetic coupling predominates. Thus, the low magnetic ordering temperature is attributed to a competition of ferromagnetic and antiferromagnetic interactions that prevent true three-dimensional order, until antiferromagnetic metal—radical interactions, and thus bulk ferrimagnetic order, prevail at low temperature. **44** was expected to show an increased magnetic, ordering temperature due to the greater number of paramagnetic linkers. Indeed, a higher magnetic transition temperature of 12 K was observed and the room-temperature $\chi_M T$ product is 11.2 emu·K/mol, compared to 10.9 emu·K/mol for **43**. Finally, low temperature (2 K) magnetic hysteresis measurements shown in Figure 32c reveal that **44** is a harder magnet than **43**, with coercive fields of 350 and 100 Oe observed, respectively. These materials are rare examples of a MOF formed by metal ions bridged by paramagnetic linkers that additionally shows ligand-centered mixed valency where magnetic ordering and semiconducting behaviors stem from the same origin, the ferric semiquinoid lattice, differently from multifunctional materials based on tetrathiafulvalene derivatives with paramagnetic counterions

where separate sub-lattices furnish the two distinct magnetic/conducting properties. Therefore they represent a challenge for pursuing magnetoelectric or multiferroic MOFs.

Anilates are also particularly suitable for the construction of microporous MOFs with strong magnetic coupling and they have been shown to generate extended frameworks with different dimensionality and large estimated void volumes, which could potentially give rise to materials with permanent porosity [112]. Very recently Harris et al. [201] have reported on the synthesis and full characterization of $(Me_2NH_2)_2[Fe_2L_3]\cdot 2H_2O\cdot 6DMF$ (**45**), the first structurally characterized example of a microporous magnet containing the Cl_2An^{3-}·chloranilate radical species, where solvent-induced switching from Tc = 26 to 80 K has been observed. **45** shows the common 2D honeycomb layered packing where the layers are eclipsed along the crystallographic *c* axis, with a H_2O molecule located between Fe centers, leading to the formation of 1D hexagonal channels (Figure 33). These channels are occupied by disordered DMF molecules, as was confirmed by microelemental analysis and thermogravimetric analysis (TGA).

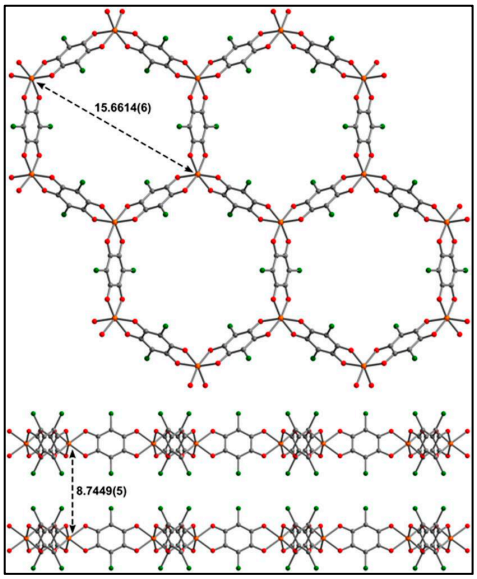

Figure 33. View of the crystal structure of $[Fe_2L_3]^{2-}$, along the crystallographic *c* axis (upper) and *b* axis (lower), with selected Fe···Fe distances (Å). Orange = Fe, green = Cl, red = O, and gray = C. Adapted with permission from Reference [201]. Copyright 2015 American Chemical Society.

X-ray diffraction, Raman spectra and and Mo··ssbauer spectra confirm the presence of Fe^{III} metal ions and mixed-valence ligands which can be formulated as $[(Cl_2An)_3]^{8-}$, obtained through a spontaneous redox reaction from Fe^{II} to Cl_2An^{2-}. Upon removal of DMF and H_2O solvent molecules, the desolvated phase $(Me_2NH_2)_2Fe_2(Cl_2An)_3]$, **45a**, showing a slight structural distortion respect to **45**, has been obtained. **45a** gives a a Brunauer-Emmett-Teller (BET) surface area of 885(105) m^2/g, from a fit to N_2 adsorption data, at 77 K, confirming the presence of permanent microporosity. This value is the second highest reported for a porous magnet, overcome only with a value of 1050 m^2/g reported for a lactate-bridged Co^{II} material [202]. Finally, the structural distortion is fully reversible and similar "breathing" behavior has been previously observed in MOFs [203–205]. The thermal variation of the magnetization shows that **45** and **45a** have a spontaneous magnetization below 80 and 26 K with magnetic hysteresis up to 60 and 20 K (Figure 34).

To precisely determine the Tcs of **45** and **45a**, variable-temperature ac susceptibility data under zero applied field were collected at selected showing for **45a** slightly frequency dependent peak in both in-phase (χ_M') and out-of-phase (χ_M'') susceptibility and give a Tc = 80 K. The frequency dependence can be quantified by the Mydosh parameter, in this case $\phi = 0.023$, which is consistent with glassy magnetic behavior. Such glassiness can result from factors such as crystallographic disorder and spin

frustration arising from magnetic topology. In contrast, the plot of χ_M' vs. T for **45a** exhibits a sharp, frequency-independent peak with a maximum at 26 K, indicating that **45a** undergoes long-range magnetic ordering at Tc = 26 K. The magnetic data demonstrate that **45** and **45a** behave as magnets that involve dominant intralayer antiferromagnetic interactions between adjacent spins. Moreover these results demonstrate that the incorporation of semiquinone radical ligands into an extended can generate a 2D magnet with Tc = 80 K, with permanent porosity and activated phase undergoing a slight structural distortion and associated decrease in magnetic ordering temperature to Tc = 26 K.

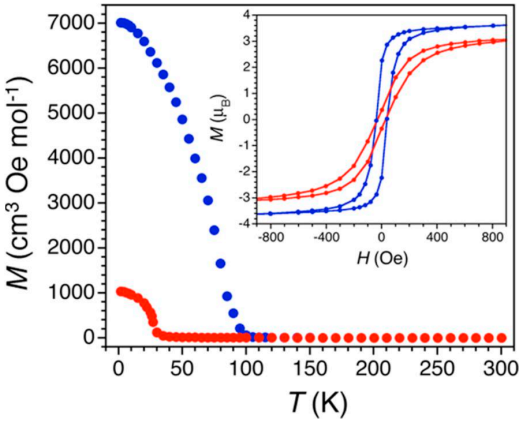

Figure 34. Thermal variation of the magnetization for **45** (blue) and **45a** (red), collected under an applied dc field of 10 Oe. Inset:Variable-field magnetization data for **45** at 60 K (blue) and **45a** at 10 K (red). Reprinted with permission from Reference [201] Copyright 2015 American Chemical Society.

The first example of a 3D monometallic lanthanoid assembly, the $Na_5[Ho(H_2An^{4-})_2]_3$ $7H_2O$ (**46**) complex, showing ferromagnetism with a Curie temperature of 11 K, has been reported by Ohkoshi et al. [206]. In this compound the Ho^{3+} ion adopts a dodecahedron (D_4d) coordination geometry and each Ho^{3+} ion is connected to eight O atoms of four bidentate H_2An^{4-} ligands directed toward the *a* and *b* axes, which resulted in a 3-D network with regular square-grid channels (Figure 35a–c). These channels (4.9 × 4.9 Å) was occupied by Na^+ ions and noncoordinated water molecules.

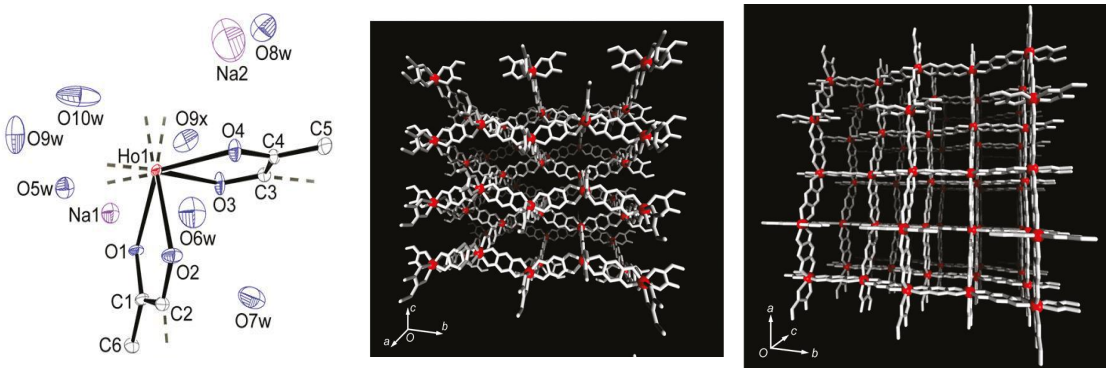

Figure 35. (**a**) Thermal ellipsoid plots (50% probability level) of the molecular structure of **46**. All independent atoms, including water and Na^+ ions, are labeled. H atoms are omitted for clarity. Ho, Na, O, and C atoms, are represented by red, purple, blue, and light gray colours respectively; (**b**) X-ray crystal structure along the *a* axis; (**c**) X-ray crystal structure along the *c* axis. Water molecules, Na^+ ions and H atoms are omitted for clarity. Adapted with permission from Reference [206]. Copyright 2009 American Chemical Society.

The thermal variation of the magnetic properties ($\chi_M T$ product vs. T) is reported in Figure 36. The $\chi_M T$ value at room temperature was 14.4 cm^3 K mol^{-1}, which nearly corresponds to the expected value of 13.9 cm^3 K mol^{-1} for Ho^{3+} ion (J = 8, L = 6, S = 2, and g = 5/4). The thermal variation of the field-cooled magnetization (FCM) and the remnant magnetization (RM) showed that a spontaneous magnetization has been observed at T_C = 11 K (Figure 36a) with a M-H hysteresis loop at 2 K indicating a value of 170 Oe for H_C and a value of 6.4 μ_B at 50 kOe for M (Figure 36b), close to the expected value of 6.8 μ_B [207].

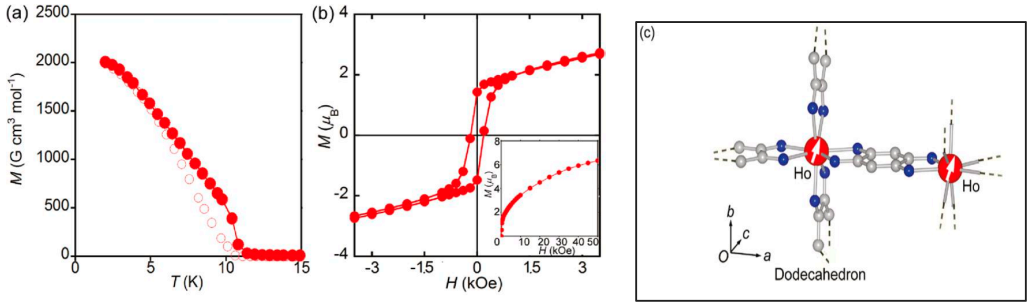

Figure 36. Thermal variation of magnetic properties of **46**. (**a**) field-cooled magnetization (FCM) obtained with decreasing temperature at an applied field of 10 Oe (red filled circles). RM obtained with increasing temperature without an applied field; (**b**) M-H hysteresis plot. Inset shows the magnetic field dependence of magnetization at 2 K; (**c**) Schematic representation of magnetic ordering. Red, blue, and light gray represent Ho, O, and C atoms, respectively. Adapted with permission from Reference [206]. Copyright 2009 American Chemical Society.

The ferromagnetic ordering is due to the effective mediation of the magnetic interactions between Ho^{3+} ions by the π orbitals of H_2An^{4-}. Interestingly this material opens the way to explore the chemistry and physical properties of related systems with different lanthanides which can result in very challenging luminescent/magnetic microporous materials.

The molecular packing and physical properties of all compounds discussed in this work are summarized in Table 2.

Table 2. Molecular Packing and Physical Properties of anilato-based magnetic/conducting molecular materials.

Compound	Molecular Packing	Physical Properties	Ref.
$[(Ph)_4P]_3[Fe(H_2An)_3]\cdot 6H_2O$ **1**	Homoleptic tris-chelated octahedral complex. strong HBs between oxygen atoms of the ligand and crystallization water molecules	PM $J/k_B = -0.020$ K	[116]
$[(Ph)_4P]_3[Cr(H_2An)_3]\cdot 6H_2O$ **2**	Homoleptic tris-chelated octahedral complex. π-π interactions	PM Weak magnetic coupling due to charge transfer between the Cr metal ions and the hydranilate ligands	[116]
$[(TPA)(OH)Fe^{III}OFe^{III}(OH)(TPA)][Fe(Cl_2An)_3]_{0.5}(BF_4)_{0.5}\cdot 1.5MeOH\cdot H_2O$ **3**	Homoleptic trischelated complex	$\mu_{eff}(RT) = 2.93$ μ_B Strong AFM interaction within $Fe^{III}OFe^{III}$ with a plateau at 55 K. Below 55 K, $\mu(T)$ is constant at 4.00 μ_B $J/k_B = -165$ K	**[117]**
$[(n\text{-}Bu)_4N]_3[Cr(Cl_2An)_3]$ **4a**	Homoleptic tris-chelated octahedral complex.	PM ZFS	[119]
$[(Ph)_4P]_3$ $[Cr(Cl_2An)_3]$ **4b**	Homoleptic tris-chelated octahedral complex. π-π interactions	PM ZFS	[119]

Table 2. *Cont.*

Compound	Molecular Packing	Physical Properties	Ref.
$[(Et)_3NH]_3$ $[Cr(Cl_2An)_3]$ **4c**	Homoleptic tris-chelated octahedral complex.	PM ZFS	[119]
$[(n\text{-}Bu)_4N]_3[Fe(Cl_2An)_3]$ **5a**	Homoleptic tris-chelated octahedral complex.	Curie-Weiss PM $J/k_B = -2.2$ K	[119]
$[(Ph)_4P]_3$ $[Fe(Cl_2An)_3]$ **5b**	Homoleptic tris-chelated octahedral complex. π-π interactions	PM ZFS	[119]
$[(Et)_3NH]_3$ $[Fe(Cl_2An)_3]$ **5c**	Homoleptic tris-chelated octahedral complex.	PM ZFS	[119]
$[(n\text{-}Bu)_4N]_3[Cr(Br_2An)_3]$ **6a**	Homoleptic tris-chelated octahedral complex.	PM ZFS	[119]
$[(Ph)_4P]_3$ $[Cr(Br_2An)_3]$ **6b**	Homoleptic tris-chelated octahedral complex. π-π interactions	PM ZFS	[119]
$[(n\text{-}Bu)_4N]_3[Fe(Br_2An)_3]$ **7a**	Homoleptic tris-chelated octahedral complex.	Curie-Weiss PM (r.t.−4.1 K), AFM coupling via halogen-bonding between the complexes forming the dimers	[119]
$[(Ph)_4P]_3$ $[Fe(Br_2An)_3]$ **7b**	Homoleptic tris-chelated octahedral complex. π-π interactions	Curie-Weiss PM	[119]
$[(n\text{-}Bu)_4N]_3[Cr(I_2An)_3]$ **8a**	Supramolecular dimers that are held together by two symmetry-related I···O interactions	Curie-Weiss PM (r.t.−4.1 K), AFM coupling via halogen-bonding between the complexes forming the dimers	[119]
$[(Ph)_4P]_3$ $[Cr(I_2An)_3]$ **8b**	Homoleptic tris-chelated octahedral complex. π-π interactions	Curie-Weiss PM	[119]
$[(n\text{-}Bu)_4N]_3Fe(I_2An)_3]$ **9a**	Homoleptic tris-chelated octahedral complex.	Curie-Weiss PM $J/k_B = 0.011$ K	[119]
$[(Ph)_4P]_3[Fe(I_2An)_3]$ **9b**	Homoleptic tris-chelated octahedral complex. iodine–iodine interactions XB interactions π-π interactions	Curie-Weiss PM $J/k_B = 0.34$ K	[119]
$[(n\text{-}Bu)_4N]_3[Cr(ClCNAn)_3]$ **10a**	Homoleptic tris-chelated octahedral complex. C–N···Cl interactions between complex anions having an opposite stereochemical configuration (Λ, Δ)	Curie-Weiss PM $J/k_B = 0.0087$ K	[120]
$[(Ph)_4P]_3$ $[Cr(ClCNAn)_3]$ **10b**	Homoleptic tris-chelated octahedral complex. π-π interactions	Curie-Weiss PM $J/k_B = -0.24$ K	[120]
$[(n\text{-}Bu)_4N]_3[Fe(ClCNAn)_3]$ **11a**	Homoleptic tris-chelated octahedral complex. C–N···Cl interactions between complex anions having an opposite stereochemical configuration (Λ, Δ)	Curie-Weiss PM	[120]
$[(Ph)_4P]_3$ $[Fe(ClCNAn)_3]$ **11b**	Homoleptic tris-chelated octahedral complex. π-π interactions	Curie-Weiss PM	[120]
$[(n\text{-}Bu)_4N]_3[Al(ClCNAn)_3]$ **12a**	Homoleptic tris-chelated octahedral complex. C–N···Cl interactions between complex anions having an opposite stereochemical configuration (Λ, Δ)	Red luminophore Ligand centred emission	[120]
$[(Ph)_4P]_3$ $[Al(ClCNAn)_3]$ **12b**	Homoleptic tris-chelated octahedral complex.	Red luminophore Ligand centred emission	[120]

Table 2. *Cont.*

Compound	Molecular Packing	Physical Properties	Ref.
$(PBu_3Me)_2[NaCr(Br_2An)_3]$ **13**	2D lattice Heterometallic anionic Honeycomb layers alternated with cationic layer in alternated manner	PM ZFS	[121]
$(PPh_3Et)_2[KFe(Cl_2An)_3](dmf)_2$ **14**	2D lattice Heterometallic anionic Honeycomb layers alternated with cationic layer in alternated manner	PM ZFS	[121]
$(NEt_3Me)[Na(dmf)]$-$[NaFe(Cl_2An)_3]$ **15**	Inter-connected 2D honeycomb	PM ZFS	[121]
$(NBu_3Me)_2[NaCr(Br_2An)_3]$ **16**	3D lattice	PM ZFS	[121]
$[(H_3O)(phz)_3][MnCr(Cl_2An)_3(H_2O)]$ **17**	Eclipsed Heterometallic anionic Honeycomb layers alternated with cationic layers	Ferrimagnet Tc = ca. 5.0 K	[125]
$[(H_3O)(phz)_3][MnCr(Br_2An)_3]\cdot H_2O$ **18**	Eclipsed Heterometallic anionic Honeycomb layers alternated with cationic layers	Ferrimagnet Tc = ca. 5.0 K	[125]
$[(H_3O)(phz)_3][MnFe(Br_2An)_3]\cdot H_2O$ **19**	Eclipsed Heterometallic anionic honeycomb layers	Weak FM due to long-range AF ordering with spin canting at ca. 3.5 K	[125]
$[(n\text{-}Bu)_4N]_3[MnCr(Cl_2An)_3(H_2O)]$ **20**	Alternated Heterometallic anionic honeycomb layers	Ferrimagnet Tc = 5.5 K $J/k_B = -8.7$ K	[125]
$[(n\text{-}Bu)_4N]_3[MnCr(Br_2An)_3(H_2O)]$ **21**	Alternated Heterometallic anionic honeycomb layers	Ferrimagnet Tc = 6.3 K $J/k_B = -8.7$ K	[125]
$[(n\text{-}Bu)_4N]_3[MnCr(I_2An)_3(H_2O)]$ **22**	Alternated heterometallic anionic honeycomb layers	Ferrimagnet Tc = 8.2 K $J/k_B = -10$ K	[125]
$Bu)_4N]_3[MnCr(H_2An)_3(H_2O)]$ **23**	Alternated Heterometallic anionic honeycomb layers	Ferrimagnet Tc = 11.0 K $J/k_B = -12$ K	[125]
$[BEDT\text{-}TTF]_3[Fe(Cl_2An)_3]\cdot 3CH_2Cl_2\cdot H_2O$ **24**	BEDT-TTF dimers not-layered structure Cl···S interactions	PM with a contribution at high temperatures from BEDT-TTF radical cations semiconductor $\sigma_{RT} = 3 \times 10^{-4}$ S cm^{-1} Intradimer Coupling Constant $J_{CC} = -2.6 \times 10^{33}$ K	[164]
δ-$[BEDT\text{-}TTF]_5[Fe(Cl_2An)_3]\cdot 4H_2O$ **25**	organic-inorganic layers segregation δ packing of BEDT TTF Cl···S interactions	PM with a contribution at high temperatures from BEDT-TTF radical cations Semiconductor $\sigma_{RT} = 2$ S cm^{-1}	[164]
α'''-$[BEDT\text{-}TTF]_{18}[Fe(Cl_2An)_3]_3\cdot 3CH_2Cl_2\cdot 6H_2O$ **26**	organic-inorganic layers segregation α''' packing of BEDT TTF Cl···S interaction	PM with a contribution at high temperatures from BEDT-TTF radical cations Semiconductor $\sigma_{RT} = 8$ S cm^{-1}	[164]
$[(BEDT\text{-}TTF)_6[Fe(Cl_2An)_3]\cdot(H_2O)_{1.5}\cdot(CH_2Cl_2)_{0.5}$ **27**	organic-inorganic layers segregation θ^{21} phase of BEDT TTF Cl···S interaction	PM with Pauli PM contribution Semiconductor σ_{RT} = ca. 10 S cm^{-1}	[166]
β-$[(S,S,S,S)\text{-}TM\text{-}BEDT\text{-}TTF]_3PPh_4[K^IFe^{III}(Cl_2An)_3]\cdot 3H_2O$ **28** β-$[(R,R,R,R)\text{-}TM\text{-}BEDT\text{-}TTF]_3PPh_4[K^IFe^{III}(Cl_2An)_3]\cdot 3H_2O$ **29**	heterobimetallic anionic honeycomb layers alternated with cationic chiral donors Cl···Cl contact, π-π stacking terminal CH_3···O contacts (segregated columns of cations and anions) β packing of TM-BEDT-TTF	Curie-Weiss PM Semiconductors $\sigma_{RT} = 3 \times 10^{-4}$ S cm^{-1}	[167]

Table 2. *Cont.*

Compound	Molecular Packing	Physical Properties	Ref.
β-[(*rac*)-TM-BEDT-TTF]$_3$ $PPh_4[K^IFe^{III}(Cl_2An)_3]\cdot 3H_2O$ **30**	heterobimetallic anionic honeycomb layers alternated with cationic chiral -(*rac*)-donors Cl···Cl contact, π-π stacking terminal $CH_3\cdots O$ contacts (segregated columns of cations and anions) β packing of TM-BEDT-TTF	Curie-Weiss PM Semiconductors $\sigma_{RT} = 3 \times 10^{-4}$ S cm^{-1}	[167]
$[Fe^{III}(sal_2\text{-trien})]MnCr(Cl_2An)_3$ **31**	2D Honeycomb bimetallic anionic layers with inserted Fe(III) cationic complexes and solvent molecules.	FerriM Inserted HS Fe(III) cations Tc = 10K $J/k_B = -10$ K Exfoliation	[168]
$[Fe^{III}(4\text{-OH-sal}_2\text{-trien})]MnCr(Cl_2An)_3$ **32**	2D Honeycomb bimetallic anionic layers with inserted Fe(III) cationic complexes and solvent molecules.	FerriM Inserted HS Fe(III) cations Tc = 10.4 K $J/k_B = -7.2$ K	[168]
$[Fe^{III}(sal_2\text{-epe})]$ $MnCr(Br_2An)_3$ **33**	2D Honeycomb bimetallic anionic layers with inserted Fe(III) cationic complexes and solvent molecules.	FerriM Inserted HS Fe(III) cations Tc = 10.2 K $J/k_B = -6.5$ K	[168]
$[Fe^{III}(5\text{-Cl-sal}_2\text{-trien})]$ $MnCr(Br_2An)_3$ **34**	2D honeycomb bimetallic anionic layers with inserted Fe(III) cationic complexes and solvent molecules.	FerriM Inserted LS Fe(III) cations Tc = 9.8 K $J/k_B = -6.7$ K	[168]
$[Fe^{II}(tren\text{-}(imid)_3)]_2$ $Mn^{II}Cl_2Cr^{III}(Cl_2An)_3]Cl\cdot$ solvent **35**	1D anionic chain formed by Cr^{III}complexes bonded to two Mn(II) ions through two bis-bidentate chloranilate bridges, and terminal third choranilate.	FerriM coupling within the chains that gives rise to a magnetic ordering below 2.6 K	[168]
$[Fe^{III}(acac_2\text{-trien})]$ $[Mn^{II}Cr^{III}(Cl_2An)_3]_3$ $(CH_3CN)_2$ **36**	Neutral layers formed by 2D honeycomb bimetallic anionic layers with cationic complexes inside the hexagonal channels. van der Waals interactions between the layers.	FerriM at ca. 10.8 K, inserted HS Fe(III) cations Exfoliation	[172]
$[Fe^{III}(acac_2\text{-trien})]$ $[Mn^{II}Cr^{III}(Br_2An)_3]_3$ $(CH_3CN)_2$ **37**	Neutral layers formed by 2D Honeycomb bimetallic anionic layers with cationic complexes inside the hexagonal channels. Van der Waals interactions between the layers	FerriM at ca. 11.4 K, inserted HS Fe(III) cations Exfoliation	[172]
$[Ga^{III}(acac_2\text{-trien})]$ $[Mn^{II}Cr^{III}(Br_2An)_3]_3$ $(CH_3CN)_2$ **38**	Neutral layers formed by 2D Honeycomb bimetallic anionic layers with cationic complexes inside the hexagonal channels. Van der Waals interactions between the layers	FerriM at ca. 11.6 K	[172]
$\{(H_{0.5}phz)_2[Fe(Cl_2An)_2(H_2O)_2]\cdot 2H_2O\}_n$ **39**	Supramolecular Framework Novel Intercalation Compounds Electrostatic interactions	Interlayer distances (Fe(1)-Fe(1′′))14.57 Å In 77–300 K temperature range, EPR silent. Intralayer AFM exchange via Hydrogen-Bonds and stacking interactions among $[Fe(Cl_2An)_2(H_2O)_2]^-$ monomers $J_{2D}/k_B = -0.10$ K	[184].
$\{[Fe(Cp)_2][Fe(Cl_2An)_2$ $(H_2O)_2]\}n$ **40**	Supramolecular Framework Novel Intercalation Compounds Electrostatic interactions	Interlayer distances (Fe(1)-Fe(1′′)) 9.79 Å In 77–300 K temperature range, EPR silent. Intralayer AFM exchange via Hydrogen-Bonds and stacking interactions among $[Fe(Cl_2An)_2(H_2O)_2]^-$ monomers and Heisenberg AFM intrachain stacking interactions in 1D arrays of $[Fe(Cp)_2]^+$ cations $J_{2D}/k_B = -0.13$ K $J_{1D}/k_B = -2.4$ K	[184]

Table 2. *Cont.*

Compound	Molecular Packing	Physical Properties	Ref.
$[Fe(Cp^*)_2][Fe(Cl_2An)_2(H_2O)_2]\}_n$ **41**	Supramolecular Framework Novel Intercalation Compounds Electrostatic interactions π-π stacking tilted columns of stacked decamethylferrocene cations	Interlayer distances (Fe(1)-Fe(1′′)) 13.13 Å. In 77–300 K temperature range, EPR silent High-spin (S = 5/2)Fe(III) ions in $\{[Fe(Cl_2An)_2(H_2O)_2]\}^{m-}$ anions Low-spin (S = 1/2) Fe(III) ions in $[Fe(Cp^*)_2]^+$ cations Intralayer AFM exchange via hydrogen-bonds and stacking interactions among $[Fe(Cl_2An)_2(H_2O)_2]^-$ monomers and Heisenberg AFM intrachains stacking interaction in 1D arrays of $[Fe(Cp)_2]^+$ cations $J/k_B = -9.5$ K $J_{1D}/k_B = -1.9$ K	[184]
$\{(TTF)_2[Fe(Cl_2An)_2(H_2O)_2]\}_n$ **42**	Novel intercalation compounds formed by the 2D hydrogen-bond supported layers and functional guests. Electrostatic interactions π-π stacking Face to Face stacking of TTF cations in columnar structure S···S distances (type A; 3.579(3) Å, and type B; 3.618(3) Å). Head-to-Tail arrangement for TTF cations in the stacked column	Interlayer distances (Fe(1)-Fe(1′′)) 13.45 Å. EPR active with g = 2.008 (2 signals) indicating TTF is present as radical species High-spin Fe(II) and Fe(III) ions (the iron-chloranilate anionic layer has a valence-trapped mixed-valence state) Isotropic intralayer AFM exchange via hydrogen-bonds and stacking interaction among iron(III)- and iron(II)-chloranilate monomers (1:1) Heisenberg alternating AFM linear chain for isotropic exchange in the 1D array of TTF cations via intrachain stacking interactions $J/k_B = -6.5$ K $J_{1D}/k_B = -443$ K	[184]
$(NBu_4)_2Fe^{III}{}_2(H_2An)_3$ **43**	3D structure MOF with Robin-Day Class II/III mixed-valency ligand	Curie-Weiss PM $J_{1D}/k_B = 0.89$ K (250–300 K) High T- FM Low T- FerriM interactions Arrhenius semiconductor $\sigma_{RT} = 0.16(1)$ S cm^{-1}	[185]
$(Na)_{0.9}(NBu_4)_{1.8}Fe^{III}{}_2(H_2An)_3$ **44**	Isostructural to **46** (PXRD) MOF with Robin-Day Class II/III mixed-valency ligand	Curie-Weiss PM $J_{1D}/k_B = 0.95$ K (250-300K) Arrhenius semiconductor $\sigma_{RT} = 0.0062(1)$ S cm^{-1}	[185]
(Me2NH2)2[Fe2Cl$_2$An3]·2H2O·6DMF **45**	Eclipsed 2D honeycomb layered packing with a H_2O between Fe centers, leading to the formation of 1D hexagonal channels	2D Microporous magnet with strong magnetic coupling. Intralayer AFM interactions Tc = 80 K, glassy Magnet, Mydosh parameter, ϕ = 0.023	[201]
(Me2NH2)2[Fe2Cl$_2$An3] **45a**	Eclipsed 2D honeycomb layered packing Desolvated phase of **48**	Intralayer AFM interactions Tc = 26 K. Permanent porosity with BET surface area of 885(105) m^2/g	[201]
$Na_5[Ho(H_2An^{4-})_2]_3$ 7H_2O **46**	3D monometallic lanthanoid assembly Ho^{3+} ion adopts a dodecahedron (D4d) geometry with regular square-grid channels	FM with a Curie Temperature of 11 K	[206]

PM = Paramagnet; FM = Ferromagnet; FerriM = Ferrimagnet; AFM = Antiferromagnet.

5. Conclusions

The compounds described in this work are summarized in Table 2. It can be envisaged that the real challenge of anilate-based materials is due to their peculiar features: (i) easy to modify or functionalize by the conventional synthetic methods of organic and coordination chemistry, with no influence on their coordination modes (ii) easy to tune the magnetic exchange coupling between the coordinated metals by a simple change of the X substituent (X = H, F, Cl, Br, I, NO_2, OH, CN, Me, Et, etc.) at the 3,6 positions of the anilato moiety; (iii) influence of the electronic nature of the X substituents on the intermolecular interactions and thus the physical properties of the resulting materials. The novel family of complexes of the anilato-derivatives containing the X=Cl, Br, I, H, and Cl/CN substituents with d-transition Fe(III) and Cr(III) metal ions (**3**–**10**) are a relevant example of the crucial role played by halogens n their physical properties, either at the electronic level, by varying the electron density on the anilate ring, or at the supramolecular level, affecting the molecular packing via halogen-bonding interactions. It is noteworthy that halogen-bonding interactions observed in **9b** are responsible for a unique magnetic behaviour in this family. Moreover the anilato derivatives having Cl/CN substituents and their complexes with Al(III) metal ions (**12a**,**b**), show unprecedented properties such as luminescence in the visible region (green and red luminophores, respectively), never observed in this family to the best of our knowledge. The paramagnetic anionic complexes has shown to be excellent building blocks for constructing via the "complex as-ligand approach": (i) new 2D and 3D heterometallic lattices with alkaline M(I) and d-transition M(III) metal ions (**13**–**16**); (ii) 2D layered molecular ferrimagnets (**17**–**23**) which exhibit tunable ordering temperature as a function of the halogen electronegativity; it is noteworthy how subtle changes in the nature of the substituents (X = Cl, Br, I, H) have been rationally employed as "adjusting screws" in tuning the magnitude of the magnetic interaction between the metals and thus the magnetic properties of the final material; the additional peculiarity of these molecular magnets is that they form void hexagonal channels and thus can behave as layered chiral magnetic MOFs with tunable size which depends, in turn, on the halogen size. The paramagnetic anionic complexes worked well as magnetic components of multifunctional molecular materials based on BEDT-TTF organic donors (**24**–**27**) which has furnished the pathway for combining electrical conductivity with magnetic properties, in analogy with the relevant class of $[M(ox)_3]^{3-}$ (ox = oxalate) tris-chelated complexes which have produced the first family of molecular paramagnetic superconductors. The introduction of chirality in the BEDT-TTF organic donor has been successful and a complete series of radical-cation salts have been obtained by combining the TM-BEDT-TTF organic donor in its (S,S,S,S) and (R,R,R,R) enantiopure forms, or their racemic mixture (rac), with 2D heterobimetallic anionic layers formed "in situ" by self-assembling of the tris(chloranilato)ferrate(III) metal complexes in the presence of potassium cations in the usual honey-comb packing pattern (**28**–**30**). Another advantage of anilato-ligands compared to the oxalato ones is their bigger size leading to hexagonal cavities that are twice larger than those of the oxalato-based layers, where a large library of cationic complexes can be inserted. When using spin crossover cations such as $[Fe^{III}(sal_2\text{-trien})]^+$, (X = Cl) (**31**) and its derivatives and the $[M^{III}(acac_2\text{-trien})]^+$, M = Fe or Ga complex (**32**–**38**), which has a smaller size than the $[Fe^{III}(sal_2\text{-trien})]^+$ complex, 2D anilate-based materials have been obtained showing in the former the typical alternated cation/anion layered structure while in the latter neutral layers never observed previously in oxalate or anilate-based 2D networks, where the spin crossover cations are inserted in the centre of the hexagonal channels. This novel type of structure opens the way to the synthesis of a new type of multifunctional materials in which small templating cations are confined into the 1D channels formed by 2D anilate-based networks and could be a useful strategy for the introduction of other properties such as electric or proton conductivity in addition to the magnetic ordering of the anilate-based network. Interestingly this type of magnetic hybrid coordination polymers can be considered as graphene related magnetic materials. In fact being formed by a 2D anionic network and cations inserted within or between the layers, with interlayer ionic or weak van der Waals interactions, they have been successfully exfoliated using either the micromechanical Scotch tape method leading to good

quality micro-sheets of these layered magnets or solvent-mediated exfoliation methods. Interestingly the hybrid nature of these magnetic layers provides the unique opportunity to generate smart layers where the switching properties of the inserted complexes can modulate the cooperative magnetism of the magnetic network. **39**–**42** are interesting examples of host-guest intercalation compounds formed by the common 2D hydrogen-bond supported layers and ferrocene/decamethylferrocene and TTF functional guests showing intralayer AFM exchange via hydrogen-bonds and stacking interactions among $[Fe(Cl_2An)_2(H_2O)_2]^-$ monomers and the Heisenberg AFM intrachain stacking interactions in 1D arrays of ferrocene/decamethylferrocene and TTF cations. Interestingly these compounds shows how hydrogen-bond-supported anionic layers based on iron-chloranilate mononuclear complexes can be used as inorganic hosts for the intercalation of guest cations to construct new types of multilayered inorganic-organic hybrid materials. It is noteworthy that these layers are so flexible that they can include and stabilize various kinds of guests in the channels showing the versatility of the anilate building blocks and the challenge of the molecular approach as synthetic procedure.

Finally **43** and **44** are rare examples of a MOF formed by metal ions bridged by paramagnetic linkers, the hydranilates, that additionally shows ligand-centered Robin—Day Class II/III mixed valency, observed for the first time in a MOF. Interestingly **43** exhibits a conductivity of 0.16 ± 0.01 S/cm at 298 K, one of the highest values yet observed in a MOF and the origin of this electronic conductivity is determined to be ligand mixed-valency. In these materials the magnetic ordering and semiconducting behaviors stem from the same origin, the ferric semiquinoid lattice, differently from multifunctional materials based on tetrathiafulvalene derivatives with paramagnetic counterions where separate sub-lattices furnish the two distinct magnetic/conducting properties. Therefore they represent a challenge for pursuing magnetoelectric or multiferroic MOFs. **45** represents also the first structurally characterized example of a microporous magnet containing the Cl_2An^{3-}·chloranilate radical species, showing Tc = 80 K and solvent-induced switching from Tc = 26 to 80 K. Upon removal of DMF and H_2O solvent molecules, this compound undergoes a slight structural distortion, which is fully reversible, to give the desolvated phase $(Me_2NH_2)_2Fe_2(Cl_2An)_3]$, **45a**, and a fit to N_2 adsorption data, at 77 K, of this activated compound gives a BET surface area of 885(105) m^2/g (the second highest reported for a porous magnet up to now) confirming the presence of permanent microporosity. These results highlight the ability of redox-active anilate ligands to generate 2D magnets with permanent porosity. **46** is another interesting example of a monometallic lanthanoid assembly which consist of a 3-D network framework showing regular square-grid channels and ferromagnetism with a curie Temperature of 11 K. This is the first structurally characterized example of magnetic lanthanoid assemblies opening the way to the preparation of 3D magnetic/luminescent MOFs.

Acknowledgments: This work was supported by the Fondazione di Sardegna—Convenzione triennale tra la Fondazione di Sardegna e gli Atenei Sardi, Regione Sardegna—L.R. 7/2007 annualità 2016—DGR 28/21 del 17.05.2015 "Innovative Molecular Functional Materials for Environmental and Biomedical Applicatons". Special Thanks are due to the Guest Editor, Manuel Leite Almeida C2TN, Instituto Superior Técnico, Universidade de Lisboa, Portugal, for its kind invitation to give a contribution to this Special Issue "Magnetism of Molecular Conductors".

Conflicts of Interest: The authors declare no conflict of interest.

References

1. Khanna, J.M.; Malone, M.H.; Euler, K.L.; Brady, L.R. Atromentin, anticoagulant from hydnellum diabolus. *J. Pharm. Sci.* **1965**, *54*, 1016–1020. [CrossRef] [PubMed]
2. Zhang, B.; Salituro, G.; Szalkowski, D.; Li, Z.; Zhang, Y.; Royo, I.; Vilella, D.; Diez, M.T.; Pelaez, F.; Ruby, C.; et al. Discovery of a small molecule insulin mimetic with antidiabetic activity in mice. *Science* **1999**, *284*, 974–977. [CrossRef] [PubMed]
3. Tsukamoto, S.; Macabalang, A.D.; Abe, T.; Hirota, H.; Ohta, T. Thelephorin a: A new radical scavenger from the mushroom thelephora vialis. *Tetrahedron* **2002**, *58*, 1103–1105. [CrossRef]
4. Puder, C.; Wagner, K.; Vettermann, R.; Hauptmann, R.; Potterat, O. Terphenylquinone inhibitors of the src protein tyrosine kinase from *stilbella* sp. *J. Nat. Prod.* **2005**, *68*, 323–326. [CrossRef] [PubMed]

5. Liu, K.; Xu, L.; Szalkowski, D.; Li, Z.; Ding, V.; Kwei, G.; Huskey, S.; Moller, D.E.; Heck, J.V.; Zhang, B.B.; et al. Discovery of a potent, highly selective, and orally efficacious small-molecule activator of the insulin receptor. *J. Med. Chem.* **2000**, *43*, 3487–3494. [CrossRef] [PubMed]
6. Wood, H.B., Jr.; Black, R.; Salituro, G.; Szalkowski, D.; Li, Z.; Zhang, Y.; Moller, D.E.; Zhang, B.; Jones, A.B. The basal sar of a novel insulin receptor activator. *Bioorgan. Med. Chem. Lett.* **2000**, *10*, 1189–1192. [CrossRef]
7. Kitagawa, S.; Kawata, S. Coordination compounds of 1,4-dihydroxybenzoquinone and its homologues. Structures and properties. *Coord. Chem. Rev.* **2002**, *224*, 11–34. [CrossRef]
8. Barltrop, J.A.; Burstall, M.L. 435. The synthesis of tetracyclines. Part I. Some model diene reactions. *J. Chem. Soc. (Resumed)* **1959**, 2183–2186. [CrossRef]
9. Jones, R.G.; Shonle, H.A. The preparation of 2,5-dihydroxyquinone. *J. Am. Chem. Soc.* **1945**, *67*, 1034–1035. [CrossRef]
10. Viault, G.; Gree, D.; Das, S.; Yadav, J.S.; Grée, R. Synthesis of a Focused Chemical Library Based on Derivatives of Embelin, a Natural Product with Proapoptotic and Anticancer Properties. *Eur. J. Org. Chem.* **2011**, *7*, 1233–1244. [CrossRef]
11. Wallenfels, K.; Friedrich, K. Über fluorchinone, ii. Zur hydrolyse und alkoholyse des fluoranils. *Chem. Ber.* **1960**, *93*, 3070–3082. [CrossRef]
12. Stenhouse, J. On chloranil and bromanil. *J. Chem. Soc.* **1870**, *23*, 6–14. [CrossRef]
13. Benmansour, S.; Vallés-García, C.; Gómez-García, C.J. A H-bonded chloranilate chain with an unprecedented topology. *Struct. Chem. Crystallogr. Commun.* **2015**, *1*, 1–7.
14. Torrey, H.A.; Hunter, W.H. The action of iodides on bromanil. Iodanil and some of its derivatives. *J. Am. Chem. Soc.* **1912**, *34*, 702–716. [CrossRef]
15. Meyer, H.O. Eine neue Synthese der Nitranilsäure. *Berichte der Deutschen Chemischen Gesellschaft (A and B Series)* **1924**, *57*, 326–328. [CrossRef]
16. Fatiadi, A.J.; Sager, W.F. Tetrahydroxyquinone. *Org. Synth.* **1962**, *42*, 90.
17. Gelormini, O.; Artz, N.E. The oxidation of inosite with nitric acid. *J. Am. Chem. Soc.* **1930**, *52*, 2483–2494. [CrossRef]
18. Hoglan, F.A.; Bartow, E. Preparation and properties of derivatives of inositol. *J. Am. Chem. Soc.* **1940**, *62*, 2397–2400. [CrossRef]
19. Junek, H.; Unterweger, B.; Peltzmann, R.Z. Notizen: Eine einfache synthese von tetrahydroxybenzochinon-1.4/A simple synthesis of tetrahydroxy-benzoquinone-1,4. *Z. Naturforsch. B* **1978**, *33B*, 1201–1203. [CrossRef]
20. Preisler, P.W.; Berger, L. Preparation of tetrahydroxyquinone and rhodizonic acid salts from the product of the oxidation of inositol with nitric acid. *J. Am. Chem. Soc.* **1942**, *64*, 67–69. [CrossRef]
21. Zaman, B.M.; Morita, Y.; Toyoda, J.; Yamochi, H.; Sekizaki, S.; Nakasuji, K. Convenient preparation and properties of 2,5-dichloro- and 2,5-dibromo-3,6-dicyano-1,4-benzoquinone (cddq and cbdq): Ddq analogs with centrosymmetry. *Mol. Cryst. Liq. Cryst. Sci. Technol. Section A Mol. Cryst. Liq. Cryst.* **1996**, *287*, 249–254. [CrossRef]
22. Wallenfels, K.; Bachmann, G.; Hofmann, D.; Kern, R. Cyansubstituierte chinone—II: 2,3-, 2,5-2,6-dicyanchinone und tetracyanbenzochinon. *Tetrahedron* **1965**, *21*, 2239–2256. [CrossRef]
23. Rehwoldt, R.E.; Chasen, B.L.; Li, J.B. 2-chloro-5-cyano-3,6-dihydroxybenzoquinone, a new analytical reagent for the spectrophotometric determination of calcium(II). *Anal. Chem.* **1966**, *38*, 1018–1019. [CrossRef]
24. Akutagawa, T.; Nakamura, T. Crystal and electronic structures of hydrogen-bonded 2,5-diamino-3,6-dihydroxy-p-benzoquinone. *Cryst. Growth Des.* **2006**, *6*, 70–74. [CrossRef]
25. Kögl, F.; Lang, A. Über den mechanismus der fichterschen synthese von dialkyl-dioxy-chinonen. *Eur. J. Inorg. Chem.* **1926**, *59*, 910–913. [CrossRef]
26. Fichter, F.; Willmann, A. Ueber synthesen dialkylirter dioxychinone durch ringschluss. *Ber. Deutsch. Chem. Ges.* **1904**, *37*, 2384–2390. [CrossRef]
27. Fichter, F. Ueber synthetische p-dialkylirte dioxychinone. *Justus Liebigs Ann. Chem.* **1908**, *361*, 363–402. [CrossRef]
28. Atzori, M.; Pop, F.; Cauchy, T.; Mercuri, M.L.; Avarvari, N. Thiophene-benzoquinones: Synthesis, crystal structures and preliminary coordination chemistry of derived anilate ligands. *Org. Biomol. Chem.* **2014**, *12*, 8752–8763. [CrossRef] [PubMed]

29. Min, K.S.; DiPasquale, A.G.; Rheingold, A.L.; White, H.S.; Miller, J.S. Observation of redox-induced electron transfer and spin crossover for dinuclear cobalt and iron complexes with the 2,5-di-tert-butyl-3,6-dihydroxy-1,4-benzoquinonate bridging ligand. *J. Am. Chem. Soc.* **2009**, *131*, 6229–6236. [CrossRef] [PubMed]
30. Semmingsen, D. The crystal and molecular structure of 2,5-dihydroxybenzoquinone at-1620c. *Acta Chem. Scand. B* **1977**, *31*, 11–14. [CrossRef]
31. Munakata, M.; Wu, L.P.; Kuroda-Sowa, T.; Yamamoto, M.; Maekawa, M.; Moriwaki, K. Assembly of a mixed-valence cu(i/ii) system coupled by multiple hydrogen bonding through tetrahydroxybenzoquinone. *Inorg. Chim. Acta* **1998**, *268*, 317–321. [CrossRef]
32. Klug, A. The crystal structure of tetrahydroxy-p-benzoquinone. *Acta Crystallogr.* **1965**, *19*, 983–992. [CrossRef]
33. Robl, C. Crystal structure and hydrogen bonding of 2,5-dihydroxy-3,6-dimethyl-p-benzoquinone. *Z. Krist. Cryst. Mater.* **1988**, *184*, 289–293. [CrossRef]
34. Andersen, E.K.; Andersen, I.G.K. The crystal and molecular structure of hydroxyquinones and salts of hydroxyquinones. Vii. Hydronium cyananilate (cyananilic acid hexahydrate) and hydronium nitranilate (a redetermination). *Acta Crystallogra. Sect. B* **1975**, *31*, 379–383. [CrossRef]
35. Andersen, E.K.; Andersen, I.G.K. The crystal and molecular structure of hydroxyquinones and salts of hydroxyquinones. VIII. Fluoranilic acid. *Acta Crystallogr. Sect. B* **1975**, *31*, 384–387. [CrossRef]
36. Andersen, E. The crystal and molecular structure of hydroxyquinones and salts of hydroxyquinones. I. Chloranilic acid. *Acta Crystallogr.* **1967**, *22*, 188–191. [CrossRef]
37. Andersen, E. The crystal and molecular structure of hydroxyquinones and salts of hydroxyquinones. II. Chloranilic acid dihydrate. *Acta Crystallogr.* **1967**, *22*, 191–196. [CrossRef]
38. Andersen, E. The crystal and molecular structure of hydroxyquinones and salts of hydroxyquinones. V. Hydronium nitranilate, nitranilic acid hexahydrate. *Acta Crystallogr.* **1967**, *22*, 204–208. [CrossRef]
39. Molcanov, K.; Stare, J.; Vener, M.V.; Kojic-Prodic, B.; Mali, G.; Grdadolnik, J.; Mohacek-Grosev, V. Nitranilic acid hexahydrate, a novel benchmark system of the zundel cation in an intrinsically asymmetric environment: Spectroscopic features and hydrogen bond dynamics characterised by experimental and theoretical methods. *Phys. Chem. Chem. Phys.* **2014**, *16*, 998–1007. [CrossRef] [PubMed]
40. Andersen, E. The crystal and molecular structure of hydroxyquinones and salts of hydroxyquinones. III. Ammonium chloranilate monohydrate. *Acta Crystallogr.* **1967**, *22*, 196–201. [CrossRef]
41. Andersen, E. The crystal and molecular structure of hydroxyquinones and salts of hydroxyquinones. IV. Ammonium nitranilate. *Acta Crystallogr.* **1967**, *22*, 201–203. [CrossRef]
42. Biliskov, N.; Kojic-Prodic, B.; Mali, G.; Molcanov, K.; Stare, J. A Partial Proton Transfer in Hydrogen Bond O–H···O in Crystals of Anhydrous Potassium and Rubidium Complex Chloranilates. *J. J. Phys. Chem. A* **2011**, *115*, 3154–3166. [CrossRef] [PubMed]
43. Molcanov, K.; Sabljic, I.; Kojic-Prodic, B. Face-to-face p-stacking in the multicomponent crystals of chloranilic acid, alkali hydrogenchloranilates, and water. *CrystEngComm* **2011**, *13*, 4211. [CrossRef]
44. Molcanov, K.; Juric, M.; Kojic-Prodic, B. Stacking of metal chelating rings with π-systems in mononuclear complexes of copper(II) with 3,6-dichloro-2,5-dihydroxy-1,4-benzoquinone (chloranilic acid) and 2,2′-bipyridine ligands. *Dalton Trans.* **2013**, *42*, 15756–15765. [CrossRef] [PubMed]
45. Molcanov, K.; Kojic-Prodic, B. Face-to-face stacking of quinoid rings of alkali salts of bromanilic acid. *Acta Crystallogr. Section B* **2012**, *68*, 57–65. [CrossRef] [PubMed]
46. Molcanov, K.; Kojic-Prodic, B.; Meden, A. π-stacking of quinoid rings in crystals of alkali diaqua hydrogen chloranilates. *CrystEngComm* **2009**, *11*, 1407–1415. [CrossRef]
47. Robl, C. Complexes with substituted 2,5-dihydroxy-p-benzoquinones: The inclusion compounds $[Y(H_2O)_3]_2(C_6Cl_2O_4)_3 \cdot 6H_2O$ and $[Y(H_2O)_3]_2(C_6Br_2O_4)_3 \cdot 6H_2O$. *Mater. Res. Bull.* **1987**, *22*, 1483–1491. [CrossRef]
48. Dei, A.; Gatteschi, D.; Pardi, L.; Russo, U. Tetraoxolene radical stabilization by the interaction with transition-metal ions. *Inorg. Chem.* **1991**, *30*, 2589–2594. [CrossRef]
49. Coronado, E.; Galan-Mascaros, J.R.; Gomez-Garcia, C.J.; Laukhin, V. Coexistence of ferromagnetism and metallic conductivity in a molecule-based layered compound. *Nature* **2000**, *408*, 447–449. [CrossRef] [PubMed]
50. Anil Reddy, M.; Vinayak, B.; Suresh, T.; Niveditha, S.; Bhanuprakash, K.; Prakash Singh, S.; Islam, A.; Han, L.; Chandrasekharam, M. Highly conjugated electron rich thiophene antennas on phenothiazine and phenoxazine-based sensitizers for dye sensitized solar cells. *Synth. Metals* **2014**, *195*, 208–216. [CrossRef]

51. Schweinfurth, D.; Klein, J.; Hohloch, S.; Dechert, S.; Demeshko, S.; Meyer, F.; Sarkar, B. Influencing the coordination mode of tbta (tbta = tris[(1-benzyl-1H-1,2,3-triazol-4-yl)methyl]amine) in dicobalt complexes through changes in metal oxidation states. *Dalton Trans.* **2013**, *42*, 6944–6952. [CrossRef] [PubMed]
52. Schweinfurth, D.; Khusniyarov, M.M.; Bubrin, D.; Hohloch, S.; Su, C.-Y.; Sarkar, B. Tuning spin–spin coupling in quinonoid-bridged dicopper(II) complexes through rational bridge variation. *Inorg. Chem.* **2013**, *52*, 10332–10339. [CrossRef] [PubMed]
53. Baum, A.E.; Lindeman, S.V.; Fiedler, A.T. Preparation of a semiquinonate-bridged diiron(II) complex and elucidation of its geometric and electronic structures. *Chem. Commun.* **2013**, *49*, 6531–6533. [CrossRef] [PubMed]
54. Nie, J.; Li, G.-L.; Miao, B.-X.; Ni, Z.-H. Syntheses, Structures and Magnetic Properties of Dinuclear Cobalt(II) Complexes $[Co_2(TPEA)_2(DHBQ)](ClO_4)_2$ and $[Co_2(TPEA)_2(DHBQ)](PF_6)_2$. *J. Chem. Crystallogr.* **2013**, *43*, 331. [CrossRef]
55. Wu, D.-Y.; Huang, W.; Wang, L.; Wu, G. Synthesis, structure, and magnetic properties of a dinuclear antiferromagnetically coupled cobalt complex. *Z. Anorg. Allg. Chem.* **2012**, *638*, 401–404. [CrossRef]
56. Chatterjee, P.B.; Bhattacharya, K.; Kundu, N.; Choi, K.-Y.; Clérac, R.; Chaudhury, M. Vanadium-induced nucleophilic ipso substitutions in a coordinated tetrachlorosemiquinone ring: Formation of the chloranilate anion as a bridging ligand. *Inorg. Chem.* **2009**, *48*, 804–806. [CrossRef] [PubMed]
57. Bruijnincx Pieter, C.A.; Viciano-Chumillas, M.; Lutz, M.; Spek, A.L.; Reedijk, J.; van Koten, G.; Klein Gebbink, R.J.M. Oxidative double dehalogenation of tetrachlorocatechol by a bio-inspired cu ii complex: Formation of chloranilic acid. *Chemistry* **2008**, *14*, 5567–5576. [CrossRef] [PubMed]
58. Ghumaan, S.; Sarkar, B.; Maji, S.; Puranik, V.G.; Fiedler, J.; Urbanos, F.A.; Jimenez-Aparicio, R.; Kaim, W.; Lahiri, G.K. Valence-state analysis through spectroelectrochemistry in a series of quinonoid-bridged diruthenium complexes $[(acac)_2Ru(\mu\text{-}l)ru(acac)2]_n$ (n = +2, +1, 0, −1, −2). *Chemistry* **2008**, *14*, 10816–10828. [CrossRef] [PubMed]
59. Guo, D.; McCusker, J.K. Spin exchange effects on the physicochemical properties of tetraoxolene-bridged bimetallic complexes. *Inorg. Chem.* **2007**, *46*, 3257–3274. [CrossRef] [PubMed]
60. Min, K.S.; Rheingold, A.L.; DiPasquale, A.; Miller, J.S. Characterization of the chloranilate(·3−) π radical as a strong spin-coupling bridging ligand. *Inorg. Chem.* **2006**, *45*, 6135–6137. [CrossRef] [PubMed]
61. Yu, F.; Xiang, M.; Wu, Q.-G.; He, H.; Cheng, S.-Q.; Cai, X.-Y.; Li, A.-H.; Zhang, Y.-M.; Li, B. Valence tautomerism and photodynamics observed in a dinuclear cobalt-tetraoxolene compound. *Inorg. Chim. Acta* **2015**, *426*, 146–149. [CrossRef]
62. Li, B.; Chen, L.-Q.; Tao, J.; Huang, R.-B.; Zheng, L.-S. Unidirectional charge transfer in di-cobalt valence tautomeric compound finely tuned by ancillary ligand. *Inorg. Chem.* **2013**, *52*, 4136–4138. [CrossRef] [PubMed]
63. Li, B.; Tao, J.; Sun, H.-L.; Sato, O.; Huang, R.-B.; Zheng, L.-S. Side-effect of ancillary ligand on electron transfer and photodynamics of a dinuclear valence tautomeric complex. *Chem. Commun.* **2008**, 2269–2271. [CrossRef] [PubMed]
64. Tao, J.; Maruyama, H.; Sato, O. Valence tautomeric transitions with thermal hysteresis around room temperature and photoinduced effects observed in a cobalt—Tetraoxolene complex. *J. Am. Chem. Soc.* **2006**, *128*, 1790–1791. [CrossRef] [PubMed]
65. Ishikawa, R.; Horii, Y.; Nakanishi, R.; Ueno, S.; Breedlove, B.K.; Yamashita, M.; Kawata, S. Field-induced single-ion magnetism based on spin-phonon relaxation in a distorted octahedral high-spin cobalt(II) complex. *Eur. J. Inorg. Chem.* **2016**, 3233–3239. [CrossRef]
66. Horiuchi, S.; Kumai, R.; Tokura, Y. High-temperature and pressure-induced ferroelectricity in Hydrogen-bonded supramolecular crystals of anilic acids and 2,3-di(2-pyridinyl)pyrazine. *J. Am. Chem. Soc.* **2013**, *135*, 4492–4500. [CrossRef] [PubMed]
67. Kagawa, F.; Horiuchi, S.; Minami, N.; Ishibashi, S.; Kobayashi, K.; Kumai, R.; Murakami, Y.; Tokura, Y. Polarization switching ability dependent on multidomain topology in a uniaxial organic ferroelectric. *Nano Lett.* **2014**, *14*, 239–243. [CrossRef] [PubMed]
68. Murata, T.; Yakiyama, Y.; Nakasuji, K.; Morita, Y. Proton-transfer salts between an EDT-TTF derivative having imidazole-ring and anilic acids: Multi-dimensional networks by acid-base hydrogen-bonds, pi-stacks and chalcogen atom interactions. *Crystengcomm* **2011**, *13*, 3689–3691. [CrossRef]

69. Horiuchi, S.; Kumai, R.; Tokura, Y. Room-temperature ferroelectricity and gigantic dielectric susceptibility on a supramolecular architecture of phenazine and deuterated chloranilic acid. *J. Am. Chem. Soc.* **2005**, *127*, 5010–5011. [CrossRef] [PubMed]
70. Ward, M.D.; McCleverty, J.A. Non-innocent behaviour in mononuclear and polynuclear complexes: Consequences for redox and electronic spectroscopic properties. *J. Chem. Soc. Dalton Trans.* **2002**, 275–288. [CrossRef]
71. Tinti, F.; Verdaguer, M.; Kahn, O.; Savariault, J.M. Interaction between copper(II) ions separated by 7.6 A. Crystal structure and magnetic properties of the μ-iodanilato bis[n, n, n′, n′ tetramethylethylenediamine copper(II)] diperchlorate. *Inorg. Chem.* **1987**, *26*, 2380–2384. [CrossRef]
72. Tamaki, H.; Zhong, Z.J.; Matsumoto, N.; Kida, S.; Koikawa, M.; Achiwa, N.; Hashimoto, Y.; Ōkawa, H. Design of metal-complex magnets. Syntheses and magnetic properties of mixed-metal assemblies $\{NBu_4[MCr(ox)_3]\}_x$ (NBu_4^+ = tetra(n-butyl)ammonium ion; ox^{2-} = oxalate ion; M = Mn^{2+}, Fe^{2+}, Co^{2+}, Ni^{2+}, Cu^{2+}, Zn^{2+}). *J. Am. Chem. Soc.* **1992**, *114*, 6974–6979. [CrossRef]
73. Decurtins, S.; Schmalle, H.W.; Oswald, H.R.; Linden, A.; Ensling, J.; Gütlich, P.; Hauser, A. A polymeric two-dimensional mixed-metal network. Crystal structure and magnetic properties of $\{[P(Ph)_4][MnCr(ox)_3]\}$. *Inorg. Chim. Acta* **1994**, *216*, 65–73. [CrossRef]
74. Atovmyan, L.O.; Shilov, G.V.; Lyubovskaya, R.N.; Zhilyaeva, E.I.; Ovanesyan, N.S.; Pirumova, S.I.; Gusakovskaya, I.G.; Morozov, Y.G. Crystal-structure of the molecular ferromagnet NBu4[$MnCr(C_2O_4)_3$] (Bu = N-C_4H_9). *J. Exp. Theor. Phys.* **1993**, *58*, 766–769.
75. Mathonière, C.; Nuttall, C.J.; Carling, S.G.; Day, P. Ferrimagnetic mixed-valency and mixed-metal tris(oxalato)iron(III) compounds: Synthesis, structure, and magnetism. *Inorg. Chem.* **1996**, *35*, 1201–1206. [CrossRef] [PubMed]
76. Coronado, E.; Galan-Mascaros, J.R.; Gómez-García, C.J.; Ensling, J.; Gutlich, P. Hybrid molecular magnets obtained by insertion of decamethylmetallocenium cations in layered bimetallic oxalate complexes. Syntheses, structure and magnetic properties of the series $[Z^{III}Cp^*_2][M^{II}M^{III}(ox)_3]$ (Z^{III}= Co, Fe; MIII = Cr, Fe; MII = Mn, Fe, Co, Ni, Cu; Cp* = pentamethylcyclopentadienyl). *Eur. J. Inorg. Chem.* **2000**, *6*, 552–563.
77. Coronado, E.; Galán-Mascarós, J.R.; Gómez-García, C.J.; Martínez-Agudo, J.M. Increasing the coercivity in layered molecular-based magnets $A[M^{II}M^{III}(ox)_3]$ (M^{II} = Mn, Fe, Co, Ni, Cu; M^{III} = Cr, Fe; ox = oxalate; A = organic or organometallic cation). *Adv. Mater.* **1999**, *11*, 558–561. [CrossRef]
78. Coronado, E.; Clemente-Leon, M.; Galan-Mascaros, J.R.; Gimenez-Saiz, C.; Gomez-Garcia, C.J.; Martinez-Ferrero, E. Design of molecular materials combining magnetic, electrical and optical properties. *J. Chem. Soc. Dalton Trans.* **2000**, 3955–3961. [CrossRef]
79. Clemente-Leon, M.; Coronado, E.; Galan-Mascaros, J.R.; Gomez-Garcia, C.J. Intercalation of decamethylferrocenium cations in bimetallic oxalate-bridged two-dimensional magnets. *Chem. Commun.* **1997**, 1727–1728. [CrossRef]
80. Coronado, E.; Galán-Mascarós, J.R.; Gómez-García, C.J.; Martínez-Agudo, J.M.; Martínez-Ferrero, E.; Waerenborgh, J.C.; Almeida, M. Layered molecule-based magnets formed by decamethylmetallocenium cations and two-dimensional bimetallic complexes $[M^{II}Ru^{III}(ox)_3]$-(M^{II}=;Mn, Fe, Co, Cu and Zn; ox = oxalate). *J. Solid State Chem.* **2001**, *159*, 391–402. [CrossRef]
81. Bénard, S.; Yu, P.; Audière, J.P.; Rivière, E.; Clément, R.; Guilhem, J.; Tchertanov, L.; Nakatani, K. Structure and NLO properties of layered bimetallic oxalato-bridged ferromagnetic networks containing stilbazolium-shaped chromophores. *J. Am. Chem. Soc.* **2000**, *122*, 9444–9454. [CrossRef]
82. Bénard, S.; Rivière, E.; Yu, P.; Nakatani, K.; Delouis, J.F. A photochromic molecule-based magnet. *Chem. Mater.* **2001**, *13*, 159–162. [CrossRef]
83. Alberola, A.; Coronado, E.; Galán-Mascarós, J.R.; Giménez-Saiz, C.; Gómez-García, C.J. A molecular metal ferromagnet from the organic donor bis(ethylenedithio)tetraselenafulvalene and bimetallic oxalate complexes. *J. Am. Chem. Soc.* **2003**, *125*, 10774–10775. [CrossRef] [PubMed]
84. Aldoshin, S.M.; Nikonova, L.A.; Shilov, G.V.; Bikanina, E.A.; Artemova, N.K.; Smirnov, V.A. The influence of an n-substituent in the indoline fragment of pyrano-pyridine spiropyran salts on their crystalline structure and photochromic properties. *J. Mol. Struct.* **2006**, *794*, 103–109. [CrossRef]

85. Aldoshin, S.M.; Sanina, N.A.; Minkin, V.I.; Voloshin, N.A.; Ikorskii, V.N.; Ovcharenko, V.I.; Smirnov, V.A.; Nagaeva, N.K. Molecular photochromic ferromagnetic based on the layered polymeric tris-oxalate of Cr(III), Mn(II) and 1-[(1′,3′,3′-trimethyl-6-nitrospiro[2H-1-benzopyran-2,2′-indoline]-8-yl)methyl]pyridinium. *J. Mol. Struct.* **2007**, *826*, 69–74. [CrossRef]
86. Kida, N.; Hikita, M.; Kashima, I.; Okubo, M.; Itoi, M.; Enomoto, M.; Kato, K.; Takata, M.; Kojima, N. Control of charge transfer phase transition and ferromagnetism by photoisomerization of spiropyran for an organic—Inorganic hybrid system, (SP)[$Fe^{II}Fe^{III}$(dto)$_3$] (SP = spiropyran, dto = $C_2O_2S_2$). *J. Am. Chem. Soc.* **2009**, *131*, 212–220. [CrossRef] [PubMed]
87. Sieber, R.; Decurtins, S.; Stoeckli-Evans, H.; Wilson, C.; Yufit, D.; Howard, J.A.K.; Capelli, S.C.; Hauser, A. A thermal spin transition in [Co(bpy)$_3$][LiCr(ox)$_3$] (ox = $C_2O_4^{2-}$; bpy = 2,2′-bipyridine). *Chemistry* **2000**, *6*, 361–368. [CrossRef]
88. Clemente-León, M.; Coronado, E.; López-Jordà, M.; Waerenborgh, J.C. Multifunctional magnetic materials obtained by insertion of spin-crossover Fe^{III} complexes into chiral 3D bimetallic oxalate-based ferromagnets. *Inorg. Chem.* **2011**, *50*, 9122–9130. [CrossRef] [PubMed]
89. Clemente-León, M.; Coronado, E.; López-Jordà, M.; Mínguez Espallargas, G.; Soriano-Portillo, A.; Waerenborgh, J.C. Multifunctional magnetic materials obtained by insertion of a spin-crossover Fe^{III} complex into bimetallic oxalate-based ferromagnets. *Chemistry* **2010**, *16*, 2207–2219. [CrossRef] [PubMed]
90. Clemente-Leon, M.; Coronado, E.; Lopez-Jorda, M.; Desplanches, C.; Asthana, S.; Wang, H.; Letard, J.-F. A hybrid magnet with coexistence of ferromagnetism and photoinduced Fe(III) spin-crossover. *Chem. Sci.* **2011**, *2*, 1121–1127. [CrossRef]
91. Clemente-Leon, M.; Coronado, E.; Lopez-Jorda, M. 2D and 3D bimetallic oxalate-based ferromagnets prepared by insertion of different Fe^{III} spin crossover complexes. *Dalton Trans.* **2010**, *39*, 4903–4910. [CrossRef] [PubMed]
92. Clemente-León, M.; Coronado, E.; Giménez-López, M.C.; Soriano-Portillo, A.; Waerenborgh, J.C.; Delgado, F.S.; Ruiz-Pérez, C. Insertion of a spin crossover Fe^{III} complex into an oxalate-based layered material: Coexistence of spin canting and spin crossover in a hybrid magnet. *Inorg. Chem.* **2008**, *47*, 9111–9120. [CrossRef] [PubMed]
93. Train, C.; Gheorghe, R.; Krstic, V.; Chamoreau, L.-M.; Ovanesyan, N.S.; Rikken, G.L.; Gruselle, M.; Verdaguer, M. Strong magneto-chiral dichroism in enantiopure chiral ferromagnets. *Nat. Mater.* **2008**, *7*, 729–734. [CrossRef] [PubMed]
94. Gruselle, M.; Train, C.; Boubekeur, K.; Gredin, P.; Ovanesyan, N. Enantioselective self-assembly of chiral bimetallic oxalate-based networks. *Coord. Chem. Rev.* **2006**, *250*, 2491–2500. [CrossRef]
95. Clemente-León, M.; Coronado, E.; Dias, J.C.; Soriano-Portillo, A.; Willett, R.D. Synthesis, structure, and magnetic properties of [(s)-[PhCH(CH$_3$)n(CH$_3$)$_3$]][Mn(CH$_3$CN)$_{2/3}$Cr(ox)$_3$]·(CH$_3$CN)_(solvate), a 2D chiral magnet containing a quaternary ammonium chiral cation. *Inorg. Chem.* **2008**, *47*, 6458–6463. [CrossRef] [PubMed]
96. Brissard, M.; Gruselle, M.; Malézieux, B.; Thouvenot, R.; Guyard-Duhayon, C.; Convert, O. An anionic {[MnCo(ox)$_3$]$^-$}$_n$ network with appropriate cavities for the enantioselective recognition and resolution of the hexacoordinated monocation [Ru(bpy)$_2$(ppy)]$^+$ (bpy = bipyridine, ppy = phenylpyridine). *Eur. J. Inorg. Chem.* **2001**, *2001*, 1745–1751. [CrossRef]
97. Sadakiyo, M.; Ōkawa, H.; Shigematsu, A.; Ohba, M.; Yamada, T.; Kitagawa, H. Promotion of low-humidity proton conduction by controlling hydrophilicity in layered metal–organic frameworks. *J. Am. Chem. Soc.* **2012**, *134*, 5472–5475. [CrossRef] [PubMed]
98. Ōkawa, H.; Shigematsu, A.; Sadakiyo, M.; Miyagawa, T.; Yoneda, K.; Ohba, M.; Kitagawa, H. Oxalate-bridged bimetallic complexes {NH(prol)$_3$}[MCr(ox)$_3$] (M = Mn^{II}, Fe^{II}, Co^{II}; $NH(prol)^{3+}$ = tri(3-hydroxypropyl)ammonium) exhibiting coexistent ferromagnetism and proton conduction. *J. Am. Chem. Soc.* **2009**, *131*, 13516–13522. [CrossRef] [PubMed]
99. Fishman, R.S.; Clemente-León, M.; Coronado, E. Magnetic compensation and ordering in the bimetallic oxalates: Why are the 2D and 3D series so different? *Inorg. Chem.* **2009**, *48*, 3039–3046. [CrossRef] [PubMed]
100. Clément, R.; Decurtins, S.; Gruselle, M.; Train, C. Polyfunctional two- (2D) and three- (3D) dimensional oxalate bridged bimetallic magnets. *Mon. Chem. Chem. Mon.* **2003**, *134*, 117–135. [CrossRef]
101. Kojima, N.; Aoki, W.; Itoi, M.; Ono, Y.; Seto, M.; Kobayashi, Y.; Maeda, Y. Charge transfer phase transition and Ferromagnetism in a mixed-valence iron complex, (N-C$_3$H$_7$)4n[$Fe^{II}Fe^{III}$(dto)$_3$] (dto = $C_2O_2S_2$). *Solid State Commun.* **2001**, *120*, 165–170. [CrossRef]

102. Hisashi, O.; Minoru, M.; Masaaki, O.; Masahito, K.; Naohide, M. Dithiooxalato(dto)-bridged bimetallic assemblies {NPr4[MCr(dto)3]}$_x$ (M = Fe, Co, Ni, Zn; NPr4 = tetrapropylammonium ion): New complex-based ferromagnets. *Bull. Chem. Soc. Jpn* **1994**, *67*, 2139–2144.
103. Carling, S.G.; Bradley, J.M.; Visser, D.; Day, P. Magnetic and structural characterisation of the layered materials AMnFe$(C_2S_2O_2)_3$. *Polyhedron* **2003**, *22*, 2317–2324. [CrossRef]
104. Bradley, J.M.; Carling, S.G.; Visser, D.; Day, P.; Hautot, D.; Long, G.J. Structural and physical properties of the ferromagnetic tris-dithiooxalato compounds, A[$M^{II}Cr^{III}(C_2S_2O_2)_3$], with A^+ = N(n-C_nH_{2n+1})$^{4+}$ (n = 3–5) and P$(C_6H_5)_4^+$ and MII = Mn, Fe, Co, and Ni. *Inorg. Chem.* **2003**, *42*, 986–996. [CrossRef] [PubMed]
105. Weiss, A.; Riegler, E.; Robl, C. Polymeric 2,5-dihydroxy-1,4-benzoquinone transition metal complexes $Na_2(H_2O)_{24}[M_2(C_6H_2O_4)_3]$ (M = Manganese(2+), Cadmium(2+). *Z. Naturforsch. Teil B Anorg. Chem.Org. Chem.* **1986**, *41*, 1501–1505.
106. Shilov, G.V.; Nikitina, Z.K.; Ovanesyan, N.S.; Aldoshin, S.M.; Makhaev, V.D. Phenazineoxonium chloranilatomanganate and chloranilatoferrate: Synthesis, structure, magnetic properties, and mössbauer spectra. *Russ. Chem. Bull.* **2011**, *60*, 1209–1219. [CrossRef]
107. Luo, T.-T.; Liu, Y.-H.; Tsai, H.-L.; Su, C.-C.; Ueng, C.-H.; Lu, K.-L. A novel hybrid supramolecular network assembled from perfect π-π stacking of an anionic inorganic layer and a cationic hydronium-ion-mediated organic layer. *Eur. J. Inorg. Chem.* **2004**, *2004*, 4253–4258. [CrossRef]
108. Abrahams, B.F.; Coleiro, J.; Hoskins, B.F.; Robson, R. Gas hydrate-like pentagonal dodecahedral $M_2(H_2O)_{18}$ cages (M = lanthanide or y) in 2,5-dihydroxybenzoquinone-derived coordination polymers. *Chem. Commun.* **1996**, 603–604. [CrossRef]
109. Abrahams, B.F.; Coleiro, J.; Ha, K.; Hoskins, B.F.; Orchard, S.D.; Robson, R. Dihydroxybenzoquinone and chloranilic acid derivatives of rare earth metals. *J. Chemical. Soc. Dalton Trans.* **2002**, 1586–1594. [CrossRef]
110. Coronado, E.; Galán-Mascarós, J.R.; Gómez-García, C.J.; Martínez-Agudo, J.M. Molecule-based magnets formed by bimetallic three-dimensional oxalate networks and chiral tris(bipyridyl) complex cations. The series [ZII$(bpy)_3$][ClO_4][MIICrIII$(ox)_3$] (ZII = Ru, Fe, Co, and Ni; MII = Mn, Fe, Co, Ni, Cu, and Zn; ox = oxalate dianion). *Inorg. Chem.* **2001**, *40*, 113–120. [CrossRef] [PubMed]
111. Abrahams, B.F.; Hudson, T.A.; McCormick, L.J.; Robson, R. Coordination polymers of 2,5-dihydroxybenzoquinone and chloranilic acid with the (10,3)-atopology. *Crys. Growth Des.* **2011**, *11*, 2717–2720. [CrossRef]
112. Frenzer, W.; Wartchow, R.; Bode, H. Crystal structure of disilver 2,5-dichloro-[1,4]benzoquinone-3,6-diolate, $Ag_2(C_6O_4Cl_2)$. *Z. Kristallogr. Cryst. Mater.* **1997**, *212*, 237. [CrossRef]
113. Junggeburth, S.C.; Diehl, L.; Werner, S.; Duppel, V.; Sigle, W.; Lotsch, B.V. Ultrathin 2D coordination polymer nanosheets by surfactant-mediated synthesis. *J. Am. Chem. Soc.* **2013**, *135*, 6157–6164. [CrossRef] [PubMed]
114. Saines, P.J.; Tan, J.-C.; Yeung, H.H.-M.; Barton, P.T.; Cheetham, A.K. Layered inorganic-organic frameworks based on the 2,2-dimethylsuccinate ligand: Structural diversity and its effect on nanosheet exfoliation and magnetic properties. *Dalton Trans.* **2012**, *41*, 8585–8593. [CrossRef] [PubMed]
115. Atzori, M.; Marchiò, L.; Clérac, R.; Serpe, A.; Deplano, P.; Avarvari, N.; Mercuri, M.L. Hydrogen-bonded supramolecular architectures based on tris(hydranilato)metallate(III) (M = Fe, Cr) metallotectons. *Cryst. Growth Des.* **2014**, *14*, 5938–5948. [CrossRef]
116. Min, K.S.; Rhinegold, A.L.; Miller, J.S. Tris(chloranilato)ferrate(iii) anionic building block containing the (dihydroxo)oxodiiron(III) dimer cation: Synthesis and characterization of [(Tpa)(OH)Fe(III)OFe(III)(OH)(Tpa)][$Fe(CA)_3]_{0.5}(BF_4)_{0.5,1.5}$MeOH,$H_2O$ [Tpa = tris(2-pyridylmethyl)amine; CA = chloranilate]. *J. Am. Chem. Soc.* **2006**, *128*, 40–41. [PubMed]
117. Hazell, A.; Jensen, K.B.; McKenzie, C.J.; Toftlund, H. Synthesis and reactivity of (.Mu.-oxo)diiron(III) complexes of tris(2-pyridylmethyl)amine. X-ray crystal structures of [Tpa(OH)feofe(H_2O)tpa]$(ClO_4)_3$ and [Tpa(Cl)FeOFe(Cl)Tpa]$(ClO_4)_2$. *Inorg. Chem.* **1994**, *33*, 3127–3134. [CrossRef]
118. Atzori, M.; Artizzu, F.; Sessini, E.; Marchio, L.; Loche, D.; Serpe, A.; Deplano, P.; Concas, G.; Pop, F.; Avarvari, N.; et al. Halogen-bonding in a new family of tris(haloanilato)metallate(III) magnetic molecular building blocks. *Dalton Transactions* **2014**, *43*, 7006–7019. [CrossRef] [PubMed]
119. Atzori, M.; Artizzu, F.; Marchiò, L.; Loche, D.; Caneschi, A.; Serpe, A.; Deplano, P.; Avarvari, N.; Mercuri, M.L. Switching-on luminescence in anilate-based molecular materials. *Dalton Trans.* **2015**, *44*, 15727–16178. [CrossRef] [PubMed]

120. Benmansour, S.; Valles-Garcia, C.; Gomez-Claramunt, P.; Minguez Espallargas, G.; Gomez-Garcia, C.J. 2d and 3d anilato-based heterometallic M(I)M(III) lattices: The missing link. *Inorg. Chem.* **2015**, *54*, 5410–5418. [CrossRef] [PubMed]
121. Mercuri, M.; Deplano, P.; Serpe, A.; Artizzu, F. Multifunctional materials of interest in molecular electronics. In *Multifunctional Molecular Materials*; Pan Stanford Publishing: Boca Raton, FL, USA, 2013; pp. 219–280.
122. Kurmoo, M.; Graham, A.W.; Day, P.; Coles, S.J.; Hursthouse, M.B.; Caulfield, J.L.; Singleton, J.; Pratt, F.L.; Hayes, W. Superconducting and semiconducting magnetic charge transfer salts: (BEDT-TTF)$_4$AFe(C_2O_4)$_3$.C6H5CN (A = H_2O, K, NH4). *J. Am. Chem. Soc.* **1995**, *117*, 12209–12217. [CrossRef]
123. Coronado, E.; Day, P. Magnetic molecular conductors. *Chem. Rev.* **2004**, *104*, 5419–5448. [CrossRef] [PubMed]
124. Atzori, M.; Benmansour, S.; Minguez Espallargas, G.; Clemente-Leon, M.; Abherve, A.; Gomez-Claramunt, P.; Coronado, E.; Artizzu, F.; Sessini, E.; Deplano, P.; et al. A Family of layered chiral porous magnets exhibiting tunable ordering temperatures. *Inorg. Chem.* **2013**, *52*, 10031–10040. [CrossRef] [PubMed]
125. Kherfi, H.; Hamadène, M.; Guehria-Laïdoudi, A.; Dahaoui, S.; Lecomte, C. Synthesis, structure and thermal behavior of oxalato-bridged Rb^+ and H_3O^+ extended frameworks with different dimensionalities. *Materials* **2010**, *3*, 1281. [CrossRef]
126. Cañadillas-Delgado, L.; Fabelo, O.; Rodríguez-Velamazán, J.A.; Lemée-Cailleau, M.-H.; Mason, S.A.; Pardo, E.; Lloret, F.; Zhao, J.-P.; Bu, X.-H.; Simonet, V.; et al. The role of order–disorder transitions in the quest for molecular multiferroics: Structural and magnetic neutron studies of a mixed valence Iron(II)–Iron(III) formate framework. *J. Am. Chem. Soc.* **2012**, *134*, 19772–19781. [CrossRef] [PubMed]
127. Kobayashi, H.; Cui, H.; Kobayashi, A. Organic metals and superconductors based on bets (bets = bis(ethylenedithio)tetraselenafulvalene). *Chem. Rev.* **2004**, *104*, 5265–5288. [CrossRef] [PubMed]
128. Enoki, T.; Miyazaki, A. Magnetic ttf-based charge-transfer complexes. *Chem. Rev.* **2004**, *104*, 5449–5478. [CrossRef] [PubMed]
129. Coronado, E.; Giménez-Saiz, C.; Gómez-García, C.J. Recent advances in polyoxometalate-containing molecular conductors. *Coord. Chem. Rev.* **2005**, *249*, 1776–1796. [CrossRef]
130. Schlueter, J.A.; Geiser, U.; Whited, M.A.; Drichko, N.; Salameh, B.; Petukhov, K.; Dressel, M. Two alternating BEDT-TTF packing motifs in α-κ-(BEDT-TTF)$_2$Hg(SCN)$_3$. *Dalton Trans.* **2007**, 2580–2588. [CrossRef] [PubMed]
131. Rashid, S.; Turner, S.S.; Day, P.; Howard, J.A.K.; Guionneau, P.; McInnes, E.J.L.; Mabbs, F.E.; Clark, R.J.H.; Firth, S.; Biggs, T. New superconducting charge-transfer salts (BEDT-TTF)$_4$[A·M(C_2O_4)$_3$]·$C_6H_5NO_2$ (A = H_3O or NH_4, M = Cr or Fe, BEDT-TTF = bis(ethylenedithio)tetrathiafulvalene). *J. Mater. Chem.* **2001**, *11*, 2095–2101. [CrossRef]
132. Martin, L.; Turner, S.S.; Day, P.; Mabbs, F.E.; McInnes, E.J.L. New molecular superconductor containing paramagnetic Chromium(III) ions. *Chem. Commun.* **1997**, 1367–1368. [CrossRef]
133. Uji, S.; Shinagawa, H.; Terashima, T.; Yakabe, T.; Terai, Y.; Tokumoto, M.; Kobayashi, A.; Tanaka, H.; Kobayashi, H. Magnetic-field-induced superconductivity in a two-dimensional organic conductor. *Nature* **2001**, *410*, 908–910. [CrossRef] [PubMed]
134. Fujiwara, H.; Fujiwara, E.; Nakazawa, Y.; Narymbetov, B.Z.; Kato, K.; Kobayashi, H.; Kobayashi, A.; Tokumoto, M.; Cassoux, P. A novel antiferromagnetic organic superconductor κ-(BETS)$_2$FeBr$_4$ [where BETS = bis(ethylenedithio)tetraselenafulvalene]. *J. Am. Chem. Soc.* **2001**, *123*, 306–314. [CrossRef] [PubMed]
135. Day, P.; Kurmoo, M.; Mallah, T.; Marsden, I.R.; Friend, R.H.; Pratt, F.L.; Hayes, W.; Chasseau, D.; Gaultier, J. Structure and properties of tris[bis(ethylenedithio)tetrathiafulvalenium]tetrachlorocopper(II) hydrate, (BEDT-TTF)$_3$CuCl$_4$·H2O: First evidence for coexistence of localized and conduction electrons in a metallic charge-transfer salt. *J. Am. Chem. Soc.* **1992**, *114*, 10722–10729. [CrossRef]
136. Martin, L.; Day, P.; Clegg, W.; Harrington, R.W.; Horton, P.N.; Bingham, A.; Hursthouse, M.B.; McMillan, P.; Firth, S. Multi-layered molecular charge-transfer salts containing alkali metal ions. *J. Mater. Chem.* **2007**, *17*, 3324–3329. [CrossRef]
137. Coronado, E.; Curreli, S.; Giménez-Saiz, C.; Gómez-García, C.J.; Alberola, A. Radical salts of bis(ethylenediseleno)tetrathiafulvalene with paramagnetic tris(oxalato)metalate anions. *Inorg. Chem.* **2006**, *45*, 10815–10824. [CrossRef] [PubMed]
138. Coronado, E.; Curreli, S.; Giménez-Saiz, C.; Gómez-García, C.J. The series of molecular conductors and superconductors ET$_4$[AFe(C_2O_4)$_3$]·PhX (ET = bis(ethylenedithio)tetrathiafulvalene; $(C_2O_4)^{2-}$ = oxalate; A+ = H_3O+, K+; X = F, Cl, Br, and I): Influence of the halobenzene guest molecules on the crystal structure and superconducting properties. *Inorg. Chem.* **2012**, *51*, 1111–1126. [PubMed]

139. Coronado, E.; Curreli, S.; Gimenez-Saiz, C.; Gomez-Garcia, C.J. A novel paramagnetic molecular superconductor formed by bis(ethylenedithio)tetrathiafulvalene, tris(oxalato)ferrate(III) anions and bromobenzene as guest molecule: $Et_4[(H_3O)Fe(C_2O_4)_3]\cdot C_6H_5Br$. *J. Mater. Chem.* **2005**, *15*, 1429–1436. [CrossRef]
140. Fourmigué, M.; Batail, P. Activation of hydrogen- and halogen-bonding interactions in tetrathiafulvalene-based crystalline molecular conductors. *Chem. Rev.* **2004**, *104*, 5379–5418. [CrossRef] [PubMed]
141. Coronado, E.; Curreli, S.; Giménez-Saiz, C.; Gómez-García, C.J.; Deplano, P.; Mercuri, M.L.; Serpe, A.; Pilia, L.; Faulmann, C.; Canadell, E. New BEDT-TTF/$[Fe(C_5O_5)_3]_3$- hybrid system: Synthesis, crystal structure, and physical properties of a chirality-induced α phase and a novel magnetic molecular metal. *Inorg. Chem.* **2007**, *46*, 4446–4457. [CrossRef] [PubMed]
142. Gomez-Garcia, C.J.; Coronado, E.; Curreli, S.; Gimenez-Saiz, C.; Deplano, P.; Mercuri, M.L.; Pilia, L.; Serpe, A.; Faulmann, C.; Canadell, E. A chirality-induced alpha phase and a novel molecular magnetic metal in the BEDT-TTF/tris(croconate)Ferrate(III) hybrid molecular system. *Chem. Commun.* **2006**, 4931–4933. [CrossRef] [PubMed]
143. Avarvari, N.; Wallis, J.D. Strategies towards chiral molecular conductors. *J. Mater. Chem.* **2009**, *19*, 4061. [CrossRef]
144. Pop, F.; Auban-Senzier, P.; Canadell, E.; Rikken, G.L.J.A.; Avarvari, N. Electrical magnetochiral anisotropy in a bulk chiral molecular conductor. *Nat. Commun.* **2014**, *5*, 3757. [CrossRef] [PubMed]
145. Rikken, G.L.J.A.; Fölling, J.; Wyder, P. Electrical magnetochiral anisotropy. *Phys. Rev. Lett.* **2001**, *87*, 236602. [CrossRef] [PubMed]
146. Krstic, V.; Roth, S.; Burghard, M.; Kern, K.; Rikken, G.L.J.A. Magneto-chiral anisotropy in charge transport through single-walled carbon nanotubes. *J. Chem. Phys.* **2002**, *117*, 11315. [CrossRef]
147. De Martino, A.; Egger, R.; Tsvelik, A.M. Nonlinear magnetotransport in interacting chiral nanotubes. *Phys. Rev. Lett.* **2006**, *97*, 076402. [CrossRef] [PubMed]
148. Rethore, C.; Fourmigue, M.; Avarvari, N. Tetrathiafulvalene based phosphino-oxazolines: A new family of redox active chiral ligands. *Chem. Commun.* **2004**, 1384–1385. [CrossRef] [PubMed]
149. Réthoré, C.; Avarvari, N.; Canadell, E.; Auban-Senzier, P.; Fourmigué, M. Chiral molecular metals: Syntheses, structures, and properties of the AsF6- salts of Racemic (±)-, (R)-, and (S)-tetrathiafulvalene—Oxazoline derivatives. *J. Am. Chem. Soc.* **2005**, *127*, 5748–5749. [CrossRef] [PubMed]
150. Madalan, A.M.; Rethore, C.; Fourmigue, M.; Canadell, E.; Lopes, E.B.; Almeida, M.; Auban-Senzier, P.; Avarvari, N. Order versus disorder in chiral tetrathiafulvalene-oxazoline radical-cation salts: Structural and theoretical investigations and physical properties. *Chemistry* **2010**, *16*, 528–537. [CrossRef] [PubMed]
151. Pop, F.; Auban-Senzier, P.; Frąckowiak, A.; Ptaszyński, K.; Olejniczak, I.; Wallis, J.D.; Canadell, E.; Avarvari, N. Chirality driven metallic versus semiconducting behavior in a complete series of radical cation salts based on dimethyl-ethylenedithio-tetrathiafulvalene (DM-EDT-TTF). *J. Am. Chem. Soc.* **2013**, *135*, 17176–17186. [CrossRef] [PubMed]
152. Karrer, A.; Wallis, J.D.; Dunitz, J.D.; Hilti, B.; Mayer, C.W.; Bürkle, M.; Pfeiffer, J. Structures and electrical properties of some new organic conductors derived from the donor molecule tmet (s,s,s,s,-bis (dimethylethylenedithio) tetrathiafulvalene). *Helvetica Chim. Acta* **1987**, *70*, 942–953. [CrossRef]
153. Wallis, J.D.; Karrer, A.; Dunitz, J.D. Chiral metals? A chiral substrate for organic conductors and superconductors. *Helvetica Chim. Acta* **1986**, *69*, 69–70. [CrossRef]
154. Pop, F.; Laroussi, S.; Cauchy, T.; Gomez-Garcia, C.J.; Wallis, J.D.; Avarvari, N. Tetramethyl-bis(ethylenedithio)-tetrathiafulvalene (TM-BEDT-TTF) revisited: Crystal structures, chiroptical properties, theoretical calculations, and a complete series of conducting radical cation salts. *Chirality* **2013**, *25*, 466–474. [CrossRef] [PubMed]
155. Galán-Mascarós, J.R.; Coronado, E.; Goddard, P.A.; Singleton, J.; Coldea, A.I.; Wallis, J.D.; Coles, S.J.; Alberola, A. A chiral ferromagnetic molecular metal. *J. Am. Chem. Soc.* **2010**, *132*, 9271–9273. [CrossRef] [PubMed]
156. Madalan, A.M.; Canadell, E.; Auban-Senzier, P.; Branzea, D.; Avarvari, N.; Andruh, M. Conducting mixed-valence salt of bis(ethylenedithio)tetrathiafulvalene (BEDT-TTF) with the paramagnetic heteroleptic anion $[Cr^{III}(oxalate)_2(2,2'\text{-bipyridine})]$. *New J. Chem.* **2008**, *32*, 333–339. [CrossRef]

157. Martin, L.; Day, P.; Horton, P.; Nakatsuji, S.I.; Yamada, J.I.; Akutsu, H. Chiral conducting salts of BEDT-TTF containing a single enantiomer of tris(oxalato)chromate(III) crystallised from a chiral solvent. *J. Mater. Chem.* **2010**, *20*, 2738–2742. [CrossRef]
158. Pop, F.; Allain, M.; Auban-Senzier, P.; Martínez-Lillo, J.; Lloret, F.; Julve, M.; Canadell, E.; Avarvari, N. Enantiopure conducting salts of dimethylbis(ethylenedithio)tetrathiafulvalene (DM-BEDT-TTF) with the hexachlororhenate(IV) anion. *Eur. J. Inorg. Chem.* **2014**, *2014*, 3855–3862. [CrossRef]
159. Coronado, E.; Minguez Espallargas, G. Dynamic Magnetic MOFs. *Chem. Soc. Rev.* **2013**, *42*, 1525–1539. [CrossRef] [PubMed]
160. Gütlich, P.; Goodwin, H.A. *Spin Crossover in Transition Metal Compounds i*; Springer: Berlin, Germany, 2004; Volume 233.
161. Halcrow, M.A. *Spin-Crossover Materials: Properties and Applications*; Wiley: New York, NY, USA, 2013.
162. Min, K.S.; DiPasquale, A.G.; Golen, J.A.; Rheingold, A.L.; Miller, J.S. Synthesis, structure, and magnetic properties of valence ambiguous dinuclear antiferromagnetically coupled cobalt and ferromagnetically coupled iron complexes containing the chloranilate(2−) and the significantly stronger coupling chloranilate(3−) radical trianion. *J. Am. Chem. Soc.* **2007**, *129*, 2360–2368. [PubMed]
163. Atzori, M.; Pop, F.; Auban-Senzier, P.; Gomez-Garcia, C.J.; Canadell, E.; Artizzu, F.; Serpe, A.; Deplano, P.; Avarvari, N.; Mercuri, M.L. Structural diversity and physical properties of paramagnetic molecular conductors based on bis(ethylenedithio)tetrathiafulvalene (BEDT-TTF) and the tris(chloranilato)FerrateIII) complex. *Inorg. Chem.* **2014**, *53*, 7028–7039. [CrossRef] [PubMed]
164. Takehiko, M. Structural genealogy of BEDT-TTF-based organic conductors i. Parallel molecule s: B and β″ phases. *Bull. Chem. Soc. Jpn.* **1998**, *71*, 2509–2526.
165. Benmansour, S.; Coronado, E.; Giménez-Saiz, C.; Gómez-García, C.J.; Rößer, C. Metallic charge-transfer salts of bis(ethylenedithio)tetrathiafulvalene with paramagnetic tetrachloro(oxalato)rhenate(IV) and tris(chloranilato)ferrate(III) anions. *Eur. J. Inorg. Chem.* **2014**, 3949–3959. [CrossRef]
166. Atzori, M.; Pop, F.; Auban-Senzier, P.; Clerac, R.; Canadell, E.; Mercuri, M.L.; Avarvari, N. Complete series of chiral paramagnetic molecular conductors based on tetramethyl-bis(ethylenedithio)-tetrathiafulvalene (TM-BEDT-TTF) and chloranilate-bridged heterobimetallic honeycomb layers. *Inorg. Chem.* **2015**, *54*, 3643–3653. [CrossRef] [PubMed]
167. Abherve, A.; Clemente-Leon, M.; Coronado, E.; Gomez-Garcia, C.J.; Verneret, M. One-dimensional and two-dimensional anilate-based magnets with inserted spin-crossover complexes. *Inorg. Chem.* **2014**, *53*, 12014–12026. [CrossRef] [PubMed]
168. Clemente-Leo, M.; Coronado, E.; Martí-Gastaldoza, C.; Romero, F.M. Multifunctionality in hybrid magnetic materials based on bimetallic oxalate complexes. *Chem. Soc. Rev.* **2011**, *40*, 473–497. [CrossRef] [PubMed]
169. Boča, R. Zero-field splitting in metal complexes. *Coord. Chem. Rev.* **2004**, *248*, 757–815. [CrossRef]
170. Teppei, Y.; Shota, M.; Hiroshi, K. Structures and proton conductivity of one-dimensional M(dhbq)·nH_2O (M = Mg, Mn, Co, Ni, and Zn, H2(dhbq) = 2,5-dihydroxy-1,4-benzoquinone) promoted by connected hydrogen-bond networks with absorbed water. *Bull. Chem. Soc. Jpn.* **2010**, *83*, 42–48.
171. Abhervé, A.; Mañas-Valero, S.; Clemente-León, M.; Coronado, E. Graphene related magnetic materials: Micromechanical exfoliation of 2D layered magnets based on bimetallic anilate complexes with inserted [FeIII($acac_2$-trien)]+ and [FeIII(sal_2-trien)]+ molecules. *Chem. Sci.* **2015**, *6*, 4665–4673. [CrossRef]
172. Castellanos-Gomez, A.; Buscema, M.; Molenaar, R.; Singh, V.; Janssen, L.; van der Zant, H.S.J.; Steele, G.A. Deterministic transfer of two-dimensional materials by all-dry viscoelastic stamping. *2D Mater.* **2014**, *1*, 011002. [CrossRef]
173. Jiang, Y.; Gao, J.; Guo, W.; Jiang, L. Mechanical exfoliation of track-etched two-dimensional layered materials for the fabrication of ultrathin nanopores. *Chem. Commun.* **2014**, *50*, 14149–14152. [CrossRef] [PubMed]
174. Li, H.; Wu, J.; Yin, Z.; Zhang, H. Preparation and applications of mechanically exfoliated single-layer and multilayer MoS_2 and WSe_2 nanosheets. *Acc. Chem. Res.* **2014**, *47*, 1067–1075. [CrossRef] [PubMed]
175. Li, P.-Z.; Maeda, Y.; Xu, Q. Top-down fabrication of crystalline metal-organic framework nanosheets. *Chem. Commun.* **2011**, *47*, 8436–8438. [CrossRef] [PubMed]
176. Gallego, A.; Hermosa, C.; Castillo, O.; Berlanga, I.; Gómez-García, C.J.; Mateo-Martí, E.; Martínez, J.I.; Flores, F.; Gómez-Navarro, C.; Gómez-Herrero, J.; et al. Solvent-induced delamination of a multifunctional two dimensional coordination polymer. *Adv. Mater.* **2013**, *25*, 2141–2146. [CrossRef] [PubMed]

177. Amo-Ochoa, P.; Welte, L.; Gonzalez-Prieto, R.; Sanz Miguel, P.J.; Gomez-Garcia, C.J.; Mateo-Marti, E.; Delgado, S.; Gomez-Herrero, J.; Zamora, F. Single layers of a multifunctional laminar Cu(I,II) coordination polymer. *Chem. Commun.* **2010**, *46*, 3262–3264. [CrossRef] [PubMed]
178. Beldon, P.J.; Tominaka, S.; Singh, P.; Saha Dasgupta, T.; Bithell, E.G.; Cheetham, A.K. Layered structures and nanosheets of pyrimidinethiolate coordination polymers. *Chem. Commun.* **2014**, *50*, 3955–3957. [CrossRef] [PubMed]
179. Saines, P.J.; Steinmann, M.; Tan, J.-C.; Yeung, H.H.M.; Li, W.; Barton, P.T.; Cheetham, A.K. Isomer-directed structural diversity and its effect on the nanosheet exfoliation and magnetic properties of 2,3-dimethylsuccinate hybrid frameworks. *Inorg. Chem.* **2012**, *51*, 11198–11209. [CrossRef] [PubMed]
180. Tan, J.-C.; Saines, P.J.; Bithell, E.G.; Cheetham, A.K. Hybrid nanosheets of an Inorganic–Organic framework material: Facile synthesis, structure, and elastic properties. *ACS Nano* **2012**, *6*, 615–621. [CrossRef] [PubMed]
181. Kumagai, H.; Kawata, S.; Kitagawa, S. Fabrication of infinite two-dimensional sheets of tetragonal metal(II) lattices X-ray crystal structures and magnetic properties of [M(CA)(pyz)]n (M^{2+} = Mn^{2+} and Co^{2+};H_2CA=chloranilic acid; pyz=pyrazine). *Inorg. Chim. Acta* **2002**, *337*, 387–392. [CrossRef]
182. Nielsen, R.B.; Kongshaug, K.O.; Fjellvag, H. Delamination, synthesis, crystal structure and thermal properties of the layered metal-organic compound $Zn(C_{12}H_{14}O_4)$. *J. Mater. Chem.* **2008**, *18*, 1002–1007. [CrossRef]
183. Nagayoshi, K.; Kabir, M.K.; Tobita, H.; Honda, K.; Kawahara, M.; Katada, M.; Adachi, K.; Nishikawa, H.; Ikemoto, I.; Kumagai, H.; et al. Design of novel inorganic—Organic hybrid materials based on iron-chloranilate mononuclear complexes: Characteristics of hydrogen-bond-supported layers toward the intercalation of guests. *J. Am. Chem. Soc.* **2003**, *125*, 221–232. [CrossRef] [PubMed]
184. Darago, L.E.; Aubrey, M.L.; Yu, C.J.; Gonzalez, M.I.; Long, J.R. Electronic conductivity, ferrimagnetic ordering, and reductive insertion mediated by organic mixed-valence in a ferric semiquinoid metal—Organic framework. *J. Am. Chem. Soc.* **2015**, *137*, 15703–15711. [CrossRef] [PubMed]
185. Kawata, S.; Kitagawa, S.; Kumagai, H.; Ishiyama, T.; Honda, K.; Tobita, H.; Adachi, K.; Katada, M. Novel intercalation host system based on transition metal (Fe^{2+}, Co^{2+}, Mn^{2+})—Chloranilate coordination polymers. Single crystal structures and properties. *Chem. Mater.* **1998**, *10*, 3902–3912. [CrossRef]
186. Wrobleski, J.T.; Brown, D.B. Synthesis, magnetic susceptibility, and moessbauer spectra of Iron(III) dimers and Iron(II) polymers containing 2,5-dihydroxy-1,4-benzoquinones. *Inorg. Chem.* **1979**, *18*, 498–504. [CrossRef]
187. Wrobleski, J.T.; Brown, D.B. Synthesis, magnetic susceptibility, and spectroscopic properties of single- and mixed-valence iron oxalate, squarate, and dihydroxybenzoquinone coordination polymers. *Inorg. Chem.* **1979**, *18*, 2738–2749. [CrossRef]
188. Clemente-León, M.; Coronado, E.; Gómez-García, C.J.; Soriano-Portillo, A. Increasing the ordering temperatures in oxalate-based 3d chiral magnets: The series [Ir(ppy)2(bpy)][MIIMIII(ox)3]·0.5H2O (MIIMIII = MnCr, FeCr, CoCr, NiCr, ZnCr, MnFe, FeFe); bpy = 2,2′-bipyridine; ppy = 2-phenylpyridine; ox = oxalate dianion). *Inorg. Chem.* **2006**, *45*, 5653–5660. [CrossRef] [PubMed]
189. Coronado, E.; Galán-Mascarós, J.R.; Gómez-García, C.J.; Martínez-Ferrero, E.; Almeida, M.; Waerenborgh, J.C. Oxalate-based 3D chiral magnets: The series [ZII(bpy)3][ClO4][MIIFeIII(ox)3] (ZII = Fe, Ru; MII = Mn, Fe; bpy = 2,2′-bipyridine; ox = oxalate dianion). *Eur. J. Inorg. Chem.* **2005**, *2005*, 2064–2070. [CrossRef]
190. Decurtins, S.; Schmalle, H.W.; Schneuwly, P.; Ensling, J.; Guetlich, P. A concept for the synthesis of 3-dimensional homo- and bimetallic oxalate-bridged networks $[M_2(ox)_3]_n$. Structural, moessbauer, and magnetic studies in the field of molecular-based magnets. *J. Am. Chem. Soc.* **1994**, *116*, 9521–9528. [CrossRef]
191. Shaikh, N.; Goswami, S.; Panja, A.; Wang, X.-Y.; Gao, S.; Butcher, R.J.; Banerjee, P. New route to the mixed valence semiquinone-catecholate based mononuclear FeIII and catecholate based dinuclear Mn^{III} complexes: First experimental evidence of valence tautomerism in an iron complex. *Inorg. Chem.* **2004**, *43*, 5908–5918. [CrossRef] [PubMed]
192. D'Alessandro, D.M.; Keene, F.R. Current trends and future challenges in the experimental, theoretical and computational analysis of intervalence charge transfer (IVCT) transitions. *Chem. Soc. Rev.* **2006**, *35*, 424–440. [CrossRef] [PubMed]
193. D'Alessandro, D.M.; Keene, F.R. Intervalence charge transfer (IVCT) in trinuclear and tetranuclear complexes of Iron, Ruthenium, and Osmium. *Chem. Rev.* **2006**, *106*, 2270–2298. [CrossRef] [PubMed]
194. Demadis, K.D.; Hartshorn, C.M.; Meyer, T.J. The localized-to-delocalized transition in mixed-valence chemistry. *Chem. Rev.* **2001**, *101*, 2655–2686. [CrossRef] [PubMed]
195. Hankache, J.; Wenger, O.S. Organic mixed valence. *Chem. Rev.* **2011**, *111*, 5138–5178. [CrossRef] [PubMed]

196. Miller, J.S. Magnetically ordered molecule-based materials. *Chem. Soc. Rev.* **2011**, *40*, 3266–3296. [CrossRef] [PubMed]
197. Ward, M.D. A dinuclear Ruthenium(II) complex with the dianion of 2,5-dihydroxy-1,4-benzoquinone as bridging ligand. Redox, spectroscopic, and mixed-valence properties. *Inorg. Chem.* **1996**, *35*, 1712–1714. [CrossRef] [PubMed]
198. Miyazaki, A.; Yamazaki, H.; Aimatsu, M.; Enoki, T.; Watanabe, R.; Ogura, E.; Kuwatani, Y.; Iyoda, M. Crystal structure and physical properties of conducting molecular antiferromagnets with a halogen-substituted donor: (EDO-TTFBr$_2$)$_2$FeX$_4$ (X = Cl, Br). *Inorg. Chem.* **2007**, *46*, 3353–3366. [CrossRef] [PubMed]
199. Clérac, R.; O'Kane, S.; Cowen, J.; Ouyang, X.; Heintz, R.; Zhao, H.; Bazile, M.J.; Dunbar, K.R. Glassy magnets composed of metals coordinated to 7,7,8,8-tetracyanoquinodimethane: M(tcnq)$_2$ (M = Mn, Fe, Co, Ni). *Chem. Mater.* **2003**, *15*, 1840–1850. [CrossRef]
200. Jeon, I.-R.; Negru, B.; Van Duyne, R.P.; Harris, T.D. A 2D semiquinone radical-containing microporous magnet with solvent-induced switching from Tc = 26 to 80 k. *J. Am. Chem. Soc.* **2015**, *137*, 15699–15702. [CrossRef] [PubMed]
201. Zeng, M.-H.; Yin, Z.; Tan, Y.-X.; Zhang, W.-X.; He, Y.-P.; Kurmoo, M. Nanoporous Cobalt(II) mof exhibiting four magnetic ground states and changes in gas sorption upon post-synthetic modification. *J. Am. Chem. Soc.* **2014**, *136*, 4680–4688. [CrossRef] [PubMed]
202. Sun, L.; Hendon, C.H.; Minier, M.A.; Walsh, A.; Dincă, M. Million-fold electrical conductivity enhancement in Fe$_2$(DEBDC) versus Mn$_2$(DEBDC) (E = S, O). *J. Am. Chem. Soc.* **2015**, *137*, 6164–6167. [CrossRef] [PubMed]
203. Murdock, C.R.; Hughes, B.C.; Lu, Z.; Jenkins, D.M. Approaches for synthesizing breathing MOFs by exploiting dimensional rigidity. *Coord. Chem. Rev.* **2014**, *258–259*, 119–136. [CrossRef]
204. Ferey, G.; Serre, C. Large breathing effects in three-dimensional porous hybrid matter: Facts, analyses, rules and consequences. *Chem. Soc. Rev.* **2009**, *38*, 1380–1399. [CrossRef] [PubMed]
205. Nakabayashi, K.; Ohkoshi, S.-I. Monometallic lanthanoid assembly showing ferromagnetism with a curie temperature of 11 k. *Inorg. Chem.* **2009**, *48*, 8647–8649. [CrossRef] [PubMed]
206. Przychodzeń, P.; Pełka, R.; Lewiński, K.; Supel, J.; Rams, M.; Tomala, K.; Sieklucka, B. Tuning of magnetic properties of polynuclear lanthanide(III)—Octacyanotungstate(V) systems: Determination of ligand-field parameters and exchange interaction. *Inorg. Chem.* **2007**, *46*, 8924–8938. [CrossRef] [PubMed]
207. Ishikawa, N.; Sugita, M.; Wernsdorfer, W. Nuclear spin driven quantum tunneling of magnetization in a new lanthanide single-molecule magnet: Bis(phthalocyaninato)Holmium anion. *J. Am. Chem. Soc.* **2005**, *127*, 3650–3651. [CrossRef] [PubMed]